National Library of Canada
Bibliothèque nationale du Canada

Canadian Theses Service
Service des thèses canadiennes

Ottawa, Canada
K1A 0N4

NOTICE

The quality of this microform is heavily dependent upon the quality of the original thesis submitted for microfilming. Every effort has been made to ensure the highest quality of reproduction possible.

If pages are missing, contact the university which granted the degree.

Some pages may have indistinct print especially if the original pages were typed with a poor typewriter ribbon or if the university sent us an inferior photocopy.

Previously copyrighted materials (journal articles, published tests, etc.) are not filmed.

Reproduction in full or in part of this microform is governed by the Canadian Copyright Act, R.S.C. 1970, c. C-30.

AVIS

La qualité de cette microforme dépend grandement de la qualité de la thèse soumise au microfilmage. Nous avons tout fait pour assurer une qualité supérieure de reproduction.

S'il manque des pages, veuillez communiquer avec l'université qui a conféré le grade.

La qualité d'impression de certaines pages peut laisser à désirer, surtout si les pages originales ont été dactylographiées à l'aide d'un ruban usé ou si l'université nous a fait parvenir une photocopie de qualité inférieure.

Les documents qui font déjà l'objet d'un droit d'auteur (articles de revue, tests publiés, etc.) ne sont pas microfilmés.

La reproduction, même partielle, de cette microforme est soumise à la Loi canadienne sur le droit d'auteur, SRC 1970, c. C-30.

Canada

THE UNIVERSITY OF ALBERTA

Isothermal Behaviour of Gassy Soils

by

© Paulo Branco Jr.

A THESIS

SUBMITTED TO THE FACULTY OF GRADUATE STUDIES AND RESEARCH,

IN PARTIAL FULFILMENT OF THE REQUIREMENTS FOR THE DEGREE

OF Doctor of Philosophy

Department of Civil Engineering

EDMONTON, ALBERTA

SPRING 1988

Permission has been granted to the National Library of Canada to microfilm this thesis and to lend or sell copies of the film.

The author (copyright owner) has reserved other publication rights, and neither the thesis nor extensive extracts from it may be printed or otherwise reproduced without his/her written permission.

L'autorisation a été accordée à la Bibliothèque nationale du Canada de microfilmer cette thèse et de prêter ou de vendre des exemplaires du film.

L'auteur (titulaire du droit d'auteur) se réserve les autres droits de publication; ni la thèse ni de longs extraits de celle-ci ne doivent être imprimés ou autrement reproduits sans son autorisation écrite.

ISBN 0-315-42757-4

THE UNIVERSITY OF ALBERTA

RELEASE FORM

NAME OF AUTHOR Paulo Branco Jr.

TITLE OF THESIS Isothermal Behaviour of Gassy Soils

DEGREE FOR WHICH THESIS WAS PRESENTED Doctor of Philosophy

YEAR THIS DEGREE GRANTED SPRING 1988

Permission is hereby granted to THE UNIVERSITY OF ALBERTA LIBRARY to reproduce single copies of this thesis and to lend or sell such copies for private, scholarly or scientific research purposes only.

The author reserves other publication rights, and neither the thesis nor extensive extracts from it may be printed or otherwise reproduced without the author's written permission.

(SIGNED) Paulo Branco Junior .....

PERMANENT ADDRESS:

Rua Miralta 79

Sao Paulo - SP

CEP 05460 - Brazil

DATED : January 29 1988

THE UNIVERSITY OF ALBERTA

FACULTY OF GRADUATE STUDIES AND RESEARCH

The undersigned certify that they have read, and recommend to the Faculty of Graduate Studies and Research, for acceptance, a thesis entitled *Isothermal Behaviour of Gassy Soils* submitted by Paulo Branco Jr. in partial fulfilment of the requirements for the degree of Doctor of Philosophy.

Dr. Z. Eisenstein .....
Supervisor

Dr. R.G. Bentsen .....

Dr. N.R. Morgenstern .....

Dr. D.W. Murray .....

Dr. J.D. Scott .....

Dr. M.B. Dusseault .....
External Examiner

Date: January 29 1988

To Nique, Ata, Pimpa

and

Lu

ABSTRACT

This thesis examines the isothermal behaviour of gassy soils.

Special attention is paid to the development of a model that appropriately simulates the transient processes that take place in gassy soils, when subjected to isothermal changes in boundary conditions.

The need for the development of this model is justified by the increasing number of underground excavations in gassy soils predicted in the near future, associated with the exploration of new hydrocarbon resources, and the lack of models that adequately simulate the transient phenomenon of gas evolution.

This model should aid those engineering projects on gassy soils in many aspects. These include enabling the choice of proper sampling techniques, guiding the design and construction of geotechnical structures, supporting the analyses of field monitoring programs and increasing the understanding of the mechanics of gassy fluids.

The development of the proposed model consists of the following steps.

1. Identification and study of the processes that control the time-dependent response of gassy soils and development of the governing equations for the problem.
2. Development of a finite element program for the solution of the governing equations, for boundary conditions usually encountered in gassy soils related works.

3. Verification of the finite element program capability to appropriately simulate the theoretical and the experimental response of oil sands. The lack of experimental data on time-dependent response of gassy soils resulted in an extensive sampling and laboratory testing program.

These three items constituted the working frame for the research and are documented herein.

ACKNOWLEDGEMENTS

The development of this research, during the past five years, would not have been possible without the love and care I received from my family.

Lucila, my wife, once again, unselfishly postponed her goals of settling down in Sao Paulo to come with me to Canada. The affection, understanding and dedication she has shown to myself and our daughters have been a source of continuous admiration. To her I express my deepest appreciation and profound thanks.

Our daughters Pimpa, Ata and Nique have been responsible for making our lives most enjoyable. The happiness in their faces, the love they have dedicated to us and the positiveness with which they have faced their lives is most rewarding, assuring Lucila and I that we have been successful in our effort to build a warm and loving environment for them.

I wish to thank Prof. Z. Eisenstein for the continuous support offered during these long years of research. To him I am grateful.

The financial support provided by the Conselho Nacional de Desenvolvimento Cientifico e Tecnologico, the Alberta Oil Sands Technology and Research Authority, Syncrude Canada Ltd. and the Fundacao Armando Alvares Penteado, is gratefully acknowledged.

Prof. J.D. Scott provided invaluable support during all phases of the sampling and laboratory programs. To him I am

thankful.

My thanks are extended to Prof. N.R. Morgenstern for the guidance and support during the outlining and implementation of the sampling and laboratory programs, and to Prof. M.B. Dusseault for lending us the hollow cylinder cell for the laboratory program.

G. Cyre and K. Ellis helped with the design and manufacture of most of the equipment used in the laboratory. H. Soderberg was responsible for the success of the sampling program and the design of some key parts of the hollow cylinder apparatus. To them I am thankful.

I owe special thanks to Tanya Schulz who not only typed and edited this thesis, but was responsible for the complete success of the laboratory program. Her seriousness at work and expertise in the laboratory were key factors for the completion of this research program.

I also owe special thanks to my friend Arsenio Negro. The support he provided before, during and after this research was extremely important. His contribution through stimulating discussions and, more important, warm friendship, will not be forgotten.

My friends Jose and Claudia Brandt once again gave us the opportunity to feel completely at home in Edmonton. Their help during the early stages of our stay in Edmonton and the friendship they have extended to us is gratefully acknowledged.

The "Brazilian Connection" in Michener Park also played an important role in our stay in Canada. I hope soon we will be together again.

Pat Collins and Sean Maloney shared with me countless miles of lunch time jogging. I thank them for bearing with me always complaining about "how fast" and "how far" we were running.

The background support offered by Andre and Gilda Ribeiro and Paulo and Myriam Sawaya during these past five years was of enormous help. To them I express my deepest gratitude.

I have very fond feelings for my brother and sisters Luiz, Cristina and Helena, who have dedicated enormous support and care throughout my life. To them I am thankful.

To my parents, Maria Helena and Paulo, I wish to express my respect and the best of my feelings. The love and support they have dedicated to me have been a driving force for all the achievements in my life. I hope now we will finally spend more time together.

In closing I would like to express my gratitude to my grandparents, Julio Braga and Isa Branco, for the incentive offered at the time I was organizing my trip back to Canada. At that time they were very proud of having a grandson starting a PhD. Were they here now, I am sure they would share with me the happiness of finishing it.

Table of Contents

Chapter Page

1. INTRODUCTION 1

1.1 General 1

1.2 Scope 8

2. MECHANICS OF GASSY FLUIDS 11

2.1 Introduction 11

2.2 Time-independent or Equilibrium Behaviour of Gassy Fluids 12

2.2.1 Compressibility of Gassy Fluids - Disregarding Surface Tensions 13

2.2.2 Compressibility of Gassy Fluids - With Surface Tensions 52

2.3 Time-dependent Behaviour of Gassy Fluids 74

2.3.1 Fundamental Gas Evolution Models 75

2.3.2 Macroscopic (descriptive) Gas Evolution Models 88

2.4 Summary and Conclusions 98

3. ANALYTICAL AND NUMERICAL SIMULATION OF THE RESPONSE OF GASSY SOILS 101

3.1 Introduction 101

3.2 Existing Stress-Relief Models for Gassy Soils 101

3.2.1 Time-Independent Models 102

3.2.2 Time-Dependent Models 107

3.3 Proposed Time-Dependent Model 110

3.3.1 Model Formulation 115

3.3.2 Finite Element Formulation 118

3.3.2.1 Temporal Discretization of Functions 119

3.3.2.2 Spatial Discretization of the Degrees of Freedom 135

3.3.2.3 Finite Element Equations 142
3.3.3 Structure and Details of CONGAS 149
3.3.4 Testing of CONGAS 176
3.3.4.1 Immediate Response 177
3.3.4.2 Transient Response 187
3.3.4.3 Independent Features 214
3.3.5 Modelling Limitations of CONGAS 221
3.3.5.1 Limitations of the Non-Linear Incremental Elastic Model 221
3.3.5.2 Limitations of the Fluid Model ...234
3.3.5.3 Limitations of the Numerical Iterative Scheme 235
3.4 Summary and Conclusions 237
4. SAMPLING AND TESTING PROGRAMS 239
4.1 Introduction 239
4.2 Sampling Program 242
4.2.1 Desirable Characteristics of Samples 242
4.2.2 Choice of Sampling Site 244
4.2.3 Choice of Core Barrels 247
4.2.4 Sampling and Storage Procedures 250
4.2.5 Piezometers 261
4.2.6 Evaluation of the Quality of Samples 264
4.3 Test Program 269
4.3.1 Classification of the Tests Performed 269
4.3.2 Physical Properties Tests (Group A) 270
4.3.2.1 Bitumen and Water Content 271
4.3.2.2 Density, Porosity and Fluid Saturation 271
4.3.2.3 Grain Size Distribution 272

4.3.2.4 Gas Content 273

4.3.2.5 Analysis of the Physical Properties Tests 280

4.3.3 Skeleton Mechanical Response Tests (Group A) 283

4.3.3.1 General 283

4.3.3.2 Triaxial Testing System 283

4.3.3.3 Sample Preparation for Testing ...292

4.3.3.4 Isotropic Drained Triaxial Tests .297

4.3.3.5 "J1" Drained Triaxial Tests 303

4.3.3.6 Standard Drained Triaxial Tests ..336

4.3.3.7 Summary of Stress-Strain Hyperbolic Parameters 341

4.3.4 Gas Evolution Response Tests (Group A) ...341

4.3.4.1 General 341

4.3.4.2 Undrained Oedometer Tests 346

4.3.4.3 Undrained Mercury Triaxial Tests .365

4.3.4.4 Summary of the Gas Evolution Test Results 430

4.3.5 Model Tests (Group B) 430

4.3.5.1 General 430

4.3.5.2 Hollow Cylinder Testing System ...432

4.3.5.3 Sample Preparation for Testing ...442

4.3.5.4 Test Type I (Undrained Isotropic Unloading) 449

4.3.5.5 Test Type II (Drained Plane Stress Shearing) 467

4.4 Summary and Conclusions 478

5. NUMERICAL SIMULATION OF MODEL TESTS AND SHAFT SINKING 485

5.1 General 485

5.2 Model Test Type I - Isotropic Undrained Unloading 486

5.3 Model Test - Type II - Drained Unloading of the Internal Bore 506

5.4 Simulation of Shaft Sinking in Oil Sands 532

5.5 Summary and Conclusions 564

6. SUMMARY AND CONCLUSIONS 570

6.1 General 570

6.2 Mechanics of Gassy Fluids 571

6.3 Development of the Finite Element Program CONGAS (CONsolidation and GAS Evolution) 573

6.4 Verification of the Prediction Capabilities of CONGAS 574

6.5 Simulation of Shaft Sinking in Oil Sands 578

6.6 Suggestions for Future Research 578

REFERENCES 581

APPENDIX A - COMPRESSIBILITY OF GASSY FLUIDS 597

APPENDIX B - DETAILS OF CONGAS 604

B.1 Introduction 604

B.2 Development of the Element Matrices in CONGAS ..604

B.3 Specification of Boundary Conditions in CONGAS .626

APPENDIX C - LABORATORY TEST DATA 629

APPENDIX D - ANALYSIS OF GAS EVOLUTION TEST DATA 686

D.1 Evaluation of Combined Solubility Coefficient from Laboratory Tests 686

D.2 Regression Analysis of Gas Evolution Test Data .687

APPENDIX E - LABORATORY EQUIPMENT DATA 694

List of Tables

Table		Page
1.1	Example of Geotechnical Groblems Involving Gassy Soils	3
3.1	Spatial Discretization Schemes - Users	136
4.1	Details of Sampling with the Pitcher Barrel Sampler	256
4.2	Details of Sampling with the Christensen Barrel	260
4.3	Evaluation of the Quality of Samples	268
4.4	Physical Properties	274
4.5	Gas Analysis	281
4.6	Triaxial Drained Isotropic Unloading Tests - Test Characteristics	298
4.7	Triaxial Drained J1 Tests - Test Characteristics	304
4.8	Strength Parameters from Triaxial Tests	322
4.9	G_i and R_f Obtained from "J1" Triaxial Tests	333
4.10	Standard Drained Triaxial Tests - Test Characteristics	337
4.11	G_i and R_F Obtained from Standard Triaxial Tests	339
4.12	Undrained Oedometer Test - Sample Characteristics	355
4.13	Gas Evolution Undrained Oedmeter Test - Sample 11-5	358
4.14	Undrained Oedometer Test - Sample 11-5 - Evaluation of the Solubility Coefficient	363
4.15	Undrained Mercury Triaxial Tests - Characteristics	377
4.16	Gas Evolution Tests - Solubility Coefficients and Bubble Point Pressures	392
4.17	Theoretical Combined Solubility Coefficients	399

Table		Page
4.18	Hollow Cylinder Test - Sample 26-1 - Saturation and Test Characteristics	451
4.19	Hollow Cylinder Test - Sample 27-2B - Saturation and Test Characteristics	452
4.20	Hollow Cylinder Test - Sample 26-1 - Sample Characteristics	454
4.21	Hollow Cylinder Test - Sample 27-2B - Sample Characteristics	455
4.22	Hollow Cylinder Test - Sample 27-2C - Saturation and Testing Characteristics	468
4.23	Hollow Cylinder Test - Sample 28-2C - Saturation and Testing Characteristics	469
4.24	Hollow Cylinder Test - Sample 27-2C - Sample Characteristics	471
4.25	Hollow Cylinder Test - Sample 28-2C - Sample Characteristics	472
5.1	Boundary Conditions, Initial Void Ratios and Initial Pore Pressures - Hollow Cylinder Tests - Type I	492
5.2	Temporal Discretization Test Type I	493
5.3	Hollow CylinderTest Type I - Numerical Simulation - Skeleton - Pore Fluid Properties	494
5.4	Boundary Conditions, Initial Void Ratios, Initial Degree of Saturation and Initial Pore Pressures - Hollow Cylinder Test - Type II	511
5.5	Temporal Discretization - Type II Test	513
5.6	Hollow Cylinder Test - Type II - Numerical Simulation - Skeleton-Pore Fluid Properties	514
5.7	Hollow Cylinder Tests - Type II - Sample Volume Changes, Step A	525
5.8	Hollow Cylinder Test - Type II - Numerical Simulation, Step B	531

Table		Page
5.9	Shaft Simulation - Stage A - Initial Stresses, Boundary Conditions and Parameters	547
5.10	Shaft Simulation - Stage B - Initial Stresses and Stress Boundary Conditions	559
A.1	Fluid Compressibility P_i = (300 + 101.325) kPa	600
A.2	Fluid Compressibility - P_i = (3000 + 101.325) kPa	601
A.3	Fluid Compressibility - P_i = (300 + 101.325) kPa	602
A.4	Fluid Compressibility - P_i = (300 + 101.325) kPa	603
C.1	Mercury Triaxial Test - Sample 3-1	630
C.2	Mercury Triaxial Test - Sample 3-1 - Evaluation of Solubility Coefficient	631
C.3	Mercury Triaxial Test - Sample 3-1 - Test Data Regression	632
C.4	Mercury Triaxial Test - Sample 6-5	633
C.5	Mercury Triaxial Test - Sample 6-5 - Evaluation of Solubility Coefficient	634
C.6	Mercury Triaxial Test - Sample 6-5 - Test Data Regression	635
C.7	Mercury Triaxial Test - Sample 9-2	636
C.8	Mercury Triaxial Test - Sample 9-2 - Evaluation of Solubility Coefficient	637
C.9	Mercury Triaxial Test - Sample 9-2 - Test Data Regression	638
C.10	Mercury Triaxial Test - Sample 11-2	639
C.11	Mercury Triaxial Test - Sample 11-2 - Evaluation of Solubility Coefficient	640
C.12	Mercury Triaxial Test - Sample 11-2 - Test Data Regression	641
C.13	Mercury Triaxial Test - Sample 11-3	642

Table Page

C.14 Mercury Triaxial Test - Sample 11-3 - Evaluation of Solubility Coefficient 643

C.15 Mercury Triaxial Test - Sample 11-3 - Test Data Regression 644

List of Figures

Figure		Page
1.1	Undrained Equilibrium Behaviour of an Element of Soil on Unloading - Modified from Sobkowicz and Morgenstern, 1984	4
2.1	Piston and Porous Stone Analogy	14
2.2	Isothermal Compressibility of Air Free Water - Modified from Fredlund, 1973	17
2.3	Effects of Pressure on Isothermal Compressibility of Air-Free Water - Modified from Fredlund, 1973	18
2.4	Solubility of Methane and Carbon Dioxide in Distilled Water	29
2.5	Solubility of Carbon Dioxide in Distilled Water	30
2.6	Solubility of Carbon Dioxide in Synthetic Sea Water	31
2.7	Volumetric Solubility of Carbon Dioxide In Bitumen - Modified from Svrcek and Mehrotra, 1982	33
2.8	Volumetric Solubility of Methane in Bitumen - Modified from Svrcek and Mehrotra, 1982	34
2.9	Volumetric Solubility of Nitrogen in Bitumen - Modified from Svrcek and Mehrotra, 1982	35
2.10	Isothermal Compressibility of Air Saturated Natural and Salt Water - Modified from Fredlund, 1973	37
2.11	Piston and Porous Stone Analogy - Two Immiscible Liquids	47
2.12	Compressibility of Pore Fluid Composed of Water and Carbon Dioxide - Initial Water and Gas Pressure = 300kPa	55
2.13	Compressibility of Pore Fluid Composed of Water and Carbon Dioxide - Initial Water and Gas Pressure = 3000kPa	56
2.14	Compressibility of Pore Fluid Composed of Bitumen and Methane - Initial Bitumen and Gas Pressure = 300 kPa	57

Figure Page

2.15 Compressibility of Pore Fluid Composed of Bitumen and Methane - Initial Bitumen and Gas Pressure = 3000 kPa 58

2.16 Critical Radius Versus Bubble Radius of a Single Bubble Immersed in a 1cc Water/Nitrogen Solution (Modified from Ward et al., 1985) 68

2.17 Bubble Growth in the Surface of Container or in the Surface of Particles Suspended in a Gas-Liquid Solution - Modified from Ward and Levart, 1984 71

2.18 Bubble Evolution in a Liquid Closed to Mass Transport - Modified from Tikuisis et al., 1983 83

2.19 Macroscopic (descriptive) Gas Evolution Model - Modified from Sobkowicz, 1982 91

2.20 Nitrogen Bubble Growth in Constant Volume and Mass of Water 92

2.21 Nitrogen Elimination in Human Beings 93

2.22 Elimination of nitrogen from the body during a course of oxygen inhalation (modified from Behnke, 1951) 96

3.1 Stress Relief Models for Gassy Soils (Isothermal Conditions) 103

3.2 Time-Dependent Models - Gassy Soils 111

3.3 Spatial Discretization of Field Variables in Consolidation Problems - Standard Elements 137

3.4 Spatial Discretization of Field Variables in Consolidation Problems - Composite Elements 138

3.5 Simplified Flow Chart of the Structure of CONGAS 151

3.6 Simple Incremental Approximation 161

3.7 Error Control Index - Bulk Modulus - Material Models 2 and 3 163

3.8 Error Control Index - Young Modulus - Material Model 2 164

Figure Page

3.9 Error Control Index - Shear Modulus - Material Model 3 165

3.10 Error Control Index - Bulk Modulus - Material Model 4 166

3.11 Error Control Index - Shear Modulus - Material Model 4 167

3.12 Finite Element Mesh Test 6-V5 178

3.13 Immediate Response - Soil Initially Fully Saturated with Drainage - Test 6-V5-1D 179

3.14 Immediate Response - Soil Initially Fully - Saturated without Drainage - Test6-V5-1D 181

3.15 Immediate Response Soil Initially Fully Saturated without Drainage - Test6-V5-2D 183

3.16 Immediate Response - Soil Partly Saturated - Test6-V5-1D 185

3.17 Finite Element Mesh - Test16-V14-1D 186

3.18 Immediate Response - Soil Initially Partly Saturated without Drainage - Test16-V14-1D 188

3.19 Immediate Response - Void Ratio and Degree of Saturation - Test16-V16-1D 189

3.20 Finite Element Meshes - Tests2-V3-1D-M1 and M2 190

3.21 One Dimensional Consolidation - Pore Pressure versus Time 191

3.22 One Dimensional Consolidation - Pore Pressure versus Time 192

3.23 One Dimensional Consolidation - Surface Vertical Displacement versus Time 194

3.24 Finite Element Mesh - Test8-V6 196

3.25 Axisymmetric Consolidation - Average Excess Pore Pressure versus Time Test8-V6 198

3.26 Finite Element Mesh - Test9-V6 199

3.27 Axisymmetric Consolidation - Excess Pore Pressure versus Time 200

Figure		Page
4.4	Sample Location	251
4.5	Piezometer Readings	263
4.6	Geophysical Log of Sampling Area	266
4.7	Degassification of Oil Sand Samples - Procedure A	277
4.8	Degassification of the Oil Sand Samples - Procedure B	279
4.9	Pressure System Schematic for Triaxial Tests	285
4.10	Bellows Volume Change	290
4.11	Variation of Bulk Modulus with Confining Pressure - Modifified from Duncan, 1980	302
4.12	Normalized Bulk Modulus versus Normalized Mean Effective stress	305
4.13	J1 Triaxial Tests (Drained) Undisturbed Samples	309
4.14	Hyperbolic Representation of a Stress-Strain Curve	312
4.15	Hyperbolic Stress-Strain Curve	315
4.16	Mohr-Coulomb and Drucker-Prager Failure Criteria	318
4.17	Curved Failure Envelope	320
4.18	Friction Angle versus Normalized Confinement Stress	323
4.19	Friction Angle versus Normalized Mean Stress	324
4.20	Transformed Hyperbolic Stress-Strain Plot	326
4.21	Comparison between Overall and Localized Strains (Modified from Jardine et al., 1984)	330
4.22	Normalized Shear Modulus versus Normalized Mean Effective Stress	334
4.23	Standard Triaxial Tests - Test Results	340

Figure		Page
4.24	Pressure System Schematic for Oedometer Tests	348
4.25	Undrained Oedometer Test - Sample 11-5 - Gas Production	360
4.26	Undrained Oedometer Test - Sample 11-5 - Equilibrium Response	361
4.27	Undrained Oedometer Test - Sample 11-5 - Solubility Coefficient	364
4.28	Pressure System Schematic for Gas Evolution Tests	369
4.29	Mercury Triaxial Test 3-1 - Equilibrium Response	381
4.30	Mercury Triaxial Test 3-1 - Solubility Coefficient	382
4.31	Mercury Triaxial Test 6-5 - Equilibrium Response	383
4.32	Mercury Triaxial Test 6-5 - Solubility Coefficient	384
4.33	Mercury Triaxial Test 9-2 - Equilibrium Response	385
4.34	Mercury Triaxial Test 9-2 - Solubility Coefficient	386
4.35	Mercury Triaxial Test 11-2 - Equilibrium Response	387
4.36	Mercury Triaxial Test 11-2 - Solubility Coefficient	388
4.37	Mercury Triaxial Test 11-3 - Equilibrium Response	389
4.38	Mercury Triaxial Test 11-3 - Solubility Coefficient	390
4.39	Bubble Point Pressures and Measured *in situ* Pore Pressures	393
4.40	Mercury Triaxial Test 3-1 - Step A	401
4.41	Mercury Triaxial Test 3-1 - Step B	402
4.42	Mercury Triaxial Test 3-1 - Step C	403

Figure		Page
4.43	Mercury Triaxial Test 6-5 - Step A	404
4.44	Mercury Triaxial Test 6-5 - Step B	405
4.45	Mercury Triaxial Test 6-5 - Step C	406
4.46	Mercury Triaxial Test 6-5 - Step D	407
4.47	Mercury Triaxial Test 6-5 - Step E	408
4.48	Mercury Triaxial Test 9-2 - Step A	409
4.49	Mercury Triaxial Test 9-2 - Step B	410
4.50	Mercury Triaxial Test 9-2 - Step C	411
4.51	Mercury Triaxial Test 11-2 - Step A	412
4.52	Mercury Triaxial Test 11-2 - Step C	413
4.53	Mercury Triaxial Test 11-2 - Step D	414
4.54	Mercury Triaxial Test 11-2 - Step E	415
4.55	Mercury Triaxial Test 11-2 - Step F	416
4.56	Mercury Triaxial Test 11-3 - Step A	417
4.57	Mercury Triaxial Test 11-3 - Step B	418
4.58	Mercury Triaxial Test 11-3 - Step C	419
4.59	Mercury Triaxial Test 11-3 - Step D	420
4.60	Mercury Triaxial Test 11-3 - Step E	421
4.61	Mercury Triaxial Test 11-3 - Step F	422
4.62	Mercury Triaxial Test 11-3 - Step G	423
4.63	Comparison Between Immediate and Time-Dependent Gas Volume Change	426
4.64	Scaling Parameter A' versus Total Degree of Saturation	428
4.65	Hollow Cylinder Tests - Schematic of Pressure Systems	434
4.66	Hollow Cylinder Test - Sample 26-1 - Step A	458

Figure

Page

4.67 Hollow Cylinder Test - Sample 26-1 - Step B 459

4.68 Hollow Cylinder Test - Sample 26-1 - Step C 460

4.69 Hollow Cylinder Test - Sample 27-2B - Step A 461

4.70 Hollow Cylinder Test - Sample 27-2B - Step B 462

4.71 Hollow Cylinder Test - Sample 27-2b - Step C 463

4.72 Hollow Cylinder Test - Sample 27-2B - Step D 464

4.73 Hollow Cylinder Test - Sample 27-2C - Step A 473

4.74 Hollow Cylinder Test - Sample 27-2C - Step B 474

4.75 Hollow Cylinder Test - Sample 28-2C - Step A 475

4.76 Hollow Cylinder Test - Sample 28-2C - Step B 476

5.1 Finite Element Mesh - Test-Test16-V16 - Hollow Cylinder Test - Type I 490

5.2 Hollow Cylinder Test Type I - Numerical Simulation - Sample 26-1 - Step B 495

5.3 Hollow Cylinder Test Type I - Numerical Simulation - Sample 26-1 - Step C 496

5.4 Hollow Cylinder Test - Numerical Simulation - Sample 27-2B - Step B 500

5.5 Hollow Cylinder Test - Numerical Simulation - Sample 27-2B - Step C 501

5.6 Hollow Cylinder Test - Numerical Simulation - Sample 27-2B - Step D 502

5.7 Finite Element Mesh - Test17-V17 - Hollow Cylinder Test - Type II 508

Figure Page

5.8 Hollow Cylinder Test - Type II - Numerical Simulation - % Consolidation versus Time, 0 to 50 minutes 516

5.9 Evaluation of % Consolidation from Numerical Tests 518

5.10 Hollow Cylinder Test - Type II - Numerical Simulation - Percent Consolidation versus Time, 0 to 2500 minutes 520

5.11 Hollow Cylinder Test - Type II - Numerical Simulation, Step A 526

5.12 Hollow Cylinder Test - Type II - Degree of Saturation versus Depth at the End of Step A - t=2882 minutes 528

5.13 UTF Shafts - Site Geology, Pore Pressures and Geotechnical Concerns 535

5.14 Blind Shaft Drilling - Construction Stages 537

5.15 Blind Shaft Drilling - Continuous Shaft Lining 540

5.16 Shaft Sinking with the Continuous Shaft Lining System - Numerical Simulation 542

5.17 Finite Element Mesh Test 13-V18 - Shaft Simulation - Stage A 545

5.18 Shaft Simulation - Stage A - Radial Stresses and Pore Pressures - Consolidation Only 549

5.19 Shaft Simulation - Stage A - Radial Stresses and Pore Pressures - A'=10 000 minutes 550

5.20 Shaft Simulation - Stage A - Radial Stresses and Pore Pressures - A'=1000 minutes 551

5.21 Shaft Simulation - Stage A - Average Seepage Forces between the Wall and a Point 0.33 m from the Shaft Wall (Element 5 - Sampling Point 3) 552

5.22 Shaft Simulation - Stage A - Progress of Tensile Zone with Time 554

Figure		Page
5.23	Finite Element Mesh - Test 18-V18 - Shaft Simulation - Stage B	557
5.24	Development of Depth of the Tensile Zone along a Vertical Line 10 cm from the Shaft Axis - Stage B	561
5.25	Tensile Zone at t=1400 minutes - Stage B	562
B.1	Triangular Element - 6-3 - Area Coordinates	605
B.2	Strain - Displacement Matrix - Triangular Element 6-3 - Axisymmetric Formulation	608
B.3	Volumetric Strain - Displacement Matrix - Triangular Element 6-3 - Axisymmetric Formulation	610
B.4	Numerical Integration of a Complete 3rd Degree Polynomial over a Triangle	612
B.5	Surface Tractions	621
B.6	Numerical Integration along Side 2-5-3 - Newton-Cotes	623
C.1	Grain Size Distribution - Sample 3-1	645
C.2	Grain Size Distribution - Sample 4-2	645
C.3	Grain Size Distribution - Sample 4-3	646
C.4	Grain Size Distribution - Sample 5-1	646
C.5	Grain Size Distribution - Sample 5-2	647
C.6	Grain Size Distribution - Sample 5-3	647
C.7	Grain Size Distribution - Sample 5-4	648
C.8	Grain Size Distribution - Sample 6-1	648
C.9	Grain Size Distribution - Sample 6-2	649
C.10	Grain Size Distribution - Sample 6-5A	649
C.11	Grain Size Distribution - Sample 7-3	650
C.12	Grain Size Distribution - Sample 7-4	650
C.13	Grain Size Distribution - Sample 7-5	651

Figure Page

C.14 Grain Size Distribution - Sample 8-1 651

C.15 Grain Size Distribution - Sample 8-2 652

C.16 Grain Size Distribution - Sample 11-3 652

C.17 Grain Size Distribution - Sample 26-1 653

C.18 Triaxial Drained Isotropic Unloading Test - Sample 5-1 654

C.19 Triaxial Drained Isotropic Unloading Test - Sample 7-4 654

C.20 Triaxial Drained Isotropic Unloading Test - Sample 8-2B 655

C.21 Triaxial Drained Isotropic Unloading Test - Sample 8-3 655

C.22 Normalized Bulk Modulus versus Normalized Mean Effective Stress - Sample 5-1 656

C.23 Normalized Bulk Modulus versus Normalized Mean Effective Stress - Sample 7-4 657

C.24 Normalized Bulk Modulus versus Normalized Mean Effective Stress - Sample 8-2B 658

C.25 Normalized Bulk Modulus versus Normalized Mean Effective Stress - Sample 8-3 659

C.26 Triaxial J1 Test - Stress Path - Sample 5-2 660

C.27 Triaxial J1 Test - Stress Path - Sample 5-3 660

C.28 Triaxial J1 Test - Stress Path - Sample 5-4 661

C.29 Triaxial J1 Test - Stress Path - Sample 8-1 661

C.30 Triaxial J1 Test - Stress Path - Sample 8-4 662

C.31 Triaxial J1 - Sample 5-2 663

C.32 Triaxial J1 - Sample 5-3 664

C.33 Triaxial J1 - Sample 5-4 665

Figure Page

C.34 Triaxial J1 - Sample 8-1 666

C.35 Triaxial J1 - Sample 8-4 667

C.36 Hyperbolic Fit - Sample 5-2 668

C.37 Hyperbolic Fit - Sample 5-3 669

C.38 Hyperbolic Fit - Sample 5-4 670

C.39 Hyperbolic Fit - Sample 8-1 671

C.40 Standard Triaxial Test - Sample 4-2 672

C.41 Standard Triaxial Test - Sample 5-1 673

C.42 Standard Triaxial Test - Sample 6-1 674

C.43 Standard Triaxial Test - Sample 6-2 675

C.44 Standard Triaxial Test - Sample 7-4 676

C.45 Standard Triaxial Test - Stress Path - Sample 4-2 677

C.46 Standard Triaxial Test - Stress Path - Sample 5-1 677

C.47 Standard Triaxial Test - Stress Path - Sample 6-1 678

C.48 Standard Triaxial Test - Stress Path - Sample 6-2 678

C.49 Standard Triaxial Test - Stress Path - Sample 7-4 679

C.50 Undrained Oedometer Test - Sample 11-5 - Step A 680

C.51 Undrained Oedometer Test - Sample 11-5 - Step B 681

C.52 Undrained Oedometer Test - Sample 11-5 - Step C 682

C.53 Undrained Oedometer Test - Sample 11-5 - Step D 683

C.54 Undrained Oedometer Test - Sample 11-5 - Step E 684

Figure		Page
C.55	Undrained Oedometer Test - Sample 11-5 - Step F	685
D.1	Linearized "Quotient + 1" Function	690
D.2	Linearized Exponential Function	693
E.1	Triaxial Cell - Base Platen and Pedestal - Top View	695
E.2	Triaxial Cell - Base Platen and Pedestal	696
E.3	Triaxial Cell - Section B-B	697
E.4	Triaxial Cell - Top Platen	698
E.5	Vertical Compliance of the Triaxial Apparatus	699
E.6	Volumetric Compliance of the Back Pressure Lines	700
E.7	Axial Load Correction for Piston Friction - Triaxial Apparatus	701
E.8	Oedometer - Expanded Cross Section	702
E.9	Oedometer - Top Plate	703
E.10	Mercury Triaxial - Sample Pedestal	704
E.11	U. of A. Volume Change Device	705
E.12	U. of A. Volume Change Device - Piston	706
E.13	Volumetric Compliance - Back Pressure System No. 2	707
E.14	Volumetric Compliance - Cell Pressure System No. 2	708
E.15	Hollow Cylinder Cell - Bottom Platen	709
E.16	Hollow Cylinder Cell - Top Platen	710
E.17	Hollow Cylinder Cell - Sketch Cross Section	711
E.18	Hollow Cylinder Cell - Sketch of Piston, Sample and Cap Assembly	712
E.19	Hollow Cylinder Cell - Piston	713

Figure Page

E.20 Hollow Cylinder Cell - Top Cap - Cross Sections A-A and B-B 714

E.21 Hollow Cylinder Cell - Top Cap - Top View 715

E.22 Hollow Cylinder Cell - Sample Top Platen 716

E.23 Hollow Cylinder Cell - Sample Bottom Platen 717

E.24 Load Cell Reading versus Jefri Pump Pressure 718

E.25 Hollow Cylinder Cell - Vertical System Compliance 719

E.26 Hollow Cylinder Cell - Volumetric Compliance of External Cell Cell System 720

E.27 Hollow Cylinder Cell - Volumetric Compliance of External Cell Cell System 721

E.28 Hollow Cylinder Cell - Volumetric Compliance of Back Pressure System 722

E.29 Hollow Cylinder Cell - Volumetric Compliance of Internal Cell System 723

E.30 Hollow Cylinder Cell - Internal Cell Latex Membrane Mold 724

List of Plates

Plate		Page
4.1	Pitcher Double Core Barrel	252
4.2	Christensen Core Barrel	252
4.3	Drill Bit - Borehole No.1 and No. 2 (Pitcher Core Barrel)	254
4.4	Drill Bit - Borehole No. 3 (Christensen Core Barrel)	254
4.5	Removal of Sample 24 from Solid Inner Tube to Storage Tray	258
4.6	Sample 28 on the Split Inner Tube	258
4.7	Triaxial Testing System	286
4.8	Lathe used for Sample Trimming	294
4.9	Diamond Bit and Frozen Sample during Trimming	294
4.10	Sample Preparation for Testing - Lateral Drains	296
4.11	Sample Preparation for Testing - Latex Membranes	296
4.12	Mercury Triaxial Cell - Stainless Steel Jacket	367
4.13	Mercury Triaxial Cell - Stainless Steel Jacket and Sample	367
4.14	Mercury Triaxial Testing System	370
4.15	Hollow Cylinder Cell and Top Cap	436
4.16	Hollow Cylinder Cell and Axial Loading System	436
4.17	Hollow Cylinder Test - Sample Preparation for Testing	446
4.18	Hollow Cylinder Test - Sample Preparation for Testing	446
4.19	Hollow Cylinder Test - Lowering of Top Plate and Collar over the Piston	448
4.20	Hollow Cylinder Test - Tightening of the Nuts Against the Collar	448

LIST OF SYMBOLS

The following is a list of symbols used in this thesis. In some cases more than one symbol has been used to represent a quantity. This is due to the fact that, whenever possible, the notation originally used by the referred authors has been preserved.

Where the use of symbols differs from that listed below, the symbol is defined in the text, immediately following its first occurrence.

SYMBOL	MEANING
A	pore pressure parameter
A, B, C	pore fluid components, pore pressure parameters, polynomial coefficients
A', E	scaling parameter
B	pore pressure parameter, bulk modulus, strain-displacement matrix
C_v	coefficient of consolidation
C	gas concentration, coupling matrix
C_{ijkl}	stress-strain tensor
d	exact differencial
D	mass diffusivity coefficient
DAMP	damping constant
E	Young's modulus
F	body force per unit mass of soil

G	shear modulus
H	solubility coefficient, constitutive matrix
J	rate of bubble formation
k, K	coefficient of permeability to water, Henry's coefficient
K_B	bulk modulus number
K_E	Young's modulus number
K_G	shear modulus number
L	Ostwald absorption coefficient
LF	liquid fraction
LG	gas fraction
m, m_B	bulk modulus exponent
M	finite element matrix, constraint modulus
n	moles, normal vector, porosity
n_q	shear modulus exponent
p	partial pressure
P	absolute pressure
q, σ	surface tensions, number of conical pits
r, R	radius of bubble, radius coordinate
R	gas constant
R_F	failure ratio
s	scaling factor
S	degree of saturation, surface
S_{ol}	volumetric solubility

t	time
T	temperature
u	pore pressure
V	filtration velocity, volume
w	displacement
x	mole ratio
X, y	mole fraction
Y, N	number of molecules
Z	compressibility factor, constant of proportionality
a	constant of proportionality, thermal diffusivity constant, time integration constant
β	compressibility
γ	unit weight, surface traction, scalar coefficient
δ	partial differential
Δ	finite increment
ϵ	strain
η, μ	dynamic viscosity
θ	angle
κ	Boltzman constant
ν	Poisson's ratio, specific volume
N	Avogrado's number
ρ	density
σ	stress, surface tension
τ	shear stress

ϕ	friction angle

Subscripts and superscripts:

a	air
aw	air/water
A,B,C,1,2,3,i	pore fluid components
c	critical
COMB	combined
d	displacement
dg	dissolved gas
e	external, effective
ext	external
EVO	evolution
f	flow
fail	at failure
fg	free gas
F	total pore fluid
g	gas
h	horizontal
i, 0	initial
int	internal
lg, l/g	liquid/gas
m	minimum
notens	no surface tensions
NTP	normal temperature and pressure
OCT	octahedral
R	reduced
t	traction, tangent

tens	with surface tensions
TOT	total
u	pore pressure
v	vertical
v, vap	vapor, volumetric
w	water, well
∞	infinity

1. INTRODUCTION

1.1 General

In the period that followed World War II, due to the high rate of construction of earth embankments, related to highway and dams, the attention of geotechnical engineers was drawn to the behaviour of partly saturated soils.

These constituted a new class of soil and its behaviour could not be explained with classical soil mechanics theories.

It has been verified (Fredlund, 1973) that this type of soil is constituted of a four phase system:

- soil skeleton
- water phase
- air phase
- water-air interface

Several years of research with partly saturated soils resulted in a good understanding of the physical processes that govern their mechanical behaviour. It has been identified that, upon changes in the boundary conditions of a soil sample, the four phases of the system interact, seeking a position of equilibrium. One of the governing processes of this dynamic problem is the migration of air molecules between the air and the water phases. It is this process, together with the presence of the water-air interface (the contractile skin, as referred to by Fredlund, 1973) that make the behaviour of these soils depart from the

behaviour predicted by the classical theories of soil mechanics.

Experiments showed that this migration process or diffusion of air molecules was fast when compared to the rates of changes in boundary conditions observed in most engineering works. Based on this assumption numerous formulations have been proposed to describe the mechanical response of partly saturated soils at equilibrium. Some of them have been incorporated into computer programs that, with the aid of numerical techniques, made possible the analysis of complex geotechnical engineering problems.

More recently, with the increase of construction work in marine environments and in oil sands deposits, as a result of an increase in exploitation of new hydrocarbon resources, the attention of geotechnical engineers was drawn to different types of soil. These include soils with fluids saturated with large amounts of gases, also called gassy or gas-laden or gas-charged soils. Some examples of problems linked to gassy soils in geotechnical engineering works are depicted in Table 1.1 .

These soils present a response to undrained stress relief very similar to that observed in partly saturated soil, except that the presence of large amounts of gas in the former results in considerably greater compressibilities of the fluids.

Figure 1.1, modified from Sobkowicz and Morgenstern, 1984, illustrates how the differences in fluid

GEOTECHNICAL WORK	GASSY SOIL TYPE	GASSY FLUID		LOCATION	OBSERVED EFFECTS	REFERENCES
		LIQUIDS	GASES			
UNDISTORBED SOIL SAMPLING	MARINE SEDIMENTS	SEA WATER	METHANE(CH_4) HYDROGEN SULFIDE(H_2S) CARBON DIOXIDE(CO_2)	GULF OF MEXICO AND MISSISSIPI RIVER DELTA	SAMPLE "GROWTH" OUT OF THE SAMPLING TUBE WHEN RETRIEVED TO THE SURFACE	SANGREY, 1977 ESRIG AND KIRBY, 1977 CHANEY ET AL., 1985
			AIR	SEA OF JAPAN		OKUMURA, 1977
	OIL SANDS	BITUMEN AND WATER	METHANE CARBON DIOXIDE	ALBERTA		HARDY AND HEMSTOCK, 1963 DUSSEAULT, 1977 DUSSEAULT AND MORGENSTERN, 1978 DUSSEAULT, 1980 MORGENSTERN, 1981
UNDERWATER EXCAVATION (PIPELINE TRENCHING)	MARINE SEDIMENTS	SEA WATER	METHANE HYD. SULFIDE CAR. DIOXIDE	GULF OF MEXICO	TRENCH SLOPE FAILURE	YEN AND ALLEN, 1977
UNDERWATER NATURAL LANDSLIDES	MARINE SEDIMENTS	SEA WATER		MISSISSIPI RIVER DELTA	RETROGRESSIVE LANDSLIDES	PRIOR AND COLEMAN, 1978 WHELAN EL AL., 1977
SURFACE EXCAVATION	SANDY CLAY	WATER	CAR. DIOXIDE	ALTO LAZIO, ITALY	FOUNDATION EXCAVATION, EXCESSIVE BOTTOM HEAVE	MORGENSTERN, 1981 SOBKOWICZ, 1982
	OIL SANDS	BITUMEN AND WATER	METHANE CAR. DIOXIDE	ALBERTA	FOUNDATION EXCAVATION EXCESSIVE BOTTOM HEAVE	SCOTT ET AL. 1985 GRIFFIN, 1986
	OIL SANDS	BITUMEN AND WATER	METHANE CAR DIOXIDE	ALBERTA	LARGE HORIZONTAL DISPLACEMENTS OF THE MINING HIGHWALLS	
	BASAL SANDS	WATER	METHANE CAR. DIOXIDE	ALBERTA	MINING WALLS INSTABILITIES	MARTSCHUK ET AL., 1985
AQUIFER DEWATERING AND DEPRESSURIZING	BASAL SANDS	WATER	METHANE CAR DIOXIDE	ALBERTA	INEFFICIENCY OF PUMPING SYSTEMS	MARTSCHUK ET AL., 1985

Table 1.1 Example of Geotechnical Problems Involving Gassy Soils

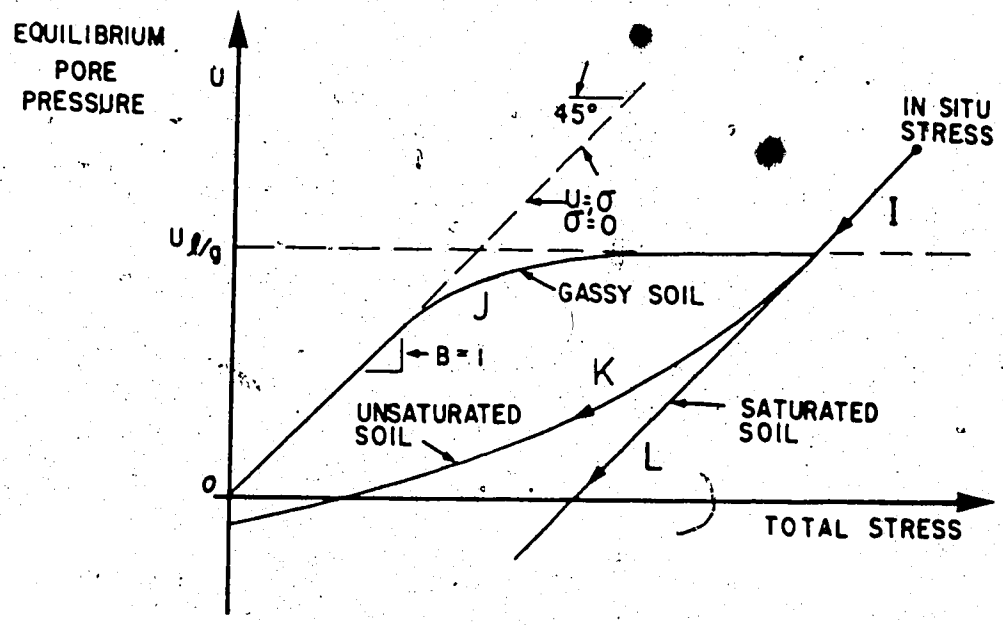

Figure 1.1 Undrained Equilibrium Behaviour of an Element of Soil on Unloading - Modified from Sobkowicz and Morgenstern, 1984

compressibilities can affect the pore pressure response of gas free fully saturated, partly saturated (small amounts of gas) and gassy (large amounts of gases) soils, when subjected to undrained, isotropic unloading.

Curves I and L in this figure represent the behaviour of a gas-free, or degassed, fully saturated soil. For a pore fluid considerably less compressible than the soil skeleton, the decreases in pore pressures (assumed to be equal in both, the gas and liquid phases) are approximately equal to the decreases in total stress resulting in a pore pressure parameter "B" equal to one (1).

Curve I , K represents the pore pressure response of a partly saturated soil, with small amounts of air in solution. For pore pressures higher than the liquid/gas saturation pressure or bubble point pressure, the air is fully dissolved in water and the pore pressure response to decreases in total stresses is similar to that of degassed soils. However, as soon as the pore pressure drops below the bubble point pressure, bubbles form and increase the compressibility of the pore fluids. This results in pore pressure decreases smaller than the decreases in total stresses. The pore pressure parameter "B" becomes less than one (1).

Curve I, J represents the pore pressure response of gassy soil. Similar to partly saturated soils, for pore pressures lower than the bubble point pressure, gas bubbles form and add compressibility to the pore fluids. However,

due to the large amounts of gas in solution, the compressibility is significantly higher than that observed in partly saturated soils. The changes in total stresses in gassy soils do not result in significant pore pressure changes up to the point when the effective stress in the soil tends to zero.

The presence of large amounts of gas in the pore fluids can occur under two circumstances:

a) The gas components of the pore fluid do not present high solubility in the pore liquids, however, due to high in situ pore pressures the number of gas molecules in solution is high.

b) The gas components of the pore fluid present high solubility in the pore liquids, and irrespective of the in situ pore pressures, the number of gas molecules in solution is high.

The diffusion of gas molecules between the free gas and liquid phases, similarly to partly saturated soil, constitutes one of the governing processes in the undrained behaviour of the pore fluids. The equations formulated to describe the equilibrium mechanical response of partly saturated soils are readily applicable to gassy soils whenever the migration processes are fast when compared to the changes in boundary condition of the soil.

This is the case of gassy fluids composed of low viscosity liquids such as those encountered in marine sediments. In oil sands, however, due to the presence of

bitumen in the pores, the mass diffusion processes are significantly slower than in marine sediments. In this case, upon undrained stress relief, the bubble growth in the pore fluids is slow, resulting in a slow increase in the fluid compressibility with time.

The compressibility of the fluids is a controlling factor in induced displacements and in the stand up time of geotechnical works such as surface and underground excavations and soil sampling. In these cases, fluids with low compressibility show a greater capacity to temporarily keep pore pressures at low levels, upon undrained stress relief. This ensures higher effective stresses in the soil skeleton resulting in smaller displacements and longer stand up times in excavation as well as better quality sampling.

Therefore, the slow mass diffusion process in gassy soils is a desirable process and the geotechnical engineer might take advantage of this fact when selecting sampling, design and construction techniques.

In order to appropriately assess the transient processes associated with gassy soils and to incorporate this knowledge in the engineering processes of decision making, an easily applicable and accurate simulation tool is required. A literature review on modelling the mechanics of gassy soil, however, reveals that such a model is not currently available. It also reveals that the models developed to simulate the equilibrium (not transient) behaviour of gassy soils have not been properly calibrated

and have not had their capability to solve engineering problems verified. The reason for that is the lack of well documented case histories or laboratory model tests in this type of soil.

The lack of appropriate simulation tools and the fact that, in the near future, the number of sampling programs and underground excavations in gassy soils, especially in oil sands deposits, is expected to increase considerably, were encouraging factors to undertake this research.

1.2 Scope

The main purpose of this thesis is to develop a model that appropriately simulates the transient processes that take place in gassy soils when subjected to isothermal boundary condition changes.

This model should aid the engineering of gassy soils in the following manner:

- To aid the choice of appropriate sampling, design and construction techniques
- To aid the analysis of field monitoring programs associated with observational techniques
- To improve the understanding of the mechanics of gassy soils

The development of the proposed model consists of the following steps:

1) The identification of the processes that govern the transient processes in the mechanics of gassy

soils and the development of the governing equations for the problem.

2) The development of a model where these governing equations are solved for boundary conditions usually encountered in gassy soils related works.

3) The verification of the capabibility of this model to appropriately simulate actual laboratory test models.

These three items constitute the working frame for the research program presented herein.

Chapter 2 presents a theoretical review of the thermodynamics of gas/liquid solutions. Its purpose is to inspect the physical processes that are thought to govern the mechanics of gassy fluids and to review the existing mathematical formulation that describes them.

Chapter 3 presents the governing differential equations that control the mechanical behaviour of gassy soils. A computer program, that uses the finite element technique, has been developed to solve these equations. All the steps required for its development are described in this chapter.

Chapter 4 describes an experimental program carried out in oil sands in order to enable the verification of the reliability of the results produced by the model proposed in Chapter 3.

That experimental program consisted of the following steps:

1) Sampling

2) Laboratory testing

The sampling program provided high quality samples used for laboratory tests. The latter involved two groups of tests:

1) Tests performed to measure the physical properties and the mechanical characteristics of the soil skeleton and of the pore fluids.

2) Tests performed to generate a case study

The parameters collected in the first group of tests were used in the finite element program, CONGAS (*CON*solidation and *GAS* evolution), in order to simulate the model tests, performed in the second test group.

The comparison between the performance predicted by the numerical model and the performance actually observed in the model tests enables the evaluation of the simulation capabilities of the former. The evaluation and calibration of CONGAS and the simulation of the construction of a shaft in oil sands are presented in Chapter 5.

Finally, Chapter 6 offers a summary of the work done and the conclusions during this research program.

2. MECHANICS OF GASSY FLUIDS

2.1 Introduction

Modelling the time-dependent response of soils has been an active area of research over the past fifty years in soil mechanics. The common basis for modelling techniques has been the identification of the equations that govern the physical process being studied and the subsequent solution of these equations by analytical or numerical techniques.

In order to develop the equations that are believed to govern the mechanics of gassy soils, additional aspects of the physical behaviour, usually not known to the geotechnical engineer, seem to be worth reviewing. In this chapter, these aspects of physical behaviour are inspected, through a review of the thermodynamics of gas/liquid solutions and through a review of the mathematical formulations that describe the mechanics of gassy fluids.

The thermodynamics of gas/liquid solutions involves a broad area of knowledge and is the basis for the understanding of various multidisciplinary topics. Examples are problems such as cavitation, in mechanical engineering, chemical reactions in chemistry, decompression sickness and tissue damage in animals undergoing decompression, studied in medical sciences.

A complete and comprehensive review of the thermodynamics of solutions is beyond the scope of this thesis. Therefore only topics that are thought to enlighten

the geotechnical aspect of the problem are dealt with herein. The present review of the thermodynamic aspects involved in gassy fluids is illustrated in this chapter using parameters from the Athabasca oil sands and from some marine sediments pore fluids.

From the geotechnical viewpoint, it is convenient to study the mechanics of fluids based on their compressibility coefficient (β). This is defined as the inverse of the bulk modulus (B), commonly used in the theory of elasticity. The boundaries of the fluid phase are assumed to be impermeable, that is to say, there is no exchange of mass th[illegible]. The fluid flow and response to shear stresses are discussed in Chapter 3.

This chapter provides the background required for the derivation of the governing equations developed subsequently in Chapter 3.

2.2 Time-independent or Equilibrium Behaviour of Gassy Fluids

In the study of the mechanical response of gassy fluids it is convenient to consider independently the effects of the interfacial tensions, existing among the components of the fluid under consideration. On the other hand, neglecting their effects simplifies the modelling of gassy soils, which is the ultimate goal of this research. Hence, the following two sections evaluate equilibrium fluid compressibilities, firstly ignoring the existence of interfacial tensions and

secondly taking into account their presence. These sections will enable the evaluation of the effects of the interfacial tensions in the behaviour of both gassy and partly saturated fluids.

2.2.1 Compressibility of Gassy Fluids - Disregarding Surface Tensions

A gassy fluid composed of a liquid, L, and a gas, G, is initially considered. The constitutive response of this hypothetical fluid, at equilibrium, is here discussed with the help of the piston and porous stone analogy presented by Fredlund, 1973 and 1976. It consists of a piston and closed cylinder arrangement with a porous stone at the base of the cylinder (Fig.2.1). The porous stone simulates the behaviour of the liquid (solvent). The free gas (solute) and the porous stone are separated by a series of imaginary valves that control the movement of the gas into the stone. The gas molecules in the stone pores simulate the gas dissolved in the liquid. In this analogy the presence of the contractile skin is neglected.

IMMISCIBLE FLUIDS - ONE LIQUID AND ONE GAS

Initially one assumes that the valves that separate the free gas from the liquid are closed. This case simulates the behaviour of *immiscible fluids*. If the absolute pressure applied by the piston is changed from P_1 to P_2, the gas and the liquid phase attain equilibrium without exchange of gas

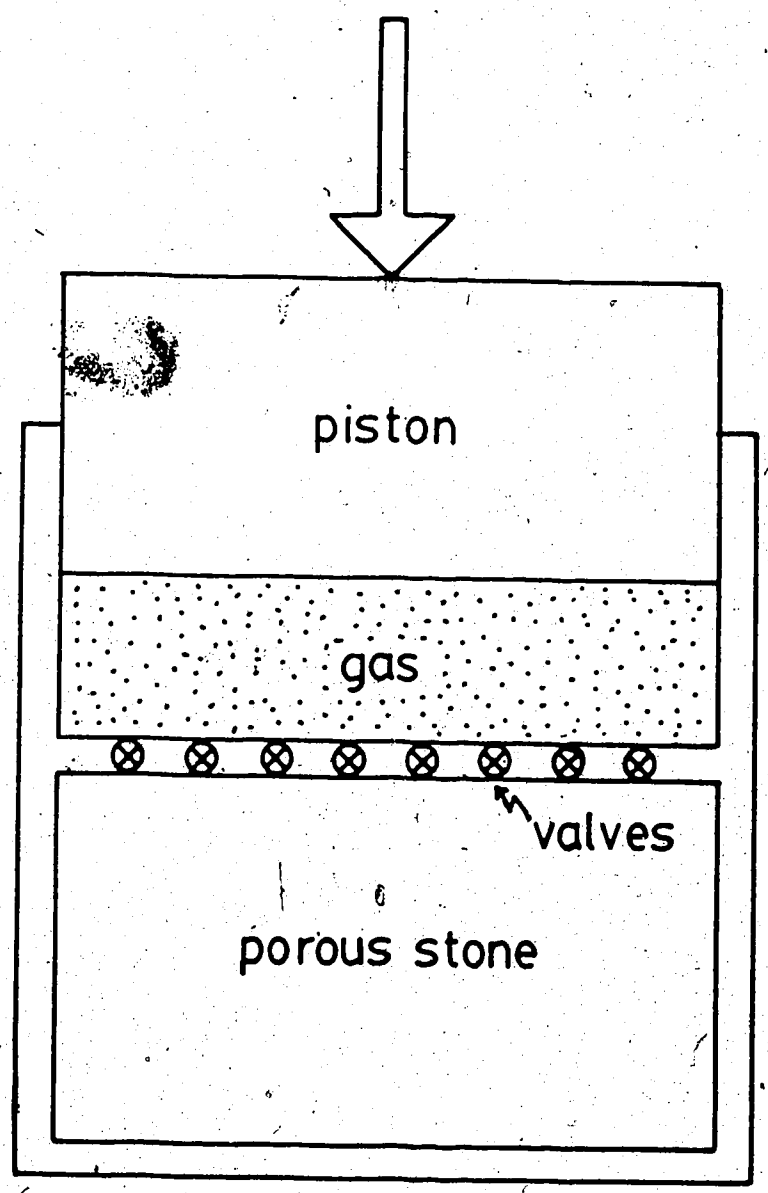

Figure 2.1 Piston and Porous Stone Analogy

molecules. The compressibility of this system is derived as follows:

$$\beta_F = -\frac{\epsilon_{VF}}{dP}$$

$$= -\frac{dV_F}{V_F dP}$$

$$= -\frac{d(V_L + V_{fg})}{V_F dP} \qquad [2.1]$$

where,

β_F = total pore fluid compressibility

ϵ_{VF} = total pore fluid volumetric strain

P = absolute pressure

V_F = total pore fluid volume

V_L = liquid volume

V_{fg} = free gas volume

Assuming that,

$$V_L = S\ V_F \qquad [2.2]$$

and,

$$V_{fg} = (1-S)\ V_F \qquad [2.3]$$

where,

S = degree of saturation of the liquid phase (assumed to be constant)

we have,

$$\beta_F = -\frac{S dV_L}{V_L dP} - \frac{(1-S) dV_{fg}}{V_{fg} dP} \qquad [2.4]$$

Assuming that the individual compressibilities of the liquid

and the gas phases are given by,

$$\beta_L = -\frac{dV_L}{V_L\ dP} \qquad [2.5]$$

and,

$$\beta_{fg} = -\frac{dV_{fg}}{V_{fg}\ dP} \qquad [2.6]$$

then, the combined total pore fluid compressibility, as given by Equation 2.4, can be rewriten in the form:

$$\beta_F = \beta_L S + (1-S)\beta_{fg} \qquad [2.7]$$

where,

β_L = gas free liquid compressibility

β_{fg} = free gas compressibility

The compressibilities of gas free water present in sea sediments and in Athabasca oil sands are presented in Figures 2.2 and 2.3.

Dodson and Standing, 1944, present compressibility coefficients for water at higher pore pressures. Figures 2.2 and 2.3 show that variations of gas free water compressibilities with pressure and temperature are relatively small.

Data published by Agar, 1984, indicate that the compressibilities of dead bitumen (no gas in solution) is very close to the gas free water compressibility.

The compressibility of the free gas phase, β_{fg}, can be readily derived from Robert Boyle's law. In 1662, Boyle verified experimentally that the volume of a gas at low density and constant temperature is inversely proportional

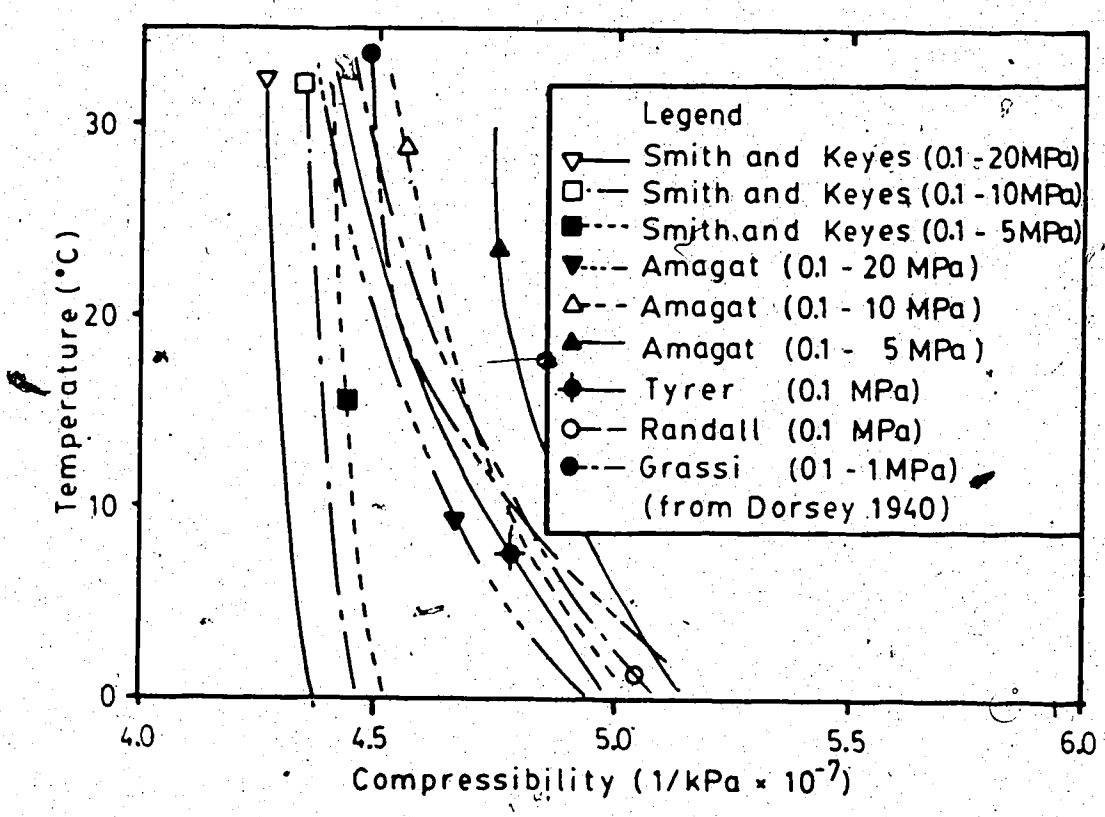

Figure 2.2 Isothermal Compressibility of Air Free Water - Modified from Fredlund, 1973

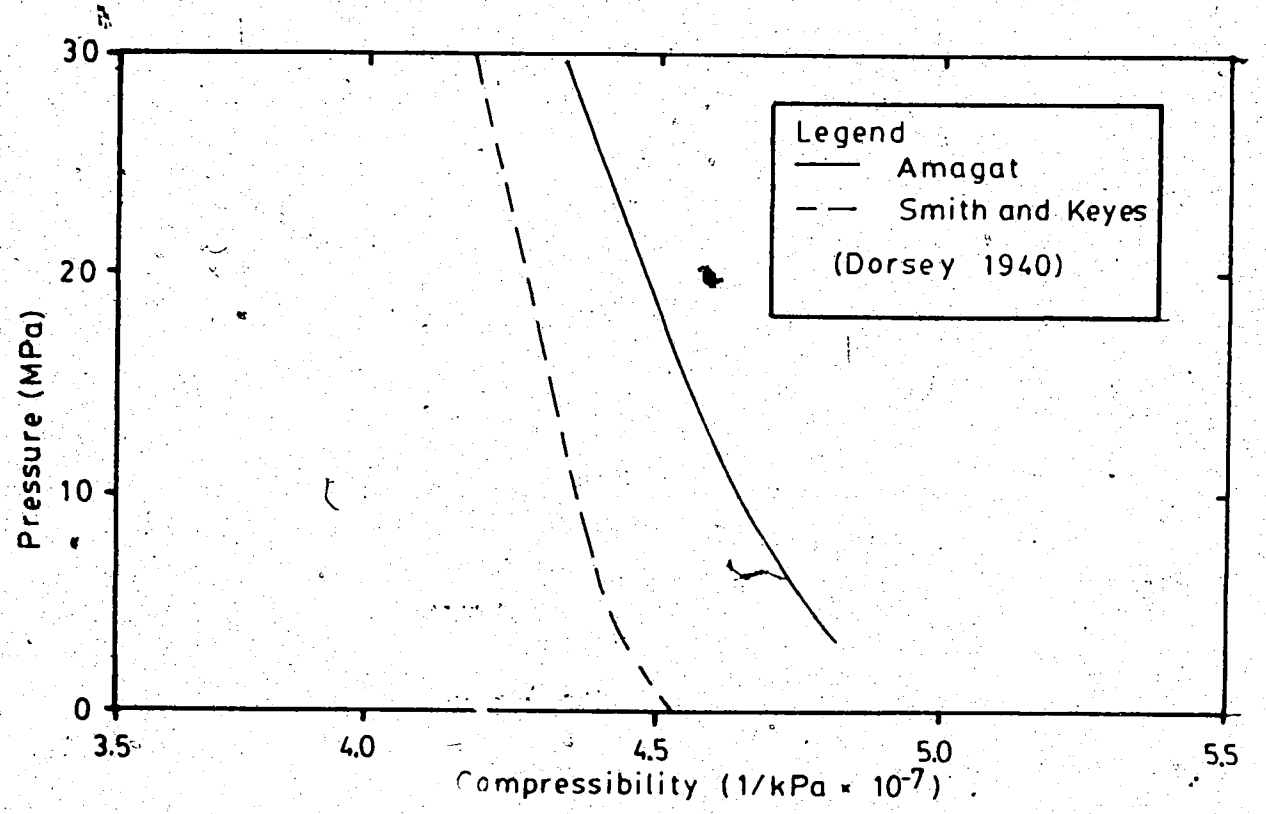

Figure 2.3 Effects of Pressure on Isothermal Compressibility of Air-Free Water - Modified from Fredlund, 1973

to the pressure

$$V = a\ (1/P) \qquad [2.8]$$

Brescia et al., 1970:22, discussed the limitation of the Boyle's law when applied to gases submitted to wider ranges of pressures. They stated that, in a real gas, the actual void space is less then the net volume of the container, since some of that volume is occupied by the gas molecules. In this case, the molecules act as if they were in a smaller container and they hit the walls of the container more frequently, which results in a greater pressure. Consequently,

$$P_{obs} > P_{Boyle}$$

where,

P_{obs} : observed pressure

P_{Boyle}: ideal gas pressure according to Boyle's law

Brescia et al. also pointed out that another reason for deviation from Boyle's law is that, in non-ideal gases, the molecules attract each other and they may stick together, even for a short period of time. In this case, the number of independent molecules in the sample, at one time, is actually reduced, resulting in a reduction of the observed pressure when compared to the one predicted by Boyle's law.

Equations of state relating P and V, that give better approximations of the behaviour of real gases, than that given by ideal gas laws, have been devised by some chemists. Silver and Nydahl, 1976, present several of these equations. Most of them measure the deviation from the Boyle's with the

compressibility factor

$$Z = \frac{PV_{measured}}{PV_{Boyle}} \qquad [2.9]$$

Silver and Nydahl, 1976, present in chart form the compressibility factor (Z) as a function of reduced pressures P_R and reduced temperature T_R, where

$$P_R = \frac{P}{P_c} \qquad [2.10]$$

and

$$T_R = \frac{T}{T_c} \qquad [2.11]$$

P_c and T_c are the highest values of pressure and temperature at which liquid and vapour can coexist in equilibrium, also called critical pressure and critical temperature respectively. They define the *critical point* in the thermodynamics *PVT surface*.

The compressibility factors of CH_4, H_2S, CO_2 and air, which are the gases most commonly encountered in the free state in gassy soils, are between [illegible] and 1.00, at *in situ* temperatures and pressures. This indicates that the use of Boyle's law result in errors lower than 1%. Brescia et al., 1970:23, confirm this assertion. Boyle's law can be used to derive the gas compressibility:

$$\beta_{fg} = \frac{dV_{fg}}{V_{fg}dP} \qquad [2.6]$$

According to Boyle's law:

$$PV_{fg} = (P+dP)(V_{fg}+dV_{fg}) \qquad [2.12]$$

$$dV_{fg} = \frac{PV_{fg}}{(P+dP)} - V_{fg}$$

$$= V_{fg}\left[\frac{P}{P+dP} - 1\right]$$

$$= V_{fg}\left[\frac{-dP}{P+dP}\right]$$

$$\frac{dV_{fg}}{V_{fg}} = \frac{-dP}{P+dP} \qquad [2.13]$$

Substituting Equation 2.13 in Equation 2.6:

$$\beta_{fg} = \frac{1}{P+dP} \qquad [2.14]$$

IMMISCIBLE FLUIDS - SEVERAL LIQUIDS AND GASES

In this case the valves that separate the free gas phase from the liquids phase are closed. The compressibility of this system is also evaluated according to Equation 2.7:

$$\beta_F = \beta_L S + (1-S)\beta_{fg} \qquad [2.7]$$

However the compressibility of liquids, β_L, is now evaluated as a function of the fraction of the total volume of the components of the liquid phase:

$$\beta_L = \frac{V_{LA}}{V_L}\beta_{LA} + \frac{V_{LB}}{V_L}\beta_{LB} + \ldots \qquad [2.15]$$

where,

V_{LA}, V_{LB} = volume occupied by the liquids

β_{LA}, β_{LB} = individual compressibilities of liquids A, B.

V_L is the total volume of the liquid phase : $V_{LA}+V_{LB}+\ldots$

The compressibility of the free gas phase composed by more than one type of gas is evaluated according to Equation 2.14. Boyle's law is equally valid for this case, being valid the remarks made in the previous section.
In this case, the total pressure of the gas phase, P, applied to the piston walls is the sum of the partial pressures, individually applied by each of the gas phase components,

$$P = p_a + p_b + \ldots \qquad [2.16]$$

This is Dalton's law of partial pressures, published in 1803 by John Dalton. This concept is required in the discussion of gas solubilities presented in the following

section.

MISCIBLE FLUIDS - ONE LIQUID AND ONE GAS

Consider again the simpler pore fluid composed of one type of liquid and one type of gas, but assume that the valves that separate the two phases of the piston-porous stone analogy are now opened.

In the gas phase the gas molecules are moving about in all directions. They frequently hit the contact between the gas phase and the porous stone. The gas molecules that are closer to the porous stone and directed toward its surface have the best chance to be "captured", being held by the attractive forces of the stone. Concurrently, molecules that have already been captured and are close to the surface have the best chance to escape to the free gas phase. Immediately after the imaginary valves are opened, the rate of molecules being captured by the porous stone is higher than the rate of molecules escaping from it, resulting in a volume decrease of the gas phase, associated with a downward movement of the piston.

A high net rate of molecules migrating from the gas phase to the porous stone is favoured by a decrease in temperature of the system and an increase in the pressure applied by the piston.

As time progresses, a condition will be reached in which the rates of gas molecules migrating to and from the porous stone will be equal. The processes of "capture" and

"escape" are still taking place but their rates are equal and there is no further net change of the volume of the gas phase. At this stage the porous stone is said to be saturated. The system is now said to be in *dynamic equilibrium*, or simply in *equilibrium*. Under this condition gas molecules are present in the gas phase (free gas) and in the liquid phase (dissolved gas).

If the pressure applied by the piston is further increased, the number of collisions of gas molecules with the porous stone surface is increased and the rate of gas molecule capture increases. This phenomenon continues, until another equilibrium condition is achieved.

The maximum quantity of solute (relative to the quantity of solvent) that will dissolve is the solubility. It increases with rising pressure.

The evaluation of the solubility of the gas in the liquid is required in order to calculate the compressibility of the system. This can be achieved with William Henry's law (1803)(Silver and Nydahl, 1976), that states that, in a dilute solution, the vapour pressure of the solute is approximately proportional to its mole fraction in the solvent,

$$p_B = K\, X_B \qquad [2.17]$$

where,

X_B = mole fraction of the gas in the liquid

$$X_B = \frac{n_{dg}}{n_{dg}+n_L} \qquad [2.18]$$

n_{dg} = moles of dissolved gas

n_L = moles of liquid

(The mole of any substance is associated with the number of molecules through the Avogadro's number, $N=6.02\times10^{23}$)

K = Henry's law coefficient (units of pressure)

p_B = partial equilibrium pressure necessary to keep n_{dg} moles of gas molecules in solution.

For dilute solutions, the partial pressure is also proportional to the mole ratio x_B, since for this condition $X_B \simeq x_B$, which leads to,

$$x_B = \frac{n_{dg}}{n_L} \qquad [2.19]$$

It follows from Henry's law that the number of moles of gas molecules that pass to the porous stone is directly proportional to the applied pressure. Assuming that the pressure applied by the piston increases from P_1 to P_2, then,

$$\frac{n_{dg1}}{n_{dg2}} = \frac{P_1}{P_2} \qquad [2.20]$$

where n_{dg1} and n_{dg2} are the moles of gas molecules dissolved at P_1 and P_2, respectively.

The volumes represented by these amounts of molecules in solution (V_{dg}) can be computed from the ideal gas law that results from Boyle's, Charle's and Avogadro's law

$$PV=nRT \qquad [2.21]$$

where R = gas constant = 0.0821 l.atm/°K.mole

Thus,

$$V_{dg1}= \frac{n_{dg1}RT}{P_1} \text{ (measured at } P_1) \qquad [2.22]$$

and

$$V_{dg2}= \frac{n_{dg2}RT}{P_2} \text{ (measured at } P_2) \qquad [2.23]$$

From Equations 2.20 and 2.23 it follows that:

$$V_{dg2}= \frac{n_{dg1}P_2RT}{P_1P_2}$$

$$= \frac{n_{dg1}RT}{P_1} \text{ (measured at } P_2) \qquad [2.24]$$

Equations 2.22 and 2.24 result:

$$V_{dg2} \text{ (at } P_2)= V_{dg1} \text{ (at } P_1) \qquad [2.25]$$

i.e, when measured at the current pressure of the solution (system), the volume of the dissolved gas is constant. Fredlund, 1973:60 and 61, and Fredlund, 1976:Appendix B, through a slightly different derivation came to the same conclusion. This conclusion allows one to express the

solubility of gases in liquids through the following:

$$V_{dg} = L\ V_L \text{ (measured at current P)} \qquad [2.26]$$

L being the Ostwald absorption coefficient. Ostwald also stated that the coefficient L is independent of pressure. He stated: "A liquid always dissolves the same volume of a given gas, independent of pressure".

Among geotechnical engineers, it has been common practice to refer to L as H, Henry's constant

$$V_{dg} = H\ V_L \qquad [2.27]$$

(Sobkowicz, 1982; Byrne et al., 1980; Chang and Duncan, 1983; Vaziri, 1986). This is probably due to pioneering geotechnical publications (e.g. Hilf, 1948 and Bishop, 1957) on the development of pore pressures in earth dams, that used this nomenclature.

Gerrard, 1980, devotes one chapter of his book on gas solubilities to a discussion about the several different ways that Henry's law is interpreted by chemists. Therefore it is not surprising that geotechnical engineers develop their own way to refer to this law. In order to avoid misinterpretation, the L and H coefficients used in Equations 2.26 and 2.27, respectively , are referred to here as the solubility coefficient, H, consistent with most geotechnical publications.

The limitations of applying the solubility relation above are summarized by Ostwald (Gerrard, 1980:6): "The assumption" (of proportionality between volume of dissolved gas and liquid) "however must remain fulfilled that the substance which is distributed undergoes no chemical change in one of the solvents."... "In general the smaller the solubility and the lower the pressure the more nearly do the laws approach actuality.".

Figures 2.4, 2.5 and 2.6 illustrate the solubility of methane, CH_4, and carbon dioxide, CO_2, in water and visually indicate the deviation from Henry's law. The more pronounced deviation from linearity is noticed for CO_2 in distilled water. This is confirmed by data published by Dorsey, 1940:541.

The data presented by Shinoda, 1978:43, also indicate deviation from Henry's law for nitrogen, N_2, and oxygen, O_2, in distilled water.

Svrcek and Mehrotra, 1982, presented experimental data of gas solubility for Athabasca bitumen and CO_2, CH_4 and N_2, at temperatures varying from 24 °C to 97 °C and pressures up to 10 MPa. The gas solubility was presented by the authors in terms of the volumetric solubility, which was defined as being the volume of gas at normal temperature (0°C) and pressure (101.325 kPa) (N.T.P.) per volume of saturated bitumen. The volumetric solubility relates to the previously defined solubility coefficient H as follows:

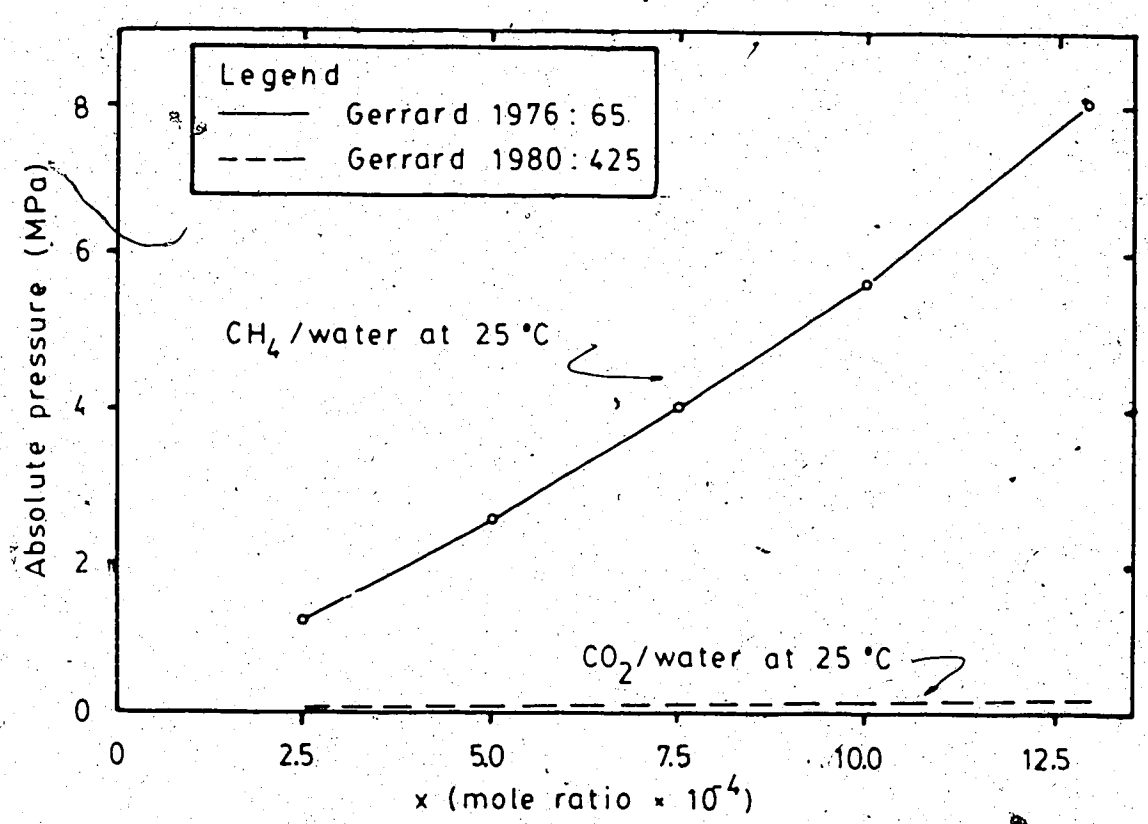

Figure 2.4 Solubility of Methane and Carbon Dioxide in Distilled Water

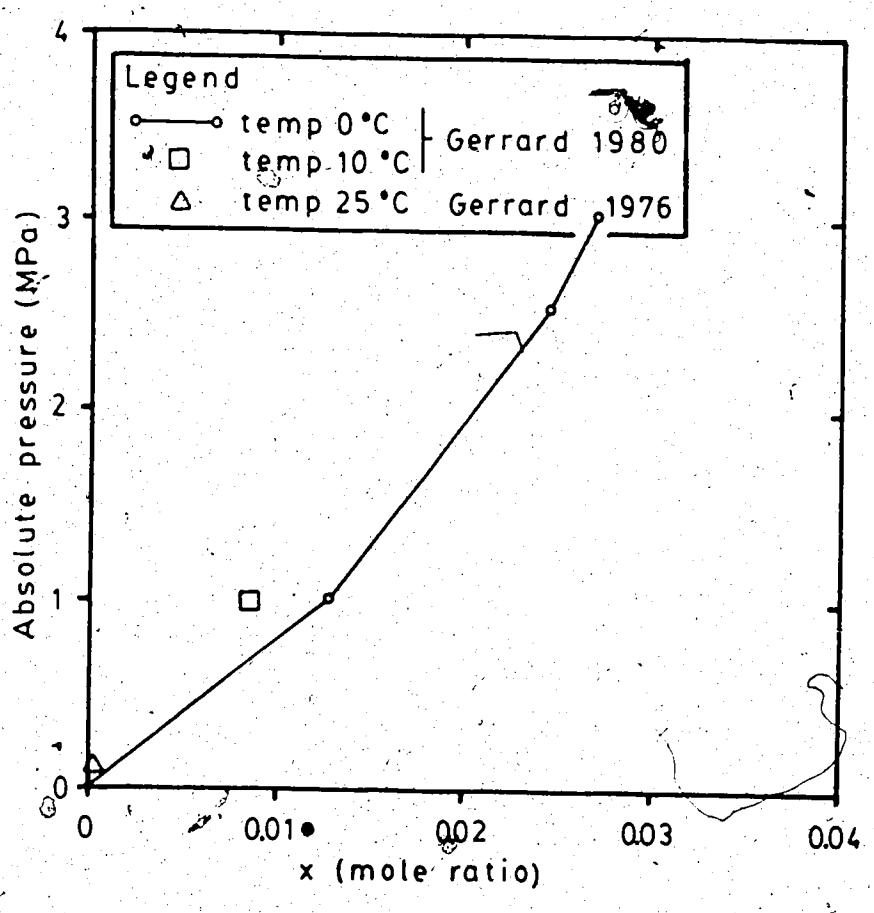

Figure 2.5 Solubility of Carbon Dioxide in Distilled Water

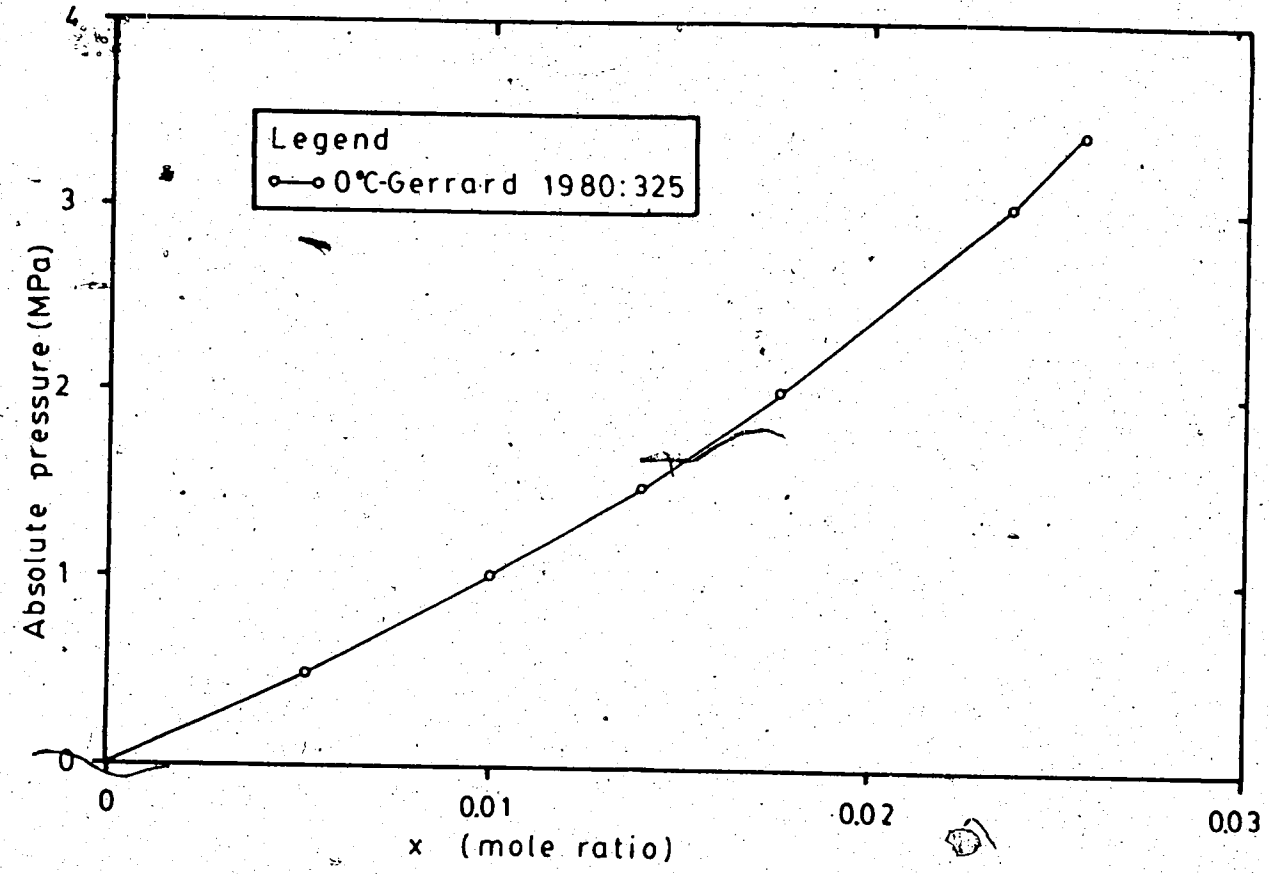

Figure 2.6 Solubility of Carbon Dioxide in Synthetic Sea Water

$$S_{ol} = \frac{V_{dg}|^{NTP}}{V_L}$$

$$= \text{volumetric solubility} \qquad [2.28]$$

according to the gas law,

$$S_{ol} = \frac{V_{dg}|^{NTP}}{V_L}$$

$$= \frac{V_{dg} P \; T_{NTP}}{V_L T \; P_{NTP}} \qquad [2.29]$$

where V_{dg} is the volume of dissolved gas measured at P and T which are the current pressure and temperatures.

According to the definition of solubility coefficient

$$H = \frac{V_{dg}}{V_L} \qquad [2.30]$$

Substituting 2.30 in 2.29,

$$S_{ol} = \frac{H \; T_{NTP} \; P}{T \; P_{NTP}} \qquad [2.31]$$

Figures 2.7 to 2.9 indicate that for the isothermal case, S_{ol} is linearly related to P for values of P lower than 5 to 8 kPa.

$$S_{ol} = \text{Constant} \times P \qquad [2.32]$$

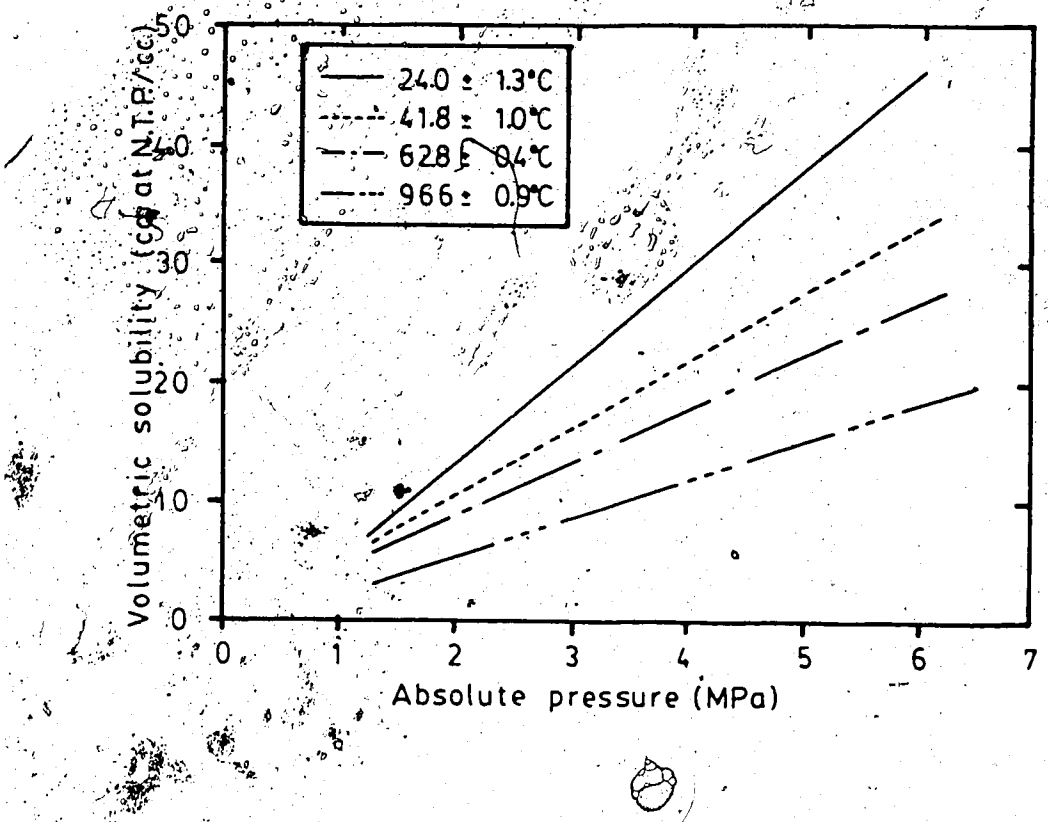

Figure 2.7 Volumetric Solubility of Carbon Dioxide In Bitumen - Modified from Svrcek and Mehrotra, 1982

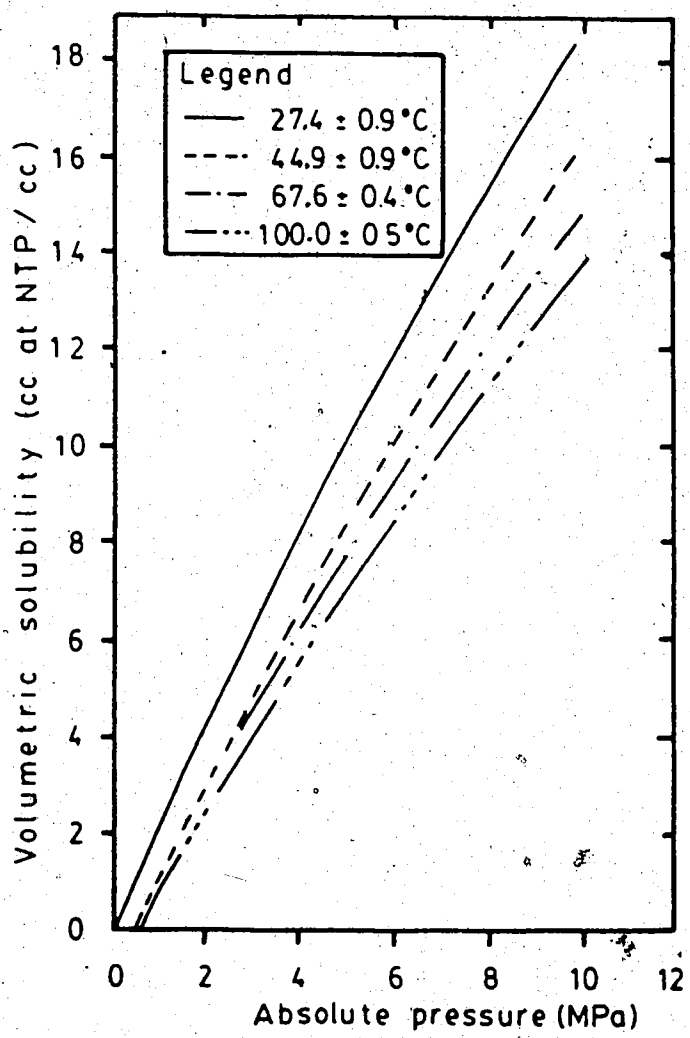

Figure 2.8 Volumetric Solubility of Methane in Bitumen - Modified from Svrcek and Mehrotra, 1982

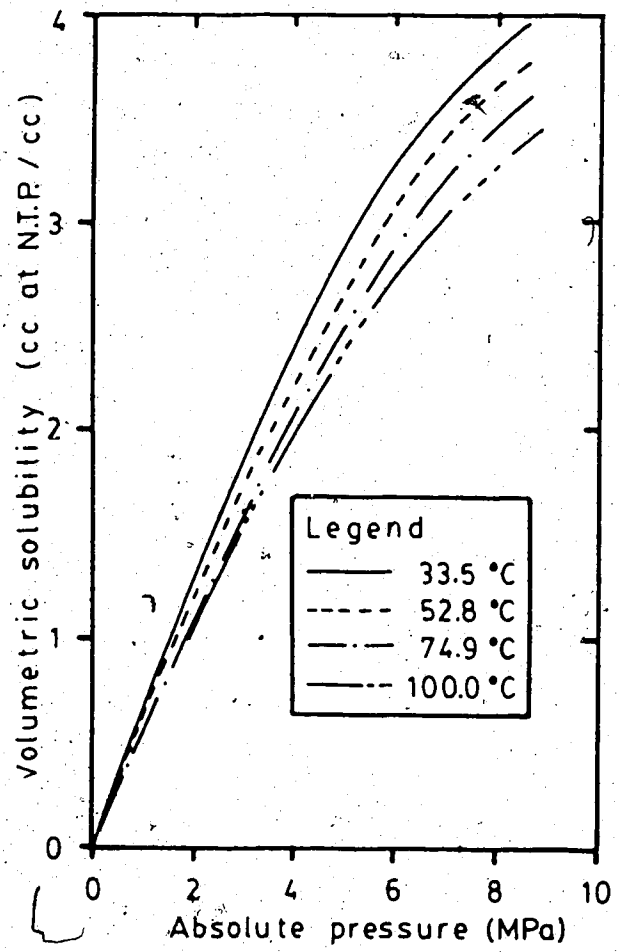

Figure 2.9 Volumetric Solubility of Nitrogen in Bitumen - Modified from Svrcek and Mehrotra, 1982

The combination of Equations 2.31 and 2.32 leads to the conclusion that, for the isothermal case, H is constant for CO_2, CH_4 and N_2, for pressures up to 5 to 8 MPa, i.e., Henry's law is applicable within these limits.

Based on laboratory tests, Mehrotra and Svrcek, 1982, presented equations that allow the evaluation of the solubility constants for CO_2, CH_4 and N_2 dissolved in bitumen.

The data published on solubility of some gases in water and bitumen allow one to conclude that, except for carbon dioxide dissolved in water, it is appropriate to assume the validity of Henry's law, as long as the pore fluid is not submitted to pore pressures higher than 5 to 8 MPa. Based on this assumption, the compressibility of the pore fluid composed of one gas and one liquid, both miscible, can be evaluated according to Equation 2.7.

The compressibility of the liquid phase is now affected by the presence of dissolved gases. Figure 2.10 presents the isothermal compressibilty of air saturated natural and sea water. The comparison of this figure with Figure 2.2 indicates that the presence of air does not significantly alter the compressibility of air-free water. Amyx et al., 1960:453 and 454, suggest that highly soluble gases result in increases in water compressibility of up to twenty percent (20 %).

Athabasca bitumen density measurements at varying pressures and temperatures and gas concentrations, carried

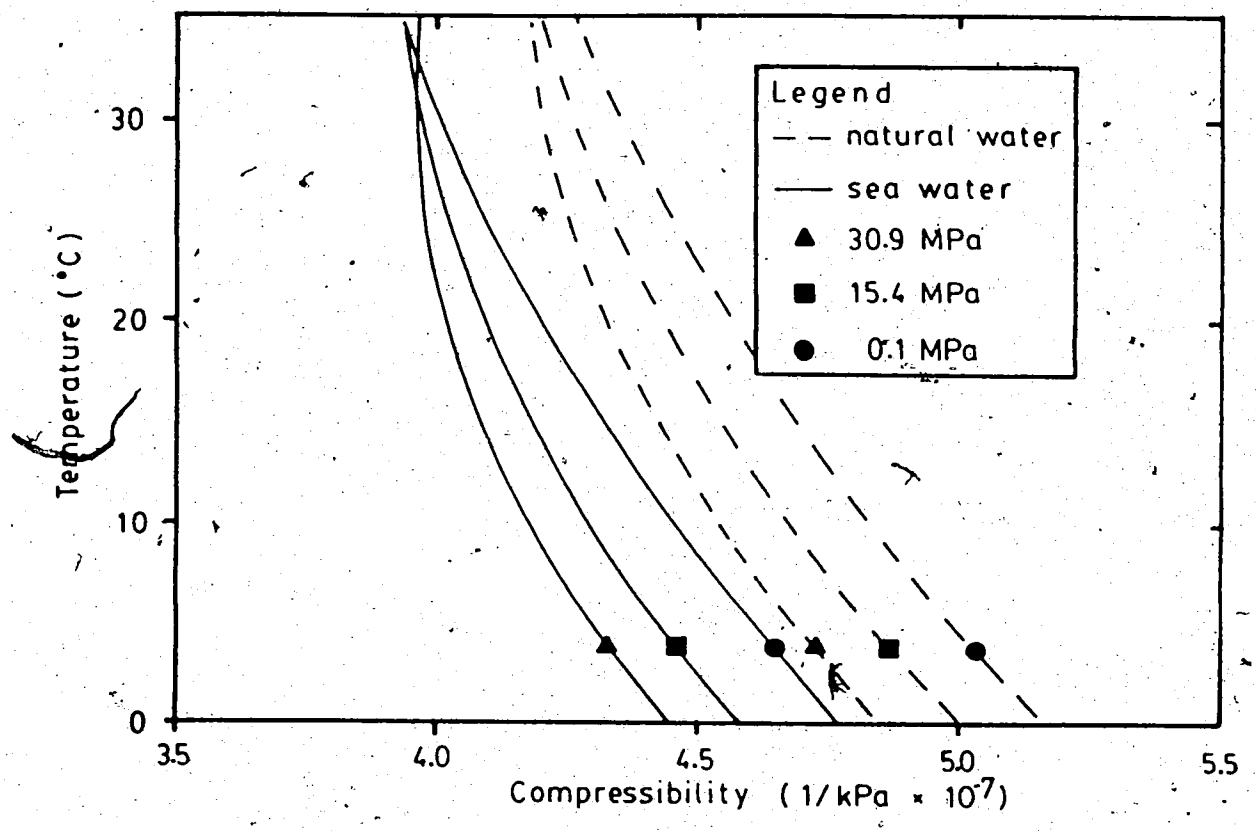

Figure 2.10 Isothermal Compressibility of Air Saturated Natural and Salt Water - Modified from Fredlund, 1973

out by Mehrotra and Svrcek, 1982, and Robinson et al., 1980, indicate that there is not a unique trend between these variables and compressibility. For pore pressure variations of up to 6 MPa, variations of the densisty of Athabasca bitumen of less than two percent (2%) were observed. Considering that the value of β_L is considerably smaller than β_{fg}, the aforementioned variability results in neglegible effects on β_f.

The compressibility of the free gas is expressed according to Equation 2.6

$$\beta_{fg} = - \frac{dV_{fg}}{V_{fg}dP} \qquad [2.6]$$

The total volume of gas is

$$V_{Tg} = V_{fg} + V_{dg}$$

$$= V_{fg} + HV_L \qquad [2.33]$$

$$dV_{Tg} = dV_{fg} \qquad [2.34]$$

Since the volume of dissolved gas remains constant, as demonstrated earlier in this chapter, it is possible to combine the free and dissolved phase and apply Boyle's law to the entire gas volume

$$dV_{Tg} = V_{Tg}\left[\frac{-dP}{P+dP}\right] \qquad [2.35]$$

and Equation 2.6 becomes

$$\beta_{fg} = \frac{V_{Tg}}{V_{fg}dP}\left[\frac{dP}{P+dP}\right]$$

$$= \frac{V_{fg}+HV_L}{V_{fg}}\left[\frac{1}{P+dP}\right]$$

$$= \frac{1-S+HS}{1-S}\left[\frac{1}{P+dP}\right] \qquad [2.36]$$

assuming S constant for the pressure increments.

Substituting 2.36 in 2.7 we have the compressibility of the fluid:

$$\beta_F=\beta_L S + (1-S+HS)\frac{1}{P+dP} \qquad [2.37]$$

In the limit, as dP approaches zero:

$$\beta_F= \beta_L S + \frac{(1-S+HS)}{P} \qquad [2.38]$$

where S and P are the values of saturation and pressure at the begining of the step under consideration.

MISCIBLE FLUIDS - ONE LIQUID AND MORE THAN ONE GAS

Returning to the piston and porous stone analogy, again with the series of valves between the gas and liquid phases opened, assume now that there is more than one type of gas in the free state. The process of "capture" and "escape" will take place at the porous stone, identical to the case

dynamic equilibrium is achieved. At this point, according to Henry's law the number of molecules in solution of each gas component is related to the partial pressure (and not the total pressure anymore) that the molecules of that specific gas component, in the free state, apply to the surface of the porous stone.

The partial pressure related to each gas component in the free state can be related to the total gas pressure according to Dalton's law:

$$p_{fg,i} = P\ y_i \qquad [2.39]$$

and

$$P = p_{fg,A} + p_{fg,B} + p_{fg,C} \ldots \qquad [2.17]$$

where

$p_{fg,i}$ = is the partial pressure of gas component i, in the free state

P = total pressure

$y_i = \frac{n_{fg,i}}{\Sigma n_{fg,i}}$ = mole fraction of gas i in the free state

$\Sigma\ y_i = 1$

According to Henry's law

$$p_A = K_A X_A \qquad [2.16]$$

Substituting 2.17 in 2.16,

$$P = K_A X_A + K_B X_B + K_C X_C \qquad [2.40]$$

Assuming,

$$P = K_{comb} X_{dg} \qquad [2.41]$$

where ,

K_{comb} = combined Henry's solubility constant

X_{dg} = mole fraction of the total dissolved gases

$$X_{dg} = \frac{\Sigma n_{dg,i}}{n_{dg}+n_L} \qquad [2.42]$$

Substitute 2.41 in 2.40,

$$K_{comb} X_{dg} = K_A X_A + K_B X_B + \ldots$$
$$= \Sigma K_i X_i \qquad [2.43]$$

Thus

$$K_{comb} = \frac{\Sigma K_i X_i}{X_{dg}} \qquad [2.44]$$

This expression can also be formulated in terms of the combined solubility coefficient H_{comb}. Assuming that each gas component can be treated independently of the other

ideal gas law becomes,

$$V_{dg,i} = \frac{n_{dg,i}RT}{p_i} \qquad [2.45]$$

and from Henry's law

$$p_i = K_i X_i \qquad [2.17]$$

where p_i, K_i and X_i are the absolute partial pressure, Henry solubility constant and total mole fraction of gas component i. Substituting 2.17 in 2.45,

$$V_{dg,i} = \frac{n_{dg,i}RT}{K_i X_i} \qquad [2.46]$$

But according to Equation 2.27,

$$V_{dg,i} = H_i V_L \qquad [2.27]$$

Substituting 2.27 in 2.46,

$$H_i V_L = \frac{n_{dg,i}RT}{K_i X_i} \qquad [2.47]$$

But,

$$X_i = \frac{n_{dg,i}}{n_{dg} + n_L} \qquad [2.48]$$

$n_{dg,i}$ = moles of gas i dissolved in liquid L

n_{dg} = total number of moles of all gases dissolved

n_L = moles of liquid

Substituting 2.48 in 2.47 and rearranging 2.47

$$K_i = \frac{(n_{dg} + n_L)RT}{H_i V_L} \qquad [2.49]$$

By analogy with 2.49 it follows that:

$$K_{comb} = \frac{(n_{dg} + n_L)RT}{H_{comb} V_L} \qquad [2.50]$$

where H_{comb} = combined solubility coefficient

Substituting 2.49 and 2.50 in 2.44

$$\frac{(n_{dg} + n_L)RT}{H_{comb} V_L} = (1/X_{dg}) \Sigma \left[\frac{(n_{dg} + n_L)RTX_i}{H_i V_L} \right]$$

$$\frac{1}{H_{comb}} = \frac{\Sigma (X_i/H_i)}{X_{dg}} \qquad [2.51]$$

Substituting 2.42 and 2.48 in 2.51, it results,

$$\frac{1}{H_{comb}} = \frac{\Sigma (n_{dg,i}/H_i)}{n_{dg}} \qquad [2.52]$$

$$H_{comb} = \frac{n_{dg}}{\Sigma (n_{dg,i}/H_i)} \qquad [2.53]$$

solubility coefficient of the solution once the solubility coefficient for each component in the liquid and the composition of the gas phase are known, at a condition of equilibrium.

The applicability of 2.53 is limited to the case where the solubility of each gas component is not affected by the presence of other gas components in solution. This limitation was introduced in the derivation through Equation 2.40.

The combined volumetric solubility of a mixture of free gases composed, in volume, of 17% of CO_2, 1% of CH_4 and 82 % of N_2 dissolved in bitumen was experimentally obtained by Mehrotra and Svrcek, 1982. It was verified that the volumetric solubility is approximately linearly related to to gas pressures up to 4 Mpa, confirming the applicability of Henry's law to certain gas mixtures up to this pressure level.

The laboratory tests performed by those authors, on the other hand, indicated that, for the specific solution tested, the assumption of non interference among dissolved gas particles is not appropriate. They verified that the volumetric solubility (Equation 2.28) of the solution obtained by the sum of the volumetric solubilities of each gas component, calculated at its associated partial pressure, can lead to errors of up to 115%.

occurred in the prediction of the individual component solubilities of CO_2 and N_2, whereas the prediction of the volumetric solubilities of CH_4 was considerably better, with errors lower than 20%. This might suggest that a gas mixture richer in CH_4, as opposed to the one tested by the authors, might involve errors in the evaluation of the combined volumetric solubility lower than those indicated. This may be the case for the Athabasca oil sands, where CH_4 is the major dissolved gas. Solubility tests for this material are discussed in the following section.

The conclusion from the discussion above is that the use of Equations 2.44 and 2.53 can lead to unacceptably large errors.

The knowledge of the combined solubility coefficient, H_{comb}, enables the evaluation of the compressibility of the pore fluids,

$$\beta_F = \beta_L S + \frac{(1-S+H_{comb}S)}{P} \qquad [2.54]$$

similar to the case of one liquid and one gas fluids. Equation 2.54 is valid for the condition of small variations in the degree of saturarion (S=constant).

MISCIBLE FLUIDS - MORE THAN ONE IMMISCIBLE LIQUID AND MORE THAN ONE GAS

In this case, the original piston and porous stone analogy is slightly modified, in order to simulate the

presence of a second immiscible liquid, as illustrated in Figure 2.11. The discussion is limited here to two immiscible liquids composing the liquid phase, since this is usually the maximum number of liquids encountered in most gassy soils.

Similar to other solutions discussed earlier in this section, the valves that separate the gas phase from the porous stone are opened and the gas molecules diffuse into the porous stone. As time progresses, a condition of equilibrium is achieved. At this stage, liquid L_1 and liquid L_2 are saturated with the gas components involved in this analysis. The pressure applied to the surface of both porous stones is P and is the result of the sum of individual partial pressures according to Dalton's law. The molecules of component i are held in solution in both liquids , L_1 and L_2, by the partial pressure $p_{fg,i}$.

In fact, this is a consequence of the principle of phase equilibrium in multi-components systems, that states that two phases are in equilibrium if, and only if, the vapor pressure of each component, common to the two phases, is the same for the two gases (Brescia et al., 1970:289, and Silver and Nydahl, 1976:396). This principle allows the evaluation of the combined solubility coefficient, for the case being studied, as a function of the individual components of the solution, as follows:

$$p_{fg,i} = \frac{n_{dg,i/L1} RT}{V_{dg,i/L1}}$$

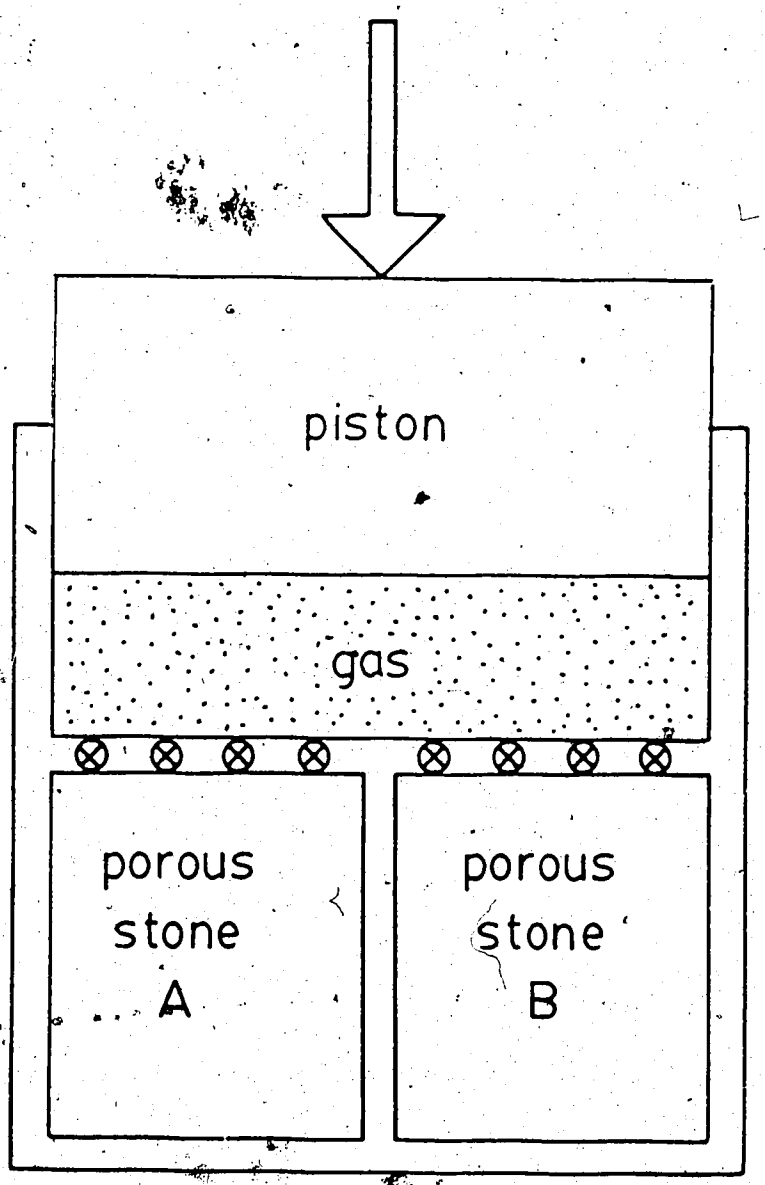

Figure 2.11 Piston and Porous Stone Analogy - Two Immiscible Liquids

$$= \frac{n_{dg,i/L2}RT}{V_{dg,i/L2}} \qquad [2.55]$$

where,

$n_{dg,i/L1}$ = moles of gas i dissolved in liquid L_1

$V_{dg,i/L1}$ = volume of gas i dissolved in liquid L_1, measured at $p_{fg,i}$

$p_{fg,i}$ = partial pressure of gas i in the gas phase.

Dalton's law yields:

$$P = \Sigma p_{fg,i} \qquad [2.16]$$

assuming that,

$$P = \frac{n_{dgTOT}RT}{V_{dgTOT}} \qquad [2.56]$$

where,

P = total pressure of the gas phase

$n_{dgTOT} = \Sigma n_{dg,i/L1} + \Sigma n_{dg,i/L2}$

n_{dgTOT} = total moles of gas dissolved in both liquids

Substituting 2.56 and 2.55 in 2.16

$$\frac{n_{dgTOT}RT}{V_{dgTOT}} = \Sigma \left[\frac{n_{dg,i/L1}RT}{V_{dg,i/L1}} \right] \qquad [2.57]$$

But, by definition

$$V_{dgTOT} = V_L H_{comb} \qquad [2.58]$$

and,

$$V_{dg,i/L1} = V_{L1} H_{i/L1} \qquad [2.59]$$

where

$V_L = V_{L1} + V_{L2}$ = total volume of liquids

H_{comb} = combined solubility coefficient

$H_{i/L1}$ = solubility coefficient of component i in liquid L_1

Thus Equation 2.57 becomes,

$$\frac{n_{dgTOT}}{H_{comb} V_L} = \Sigma \frac{n_{dg,i/L1}}{H_{i/L1} V_{L1}} \qquad [2.60]$$

In an enclosed system as the one being considered,

$$n_{dg,i/L1} + n_{dg,i/L2} = n_{dg,i/TOT} \qquad [2.61]$$

where,

$n_{dg,i/TOT}$ is the total number of moles of gas i in solution

Equations 2.55, 2.59 and 2.61 can be combined to yield,

$$n_{dg,i/L1} = n_{dg,i/TOT} \left[\frac{H_{i/L1} V_{L1}}{H_{i/L1} V_{L1} + H_{i/L2} V_{L2}} \right] \qquad [2.62]$$

Substituting 2.62 in 2.60,

$$\frac{n_{dgTOT}}{H_{comb}V_L} = \Sigma \left[\frac{n_{dg,i/TOT}}{H_{i/L1}V_{L1} + H_{i/L2}V_{L2}}\right] \qquad [2.63]$$

$$H_{comb} = \left[\frac{n_{dgTOT}}{V_L}\right] \left[\sum \left[\frac{n_{dg,i/TOT}}{H_{i/L1}V_{L1} + H_{i/L2}V_{L2}}\right]\right]^{-1} \qquad [2.64]$$

The latter equation shows that, with the knowledge of the total number of moles of gas molecules in solution, the composition of the mixture of gases and liquids, and the individual solubility constant of each gas component for each liquid, it should be possible theoretically to evaluate the combined solubility constant.

Here, once more, it is assumed that the solubility of one gas in solution is not affected by the presence of other gases in solution.

Peacock, 1988, tested Athabasca oil sands with average water and bitumen weight contents of 3% and 14%, respectively, saturated with CH_4 and CO_2, at 80% and 20% respectively. He concluded that the average solubility can be reasonably predicted from the individual solubility of each component.

With the knowledge of H_{comb}, the fluid compressibility can be evaluated according to Equation 2.65

$$\beta_F = \beta_L S + \frac{(1-S)H_{comb}S}{} \qquad [2.65]$$

In this case β_L relates to the combined isothermal compressibility of the two immiscible liquids, L_1 and L_2, according to Equation 2.15, previously derived in this

chapter

$$\beta_L = \frac{V_{L1}}{V_L}\beta_{L1} + \frac{V_{L2}}{V_L}\beta_{L2} \qquad [2.15]$$

Equations 2.15 and 2.65 allow evaluation of the fluid compressibility for the most general case of gassy fluids considered in this thesis.

The applicability of the coefficients of compressibility derived above is limited to cases where there are gas molecules in the free state, i.e., not in solution. There is a pressure, applied to the system by the piston, that drives all free gas into solution. This is called the *bubble point pressure* or *critical pressure*. For further increases in the piston pressure the compressibility of the system becomes equal to the compressibility of the liquid phase.

For an ideal solution of gases and liquids, i.e. a solution in which the presence of one gas component does not affect the dissolution of another gas component, Dalton's and Raoult's laws enable the evaluation of the bubble point pressure of the solution. This is done for a given solution composition, for a given temperature, and a given saturation pressure of each gas component dissolved individually in each pure liquid. This assessment was demonstrated by Silver and Nydahl, 1976. They concluded that the bubble point pressure is given by

$$\frac{1}{P} \Sigma P_i^0 Z_i = 1.0 \qquad [2.66]$$

where,

P = total pressure of the system

P_i^0 = saturation pressure of each individual component when separately dissolved in the pure liquid

Z_i = total mole fraction of component i in the solution (dissolved + free)

Field observations and laboratory tests (Peacock, 1988) have indicated that the bubble point pressure for the Athabasca oil sands is approximately equal to the *in situ* pore pressure.

From data presented in Esrig and Kirby, 1977, and Hulbert and Bennett, 1982, one can conclude that in marine sediments the bubble point pressure can be higher than the hydrostatic pore pressure and it varies from point to point in the ocean bottom.

2.2.2 Compressibility of Gassy Fluids - With Surface Tensions

The compressibility equations in the previous section were derived assuming that both the gas and the liquid phases are subjected to the same pressure. However this is a simplification of the real case, since the membrane that separates the two phases has physical and mechanical properties different from both phases and can affect its

compressibility (Fredlund, 1973).

Schuurman, 1966, and later Teunissen, 1982, derived the compressibility of an air/water mixture taking into account the existence of the interfacial membrane. In order to relate the air pressure inside the bubbles to the water pressure, they used Laplace's equation (Prigogine, 1964:147),

$$u_w = u_a - \frac{2q}{r} \qquad [2.67]$$

derived from the static equilibrium of an occluded bubble where,

u_w = pressure in the water (liquid) phase

u_a = pressure in the air (gas) phase (in the bubble)

q = surface tension between the water and air phases

r = radius of the bubble

The water is assumed to be incompressible ($\beta_L=0$) and the following relationship for the fluid compressility is obtained,

$$C_w = \frac{1}{V_a + V_w}\left[\frac{(V_{a0} + V_s)u_{a0}}{(V_a + V_s)^2} - \frac{2q}{3r_0 V_a}\left[\frac{V_{a0}}{V_a}\right]^{1/3}\right]^{-1} \qquad [2.68]$$

where, according to Schuurman's notation,

V_a = volume of air in the free state for air pressure u_a

V_{a0} = volume of air in the free state for air pressure u_{a0}

V_w = volume of water

V_s = volume of dissolved air

u_{a0} = atmospheric pressure

r_0 = radius of bubble equivalent to V_{a0}

In order to be consistent with the nomenclature used in this thesis, Equation 2.68 is modified to

$$\beta_{fg} = \frac{1}{V_{fg} + V_L}\left[\frac{(V_{fg0} + V_{dg})P_{atm}}{(V_{fg} + V_{dg})^2} - \frac{2q}{3r_0V_{fg}} \left[\frac{V_{fg0}}{V_{fg}}\right]^{1/3}\right]^{-1} \quad [2.69]$$

that can be further rearranged as,

$$\beta_{fg} = \frac{1}{V_{fg} + V_L}\left[\frac{P_{fg}}{(V_{fg} + V_{dg})} - \frac{2q}{3r_0V_{fg}} \left[\frac{V_{fg0}}{V_{fg}}\right]^{1/3}\right]^{-1} \quad [2.70]$$

Schuurman demonstrates that for the case where q=0 ($u_a = u_w$), Equation 2.70 transforms into the second term of Equation 2.38, that gives the compressibility of the fluid for an incompressible liquid.

Figures 2.12 to 2.15 depict the compressibility of water saturated with CO_2, and bitumen saturated with CH_4, respectively, for the case where the surface tension is considered or not in the calculations, and for two pore pressure levels (300 and 3000 kPa). These combinations simulate, in an approximate manner, the pore fluids of a marine sediment and a bitumen rich Athabasca oil sand.

The gassy soils considered in these figures are assumed to be initially at equilibrium, with the voids fully saturated with the liquid being considered, which in turn,

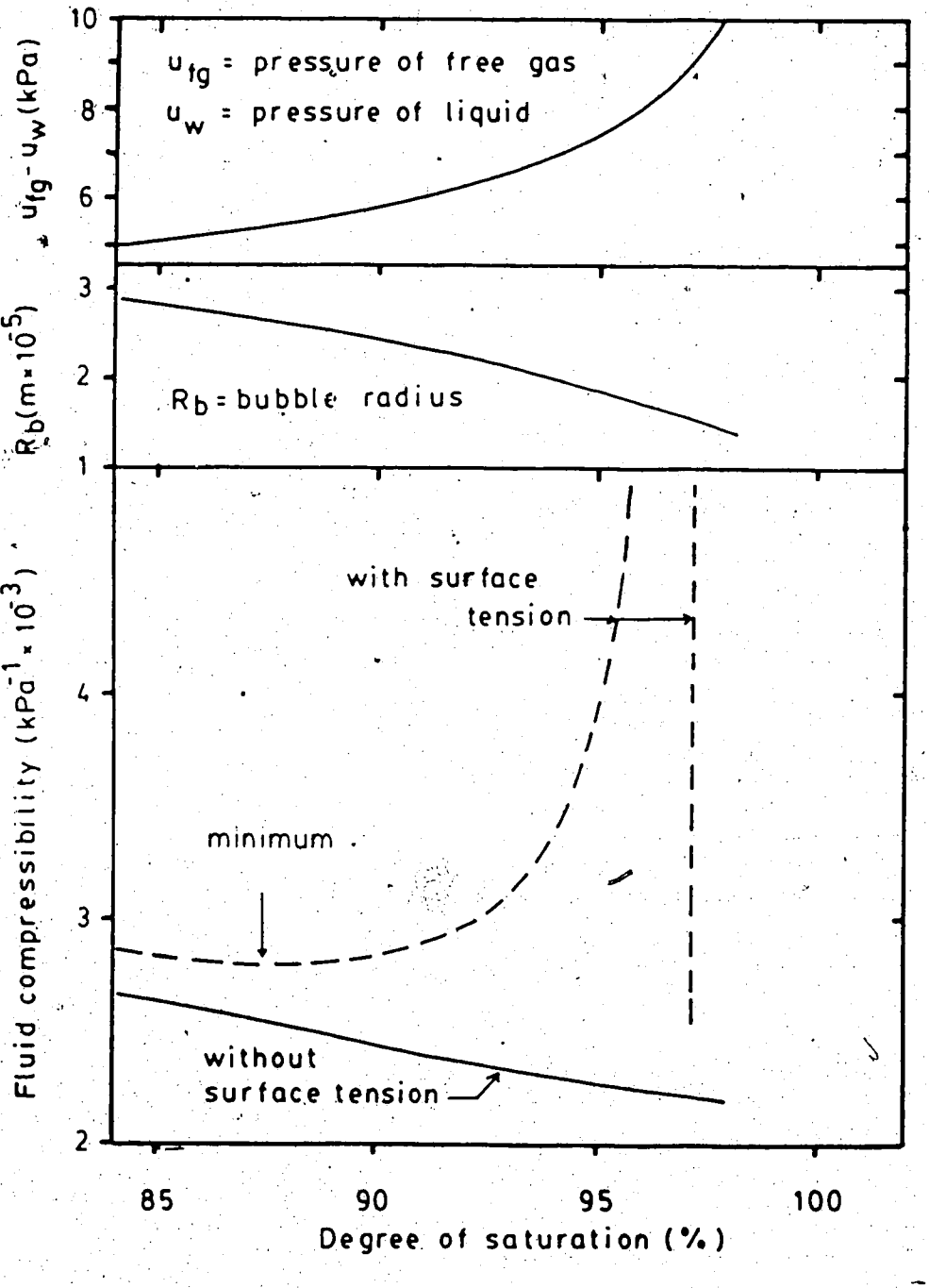

Figure 2.12 Compressibility of Pore Fluid Composed of Water and Carbon Dioxide - Initial Water and Gas Pressure = 300kPa

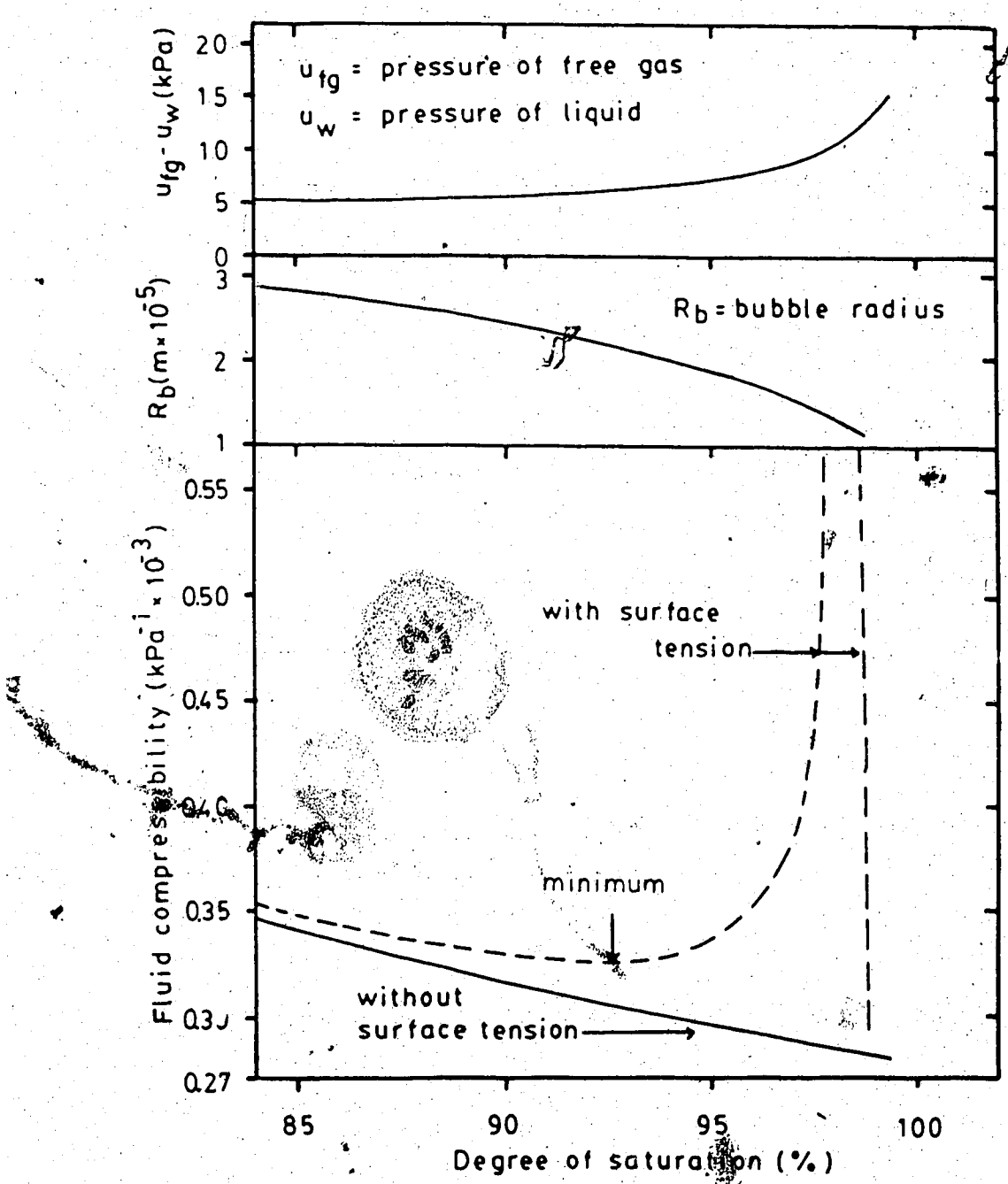

Figure 2.13 Compressibility of Pore Fluid Composed of Water and Carbon Dioxide - Initial Water and Gas Pressure = 3000kPa

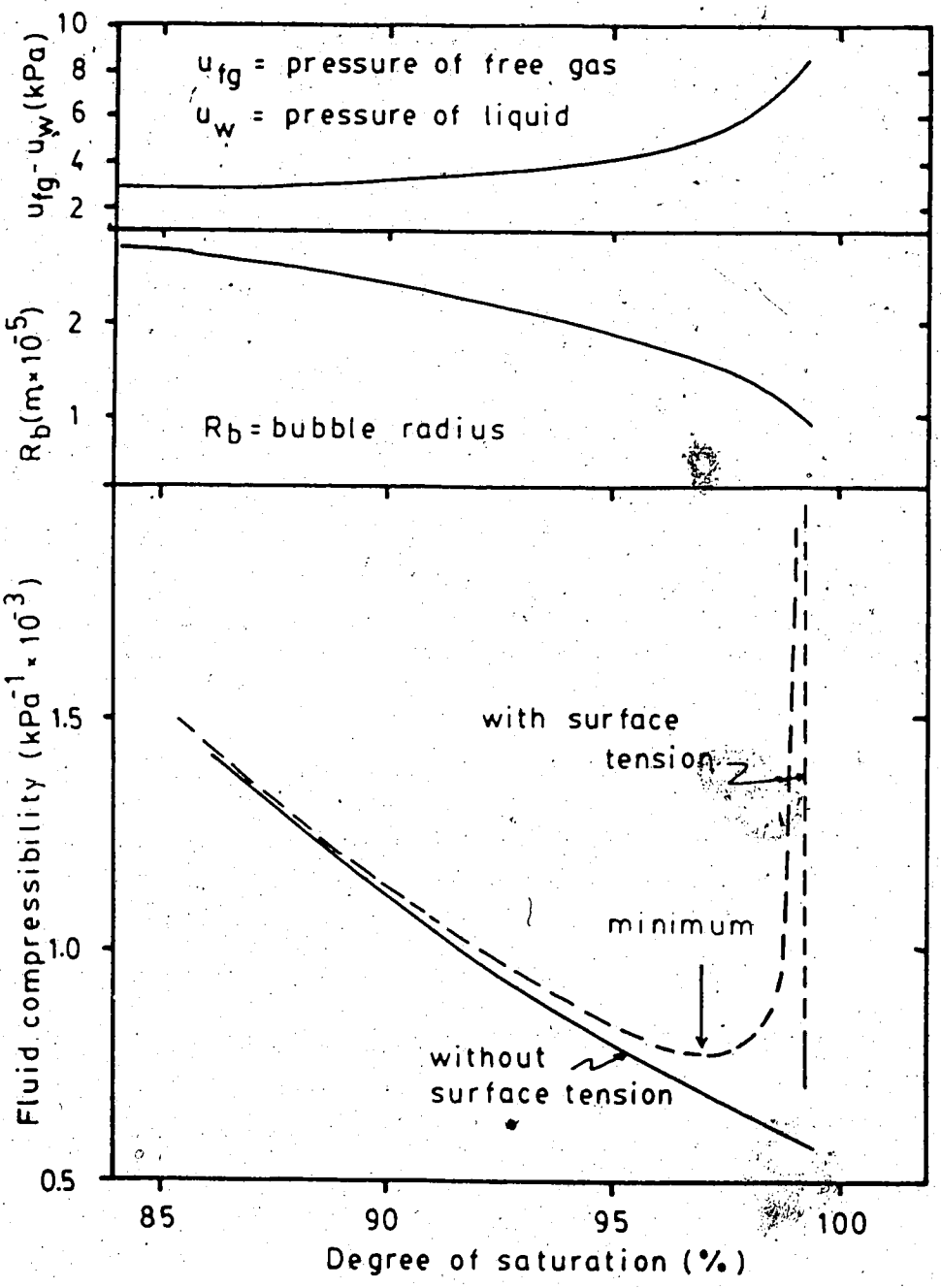

Figure 2.14 Compressibility of Pore Fluid Composed of Bitumen and Methane - Initial Bitumen and Gas Pressure = 300 kPa

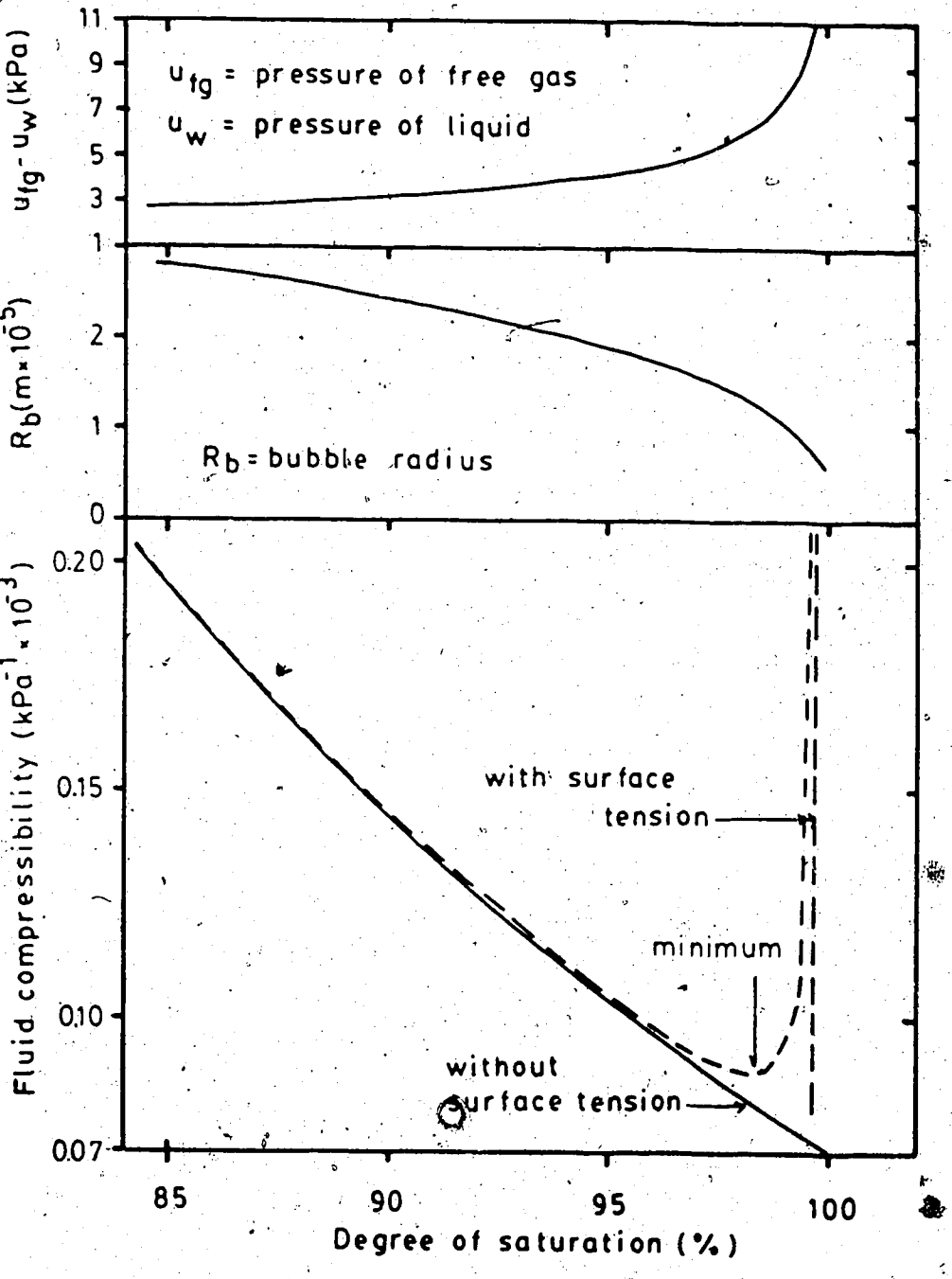

Figure 2.15 Compressibility of Pore Fluid Composed of Bitumen and Methane - Initial Bitumen and Gas Pressure = 3000 kPa

is also fully saturated with the corresponding gas. The calculations are carried out assuming that the pore pressure measured at the liquid phase drops from the initial value, to lower equilibrium values. For each pore liquid pressure, the compressibility of the fluid, the radius of the average bubble, the degree of saturation and the pore pressure inside the bubble can be evaluated.

Equation 2.70, derived from Schuurman and Teunissen works and used to obtain Figures 2.12 to 2.15, is restricted to the case where the bubbles are occluded. According to Sparks, 1963, this situation occurs only for degrees of saturation greater than 85%. In these cases the radii of the bubbles at equilibrium can be directly related to the surface tension and the degree of saturation. For non-occluded bubbles the surface tension is related to the minimum radius of the bubble, which may not bear any simple geometric relation with its volume and, consequently, with the degree of saturation.

More details about the construction of these figures are given in Appendix A.

Figures 2.12 to 2.15 indicate that, for degrees of saturation greater than 85%, the fluid compressibility when surface tension is considered, is slightly greater than when it is not considered. At this degree of saturation (85%), the difference in compressibility, accounting or not accounting for surface tension, increases with increasing solubility of the gas into the liquid and with decreasing

initial equilibrium bubble point pressures. In Figures 2.12 and 2.13, where CO_2 and water are the fluid constituents, the difference in compressibility values at S=85% is lower than 10% whereas this difference reduces to values lower than 1% for the other cases considered. However, by further inspecting Figures 2.12 and 2.13, and Tables A1 to A4 (Appendix A), one can observe that for S approaching 100%, β_{tens} (compressibility of fluid considering surface tension) increases rapidly, followed by a sharp drop, resulting in negative values, whereas $\beta_{no\ tens}$ (compressibility of fluid neglecting surface tension) decreases monotonically to zero.

According to Teunissen, 1982, unstable behaviour of the fluid, in the presence of surface tension, occurs at the critical pressure (bubble point pressure), when the bubbles collapse. This may occur in two different ways, depending upon which variable of the system is controlled: the fluid pressure or the fluid volume. For the fluid pressure controlled system, the free gas will dissolve suddenly, whereas for the volume controlled system, the fluid pressure will drop after reaching the critical pressure. The critical pressure is a bifurcation point, with an unstable branch for the volume controlled system and a stable one for the fluid pressure controlled system. This agrees with Schuurman's, 1966, comments that at the minimum points in the $\beta \times S$ curves, as indicated in Figures 2.12 to 2.15, the bubbles might have reached an unstable state of equilibrium, which cannot be described by the proposed formulation. Schuurman

suggested (Schuurman 1966:278, Figure 7) that from this point on, β_{tens} gradually approaches β_L, when S approaches 100%.

Assuming that, for degrees of saturation lower than those observed at the minimum points, (Figures 2.12 to 2.15), Schuurman's equation closely reflects reality, one can observe that the difference in the pore pressures measured in the liquid and in the gas phase is small when compared to the magnitude of the pore pressures involved in the calculations.

Fredlund, 1973 and 1976, presented the following formulation for the compressibility of a fluid where surface tensions are considered

$$\beta_F = S\beta_L + B_{av}\frac{(1-S)}{P_{fg}} + B_{av}\frac{SH}{P_{fg}} \qquad [2.71]$$

where,

$$B_{av} = \frac{dP_{fg}}{dP_L} \quad (< 1) \qquad [2.72]$$

and all other terms have the previously defined meaning. This equation was derived assuming the gas phase to be continuous inside the sample, thus, being valid for S smaller than 85%. The B_{av} values are determined experimentally. They are stress and wetting history dependent.

For the case where the bubbles are not connected (S>85%) Fredlund contends that $u_a=u_w$ and there is no interfacial tension present any more. According to him air and water pressures in a partly saturated soil cannot differ, apart from the inclusion of a solid medium. With this statement Fredlund questioned the validity of Schuurman's and Teunissen's compressibility equations. The reasoning that led him to this conclusion is described in Appendix A of his 1976 paper. Through a very simple model, that uses Boyle's, Henry's and Laplace's equations for the equilibrium of a bubble, Fredlund concluded that an occluded bubble, in the presence of interfacial tension, always collapses upon an increase of the fluid pressure. He reasoned that since laboratory tests show that soils exist in a stable condition at degrees of saturation higher than 85%, thus, with occluded bubbles, one can conclude that there is no surface tension in occluded bubbles and Laplace's equation cannot be applied to this case.

Sobkowicz, 1982:Chapter 5, through a comprehensive literature review on the behaviour of occluded bubbles, concluded that Schuurman's work was correct, lacking only the consideration of a critical radius of the bubble, below which the bubble cannot exist anymore and collapses, as recognized by Schuurman himself. Sobkowicz stated that Fredlund's statement about occluded bubbles was incorrect and ill-founded.

In fact, Fredlund's simple model of the behaviour of an occluded bubble, which led him to the conclusions above, is correct if one considers the equilibrium of a bubble in an infinite liquid.

The pioneering work by Gibbs, 1878, (Ward et al., 1982, 1984, 1985) and followed by Epstein and Plesset, 1950, and Keller, 1964 (Davies, 1964) indicates that if interfacial tensions are considered, a bubble cannot exist in an unbounded liquid, in a state of stable equilibrium. According to their formulation, there are five possible situations for this bubble in an unbounded liquid:

1) The solution is initially undersaturated

The bubble looses gas molecules to the liquid, decaying in size and disappearing.

2) The solution is just saturated

Due to the presence of interfacial tension, the bubble also decays in size and disappears. Theoretically, in the absence of interfacial tension, the bubble should remain in neutral equilibrium.

3) The solution is supersaturated with $r_0 = r_e$

r_0 and r_e are the initial and equilibrium radii of the bubble, respectively. In this case the bubble remains in unstable equilibrium.

4) The solution is supersaturated with $r_0 \leq r_e$

The bubble decays and disappears in a finite time, similar to items 1 and 2 above.

5) The solution is supersaturated with $r_0 > r_e$

The solution looses molecules to the bubble, and it grows indefinetely.

More recently, Tucker and Ward, 1975, expressed the critical radius in terms of the thermodynamic properties of the solution:

$$r_c = \frac{2\gamma_{lg}}{\eta P_{vap} + (C_2 P'/C_{2s}) - P'} \qquad [2.73]$$

$$\eta = e^{(\nu_1 (P' - P_{vap})/\kappa T} - C_2) \qquad [2.74]$$

where,

γ_{lg} = surface tension of the liquid/gas interface

P' = total pressure

κ = Boltzman constant

T = temperature

C_2 = gas concentration in the solution surrounding the bubble

C_{2s} = equilibrium gas concentration in the absence of the liquids vapor, at P' and T

ν_1 = specific volume of pure liquid (without dissolved gas)

P_{vap} = vapor pressure of the pure liquid.

If for given P', T and C_2 the bubble does not achieve the critical radius, it cannot reach unstable or stable equilibrium and it disappears at a finite time.

The validity of the above equations was experimentally checked by the authors, using oxygen (O_2) as solute and water as solvent.

Tucker and Ward, 1975, showed that the derivations by Epstein and Plesset, 1950, and Plesset, 1964, neglected the presence of vapour pressure inside the bubble. As a result, the prediction from their derivation would be that, unless the solution were oversaturated, all bubbles would dissolve. The Tucker and Ward experiments clearly showed that even for cases where C_2/C_{2s} is less than unity, the bubble can grow. Their equation and experiments show that due to the presence of the vapor term in Equations 2.73 and 2.74, in the presence of interfacial tension, there is a finite critical radius for C_2/C_{2s}, i.e., the bubble might not dissolve for $r_0=r_e$. The practical consequences of the theories developed for bubbles in an infinite liquid are of limited value when applied to gassy soils, since they cannot be directly applied to a confined pore space. As previously mentioned in this section, the extrapolation of the theories on behaviour of isolated bubbles, presented so far, to the pore space of a soil sample led Fredlund, 1973 and 1976, to debatable conclusions.

In the pore space of soils, the bubbles can nucleate and form at sites extremely close to each other. Due to this proximity, the liquid that surrounds each bubble has a limited capacity to exchange gas molecules. The result is that the growth or decay of a bubble occurs concurrently with a change in the saturation gas concentration of the surrounding liquid. This situation is analogous to the case of a bubble in a liquid of finite volume. Ward et al., 1982, studied the stability of bubbles in a closed volume of liquid/gas solution, and showed that for this boundary condition there exists a second equilibrium state, i.e. one in addition to that considered by Gibbs and that this second state is a stable equilibrium state. The following illustrates their conclusion. Ward et al., opt. cit., derived the relationship between the bubble radius, r, and the critical radius, r_c, for given values of the total number of moles of the gas component (N_2), the total number of moles of the solvent (liquid) component (N_1), the pressure in the liquid phase (P') and the temperature (T):

$$r_c = \frac{2C_s\chi}{C_{01}P'}\left[N_1 - \frac{4\pi\eta P_- R^3}{3\kappa T}\right]\left[N_2 - \frac{4\pi R^3}{3\kappa T}\left(P' - \eta P_- + \frac{2\gamma}{R}\right) - \right.$$

$$\left. - \frac{C_s}{C_{01}}(1-(\eta P_-/P'))\left(N_1 - \frac{4\pi\eta P_- R^3}{3\kappa T}\right)\right]^{-1} \qquad [2.75]$$

where,

C_s = saturation concentration of the gas in the liquid phase, and for a weak solution:

$$C_3 = \frac{C'_1 P}{K_H} \qquad [2.76]$$

K_H = Henry's law constant

C'_1 = Concentration of the liquid in the liquid phase

γ = interfacial tension between liquid and gas phases

C_{01} = density of the pure liquid

$$\eta = e^{(\nu_0(P'-P_-)/\kappa T - C'_2/C'_1)} \qquad [2.77]$$

ν_0 = specific volume of the pure liquid

P_- = saturation or vapor pressure of the pure liquid

κ = Boltzman constant

C'_2 = concentration of gas molecules in the liquid phase (n_{dg}/V_L)

Figure 2.16 illustrates the variation of the critical radius with the radius (according to Equation 2.75) of a single bubble immersed in a 1.0 cc water/nitrogen solution at 25 °C and 101.325 kPa, as obtained by Ward et al., 1982. Three curves are shown in this figure, each of them plotted for different total gas contents: N_{2m}, $N_2^{(1)}$ and $N_2^{(2)}$. According to the authors' derivation the equilibrium of a bubble is only possible if its radius is equal to the critical radius. The dashed line in this figure indicates the points where this condition is satisfied. The intersection of this line with the curves given by Equation 2.75 represents possible equilibrium states for this system. Hence, for the case with the smallest total number of gas molecules, associated with the curve labelled $N_2^{(2)}$, there are no possible equilibrium

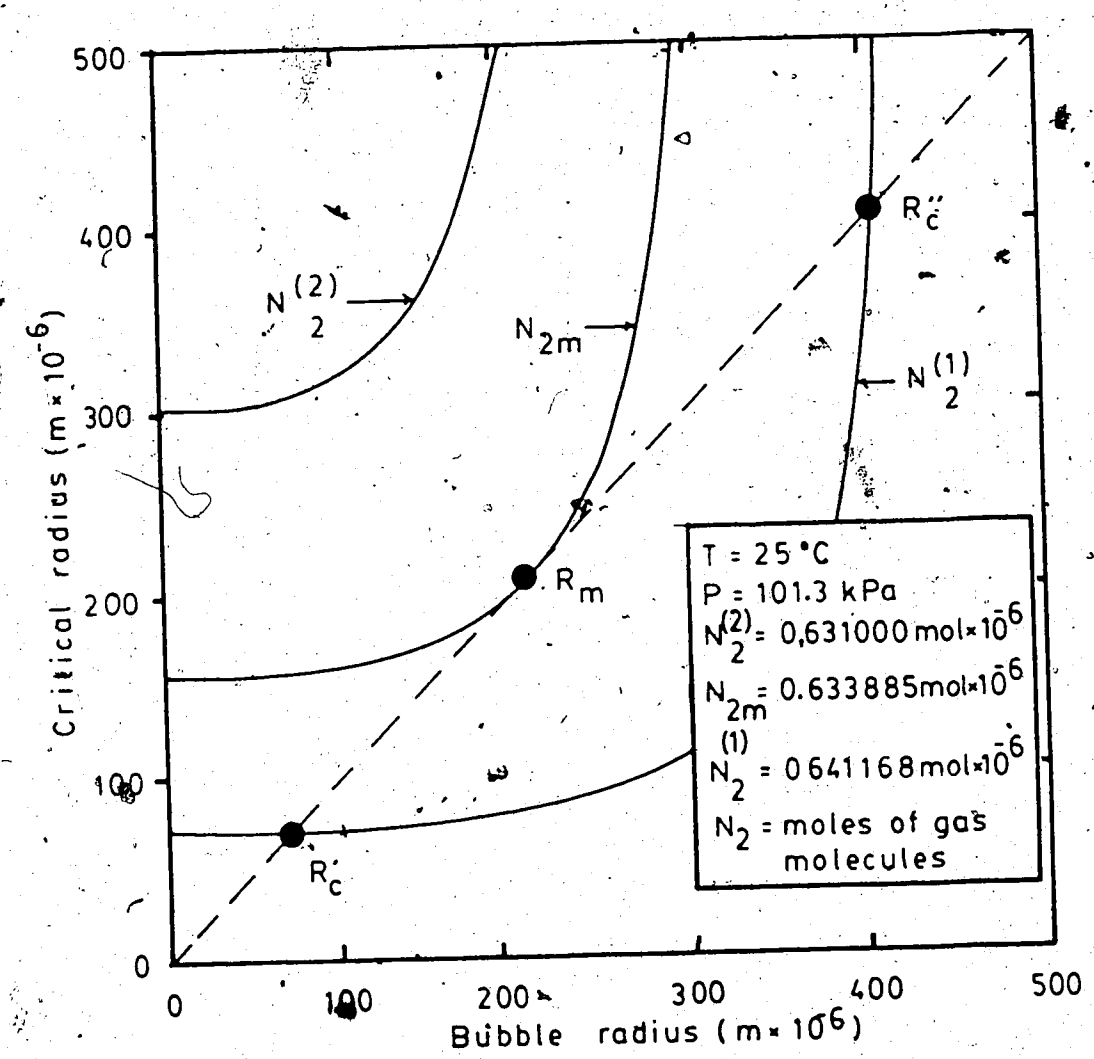

Figure 2.16 Critical Radius Versus Bubble Radius of a Single Bubble Immersed in a 1cc Water/Nitrogen Solution (Modified from Ward et al., 1985)

states. The figure shows that if N_2 is smaller than a minimum number, N_{2m}, a bubble cannot exist. For $N_2 = N_{2m}$, $R = R_m$, the existence of a bubble is possible and there is only one possible equilibrium state.

For $N_2 > N_{2m}$, the existence of a bubble is possible and there are two possible equilibrium states associated with the critical radii, R'_c and R''_c, as indicated in the figure.

The analysis of the state of equilibrium associated with the radii, R_m, R'_c and R''_c is possible by considering situations in which the bubble under consideration, initially at equilibrium, with a radius equal to R_c (critical radius), is perturbed. The perturbation results in the modification of the radius of the bubble.

For example, if the initial equilibrium radius is R'_c and the perturbation results in a decrease in the radius of the bubble, according to Figure 2.16, this new radius is larger than the new equivalent critical radius. Thus, gas molecules are transferred from the bubble to the liquid, leading to a further reduction in bubble size. This situation is clearly an unstable one, in which the bubble continuously decreases in size and collapses. A similar analysis could be done for the other points of equilibrium, R''_c and R_m.

Ward et al., 1982, carried out this analysis and concluded that points R_m and R'_c represent conditions of unstable equilibrium, whereas point R''_c represents a condition of stable equilibrium. The authors verified the validity of Equation 2.75 through a series of experiments where water

and nitrogen were used as solvent and solute, respectively, in a closed container. Their conclusion agreed with the previous work by Mori et al., 1977, that testing a mixture of non-condensable gases (N_2, O_2, CO_2) dissolved in Freon 21, also verified the possibility of the existence of a bubble, in stable equilibrium, in the presence of surface tension. Ward et al. further extended their equations to the case where more than one bubble is present in a closed volume of liquid. They concluded that the greater the number of bubbles, the smaller the minimum radius required for stable equilibrium of these bubbles. This conclusion has a major impact on the behaviour of gassy soils where a great number of bubbles is likely to exist. In this case, the bubbles occupying the pores might exist in stable equilibrium at extremely small radii. The papers by Ward el al., 1983, and Ward and Levart, 1984, on the stability of bubble nuclei, in solid surfaces contacting a liquid/gas solution of finite volume, indicate that gas bubbles are not spherical when they nucleate in the presence of rough surfaces, as is the case of soils. By modelling the solid surface roughness through a collection of conical pits, the authors mathematically described the growth of bubbles which are observed to nucleate at the apex of the pit (Griffith and Wallis, 1982, cited by Ward et al., 1983:1841 and Harvey, 1951), growing outwardly, as illustrated in Figure 2.17.

They showed that, as for the spherical bubbles, the bubble can exist inside the conical pit, in a condition of

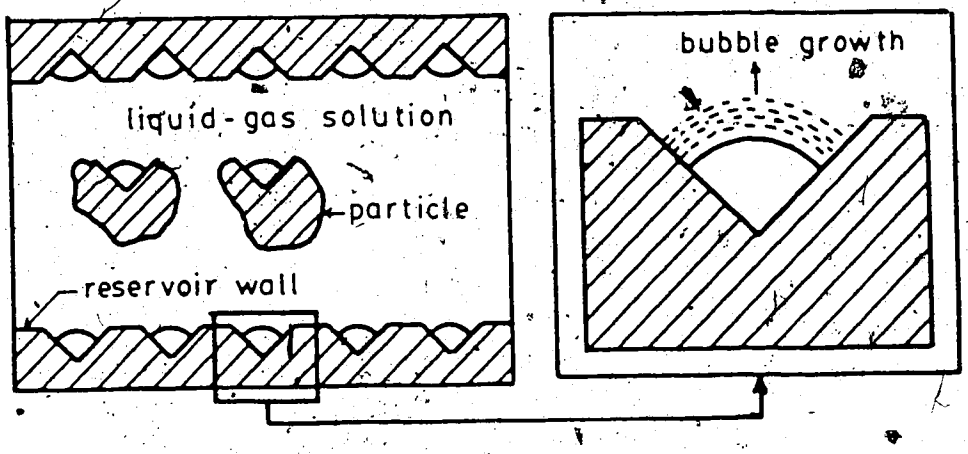

Figure 2.17 Bubble Growth in the Surface of Container or in the Surface of Particles Suspended in a Gas-Liquid Solution - Modified from Ward and Levart, 1984

stable equilibrium, with a critical radius given by the expression:

$$r_c = 2\gamma_{lg}(q_c V^B K_H + N_1 KT - q_c \eta P_- V^B) \times$$

$$\times \left[(\eta P_- - P') \ (q_c V^B K_H + N_1 KT - q_c \eta P \ V^B) + K_H KT N_2 \right]^{-1} \qquad [2.78]$$

where,

N_1 and N_2 = total number of liquid and gas molecules respectively in the system

q_c = number of conical pits

V^B = volume of a bubble nucleus

All other variables have the same meaning as before.

Upon a continuous decrease in the liquid pressure, the bubble grows out of the pit, eventually leaving and transforming itself into an occluded bubble, surrounded by the liquid solution.

The work on the equilibrium of gas bubbles in a liquid/gas solution indicates the complexity of the approximate evaluation of the compressibility of gassy fluids discussed previously. The equations presented in this section, when applied to the pore fluids of a gassy soil, clearly indicate that the unknowns of the problem, such as number of bubbles, volume and shape of roughness are numerous and impossible to accurately estimate in practice. This fact along with the works by several authors, described in this section, allow the following conclusion to be drawn:

- For degrees of saturation greater that 85%, the bubbles in the pores are not interconnected. Neglecting of the interfacial tensions in the calculations of fluid compressibility can result in errors up to 10% in high solubility gas-liquid solutions, such as CO_2 and H_2O. On the other hand, neglegible errors may be found in low solubility gas liquid solutions, such as CH_4 and bitumen, when compared to Schuurman's solution.

- For degrees of saturation smaller than 85%, the bubbles are interconnected. When the effects of interfacial tensions are neglected in the evaluation of the fluid compressibility, the errors that can result are theoretically unknown. Laboratory experiments have shown, however, that the larger the degree of saturation is, the smaller the interfacial tensions are and, consequently, the smaller are the errors involved in disregarding its effects.

Considering that in most geotechnical problems related to gassy soils, the soil is found with high degrees of saturation, the equations developed in Section 2.1.1, for fluid compressibility without surface tensions are valid for all practical purposes.

2.3 Time-dependent Behaviour of Gassy Fluids

As a result of pressure changes in a gassy fluid, assumed to be initially in equilibrium, it can be observed that the fluid shows an instantaneous volume change, governed by time-independent processes, and, as time progresses, under a constant pressure, it presents a time-dependent volume change, governed by pressure independent processes.

The time-independent processes are basically pressure-dependent and can be described by an equation of state and the solubility laws described earlier in this chapter.

In the preceding section, the relationship between changes in pore pressure and changes in the volume of gassy fluids were evaluated on the assumption that the time-dependent processes, associated with the decay or growth of the volume of the fluid, had ceased and a condition of equilibrium had been achieved.

In this section, these transient processes are examined and their effects on the mechanical response of gassy fluids are analysed.

The existing modelling techniques used to simulate the physical phenomena that cause the time-dependent response of gassy fluids, upon undrained stress changes, can be classified in two categories: the microscopic technique and the macroscopic technique.

In the microscopic technique the time-dependent response is expressed in terms of fundamental thermodynamic properties of the fluids.

In the macroscopic technique the time-dependent response is expressed in terms of non-fundamental variables. The following sections describe the models that fall into these categories.

2.3.1 Fundamental Gas Evolution Models

The dominant physical processes that are thought to control the time dependent volume change of gassy fluids are:

- Bubble nucleation or "birth" of bubbles, and
- Bubble sorption in a liquid.

These phenomena are inspected below.

BUBBLE SORPTION

With the help of the piston and porous stone analogy, it has been shown that, upon an instantaneous drop in the pressure applied by the vertical piston, when the valves separating the gaseous phase from the porous stone are opened (miscible fluids), a process of gas molecules transfer between these two phases is initiated. Upon examination, it becomes apparent that immediately after the application of the change in piston load, the mechanical response of the system is identical to the case where the valves are closed and the system models the behaviour of

immiscible fluids. The compressibility of the fluids can be evaluated through Equation 2.7,

$$\beta_F = \beta_L S + (1-S)\beta_{fg} \qquad [2.7]$$

where the variables, previously defined, refer to the equilibrium state prior to the application of the piston load.

With time, the migration of gas molecules from the porous stone to the gaseous phase results in an upward movement of the piston, with an increase in volume of the fluid system. Since we have considered here that the pressure applied by the piston is constant, the increase in volume of the gas phase results in an increase in the compressibility of the system.

Based on this conceptual model and assuming the fluid incompressible, the combined compressibility of the total pore fluid (β_F) can be evaluated as follows,

$$\beta_F = \frac{-dV_{fg}}{V_F^0 dP} \qquad [2.6]$$

where,

$$dV_{fg} = dV_{fg}(\text{immediate}) + dV_{fg}(\text{transient}) \qquad [2.79]$$

dV_{fg}(immediate) can be expressed by Equation 2.13

$$dV_{fg}(\text{immediate}) = V^0_{fg}\left[\frac{-dP}{P+dP}\right] \qquad [2.13]$$

and,

$$dV_{fg}(\text{transient}) = dV_{fg}\Big|_{t0}^{t1}$$

$$= \int_{t0}^{t1} \dot{V}_{fg}\,dt \qquad [2.80]$$

$\dot{V}_{fg} = dV_{fg}/dt$ = rate of change in volume of free gas due to time-dependent processes.

Substituting 2.13, 2.80 and 2.79 in 2.1, and assuming the pore liquids incompressible:

$$\beta_F = \frac{V^0_{fg}}{V^0_F(P+dP)} - \frac{\int_{t0}^{t1}\dot{V}_{fg}\,dt}{V^0_F dP} \qquad [2.81]$$

Except for the rate term in the volume of free gas, all other terms in Equation 2.81 are known for an equilibrium condition, prior to changes in the piston load.

The time dependent change in bubble volume has been the subject of extensive and detailed studies related to the thermodynamics of weak gas/liquid solutions.

Westwater, 1964, pointed out that three regulatory mechanisms are evident in the rate of growth of a bubble:

1) Mechanical forces, described by the force balance equation in spherical coordinates (body forces are not considered):

$$R\frac{d^2R}{dt^2} + \left[2 - \frac{\epsilon}{2}\right]\left[\frac{dR}{dt}\right]^2 + \frac{2\sigma}{\epsilon\rho_L R} + \frac{4\mu_L}{\rho_L R}\left[\frac{dR}{dt}\right] = \frac{p_v + p_i - p_\infty}{\epsilon\rho_L} \qquad [2.82]$$

where:

R = bubble radius

t = time

$e = (\rho_L - \rho_v)/\rho_L$

ρ_L = density of liquid

ρ_v = density of vapour phase

α = surface tension

μ_L = viscosity of liquid

p_v = partial pressure of vapour in bubble

p_∞ = vapor pressure of liquid

Notice that the time-independent version of this equation reduces to Laplace's mechanical equilibrium of an occluded bubble previously referred to in this chapter.

2) Transfer of heat, described by the heat balance equation:

$$\frac{Q}{\rho_L C_L} + a_L\left[\frac{\delta^2 T}{\delta r^2} + \frac{2\delta T}{r\delta r}\right] = \frac{\delta T}{\delta t} + \frac{\epsilon R^2}{r^2} \qquad [2.83]$$

where:

Q = heat generated by distributed source

C_L = heat capacity of liquid

a_L = thermal diffusivity of liquid

T = temperature

r = radial coordinate in liquid, measured from bubble centre

This equation includes heat conduction in and out, heat transport by radial flow of the liquid, possible heat

generation and sensible heat storage and depletion.

3)Mass diffusion, described by the mass balance equation on solute

$$D\left[\frac{\delta^2 C}{\delta r^2} + \frac{2}{r}\frac{\delta C}{\delta r}\right] = \frac{\delta C}{\delta t} + \frac{\epsilon R^2}{r^2}\frac{dR\delta C}{dt\delta r} \qquad [2.84]$$

where,

D = mass diffusivity coefficient

C = solute concentration

Westwater's time-dependent equations assume that the gas molecule diffusion through the gas bubble and through the gas liquid interface membrane produces negligible effects on the transient growth of bubbles. This assumption is in agreement with Davies and Rideal, 1961, who concluded that, for the case of a molecule of CO_2 moving through water, across an interface and into a bubble, the forces opposing this movement, in the liquid phase, are approximately two orders of magnitude greater than the forces in the gas phase and at the interface.

The time-dependent isothermal growth of a bubble can be obtained by solving Equations 2.82 and 2.84 simultaneously. The solution of Equation 2.84 has raised the interest of several investigators. Sobkowicz, 1982, collected approximately twenty references where the mass transfer equation is solved for the case of a single bubble in an

infinite liquid. In this case, the appropriate boundary conditions are:

$$C(R,t) = C_s, \quad t>0$$

$$C(\infty,t) = C_i, \quad t>0$$

$$C(r,0) = C_i, \quad r>R$$

where:

$C(r,t)$ = gas concentration at distance r from the centre of bubble at time t

C_s = gas concentration in the saturated solute

C_i = initial gas saturation

R = bubble radius

Westwater presented results of tests performed with carbon dioxide in water. He compared the observed rate of bubble growth with that predicted by the numerical solution of Equations 2.82 and 2.84. He concluded that the differential Equations closely model the physical phehomenon, and that for the case studied, the growth of the bubble radius is linearly proportional to the square root of time. However, as previously mentioned, the boundary conditions above cannot be applied to the pores of soils.

Lee and Black, 1972, studied the time required to dissolve air bubbles trapped in laboratory drain lines. They assumed the bubbles were surrounded by infinite liquid. In a later publication, in order to estimate the time required to saturate an initially partly saturated soil, Black and Lee, 1973, generalized the results obtained for a bubble in an

infinite liquid to a bubble in the soil pores. They suggested a relationship similar to that presented by Westwater:

$$\Delta V = K_s t^x \qquad [2.85]$$

where,

ΔV = change in volume of air voids

K_s and x = empirical constants that depend on the condition of the problem ($0<x<1$)

Although their generalization proved to be acceptable for bubbles dissolving in water, and disappearing after a limited amount of time, it proved to be unacceptable as model for the growth of gas bubbles in a confined volume of liquid. As inferred from Equation 2.85, for time tending to infinity, the change of volume of the bubble also tends to infinity.

Sobkowicz, 1982, extended Epstein and Plesset's, 1950, formulation, originally derived for a single bubble in infinite liquid, for the case of a bounded liquid. He neglected the effects of mechanical forces (Equation 2.82) on the time dependency of bubble growth and assumed stationary bubble walls. The following boundary conditions were imposed:

$$C(r,0) = C_i, \quad R<r<S$$

$$C(R,t) = C_s, \quad t>0$$

$$\delta C(S,t)/\delta r = 0, \quad t>0$$

The following equation was obtained,

$$\frac{dV}{dt} = 8\pi KH\left(1-\frac{C_i}{C_s}\right)\frac{R}{(S-R)}\times$$

$$\times\sum_{n=1}^{\infty}\left[e^{-Ka^2t}\left[\frac{\sin(\pi(2n+1))}{2a} - R\sin^2\left(\frac{\pi(2n+1)}{2}\right)\right]\right] \qquad [2.86]$$

where, H = solubility coefficient

K = mass diffusivity coeficient

= radius of the spherical container

$$a = \frac{(2n+1)\pi}{2(S-R)} \qquad [2.87]$$

V = volume of the bubble

and the other variables have the same meaning as before.

The sum of the exponential terms reduces dV/dt to near zero values and gives an asymptotic character to the volume-time relationship, an observable occurrence in closed volumes of liquids.

Tikuisis et al., 1983, solved the problem of a gas bubble dissolving in a liquid closed to mass transport, for boundary conditions different than those assumed by Sobkowicz. These are illustrated in Figure 2.18.

They assumed that the mass diffusion process takes place within a thin layer of unstirred liquid surrounding the bubble. Outside this layer, this fluid is continuously stirred resulting in an uniform (but not constant with time) gas concentration. For this problem, the rate of change of the bubble radius is given by:

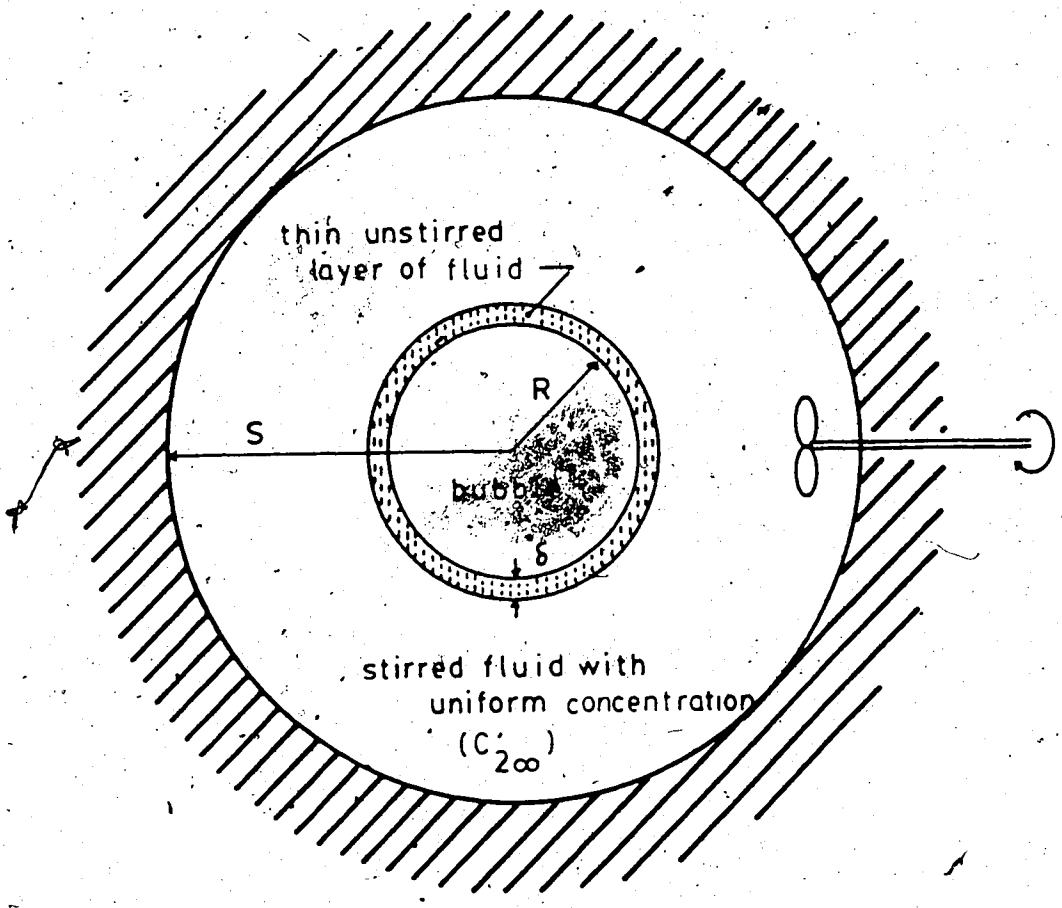

Figure 2.18 Bubble Evolution in a Liquid Closed to Mass Transport - Modified from Tikuisis et al., 1983

$$\frac{dR}{dt} = \frac{-KT\bar{D}}{P'-P_\infty+(4\gamma/3R)} \frac{\delta C'_2(R,t)}{\delta r} \qquad [2.88]$$

The term "$D \frac{\delta C'_2(R,t)}{\delta r}$" is the flux of gas molecules across the interface and is given by:

$$D \frac{\delta C'_2(R,t)}{\delta r} = K_{gl}\left[\frac{a(t)}{C'_2(R,t)} - \frac{C'_2(R,t)}{a(t)}\right] \qquad [2.89]$$

and,

$$K_{gl} = \left[P'-P_\infty+\frac{2\gamma}{R_c(\infty)}\right] \frac{\pi r_g^3 P_\infty}{K_H} \sqrt{2\pi m_g KT} \qquad [2.90]$$

$$a(t) = \left[\frac{C'_1}{K_H}\right]\left[P'-P_\infty+\frac{2\gamma}{R(t)}\right] \qquad [2.91]$$

where,

D = diffusivity coefficient

P' = pressure on the liquid

P∞ = vapor pressure in the bubble

C'_2 = gas concentration in the liquid phase

C'_1 = liquid concentration in the liquid phase

K_H = Henry's solubility constant

r_g = effective radius of the gas molecules

m_g = mass of the gas molecules

$R_c(\infty)$ = critical radius of the solution in the final equilibrium state

and where other variables have the same meaning as before.

Equation 2.89 has been numerically solved by Tikuisis et al., 1983. The solution allowed the term $\delta C'_2(R,t)/\delta r$ to be expressed as a function of the bubble radius, R, the diffusivity coefficient, D, the thickness of the unstirred fluid, δ (Figure 2.18) and the summation of infinite series, similar to Sobkowicz's solution.

The thickness δ is given by $Z(1-e^{(-R/z)})$ where Z is the thickness of the unstirred layer when the interface between the liquid and gas phase is flat. This is an unknown parameter and must be obtained experimentally.

The term $\delta C'_2(R,t)/\delta r$ when substituted in Equation 2.88 allows the evaluation of the rate of growth of a bubble.

BUBBLE NUCLEATION

In the preceding section, the currently available solutions for the problem of rate of growth of bubbles and the boundary conditions associated with them were presented. The boundary conditions adopted for each case are extremely simple when compared to the real case, where, upon relief in pressure of the liquid below certain values (bubble point pressure), bubbles start forming at different sites and different rates, with time.

The birth of a bubble in the neighbourhood of an already existing bubble, affects the rate of sorption of the latter, since it modifies the boundary conditions that govern its growth.

The number of publications on bubble nucleation is not as abundant as those dedicated to the phenomenon of gas sorption. This observation agrees with Sobkowicz's conclusion that "one might speculate that sorption is the dominant process influencing the gas sorption behaviour".

Bubble nucleation has drawn the attention of some researchers. In the cases discussed herein, some solutions have been proposed involving simplifications which restrain their use to simpler cases. One such solution is given by Ward et al., 1970,

$$J = Z\, e^{\left[\frac{-16\pi\sigma^3}{3KT(\eta P_\infty + (P'C'/C_s) - P')^2}\right]} \qquad [2.92]$$

where the new variables are,

J = rate of formation of nuclei per unit volume

Z = constant of proportionality (experimentally estimated)

σ = surface tension

This equation expresses the number of bubbles formed in a given time, as a function of the thermodynamic variables of the system (P', P", C'/C_s)

This theory does not include the phenomenon of dissolved gas "nucleating" at imperfections or included solids.

According to Harvey, 1951, the origin of gas nuclei is intimately connected with the character of the bounding

surface. In the presence of a surface crack or an acute angled cavity, gas nucleation may occur even if ΔP is zero, at the bottom of the cavity. This is due to statistical fluctuations in the molecular behaviour, similar to those associated with Brownian movement. Once a bubble is formed, its growth is controlled by factors discussed earlier in this chapter.

Harvey showed that, in the absence of a gas nucleus, enormous supersaturation may be attained in homogeneus liquids at rest. Laboratory experiments have shown that water initially saturated with oxygen at 250 atmospheres, can be reduced to 1 atmosphere, without the production of gas bubbles.

In the pores of soils, the phenomenon of bubble nucleation is clearly geometrically dictated by the imperfections or irregularities of the soil skeleton.

The currently available solutions, based on fundamental thermodynamic properties, to the problem of bubble nucleation and gas sorption, presented in this section, provide a means of evaluating the rate of volume growth of bubbles, dV/dt. The latter, when applied to Equation 2.81, enables the evaluation of the time-dependent compressibility of the gassy fluids under consideration, provided the appropriate boundary conditions used to develop these equations are respected.

Unfortunately these simple boundary conditions have little resemblances with those found in the pores of soils.

For a particular soil sample, the correct solution for the rate of volume growth of a bubble should properly evaluate the sites where bubbles would form, and accordingly, should simulate the initial stages of bubble formation, based on heterogeneous bubble nucleation theories; it should also take into account the proximity of neighbouring bubbles, the irregular shape of the pores and the critical radii of bubbles.

Considering that the current solutions to the problem, even for the simplest boundary conditions, are very complex, one may conclude that an ideal solution for the actual boundary condition of soil pores is not a simple task. Keeping in mind the current lack of complete knowledge on the physical processes that govern the problem, it seems that efforts towards the solution of the governing equations discussed in this chapter may not render substantial practical results.

Realizing these facts, alternative and possibly more practical approaches can be proposed to the solution of the problem. These are presented in the following section.

2.3.2 Macroscopic (descriptive) Gas Evolution Models

In an attempt to solve the problem of the transient mechanical response of gassy fluids and, concurrently to avoid some of the pitfalls inherent to the fundamental models, discussed in the previous section, Sobkowicz, 1982, and Sobkowicz and Morgenstern, 1987, postulated a simple

descriptive model, based on observed behaviour of soil samples in the laboratory.

This model provides a general empirical relationship between the volume of the free gas and the time, for a situation where the pore fluid pressure is assumed to be constant. This model, called the "macroscopic" theory of evolution, predicts rates of bubble volume increase without identification of the physical processes which might be governing the observed results.

Sobkowicz performed a series of tests with Ottawa sand samples, artificially prepared and saturated with CO_2 saturated water. He performed, among other tests, isotropic undrained unloading triaxial tests and noted that, during specific steps of these tests, it was possible to measure the gas volume changes due to gas evolution independently. This was done by maintaining the effective stresses in the samples equal to zero, which enables the control of the undrained pore pressures, kept constant during each unloading stage. In this case, any time-dependent volume change, that occurs during any specific step, can be directly associated with the gas evolution.

Performing nonlinear regression analyses on the data collected at these test steps, he concluded that the "quotient+1" function would better model the observed process:

$$V_{fg}(t) = V_{fg}(0) + (V_{fg}(\infty) - V_{fg}(0)) \frac{t}{t+A'} \qquad [2.93]$$

where,

$V_{fg}(0)$ = initial volume of free gas, before the liquid pressure is set to P_L

$V_{fg}(\infty)$ = final (equilibrium) volume of free gas

t = time

A' = scaling parameter

Figure 2.19 illustrates the proposed function.

Ward et al., 1985, performed tests with nitrogen dissolved in water. The solution pressure was instantaneously dropped from an initial value higher than the bubble point pressure. After this pressure drop, the volume of the solution was kept constant and the pressure was monitored. The test results and the best fit quotient+1 curve from statistical regression are presented in Figure 2.20. It shows that the proposed function describes reasonably well the observed phenomenon. As another example of a similar problem, Figure 2.21 presents data on nitrogen elimination from fluid and fat tissues in the human body and the best fit quotient+1 curve. The similarities of these two curves with that obtained from gas evolution in soil samples is unequivocal. The rate of gas bubble growth at any time can be obtained from the quotient+1 function by taking the derivative with respect to time of Equation 2.93,

$$\frac{dV_{fg}}{dt} = \frac{V_{fg}(\infty)-V_{fg}(t)}{t+A'} \qquad [2.94]$$

In order to further simplify the solution of the

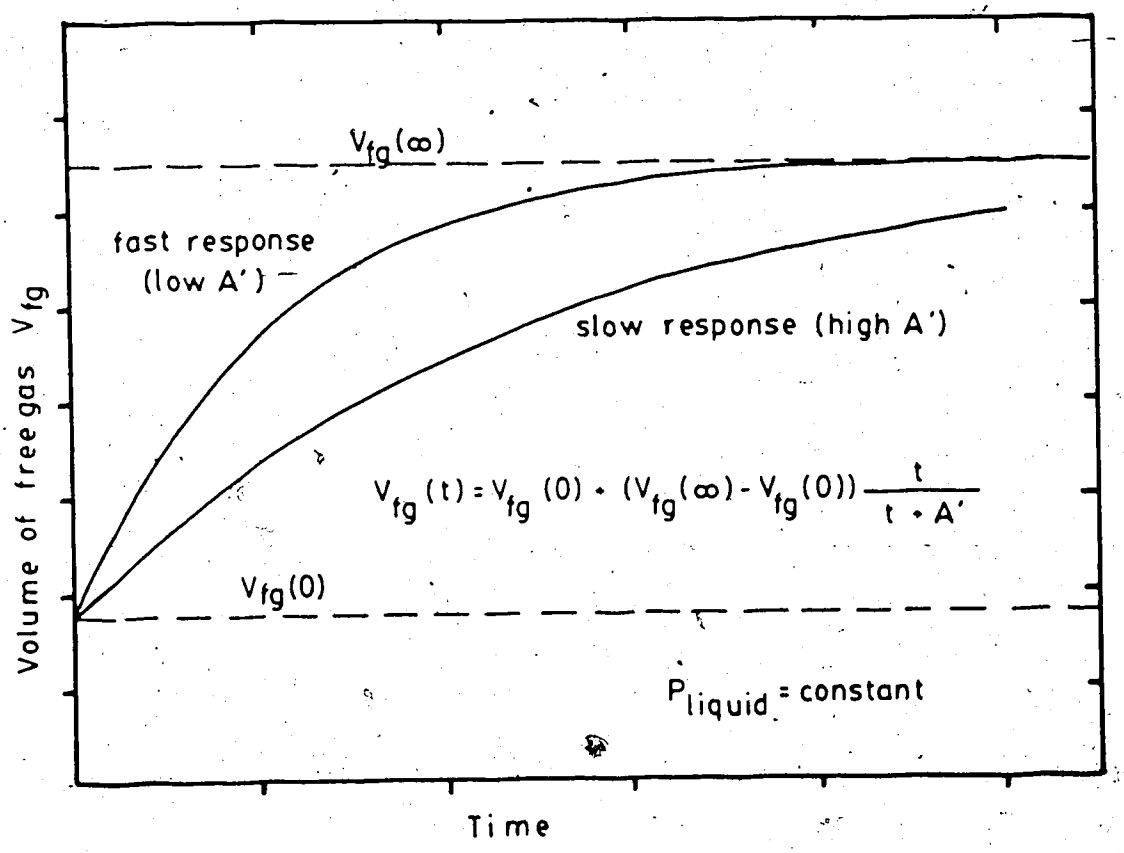

Figure 2.19 Macroscopic (descriptive) Gas Evolution Model - Modified from Sobkowicz, 1982

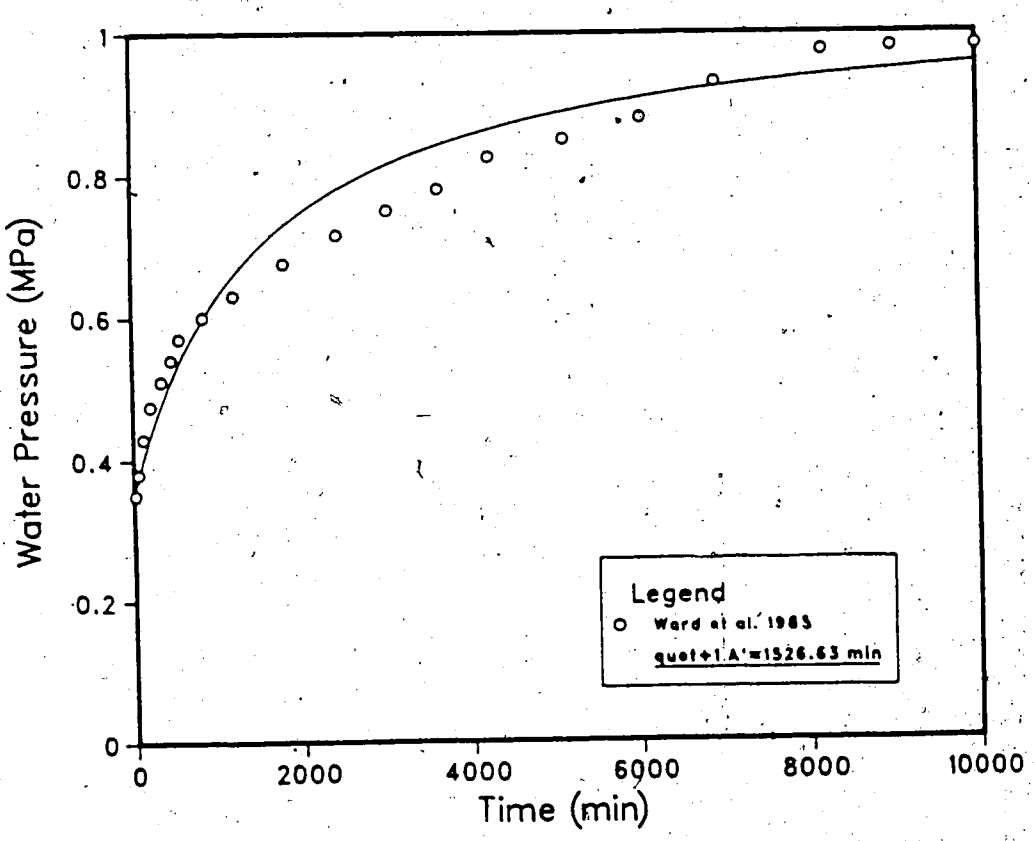

Figure 2.20 Nitrogen Bubble Growth in Constant Volume and Mass of Water

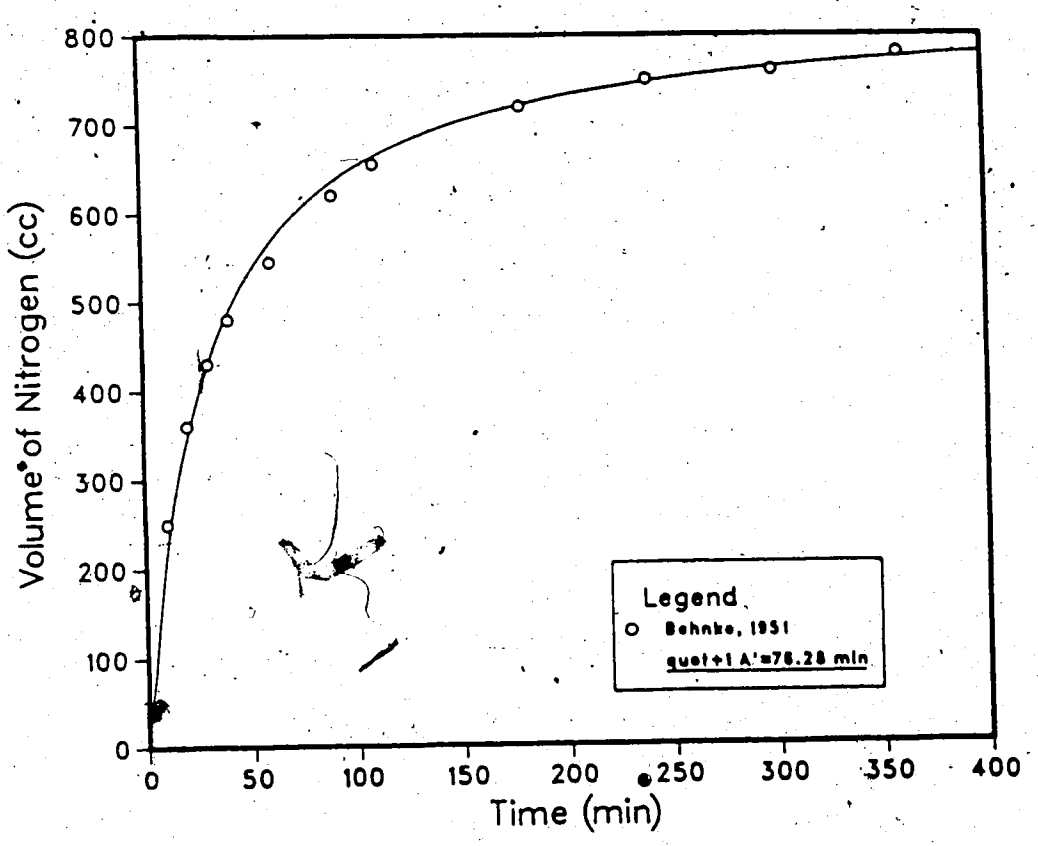

Figure 2.21 Nitrogen Elimination in Human Beings

differential equations, Sobkowicz reduced equation 2.94 to,

$$\frac{dV_{fg}}{dt} = E(V_{fg}(\infty)-V_{fg}(t)) \qquad [2.95]$$

The simplicity of the above equations when compared to the equations derived earlier in this chapter is unquestionable. It still retains the form of the more fundamental equations but enables a simpler solution for the time-dependent problem.

Identical approaches have been applied to the prevention of decompression sickness in divers, fliers, caisson and mining workers.

When exposed to air at pressures higher than atmospheric, the fluids and body tissues of animals and human bodies are subjected to the diffusion of gases present in the air (basically N_2 and O_2). The nitrogen shows a very low rate of penetration when diffusing in fat tissues. Upon decompression at slow rates, the body's excess dissolved nitrogen has sufficient time to diffuse from the tissues into the blood and to be eliminated through the lungs. However, if the decompression is too rapid, the excess nitrogen begins to escape from the dissolved state and eventually forms bubbles in the tissues. This phenomenon results in *decompression sickness*. Its effects and symptoms are described by Ferris et al., 1951, Behnke, 1951, Tobias, 1951, Spetch, 1958, Shchupakov, 1967, Walder and McCallum, 1975, McArdle et al., 1981, among others.

Due to the recognized difficulties in appropriately considering all intervening boundary conditions, best fit equations have been proposed to model the denitrogenation process. Behnke et al., 1935, and Behnke, 1951, proposed that the process can be modelled through the sum of exponential terms of the form:

$$Y=Q(1-e^{-Kt}) \qquad [2.96]$$

where,

Y = quantity of N_2

Q = total excess amount of N_2 in solution

K = rate of change in the slope of the curve (equivalent to Sobkowicz's E scaling parameter)

$(1-e^{-Kt})$ = rate of decrease of the total N_2 during time t

Behnke stated that only one value for K would not fit properly the experimental data since the concentration of N_2 in the various tissues and fluids of the body would vary according to the local diffusion coefficient and the available blood supply. It was verified that the value of K does not remain constant, but progressively decreases with time.

The curve for total N_2 (curve (a) in Figure 2.22) can be more accurately represented by two exponential expressions on the basis of a high value for K during the first hour and a low value for K after the first hour. This figure illustrates that the N_2 evolution process takes place faster in the body fluids than in the fat tissues, and that the

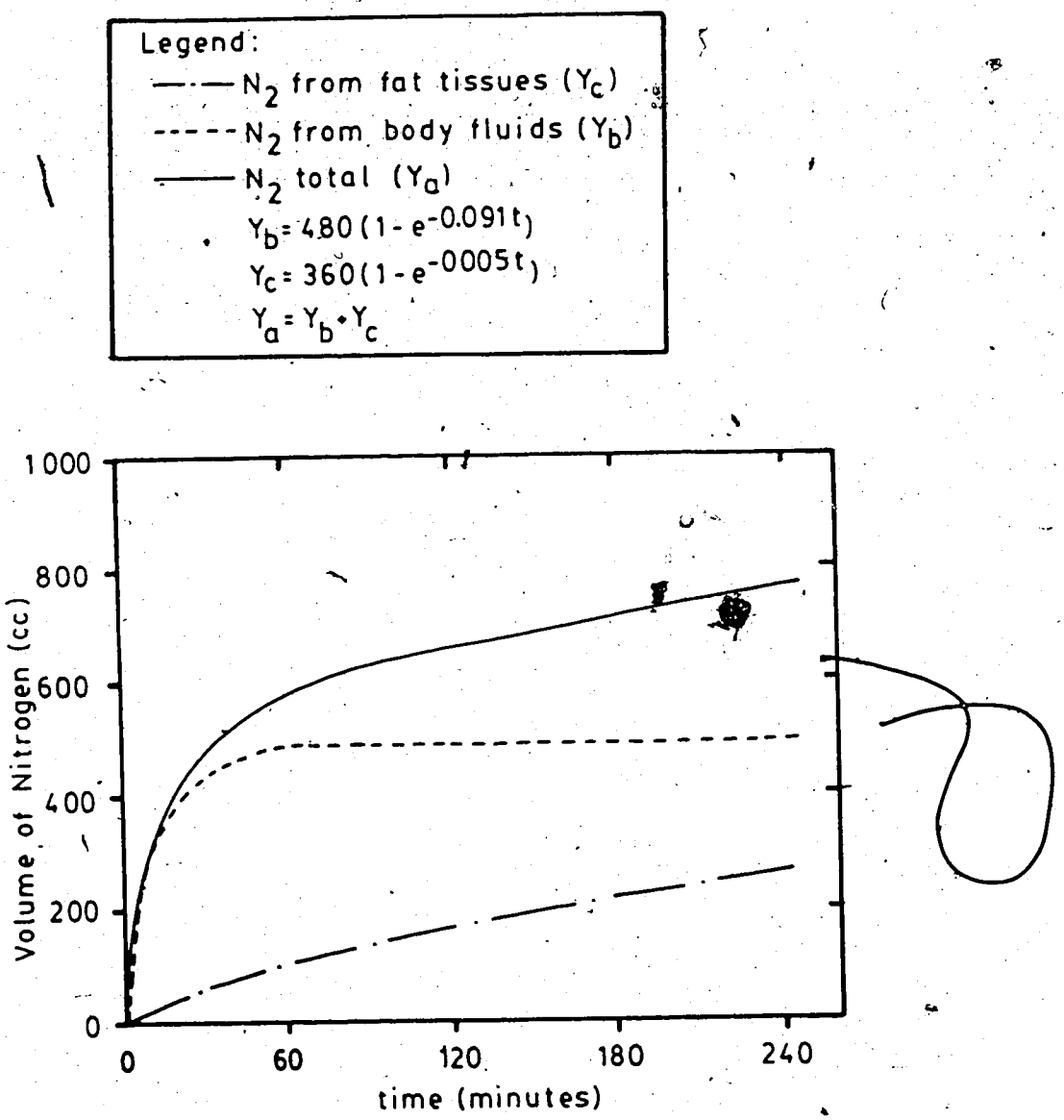

Figure 2.22 Elimination of nitrogen from the body during a course of oxygen inhalation (modified from Behnke, 1951.)

composition of these two curves result in the total measured N_2 amount.

Smith and Morales, 1944, used three exponential curves, instead of two, to fit the experimental data collected during the denitrogenation of human bodies.

The advantage of using the quotient+1 fit, instead of the exponential fit, is that the effect of a decreasing value of K as time progresses , is naturally taken into account, since:

$$K'(\text{or Sobkowicz's } E) \equiv \frac{1}{t+A'} \qquad [2.97]$$

The scaling parameter A' in Sobkowicz's model is the only unknown in the relationship and can be obtained readily from laboratory tests. Its value is a characteristic of the specific pore fluid being analyzed. This means that the extrapolation of A' values obtained for gassy fluids composed of specific components, to gassy fluids composed of different components, or even the same components but at different composition, cannot be made readily. In fact this is a drawback inherent to every descriptive or empirical method. A typical example of such a model is the *stress-path* method, initially proposed by Lambe, 1967, and later discussed by Lambe and Marr, 1979. It proposes to simulate complex stress-path dependent soil mechanical response,

based on simpler stress-path independent mathematical models and laboratory tests.

The substitution of Equation 2.94 in Equation 2.81 enables the evaluation of the time dependent compressibility of gassy fluids:

$$\beta_{fg}(t) = \frac{\cdot V_{fg}}{V_F^0(P+dP)} - \left(\frac{1}{V_F^0 dP}\right) \int_{t1}^{t2} \frac{V_{fg}(\infty)-V_{fg}(t)}{t+A'} dt \qquad [2.98]$$

A more general treatment of this equation is given in Chapter 3.

2.4 Summary and Conclusion

The mechanical response to isothermal pore pressure changes of gassy fluids has been analysed in this chapter. This analysis was carried out with the development of the compressibility of the fluids, a constitutive parameter which is familiar to geotechnical engineers.

Initially, the fluid compressibilities were evaluated under the assumption that all the physical processes associated with changes in the boundary conditions of the problem have ceased, reflecting a condition of equilibrium.

The equations developed are functions of fundamental thermodynamic properties and should be applicable to engineering cases, where the rate of change in the boundary condition is slow compared to transient processes involved in the response of the fluids.

For the development of the time-independent fluid compressibility, a review of the basic principles that control the equilibrium behaviour of a gassy fluid was carried out. This review revealed the limitations of the ideal gas and solution laws when applied to real cases. It was concluded that the laws are applicable to marine sediments and oil sands gas saturated with small amounts of carbon dioxide, subjected to fluid pressures up to 8MPa. An exception to this assertion is the evaluation of the combined solubility coefficient (H_{comb}) from individual gas and liquid solubility coefficients. Laboratory experiments have shown that, for methane rich solutions, errors up to 20% might result in theoretical evaluations of H_{comb}. The review also indicated that, when the surface tensions between the gas and liquid phases are neglected, the errors in the evaluation of the fluid compressibility are small (<1%), provided that the carbon dioxide content is small and/or the fluid pressures are high (>3 MPa).

The effects of the surface tensions on the stability of bubbles were also discussed. It was concluded that extremely small bubbles can exist, in a stable condition, irrespective of the presence of the soil skeleton. This conclusion does not support Fredlund's view, as presented in his thesis in 1973.

Finally, the fluid compressibilities have been evaluated taking into account the time-dependent processes, namely:

- gas nucleation
- gas sorption

It has been shown that the appropriate evaluation of the time-dependent compressibility of gassy fluids, in the pores of soils, based on fundamental thermodynamic variables, is a difficult task due to the complexities in assessing the involved boundary conditions.

More general descriptive time-dependent models have been presented. It has been shown that they are valuable to the solution of the problems dealt with in this thesis, in a case by case basis, despite their inherent limitations.

It has also been shown that an identical approach has been applied to the prevention of decompression sickness in divers, fliers, caisson and mining workers.

3. ANALYTICAL AND NUMERICAL SIMULATION OF THE RESPONSE OF GASSY SOILS

3.1 Introduction

The increase of construction works in marine sediments and oil sands in the last two decades was naturally followed by an increase in the need for reliable simulation tools. As a result, simulation models, aimed at making mining and geotechnical works more economical with no loss of safety, have been developed.

In the first part of this chapter, a review of the models developed up to date is presented.

In the second part of the chapter, the formulation that takes into account the time-dependent gas evolution is developed. The governing differential equations are solved by numerical techniques using a finite element program CONGAS (CONsolidation and GAS evolution). The development and testing of the predictive capabilities of this numerical model are also presented in detail in this chapter.

3.2 Existing Stress-Relief Models for Gassy Soils

As was the case in Chapter 2, the existing models developed to simulate the mechanical response of gassy soils are here classified according to their capability to simulate the transient processes that take place in gassy soils when subjected to stress relief: pore fluid drainage and gas evolution.

The models classified as time-independent yield a frozen picture of the soil response, neglecting when and how such conditions occurred, whereas the time-dependent models reflect the soil response as a function of time.

Figure 3.1 depicts how the models discussed herein are grouped according to this classification. In this figure the terms long term and short term refer to an equilibrium and to a non-equilibrium situation, respectively. An equilibrium situation is one in which the processes that govern the soil behaviour, such as pore fluid drainage and gas evolution have ceased. The terms undrained and short term and drained and long term cannot be equated. The conditions of drainage refer to situations where the pore fluids are permitted (drained) or not permitted (undrained) to move across the boundaries of infinitesimal soil elements that constitute the soil mass being considered.

All models assume that interfacial tensions for water and gas and bitumen are small, compared to the magnitude of the stresses involved in the analysis. This implies that the gas bubbles and the pore liquid pore pressures are the same and that the concept of an "homogenized pore fluid" as discussed by Chang and Duncan, 1983, is valid.

3.2.1 Time-Independent Models

Harris and Sobkowicz, 1977, developed a two-dimensional model that relates undrained changes in fluid pore pressure to changes in total stresses and temperatures. The model is

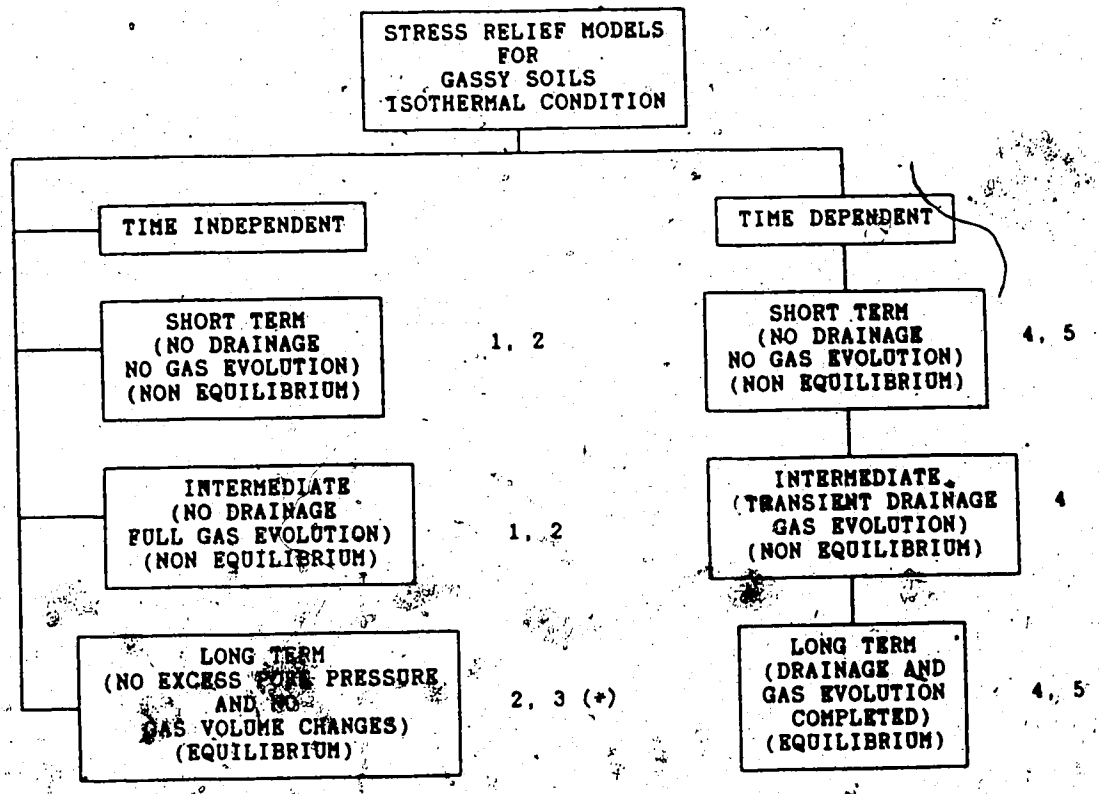

(*) - INCORRECT FOR QUICK UNLOADING

MODELS:

1 - HARRIS AND SOBKOWICZ (1977), DUSSEAULT (1979)
2- NEAT, OILSTRESS, INCOIL, BYRNE AND VAZIRI (1985)
3- ROWE ET AL. (1982)
4- SOBKOWICZ (1982)
5- GHABOUSSI AND WILSON (1973), GHABOUSSI AND KIM (1982)
CHANG AND DUNCAN (1983), VAZIRI (1986)

Figure 3.1 Stress Relief Models for Gassy Soils (Isothermal Conditions)

derived for an elastic response of the soil skeleton and includes the pore pressure parameters A and B (Skempton, 1954). The parameter A enables the simulation of pore pressure changes due to volume changes associated with shear. This model simulates non-equilibrium situations, where no pore fluid drainage is allowed. The short-term or immediate response, where, besides no fluid drainage, it is assumed that no gas evolution takes place, can be simulated by making the solubility coefficient equal to zero. On the other hand, an intermediate response, where no fluid drainage has taken place but the gas evolution processes have ceased, can be simulated by making the solubility coefficient equal to its value at equilibrium.

Dusseault, 1979, presented a one-dimensional formulation, where pore fluid pressure changes are related to total stress relief for a soil with a non-linear elastic constitutive law. The undrained situation before or after the dissolved gases have come out of solution can be simulated by assigning appropriate values to the solubility coefficients.

The two models above do not allow a coupled analysis of total stress changes and pore pressure changes in problems where the geometry is more complex or the soil presents a more complex constitutive behaviour. For these purposes, finite element programs have been developed and are discussed next.

The NEAT finite element program (*N*on-Linear *E*ffective Stress *A*nalysis for *T*arsand), presented by Harris and Smith, 1979, and discussed by Piche, 1980, enables a two-dimensional analysis for the undrained condition before or after gas evolution takes place. It also allows analysis for the fully drained equilibrium condition in which the effects of the presence of gas on the soil mass behaviour are not considered. In the undrained analysis it is assumed that there exists a discrete value of the critical gas saturation (or venting porosity) at which gas mobility occurs. When this gas saturation is reached, the program resets the pore fluid pressure to a reduced value, specified by the user.

The soil skeleton has a curved failure envelope and is assumed to behave in a non-linear elastic manner. Its response to stress changes is described by the secant values of the bulk modulus (B_s) and the secant values of the shear modulus (G_s).

As the solution is piece-wise linear elastic, the model does not simulate volume changes due to shear.

As reported by Byrne et al., 1980, Byrne and Grigg, 1980, further extended the program NEAT to include shear dilation. In the undrained analysis, for this new program, OILSTRESS, for pore pressures higher than the bubble point pressure, the pore pressure changes are defined by Skempton's A and B parameters, whereas for pore pressures below the bubble point pressure, the pore pressure changes

are governed by the gas laws. Application of the OILSTRESS program can be found in Byrne et al., 1980).

Byrne and Janzen, 1984, developed a finite element program (INCOIL) in which the soil skeleton also behaves as a non-linear elastic material. The program uses an incremental approach, where a tangent modulus rather that a secant modulus is used. This type of approach is more desirable because it allows the field loading sequence to be followed, instead of the single step loading used in NEAT and OILSTRESS.

The simulation of the pore pressure response and of the shear dilatancy is done in the same way as in the OILSTRESS program. In the three finite element programs above the solution of the equilibrium equations for the undrained analysis is obtained iteractively. This is required because the pore pressures within the soil are input data for the solution and also are the unknowns of the problem.

Byrne and Vaziri, 1985, presented a formulation slightly different than the one used in INCOIL. The pore pressures were incorporated into the stiffness matrix of the finite element equations and these, for each load increment, were not dealt with as unknowns.

Rowe, et al., 1982, presented a study of the excavation of a tunnel in oil sands. An elastic-plastic model was adopted, which allowed the incorporation of a curved failure surface and related stress dependent dilatancy. The model developed allows only for fully drained analyses, in which

volume changes due to gas expansion are neglected.

The fully drained type of analysis, if carried out with the four finite element programs described above, can lead to unrealistic results that might not reflect the final, steady-state condition of equilibrium. In gassy soils, rapid unloading can lead to situations where decreases in total stresses are larger than the decreases in pore pressure. Depending on the magnitude of the decreases in total stress, the effective stresses are governed only by the gas laws. At this stage, due to the eventually large volumetric changes, the soil structure might have no similarity with the original state. With time, the excess pore pressure dissipates and the fully drained equilibrium condition prevails, but the original soil structure is never recovered. In this case, the final displacements and stress states within the soil mass can be computed only if the intermediate conditions described above are considered.

For that purpose, time-dependent models have been developed.

3.2.2 Time-Dependent Models

The time-dependent models discussed below were developed based on the concept of a "homogenized pore fluid", as mentioned previously.

In 1982, based on his macroscopic theory of gas evolution, Sobkowicz developed a finite difference program to solve the one-dimensional diffusion equations of combined

consolidation and gas evolution around a shaft or borehole.

The soil was assumed to behave as a linear elastic material and the pore liquid and gas properties required to perform the analysis are liquid compressibility, solubility coefficient and a time scaling factor. This model is extremely useful in illustrating how the pore liquid drainage and the pore gas evolution processes can have counteracting effects and how they govern the pore pressure distribution around boreholes or shafts.

The diffusion theory of consolidation and gas evolution developed by Sobkowicz, 1982, does not model all aspects of the behaviour of the soil mass. Similarly to the Terzaghi-Rendulic solutions for the problem of consolidation, Sobkowicz's solution assumes that the total stresses within the soil mass are constant with time. This assumption allows the solution of the diffusion equations independently of the stress equilibrium of the soil skeleton.

From the theoretical point of view, theories that incorporate total stress equilibrium and strain compatibility during the transient processes are preferable.

Ghaboussi and Wilson, 1973, extended the previous work by Sandhu and Wilson, 1969, originally based on Biot's theory of coupled consolidation (Biot, 1941 and 1955), and included the solid and fluid compressibility in the finite element analysis. This enabled the simulation of partly saturated and gassy soils.

In 1982, Ghaboussi and Kim presented an extension of Ghaboussi and Wilson's formulation and included material non-linearity. A constant value of the air-water interfacial tensions was used in the evaluation of the pore fluids compressibility. Chang and Duncan, 1983, presented a finite element program also based on Biot's theory of consolidation, that allowed the analysis of the consolidation of inelastic, partly saturated and gassy soils. In their analysis, the Cam-Clay model originally derived to simulate the stress-strain behaviour of normally and lightly over-consolidated natural clays, was used. Vaziri, 1986, developed a finite element formulation similar to Chang and Duncan's, except that in the former, the soil skeleton stress-strain response is modelled with a non-linear elastic, hyperbolic, stress-strain relationship. Ghaboussi and Wilson's, Ghaboussi and Kim's, Chang and Duncan's and Byrne and Vaziri's, 1985, models use the concept of an homogenized pore fluid. The compr[illegible] of the mixture of air and water is calculated assuming that the water is incompressible and that the gas volume changes are governed by Boyle's law and the equilibrium value of the solubility coefficient, similar to what was done in the formulations presented in the previous section. By assuming an equilibrium value for the solubility coefficient, the method of analysis becomes time-dependent as far as pore fluid drainage is concerned, but time-independent as far as gas evolution is concerned. This type of simulation is valid

for cases where the gas evolution takes place much faster than pore fluid drainage, which is the case for most partly saturated soils where water and air usually constitute the pore fluid. In cases where the rate of gas evolution is comparable to the rate of water drainage, the use of an equilibrium solubility coefficient is not acceptable.

Figure 3 summarizes the details of the time-dependent models described above.

3.3 Proposed Time-Dependent Model

The review of the existing models that simulate the time-dependent mechanical response of gassy soils reveals that none of them appropriately couples the transient response of the pore fluid upon stress relief with the sand skeleton deformation. This fact revealed the need for the development of a numerical model, described in detail in the following sections.

In order to properly simulate the mechanical response of gassy soils (in particular oil sands) the model should appropriately account for the following aspects:

a) Soil skeleton stress-strain response
   - anisotropy
   - non-linearity
   - plasticity
   - volumetric straining associated with shear stresses
   - strain softening (with stress induced anisotropy)

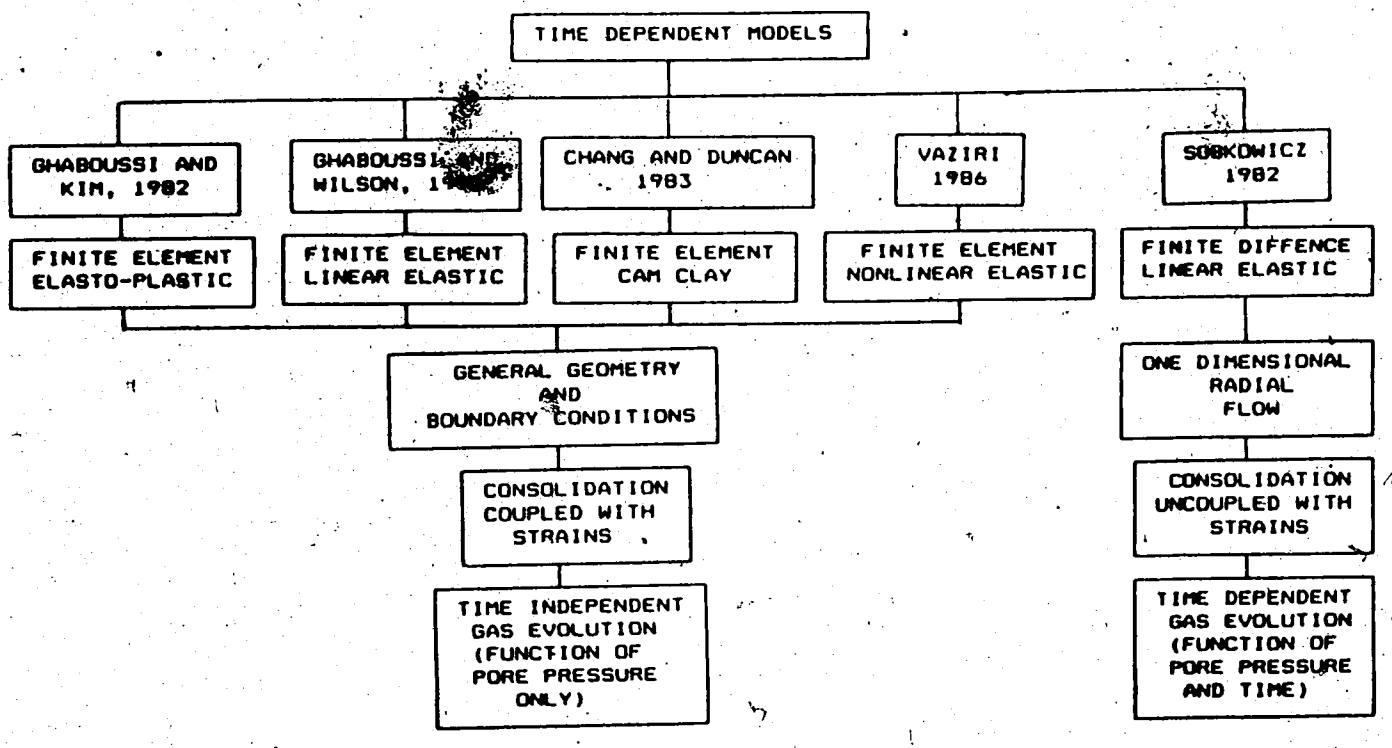

Figure 3.2 Time-Dependent Models - Gassy Soils

b) Pore fluid response

- time-dependent flow of multiple phase fluid
- time-dependent gas evolution in each of the liquid phases

c) a) and b) through appropriate consideration of volumetric strain compatibility of each phase and by ensuring dynamic equilibrium among them (with appropriate consideration of surface tensions)

Among these features, the time-dependent gas evolution in the pore fluids is undoubtedly the one that has received the least attention, despite its importance, as stated previously.

The inclusion in a numerical model of all the desirable features listed above would require concentration of attention in areas that are currently the subject of very active research such as plasticity, volume change due to shear and strain-softening. This would result in a digression from the main subject of this research. Therefore it was decided to concentrate efforts on the development of an appropriate model for the pore fluid phase, and, for the soil-skeleton model, using a well proven constitutive relationship.

The pore fluid is modelled as a multi-phase fluid composed of a liquid and a gas phase.

The gas phase is assumed to be present in the form of occluded bubbles that are immobile. The gas volume changes

are governed by the gas laws, as far as the time-independent response is concerned, and by Sobkowicz's macroscopic model, as far as the time-dependent response is concerned.

The liquid phase is treated as a homogeneous liquid, that flows according to Darcy's law. The bubble formation is assumed to take place homogeneously within the homogeneized fluid. The simulation of liquid phases composed of more than one liquid is possible with the choice of appropriate parameters for the homogeneized liquid. For instance, the simulation of the liquid flow in oil sands, at *in situ* temperatures, is performed under the assumption that the bitumen phase is immobile and that the water phase flows according to Darcy's law. In this case the coefficient of permeability is related to the effective permeability of the water phase.

The strains are related to effective stresses through a linear or a non-linear elastic hyperbolic model. The classical principle of effective stress is assumed to be valid, i.e., it is assumed that the surface tensions do not affect the intergranular contact. This assumption is supported by the discussion presented in the previous chapter.

Volumetric deformation of the sand skeleton is coupled with volumetric changes of the fluid and gas phase. The coupled solution was chosen, as opposed to the uncoupled solution, because the former describes better the physical phenomena, that in fact are actually coupled in nature. The

solution of the transient process of pore pressure change in soil masses in an uncoupled matter is an unnecessary oversimplification of the problem. According to Zienkiewicz, 1982, the use of uncoupled solutions is numerically interesting for the case of the dynamic excitation of soil structures. In this case the finite element equations result in non-symmetric matrices, which makes their solution significantly more time consuming.

For most common consolidation problems, where the acceleration term of the equilibrium equation is neglected, the governing equations are reduced to a system of linear equations which, due to its symmetric nature, can be solved by conventional methods used in finite element programs.

The use of uncoupled solutions for the solution of consolidation problems is probably preferred by some researchers due to the convenience of using computer codes originally written to independently solve the diffusion and the skeleton time-independent response. Yamagami, et al., 1985, reported that for some consolidation problems studied, the uncoupled solution consumed less CPU time than the coupled solution. On the other hand, the 2D study presented by Wan, 1985:222, showed that for some cases, the pore pressure prediction from the uncoupled solution can significantly depart from those predicted by the coupled solution. These facts, associated with the inability of the uncoupled solution to predict the immediate undrained response of the soil mass, upon application of internal

loads, led to the development of a fully coupled formulation.

3.3.1 Model Formulation

Governing Equations

a) Equilibrium equation

$$\sigma_{ij,j} + F_i \rho_s = 0 \qquad [3.1]$$

where,

σ_{ij} = total stress tensor

F_i = body force per unit mass of soil

ρ_s = total density of the soil

b) Principle of effective stresses

$$\sigma'_{ij} = \sigma_{ij} - u\,\delta_{ij} \qquad [3.2]$$

where,

σ'_{ij} = effective stress tensor

u = pore fluid pressure

δ_{ij} = kronecker delta

c) Continuity equation

$$V_{i,i} + \dot{W}_{i,i} - \frac{\dot{u}}{Q_L} - \dot{e}_v^{FG} = 0 \qquad [3.3]$$

where,

V_i = water velocity vector

W_i = displacement vector

$1/Q_L$ = combined compressibility of liquid phase

= Partial differentiation with respect to time

ϵ_v^{FG}: volumetric variation of the gas phase per unit volume of soil.

d) Effective stress-strain relationship

$$\sigma'_{ij} = C_{ijkl} \cdot \epsilon_{kl} \qquad [3.4]$$

where,

ϵ_{kl} = strain tensor

C_{ijkl} = tensor relating strains to stresses

e) strain-displacement relationship

$$\epsilon_{kl} = \frac{1}{2} (W_{k,l} + W_{l,k}) \qquad [3.5]$$

where, $W_{k,l}$ = partial differentiation of the displacement vector

f) Darcy's law

$$V_i = -k_{ij}(u_{,j} + \rho_w F_j) \qquad [3.6]$$

where, k_{ij} = permeability tensor (coefficient of permeability/unit weight of water).

F_j = body force per unit mass of water.

ρ_w = density of water

Boundary Conditions

a) Displacement boundary condition

$$S = S_t + S_d \qquad [3.7]$$

where, S_t = part of the surface subjected to known applied tractions $\bar{T}_i$

S_d = part of the surface subjected to specified displacements $\bar{W}_i$

b) Flow boundary condition

$$S = S_q + S_u \qquad [3.8]$$

where, S_q = part of the surface subjected to specified flow velocity, $\bar{q}$

S_u = part of the surface subjected to specified pore pressures, $\bar{u}$

The boundary conditions may be written in the form:

$$W_i = \bar{W}_i \text{ on } S_D \text{ for } t \geq 0 \qquad [3.9]$$

$$\sigma_{ij} n_j = \bar{T}_i \text{ on } S_T \text{ for } t \geq 0 \qquad [3.10]$$

$$V_i n_i = \bar{q} \text{ on } S_Q \text{ for } t > 0 \qquad [3.11]$$

$$u = \bar{u} \text{ on } S_u \text{ for } t > 0 \qquad [3.12]$$

where, n_i = vector normal to the boundary surface.

and, to complete the definition of the problem, at $t=0^+$:

$$W_{i,i} = \frac{1}{Q_L}\dot{u} + \dot{e}_{vo}^{FG} \qquad [3.13]$$

Combining the governing equations and integrating the continuity equation over time, it follows:

$$(C_{ijkl}\frac{1}{2}(W_{k,l}+W_{l,k}))_{,j}+u_{,j}+\rho_s F_j = 0 \qquad [3.14]$$

$$\int^t - \left[\left[k_{ij}(u_{,j}+\rho_w F_j)\right]_{,i}\right]dt + \int^t \dot{W}_{i,i}\,dt - \int^t \frac{\dot{u}}{Q_L}dt - \int^t \dot{\epsilon}_v^{FG}dt=0 \qquad [3.15]$$

3.3.2 Finite Element Formulation

Most of the solutions by finite elements of the governing equations associated with the consolidation of soil masses have been based either on techniques based on variational principles or based on weighted residual methods (Khaled, et al., 1984).

Sandhu and Wilson, 1969, published the first finite element formulation for the problem of consolidation. The authors postulated a variational formulation of the coupled problem in terms of displacements and pore pressures. The formulation developed, described in detail by Sandhu and Pister, 1970, and later by Yokoo, et al., 1971-a and 1971-b, was the basis of the work later developed by Hwang et al., 1971, Ghaboussi and Wilson, 1973 and Osaimi and Clough, 1979, among several other researchers. Yokoo, et al., 1971-c, relaxed the inter-element continuity of pore pressures and developed another variational formulation.

The complexity associated with the development of equations for the use of variational principles is avoided with the use of weighted residual methods.

In the latter, the finite element equations are easily derived from the differential governing equations, as demonstrated later in this section. Galerkin's version of the method of weighted residuals has been used by several researchers for the solution of coupled consolidation problems. Among them, Hwang, et al., 1972, Chang and Duncan, 1983, Zienkiewicz and Shiomi, 1984, Meijer, 1984, Khaled et al., 1984, Wan, 1985 and Vaziri, 1986.

The solution of the governing Equations 3.14 and 3.15, developed in the preceding sections, is obtained herein with the aid of Galerkin's method, which is preceded by the temporal and spatial discretization of the functions involved in the solutions.

3.3.2.1 Temporal Discretization of Functions

In the absence of any second derivative with respect to time, the "θ - Wilson" or "θ - method " (Kujawski and Desai, 1985) scheme is appropriate for the temporal discretization of functions. It states that the integral of a function $f(t)$, in the time domain, can be discretized as follows:

$$\int_{tN-1}^{tN} f(t)dt = \alpha\Delta t\ f(t_N) + (1-\alpha)\Delta t\ f(t_{N-1}) \qquad [3.16]$$

where

α = time integration constant

$\Delta t = t_N - t_{N-1}$

Some of the most popular values used for α are (Kujawski and

Desai, 1985):

$\alpha = 0$ Euler forward explicit scheme [3.17]

$\alpha = 1/2$ Trapezoidal or Crank-Nicolson scheme [3.17b]

$\alpha = 2/3$ Galerkin or Parabolic scheme [3.17c]

$\alpha = 0.878$ Linear Scheme [3.17c]

$\alpha = 1$ Euler Backward, fully implicit scheme (Owen and Damjanic, 1981) [3.17e]

$\alpha = 1+\frac{1}{\Delta t} - \frac{1}{\ln(1+\Delta t)}$ Logarithmic scheme (Sandhu, 1968) [3.17f]

$\alpha = 1+\frac{1}{\tau_o} + \frac{1}{\ln(1-\tau_o)}$ Logarithmic scheme (Hwang et al., 1971) [3.17g]

where $\tau_o = \frac{\Delta t}{t_{N-1}}$ [3.17h]

According to Booker and Small, 1975, and Owen and Damjanic, 1981, the numerical solutions are unconditionally stable for $0.5<\alpha<1.0$. Within this range, α values have shown to affect slightly the accuracy of the numerical solutions. Sandhu, et al., 1977, verified that in temporal meshes involving drastic changes in the size of the time step, the logarithmic scheme yielded more accurate results than the Crank-Nicolson scheme ($\alpha=1/2$). Reed, 1984, showed that, for cases where the "smoothing" technique (discussed later in this section) was used, Galerkin's scheme ($\alpha=2/3$) yielded more accurate results than the Crank-Nicolson scheme.

The temporal discretization of the continuity equation (3.15) can, therefore, be carried out as follows:

$$-a\Delta t\left[k_{ij}\ (u_{,j}+\rho_w F_j)\right]_{,i}\Big|^{tN}$$

$$-\ (1-a)\Delta t\left[k_{ij}(u_{,j}+\rho_w F_j)\right]_{,i}\Big|^{tN-1}\ +$$

$$+\ W_{i,i}\Big|^{tN} - W_{i,i}\Big|^{tN-1} - \frac{u}{Q_L}\Big|^{tN} + \frac{u}{Q_L}\Big|^{tN-1} - \epsilon_v^{FG}\Big|_{tN-1}^{tN} = 0 \qquad [3.18]$$

The value of $\epsilon_v^{fg}|_{tN-1}^{tN}$ in the equation above is further expanded as follows:

For an infinitesimal element with volume dV, the variation of the volume of free gas, per unit volume, from time t_{N-1} to time t_n, is given by the expression

$$\epsilon_v^{FG}\Big|_{tN-1}^{tN} = \frac{1}{dV}\int_{tN-1}^{tN}\frac{dV_{fg}}{dt}dt \qquad [3.19]$$

where, dV = total volume of the element

dV_{fg} = volume of free gas

The calculation of the variation of the volume of free gas must consider two phenomena that occur simultaneously:

- migration of gas molecules from the pore liquids to the gas phase (for the case where the pore fluid decreases). This is a time dependent process, as discussed in Chapter 2.
- change of volume of gas in the free state due to changes in fluid pore pressure, according to Boyle's law.

In the present derivation, the change of the volume of free gas is calculated in two separate steps:

a) the volume of free gas produced due to gas evolution is calculated initially and corrected for the pore fluid pressure at the beginning of the time step (t_{N-1}).

b) The volume of free gas existing at the beginning of the time step (t_n) plus the volume of free gas produced due to gas evolution (calculated in a)) are corrected to the pore fluid pressure at the end of the time step (t_n) according to Boyle's law.

This procedure can be expressed by the following equations:

$$\text{a)}\quad \Delta V_{fg}^{EVO}\Big|^{PN-1} \qquad [3.20]$$

$$\text{b)}\quad V_{fg}^{N}=(V_{fg}^{N-1}+\Delta V_{fg}^{EVO}\Big|^{PN-1})\cdot\frac{P_{N-1}}{P_N} \qquad [3.21]$$

where

$\Delta V_{fg}^{EVO}\Big|^{PN-1}$ = volume of free gas produced due to gas evolution only, measured at P_{N-1}

V_{fg}^{N}, V_{fg}^{N-1} = volumes of free gas at times t_N and t_{N-1}, respectively

P_N, P_{N-1} = absolute pressures at t_N and t_{N-1}, respectively.

The integration of the rate of gas evolution in Equation 3.19 can, therefore, be expressed as follows:

$$\int d\dot{V}_{fg}dt = V_{fg}^{N-1}\left(\frac{P_{N-1}-P_N}{P_N}\right) + \Delta V_{fg}^{EVO}\Big|^{PN-1}\frac{P_{N-1}}{P_N} \qquad [3.22]$$

The value of $\Delta V_{fg}^{EVO}\Big|^{PN-1}$ is calculated as follows:

$$\Delta V_{fg}^{EVO}\Big|^{PN-1} = \int_{tN-1}^{tN} d\dot{V}_{fg}^{EVO}dt \qquad [3.23]$$

According to Sobkowicz's model, presented in Chapter 2, at a constant fluid pressure:

$$d\dot{V}_{fg}^{EVO} = \frac{V_2 - V_{fg}}{t + A'} \qquad [3.24]$$

where,

V_2 = equilibrium volume of free gas after gas evolution has ceased

A' = scaling parameter

Substituting 3.24 in 3.23

$$\Delta V_{fg}^{EVO}\Big|^{PN-1} = \int_{tN-1}^{tN}\frac{V_2 - V_{fg}}{t + A'}dt \qquad [3.25]$$

This equation can be further expanded as follows:

$$\Delta V_{fg}^{EVO}\Big|^{P_{N-1}} = \frac{\Delta t(1-a)}{t_{N-1}+A'}\,(V_2^{N-1} - V_{fg}^{N-1}) + \left[\frac{\Delta t a}{t_N+A'}(V_2^N - V_{fg}^N)\right]\frac{P_N}{P_{N-1}} \qquad [3.26]$$

The first term of the right hand side of Equation 3.26 is the rate of gas evolution, at pressure P_{N-1}, times $(1-a)\Delta t$. The second term of the right hand side of this equation is the rate of gas evolution at P_N times $a\Delta t$, corrected according to Boyle's law to the pressure P_{N-1}

Equation 3.26 is substituted in 3.22, which in turn is substituted in 3.19 to result in:

$$\epsilon_v^{fg}\Big|_{tN-1}^{tN} = \frac{1}{dV}\left[V_{fg}^{N-1}\left(\frac{P_{N-1}-P_N}{P_N}\right) + \frac{\Delta t(1-a)}{t_{N-1}+A'} \cdot (V_2^{N-1}-V_{fg}^{N-1})\cdot\frac{P_{N-1}}{P_N} + \frac{\Delta t a}{t_N+A'}(V_2^N - V_{fg}^N)\right] \qquad [3.27]$$

It is numerically desirable to express Equation 3.27 in terms of the degrees of freedom of the problem (pore fluid pressure and nodal displacements) and the volumes of free gas at the beginning of the time step. Therefore, the term $(V_2^N - V_{fg}^N)$ can be further modified.

According to Fredlund, 1973, and discussion presented in Chapter 2, the gas laws can be applied to the total volume of gases (dissolved and in the free state).

For an element where water cannot move across its boundaries, the total volume of gas can be obtained at

different pore fluid pressures from the Boyle's equation

$$V_{Tg}^{N} = \frac{P_{N-1} \cdot V_{Tg}^{N-1}}{P_N} \qquad [3.28]$$

where,

V_{Tg} = total volume of gas within the element $= V_{fg} + V_{dg}$

V_{dg} = volume of gas dissolved into the pore liquid.

For the case where the water is allowed to move across the element boundaries:

$$V_{Tg}^{N} = \frac{P_{N-1} \cdot V_{Tg}^{N-1}}{P_N} + \Delta V_w . \bar{H}^{N} \qquad [3.29]$$

$$\bar{H}^{N} = \frac{V_{dg}^{N}}{V_L^{N}} \quad (\neq H) \qquad [3.30]$$

where,

ΔV_w = amount of water that drained to or from the element between times t_{N-1} and t_N

H = equilibrium solubility coefficient

V_L^N = total volume of liquids in the element at t_N.

$\bar{H}^N$ can also be expressed as follows:

$$V_L^N . \bar{H}^N = V_L^N H + (V_2^N - V_{fg}^N) \qquad [3.31]$$

thus,

$$\bar{H}^N = H + \frac{V_2^N - V_{fg}^N}{V_L^N} \qquad [3.32]$$

In order to simplify the analytical solution to the problem, Sobkowicz, 1982, assumed that

$$\frac{V_2^N - V_{fg}^N}{V_L^N} \simeq \frac{V_2^{N-1} - V_{fg}^{N-1}}{V_L^{N-1}} \qquad [3.33]$$

In this thesis, however, the rigorous solution, expressed by Equation 3.32 is preferred. It is assumed that the mass of water that flows into the element has a concentration of gas molecules identical to the gas concentration of the water already within the element.

The term $(V_2^N - V_{fg}^N)$ can, therefore, be expressed as follows:

$$V_2^N - V_{fg}^N = V_{Tg}^N - HV_L^N - V_{fg}^N \qquad [3.34]$$

Substituting 3.29 in 3.34 it follows:

$$V_2^N - V_{fg}^N = \frac{V_{Tg}^{N-1} P_{N-1}}{P_N} + \bar{H}^N \Delta V_w - HV_L^N - V_{fg}^N \qquad [3.35]$$

V_{Tg}^{N-1} can also be expressed by:

$$V_{Tg}^{N-1} = \bar{H}^{N-1} . V_L^{N-1} + V_{fg}^{N-1} \qquad [3.36]$$

Substituting 3.36 and 3.32 in 3.26:

$$V_2^N - V_{fg}^N = \frac{(\bar{H}^{N-1} . V_L^{N-1} + V_{fg}^{N-1}) P_{N-1}}{P_N} + (H + \frac{V_2^N - V_{fg}^N}{V_L^N}) \Delta V_w - HV_L^N - V_{fg}^N \qquad [3.37]$$

which can be rearranged in order to isolate the term $(V_2^N - V_{fg}^N)$ from other terms, as follows:

$$(V_2^N - V_{fg}^N) \left(1 - \frac{\Delta V_w}{V_L^N}\right) = \frac{(\bar{H}^{N-1} V_L^{N-1} + V_{fg}^{N-1}) . P_{N-1}}{P_N} + H\Delta V_w - HV_L^N - V_{fg}^N \qquad [3.38]$$

However,

$$H\Delta V_w - HV_L^N = HV_L^{N-1} \qquad [3.39]$$

Substituting 3.39 into 3.38 and rearranging 3.38:

$$V_2^N - V_{fg}^N = \frac{V^N}{V_L^{N-1}} \left[\frac{P^{N-1}(\bar{H}^{N-1} V_L^{N-1} + V_{fg}^{N-1})}{P^N} - H V_L^{N-1} - V_{fg}^N \right] \quad [3.40]$$

V_{fg}^N and V_L^N can also be expressed as functions of the soil physical properties:

$$V_L^N = \left[(S^N e^N)/(1+e^N) \right] V^N \quad [3.41]$$

$$V_{fg}^N = \left[(1-S^N) e^N/(1+e^N) \right] V^N \quad [3.42]$$

where, V^N = total volume of the element at t_N

e^N = void ratio at t_N

S^N = total degree of saturation at t_N

Substituting 3.41 and 3.42 in 3.40:

$$(V_2^N - V_{fg}^N) = \frac{S^N e^N (1+e^{N-1})}{S^{N-1} e^{N-1} (1+e^N)} \cdot V^N \left[\frac{P^{N-1}}{P^N (1+e^{N-1})} \right.$$

$$(\bar{H}^{N-1} \cdot S^{N-1} e^{N-1} + (1-S^{N-1}) e^{N-1})$$

$$\left. - \frac{H S^{N-1} e^{N-1}}{1+e^{N-1}} - \frac{(1-S^N) e^N}{1+e^N} \frac{V^N}{V^{N-1}} \right] \quad [3.43]$$

The term V^N/V^{N-1} in this equation can be expressed as:

$$\frac{V^N}{V^{N-1}} = \frac{V^{N-1}+\Delta V}{V^{N-1}}$$

$$= 1+\epsilon_v$$

$$= 1+\frac{\Delta e}{1+e^{N-1}}$$

$$= \frac{1+e^N}{1+e^{N-1}} \qquad [3.44]$$

Substituting 3.44 in 3.43

$$(V_2^N - V_{fg}^N) = \frac{S^N e^N (1+e^{N-1})}{S^{N-1} e^{N-1} (1+e^N)} \cdot V^N \left[\frac{P^{N-1}}{P^N (1+e^{N-1})} \right.$$

$$(\bar{H}^{N-1} \cdot S^{N-1} e^{N-1} + (1-S^{N-1}) e^{N-1})$$

$$\left. - \frac{HS^{N-1} e^{N-1}}{1+e^{N-1}} - \frac{(1-S^N)e^N}{1-e^{N-1}} \right] \qquad [3.45]$$

The values of e^N and S^N of Equation 3.45 can also be expressed in terms of the initial parameters and the degrees of freedom of the problem as follows:

Calculation of e^N

$$e^N = e^\circ + \Delta e$$

$$= e^\circ + (1+e^\circ)\epsilon_{V\text{total}} \qquad [3.46]$$

where,

e° = void ratio at the beginning of the first time step

Δe = total change in void ratio from the beginning of the solution

ϵ_{Vtotal} = total volumetric strain

Calculation of S^N

$$V_{fg}^N = V_{fg}^{N-1} + \Delta V_{fg} \qquad [3.47]$$

$$\frac{(1-S^N)e^N}{(1+e^N)} \cdot V^N = \frac{(1-S^{N-1})e^{N-1}}{1+e^{N-1}} \cdot V^{N-1} + \epsilon_v^{fg}\Big|_{tN-1}^{tN} \cdot V^{N-1} \qquad [3.48]$$

Substituting 3.44 in 3.48

$$\frac{(1-S^Ne^N)}{(1+e^N)} \cdot \frac{(1+e^N)}{(1+e^{N-1})} = \frac{(1-S^{N-1})e^{N-1}}{1+e^{N-1}} + \epsilon_v^{fg}\Big|_{tN-1}^{tN} \qquad [3.49]$$

$$(1-S^N)e^N = (1-S^{N-1})e^{N-1} + \epsilon_v^{fg}\Big|_{tN-1}^{tN} \cdot (1+e^{N-1}) \qquad [3.50]$$

$$(1-S^N) = (1-S^{N-1})\frac{e^{N-1}}{e^N} + \epsilon_v^{fg}\Big|_{tN-1}^{tN} \cdot \frac{(1+e^{N-1})}{e^N} \qquad [3.51]$$

$$S^N = 1 - \frac{1}{e^N}\left[(1-S^{N-1})e^{N-1} + \epsilon_v^{fg}\Big|_{tN-1}^{tN} \cdot (1+e^{N-1})\right] \qquad [3.52]$$

Substituting 3.46 in 3.52

$$S^N = 1 - \left(\frac{1}{e_o + (1+e_o)\epsilon_{Vtotal}}\right) \cdot \left[(1-S^{N-1})e^{N-1} + \epsilon_v^{fg}\Big|_{tN-1}^{tN} \cdot (1+e^{N-1})\right] \qquad [3.53]$$

Equation 3.53, 3.46, and 3.45 enable the expression of $(V_2^N - V_{fg}^N)$ as a function of the initial soil parameters and the degrees of freedom of the problem.

The term $(V_2^{N-1} - V_{fg}^{N-1})$ can also be expressed as a function of the initial soil parameters:

$$V_2^{N-1} - V_{fg}^{N-1} = (\bar{H}^{N-1} - H) \cdot V_L^{N-1}$$

$$= \frac{(\bar{H}^{N-1} - H) \cdot S^{N-1} \cdot e^{N-1} \cdot V^{N-1}}{1+e^{N-1}} \qquad [3.54]$$

Equation 3.54 and 3.45 can be substituted in Equation 3.26 and the change of volume of free gas due to gas evolution measured at P_{N-1} is given by:

$$\Delta V_{fg}^{EVO}\Big|^{PN-1} = \frac{\Delta t(1-a)(\bar{H}^{N-1} - H) S^{N-1} e^{N-1} V^{N-1}}{(t_N + A')(1+e^{N-1})}$$

$$+ \frac{P_N}{P_{N-1}} \cdot \frac{\Delta t a}{t_N + A'} \frac{S^N e^N (1+e^{N-1}) V^N}{S^{N-1} e^{N-1} (1+e^N)}$$

$$\left[\frac{P_{N-1}}{P_N(1+e_{N-1})}(\bar{H}^{N-1} S^{N-1} e^{N-1} + (1-S^{N-1})e^{N-1}\right)$$

$$- \frac{HS^{N-1}e^{N-1}}{(1+e^{N-1})} - \frac{(1-S^N)e^N V^N}{(1+e^N)V^{N-1}} \Bigg] \qquad [3.55]$$

Substituting Equation 3.44 in the second term of the right hand side of Equation 3.55, and rearranging this latter equation, leads to:

$$\Delta V_{fg}^{EVO}\Big|^{PN-1} = V_{N-1}\frac{\Delta t(1-\alpha)(\bar{H}^{N-1}-H)S^{N-1}e^{N-1}}{(t_{N-1}+A')\ (1+e^{N-1})}$$

$$+ \frac{P_N}{P_{N-1}}\ \frac{\Delta t\alpha}{(t_N+A')}\ \frac{S^N e^N}{S^{N-1}e^{N-1}}\ \frac{V_{N-1}}{(1+e^{N-1})}$$

$$\left[\frac{P_{N-1}}{P_N}\ (\bar{H}^{N-1}\ S^{N-1}\ e^{N-1} + (1-S^{N-1})e^{N-1}\right)$$

$$- HS^{N-1}e^{N-1} - (1-S^N)\ e^N\Big] \qquad [3.56]$$

Substituting Equation 3.56 in 3.22 and then 3.22 in 3.19, and assuming that

$$V^{N-1} = dV\ \frac{(1+e^{N-1})}{(1+e^{\circ})} \qquad [3.57]$$

where

dV = inital total volume of the soil element

The term $\int_{tN-1}^{tN} \epsilon_v^{fg} dt$ can be expressed as follows

$$\int_{tN-1}^{tN} \dot{\epsilon}_v^{fg} dt = \frac{1}{dV} \int_{tN-1}^{tN} d\dot{V}_{fg}\, dt$$

$$= \frac{(1-S^{N-1})e^{N-1}}{(1+e^{N-1})} \cdot \frac{(1+e^{N-1})}{(1+e^{\circ})} \cdot \frac{(P_{N-1}-P_N)}{P_N}$$

$$+ \frac{P_{N-1}}{P_N} \cdot \frac{(1+e^{N-1})}{(1+e^{\circ})} \cdot \left[\frac{\Delta t(1-a)(\bar{H}^{N-1}-H)S^{N-1}.e^{N-1}}{(t_{N-1}+A')(1+e^{N-1})} \right.$$

$$+ \frac{P_N \Delta t a S^N e^N}{P_{N-1}(t_N+A')S^{N-1}e^{N-1}(1+e^{N-1})}$$

$$\cdot \left[\frac{P_{N-1}}{P_N} (\bar{H}^{N-1}.S^{N-1}.e^{N-1}+(1-S^{N-1})e^{N-1}) \right.$$

$$\left. \left. - H.S^{N-1}e^{N-1}-(1-S^N)e^N \right] \right]$$

$$= \frac{(1-S^{N-1})e^{N-1}(P_{N-1}-P_N)}{(1+e^{\circ})\ P_N} + \frac{P_{N-1}\Delta t(1-a)(\bar{H}^{N-1}-H)S^{N-1}e^{N-1}}{P_N(1+e^{\circ})\ (t_{N-1}+A')}$$

$$+ \frac{\Delta t a S^N e^N}{(t_{N-1}+A')S^{N-1}e^{N-1}(1+e^{\circ})} \left[\frac{P_{N-1}}{P_N} (\bar{H}^{N-1}\ S^{N-1}\ e^{N-1} \right.$$

$$\left. + (1-S^{N-1})\ e^{N-1} - HS^{N-1}e^{N-1} - (1-S^N)\ e^N \right] \qquad [3.58]$$

where the values of e^N and S^N are given by Equations 3.46 and 3.53.

Equation 3.58 indicates that, for the solution of the continuity equation (Equation 3.18), $\bar{H}$, the non-equilibrium solubility constant, must be known at the beginning of every solution step. This is possible with a knowledge of the degrees of freedom and soil parameters at the beginning and end of the preceding time increment, as demonstrated below:

Calculation of $\bar{H}^N$

$$\bar{H}^N = H + \frac{V_2^N - V_{eq}^N}{V_L^N}$$

$$= H + \frac{S^N e^N (1+e^{N-1})}{S^{N-1} e^{N-1} (1+e^N)} V^N \frac{(1+e^N)}{S^N e^N V^N}$$

$$\left[\frac{P_{N-1}}{P_N (1+e^{N-1})} (\bar{H}^{N-1} S^{N-1} e^{N-1} + (1-S^{N-1}) e^{N-1}) \right.$$

$$- H \frac{S^{N-1} e^{N-1}}{(1-e^{N-1})} - \frac{1-S^N e^N}{(1+e^{N-1})}$$

$$= H + \frac{1}{S^{N-1} e^{N-1}} \left[\frac{P_{N-1}}{P_N} (\bar{H}^{N-1} S^{N-1} e^{N-1} + (1-S^{N-1}) e^{N-1}) \right.$$

$$\left. - H S^{N-1} e^{N-1} - (1-S^N) e^N \right]$$

$$= H + \frac{P_{N-1}}{P_N} \left[\bar{H}^{N-1} + \frac{e^{N-1}}{S^{N-1} e^{N-1}} - \frac{S^{N-1} e^{N-1}}{S^{N-1} e^{N-1}}\right]$$

$$- H - \frac{(1-S^N) e^N}{S^{N-1} e^{N-1}}$$

$$= \frac{P_{N-1}}{P_N} \left[\bar{H}^{N-1} + \frac{1}{S^{N-1}} - 1\right] - \frac{(1-S^N) e^N}{S^{N-1} e^{N-1}} \qquad [3.59]$$

e^N and S^N can be evaluated with Equation 3.46 and 3.53.

Therefore, the complete formulation for the gas evolution problem at a point within the soil mass is given by Equations 3.46, 3.53, 3.58 and 3.59, which is a function of the soil physical properties at the beginning of a given time step, and also a function of the degrees of freedom of the problem, both at the beginning and end of the time step under consideration. The spatial discretization of the degrees of freedom under consideration is discussed in the

following section.

3.3.2.2 Spatial Discretization of the Degrees of Freedom

The spatial discretization of the field variables involved in the solution of soil consolidation problems has been done with the use of either triangular or quadrilateral elements, where, in most cases, the displacements and pore pressures are interpolated linearly or quadratically. The elements can be grouped into two classes, standard and composite (Reed, 1984).

In the standard elements, both the displacements and pore pressures are approximated with the same order of interpolation. Belonging to this group are the triangular and quadrilateral elements illustrated in Figure 3.3. In the composite elements, the order of interpolation of pore pressures is lower than the order of interpolation of displacements. These elements are illustrated in Figure 3.4. Table 3.1 presents a list of some publications by researchers involved in the finite element simulation of consolidation problems, and the elements used by them. The development of the composite elements was probably based on the consideration that according to the theory of small deformations, stresses are proportional to the derivative of displacements. Therefore, it is reasonable to assume that the pore pressures are also proportional to the derivative of displacements. Sandhu et al., 1977, undertook an analysis on the performance of the standard elements and of the composite elements, Types 6-3 and 8-4, on the basis of

PUBLICATION	STANDARD ELEMENT		COMPOSITE ELEMENT			
	TRIANG.	QUADRILAT	TRIANGULAR		QUADRILATERAL	
	6-6	8-8	6-3	15-3	8-4	SING.
SANDHU AND WILSON 1969			X			
HWANG ET AL. 1971			X			
YOKOO ET AL. 1971		X				
GHABOUSSI AND WILSON 1973			X			
SANDHU ET AL. 1977	X	X	X		X	
SIRIWARDANE AND DESAI 1981			X			
CHANG AND DUNCAN 1983					X	
REED 1982,1984		X				
MEIJER 1984			X			
KHALED ET AL. 1985					X	
SANDHU ET AL. 1985						X
WAN 1985		X				
VAZIRI 1986			X	X		

Table 3.1 Spatial Discretization Schemes - Users

STANDARD ELEMENTS

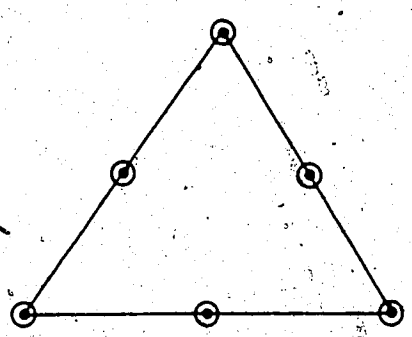

triangular 6-6

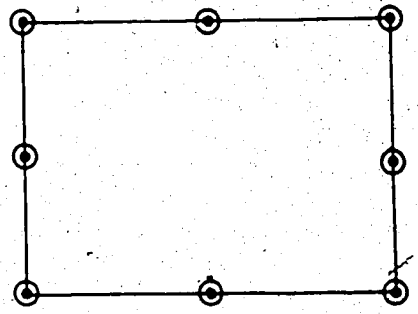

quadrilateral 8 - 8

○ pore pressure node (1 d.o.f.)

• displacement node (2 d.o.f.)

Figure 3.3 Spatial Discretization of Field Variables in Consolidation Problems - Standard Elements

COMPOSITE ELEMENTS

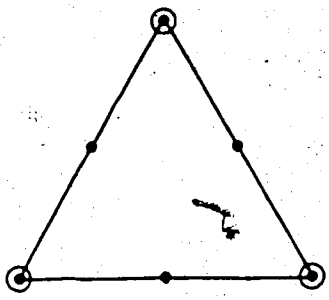

triangular 6-3

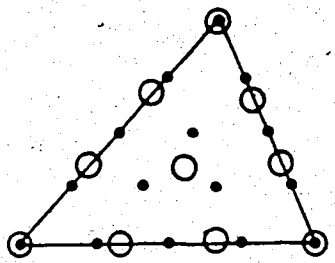

triangular 15-10

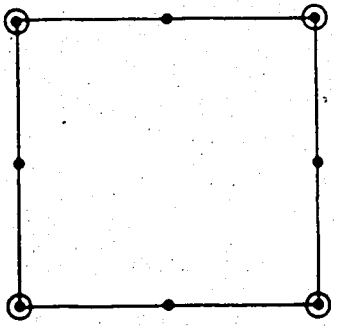

quadrilateral 8-4

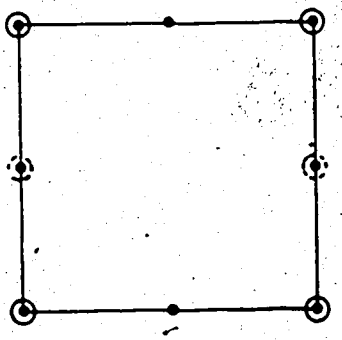

quadrilateral singular 8-4 and 8-6

○ pore pressure node (1 d.o.f.)

• displacement node (2 d.o.f.)

◌ pore pressure node (1 d.o.f.) present only in the quadrilateral singular 8-6 element

Figure 3.4 Spatial Discretization of Field Variables in Consolidation Problems - Composite Elements

analytical results for 1-D elastic consolidation. Within the same class of elements, both the triangular and quadrilateral elements, presented similar numerical performance, i.e. accuracy of results and CPU time efficiency. The standard elements were unable to perform immediate response analyses by simply setting $\Delta t=0$ for the first time increment because, by following this procedure, the stiffness matrix became singular.

The element Types 6-6 and 8-8 also did not give satisfactory answers when a very small time step was used, just after the application of a load. On the other hand, element Types 6-3 and 8-4 gave reasonable estimates for the "undrained immediate response" and improved results at later time-steps. The standard elements gave better estimates of settlement at early time stages than the composite elements. However, at later stages, the differences were insignificant. The standard elements gave errors in pore pressures which did not dissipate in time and were oscillating in space.

By relaxing the inter-element continuity of pore pressures, Yokoo et al., 1971-c, developed a new variational formulation which, when applied to the 1-D consolidation case with the element Type 8-8, resulted in predictions of the immediate response more accurately than the ones reported by Sandhu et al., 1977, for the same type of element.

Reed, 1982 and 1984, developed a so-called "smoothing" technique, that aimed at improving the performance of the standard quadrilateral element 8-8. The basic premise of Reed's technique is that the pore pressure distribution produced by the isoparametric element gives the exact solution at the four integration points.

Under this assumption, he further assumed that the "correct" pore pressure distribution within the element is given by a bi-linear surface that satisfied the pore pressure values at the four integration points. With this assumption, the "correct" pore pressures at the nodes can be evaluated. The displacement field associated with the "correct" pore pressure can be calculated by re-solving the finite element equations, with the same time step, Δt, and the same loading, but with the "correct" pore pressures taken as additional specified degrees of freedom.

This technique eliminated the oscillatory nature of the pore pressure within the meshes and yielded excellent prediction of the pore pressures and displacements.

In order to avoid the ill-conditioning of the stiffness matrix for cases when Δt_o is made too small, for the initial immediate response solution, Reed developed a technique which is presented later in this chapter. The good results obtained by Reed were later confirmed by Wan, 1985.

The good accuracy of solutions produced by Reed's technique is, however, obtained at higher computational time, and consequently, higher cost. As reported by Reed,

1984:256, the smoothing process takes only a small fraction of the total time of the solution, however, the re-solution of the finite element equations for the same time increment, increased the total time of solution by approximately 50%.

Other not so popular composite elements, also illustrated in Figure 3.4, are the quadrilateral singular elements. They were introduced by Sandhu et al., 1985, aiming at modelling pore pressures in the vicinity of the free draining surfaces. In this region, the field variables are interpolated with functions of the type,

$$f(x) = 1 - ax - (1-a)x^N \qquad [3.60]$$

where $a = 1 - (1/e^{\gamma\tau})$

γ = scalar coefficient

τ = non-dimensional time factor

The numerical test results presented by the authors indicated that the 8-6 singularity element scheme was unsatisfactory. The errors in pore pressure prediction near the draining surface were high. The accuracy of the results obtained with the 8-4 singularity element was highly dependent on the values arbitrarily assigned for N and γ of Equation 3.60. More numerical testing of this element is required before it can be used with confidence in more general consolidation problems.

The triangular 15-10 element was discussed in detail by Vaziri, 1986. The element allows a quartic displacement and a cubic pore pressure interpolation. The higher degree of interpolation used in this element aims at improving

mechanical performance at the mesh at nearly incompressible or highly restrained conditions. However, as reported by Sandhu et al., 1985, the use of higher order interpolation near loaded boundaries has had limited success.

Considering the facts exposed in this section, and the availability of some subroutines used by Hwang, 1970, at the time the program CONGAS was developed, it was decided to use the triangular 6-3 composite element.

3.3.2.3 Finite Element Equations

The derivation of the finite element equations presented in this section follows, with a few modifications, the derivation published by Chang and Duncan, 1983.

The four independent variables, W_i (displacements) and u, are approximated by interpolation (shape) functions, as described in the preceding section. The soil domain is subdivided into triangular 6-3 finite elements. Within the elements, the independent variables are approximately represented by the values of $W_{i\alpha}$ and u_α, defined at the nodes of the finite elements.

$$W_i^* = \phi_{i\alpha}^w . W_{i\alpha} = \langle \phi_w \rangle \{\bar{W}_i\} \qquad [3.61]$$

$$u^* = \phi_\alpha^u . u_\alpha = \langle \phi_u \rangle \{\bar{u}\} \qquad [3.62]$$

where, $\phi_{i\alpha}^w$ = interpolation function for displacements

ϕ_α^u = interpolation function for pore pressures

Therefore, the W_i^* vary quadratically and u^* varies linearly within the elements. As a consequence, the volumetric strains of the element, $W_{i,i}^*$, vary linearly within the element. The volumetric change of gas per unit volume of soil is also assumed to vary linearly within the elements and can be expressed as:

$$\epsilon_v^{*fg} = \phi_a^u \epsilon_{va}^{fg}\Big|_{tN-1}^{tN} = \langle \phi_u \rangle \left[\bar{\epsilon}_v^{fg}\right]_{t_{N-1}}^{t_N} \qquad [3.63]$$

Substituting Equations 3.63, 3.62 and 3.61 into the governing equations, it follows:

$$\left[C_{ijkl}\frac{1}{2}(W_{k,l}^* + W_{l,k}^*)\right]_{,j}\Big|^{tN}$$

$$+ u_{,j}^* + \rho_s F_j = ER_j \qquad [3.64]$$

$$- a\Delta t\left[k_{ij}(u_{,j}^* + \rho_w F_j)\right]_{,i}\Big|^{tN}$$

$$- (1-a)\Delta t\left[k_{ij}(u_{,j}^* + \rho_w F_j)\right]_{,i}\Big|^{tN-1}$$

$$+ W_{i,i}^*\Big|^{tN} - W_{i,i}^*\Big|^{tN-1} - \frac{u^*}{Q}\Big|^{tN}$$

$$+ \frac{u^*}{Q}\Big|^{tN-1} - \epsilon_v^{*fg}\Big|_{tN-1}^{tN} = ER \qquad [3.65]$$

where ER_j and ER are the errors of the residuals arising from the approximations resulting from the interpolations

from nodes.

The weighted residual methods assume that the best solution can be found if the integrals of Equations 3.64 and 3.65, times the weighting functions are zero,

$$\int W \cdot ER \cdot dV = 0 \qquad [3.66]$$

where,

ER = error

W = weighting function.

Following Galerkins's procedure, the weighting functions are assumed to be the interpolation functions. Substituting 3.64 and 3.65 in 3.66 and imposing boundary conditions given by the Equations 3.9 to 3.12, the governing equations can be expressed in the matrix form, as follows:

$$[K_1]\{W\}_{tN} + [C]\{u\}_{tN} = \{M_1\} + \{M_2\} + \{T\} \qquad [3.67]$$

and

$$[C]^T\{W\}_{tN} - a\Delta t[K_2]\{u\}_{tN} - [E]\{u\}_{tN} =$$

$$[C]^T\{W\}_{tN-1} - (1-a)\Delta t[K_2]\{u\}_{tN-1} - [E]\{u\}_{tN-1}$$

$$+ a\Delta t\{M_3\}_{tN} + (1-a)\Delta t\{M_3\}_{tN-1} - a\Delta t\{Q\}_{tN}$$

$$- (1-\alpha)\Delta t\{Q\}_{tN-1} + \{\epsilon_v^{fg}\}_{tN-1}^{tN} \qquad [3.68]$$

$[K_1]\{w\}_{tN}$ is the nodal force vector due to the straining of the soil skeleton.

$[C]\{u\}_{tN}$ is the nodal force vector resulting from the pore pressure gradient;

$\{M_1\}$ is the initial stress vector;

$\{M_2\}$ is the body force vector;

$\{T\}$ is the specified boundary traction vector;

$[C]^T\{W\}_{tN}$ is the volumetric strain of the soil skeleton;

$\alpha\Delta t[K_2]\{u\}_{tN}+(1-\alpha)\Delta t[K_2]\{u\}_{tN-1}$ is the fluid inflow due to pore pressures;

$[E]\{u\}_{tN}-[E]\{u\}_{tN-1}$ is the volumetric strain of the liquid phase due to changes in pore pressure;

$\alpha\Delta t\{M_3\}_{tN}+(1-\alpha)\Delta t\{M_3\}_{tN-1}$ represents the gravity forces;

$\alpha\Delta t\{Q\}_{tN}+(1-\alpha)\Delta t\{Q\}_{tN-1}$ is the specified boundary flow; and

$\{\epsilon_v^{fg}\}_{tN-1}^{tN}$ is the volumetric strain due to volume change of free gas.

Equations 3.67 and 3.68 can be grouped and expressed as follows:

$$\left[\begin{array}{c|c} [K_1] & [C] \\ \hline [C]^T & [-\alpha\Delta t[K_2]-[E]] \end{array}\right] \times \left\{\begin{array}{c} W_{tN} \\ \hline V_{tN} \end{array}\right\} = \left\{\begin{array}{c} \\ \hline \{M_1\} + \{M_2\} + \{T\} \end{array}\right\}$$

$$\left\{ \begin{array}{l} [C]\{W\}_{tN-1} + (1-\alpha)\Delta t[K_2]\{u\}_{tN-1} + \\ + \alpha\Delta\{M_3\}_{tN} + (1-\alpha)\Delta t\{M_3\}_{tN-1} - \\ - \alpha\Delta t\{Q\}_{tN} - (1-\alpha)\Delta t\{Q\}_{tN-1} + \\ [E]\{u\}_{tN-1} + \{e_v^{fg}\}_{tN-1}^{tN} \end{array} \right\} \qquad [3.69]$$

where, for each element:

$$[K_1]_{\delta\alpha} =$$

$$= \int_{Ve} \frac{1}{2} (\phi^w_{i\delta,j} + \phi^w_{j\delta,i}) C_{ijkl} \frac{1}{2} (\phi^w_{k\alpha,l} + \phi^w_{l\alpha,k}) \, dV$$

$$= \int_{Ve} [B_e]^T [H] [B_e] dV \qquad [3.70]$$

$$[K_2]_{\tau\gamma} = \int_{Ve} \phi^u_{\tau,i} K_{ij} \phi^u_{\gamma,j} dV = \int_{Ve} [B_q][R][B_q]^T dV \qquad [3.71]$$

$$[C]_{\delta\gamma} = \int_{Ve} \phi^w_{i\delta,i} \phi^u_{\gamma} dV = \int_{Ve} [B_w] \langle \phi_u \rangle dV \qquad [3.72]$$

$$\{M_1\}_\delta = \int_{Ve} \frac{1}{2} (\phi^w_{i\delta,j} + \phi^w_{j\delta,i}) . \sigma_{oij} \, dV$$

$$= \int_{Ve} [B_e]^T \{\sigma_o\} \, dV \qquad [3.73]$$

$$\{M_2\}_\delta = \int_{Ve} \phi^w_{i\delta} \rho_s F_i dV = \int_{Ve} \langle \phi_w \rangle^T \rho_s F_i \, dV \qquad [3.74]$$

$$\{M_3\}_r = \int_{Ve} \phi^u_{r,i} K_{ij} \rho_w F_j dV = \int_{Ve} [B_q]^T [R] \rho_w F_i dV \qquad [3.75]$$

$$\{T\}_\delta = \int_{ST} \phi^w_{i\delta} T_i dS = \int_{ST} <\phi_w>^T \bar{T}_i dS \qquad [3.76]$$

$$\{Q\}_r = \int_{SQ} \phi^u_r \bar{q} dS = \int_{SQ} <\phi_u>^T \bar{q} dS \qquad [3.77]$$

$$\{\epsilon^{fg}_v\}^{tN}_{tN-1} = \int_{Ve} \phi^u_r \epsilon^{fg}_v \Big|^{tN}_{tN-1} dV$$

$$= \int_{Ve} <\phi_u>^T \epsilon^{fg}_v \Big|^{tN}_{tN-1} dV \qquad [3.78]$$

$$[E]_{rr} = \int_{Ve} \frac{1}{Q} \phi^u_r \phi^u_r dV$$

$$= \int \frac{1}{Q} \{\phi_u\} <\phi_u> dV \qquad [3.79]$$

In order to introduce material non-linearity for the simulation of the soil skeleton response, it is convenient to express the stress-strain relationship as follows:

$$\{\dot{\sigma}\} = [C_t] \{\dot{\epsilon}\} \qquad [3.80]$$

where,

$\{\dot{\sigma}\}$ = increment in effective stress

$\{\dot{\epsilon}\}$ = corresponding increment in strains

$[C_t]$ = matrix of tangent values which are functions of the current state of stress and are derived from the non-linear elastic model, presented later in

this chapter.

With the aid of Equation 3.80, Equation 3.69 can be expressed in terms of incremental displacements and total pore pressures as follows:

$$\left[\begin{array}{c|c} [K_1]_t & [C] \\ \hline [C]^T & -a\Delta t[K_2]_t - [E] \end{array}\right] \times \left\{\begin{array}{c} \Delta W \Big|_{tN-1}^{tN} \\ \hline u_{tN} \end{array}\right\} = \left\{\begin{array}{l} \{M_1\}^{**} + \{M_2\}^{**} + \{\Delta T_t\} + C\{u\}_{tN-1} \\ \hline (1-a)\Delta t[K_2]_{tN-1}\{u\}_{tN-1} + a\Delta\{M_3\}_{tN} + \\ + (1-a)\Delta t\{M_3\}_{tN-1} - a\Delta t\{Q\}_{tN} - \\ - (1-a)\Delta t\{Q\}_{tN-1} + \{\bar{\epsilon}_v^{fg}\}_{tN-1}^{tN} - [E]\{u_{tN-1}\} \end{array}\right\} \quad [3.81]$$

** included only in the first time increment.

The development of the finite element program CONGAS aimed at solving the Equation 3.81. The structure and details of this program are presented in the following section.

3.3.3 Structure and Details of CONGAS

Equation 3.81, developed in the preceding section, except for the term $\{\epsilon_v^{fs}\}_{tN-1}^{tN}$ in the load vector, is identical to the equation previously developed by Chang and Duncan, 1983. By imposing [E] equal to zero, i.e. assuming the pore fluids incompressible, the equations become identical to the ones presented by Sandhu and Wilson, 1969, and by Hwang et al. 1971. Due to this similarity, it was possible to develop CONGAS based on the structure of existing finite element programs for coupled consolidation. As mentioned in the preceding section, at the time of the beginning of the development of CONGAS, the code of the program developed by Hwang, 1970, was available. At that time, Hwang's program allowed the simulation of plane strain, coupled consolidation of a linear elastic soil skeleton, subjected to homogeneous displacement boundary conditions and constant boundary stresses. The frame of Hwang's program was used as the starting point for the development of CONGAS. With a series of modifications, it was possible to upgrade CONGAS in order to include:

- pre-processing facility
- option for coupled consolidation only or coupled consolidation and gas evolution
- option for linear elastic or three other non-linear elastic material models
- option for plane strain or axisymmetric formulation
- option for constant or variable coefficient of

permeability

- option for compressible or incompressible pore liquids
- re-start facility

The main structure of CONGAS is depicted, in a simplified form, in Figure 3.5. A detailed flowchart of CONGAS is given in a report by Branco, 1988. This report also presents a detailed description of the variables involved and the subroutines.

Appendix B presents details of the integration schemes and procedures adopted for the evaluation of the element stiffness matrices.

The most relevant points based on which CONGAS was structured, are discussed in the following items.

Iterative Scheme for Solutions of Non-Linear Fluid Flow

The analysis of the terms of Equation 3.81 indicates that the vector $\{\epsilon_v^{fg}\}_{tN-1}^{tN}$ given by Equations 3.78, 3.58 and 3.59, representing the gas volume increase that occurred between times t_{N-1} and t_N, introduces a nonlinearity in the finite element equations. This occurs because $\{\epsilon_v^{fg}\}_{tN-1}^{tN}$, present in the load vector of Equation 3.81, requires knowledge of the field variables W_1 and u, both at t_N and t_{N-1}, for its evaluation. This procedure is presented in detail by Branco, 1988, and is summarized as follows.

1. For the first iteration of a given time increment, Equation 3.81 is solved with $\{\epsilon_v^{fg}\}_{tN-1}^{tN}$ obtained from the preceding time increment. If the time increment under consideration is the first one (i.e. $t_{N-1}=0$, the elements

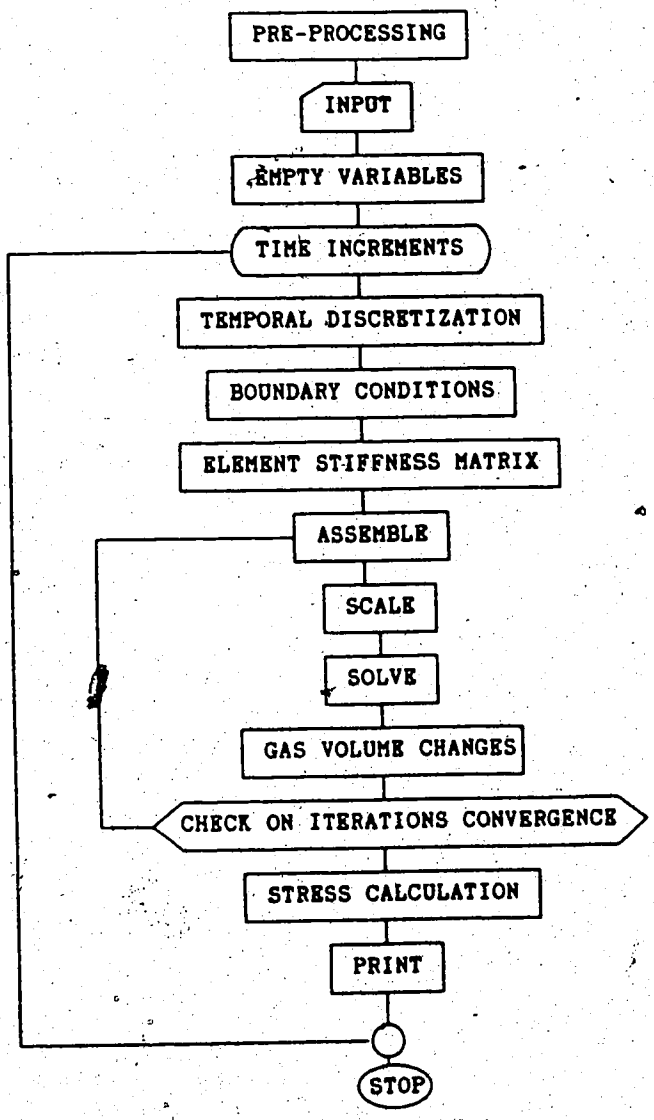

Figure 3.5 Simplified Flow Chart of the Structure of CONGAS

of $\{\epsilon_v^{fg}\}_{tN-1}^{tN}$ are assumed to be equal to zero.

2. The solution of Equation 3.81 produces the values of ΔW_i and u at the nodal points of the finite element mesh, at time t_N or $(\Delta W_i, u)$. Therefore, at the end of this time step, i.e. iteration I, the values of $(W_i,u)_{tN-1}$ and $(\Delta W_i,u)_{tN}^{I}$ are known.

3. Knowledge of $(\Delta W_i,u)_{tN}^{I}$ and $(W_i,u)_{tN-1}$ allows the evaluation of $\epsilon_{v,I}^{fg,tN}$, i.e., the volumetric gas change at t_N during iteration I, at the nodes of the mesh elements. With $\epsilon_{v,I}^{fg,tN}$, the vector $\{\epsilon_v^{fg}\}_{tN-1}^{tN,I}$ can be evaluated.

4. The vector $\{\epsilon_v^{fg}\}_{tN-1}^{tN}$, to be used in Equation 3.81, is evaluated as follows:

$$\{\epsilon_v^{fg}\}_{tN-1}^{tN} = \{\epsilon_v^{fg}\}_{tN-1}^{tN,I-1} + \left[\{\epsilon_v^{fg}\}_{tN-1}^{tN,I} - \{\epsilon_v^{fg}\}_{tN-1}^{tN,I-1}\right] * DAMP \qquad [3.82]$$

The damping factor, DAMP, is included in the evaluation of the new "lumped" volumes of free gas, in order to allow faster convergence of the iterations. Section 3.3.5.3 discusses in more detail the values for DAMP.

5. With the new value of $\{\epsilon_v^{fg}\}_{tN-1}^{tN}$ step (2) is repeated, i.e., finite element equation 3.81 is re-solved and the values $(\Delta W_i, u)_{tN}^{I+1}$ are obtained. At this stage the values $(\Delta W_i,u)_{tN-1}$, $(\Delta W_i,u)_{tN}^{I}$ and $(\Delta W_i,u)_{tN}^{I+1}$ are known.

6. The error associated with the calculations in iteration I can be evaluated at each nodal point.

$$\text{ERROR}\Big|_{I}^{I+1} = \left| \frac{(\Delta W_i, u)_{tN}^{I+1} - (\Delta W_i, u)_{tN}^{I}}{(W_i, u)_{tN-1}} \right| \qquad [3.83]$$

7. With values of $(\Delta W_i, u)_{tN}^{I+1}$ and $(W_i, u)_{tN-1}$

$\{\epsilon_v^{fg}\}_{tN-1}^{tN,I+1}$ can be evaluated, and together with

$\{\epsilon_v^{fg}\}_{tN-1}^{tN,I}$, according to Equation 3.82, allows evaluation of the new $\{\epsilon_v^{fg}\}_{tN-1}^{tN}$ to be used in Equation 3.81.

8. Step 5 is repeated and values of $(\Delta W_i, u)_{tN}^{I+2}$ are obtained.

9. Step 6 is repeated and the new error, associated with iteration I+1, is evaluated according to Equation 3.83.

10. At this stage, the values of the errors associated with iterations, I and I+1, allow verification of convergence of the iteration procedure. Convergence is achieved if the error in successive iterations decreases.

    If convergence is verified in the previous two iterations, but the error associated with the last iteration is higher than a specified tolerance, a new iteration is carried out with the repetition of steps 7 to 10.

11. Successive iterations are performed until the error, evaluated in the last iteration, is lower than the specified tolerance. When this occurs, the last values of $(\Delta W_i, u)_{tN}$ are assumed to be the correct answer. The converged values of $(W_i, u)_{tN}$ are evaluated and the calculations for the subsequent time step can be performed.

12. If, however, after successive iterations it is verified

that the errors increase, i.e. the solution diverges, the program stops. Section 3.3.5.3 discusses the measures to be taken when divergence takes place.

It is worth noting that between successive interations the solution scheme presented above does not require the re-evaluation and re-assembling of the total stiffness matrix on the left hand side of the finite element equations. Between successive iterations, only the load vector is re-assembled with the new values of $\{\epsilon_v^{fg}\}_{tN-1}^{tN}$ (the values of the coefficient of permeability are assumed to be constant during the iterative procedure). This efficient computational scheme not only eliminates the necessity of evaluating the element stiffness matrices between iterations, but also allows simplifications in the solution scheme of the finite element equations, described later in this section

The solution scheme described above is schematically illustrated as the internal loop of the flow chart in Figure 3.5.

Material Models

Four elastic material models are available in CONGAS:

1. Linear elastic, based on ν (Poisson's ratio) and E (Young's modulus)
2. Hyperbolic conventional, based on E and B (bulk modulus), both obtained as a function of σ'_3 (minor principal effective stress).
3. Hyperbolic modified I, based on G (shear modulus) and B,

both obtained as functions of σ'_3.

4. Hyperbolic modified II, based on G and B, both obtained as a function of σ'_{oct} (octahedral effective stress).

Depending on the material model used, one of the following constitutive matrices is used for the evaluation of $[K_1]_t$ (Equation 3.70):

1. Linear elastic:

axisymmetric formulation:

$$[H] = \frac{E(1-\nu)}{(1+\nu)(1-2\nu)} \begin{bmatrix} 1 & \frac{\nu}{1-\nu} & 0 & \frac{\nu}{1-\nu} \\ \frac{\nu}{1-\nu} & 1 & 0 & \frac{\nu}{1-\nu} \\ 0 & 0 & \frac{1-2\nu}{2(1-\nu)} & 0 \\ \frac{\nu}{1-\nu} & \frac{\nu}{1-\nu} & 0 & 1 \end{bmatrix} \quad [3.84]$$

2. Hyperbolic conventional:

axisymmetric formulation:

$$[H] = \frac{3B}{9B-E} \begin{bmatrix} (3B+E) & (3B-E) & 0 & (3B-E) \\ (3B-E) & (3B+E) & 0 & (3B-E) \\ 0 & 0 & E & 0 \\ (3B-E) & (3B-E) & 0 & (3B+E) \end{bmatrix} \quad [3.85]$$

3. Hyperbolic modified, both I and II:

axisymmetric formulation:

$$[H] = \begin{bmatrix} (B+(4/3)G) & (B-(2/3)G) & 0 & (B-(2/3)G) \\ (B-(2/3)G) & (B+(4/3)G) & 0 & (B-(2/3)G) \\ 0 & 0 & 2G & 0 \\ (B-(2/3)G) & (B-(2/3)G) & 0 & (B+(4/3)G) \end{bmatrix} \quad [3.86]$$

The constitutive matrices for the plane strain formulation are obtained from the matrices above, by imposing H(I,4)=H(4,I)=0 (I=1 to 4).

The strains tensors associated with the constitutive matrices above are:

Axisymmetric formulation:

$$\langle \epsilon \rangle = \langle \epsilon_x \ \epsilon_y \ \epsilon_{xy} \ \epsilon_z \rangle_{1x4} \quad [3.87]$$

Plane Strain Formulation:

$$\langle \epsilon \rangle = \langle \epsilon_x \ \epsilon_y \ \epsilon_{xy} \rangle_{1x3} \quad [3.88]$$

The tangent elastic moduli for each of the materials models are evaluated as follows:

1. Linear elastic model.

$$E_t = E \text{ (constant)}$$

$$\nu_t = \nu \text{ (constant)}$$

2. Hyperbolic conventional model

$$E_t = K_E P_a \left(\frac{\sigma'_3}{P_a}\right)^n \left[1 - \frac{R_F(\sigma_1-\sigma_3)(1-\sin\phi)}{2\,\sigma_3\,\sin\phi}\right]^2 \quad [3.89]$$

$$\text{where, } \phi = \phi_o - \Delta\phi \log\left(\frac{\sigma'_3}{P_a}\right) \quad [3.90]$$

$$B_t = K_B P_a \left(\frac{\sigma'_3}{P_a}\right)^m \qquad [3.91]$$

The terms of the three equations above are described by Duncan et al., 1980.

3. Hyperbolic modified I model

$$G_t = K_G P_a \left(\frac{\sigma_3'}{P_a}\right)^n \left[1 - \frac{R_F(\sigma_1-\sigma_3)(1-\sin\phi)}{2\sigma_3'\sin\phi}\right]^2 \qquad [3.92]$$

where

K_G = shear modulus number

ϕ and B_t are obtained from Equations 3.90 and 3.91 respectively. The other variables are defined by Duncan et al., 1980.

4. Hyberbolic modified II model

$$G_t = K_G P_a \left(\frac{\sigma'_{oct}}{P_a}\right)^n \left[1 - \frac{R_F \tau_{oct}(3-\sin\phi)}{2\sqrt{2}\sigma'_{oct}\sin\phi}\right]^2 \qquad [3.93]$$

$$B_t = K_B P_a \left(\frac{\sigma'_{oct}}{P_a}\right)^m \qquad [3.94]$$

$$\phi = \phi_o - \Delta\phi \log\left(\frac{\sigma'_{oct}}{P_a}\right) \qquad [3.95]$$

A complete description on the development of the three Equations above, and how to obtain the required constants from laboratory tests, is given in Sections 4.3.3.4 and 4.3.3.5 of Chapter 4.

The fact that the elastic constants in models 2, 3 and 4 are independently evaluated from laboratory tests can lead to situations incompatible with the theory of elasticity. Therefore, restrictions are imposed on the values of these constants, as follows:

For material model 2, the constitutive matrix is expressed in terms of E_t and B_t. In order to obtain values of Poisson's ratio betwen 0.0 and 0.5, E_t and B_t must obey the following relationships:

$$\nu_t = \frac{3B_t - E_t}{6B_t} \qquad [3.96]$$

Thus,

$$\text{for } \nu_t \geq 0 \ , \ B_t \geq E_t/3 \qquad [3.97]$$

$$\text{for } \nu_t \leq 0.5 \ , \ E_t \geq 0 \qquad [3.98]$$

$$\text{or for } \nu_t \leq 0.4998 \ , \ E_t \geq 0.001 \ B_t \qquad [3.99]$$

Notice that the condition imposed by Equation [3.98] is always satisfied in the hyperbolic model. The condition imposed by Equation 3.99 was introduced in CONGAS in order to guarantee numerical stability. Equation 3.97 is also verified in CONGAS.

For material models 3 and 4 the constitutive matrices are expressed in terms of G_t and B_t. In order to obtain

values of Poisson's ratio between 0 and 0.5, the following relationships are imposed in CONGAS:

$$\nu_t = \frac{3B_t - 2G_t}{6B_t + 2G_t} \qquad [3.100]$$

Thus,

$$\text{for } \nu_t \geq 0 \ , \ B_t \geq (2/3)G_t \qquad [3.101]$$

$$\text{for } \nu_t \leq 0.5 \ , \ G_t \geq 0 \qquad [3.102]$$

$$\text{or for } \nu_t \leq 0.4995 \ , \ G_t \geq 0.001\ B_t \qquad [3.103]$$

For the same reason discussed in the case of model 2, the condition imposed by Equation 3.103 is imposed in CONGAS.

In order to account for the non-linearity of material models 2 to 4, CONGAS uses an incremental approach for the solution of the problem. In this approach, the external boundary loads are applied in increments. For each load increment, the constitutive parameters (B_t, E_t or G_t) are evaluated based on the stress state at the beginning of the load step. These parameters are assumed to be constant during that time increment and the finite element equations are solved linearly, as in a linear elastic material problem. This is the piecewise-linear procedure. The assumption that, during one load increment, the constitutive

parameters are constant, introduces an error in the evaluated strains and stresses. There are several methods to correct the evaluated strains and stresses, in order to account for the true non-linear response of the soil skeleton during one load step. Most solution methods use iterations, which often significantly increase the cost of the solution.

In CONGAS, due to the relatively high computational costs associated with the iteration procedure required for the solution of the non-linear continuity equation, a simple incremental approximation or the basic Euler procedure (Vaziri, 1986) was adopted to solve the material non-linearity problem. In this procedure, the errors associated with the linearization of the constitutive curve are neglected. Therefore, the strains and stresses obtained at the end of each of the load increments are assumed to be correct. Figure 3.6 illustrates the theoretically correct solution and the ones obtained from a simple incremental approximation. One can observe that, depending on the curvature of the true soil mass response, and on the number of load increments in which the external load is subdivided, the error of the predicted load - displacement curve can be high. In order to keep track of the error involved in the solution adopted, a control procedure was developed. It consists of comparing the state of stress at the point of equilibrium at the end of each load step, with the state of stress given by the constitutive model, associated with the

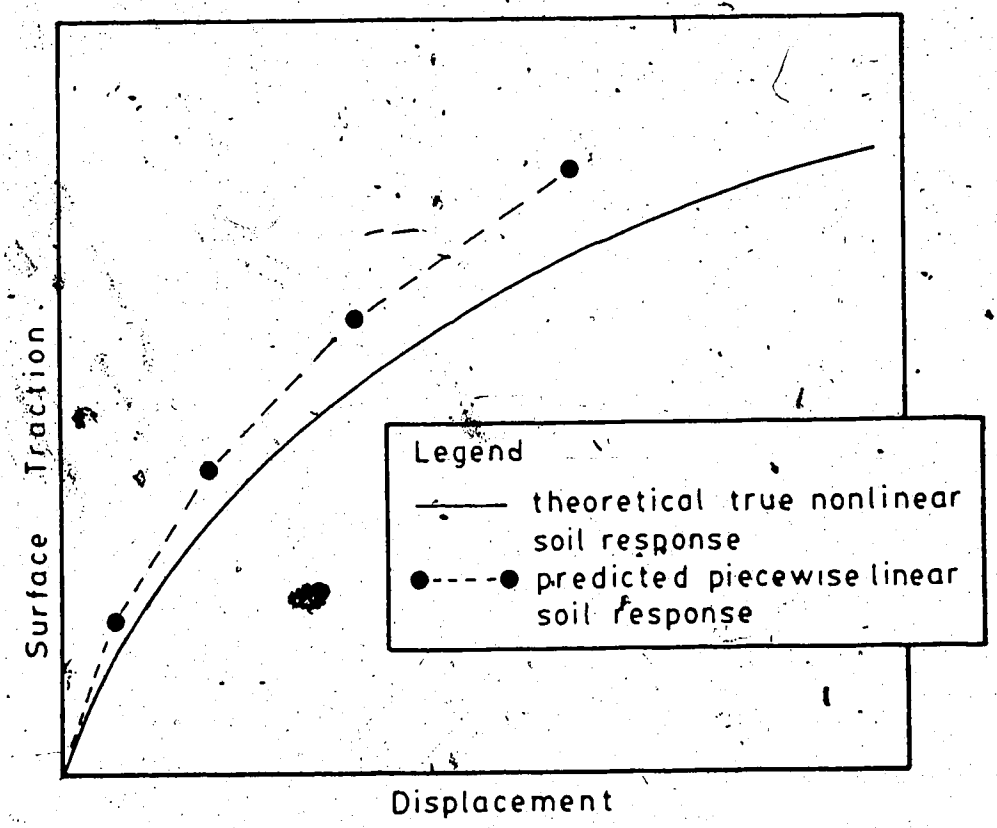

Figure 3.6 Simple Incremental Approximation

same state of strain from the numerical solution.

For material model 2, two control indices are defined:

$$\text{ERRORB} = \frac{\sigma'_{3,\text{OBTAINED}}}{\sigma'_{3,\text{TRUE}}} \qquad [3.104]$$

$$\text{ERRORE} = \frac{(\sigma_1 - \sigma_3)_{\text{OBTAINED}}}{(\sigma_1 - \sigma_3)_{\text{TRUE}}} \qquad [3.105]$$

The terms in these equations are shown in Figures 3.7 and 3.8.

The evaluation of the error in the maximum deviatoric stress, ERRORG, for material type 3, is slightly different than for material type 2, since model 3 is defined in terms of B_t and G_t, both expressed in terms of σ'_3. This error evaluation is illustrated n Figure 3.9.

Material type 4 is also expressed in terms of B_t and G_t; however, these are expressed in terms of σ'_{OCT}. In this case, ERRORB and ERRORG are evaluated according to Figures 3.10 and 3.11.

Liquid Compressibility

The compressibility of the liquid phase, in the finite element Equation 3.81, is taken into account through the vector [E], which is given by Equation 3.73. The term 1/Q in that equation accounts for the combined compressibility of all liquids in the pore. For the case of oil sands, where there are two pore liquids, water and bitumen, the combined liquid compressibility is evaluated as follows:

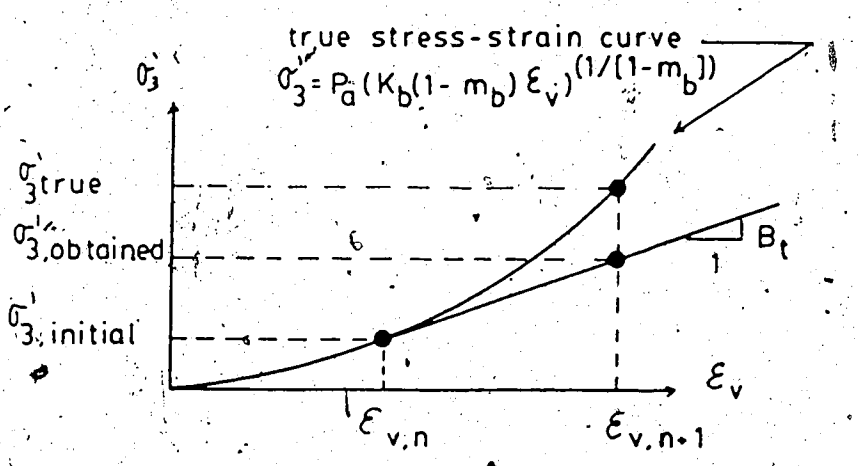

$\sigma'_{3,initial}$ = initial minor effective stress

$\sigma'_{3,obtained}$ = minor effective stress obtained from numerical solution, associated with $\epsilon_{v,n+1}$

$\sigma'_{3,true}$ = minor effective stress in the true stress-strain curve associated with $\epsilon_{v,n+1}$

$\epsilon_{v,n}$ = total volumetric strain at the beginning of the load step

$\epsilon_{v,n+1}$ = total volumetric strain at the end of the the load step, obtained from numerical solution

B_t = tangent bulk modulus evaluated in terms of $\sigma'_{3,initial}$

ERRORB = $(\sigma'_{3,obtained}/\sigma'_{3,true})$

$K_{a,ma}$ = bulk modulus coefficients

Figure 3.7 Error Control Index - Bulk Modulus - Material Models 2 and 3

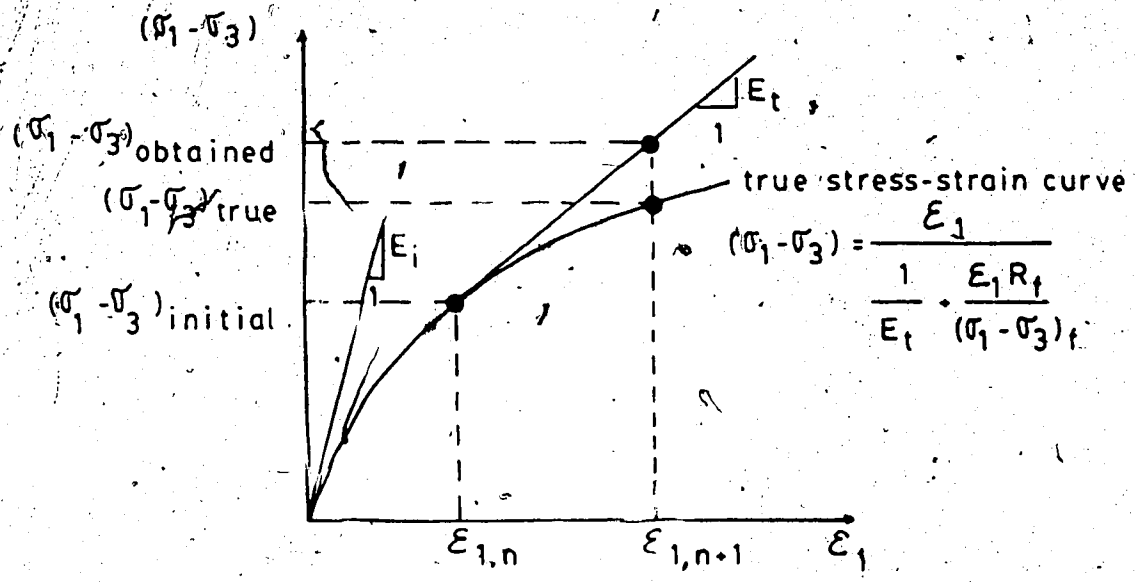

$(\sigma_1-\sigma_3)_{initial}$	= initial maximum deviatoric stress
$(\sigma_1-\sigma_3)_{obtained}$	= maximum deviatoric stress obtained from numerical solution, associated with $\epsilon_{1,n+1}$
$(\sigma_1-\sigma_3)_{true}$	= maximum deviatoric stress in the true stress-strain curve, associated with $\epsilon_{1,n+1}$
$(\sigma_1-\sigma_3)_f$	= maximum deviatoric stress at failure
R_f	= failure ratio
$\epsilon_{1,n}$	= total maximum principal strain at the beginning of the load step
$\epsilon_{1,n+1}$	= total maximum principal strain at the end of the load step, obtained from numerical solution
E_t	= tangent Young modulus evaluated in terms of $\sigma'_{3,initial}$ and $(\sigma_1-\sigma_3)_{initial}$
E_i	= initial tangent Young modulus
ERRORE	= $(\sigma_1-\sigma_3)_{obtained}/(\sigma_1-\sigma_3)_{true}$

Figure 3.8 Error Control Index - Young Modulus - Material Model 2

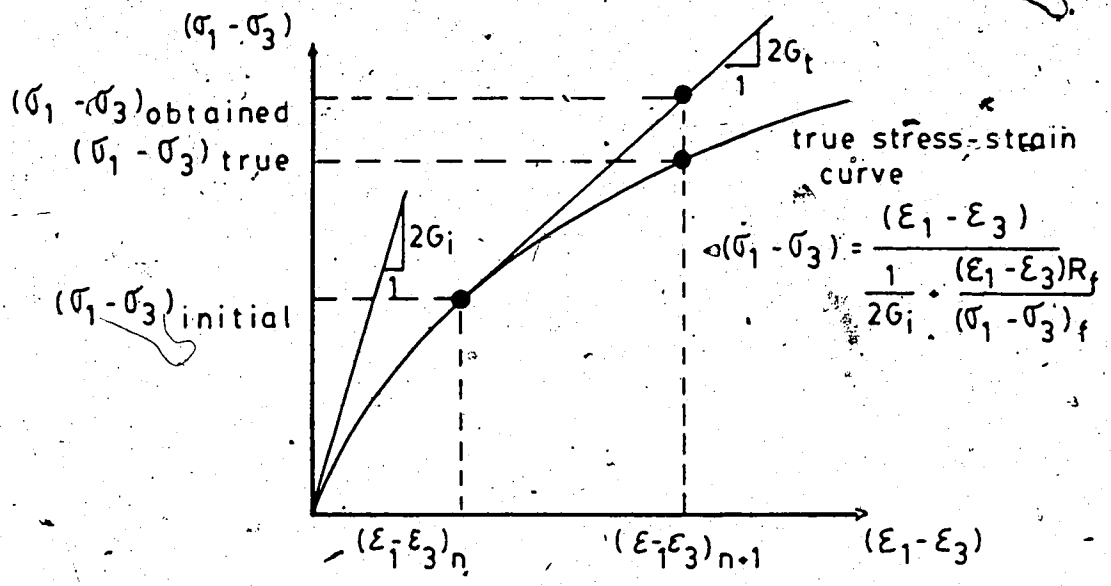

$(\sigma_1-\sigma_3)_{initial}$	= initial maximum deviatoric stress
$(\sigma_1-\sigma_3)_{obtained}$	= maximum deviatoric stress obtained from numerical solution, associated with $(\epsilon_1-\epsilon_3)_{n+1}$
$(\sigma_1-\sigma_3)_{true}$	= maximum deviatoric stress in the true stress-strain curve, associated with $(\epsilon_1-\epsilon_3)_{n+1}$
$(\sigma_1-\sigma_3)_f$	= maximum deviatoric stress at failure
R_f	= failure ratio
$(\epsilon_1-\epsilon_3)_n$	= total max. deviatoric strain at the beginning of the load step
$(\epsilon_1-\epsilon_3)_{n+1}$	= total max. deviatoric strain at the end of the load step, obtained from numerical solution
G_t	= tangent shear modulus evaluated in terms of $\sigma'_{3,initial}$ and $(\sigma_1-\sigma_3)_{initial}$
G_i	= initial tangent shear modulus
ERRORG	= $(\sigma_1-\sigma_3)_{obtained}/(\sigma_1-\sigma_3)_{true}$

Figure 3.9 Error Control [illegible] - Shear Modulus - Material Model 3

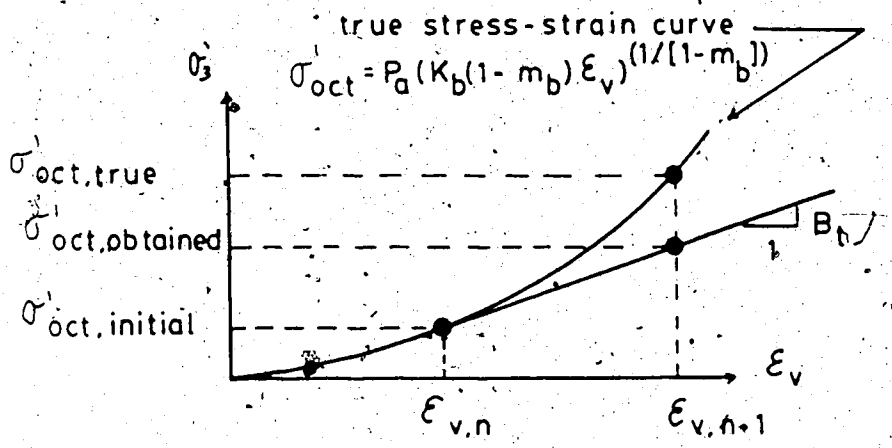

$\sigma'_{oct,initial}$ = initial octahedral effective stress

$\sigma'_{oct,obtained}$ = octahedral effective stress obtained from numerical solution, associated with $\epsilon_{v,n+1}$

$\sigma'_{oct,true}$ = octahedral effective stress in the true stress-strain curve, associated with $\epsilon_{v,n+1}$

$\epsilon_{v,n}$ = total volumetric strain at the beginning of the load step

$\epsilon_{v,n+1}$ = total volumetric strain at the end of the load step, obtained from numerical solution

B_t = tangent bulk modulus evaluated in terms of $\sigma'_{oct,initial}$

ERRORB = $\sigma'_{oct,obtained}/\sigma'_{oct,true}$

Figure 3.10 Error Control Index - Bulk Modulus - Material Model 4

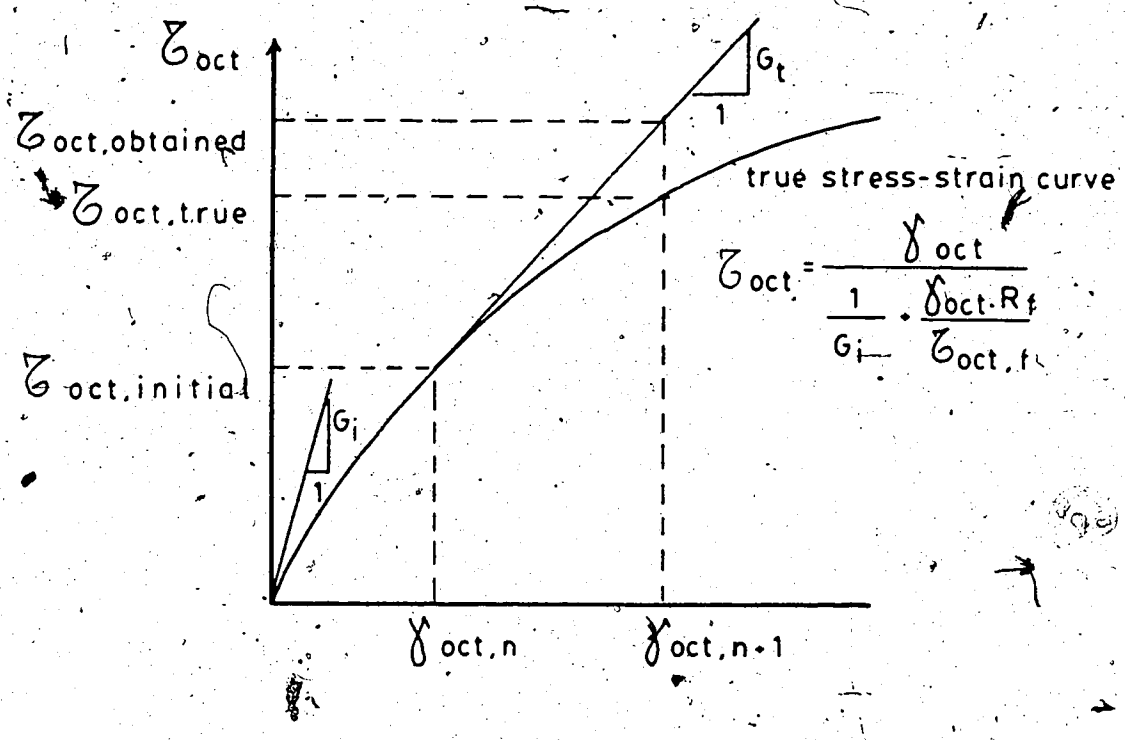

$\tau_{oct,initial}$ = initial octahedral shear stress

$\tau_{oct,obtained}$ = octahedral shear stress obtained from numerical solution associated with $\gamma_{oct,n+1}$

$\tau_{oct,true}$ = octahedral shear stress in the true stress-strain curve associated with $\gamma_{oct,n+1}$

$\tau_{oct,f}$ = octahedral shear stress at failure

R_f = failure ratio

$\gamma_{oct,n}$ = total octahedral shear strain at the beginning of step

$\gamma_{oct,n+1}$ = total octahedral shear strain at the end of step, obtained from numerical solution

G_t = tangent shear modulus evaluated in terms od $\sigma'_{oct,initial}$ and $\tau_{oct,initial}$

G_i = initial tangent shear modulus

ERRORG = $\tau_{oct,obtained}/\tau_{oct,true}$

Figure 3.11 Error Control Index - Shear Modulus - Material Model 4

$$\frac{1}{Q} = \frac{d\epsilon_v^{liq}}{du} = \frac{dV_{bit} + dV_{wat}}{V_{tot} \cdot du} \qquad [3.106]$$

where,

$$dV_{bit} = \frac{1}{Q_{bit}} \cdot du \cdot V_{bit}$$

$$= \frac{1}{Q_{bit}} \cdot du \cdot \frac{e_{bit}}{1+e} \cdot V_{tot} \qquad [3.107]$$

$$dV_{wat} = \frac{1}{Q_{wat}} \cdot du \cdot V_{wat}$$

$$= \frac{1}{Q_{wat}} \cdot du \cdot \frac{e_{wat}}{1+e} \cdot V_{tot}$$

$$= \frac{1}{Q_{wat}} \cdot du \cdot \frac{eS - e_{bit}}{1+e} \cdot V_{tot} \qquad [3.108]$$

where,

V_{bit}, V_{wat} = volume of bitumen and water respectively,

V_{tot} = total volume of the element being considered, including the pores and soil grains.

ϵ_v^{liq} = portion of the total volumetric strain of the element being considered, due to volumetric strain of the liquids.

e = total void ratio

e_{bit}, e_{wat} = void ratio of bitumen and water phases, respectively.

S = total degree of saturation (of both, bitumen and water)

Q_{bit}, Q_{wat} = volumetric compressibility of bitumen and water, respectively.

du = change in liquid pore pressure.

Substituting Equations 3.107 and 3.108 in 3.106 and rearranging the latter,

$$\frac{1}{Q} = \frac{1}{1+e}\left[e_{bit}\left(\frac{1}{Q_{bit}} - \frac{1}{Q_{wat}}\right) + \frac{eS}{Q_{wat}}\right] \qquad [3.109]$$

It is worth noting that for $e_{bit}=0$, Equation 3.109 becomes

$$\frac{1}{Q} = \frac{eS}{(1+e)Q_{wat}} \qquad [3.110]$$

as opposed to

$$\frac{1}{Q} = \frac{1}{Q_{wat}} \qquad [3.111]$$

This occurs because the combined liquid compressibility in Equation 3.106 is defined in terms of the total volumetric strain of the element being considered, whereas the value of Q_{wat}, is defined in terms of the unit volume of water, as depicted in 3.108.

The terms e_{bit}, Q_{bit} and Q_{wat} of Equation 3.109 are approximately constant and e and S vary during the processes of gas evolution and consolidation. Thus, the values of Q should always be evaluated between successive time increments, and between successive iterations. It is possible to conclude, however, that for an oil sand sample with the following characteristics:

$e_o = 0.470$

$e_{vat} = 0.14$

$e_{bit} = 0.33$

$Q_{vat} = 4.5 \times 10^{-7}$ 1/kPa

$Q_{bit} = 20.7 \times 10^{-7}$ 1/kPa,

with degrees of saturation varying between the extremes allowed by the current formulation, i.e. S=0.85 to 1.00, associated with volumetric strain increases of up to 10%, above which the small displacements formulation would not be applicable any longer, e = 0.47 to 0.52, the variations of the value 1/Q vary within a very narrow band of values (±0.6%). Due to this fact, and the inaccuracies inherent in the evaluation of Q_{vat} and Q_{bit}, in CONGAS, 1/Q is evaluated based on the initial values of the problem, which are assumed to be constant throughout the calculations.

Coefficient of Permeability

In CONGAS, the permeability tensor of the soil skeleton is assumed to be symmetric and its components are assumed to vary according to the following equation:

$$K_{ij\ WAT} = K_{ij\ WAT}(S=100\%) \cdot \frac{e_{WAT}^3\ (1+e_{owat})}{e_{owat}^3\ (1+e_{wat})} \cdot \left[\frac{S_{wat}}{S_{wat}(S=100\%)}\right]^3 \qquad [3.112]$$

where,

$K_{ij\ WAT}(S=100\%)$ = permeability tensor with respect to water, for a fully saturated pore fluid.

e_{owat}, e_{wat} = initial and current void ratios of the

water phase.

$S_{wat}(S=100\%) = V_{wat}/V_{voids}$ [3.113]

= degree of saturation with respect to the water phase, for a fully saturated condition.

S_{wat} = current degree of saturation.

Equation 3.112 is an extension of the Chang and Duncan, 1983, equation for the case of a two-component liquid phase, in which only one of the components (in the case of oil sands at *in situ* temperatures, the water phase) is assumed to flow.

It is possible to demonstrate that Equation 3.112 can be further modified to the form:

$$K_{ij\ WAT} = K_{ij\ WAT}(S=100\%) \cdot \frac{e_{WAT}^3\ (1+e_{owat}) \cdot e_o^3}{e_{owat}^6\ (1+e_{wat})} S_{wat}^3 \quad [3.114]$$

where e_o is the initial total void ratio.

A sensitivity study of the equation above, performed with extreme values for the degree of saturation and void ratios indicated that the coefficient of permeability can vary up to three orders of magnitude.

During each load or time increment, the coefficient $K_{ij\ WAT}$ is assumed to be constant. This assumption is based on the hypothesis that the degree of saturation and void ratio do not vary significantly during a load step. This assumption simplifies, to a significant extent, the iterative procedure required for the solution of the

non-linear continuity equation, as described earlier in this section. This occurs due to the fact that, by assuming K_{ij}^{WAT} constant in a given load step, the matrix $[K_2]$ in the load vector of Equation 3.81, does not have to be updated between successive iterations.

Boundary Conditions

As depicted in Section 3.3.1, the solution of the governing equations requires a knowledge of the boundary conditions. These can be classified as displacement boundary conditions (specified surface tractions and specified displacements) and flow boundary conditions (specified boudary flows and specified pore pressures).

In CONGAS, the surface tractions and boundary flows are evaluated according to Equations 3.76 and 3.77, and included in the load vector of the finite element Equation 3.81. The detailed development of the traction and flow vectors is given in Appendix B. An algorithm was developed in order to allow modification of the surface tractions during the calculations, as explained in Branco, 1988.

CONGAS allows the imposition of homogeneous specified displacements (=0) in directions varying from 0 to 90 degrees. Pore pressures can also be specified at the external nodes of the element at the boundary of the finite element mesh. A detailed description of the specification of boundary conditions in CONGAS is presented in Appendix B.

Scaling of the Stiffness Matrix

In trying to solve the problem associated with the analysis of the immediate response, for incompressible pore fluids, Reed, 1982 and 1984, concluded that the adoption of extremely small time increments (Δt) can lead to ill-conditioning of the stiffness matrix. According to Reed, the value of Δt at which ill-conditioning occurs is determined by the relative orders of magnitude of the elements of the constitutive submatrix K1 (Equation 3.81) and those of the flow submatrix K2. It is not uncommon in consolidation problems, to find the maximum pivot of the stiffness matrix twenty orders of magnitude larger than the minimum pivot (Reed, 1982:535).

Therefore, in trying to reduce the problem of ill-conditioning, Reed introduced a scaling factor S, that multiplies certain terms of the finite element equation as follows:

$$\begin{bmatrix} [K_1]_t & s.[C] \\ \hline s[C]^T & s^2\{-\alpha\Delta t[K_2]-E\} \end{bmatrix} \cdot \begin{Bmatrix} W \\ \hline \frac{u}{s} \end{Bmatrix} = \begin{Bmatrix} R \\ \hline V.s \end{Bmatrix} \qquad [3.115]$$

The value of s is chosen in order to bring the values of the minimum pivot up to the same order of magnitude as the maximum pivot in $[K_1]$.

Reed's approach was introduced into CONGAS and its efficiency analysed. A series of numerical tests indicated that due to the fact that the composite triangular element 6-3 was used in CONGAS, ill-conditioning of the stiffness matrix was never a problem. This verification agrees with

the numerical tests performed by Sandhu et al., 1977.

The use of Reed's scaling technique proved to be useful in the analysis of the drained response of the meshes under consideration. By setting s=0, the finite element equation reduces to the time-independent problem, with pore pressures equal to zero within the mesh.

Finite Element Equation Solver

The solution of the finite element equation was performed with the Gaussian Elimination technique. The algorithm developed by Hwang, 1970, was used in CONGAS. It consists of, in a first phase, "triangularize" the originally symmetric stiffness matrix and, in a second and final phase, proceed with direct back substitution.

As mentioned earlier in this section, the iterative procedure, developed to solve the finite element equations, does not require re-assembly of the stiffness matrix between successive iterations belonging to a given time increment. Therefore, for each time increment, the stiffness matrix is "triangularized" only once, at the beginning of the first iteration. For the subsequent iterations only the load vector is re-assembled and modified in order to be compatible with the "triangularized" stiffness matrix.

In the case of the linear elastic material model, the components of $[K_1]$ and $[C]$ of the stiffness matrix are constant throughout the calculations. Therefore, the use of the procedure of temporarily storing the stiffness matrix in its triangularized form, and re-using it during the solution

of the linear equation, is possible and desirable.

Calculation of Strains and Stresses

The solution of the finite element equation produces nodal displacements and pore pressures at the nodal points. The evaluation of strains and stresses within the elements is, possible then with the following relationship:

$$\{\Delta\epsilon\} = [B]\{\Delta w\} \qquad [3.116]$$

where,

$\{\Delta\epsilon\}$ = incremental strain tensor

$[B]$ = strain-displacement matrix

$\{\Delta w\}$ = incremental nodal displacement tensor

$[B]$ is a function of the coordinates of the triangular elements and can be evaluated at any point within the element.

As discussed in Appendix B, the exact integration of functions over the volume of the triangular elements for the axisymmetric case with non-linear material model was performed numerically with four optimum sampling points. Following Zienkiewicz, 1983:280, the strains and stresses in CONGAS are evaluated at these points, where, theoretically, they present minimum deviations from the "correct" values. For the sake of consistency, irrespective of the number of sampling points required for the integration of functions over the volume of the elements, in the development of the elements stiffness matrices, CONGAS presents strains and stresses at the four sampling points illustrated in Appendix B.

Once strains are available at the sampling points, stresses can be evaluated as follows:

$$\{\Delta\sigma\} = [H]_t\{\Delta\epsilon\} \qquad [3.117]$$

where,

$\{\Delta\sigma\}$ = incremental stress tensor

$[H]_t$ = tangential constitutive matrix.

For the case where gas evolution is considered, the evaluation of the volumetric strains is performed at the nodal points. The strains at this point are assumed to be the average strains evaluated at that specific node, obtained from each of the neighbouring elements that share that node.

3.3.4 Testing of CONGAS

The testing of CONGAS consisted of comparing its results with closed form solutions, or approximate solutions published by other authors, whenever these were available.

The subsequent sections describe the testing of CONGAS, according to the following outline:

Immediate Response

- Soil initially fully saturated
- Soil initially partly saturated

Transient Response

- Consolidation only

- Gas evolution only
- Consolidation and gas evolution

Independent Features

- Liquid Compressibility
- Variable Coefficient of Permeability

3.3.4.1 Immediate Response

Soil Initially Fully Saturated

Figure 3.12 illustrates the finite element mesh chosen to illustrate the case of one dimensional-immediate response as predicted by CONGAS. This is the two-dimensional version of the oedometer test, with drainage allowed only at the top.

Figure 3.13 depicts the pore pressure response for $\Delta t=0$, i.e., the immediate response. The significant deviation from the theoretical response is attributed to the fact that the linear pore pressure shape function cannot accommodate sharp variations of pore pressures within the element, as it occurs in the early stages of unloading, close to the drainage boundary. Some procedures followed by other authors to overcome this problem were described in Section 3.3.2.2. Vermeer and Verruijt, 1981, carried on a study on the accuracy conditions for solutions of consolidation problems by finite elements. The authors showed that there is a lower limit for the time steps below which spatial oscillations occur:

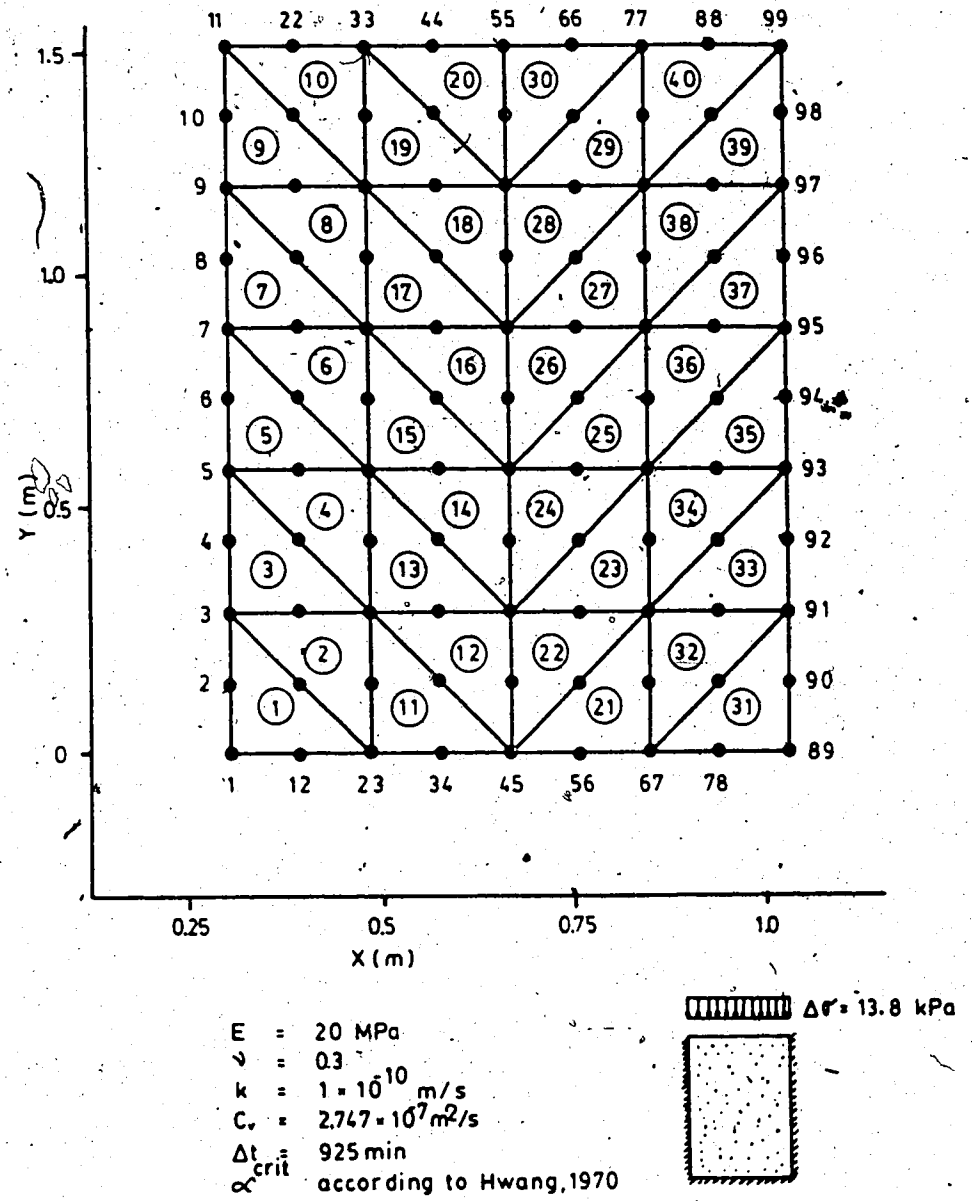

Figure 3.12 Finite Element Mesh Test 6-V5

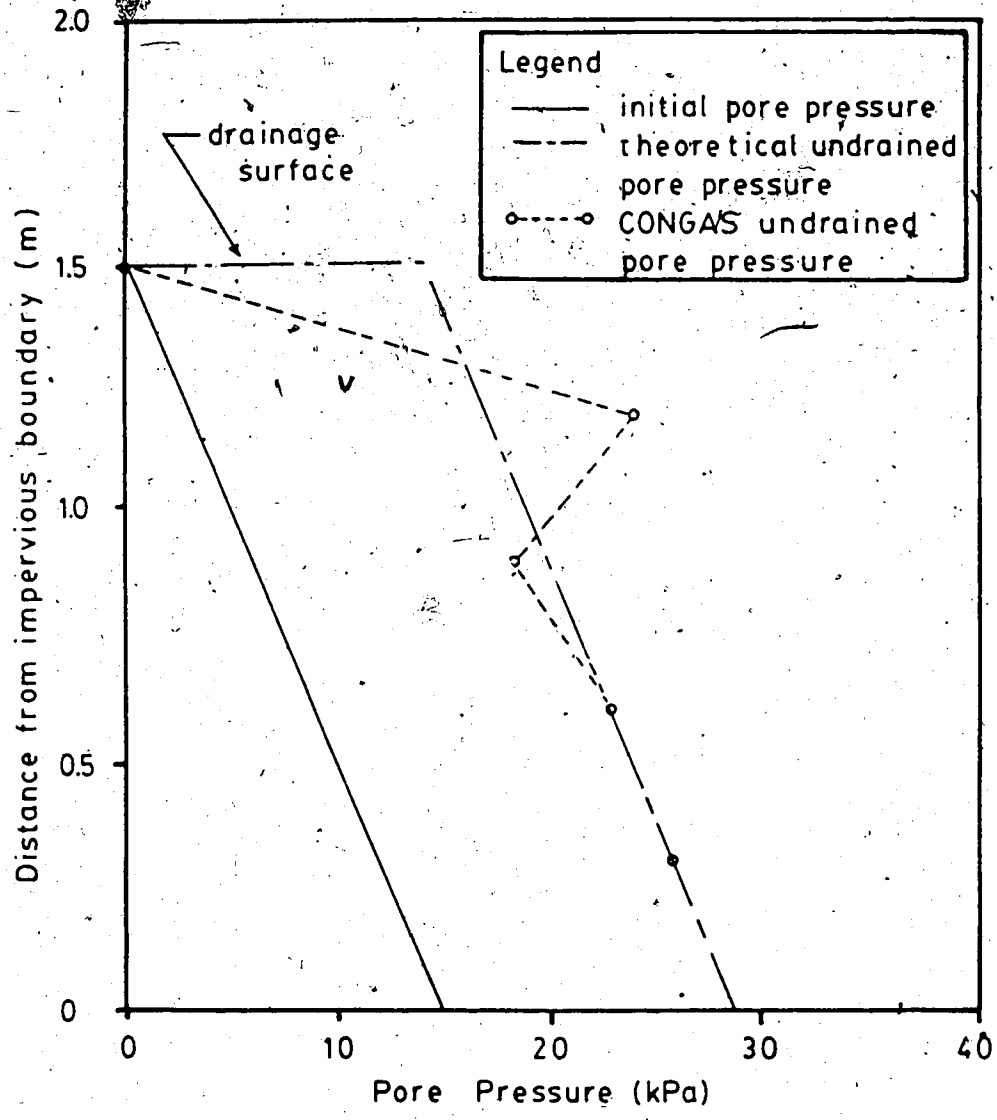

Figure 3.13 Immediate Response - Soil Initially Fully Saturated with Drainage - Test 6-V5-1D

$$Dt > \frac{1}{6} \frac{(\Delta h)^2}{a c_v} \qquad [3.118]$$

where,

Δh = average size of element, close to the drainage surface.

a = time integration constant (Section 3.3.2.1)

c_v = coefficient of consolidation

This equation was derived from the one-dimensional case of consolidation of an elastic soil mass. It guarantees that, everywhere within the soil, the excess pore pressure is equal to or smaller than the externally applied boundary load. For the case considered in Figure 3.12, the following condition must be satisfied.

$$\Delta t > 940/a \text{ (minutes)} \qquad [3.119]$$

Therefore, for a varying between 0.5 and 1.0, Δt should be greater than 940 to 1880 minutes.

If however, the immediate response is imperative to the solution of the problem, an alternative approach can be used. It consists of, for the first time increment, eliminating the drainage at the drainage boundaries and imposing $\Delta t = 0$. For the subsequent steps, drainage is imposed and Δt chosen in accordance with Vermeer and Verruijt's suggestion. Figure 3.14 depicts the results of the immediate response for the same case of Figures 3.12 and 3.13, except that drainage is temporarily impeded for $\Delta t = 0$.

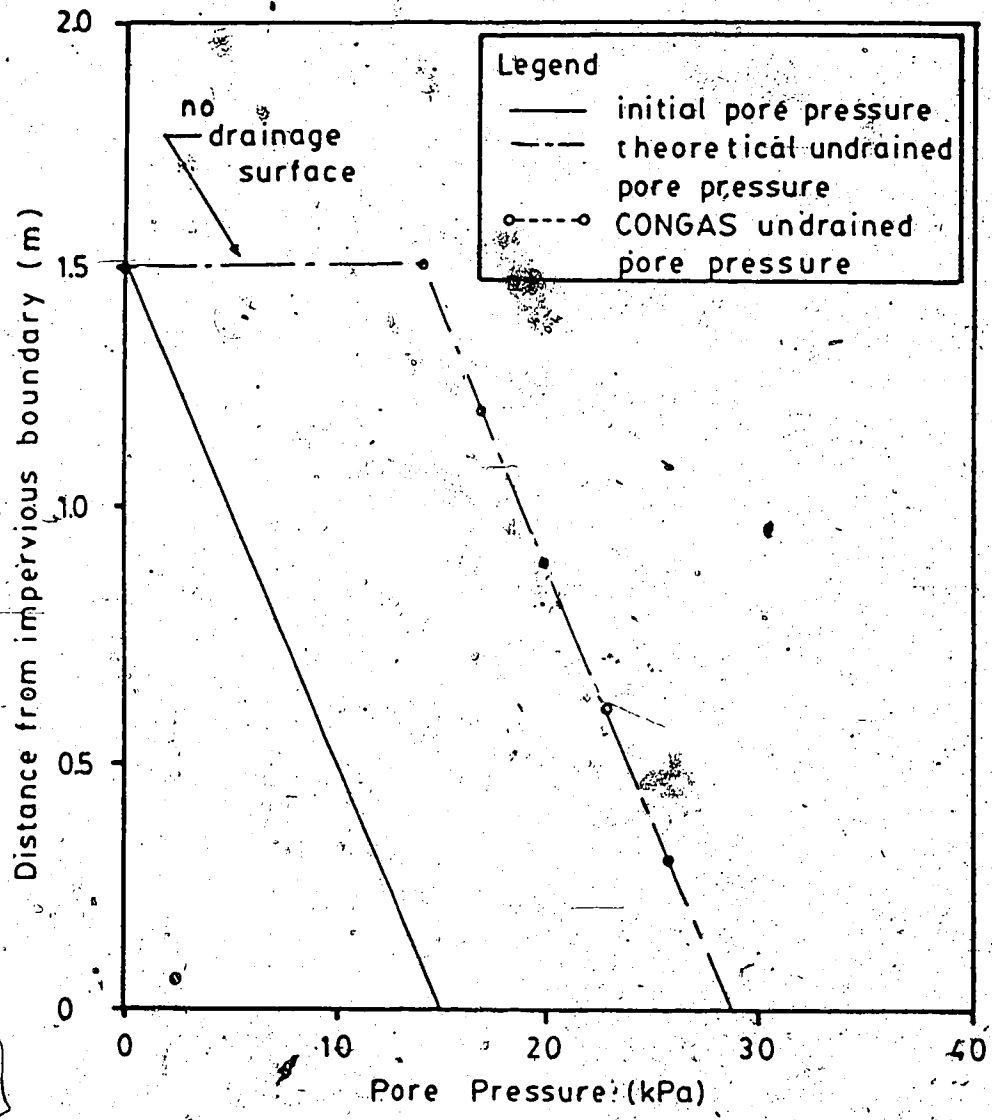

Figure 3.14 Immediate Response - Soil Initially Fully Saturated without Drainage - Test6-V5-1D

The mesh presented in Figure 3.12 was also used to analyse the immediate response of a linear elastic soil mass, subjected to a two dimensional mode of deformation. This was done by simply relaxing the constraint imposed on the lateral deformation on the oedometer one dimensional case. In this case, the theoretical pore pressure response can be evaluated according to Skempton's equation

$$\Delta u = B(\Delta\sigma_3 + A(\Delta\sigma_1 - \Delta\sigma_3)) \qquad [3.120]$$

where, for the elastic two dimensional case

$A = 1/2$ and $B = 1.0$

and $\Delta\sigma_1 = \Delta\sigma_{ext}$ and $\Delta\sigma_3 = 0$ yields

$$\Delta u = 0.5\ \Delta\sigma_{ext}$$

Figure 3.15 illustrates the accuraty of pore pressures and strains predicted by CONGAS when drainage is impeded for $\Delta t=0$. The results obtained for this case are highly satisfactory.

Soil Initially Partly Saturated

The theoretical response for the one dimensional case can be obtained from Sobkowicz, 1982:33. By imposing volume change compatibility between the soil skeleton and pore fluid, Sobkowicz derived the following equation:

$$A.\Delta u^2 + B.\Delta u + C = 0 \qquad [3.121]$$

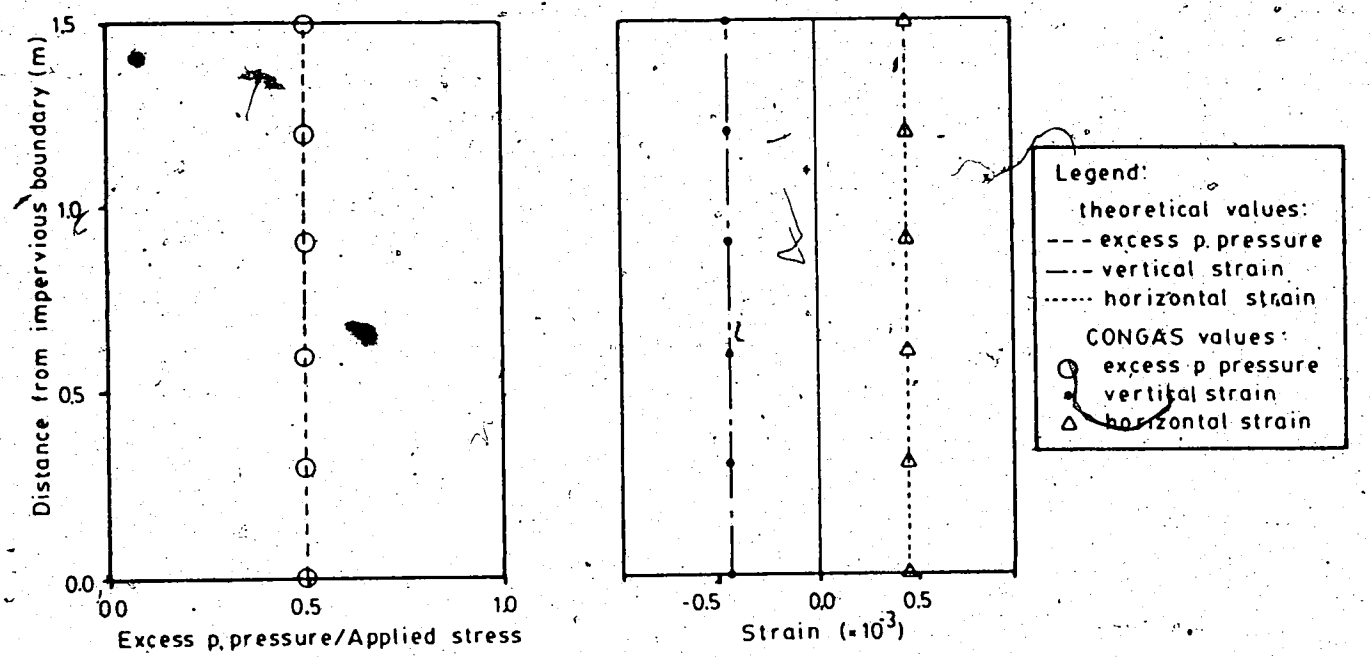

Figure 3.15 Immediate Response-Soil Initially Fully Saturated without Drainage - Test6-V5-2D

where,

$$A = \beta_T + nS\beta_L$$

$$B = \beta_T(P_o - \Delta\sigma) + n(\beta_L S P_o + 1 - S + SH)$$

$$C = -\beta_T \Delta\sigma P_o$$

n, S and P_o are the initial values of porosity, degree of saturation and absolute pore pressure taken at the beginning of the step increment.

β_T is the soil skeleton compressibility

β_L is the pore liquid compressibility

H is the solubility coefficient

The solution for the immediate pore pressure response within the soil mass is possible by making the solubility coefficient, H, equal to zero, and solving the quadratic equation above.

Figure 3.16 depicts the theoretical results and results predicted by CONGAS, for a case identical to the one illustrated in Figure 3.12 except that the soil is now initially partly saturated and the sample is subjected to unloading. In this case, once more, the immediate pore pressure response by CONGAS compares very well with the theoretical solution by Sobkowicz.

Another series of immediate response analyses was performed with the mesh depicted in Figure 3.17. In this case, similar to the case presented in Figure 3.16, the soil mass, initially at equilibrium, is subjected to unloading in the vertical direction. Moreover, gravity was neglected. Figures 3.18 and 3.19 allow a comparison of the pore

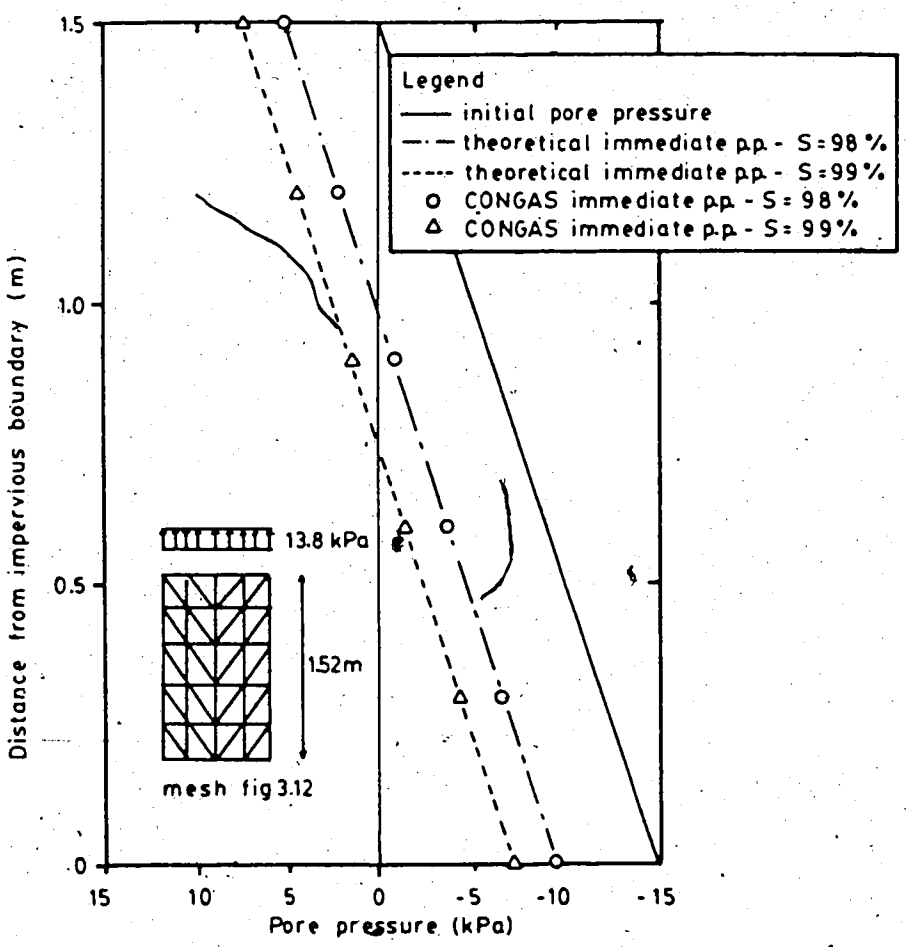

Figure 3.16 Immediate Response - Soil Partly Saturated - Test6-V5-1D

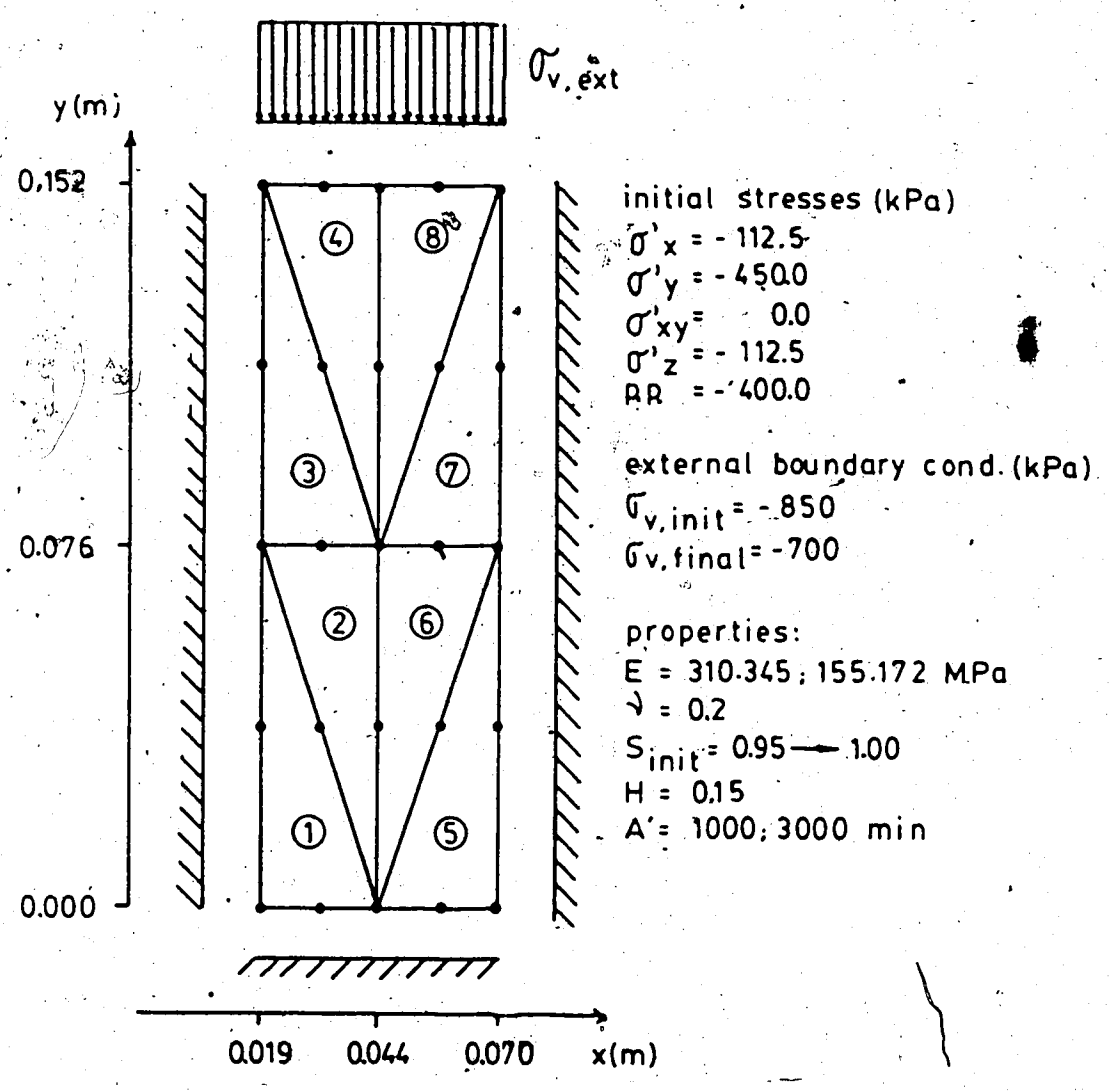

Figure 3.17 Finite Element Mesh - Test16-V14-1D

pressures, degree of saturation and void ratio predicted by CONGAS with the ones obtained from Sobkowicz's analytical solution.

The predictive capabilities of CONGAS are, once again, satisfactory.

3.3.4.2 Transient Response

Consolidation Only (Degassed Fluid)

Two series of tests were performed in order to verify the accuracy of the prediction of the consolidation problem with no gas evolution, by CONGAS:

- One dimensional consolidation
- Axisymmetric consolidation

Some of the tests performed are presented in the following sub-sections.

One Dimensional Consolidation (Degassed Fluid)

Figure 3.20 depicts two of the finite element meshes used to study the one dimensional consolidation of a linear elastic soil mass. For the coarser mesh (Test2-V3-1D-M1) the minimum time increment allowed to satisfy Vermeer and Verruijt's condition varies between 925 and 1851 minutes, whereas for the finer mesh, this value drops to 231 to 462 minutes. Figures 3.21 and 3.22 present the pore pressure response at points located at two different distances from the drainage boundaries. The results obtained with CONGAS, as well as the ones predicted by Taylor's solution, 1948, are compared. The comparison of the two curves associated with the coarser mesh (Test 2-V3-1D-M1 - Δt=475 min. and

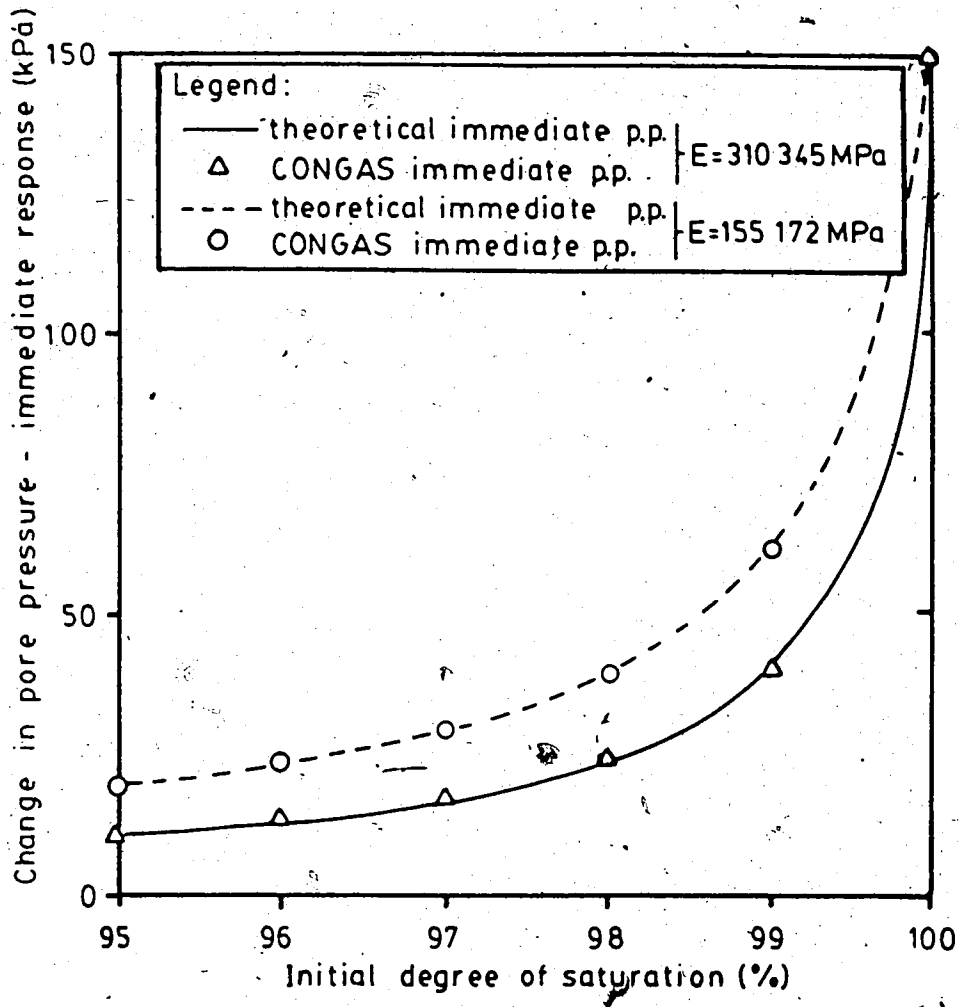

Figure 3.18 Immediate Response - Soil Initially Partly Saturated without Drainage - Test16-V14-1D

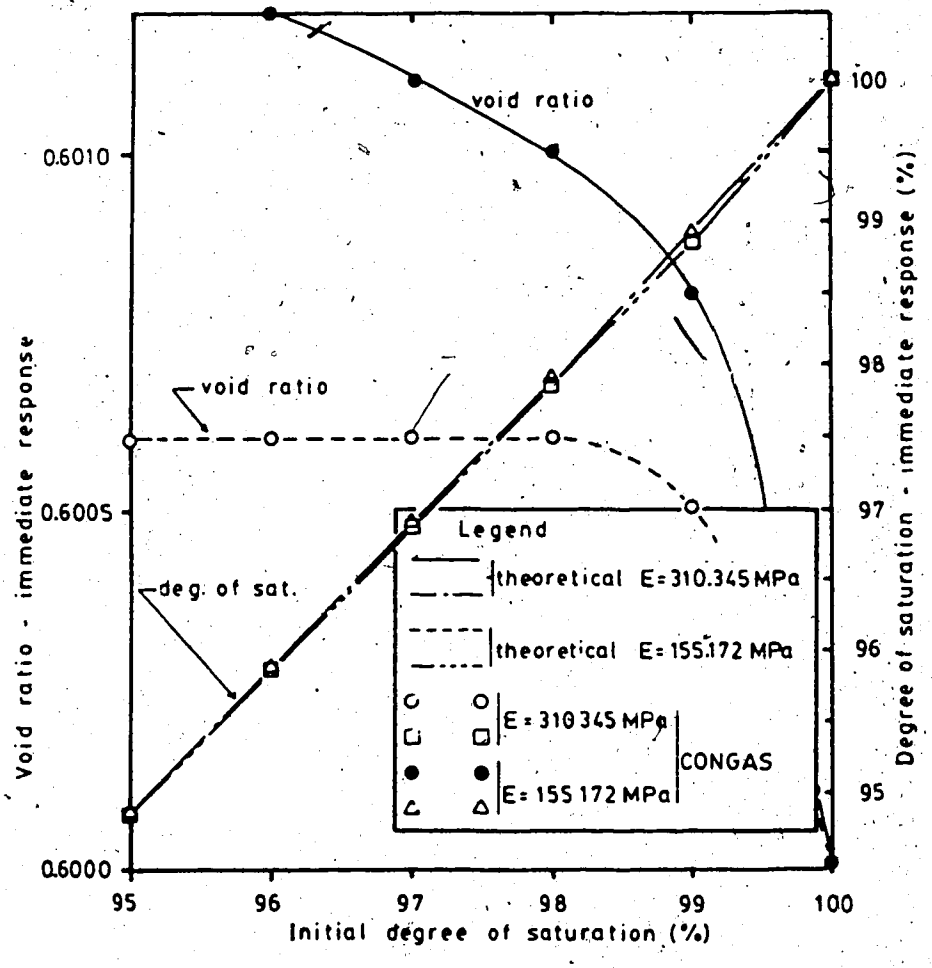

Figure 3.19 Immediate Response - Void Ratio and Degree of Saturation - Test 16-V16-1D

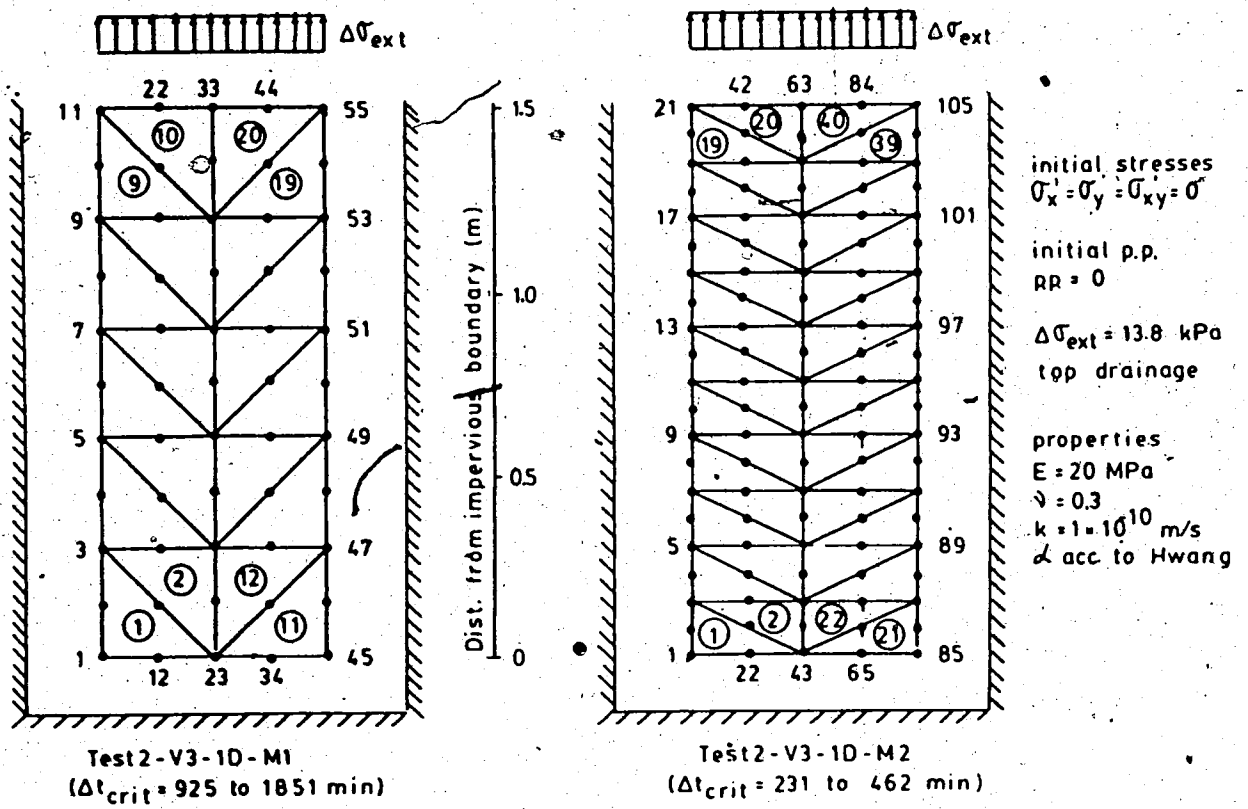

Figure 3.20 Finite Element Meshes - Tests2-V3-1D-M1 and M2

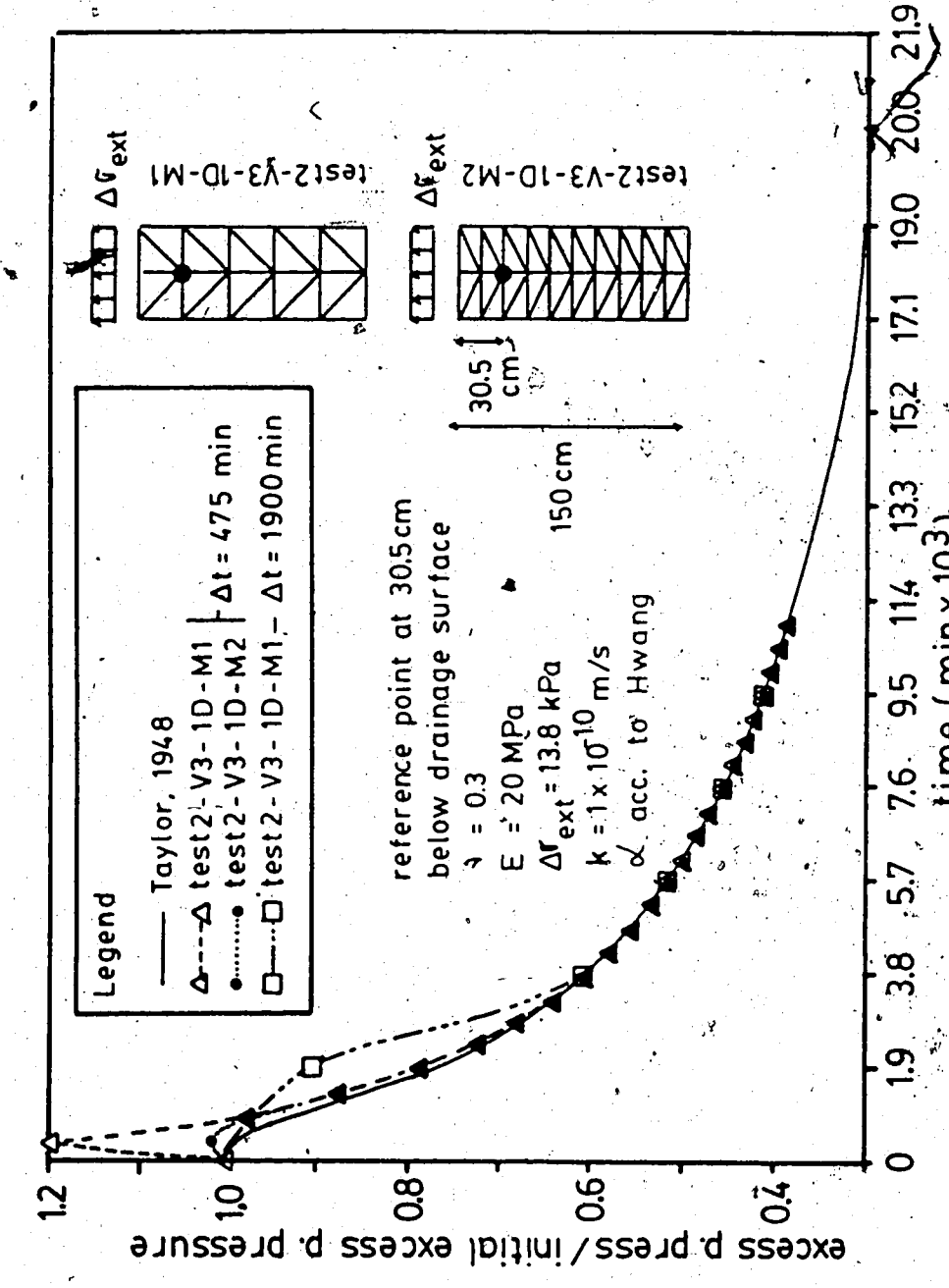

Figure 3.21 One Dimensional Consolidation - Pore Pressure versus Time

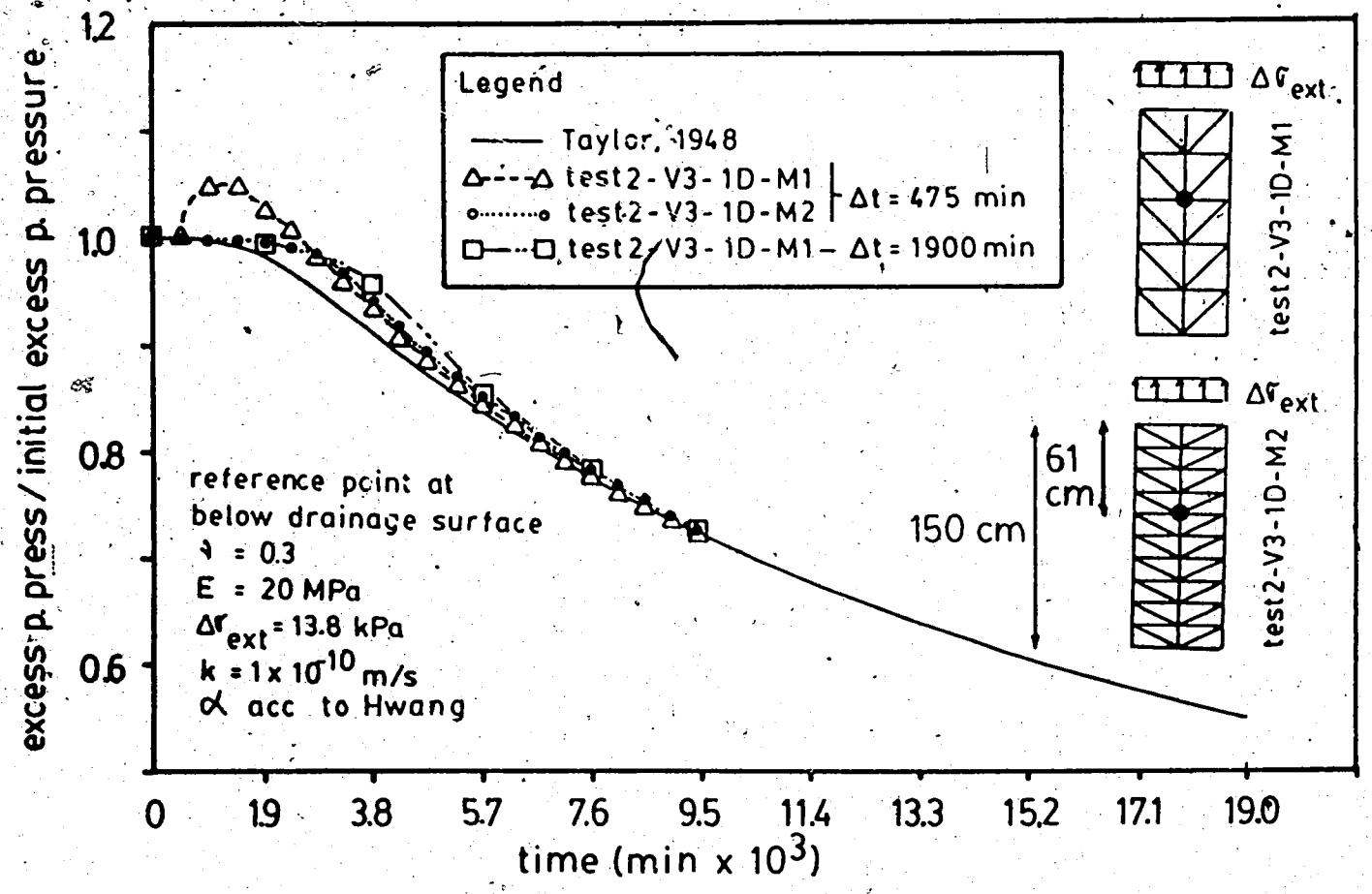

Figure 3.22 One Dimensional Consolidation - Pore Pressure versus Time

Δt=1900 min.) indicates that, as predicted by Vermeer and Verruijt, the use of time increments smaller than the critical values indicated above, results in the overprediction of the change in pore pressures to values even higher than the applied boundary stresses. The overprediction is high in the early stages of consolidation, but disappears quickly with time.

The use of a time increment equal to 1900 minutes, that is higher than the critical values of time increments, decreases the maximum error in pore pressure prediction at the early stages of consolidation but, on the other hand, induces a slower convergence of the predicted pore pressures towards Taylor's solution.

The results associated with the finer mesh (Test2-V3-1D-M2), with a time increment equal to 475 minutes, that is higher than the minimum values presented previously, confirm the assertions above and illustrate the effectiveness of mesh refinement on the quality of the prediction.

The predicted and theoretical vertical displacements at the top surface of the soil are plotted in Figure 3.23. This figure shows that for both meshes studied, irrespective of the temporal discretization adopted, the predicted vertical displacements agreed very well with Terzaghi's closed form solution.

Tests performed with the mesh Test6-V5, illustrated in Figure 3.12 and mesh Test2-V3-1D-M1, in Figure 3.20, allowed

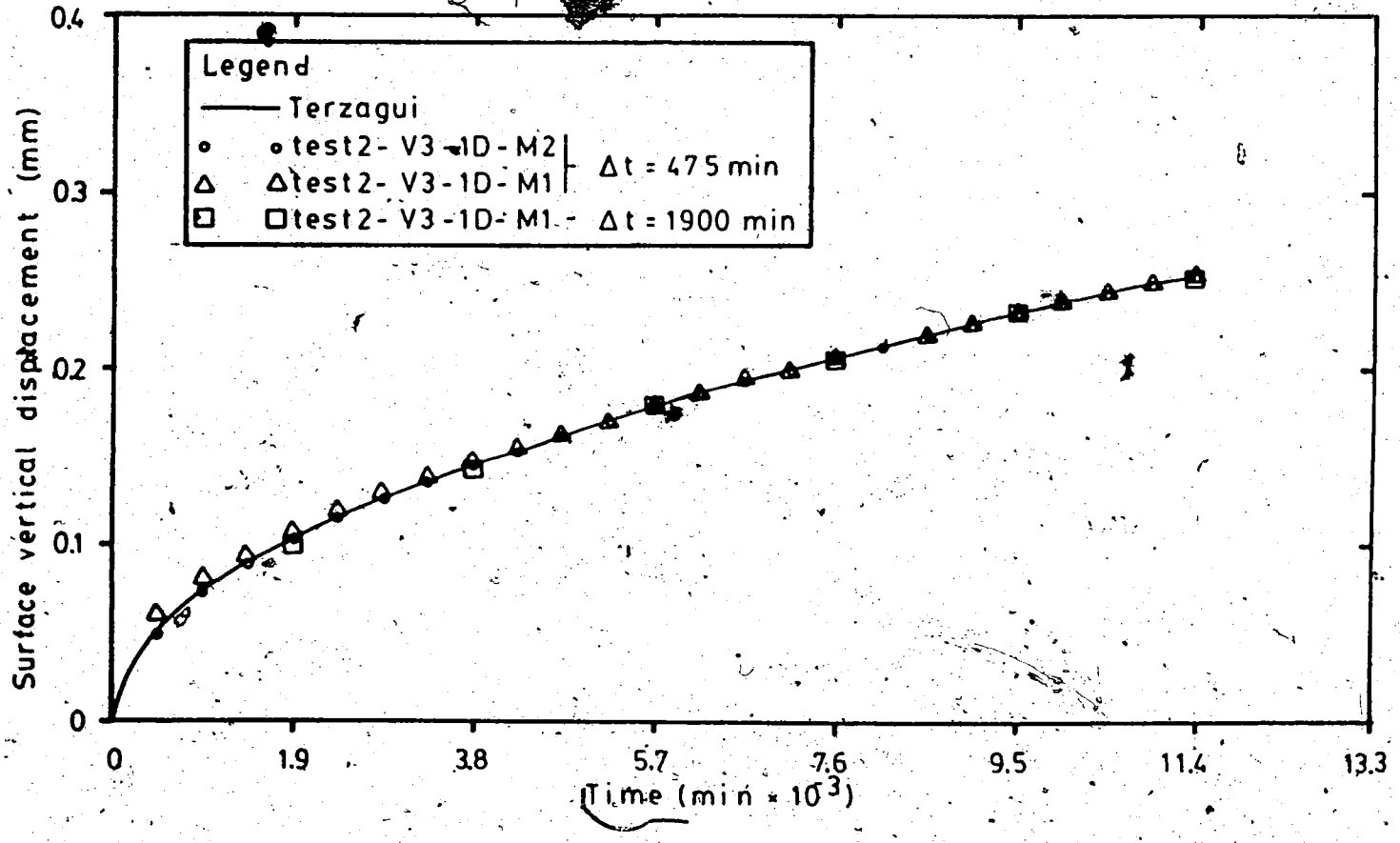

Figure 3.23 One-Dimensional Consolidation - Surface Vertical Displacement versus Time

the verification of the horizontal refinement of the mesh on the numerical results. In both meshes, the pressures along a horizontal line can vary up to 10%, provided that $\Delta t > \Delta t_{crit}$. This occurs in the first time increments and the difference decreases as time progresses.

Axisymmetric Consolidation (Degassed Fluid)

The analytical solution for the axisymmetric consolidation of a hollow cylinder subjected to drainage both at the internal bore and top surfaces, was offered by Barron, 1948. The solution is limited to the case where the soil mass is only allowed to move vertically. Thus, the internal and external walls of the cylinder are laterally restrained. Barron produced charts that relate the pore pressure dissipation within the soil, and the average degree of consolidation varying with time, for some specific cases. In this section, two cases are presented and compared with the results from CONGAS.

Figure 3.24 presents the finite element mesh used to study the consolidation of a hollow cylinder with external to internal radius ratio (r_e/r_i) equal to 5. Drainage is allowed only at the internal bore. As in Barron's solution, both internal and external walls are restrained from movement in the horizontal direction. An external load is instantaneously applied to the top surface. This load generates pore pressures that dissipate with time, resulting in the vertical straining of the soil. The soil properties used in this analysis are presented in Figure 3.24.

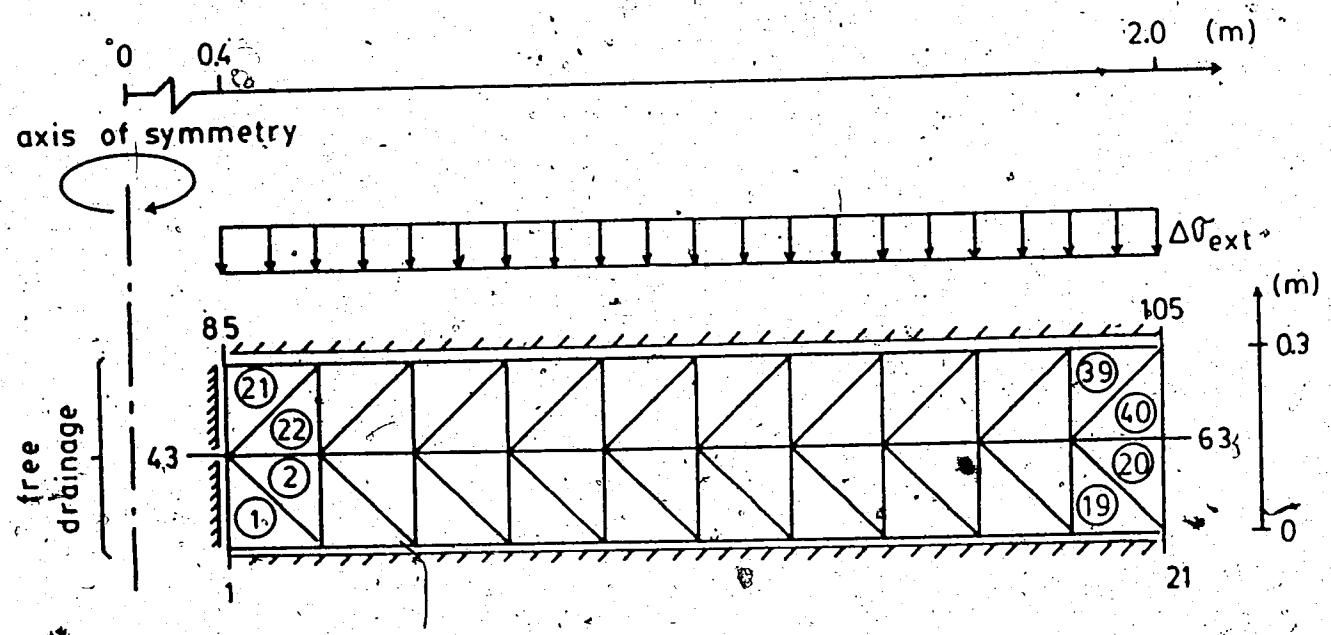

E = 240 MPa
ν = 0.3
k = 1×10^{-9} m/s
e_i = 0.47
S_i = 1.00

Figure 3.24 Finite Element Mesh - Test8-V6

Figure 3.25 presents the average excess pore pressure dissipation with time for both Barron's solution and CONGAS. It illustrates that the values predicted by CONGAS are very close to Barron's solution.

Figure 3.26 presents a mesh with external to internal radius ratio of 40. Its horizontal refinement is not uniform, being denser closer to the drainage boundary at the internal wall. This mesh is subjected to boundary conditions identical to those associated with the mesh presented in Figure 3.24. This mesh (Test9-V6) allows a comparison of the dissipation of excess pore pressure predicted by CONGAS at specific locations within the soil mass, with the solution presented by Barron, op.cit.. Figure 3.27 illustrates both results. The analysis of the results presented in this figure reveals that at the early stages of consolidation, the pore pressure prediction is rather poor at points located near the drainage boundary. The errors, however, disappear quickly as time progresses. For time factors (Th) greater than 0.02, the pore pressures indicated by CONGAS are very close to the ones offered by Barron's solution.

Better pore pressure predictions close to the drainage boundary, in the early stages of consolidation, would be possible with the use of a more refined temporal discretization. The minimum time increment equation, developed by Vermeer and Verruijt, 1981, presented earlier in this section, is not directly applicable to the axisymmetric case, but, if used simply as an indicator,

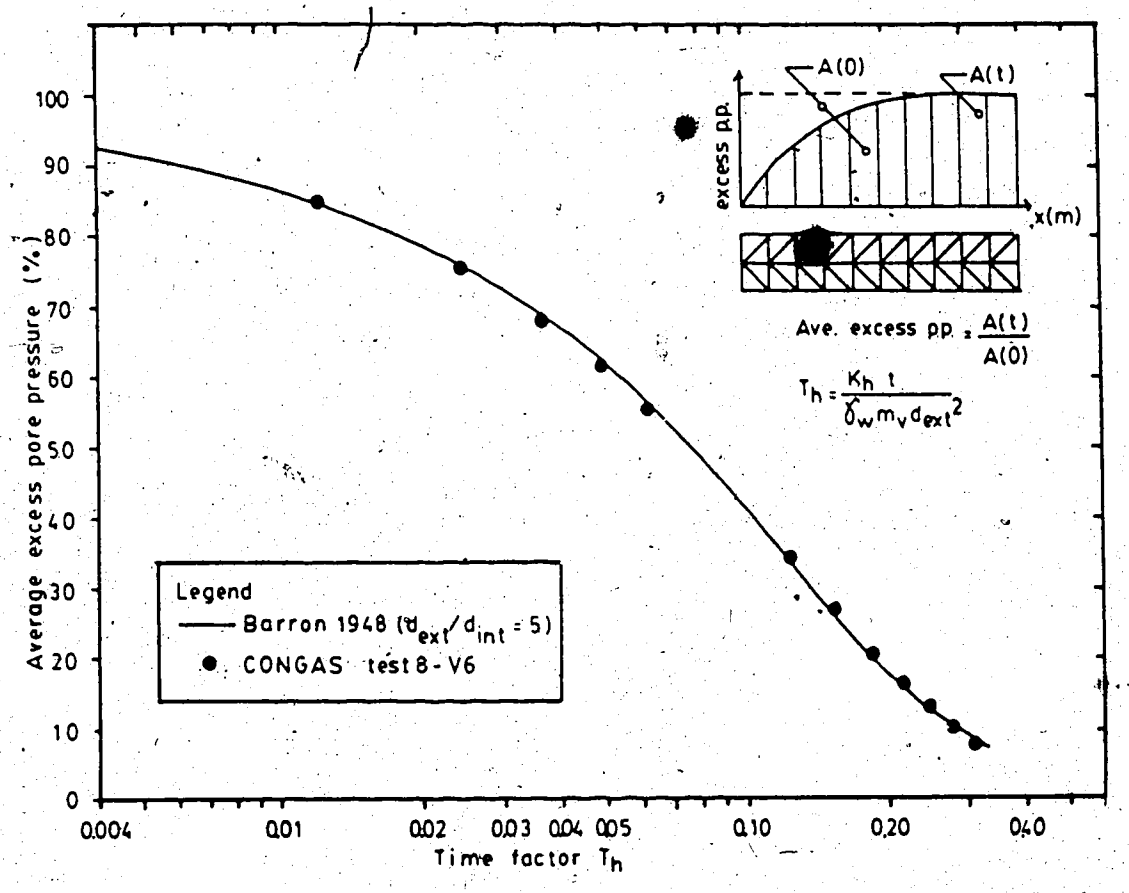

Figure 3.25 Axisymmetric Consolidation - Average Excess Pore Pressure versus Time Test8-V6

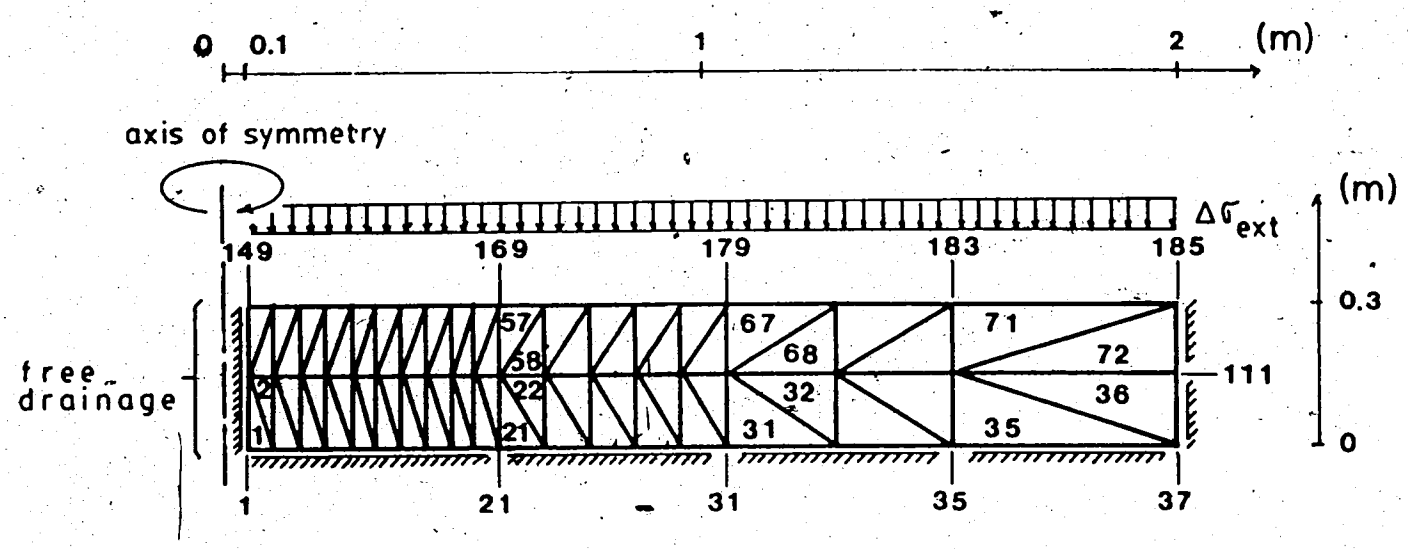

E = 240 MPa
ν = 0.3
k = 10^{-10} m/s
α - according to Hwang, 1970
$\Delta\sigma_{ext}$ = 2.69 MPa

Figure 3.26 Finite Element Mesh - Test9-V6

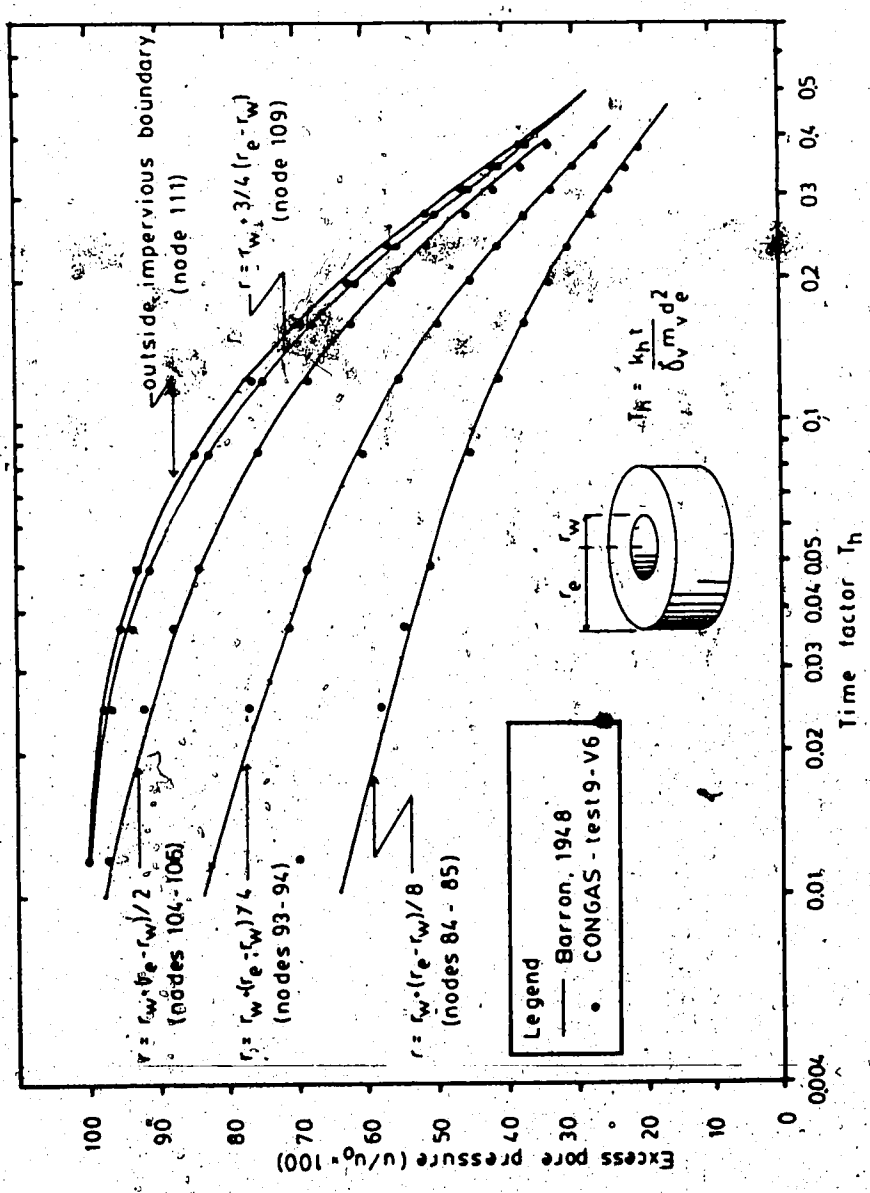

Figure 3.27 Axisymmetric Consolidation - Excess Pore Pressure versus Time

reveals that time increments as small as 1 minute could be used for the study of this case.

Gas Evolution Only

Sobkowicz, 1982:248, developed an approximate analytical solution for the problem of pore pressure generation due to gas evolution of a linearly elastic, gassy soil, subjected to undrained unloading.

The pore pressures as a function of time, are obtained from the quadratic equation.

$$A\Delta u^2 + B\Delta u + C = 0 \qquad [3.122]$$

where,

$A = \beta_T + nS\beta_L$

$B = \dot{P}.A + n.(1-S+SH[E_{SOB}.\Delta t/2])$

$C = -P.D$

$D = E_{CONST}.\Delta t.(K'/P/V_T - n[1-S+SH])$

where,

P = absolute pore pressure at the beginning of the time step.

E_{CONST} = gas evolution scaling factor.

Δt = time increment

K' = total equilibrium volume of dissolved and free gas in the pore space at any pressure P', multiplied by P'.

V_T = total volume of sample.

All other variables are defined in Equation 3.121.

This equation was derived based on the assumption that the volume of free gas produced during a time increment can

be evaluated in two-independent steps:

1. The rate of gas formation, due to evolution only, is evaluated based on the average of the gas formation rates at the beginning and end of the time step, i.e. at pressures P and (P+ΔP), respectively.
2. Boyle's law is applied to the initial volume of free gas plus the additional volume of gas calculated according to 1).

Step 1) above is, in fact, a particular case of the temporal discretization used in CONGAS, for time integration constant, α, equal to 0.5. Sobkowicz developed his equations based on an exponential form for the gas formation rate, as discussed in Chapter 2. In that formulation, thus, the scaling parameter is E_{CONST}.

The finite element mesh presented in Figure 3.20 (Test2-V3-1D-M1) was used to study the undrained behaviour of an idealized gassy soil. The soil properties and dimensions are presented in Figure 3.28. The soil, initially in equilibrium, is subjected to an external load of 13.8 kPa, applied to the top surface, acting upwards, as indicated in Figure 3.28. Initially, the pore pore pressure drops, to counteract the external load, and, as time progresses, bubbles in the pores increase in size, resulting in a gradual increase in pore pressure.

The pore pressure response versus time, as predicted by Equation 3.122, with a time increment equal to 4 min, is presented by the curves in Figure 3.28, for three different

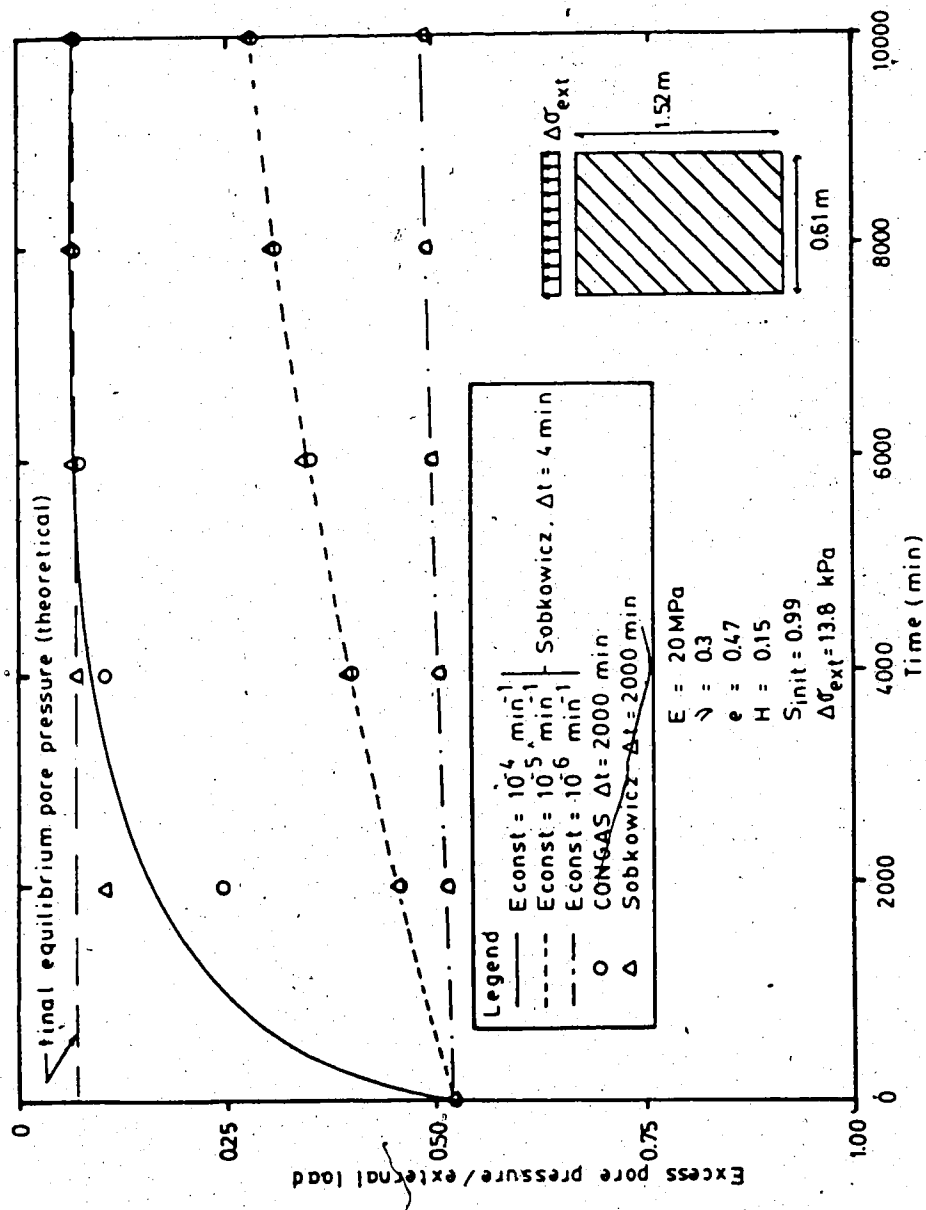

Figure 3.28 Undrained Transient Gas Evolution - Test2-V2-M1

values of the scaling parameter: 10^{-4}, 10^{-5} and 10^{-6} (1/minute). The time increment of 4 minutes was chosen based on a study that showed that time increments smaller than this value resulted in negligible variation of the resultant pore pressures. The three curves are probably very close to the "exact" solution for the problem.

The pore pressure response for the three values of scaling parameter given above, as predicted by equation 3.122 and by CONGAS, with time increments of 2000 minutes are represented by scattered points in Figure 3.28. These points show that this large time increment is appropriate for the lower values of the scaling parameter. However, for E_{CONST} equal to 10^{-4} 1/min, both CONGAS and Equation 3.122 produce erroneous predictions. This illustrates the fact that the gas evolution properties of the soil being studied also affect the choice of the appropriate temporal discretization.

It is worth noting that, for $E_{CONST}=10^{-4}$ 1/min, and $\Delta t=2000$ minutes, CONGAS predicts pore pressures lower than those predicted by Equation 3.122. This is attributed to differences in approach followed in each solution for the calculation of the average rate of gas evolution during the time increment. In CONGAS, for the case being studied, the time integration scheme adopted (logarithmic, Hwang et al., 1971) results in time integration constants that vary between 1 and 0.5. The analysis of Equation 3.81 indicates that for these values of α, the rate of gas evolution at the

end of the time step affects the solution to a greater extent than the rate of gas at the beginning of the time increment. Thus, the average rate of gas evolution predicted in CONGAS, for a given time increment, is smaller than that evaluated by Equation 3.122, where the average rate of gas evolution is equally affected by the rates of gas produced at the beginning and end of the time step.

Both solutions, Sobkowicz's and CONGAS, predicted pore pressures that asymptotically tended to a maximum equilibrium value, very close to the theoretical one, predicted according to Equation 3.121.

The results of the study on the effects of the refinement of the temporal discretization for the case presented above, with $E_{CONST}=10^{-4}$ 1/min, is illustrated in Figure 3.29. This figure shows that, for $\Delta t=500$ minutes, CONGAS predicts pore pressure response similar to Sobkowicz's solution with $\Delta t=4$ minutes.

The finite element mesh presented in Figure 3.17 was also used to study the accuracy of the prediction of pore pressures by CONGAS, for the case where transient gas evolution is the only process taking place within the soil. The soil and pore fluid properties used in the analysis are presented in Figure 3.17. The scaling parameter A', rather then E_{CONST}, was used in this analysis. Two values of A' were tested, 1000 and 3000 minutes. Figures 3.30 and 3.31 present the results of the two tests performed. In both cases, the results associated with $\Delta t=100$ minutes offer solutions very

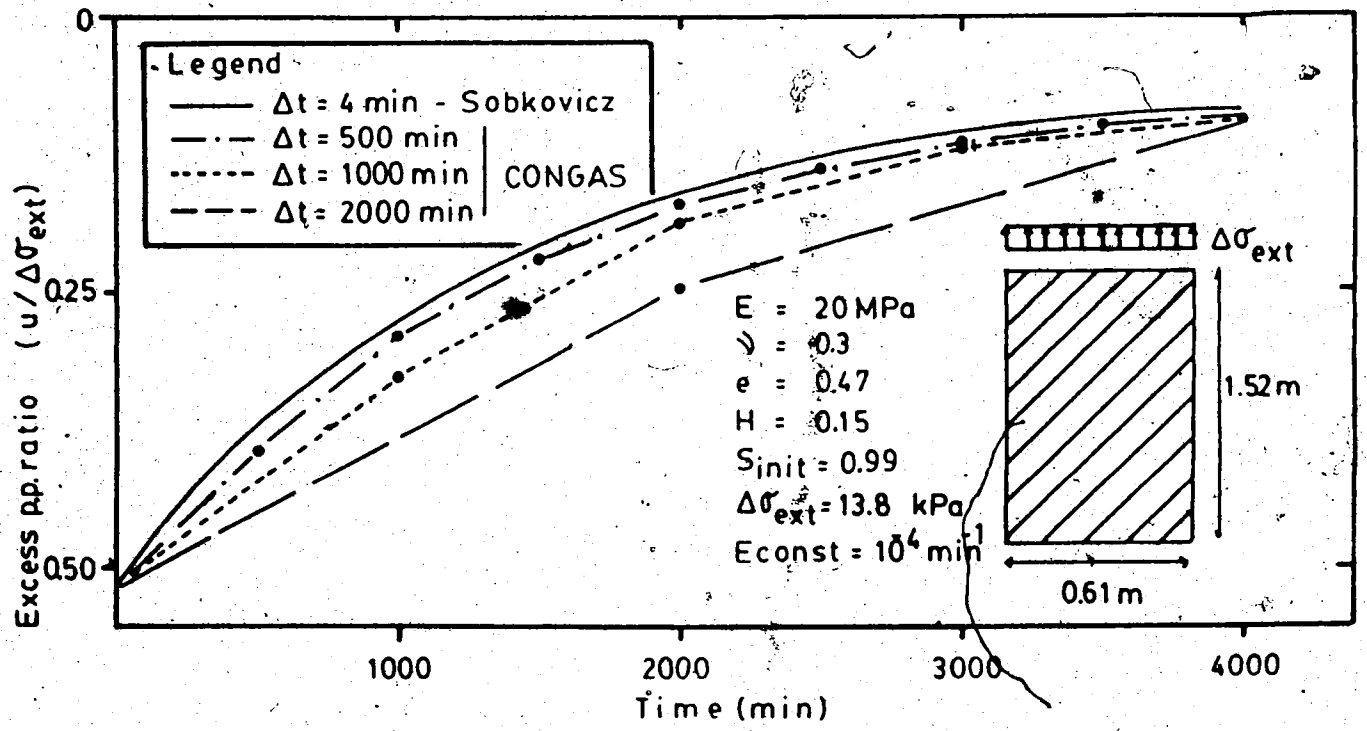

Figure 3.29 Undrained Transient Gas Evolution -

Test2-V2-M1-E_c=10^{-4} 1/min

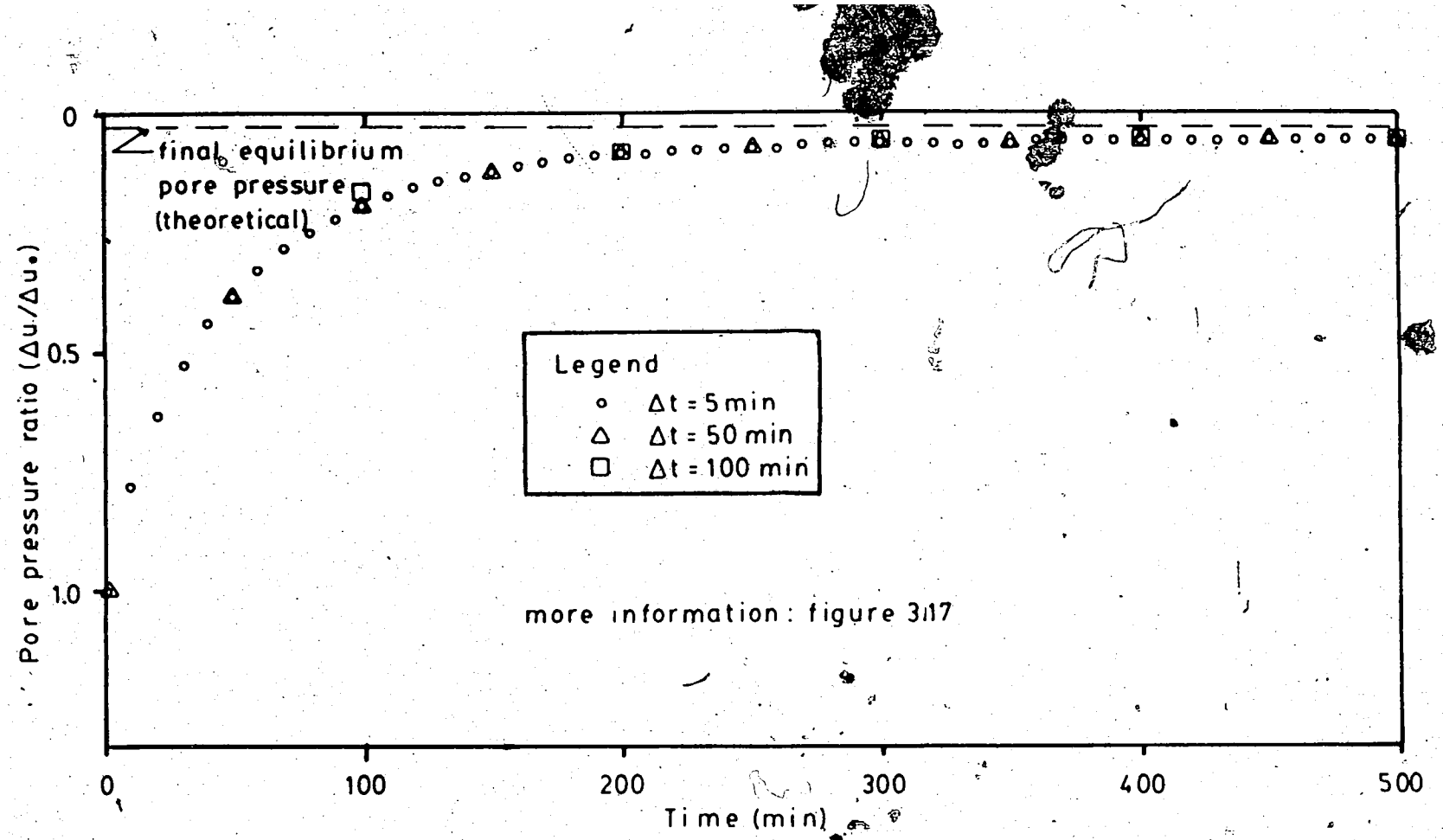

Figure 3.30 Undrained Transient Gas Evolution - Test 16-V14-1D - A' = 1000 min

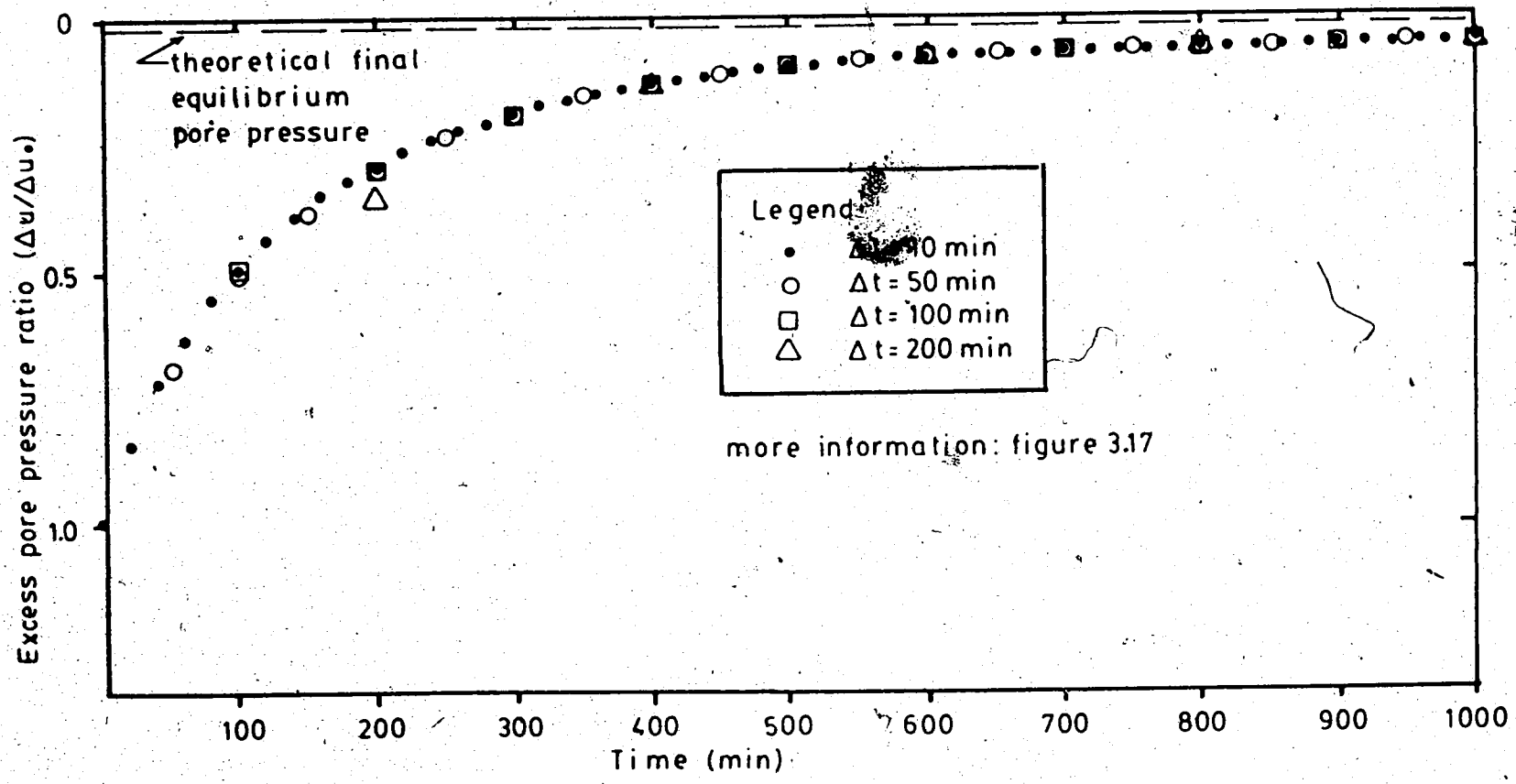

Figure 3.31 Undrained Transient Gas Evolution - Test16-V14-1D - A'=3000 min

similar to those in which a time increment of 5 minutes was used. Irrespective of the time increment used, all solutions produced pore pressures that asymptotically approached the theoretical equilibrium pore pressure.

All numerical tests presented in this section were performed with an allowable error, in the evaluation of the convergence of the gas evolution iterations, of 0.1%. The DAMP values, presented in Section 3.3.3, varied between 0.1 and 0.8.

Consolidation and Gas Evolution

The predictive capabilities of CONGAS, for the case, where both transient processes of consolidation and gas evolution take place simultaneously, was verified with the finite element mesh presented in Figure 3.32.

Due to the unavailability of solutions by other authors, for the case being considered herein, the performance of CONGAS was analysed qualitatively. This analysis was based on a comparison of two numerical tests, performed with the mesh of Figure 3.32, with identical soil and fluid properties and boundary conditions. In one of the tests, however, the pore fluid was assumed to be degassed, whereas, in the other test, gases were present in the pore fluids. Therefore, in the former test, consolidation was the only transient process involved, whereas in the latter, both consolidation and gas evolution took place.

In these idealized tests, the soil, initially at equilibrium, had the boundary pore pressure at the top

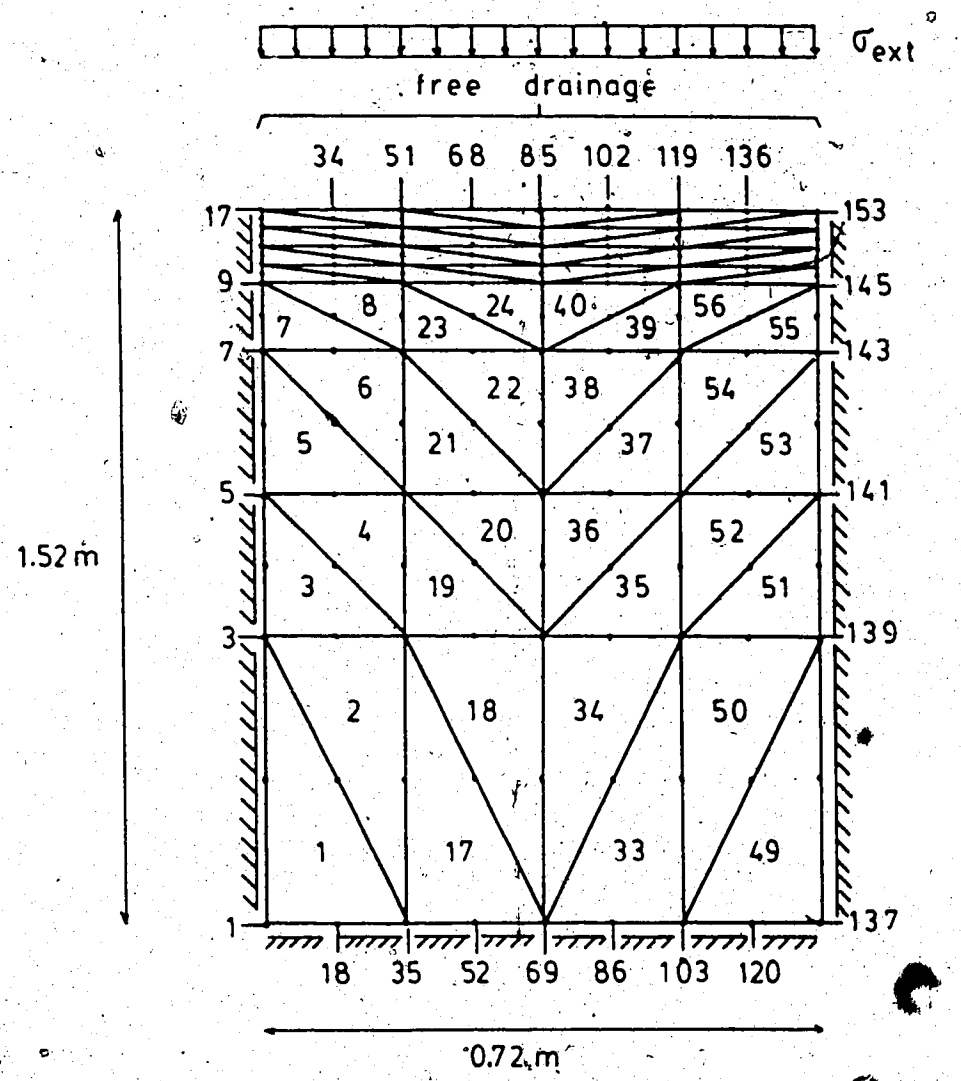

boun. conditions:

$\sigma_{ext,init} = \sigma_{ext,final} = 551.7$ kPa

$u_{init} = 137.9$ kPa

$u_{final} = 69$ kPa

properties

E = 200 MPa

ν = 0.3

$k = 10^{10}$ m/s

initial stress state

$\sigma'_x = 177.5$ kPa

$\sigma'_y = 413.8$ kPa

$\sigma'_{xy} = 0.0$ kPa

$u = 137.9$ kPa

Figure 3.32 Finite Element Mesh Test15-V15-1D

surface modified from the initial value of 137.9 kPa to 69 kPa. The external boundary traction, applied to the top surface was maintained constant, before and after the modification of the boundary pore pressures. The soil was allowed only to move vertically, thus being allowed to deform in the one dimensional mode. The soil and fluid properties used in the tests are presented in Figure 3.32. Figures 3.33 and 3.34 present the dissipation of excess pore pressure with time elapsed after the modification of the boundary pore pressure, for two points located at different distances from the drainage boundary. Three sets of data are presented in each curve. The solid curve represents the analytical solution of the one dimensional consolidation of a linearly elastic soil mass, saturated with degassed fluid. The scattered points represent the CONGAS results for both the degassed and the gassy fluids. The data plotted in both figures show that both the temporal and spacial discretization used in CONGAS resulted in an accurate prediction of pore pressures for the degassed fluid, when compared with the results from Taylor's solution. As expected, the pore pressure dissipation in the sample with gassy fluid is slower than the degassed sample. In the former, the decreases in pore pressure near the drainage boundary result in the formation of bubbles that tend to decrease the rate of pore pressure decrease. This situation was verified in the field by Martschuk et al., 1985 during the dewatering of basal sands for the oil sands mining at

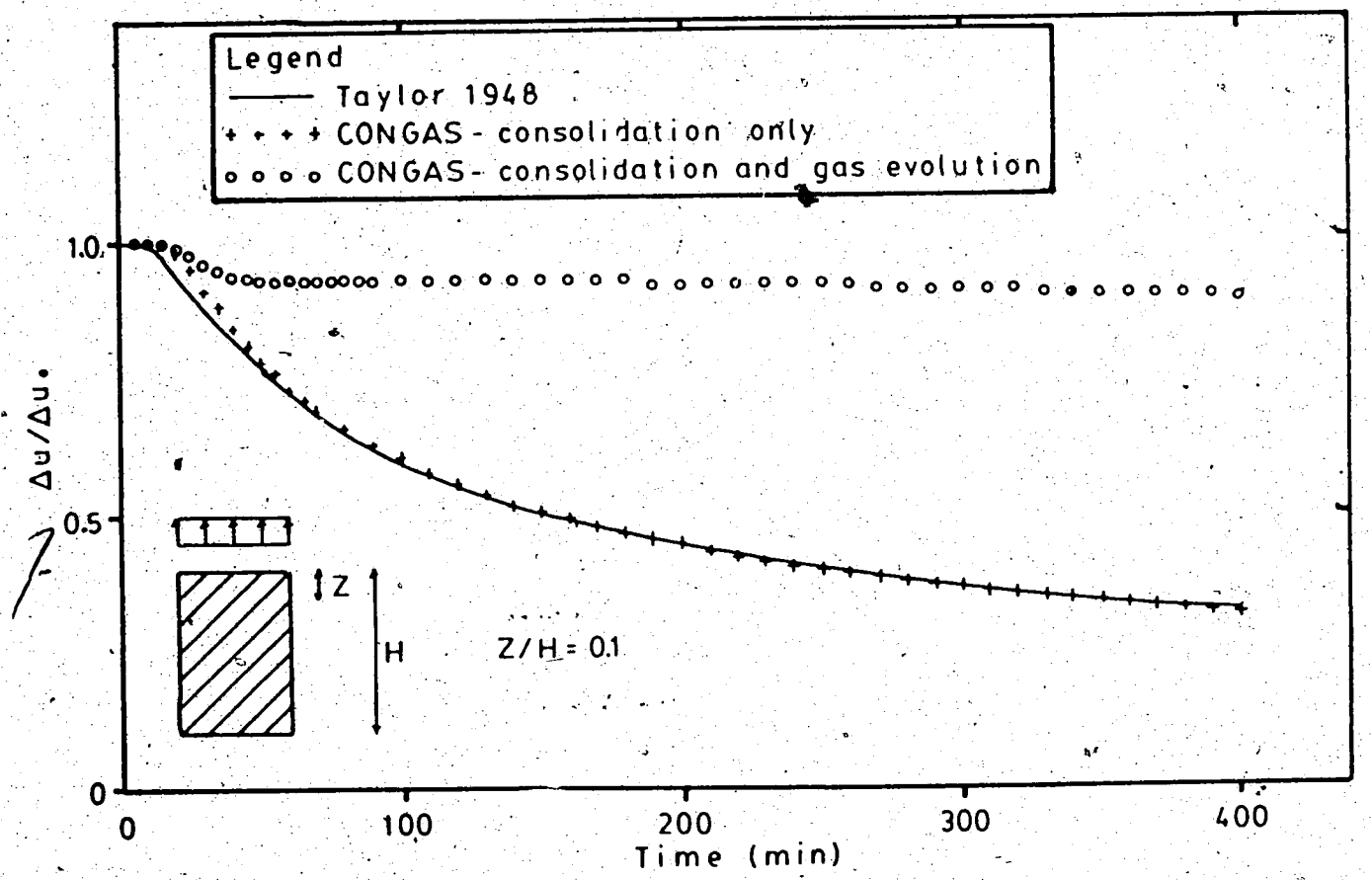

Figure 3.33 Coupled Consolidation and Gas Evolution - Test 15-V15-1D (z/H=0.1)

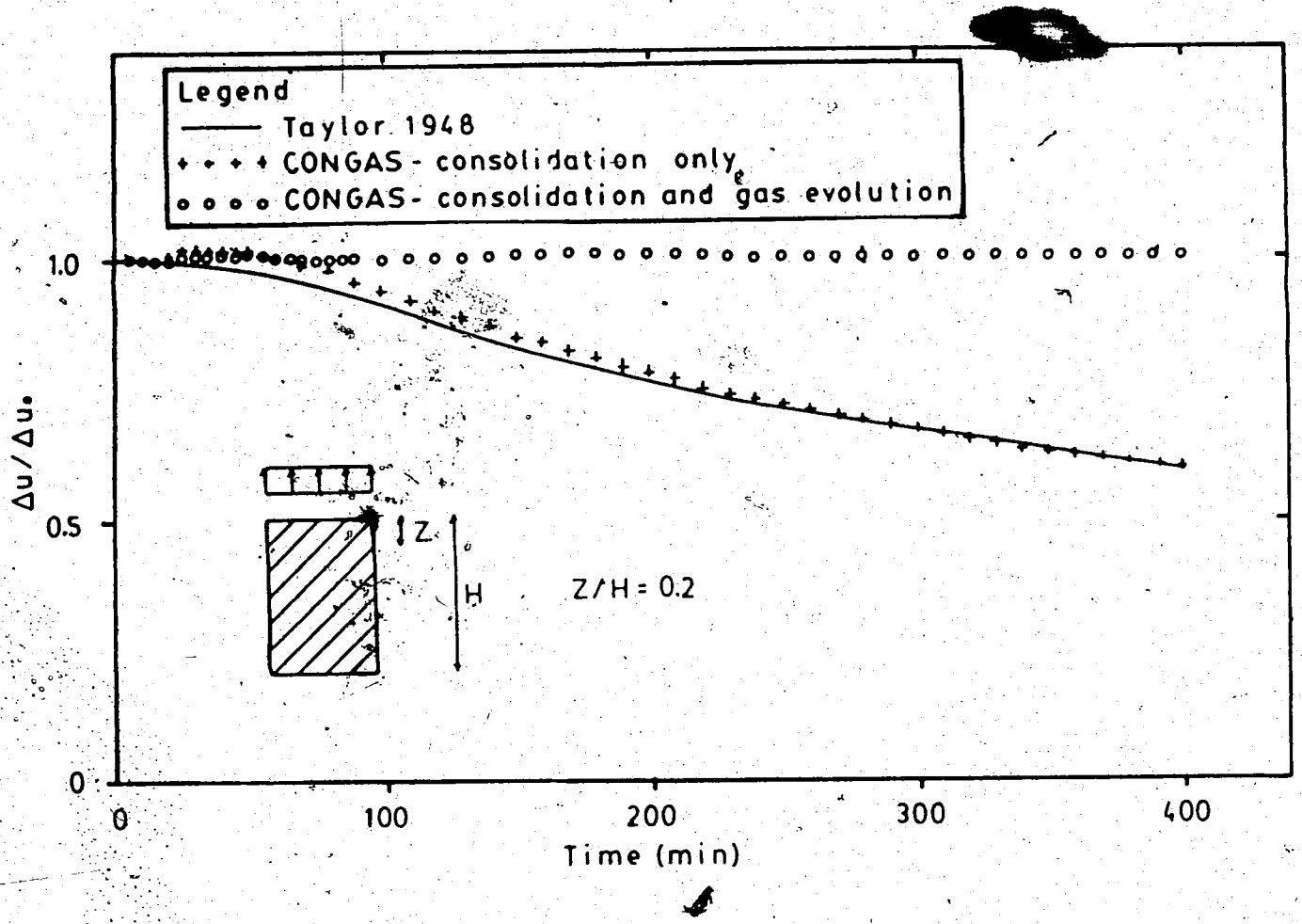

Figure 3.34 Coupled Consolidation and Gas Evolution - Test 15-V15-1D (z/H=0.2)

Suncor Inc., in Fort McMurray, Alberta. The authors verified that "the net effect of having gas dissolved in the aquifer water is the potential for pore pressures to decrease more slowly with dewatering than if no gas were present."

Figure 3.35 illustrates the pore pressure profile within the sample, for both cases, degassed and gassy fluid, at three different times. The delay in pore pressure response for the gassy soil, near the drainage boundary is clearly shown in this figure.

The settlement of the top surface for the two cases studied are displayed in Figure 3.36. In this figure, once again, the effect of gas evolution on the consolidation process is clearly shown.

3.3.4.3 Independent Features

Liquid Compressibility

The capability of CONGAS to correctly incorporate the compressibility of the liquids in the simulation of the behaviour of soils was verified with a numerical test performed with the finite element mesh Test2-V3-1D-M1, presented in Figure 3.20. The soil and fluid properties considered in this analysis are the same as those present in Figure 3.20, with the following additional information:

bitumen void ratio: 0.33

total initial void ratio: 0.47

water compressibility ($1/Q_{wat}$) = 0.45×10^{-4} kPa^{-1}

bitumen compressibility ($1/Q_{bit}$) = 2.05×10^{-4} kPa^{-1}

pores fully saturated with degassed liquids.

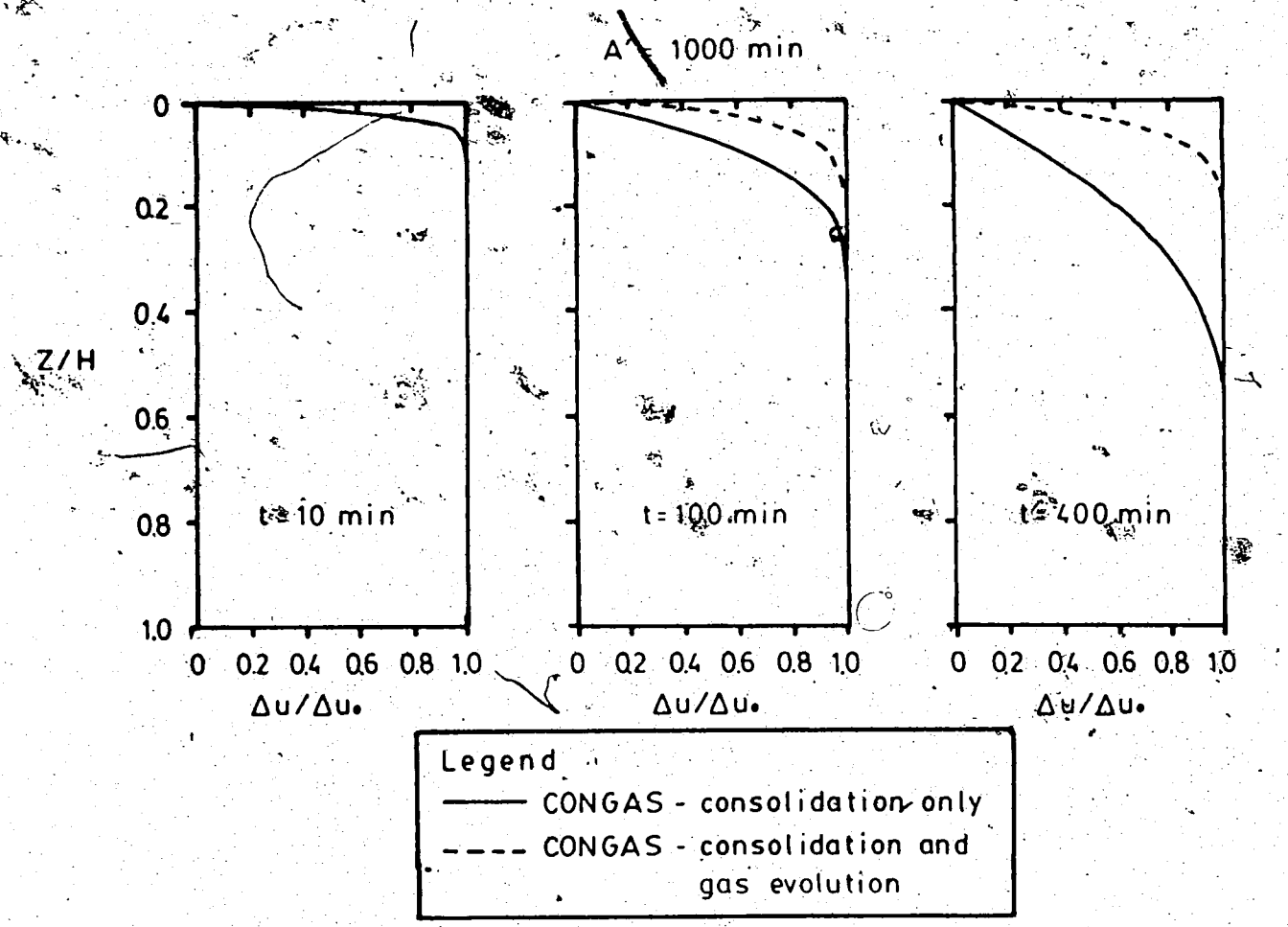

Figure 3.35 Coupled Consolidation and Gas Evolution - Test 15-V15-1D Excess Pore Pressure versus Depth

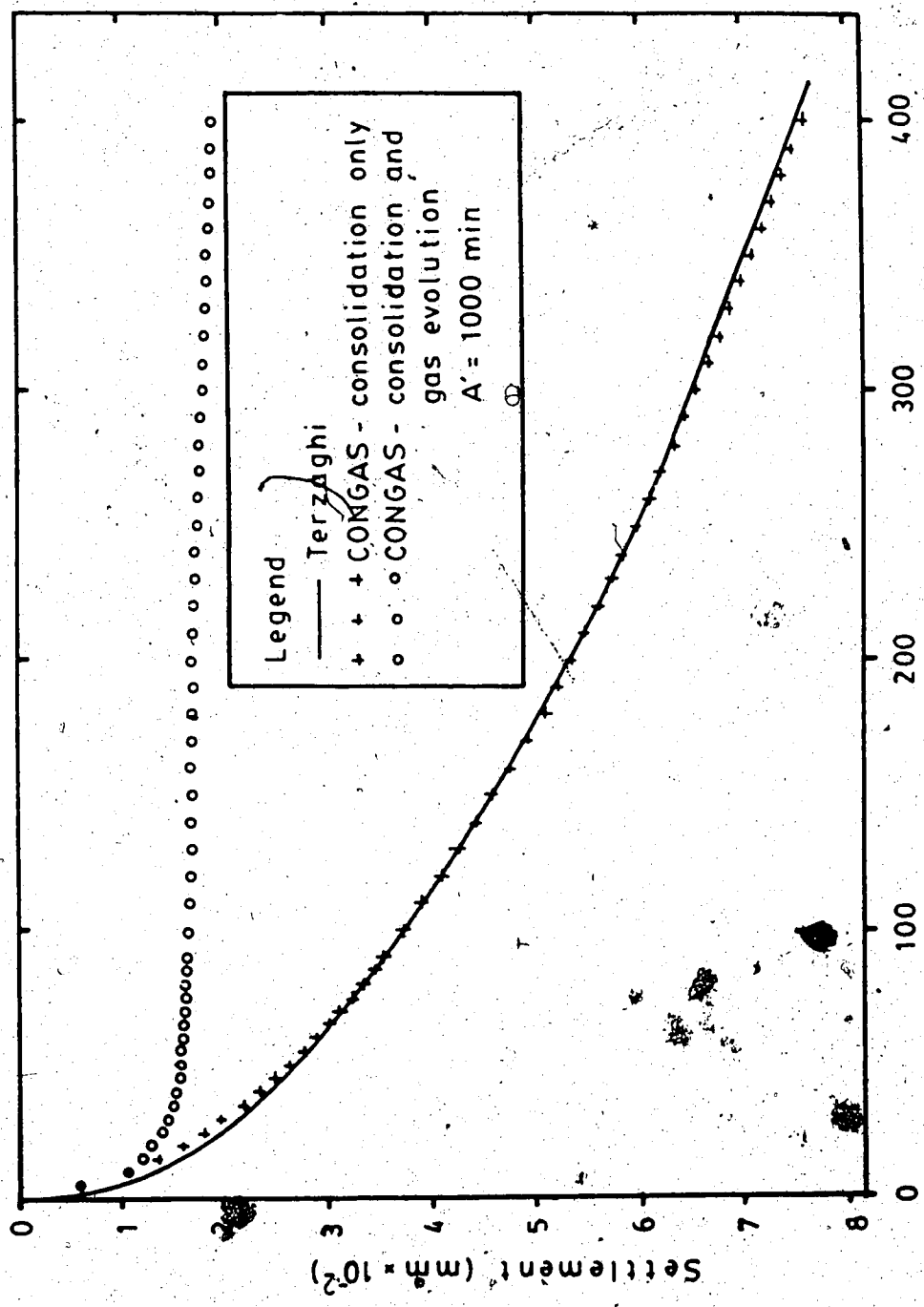

Figure 3.36 Coupled Consolidation and Gas Evolution - Test15-V15-1D - Surface Settlement versus Time

For the oedometer case, as the one simulated herein, it is possible to calculate theoretically the immediate undrained pore pressure response and vertical deformation for the soil saturated with compressible liquid. This is done by imposing volumetric strain compatibility between the skeleton and liquid phases:

volumetric strain due to liquid compression:

$$\epsilon_{v,liq} = \Delta u \frac{1}{Q} \qquad [3.123]$$

volumetric strain due to soil skeleton compression:

$$\epsilon_{v,skel} = (\Delta\sigma_{ext} - \Delta u).m_v \qquad [3.124]$$

where, Δu = pore pressure change

$\Delta\sigma_{ext}$ = external tractions

m_v = coefficient of volume change

$1/Q$ = combined liquid compressibility (Equation 3.109)

In the undrained case (or immediate response):

$$\epsilon_{v,liq} = \epsilon_{v,skel} \qquad [3.125]$$

and the following can be obtained,

$$\Delta u = \frac{\Delta\sigma . m_v}{((1/Q)+m_v)} \qquad [3.126]$$

Therefore, for the case studied,

Δu = 13.61 kPa

and $\epsilon_v = 6.83 \times 10^{-6}$

The results produced by CONGAS match exactly these values.

The time-dependent response for the compressible fluid case, during the first 9000 minutes that followed the immediate undrained response, resulted in excess pore pressures between 2 and 5% lower than those predicted for the incompressible fluid case, depicted in Figures 3.21 and 3.22, Test2-V3-1D-M1.

If a gassy fluid had been considered, the effects of fluid compressibility on the transient response of the soil would be minimized. The presence of gases in the pore fluid results in a net compressibility of the fluid significantly larger than the compressibility of the liquids usually encountered in the pores of gassy soils.

Variable Coefficient of Permeability

The effects of the variability of the coefficient of permeability in the results produced by CONGAS were also studied with the mesh Test2-V3-1D-M1, presented in Figure 3.20. The soil and fluid properties indicated in this figure

and in the preceding sub-section were used in the analysis, except that the pore liquids were considered incompressible and the coefficient of permeability variable, according to Equation 3.114. Two different values of surface boundary tractions were considered separately. In the first one, a value of $\Delta\sigma_{ext}$=13.8 kPa was used, and in the second, a value one hundred times greater was used, $\Delta\sigma_{ext}$=1379.3 kPa. All other variables were maintained identical for the two analyses.

The results from the first analyses showed that due to the small variation of void ratio, associated with the small boundary traction applied, the effects of the variation of the coefficient of permeability on the soil response were negligible. The results of this analysis were almost identical to the ones in which the coefficient of permeability was considered constant.

The results from the second analysis, however, showed that the increase in void ratio associated with the expansion of the soil mass increases the coefficient of permeability and consequently hastens the expansion process. This is illustrated by the pore pressure responses obtained from the cases where the coefficient of permeability is considered constant and where it is considered variable, as depicted in Figure 3.37.

The effects of the variation of the degree of saturation on the coefficient of permeability and consequently on the consolidation process, are inspected in

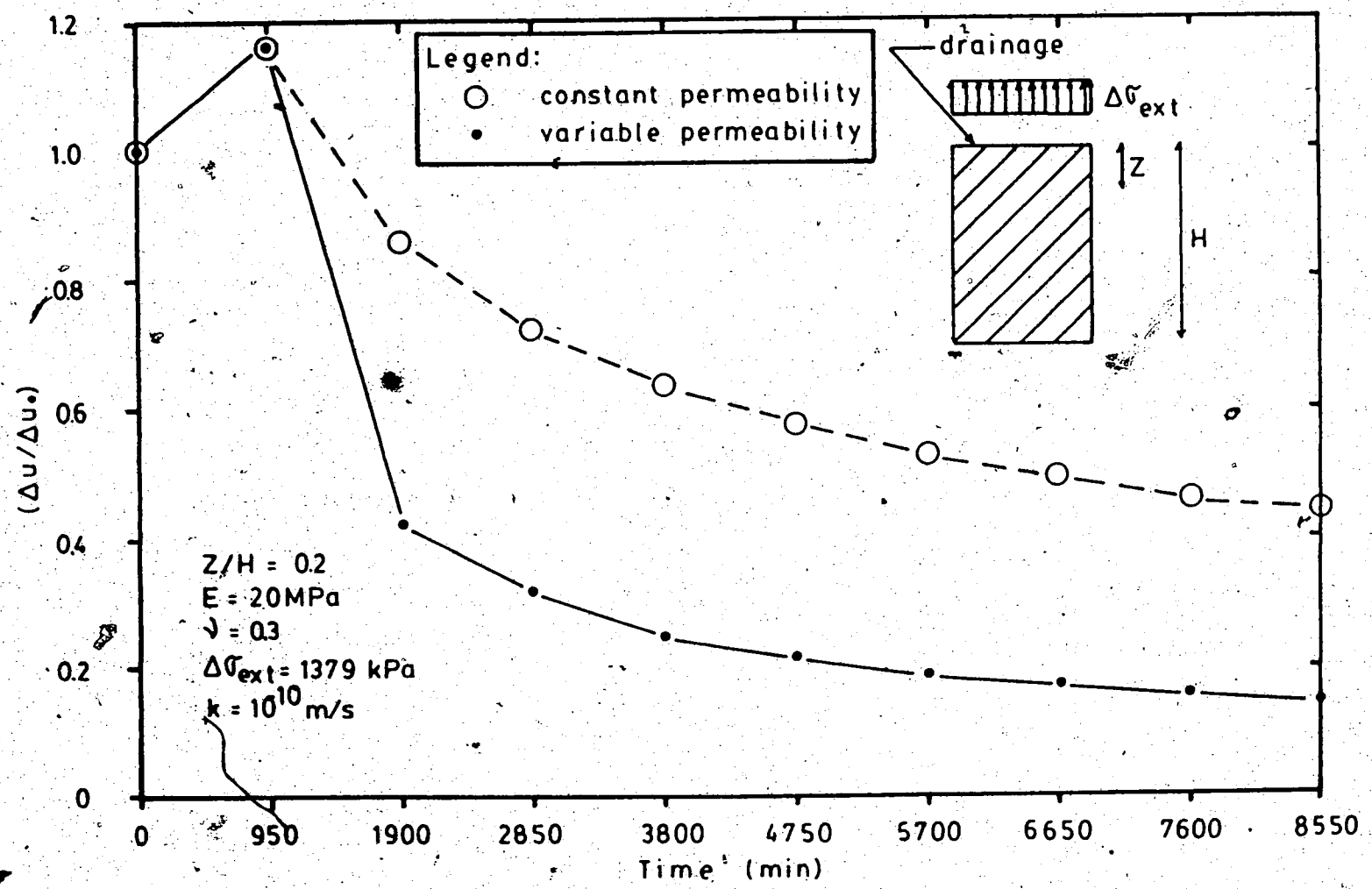

Figure 3.37 One Dimensional Consolidation - Variable Coefficient of Permeability

Chapter 5, Section 5.4.

3.3.5 Modelling Limitations of CONGAS

The preceding section highlighted the capability of CONGAS to simulate some idealized cases where closed form solutions or approximate solutions were available. When used to model more general cases, however, CONGAS has some limitations that are presented and discussed in the following sections.

3.3.5.1 Limitations of the Non-Linear Incremental Elastic Model

Stress Path and Failure

In order to illustrate the modelling limitations of the use of piecewise linear elastic solutions, associated with non-linear elastic models, the analysis of the behaviour of an element located at the wall of a shaft, is presented next.

The material model adopted for the soil mass is the hyperbolic model presented in Section 3.3.3. where the elastic parameters are expressed in terms of the minimum principal effective stress. Figure 3.38 illustrates the stresses the element considered is being subjected to, and the material model chosen.

Initially, before the shaft excavation, the radial stresses at the shaft contour equal the in situ stresses and for the case where the horizontal stress ratio is equal to one, the tangential stresses equal the radial stresses. A

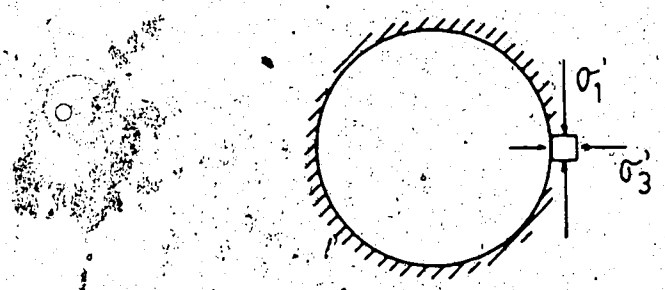

stresses at wall shaft

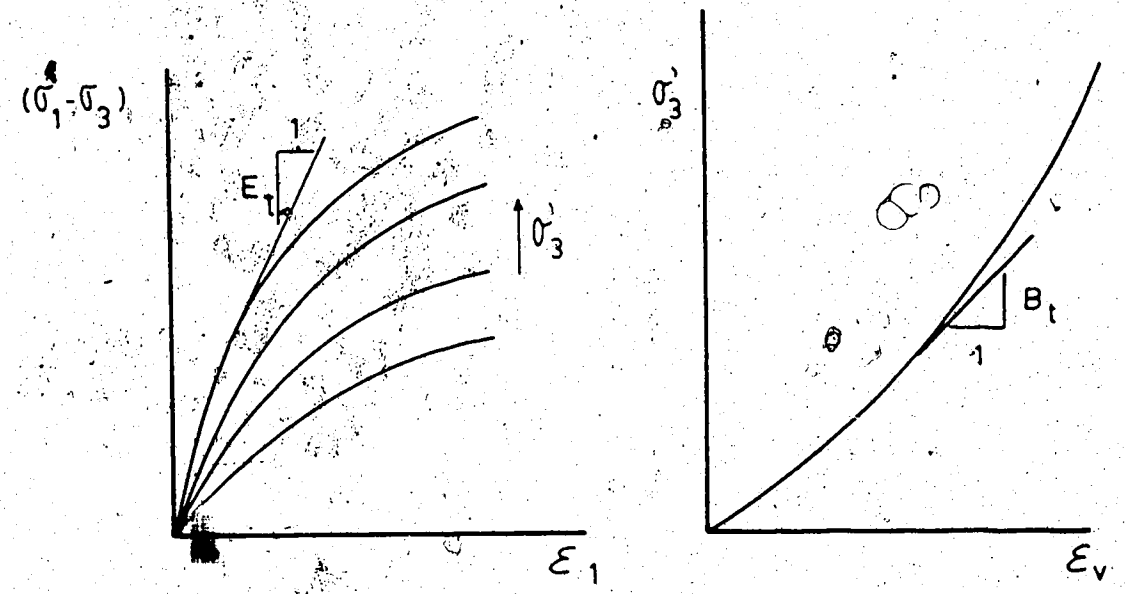

hyperbolic model (σ'_3) - CONGAS material model 2

Figure 3.38 Two Dimensional Simulation of Shaft Sinking - Hyperbolic Model

simple and approximate simulation of the shaft excavation in the two dimensional analysis considered herein can be carried out by reducing the radial stresses at the shaft contour. Since the material model is non-linear, this stress reduction should be made in steps.

For each of the unloading steps, the elastic constants used are obtained from the equations that describe the material model, as a function of σ'_3, among some soil strength properties and model constants at the beginning of the unloading step. For this step, the solution is solved then as a linear elastic one, where the elastic parameters are assumed to be constant. Irrespective of the elastic constants, the solution always produces a situation of equilibrium in the element considered in which the decrease in the minimum effective stress is associated with an increase in the deviatoric stress $(\sigma_1-\sigma_3)$. This stress path, obtained from successive unloading steps, might not be compatible with the stress path required to ensure that the equilibrium stresses, at the end of each increment, belong to the stress strain surface described by the hyperbolic model. An equilibrium condition might be predicted by the incremental formulation, such as the state of stress is distant from the stress-strain surface. This condition is illustrated in Figure 3.39. The stress path predicted by the incremental formulation associated with the shaft excavation, is represented by the curve A-B in Figure 3.39. Curve A-C represents the vertical projection of the stress

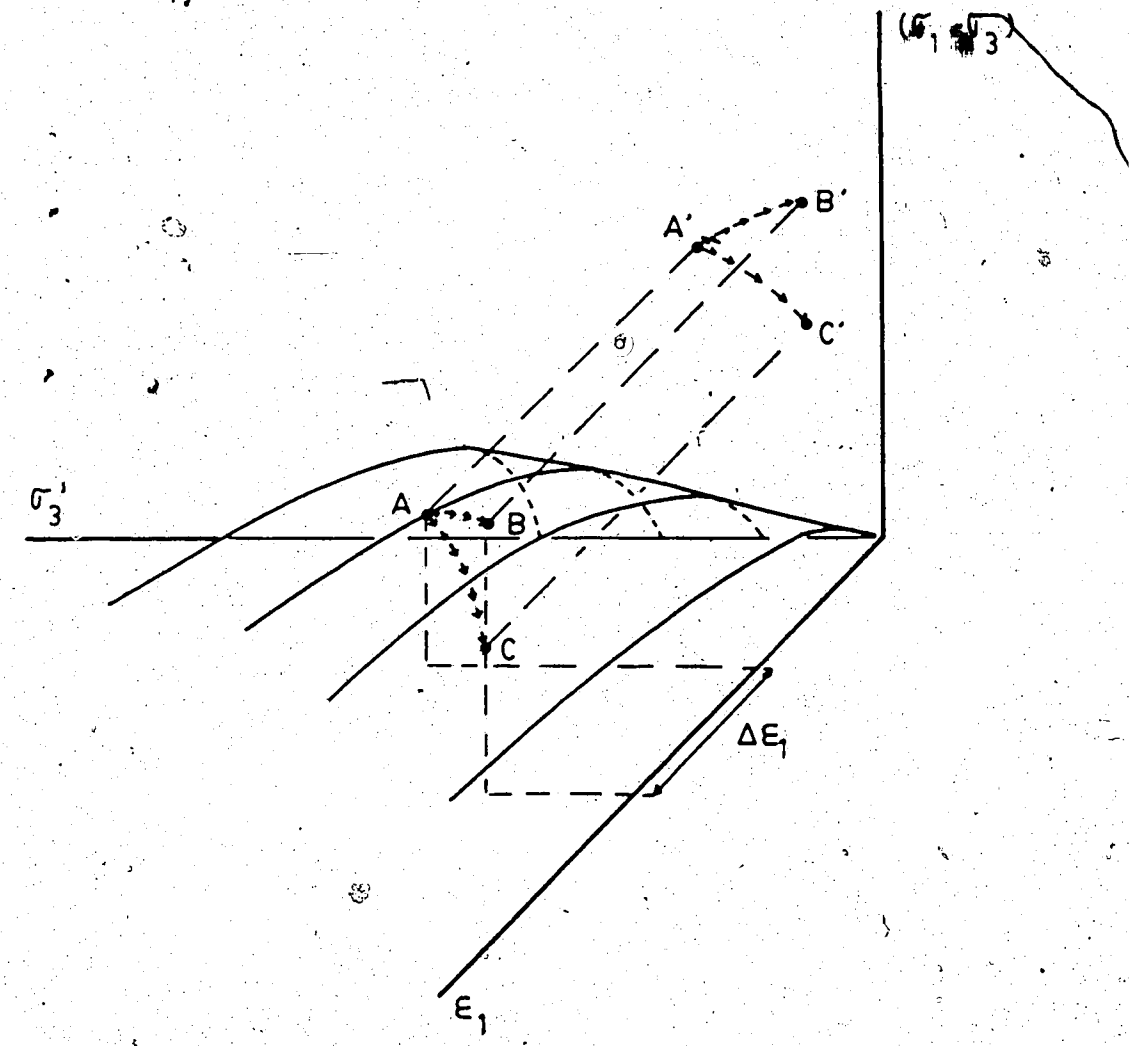

Figure 3.39 Shaft Sinking Simulation - Stress Path - Material Model 2

path A-B on the stress-strain surface. The vertical distance between points B and C gives a qualitative indication of how erroneous the solution by CONGAS might be. The implementation of the error indices in CONGAS, described in Section 3.3.3, was carried out in order to provide a means of evaluating the resultant equilibrium strains and stresses.

If, however, a non-linear material model described in terms of σ'_{oct}, τ_{oct} and the elastic constants G_t and B_t (material model 4 in CONGAS) are used, the errors associated with the state of equilibrium are smaller than those obtained if material model 2 is used. The reason for that follows directly from the shaft excavation example described herein, where σ'_{oct} is constant throughout the unloading steps. The stress paths associated with this latter case are illustrated in Figure 3.40.

A direct consequence of the inability of the numerical results to follow a stress-path that belongs to the stress-strain curve is that the equilibrium stress state at the end of an unloading step might violate the failure criterion. This is illustrated in Figure 3.41. Byrne and Janzen, 1984, proposed a technique called "Load Shedding", in which the stresses at a point of equilibrium that violate the failure criterion, are redistributed within the mesh in such a way that the new equilibrium stress state is in accordance with the failure criterion. Vaziri, 1986, implemented in Byrne and Janzen's technique two new methods

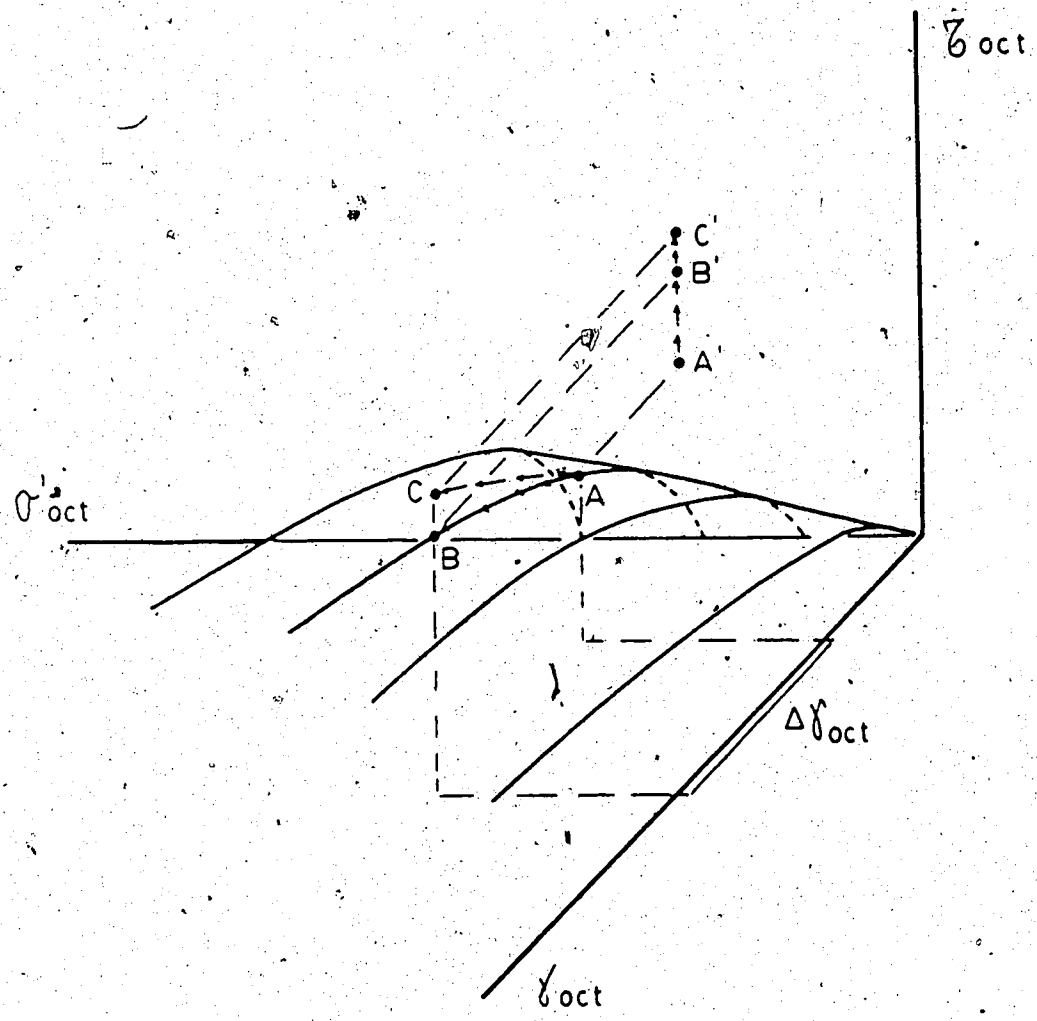

Figure 3.40 Shaft Sinking Simulation -- Stress Paths - Material Model 4

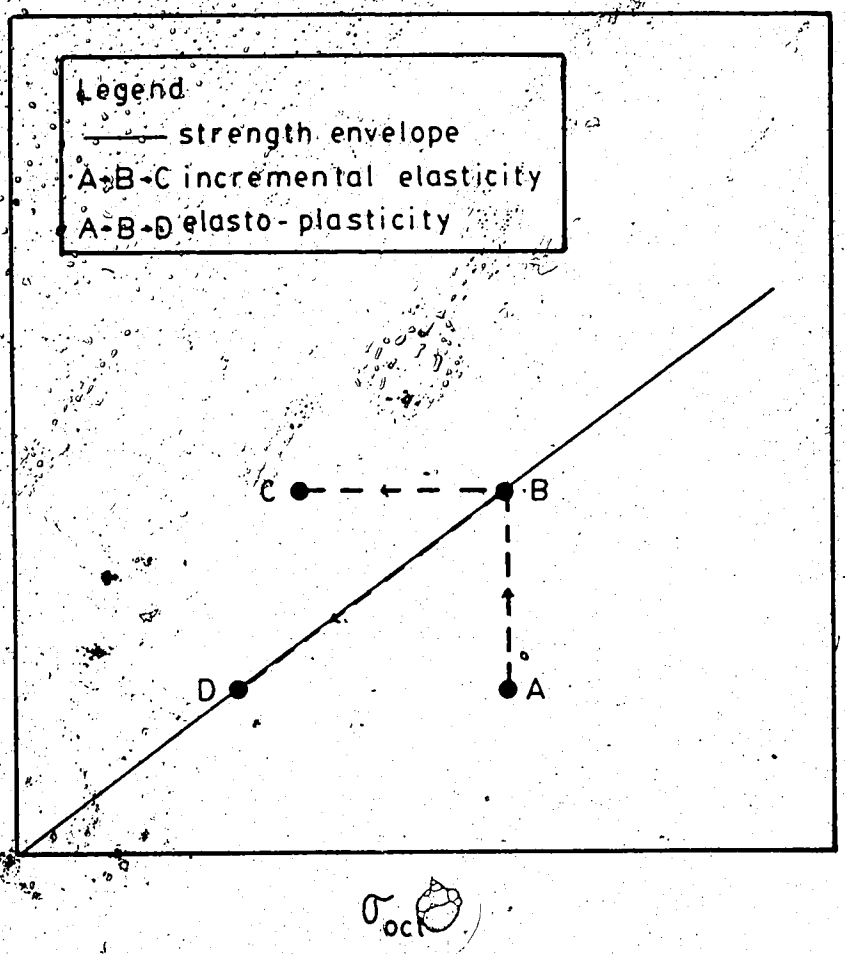

Figure 3.41 Failure Criteria Violation - Incremental Elasticity

of redistributing unbalanced loads in an element at failure.

According to the stress paths shown in Figure 3.39, it is possible to conclude that, for the sake of consistency, the "load shedding" technique should also be applied to points of equilibrium prior to failure.

In the writer's opinion, the implementation of additional features in the non-linear elastic material models, aiming at simulating plastic deformations, unnecessarily adds numerical complexities and approximations to the solution. The use of incremental elasticity should be chosen for specific types of problems that require a simple numerical solution. The limitations of the elastic solution should be recognized and incorporated in the analysis of the results, through a sensible application of engineering judgement. If, however, plastic deformations are of prime concern, one might opt for more comprehensive non-linear plastic models, thus abandoning the non-linear elastic models. In accordance with these thoughts, the simplest form of the incremental elasticity solution was maintained in CONGAS. This means that its use should be limited to cases where the stresses at equilibrium are not close to the strength envelope.

Volume Changes due to Shear

In the incremental elasticity formulation, changes in shear stress do not cause changes in volume. This is a limitation of the non-linear elastic material models which

Byrne and Eldridge, 1982, tried to overcome by implementing the "pseudo-dilatant" technique.

In this technique, for a given load increment, an equilibrium stress state is obtained simply by means of the theory of elasticity, i.e., without shear dilation. Based on Rowe's, 1971, and Hughe's et al. 1977, stress dilation theory, a volumetric strain is evaluated based on the shear strains at the end of the load increment. The hydrostatic load vector to cause this volumetric strain is evaluated and reapplied to the system, along with the load increment, and the new stress and strain equilibrium states are computed. Therefore, according to this model, dilation due to shear is always associated with some decrease in the hydrostatic stresses. It happens, however, that in some cases, as in the case of pressuremeter tests performed in dense sand as illustrated by Baguelin et al., 1978:387, the shear dilation occurs with increases in the octahedral stress. This situation cannot be simulated by the model proposed by Byrne and Eldridge, which is described above. Chen and Saleeb, 1982:529, presented another form of implementing shear dilatancy in incremental elasticity. The shortcomings of the proposed method, such as handling non-symmetric stiffness matrices, were highlighted by the authors.

Given the weaknesses and shortcomings of the methods above, it was decided not to include shear-volume coupling in CONGAS. This undoubtedly limits its applications to nearly no dilatant/contractile soils. Once again, the facts

presented in this sub-section indicate that if shear-volume coupling is a feature of major importance in the system being simulated, the use of more comprehensive plastic models might be more appropriate.

Shear Stress Reversal

Shear stress reversal or "unloading-reloading" behaviour, was modelled by Duncan and Chang, 1970. The authors proposed that upon unloading, Young's modulus of the material is higher than upon loading. This feature was implemented in the hyperbolic model, and according to Chen and Saleeb, 1982, simulated with accuracy the actual behaviour of soils.

This feature was not implemented in CONGAS because most of the situations for which the program was developed do not involve shear stress reversal or, as more commonly referred to, unloading situations.

Non-Viscous Stress-Strain Response

The transient response of the soil mass in CONGAS, occurs solely due to the phenomena of consolidation and gas evolution. However, in soils like oil sands, the bitumen present in the pores exhibits viscous behaviour, which might alter the transient response predicted by CONGAS.

In order to inspect how the viscous response of the bitumen affects the transient response of oil sands, a simple study was carried out based on the visco-elastic model developed by Zienkiewicz et al., 1968. According to

the authors, experiments have shown that, in some materials, creep occurs only due to the deviatoric stress components, the volumetric behaviour being elastic. Therefore, the mechanical response of these materials is conveniently analysed in two separate parts:

- volumetric response - function of the bulk modulus
- pure shear response - function of the shear modulus

Figure 3.42 depicts the model dicussed herein. The shear component is defined according to Kelvin's model, in terms of the elastic shear modulus of the soil skeleton and the viscosity of the bitumen.

Assuming that the soil is subjected to constant shear stress, the rate of shear strain due to creep is given by the equation:

$$\dot{\gamma}_{cr} = \frac{d\gamma_{cr}}{dt}$$

$$= \frac{\tau}{\eta} - \frac{G}{\eta} \cdot \gamma_{cr}$$

$$= a\tau - b\gamma_{cr} \qquad [3.127]$$

The shear strain that occurs from time t to time Δt, for a constant shear stress is:

$$(\gamma_{cr})_{t+\Delta t} = (e^{-b\Delta t})\ (\gamma_{cr})_t + \frac{a\tau}{b}(1-e^{-b\Delta t})$$

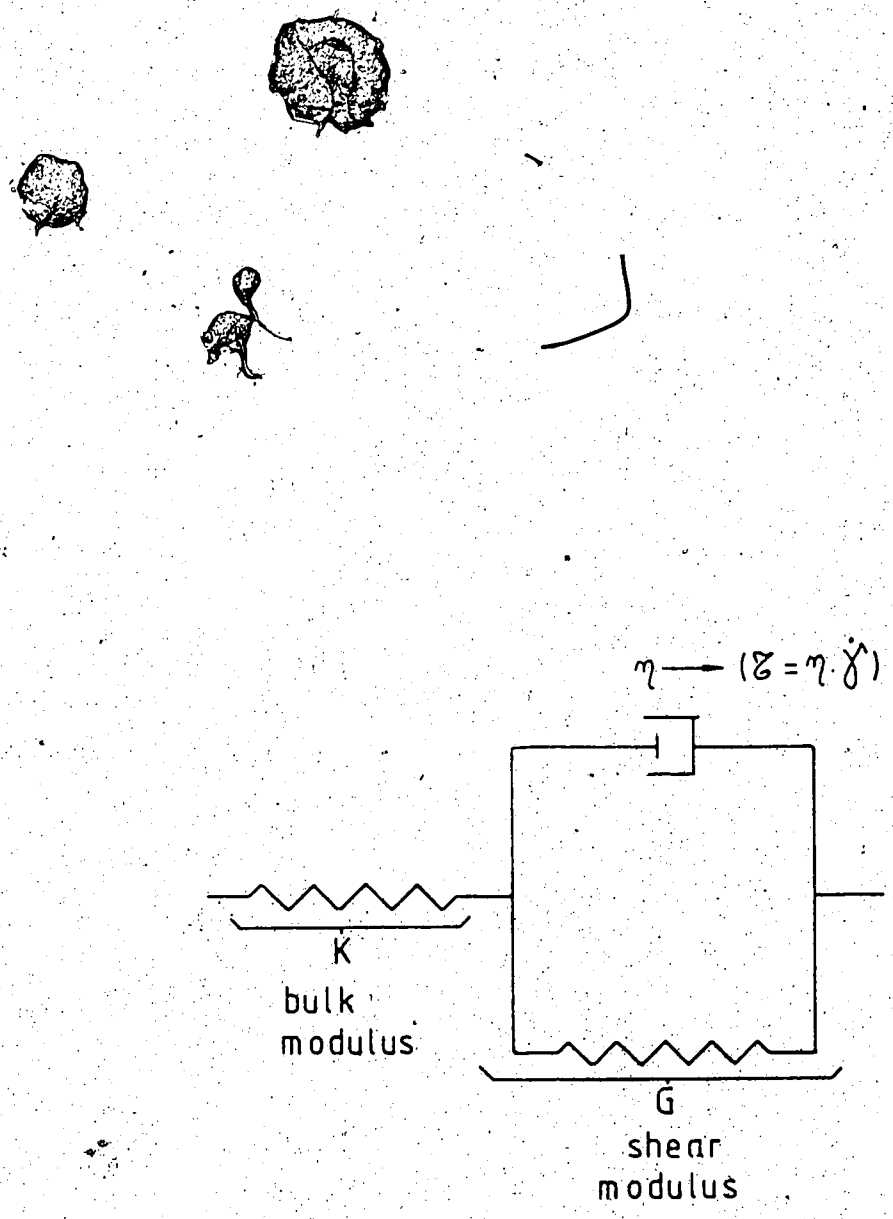

Figure 3.42 Visco-Elastic Model - Modified from Zienkiewicz et al., 1968

$$= \frac{a\tau}{b} + \left[(\gamma_{cr})_t - \frac{a}{b}\tau\right] \qquad [3.128]$$

since $\frac{a}{b} = \frac{1}{G}$,

$$(\gamma_{cr})_{t+\Delta t} = \frac{\tau}{G} + \left[(\gamma_{cr})_t - \frac{\tau}{G}\right] e^{-b\Delta t} \qquad [3.129]$$

The first term of the right hand side of this equation is the total additional shear strain due to the shear stress τ, if the time-dependent strains are neglected. The second term refers to the time-dependent shear strains.

If the following typical oil sands parameters are considered:

$G = 80$ MPa

$\eta = 1.3 \times 10^4$ Pa.s (Athabasca bitumen viscosity at 6°C according to Hardy and Hemstock, 1963).

$\therefore \quad b = \frac{G}{\eta} = 6154$ 1/sec

the second term on the right hand side of Equation 3.129 is multiplied by the term $e^{-6154.\Delta t}$. Considering that the time increments usually used in numerical analyses of consolidation and time evolution problems, are not smaller than 60 seconds, one can verify that, for the case considered, the second term of the right hand side of Equation 3.129 is orders of magnitude smaller than the total, time independent first term. Hence, it can be concluded that the creep effects in the shear strain

deformation for the case considered, which represents most of the in situ situations, can be neglected.

For cases where the temperature of the reservoir is higher than considered above, the viscous response of the bitumen has even less effect on the overall behaviour of the soil mass.

For cases where the temperature of the oil sands are lowered, to improve the stability of excavation, (Jessberger, 1979) the viscous response of the soil mass might have to be considered in the analysis.

3.3.5.2 Limitations of the Fluid Model

The limitations of the fluid model are a consequence of the hypothesis adopted for its development. Some of these limitations are discussed in the following subsections.

Gas Venting

The term "gas venting" is used to describe the situation in which the gas bubbles present in the pores of the soil grow to a size that they become interconnected. If this process propagates to a drainage boundary in which the pore pressures are lower than the ones inside the now interconnected bubbles, the gas escapes from the pores. As discussed in Chapter 2, experiments have shown that bubbles become interconnected at degrees of saturation between 80 and 85%.

Based on the fact that soil permeability to gases is higher than is the permeability to water and bitumen, Harris and Smith, 1979, proposed the simulation of gas venting to

be performed by the imposition of immediate dissipation of excess pore pressures at points where the degree of saturation exceeds the lower limits prescribed above. According to the authors, this process is equivalent to imposing an extremely high value of gas permeability in regions where venting occurs.

In CONGAS, this feature was not included. Thus, it is limited to simulating cases where the degree of saturation is higher than 85%.

Bubble Point Pressure

The solution scheme adopted in CONGAS assumes that the initial pressures are equal to or smaller than the bubble formation or critical pressure. As discussed in Chapter 2, this seems to be a reasonable assumption for simulation of most stress relief situations in the Athabasca oil sands deposits or in marine sediments.

In order to give more flexibility to CONGAS, future versions should include the possibility of specifying bubble point pressures smaller than the initial pore pressures.

3.3.5.3 Limitations of the Numerical Iterative Scheme

The iterative scheme adopted in CONGAS, for the solution of the non-linear flow in the soil mass, results in the successive solution of the finite element equations for different values of the gas volume vector $\{e_v^{fg}\}$. As stated in Section 3.3.3, iterations are performed until two successive solutions yield results within a prescribed tolerance.

However, depending on a series of variables involved in the solution of the system, such as the magnitude of stress relief, the initial stresses and pore pressures within the soil mass, the gas evolution and solubility constants, two situations can be encountered.

1. During successive iterations, the absolute pore pressure at a point might become lower than the absolute zero pressure, which is physically impossible.
2. During successive iterations, the resultant degrees of freedom might diverge, i.e., the error, as defined in Section 3.3.3, might increase as iterations proceed.

For cases where situation 1) above is encountered, the calculations in CONGAS are halted. Provided that the correct solution for the problem is related to pore pressures above absolute zero, situation 1) can be avoided with the use of small values for DAMP constants (defined in Section 3.3.3).

Calculations in CONGAS are also stopped whenever situation 2) is encountered. There are two possible means of avoiding this situation: the use of smaller DAMP values or the use of smaller time increments. Both approaches reduce the magnitude of the gas volume vector $\{\epsilon_v^{tg}\}$ which results in more stable solutions at the cost of a larger number of iterations. Care must be taken not to decrease the time increment below critical values, as discussed in Section 3.3.4.2. If time increments smaller than the critical ones are required, refinement of the mesh might be necessary. The use of lower DAMP values is an efficient way of eliminating

solution divergence. Values of DAMP as low as 0.01 were required in some cases presented in this thesis. The exact DAMP value to be used in a solution is a function of several variables involved in the problem. Generally speaking, the larger the amount of gas produced in a given time increment, and the greater the freedom the finite element mesh has to move, as a result of the transient processes involved, the smaller the DAMP values should be.

3.4 Summary and Conclusions

In this chapter, the techniques to simulate the mechanical response of gassy fluids were discussed. A review of the existing models was presented. This review indicated that most of the models that consider the time-dependent response of gassy soils do not simulate properly the transient evolution of gases. In these models, the transient pore pressure occurs solely due to consolidation, whereas the gas evolution is assumed to take place instantaneously, as a function of the pore pressures, and not as a function of time. The need for the development of a model that properly simulates the transient behaviour of gassy soils was, therefore, identified. As a result, a model was developed. This development consisted of the derivation of the governing equations and their solution by the finite element technique. A computer program, CONGAS, was developed. In this program, the soil skeleton mechanical response is modelled with a linear elastic or three

different versions of the non-linear elastic hyperbolic model.

The pore fluid is assumed to be a two phase system, formed by one liquid and miscible gases, that can be both, dissolved in the liquid and in the free state.

The gas bubbles are assumed to be immobile and the liquid phase is assumed to flow according to Darcy's law. The formulation allows the liquid phase to be considered compressible and the coefficient of permeability to vary as a function of the void ratio and degree of saturation.

The program is limited to solve cases where the bubbles are not interconnected.

A series of numerical tests was performed. These tests indicated that CONGAS accurately simulated the idealized conditions. The limitations of the program were discussed in detail.

4. SAMPLING AND TESTING PROGRAMS

4.1 Introduction

The preceding chapters of this thesis presented a review of the physics of gas evolution in gassy fluids and a review of the existing analytical models that simulate these transient processes. It was shown that the models that use the fundamental thermodynamic properties of the fluids are difficult to apply to the simulation of the time-dependent response of gassy soils and that macroscopic, or descriptive models, are more suitable for this purpose.

A macroscopic gas evolution model was implemented in the equations that govern the time-dependent response of gassy soils which were solved by numerical techniques and implemented in the finite element program CONGAS.

The present chapter presents the sampling and testing program that was designed in order to fulfill two objectives:

1. To observe the equilibrium and non-equilibrium (transient) mechanical behavior of a natural gassy sediment (oil sand). This observation should allow the verification of the applicability of the simple macroscopic gas evolution models described in Chapter 2, to simulate the response of gassy sediments.
2. To verify the predicitive capabilities of the numerical model (CONGAS) developed in Chapter 3.

The Athabasca oil sand was chosen as soil material for the testing program. It is a dense, fine to medium grained uniform quartz sand containing water, bitumen and occasionally free gas, as pore fluids. Its structure is interpenetrative due to diagenesis which resulted in dissolution and recrystallization of quartz at grain boundaries, after the time of burial (Dusseault, 1977). The sand grains are water wet, i.e., completely surrounded by water, which forms a continuous phase throughout the oil sand matrix. The bitumen also forms a continuous phase and, together with any existing free gas, occupies the remaining pore space.

At *in situ* temperatures, (≃6°C), Strausz et al., 1977, reported the presence of gases, predominantly methane, neopentane and carbon dioxide. Figure 4.1 illustrates the structure of an oil rich sand.

The choice of Athabasca oil sand as the testing material was based on the interest of the oil sands mining industry in Alberta in the research developed herein, the availability of this material and the extensive experience in sampling and testing oil sands gained in the last decade by the geotechnical group of the University of Alberta.

The series of tests performed with the oil sands samples can be divided in two groups:

Group A) Tests performed in order to produce fundamental skeleton and fluid mechanical parameters. These are used as input data for the finite element program CONGAS.

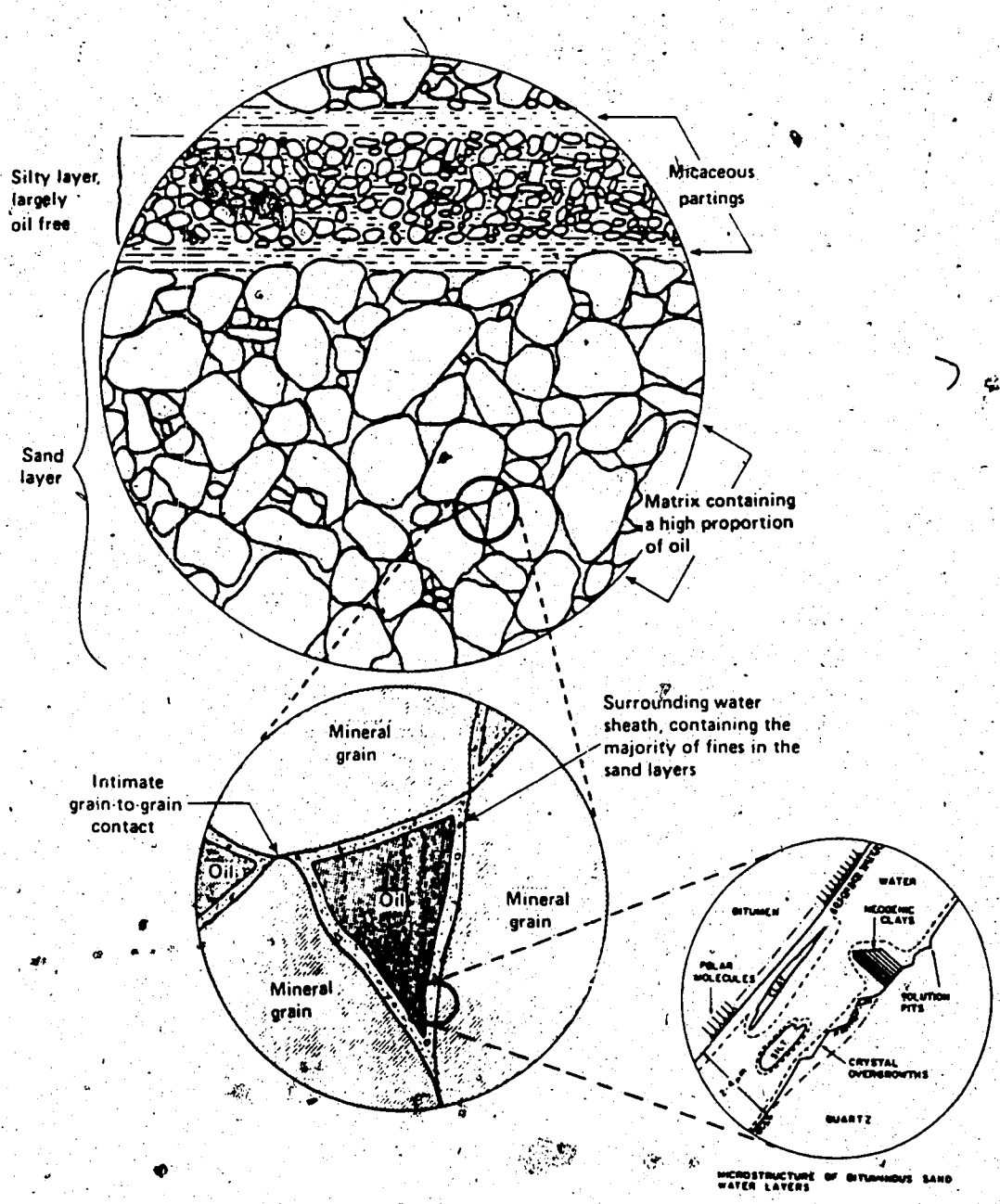

Figure 4.1 Composition of *in situ* Oil Sands - Modified from Dusseault, 1988

This program requires the physical properties, skeleton mechanical properties, i.e., the stress-strain characteristics of the sand skeleton and the pore fluid flow and gas evolution characteristics. The tests performed with the pore fluids of the collected samples enable further insight into the complex phenomenon of gas evolution.

Group B) Tests performed in order to produce a case study. These tests are conducted under controlled boundary conditions and, when compared with numerical tests performed with similar boundary conditions, allow the verification of the predictive capabilities of the numerical model proposed in CONGAS. Hollow cylinder tests were performed for this purpose.

Figure 4.2 illustrates the role of the laboratory program in this research.

The following sections describe in detail the sampling and testing program.

4.2 Sampling Program

4.2.1 Desirable Characteristics of Samples

Due to reasons explained in the preceding section, it was decided to carry out the laboratory program with the Athabasca oil sands samples.

The following characteristics were desirable in the samples:

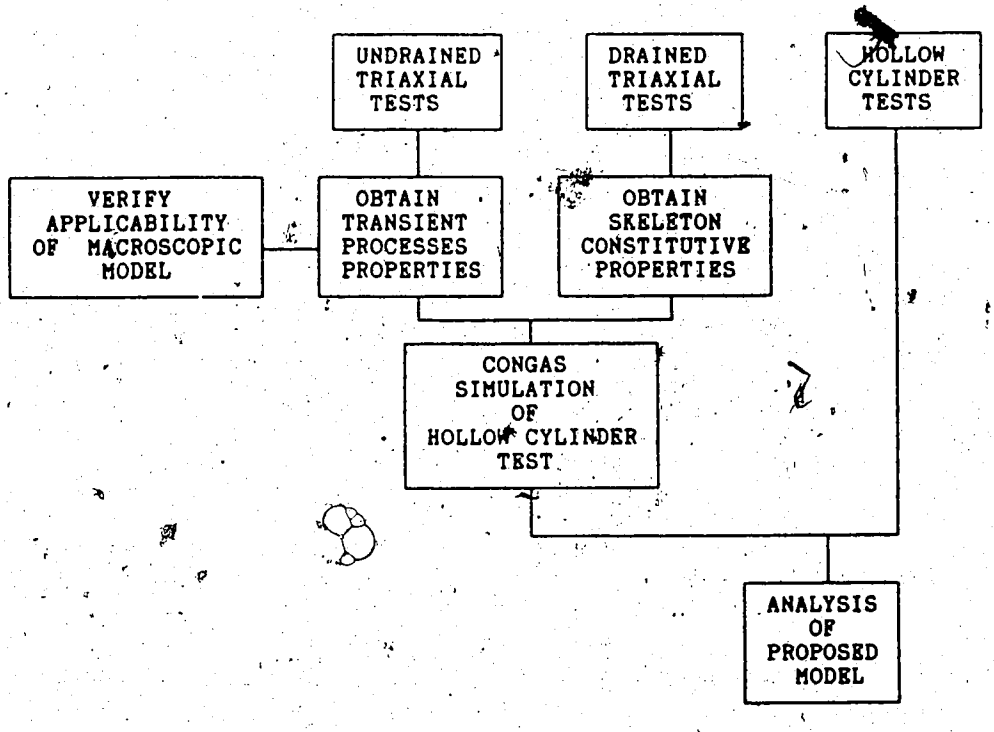

Figure 4.2 Role of the Laboratory Program

1. They should be relatively undisturbed so that the geotechnical properties obtained would be representative of the oil sands *in situ* and could be used in the future analysis of the geotechnical behaviour of oil sands.
2. They should contain a high quantity of gas in the pore fluids in order to increase the accuracy of measurements of gas volume change.
3. They should have a high bitumen content which would allow the study of the influence of a high viscosity fluid in the time-dependent gas evolution process.
4. The samples required to perform the Group B tests, i.e., the model tests, should have large dimensions in order to minimize the effects of local heterogeneity on the test results, and to allow a wider range of strains, stresses and pore pressures within the sample.

These requisites should provide a better means of verifying the predictive capabilities of CONGAS.

4.2.2 Choice of Sampling Site

Item 2, cited in the preceding section, eliminates the possibility of using samples obtained from oil sands outcrops, along river valleys, similar to the procedures used by Smith et al., 1978 and Agar, 1984, at the Saline Creek valley, Fort McMurray. Oil sands at this location have experienced a gradual removal of confining stress and reduction of pore pressures due to erosion and formation of the Saline Creek valley over a period of approximately

10,000 years (Dusseault and Domselaar, 1982:346). This slow stress relief has allowed the gases that were dissolved in the pore fluids to diffuse from the oil sands without disturbing the sand microstructure (Agar, 1984:94). In order to fulfill the requirements listed above, it was decided that the mining benches at Syncrude Canada Ltd., located north of Fort McMurray, on an extensive deposit of Athabasca oil sands, as illustrated in Figure 4.3, would be the ideal site for sampling. The geology of this area has been extensively discussed and has been the subject of several publications (Vigras, L.W., 1968, Jardine, D., 1974, Carrigy and Kramers, 1974, Stewart and MacCullum, 1978, Mossop et al., 1979). The Athabasca oil sand belongs to the McMurray Formation which overlies the Devonian limestones and, in some places, is separated from these limestones by a coarse-grained quartzose sandstone. Overlying the oil sands of the McMurray formation are the marine shales of the Clearwater Formation.

At the north-east region of the mining area at Syncrude, borehole loggings indicated the presence of bitumen and gas rich oil sands at depths between 33 to 40 meters and 46 to 53 meters, measured from the original ground surface. At this site, the top 16 metres of overburden has been removed in order to facilitate the surface mining of oil rich sands. This surface stripping of the overburden is beneficial in the sense that it would minimize the drilling depths, allowing faster access to the

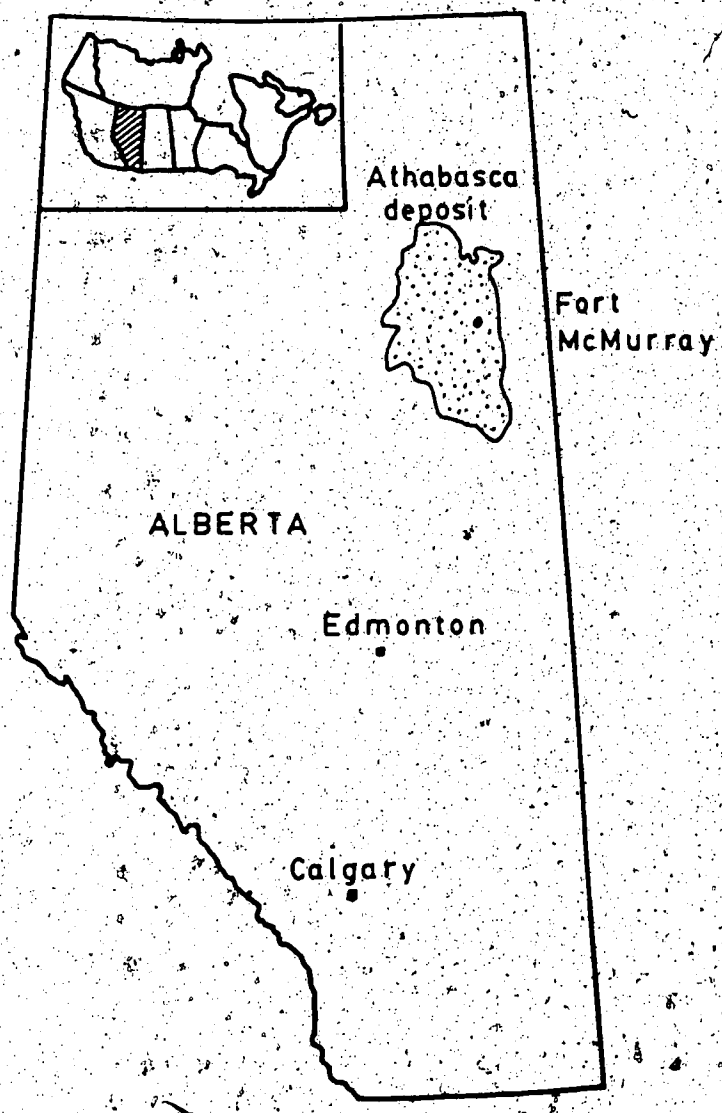

Figure 4.3 Athabasca Oil Sands Deposit

gas rich sand layer and faster retrieval of the sampler. However, on the other hand, it reduces the *in situ* vertical confinement of the deposit, resulting in volumetric expansion of the sand skeleton and the eventual formation of gas bubbles in the pores, prior to sampling.

The location and description of the sampling boreholes and the evaluation of the quality of samples is presented in Sections 4.2.4 and 4.2.5.

4.2.3 Choice of Core Barrels

During core sampling, the sample, initially at *in situ* confining stresses, is subjected to total stress relief, which results in decreases in the pore pressure. In gassy soils, the decreases in the pore pressure induce the birth and growth of gas bubbles, which tend to maintain the pore pressures high and, consequently, the effective stress low.

Due to the lack of cementation between the Athabasca oil sand grains, the decrease in effective stress induces volumetric expansion of the sample and loss of the interpenetrative structure.

A complete description of the observed disturbances of oil sands during sampling is given by Dusseault and Domselaar, 1982. The authors suggested that volumetric expansion in downhole sampling could be minimized by pressure coring or downhole freezing. The former consists of locking in downhole pressures before retrieving the sample to the surface, then freezing it to temperatures low enough

to guarantee that the sample expansion is kept to a minimum by the time sample pressure is relieved.

Downhole freezing consists of prefreezing the oil sands *in situ* before sampling. Upon a decrease in temperature of the pore fluids, one can observe a decrease in the bubble point pressure, an increase in the solubility coefficient and an increase in the tensile resistance to expansion, associated with increases of the bitumen viscosity and the freezing of the water phase.

The major advantage of the downhole freezing, when compared to the pressure coring technique, is that it provides a better means of closely maintaining the sand skeleton under *in situ*, and eventually unknown, non-uniform state of stress, commonly present in the Athabasca deposits at shallower depths. The preservation of non-homogeneous stresses by means of downhole pressures is technologically difficult.

Considering the large quantities of gas (and consequent high potential for fluid expansion during sampling) required in the samples to be tested herein, it would be desirable to use one of the two sampling techniques, briefly described above. However the unavailability of appropriate hardware, for the case of the pressure coring technique, and the elevated costs of *in situ* prefreezing resulted in the search for alternative techniques. At the Syncrude site, core samples have been retrieved with a Pitcher double core barrel, with a non-rotating inner barrel that collects the

sample. The inner barrel is spring loaded providing automatic adjustment of the distance by which the cutting edge of the barrel leads the coring bit (Plate 4.1). Cross sections of a Pitcher sampler during operation are provided by Hunt, 1984:101.

The Pitcher sampler used at Syncrude allows the retrieval of 7.3 cm (2.875 in) diameter samples up to 83 cm long. The internal diameter of the inner barrel is smaller than the internal diameter of the drill bit to prevent any additional radial expansion of the core during drilling. The relatively small length of the inner barrels prevented "jamming" of the core within the barrel that would normally occur in sampling operations with longer barrels without additional internal clearance.

Since by the time the sampling program was implemented, the Syncrude Pitcher sampler was available, it was chosen to obtain the samples required to run tests belonging to Group A.

The tests belonging to Group B, however, required larger samples which could not be obtained with the available Syncrude Pitcher sampler.

A survey of the large diameter core samplers suitable for the oil sands sampling indicated that the Christensen double core barrel was the only one available.

Similar to the Pitcher sampler, it has a non-rotating inner barrel that collects the sample. This inner barrel, however, is not spring loaded and cannot travel

longitudinally within the outer barrel. The model used in this research, the 7.75" X 5.875" Christensen Core Barrel, (Plate 4.2), had a drill bit with an internal diameter of 14.923 cm (5.875") and an inner barrel with internal diameter of 15.558 cm.

Two types of inner barrels were available for this core barrel, a solid and a split inner barrel, both allowing the retrieval of samples up to 300 cm long.

The difference in diameter between the drilling bit and the inner barrel, which allows diametral expansion of the sample, and the large dimensions and the weight of this sampler that significantly slow the sampling process, would certainly result in losses of quality of the samples. The quality of the core samples is discussed in the following sections.

4.2.4 Sampling and Storage Procedures

Figure 4.4 schematically presents the depths and lengths of the samples obtained from three boreholes. Boreholes 1 and 2 were used to retrieve the small diameter samples, with the Pitcher Sampler. Borehole 3 was used for the sampling with the larger diameter Christensen sampler.

Borehole 1 was located at coordinates 49,004.8N and 52,328.1E at an elevation of 294 m. Boreholes 2 and 3 had the same elevation and were located at approximately 4 and 20 metres, respectively, south of Borehole 1.

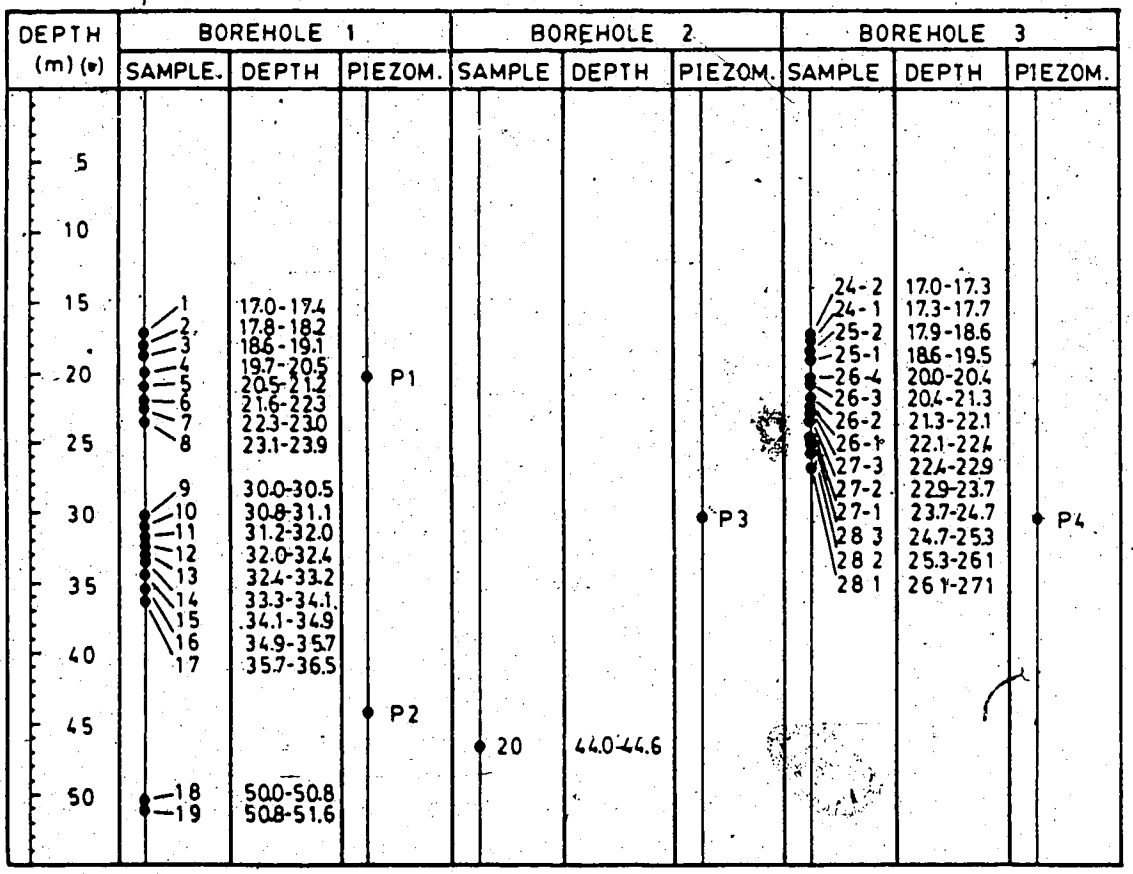

(*) Refered to the mining bench elevation (El. 294.0 m)

Figure 4.4 Sample Location

Plate 4.1 Pitcher Double Core Barrel

Plate 4.2 Christensen Core Barrel

The three boreholes were drilled by rotary drilling with circulation of drilling mud to the depths where sampling had been planned. The holes were uncased and their stability guaranteed by the drilling mud. The bits used in this phase of drilling are presented in Plates 4.3 and 4.4.

Sampling in Borehole 1 took place in two distinct intervals, defined by the depths between 17.0 and 23.9 metres and 30.0 to 36.5 metres, below the mining bench surface. These layers had been chosen based on the high grade of bitumen indicated by the geophysical logging previously performed in this area (resistivity, porosity and density logs). The analysis of the geomechanical performance of highwalls in the mining area indicated that the deeper interval consisted of bitumen rich oil sand saturated with large amounts of gas.

After removal from the Pitcher sampler, the extremities of the inner tubes were cut so that their length would be the same as the length of the sample. The inner tubes had their ends capped with a plastic cap, and were tagged, bagged and placed on dry ice in insulated wooden boxes.

Table 4.1 depicts additional details about the retrieval of samples obtained with the Pitcher sampler, i.e. at what time the sample was being retrieved, the time it reached the surface and the time at which they were wrapped and placed on dry ice. This information together with the amount of longitudinal expansion of the samples and the observed bitumen and gas content were helpful in choosing

Plate 4.3 Drill Bit - Borehole No.1 and No. 2 (Pitcher Core Barrel)

Plate 4.4 Drill Bit - Borehole No. 3 (Christensen Core Barrel)

the samples to be used in the laboratory tests.

Table 4.1 indicates that the elapsed time from removal of the sampler from the hole to final placement on dry ice ranged from 4 to 17 minutes. For the majority of the samples, this time was reduced to less than 6 minutes. The reduction of this time was considered important, in order to minimize the longitudinal expansion of the cores, which is governed by the time-dependent expansion of the gas fluid phase.

The relatively low atmospheric temperatures, also recorded in Table 4.1, helped to inhibit the expansion of the cores.

Samples 9 to 18, cored from the deeper interval, expanded from 3 to 15 cm out of the inner tube, before they were appropriately stored on dry ice. This confirmed the high gas content expected at these depths.

Sampling in Borehole 3 took place only in the top interval of the oil sand deposit, between 17.0 and 27.1 metres of depth, measured from the mining bench at an elevation of 294 metres, as indicated in Figure 4.4. It was decided not to obtain large diameter samples from the deeper interval because the large amounts of gas at those depths combined with the large internal clearance between the cutting bit and inner tube would inevitably result in excessive expansion of the sample. The time required to take the Christensen sampler apart and the appropriate storage of the samples would also contribute to the deterioration of

	SAMPLE	INTERVAL (M) (*)	LENGTH (CM)	TIME OF DAY FOR: A	B	C	AMBIENT TEMP (C)	DATE	COMMENTS
	1	17.0-17.4	36	-	14:26	14:29	0 TO -2	APRIL 1, 1986	NO OBSERVED GROWTH
	2	17.8-18.2	40	-	15:00	15:17	"	"	LOST THE LOWER END
	3	18.6-19.1	50	-	15:30	15:37	"	"	SLIGHT EXPANSION
	4	19.7-20.5	80	-	16:20	16:32	"	"	SAMPLER HIT BADLY TO REMOVE INNER LINER. BUBBLES THROUGH MUD
B	5	20.5-21.2	66	-	16:49	16.55	"	"	LOOSE AT THE TOP
O	6	21.6-22.3	71	-	17:01	17:05	"	"	TOP SIGHTLY DISTURBED
R	7	22.3-23.0	71	-	17:13	17:17	"	"	GAS BUBBLING IN THE DRILLING MUD
E	8	23.1-23.9	76	-	17:25	17:39	"	"	-
H	9	30.0-30.5	50	-	9:53	10:00	-5 TO -7	APRIL 2, 1986	EXPANSION OF 5 CM OUT OF TUBE
O	10	30.8-31.1	30	-	10:15	10:20	"	"	VERY RICH SAND
L	11	31.2-32.0	48	-	10:25	10:30	"	"	EXPANSION OF 5 CM OUT OF TUBE
E	12	32.0-32.4	40	10:42	10:48	10:52	"	"	EXPANSION OF 8 CM OUT OF TUBE
	13	32.4-33.2	81	10:58	11:02	11:06	"	"	EXPANSION OF 8 TO 10 CM OUT OF TUBE
1	14	33.3-34.1	81	11:17	11:22	11:28	"	"	EXPANSION OF 8 CM OUT OF TUBE
	15	34.1-34.9	81	11:41	11:43	11:47	"	"	EXPANSION OF 3 CM OUT OF TUBE
	16	34.9-35.7	81	-	13:09	13:14	"	"	EXPANSION OF 13 TO 15 CM OUT OF TUBE
	17	35.7-36.5	81	13:26	13:31	13:38	"	"	EXPANSION OF 8 CM OUT OF TUBE. CLAY SHALE LAYERS PRESENT
	18	50.0-50.8	81	-	-	-	"	"	CLAY SHALE SAMPLE
	19	50.8-51.6	81	-	-	-	"	"	CLAY SHALE SAMPLE
B	20	44.0-44.5	53	17:39	17:43	17:50	"	"	CLAY SHALE AT BOTTOM. EXPANDED 2 CM OUT OF TUBE. LOOSE TOP
H	21	44.8-45.6	12	17:58	18:00	-	"	"	VERY LOOSE LEAN SAND. SAMPLE THROWN AWAY
	22	45.6-45.7	8	18:17	18:23	-	"	"	CLAYEY LEAN SAND, LOOSE. SAMPLE THROWN AWAY
2	23	46.4- -	-	18:45	18:50	-	"	"	LEAN SAND WITH PEBBLES. SAMPLE THROWN AWAY.

(*) - REFERRED TO THE MINING BENCH - ELEVATION 294 M

A - TIME AT WHICH THE SAMPLE STARTED TO BE BROUGHT FROM THE BOTTOM OF THE BOREHOLE TO THE SURFACE

B - TIME AT WHICH THE SAMPLE REACHED THE SURFACE

C - TIME AT WHICH THE SAMPLE WAS CAPPED, BAGGED AND PUT OF DRY ICE

Table 4.1 Details of Sampling with the Pitcher Barrel Sampler

the samples obtained at those depths.

Sample 24 was the first large diameter sample obtained with the Christensen barrel. It was an 80 cm long core retrieved to surface in a solid inner tube. As opposed to the smaller samples that were stored on ice within the steel inner liners used in the Pitcher sampler, the bigger samples had to be removed from the liner before being wrapped and stored on dry ice. This occurred due to the high price of the inner tube used with the Christensen barrel.

The removal of Sample 24 from the inner tube indicated that the process of sliding the sample down the inner tube, into some circular shaped trays, as illustrated in Plate 4.5, was inducing excessive disturbance of the sample. For Samples 25 to 28 it was decided to use the split inner tube. For these samples, after the inner split tube was removed from the Christensen barrel, it was laid on steel supports and had its sides separated. At this stage the samples were exposed for visual inspection, as illustrated in Plate 4.6. The following step consisted of the placement of the 91.4 cm long semi-circular shaped trays (which had been previously chilled on dry ice and covered with a plastic sheet) on top of the exposed upper side of the sample. At this stage the bottom half of the split liner, which, up to that moment, was holding the sample, and the semi-circular trays, were rotated 180° along the axis of the sample, in such a way that the samples were now being supported by the trays. The number of trays required to

Plate 4.5 Removal of Sample 24 from Solid Inner Tube to Storage Tray

Plate 4.6 Sample 28 on the Split Inner Tube

support one sample would depend on the length of the sample and on the number of good continuous and homogeneous portions of the sample that would be adequate for laboratory testing.

Both the tray and the core were wrapped with a minimum of two layers of thick plastic bags and metal tape and stored on dry ice.

Samples 24 and 25 were removed from the steel trays and slid into PVC tubing, approximately one hour after they had been put on dry ice. This procedure proved to be time consuming and inadequate when performed at the local atmospheric temperatures. Samples 26, 27 and 28 were, instead, together with the steel trays, kept wrapped in plastic bags on dry ice until all the samples were permanently stored at the University of Alberta.

Table 4.2 depicts the details of sampling with the Christensen barrel. It shows that, when the split inner tube was used, the elapsed time between the removal of the sampler from the borehole and the placement of the samples on dry ice varied from 24 to 38 minutes. During this period of time the samples were exposed to a condition of no lateral or longitudinal confinement, which, associated with the slightly higher atmospheric temperatures, might result in lower quality when compared to the samples obtained with the Pitcher sampler.

At the end of the sampling program, the samples were transported to the University of Alberta and transferred

BOREHOLE	SAMPLE SECTION	INTERVAL (m) (a)	LENGTH (cm)	TIME OF DAY FOR: A	B	C	AMBIENT TEMP (C)	DATE	COMMENTS
3	24-2	17.0-17.3	27.5	-	11:00	12:00	0	APRIL 3, 1986	SPLIT INNER TUBE WAS USED. EXCESSIVE TIME REQUIRED TO TAKE SAMPLER APART. NO EXPANSION OBSERVED.
	24-1	17.3-17.7	38.5						
	25-2	17.9-18.6	71.0	-	12:12	12:59	+5	APRIL 4, 1986	SPLIT INNER TUBE WAS USED. 2 TO 5 CM OF LONGITUDINAL EXPANSION. SAMPLE DISTURBED WHEN PUT INTO PVC LINER.
	25-1	18.6-19.5	91.0						
	26-4	20.0-20.4	40.0	-	13:55	14:53	"	"	SPLIT INNER TUBE WAS USED. TOP SECTION (4) CAME BADLY SHEARED.
	26-3	20.4-21.3	90.0						
	26-2	21.3-22.1	78.0						
	26-1	22.1-22.4	32.0						
	27-3	22.4-22.9	46.0	-	15:42	16:12	"	"	SPLIT INNER TUBE WAS USED.
	27-2	22.9-23.7	80.0						
	27-1	23.7-24.7	90.0						
	28-3	24.7-25.3	62.0	-	17:09	17:35	"	"	SPLIT INNER TUBE WAS USED. TOP SECTION (3) PRESENTED SEVERAL CRACKS ALONG BEDDING
	28-2	25.3-26.1	79.0						
	28-1	26.1-27.1	95.0						

(a) - REFERRED TO THE MINING BENCH - ELEVATION 294 M

A - TIME AT WHICH THE SAMPLE STARTED TO BE BROUGHT FROM THE BOTTOM OF THE BOREHOLE TO THE SURFACE

B - TIME AT WHICH THE SAMPLE REACHED THE SURFACE

C - TIME AT WHICH THE SAMPLE WAS BAGGED AND PUT OF DRY ICE

Table 4.2 Details of Sampling with the Christensen Barrel

from the insulated wooden boxes, filled with dry ice, to a freezer at approximately -20°C, where they were kept before being removed for trimming and testing.

Samples 26, 27 and 28 were transferred from the steel trays to PVC tubes, before being stored in the freezer.

4.2.5 Piezometers

Four pneumatic piezometers (Slope Indicator Company) were installed in the three boreholes, after sampling was completed, at the depths indicated in Figure 4.4. The piezometer tips were encased in a slotted PVC casing. Their installation consisted of the the following activities:.

1. Pour bentonite pellets in the hole in order to produce a bottom plug of at least 7 m long.
2. Pour clean sand, up to 1.5 metres above the top of the bentonite plug.
3. Lower the piezometer down the hole.
4. Pour an additional 3.0 m of sand.
5. Pour additional 7.0 m of bentonite pellets to form the top plug.

Piezometer P3, installed at 30 m depth in Borehole 2 malfunctioned after installation and was abandoned.

The piezometer readings taken on May 27, 1986, approximately 54 days after installation are illustrated on Figure 4.5. The data indicates that the local mining activities significantly altered the initially hydrostatic pore pressure profile. The pore pressures closer to the

mining bench elevation have dropped probably due to the generalized drawdown that is taking place in the region due to the proximity of the highwalls.

The sampling of the deeper oil sands indicated the presence of a very clean, coarse-grained sand overlying a clay shale deposit. This clean sand might be working as a basal drain for the oil sand deposit and might be responsible for low pore pressures measured in P4. A more conclusive analysis of the pore pressure distribution within the oil sand deposit would require a greater number of piezometers, which would preferably use a mechanical packer system (Lalonde, 1983:20) as a means of isolating the chamber that contains the piezometer tip from the rest of the borehole. The efficiency of the use of bentonite mud as a sealing plug for piezometers is questionable when applied to gassy deposits. During the pouring of mud, the flow of gas bubbles from the gas rich layer to the surface might open small channels in the bentonite plug. This could connect the piezometer chamber to the rest of the borehole, which would result in piezometer readings equal to the hydrostatic pressure determined by the height of bentonite mud and water above the piezometer tip.

The pore pressure readings should provide valuable information on the bubble pressure, to be expected from gas evolution laboratory tests.

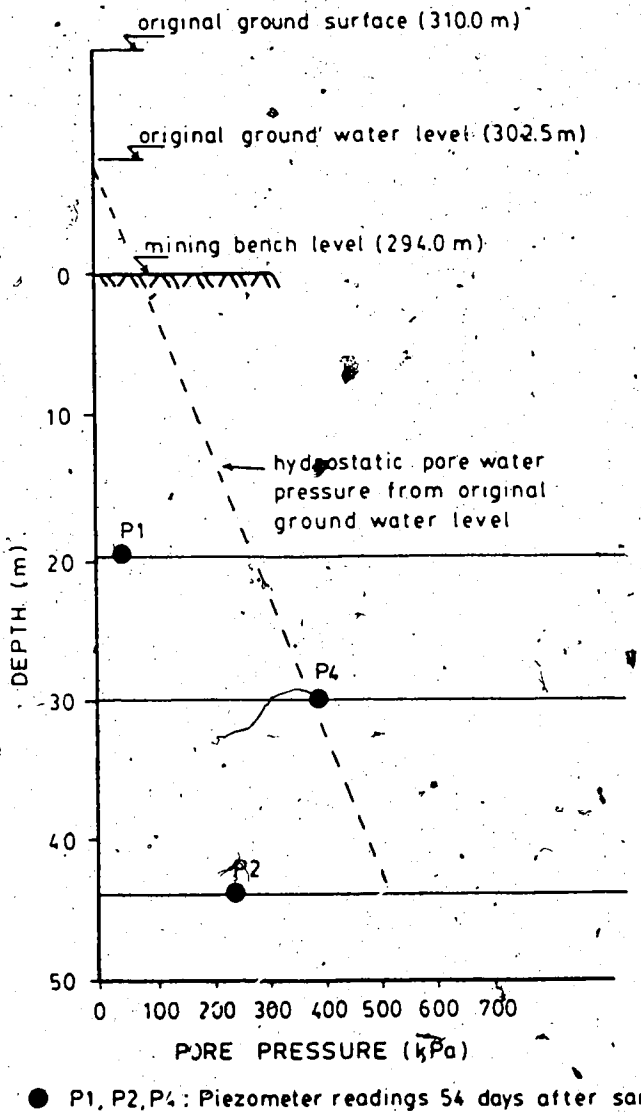

Figure 4.5 Piezometer Readings

4.2.6 Evaluation of the Quality of Samples

The evaluation of the quality of samples is performed in order to identify a common denominator among the test results performed with various cores, obtained with different sampling techniques.

Dusseault and Domselaar, 1982:338, recommended the use of the Index of Disturbance, (I_D) in order to quantify the core damage. It is defined as:

$$I_D = \frac{n_s - n_i}{n_i} \times 100 \qquad [4.1]$$

where,

n_s = porosity of the sample obtained in the laboratory

n_i = *in situ* porosity of the deposit, obtained with geophysical methods.

Dusseault, 1977:Appendix 9, and Dusseault and Domselaar, 1982:238, recommended that the evaluation of the *in situ* measurement of the *in situ* porosity be made from the geophysical measurement of the *in situ* bulk density. Porosity values may be obtained from bulk densities if the soil constituents (minerals and pore fluids), their amounts and specific gravities are known.

The authors stated that the use of geophysical methods for the direct measurement of the *in situ* porosity (neutron porosity) results in porosities less accurate than those obtained from the direct measurement on the *in situ* bulk densities.

Figure 4.6 presents the gamma ray and the *in situ* density logs obtained from a borehole located adjacent to Borehole 1. The gamma ray log is a measure of natural radioactivity. According to Dusseault, 1977:440, medium to coarse-grained sands in the Athabasca Oil Sands are generally extremely quartzose (greater than 95% quartz) and display low natural radioactivities. The natural radioactivities increase with the increase in quantities of clay minerals. He stated that argillaceous strata have radioactive values above 60 API (American Petroleum Institute, standard radioactivity units).

In the bulk density logs densities "are determined by the measurement of gamma ray intensity at a fixed distance from a strong, constant, activating gamma ray source. Radiation is converted to bulk density by direct comparison to a calibration of materials of known bulk density, and all raw data are automatically compensated within the recording apparatus" (Dusseault, 1977:440).

The geophysical logs of Figure 4.6 were performed prior to the removal of the top 16 metres of overburden. This means that, at the time the sampling program was implemented, the *in situ* bulk densities were most likely lower, and the *in situ* porosities were most likely higher than the original *in situ* ones. A brief evaluation of the volumetric expansion that took place due to the removal of the overburden, at the depths where samples were taken, indicated that the volumetric expansion was less than 0.1%

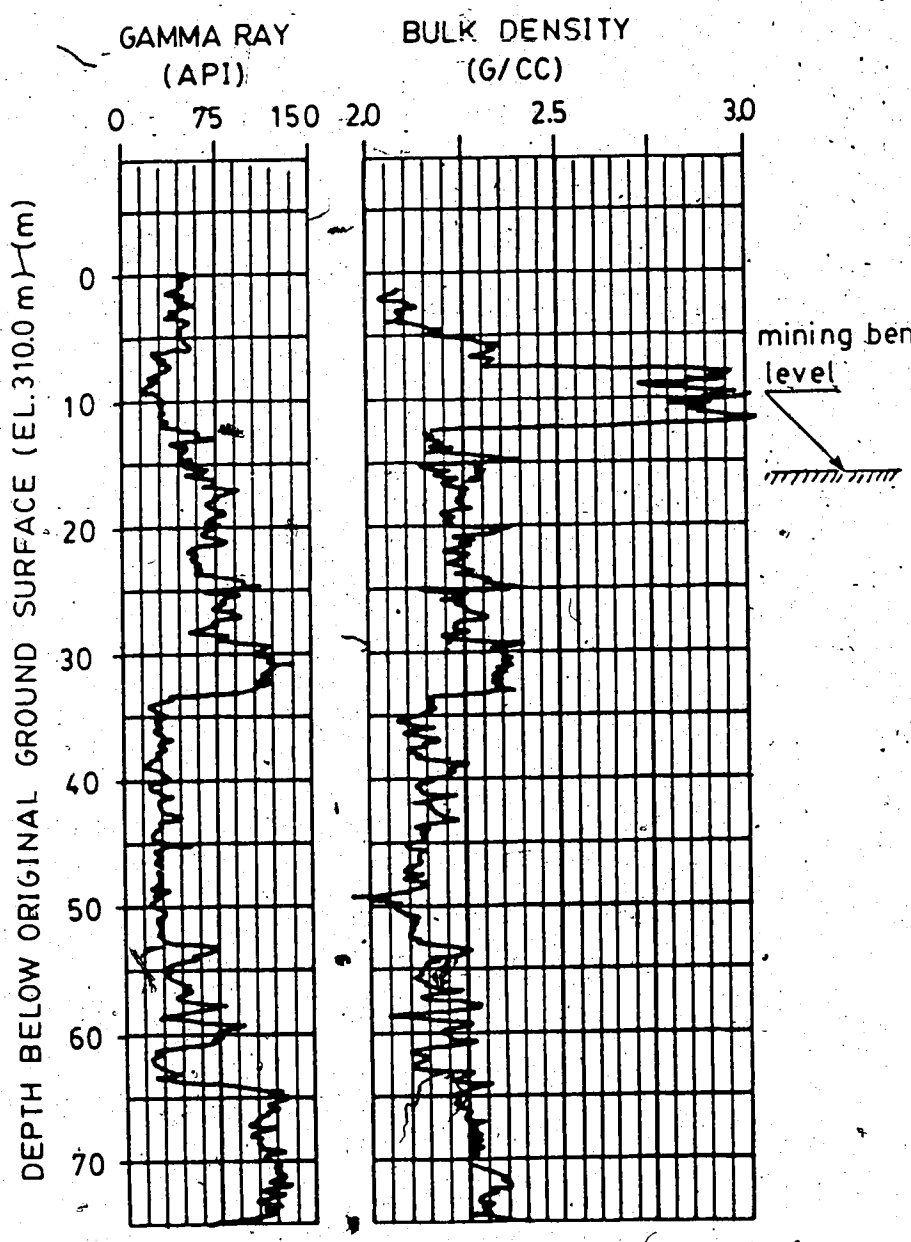

Figure 4.6 Geophysical Log of Sampling Area

which resulted in variations of less than 0.1% in the original *in situ* porosities. This means that the Index of Disturbance can be approximately evaluated directly with the aid of the geophysics logs, presented in Figure 4.6, without considering the removal of the overburden.

Table 4.3 presents the average Index of Disturbance for the samples tested in the laboratory. The *in situ* porosities were obtained from the bulk densities according to the simplified equation.

$$n = 100 \frac{(2.65 - D)}{1.64} \qquad [4.2]$$

as suggested by Dusseault and Domselaar, 1982:338. It estimates oil sands porosities accurate to within one porosity unit (n ±1%).

The laboratory porosities refer to the frozen samples, before sampling. Considering that, during freezing, bitumen rich oil sands, with water saturation less than 10%, undergo less than 0.2% of volumetric expansion, (Dusseault, 1980;91), it is reasonable to assume that the porosities of the frozen samples are representative of their state immediately after sampling.

According to the disturbance classification proposed by Dusseault and Domselaar, 1982:340, samples with indices of disturbance between 20% and 40% are considered highly disturbed. This is the case for most of the samples listed

SAMPLE	INTERVAL (M) (****)	SAMPLER	IN SITU		LAB POROSITY (%) (***)	Id (%)
			BULK DENSITY (G/CC) (*)	POROSITY (%) (**)		
3	18.6-19.1	P	2.12	32.3	36.2	12.1
4	19.7-20.5	P	2.12	32.3	37.9	17.3
5	20.5-21.2	P	2.13	31.7	39.9	25.9
6	21.6-22.3	P	2.13	31.7	41.0	29.3
7	22.3-23.0	P	2.20	27.4	40.3	47.1
8	23.1-23.9	P	2.18	28.7	40.3	40.4
9	30.0-30.5	P	2.12	32.3	42.1	30.3
11	31.2-32.0	P	2.12	32.3	46.1	42.7
14	33.3-34.1	P	2.05	36.6	38.9	6.3
26-1	22.1-22.4	C	2.16	29.9	40.0	33.8
27-2	22.9-23.7	C	2.19	28.0	38.9	38.9
28-2	25.3-26.1	C	2.15	30.5	41.1	35.1

P - PITCHER SAMPLER
C - CHRISTENSEN SAMPLER
(*) - DATA FROM GEOPHYSICAL LOG
(**) - CALCULATED FROM BULK DENSITY ACCORDING TO DUSSEAULT AND DOMSELAAR, 1982:338
(***) - FROZEN SAMPLE, AFTER TRIMMING
(****) - DEPTHS MEASURED FROM MINING BENCH LEVEL : 294 M

Table 4.3 Evaluation of the Quality of Samples

in Table 4.3. The low quality of the samples, as far as porosity is concerned, indicates that some of the physical properties and the stress-strain relationship obtained from the laboratory tests are not representative of the *in situ* oil sands. However, the large volumetric expansions that resulted in the low quality of the samples, might indicate that most of the *in situ* originally dissolved gases might have been kept within the pores.

The Index of Disturbance of the samples retrieved by the Pitcher sampler and by the Christensen barrel are comparable, allowing one to conclude that the geotechnical properties of both types of samples are similar. This similarity was a necessary condition for the appropriate comparison of the results from the numerical simulation of the hollow cylinder test with the actual test performed in Chapter 5. The former requires geotechnical parameters as input data, which in this research were obtained from tests performed with the Pitcher Sampler samples whereas the latter requires test data obtained from the hollow cylinder tests, performed with the Christensen barrel samples.

4.3 Test Program

4.3.1 Classification of the Tests Performed

The classification of the tests performed in this research was briefly presented in Section 4.1, the introduction of this chapter. This classification divides

the tests into two distinct groups: Group A and Group B.

Tests belonging to Group A are those performed in order to provide the basic, fundamental geotechnical information about the oil sand. Their results are used as input data for the finite element program CONGAS. Tests belonging to Group B are those performed in order to produce a case study. In Chapter 5, the results of these tests are compared with the results of similar tests performed numerically with CONGAS. This comparison enables the evaluation of the numerical models and techniques employed in CONGAS.

The tests belonging to Group A were designed in order to yield:

Physical properties;

Skeleton mechanical response;

Gas evolution response.

The tests belonging to Group B were hollow cylinder tests. These tests allow the accurate control of all boundary conditions involved in the numerical simulation and enable the simulation of conditions commonly encountered in underground excavations.

The following sections describe in detail the laboratory tests performed in this research program.

4.3.2 Physical Properties Tests (Group A)

4.3.2.1 Bitumen and Water Content

The quantities of bitumen and water occupying the pore space in oil sand samples were determined using soxhlet refluxing. The laboratory procedure associated with this system was described in detail by Agar, 1984:142 and will not be repeated here.

The system separates the three phases of the oil sand, i.e., sand skeleton, bitumen and water, and allow the independent measurement of the volume and weight of each phase.

Table 4.4 presents the weight percentages of bitumen, water and sand, obtained from the end trimmings of the samples tested.

4.3.2.2 Density, Porosity and Fluid Saturation

The bulk density of all samples was determined after sample preparation in the cold room. This was possible with the accurate weighing and measurement of the volume of the samples which was made through multiple direct measurements of the height and diameter with a caliper.

The knowledge of the bulk density, the mass of the bitumen, water and mineral grain contents, and the volume of the frozen sample allows the evaluation of its pore fluids saturation and porosity as follows:

$$V_{wat} = \frac{m_{wat}}{G_{wat}} \qquad [4.3]$$

$$V_{bit} = \frac{m_{bit}}{G_{bit}} \quad [4.4]$$

$$V_{sand} = \frac{m_{sand}}{G_{sand}} \quad [4.5]$$

$$V_{fg} = V_{tot} - V_{wat} - V_{bit} - V_{sand} \quad [4.6]$$

$$n = \frac{(V_{fg} + V_{wat} + V_{bit})}{V_{TOT}} \quad [4.7]$$

$$S_{wat} = \frac{V_{wat}}{V_{fg} + V_{wat} + V_{bit}} \quad [4.8]$$

$$S_{bit} = \frac{V_{bit}}{V_{fg} + V_{wat} + V_{bit}} \quad [4.9]$$

where

m_{wat}, m_{bit}, m_{sand} = mass of water, bitumen and sand, respectively, obtained from extraction tests.

G_{wat}, G_{bit}, G_{sand}= specific gravity of water, bitumen and mineral grains.

V_{wat}, V_{bit}, V_{sand}, V_{fg}= volume of the water, bitumen and sand grains and the free gas phases.

n = total porosity of the frozen sample

S_{wat}, S_{bit} = water and bitumen saturation.

4.3.2.3 Grain Size Distribution

Mechanical sieve analyses were performed according to standard ASTM D422-72, for the materials portion retained in the #325 sieve.

The grain size distribution was determined with the grain minerals after bitumen and water had been extracted by soxhlet refluxing with toluene, as described in Section 4.3.2.1. A small portion of the fine particles was absorbed by the "thimble" (filter bag) during the process.

The ends of the samples that resulted from trimming the sample in the cold room were used both for the determination of materials content and grain size distribution.

Table 4.4 summarizes the results from the grain size analyses. The grain size distribution curves are presented in Appendix C.

4.3.2.4 Gas Content

The chemical composition of gases in Athabasca bitumen was the subject of a detailed study published by Strausz et al., 1977. The authors conducted experiments at different temperatures that consisted of the collection and subsequent analysis of the gases that evolved from oil sand specimens. The degassing of the specimens was carried out with a high vacuum apparatus that lowered the pressure in a Pyrex vessel, containing the oil sand, to 0.1 kPa. The volatile gases that evolved at the equilibrium temperature were analysed by gas chromatography.

At 5°C, approximately the formation temperature, nitrogen (N_2,16600), oxygen (O_2,11000), carbon dioxide (CO_2,5860), neopentane (C_5H_{12},134) and methane (CH_4,114) were the major components of the evolved gas phase. The numbers between parenthesis are the number of moles times

SAMPLE	TEST	BULK	WEIGHT %			SATURAT.		VOID	GRAIN SIZE-DIS.		
		DENS G/CC	BIT %	WAT %	SAND %	SBIT %	SWAT %	RATIO	D10 MM	D60 MM	CU
8-4	J1-TRIAX	1.888	14.7	3.6	81.7	64.5	16.3	0.718	0.102	0.209	2.0
5-3	..	1.950	14.5	1.8	83.7	71.5	9.1	0.623	0.092	0.194	2.1
8-1	..	1.946	12.4	3.5	84.1	61.3	17.8	0.619	0.090	0.230	2.6
5-2	..	1.918	13.3	2.8	83.9	63.1	13.9	0.647	0.115	0.240	2.1
5-4	..	1.901	13.5	4.0	82.5	61.0	18.6	0.690	0.104	0.209	2.0
4-2	STD-TRIA	1.949	13.3	2.3	84.4	66.4	11.8	0.611	0.837	0.208	2.5
7-3	..	1.934	13.9	4.1	82.0	65.0	19.7	0.671	0.080	0.175	2.1
6-2	..	1.963	14.2	2.6	83.2	70.6	13 3	0.622	0.108	0.201	1.9
6-1	..	1.883	15.3	4.6	80.1	64.9	20.1	0.757	0.107	0.220	2.1
7-5	..	1.915	14.4	3.4	82.2	66.0	16.1	0.683	0.091	0.197	2.2
5-1	ISO-UNL. STD-TRIA	1.915	13.9	4.5	81.6	64.4	21.5	0.680	0.091	0.200	2.2
7-4	..	1.937	15.6	2.5	81.9	73.1	12.1	0.671	0.092	0.198	2.2
8-2B	ISO-UNL.	1.824	7.1	8.0	84.9	30.3	35.2	0.710	--	0.180	--
8-3	..	1.924	14.0	2.8	83.2	66.0	13.6	0.656	0.080	0.200	2.5
11-5	UND-OED.	1.724	14.6	4.6	80.8	52.4	17.0	0.885	--	--	--
11-2	MERC-TRI	1.786	15.8	1.9	82.3	61.6	7.6	0.803	--	--	--
11-3	..	1.733	14.6	4.6	80.8	52.2	17.0	0.884	0.149	0.205	1.4
3-1	..	1.988	12.4	2.5	85.1	66.2	13.7	0.566	--	--	--
6-5	..	1.920	11.3	7.9	80.8	50.8	36.6	0.709	0.127	0.248	2.0
9-2	..	1.808	12.8	2.4	84.8	53.3	10.3	0.728	--	--	--
14-3	..	1.936	14.1	2.2	83.7	68.2	11.0	0.637	--	--	--
4-3	..	1.984	--	--	--	--	--	--	0.132	0.207	1.7
26-1	HOL.CYL.	1.908	14.0	2.7	83.3	64.8	12.9	0.667	0.110	0.180	1.6
27-2B	..	1.962	15.6	1.3	83.1	76.3	6.6	0.633	0.080	0.180	2.3
27-2C	..	1.942	15.6	1.3	83.1	75.3	6.5	0.642	--	--	--
28-2T	..	1.895	16.2	2.1	81.7	71.7	9.8	0.711	--	--	--
28-2C	..	1.929	16.2	2.1	81.7	74.8	10.0	0.682	--	--	--

NOTE : ALL DATA IS RELATED TO THE TEST SAMPLE FROZEN, BEFORE TEST

Table 4.4 Physical Properties

10^{-8} of that specific component collected per kilogram of oil sand. They indicate that the air constituents, N_2, O_2 and CO_2 were responsible for more than 99% of the total number of gas molecules present in the free state. One might suggest that these components occurred basically due to air contamination during the preparation of the specimens. However, the percentage volumes of N_2, O_2 and CO_2 in air are 79.04, 20.93 and 0.03 (McArdle et al., 1981:169) respectively, as opposed to the 49.61, 32.88 and 17.51 percentages obtained by the authors.

Tests at 70°C, 95°C, 130°C and 210°C have also been performed by Strausz et al., 1977. The results of the chemical composition of gases at these temperatures are beyond the interest of this thesis.

It was the interest of the research presented herein to identify the gases that evolve from oil sand specimens at 24°C, the temperature at which the gas evolution tests, described in Section 4.3.4, were performed. Four oil sands specimens had their gases collected and analysed at 24°C, in order to fulfill this interest.

The oedometer cell, described in Section 4.3.4.2, was used to degassify the oil sand specimen.

Two procedures were followed:

Procedure A

1. The samples were placed in the oedometer cell after being stored in an air tight container which was kept on dry ice for a period of at least 24 hours. The container

prevents contamination of the samples with CO_2 from the dry ice.

2. The frozen sample was placed in the oedometer cell. The top piston was positioned against the top of the frozen sample, as illustrated in Figure 4.7.
3. A glass container was connected to valve B on the piston of the cell and a vacuum pump was connected to the bottom valve A of the cell as indicated in Figure 4.7.
4. Valve C was closed and all the others remained opened.
5. The air pressure inside the cell was then dropped from atmospheric to approximately 20 kPa with the help of the vacuum pump. The purpose of this step was to minimize the amount of air existing in the system. This step took approximately 3 minutes before valve A was closed.
6. The system was kept under low pressure for approximately 24 hours to allow the oil sand samples to thaw and gas to evolve from the fluid phase.
7. The vacuum pump was connected to valve D and with valve C still closed, the pressure in the gas bottle was lowered from atmosphere to approximately 20 kPa.
8. With the sample now fully thawed, valve D was closed and valve C opened. This procedure allowed the gas that evolved in the oedometer cell from the oil sand sample to flow into the gas bottle.
9. Valve D was closed and the gas sample was ready to be analysed.

<u>Procedure B</u>

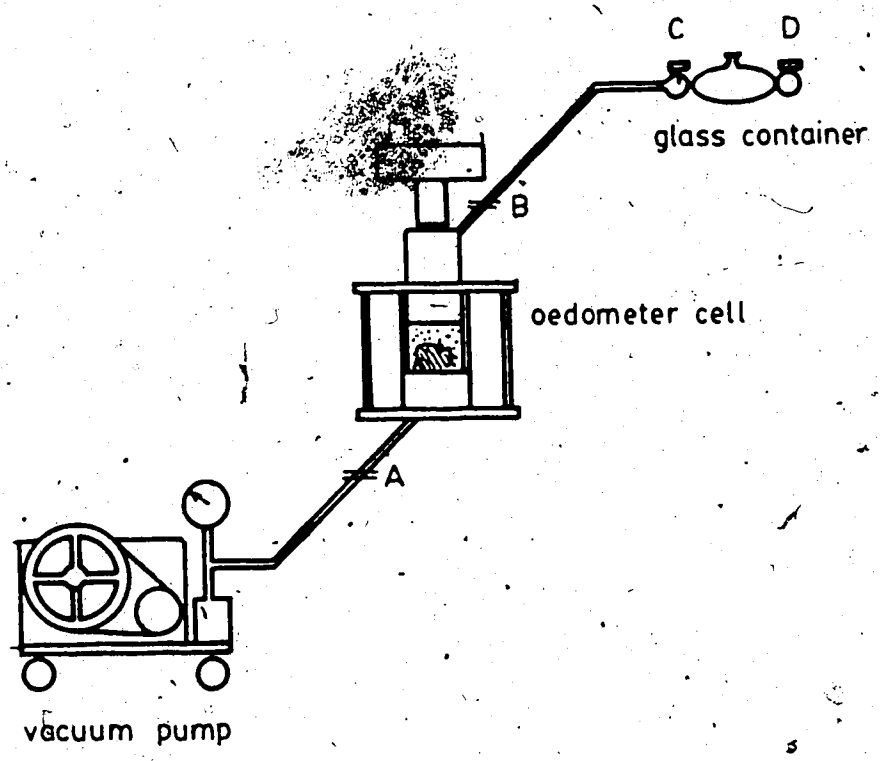

Figure 4.7 Degassification of Oil Sand Samples - Procedure A

Step 1 and 2 are identical to the first two steps in Procedure A.

3. A gas container was connected to valve B in the piston of the cell, and a bottle of helium was connected to valve A at the bottom of the cell, as indicated in Figure 4.8.
4. Valve D was connected to a plastic tube which had one end immersed in water.
5. With all valves opened the system was flushed with helium, that bubbled in the water cup for approximately 2 minutes, in order to allow all the air in the system to be substituted by helium. This gas was chosen because it was the "carrier" gas in the HP-5830A-gas chromatograph used for the gas analysis discussed later in this section.
6. Valves A and D were closed and the oil sand sample was allowed to thaw for approximately 24 hours.
7. Valve A was opened and a pressure of approximately 70 kPa above atmospheric was applied to the system.
8. Valve C was closed and the gas sample was ready to be analysed.

The gases collected from the oil sand samples, by following one of the procedures described above, were removed from the gas bottle with a syringe and inserted into a Hewlett Packard HP-5830A gas chromatograph. The gas was analysed and the data was output on a Hewlett Packard HP-18850A-GC Terminal. The data obtained from

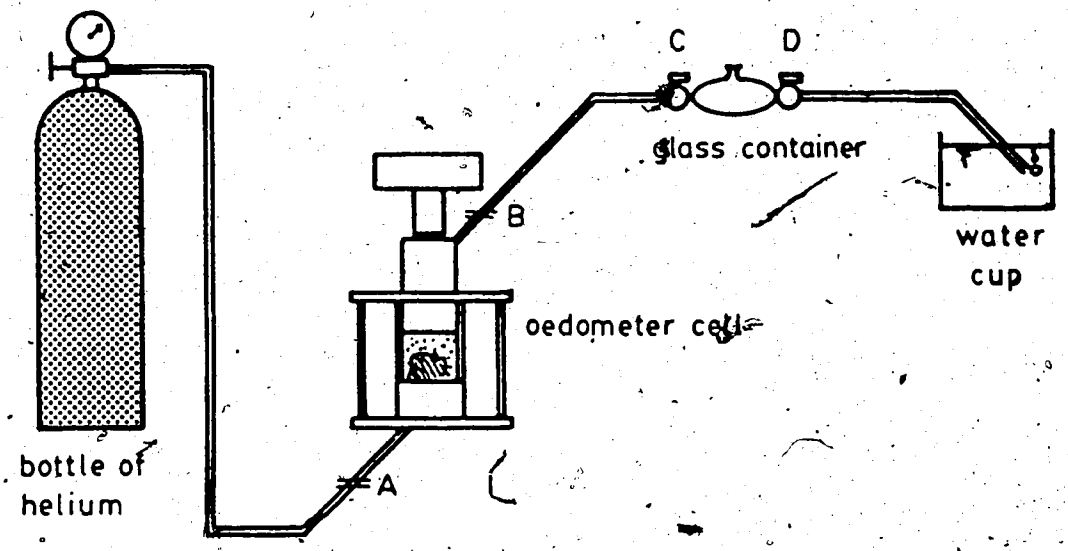

Figure 4.8 Degassification of the Oil Sand Samples - Procedure B

these tests are summarized in Table 4.5.

4.3.2.5 Analysis of the Physical Properties Tests

The tests performed in order to obtain the physical properties of the oil sand samples used in this research indicate that samples tested were extremely uniform as far as bitumen and water content are concerned. In most cases, the bitumen and water content were 14 and 4%, respectively. The bitumen and water saturations were 65 and 16%, respectively.

The void ratios of the frozen trimmed samples varied between 0.57 and 0.89, with the majority of the samples having a void ratio of 0.65.

The sieve analyses showed that all the samples have a uniform sand structure, with a uniformity coefficient, CU, ranging from 1.9 to 2.5.

The gas chromatography analysis, summarized in Table 4.5 indicates that, irrespective of the procedure followed to degassify the soil specimens, air is the major constituent of the gas phase, followed by CH_4 and CO_2.

Air might be present in large amounts in the collected gas samples due to one or a combination of the following possibilities.

1. The oedometer cell might not have been properly deaired, before the oil sand samples thawed.
2. The gas samples might have been contaminated by air, when removed with a syringe from the gas bottle to the gas analyser.

SAMPLE	TEST PROCEDURE	GAS TYPE VOLUME (%)		
		N_2 /O_2	CH_4	CO_2
4-3	A	91.3	3.7	5.0
3-1	A	91.8	5.5	2.7
26-1	B	97.3	2.1	0.5
27-2	B	*	*	*
28-2C	B	93.9	5.1	1.0

(*) - EXCESSIVE AIR CONTAMINATION PRIOR TO GAS ANALYSIS

Table 4.5 Gas Analysis

3. Air might have penetrated the sample during sampling and storing.

The large amounts of air detected in the gas chromatography analyses are comparable to the ones obtained by Strausz et al., 1977.

It was initially thought that the flushing of the system with helium would minimize the presence of air in the cell prior to gas evolution from the thawing sample. The results, however, indicate that, irrespective of the procedure followed to deair the system, the amounts of air measured were approximately the same. It is believed that items 2 and 3 are responsible for most of the air present. The freezing of the samples immediately after sampling in the field might have significantly increased the solubility coefficient of the bitumen. This may have caused some additional quantities of air to be absorbed by the bitumen. To the author's knowledge there is no data published on the solubility coefficient of bitumen at extremely low temperatures.

Table 4.5 also indicates that, as opposed to Strausz et al., 1977, who measured neopentane, C_5H_{12}, as the gas present in larger amounts in Athabasca bitumen, the gas tests performed here did not detect the presence of this gas. The small number of tests, and the variability of the results obtained do not allow a more conclusive analysis of the gas test results.

4.3.3 Skeleton Mechanical Response Tests (Group A)

4.3.3.1 General

Drained triaxial tests were performed in order to obtain the skeleton constitutive behavior of the samples retrieved with the Pitcher sampler. Two types of tests had originally been planned.

- drained, isotropic triaxial tests,
- drained, "J1" triaxial tests.

These tests would independently allow the evaluation of the bulk modulus (B) and the shear modulus (G), respectively. These constitutive parameters are required for the numerical simulation of the hollow cylinder tests, described later in this chapter. However, problems encountered in maintaining the octahedral normal stress constant throughout the "J1" tests resulted in the performance of some standard triaxial tests, where the minor effective stress (σ'_3) is kept constant during the test.

The stress levels chosen for the performance of the drained triaxial tests are compatible with the stress levels encountered in the hollow cylinder tests.

The following subsections describe the system used and the procedure followed to perform the triaxial tests, the test results and their interpretation.

4.3.3.2 Triaxial Testing System

The triaxial testing system consisted of:

- triaxial cell

- back and confining pressure system
- axial loading system
- monitoring devices.

Plate 4.7 and Figure 4.9 illustrate this system.

Triaxial Cell

Figures E1 to E4 of Appendix E show in detail the triaxial cell used in this research. The maximum allowable confining pressure in this cell is 6.2 MPa.

The aluminum sample pedestal rests on a stainless steel base platen and allows the testing of samples 5.72 cm in diameter.

Back Pressure and Confining Pressure System

The back pressure was applied to the sample through a line that was connected to the base platen. The system used did not allow the control of the pore pressures at the top of the sample.

The schematic of the pore pressure system for the triaxial tests is presented in Figure 4.9. Through this system, it was possible to use two different sources of pressures: compressed air and nitrogen sources.

The compressed air system was connected to the central compressor that supplies air to all the laboratories of the Civil Engineering building. It allows the accurate application of pressures up to approximately 1.0 MPa. The source line coming from the compressor was connected to a pressure regulator (Nullmatic Pressure Regulator - More Instruments Co. Ltd.) that controlled the pressure in the

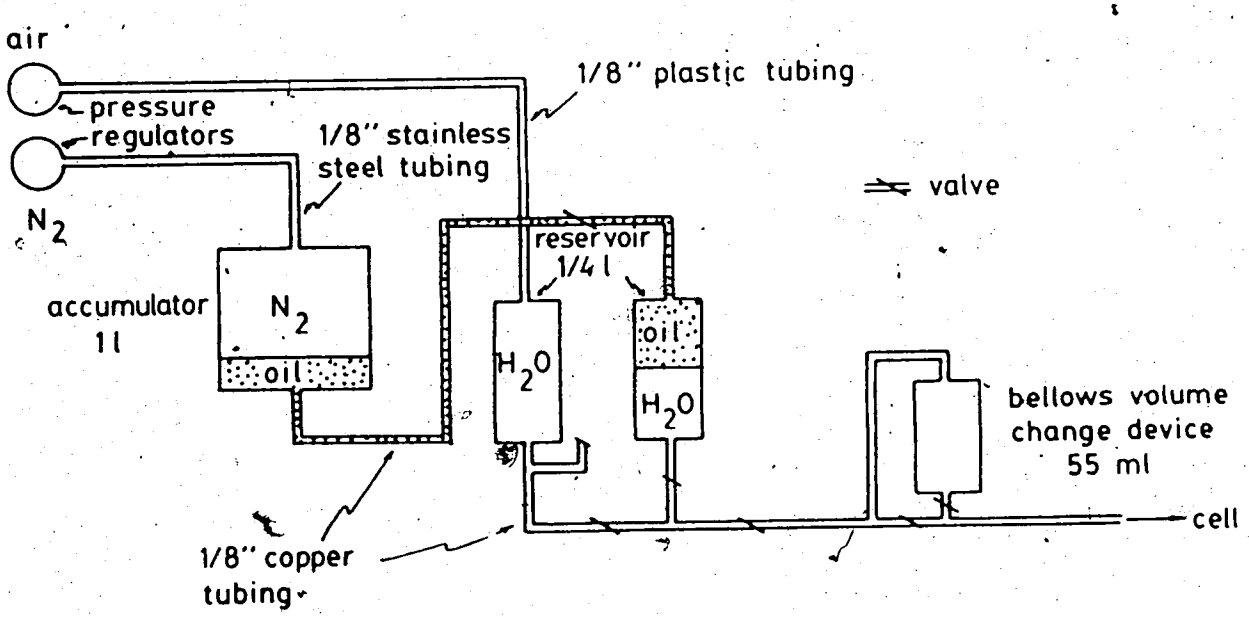

Figure 4.9 Pressure System Schematic for Triaxial Tests

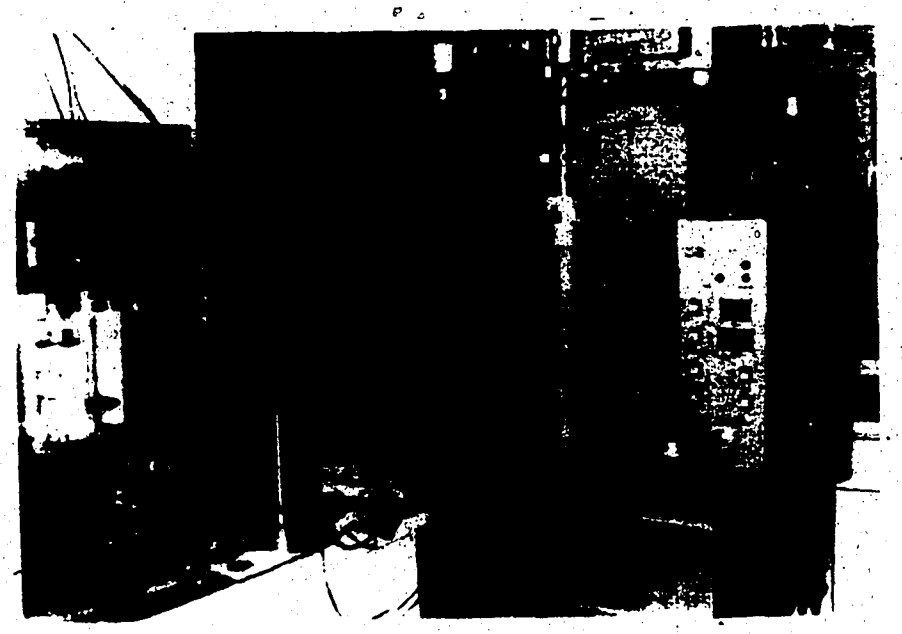

Plate 4.7 Triaxial Testing System

test system. Three millimetre plastic tubing connected the pressure regulator to a 250 cc water reservoir. A film of silicon oil with thickness of approximately 3 cm, was placed between the air and the water in order to slow down and minimize the contamination of the water with large amounts of air. This reservoir supplied the water for saturation of the sample.

A nitrogen pressure source was available for the application of back pressures higher than 1.0 MPa. The nitrogen source was a cylinder initially charged to 18.6 MPa. A Circle Seal self-relieving pressure regulator (maximum inlet pressure 41.4 MPa; maximum outlet pressure 5.5 MPa) connected to the nitrogen bottle was used to regulate the pressure.

Stainless steel Swaglock fittings and 3 mm stainless steel tubing joined the nitrogen pressure regulator to the accumulator. This was a "bladder-type" accumulator which was used for maintaining approximately constant the applied pressures in the high pressure range. The nitrogen pressurizes the bladder which in turn pressurizes the silicon oil. The accumulator was connected to an oil water reservoir with 3 mm brass fittings and copper tubing. Both pressure systems allowed the application of pressures with an accuracy of approximately ±0.5%.

The confining pressure system was identical to the back pressure system.

Axial Loading System

A 10,000 kg Wykeham Farrance stepless compression test machine was used to apply the vertical stresses to the samples. It allows the accurate control of the rate of vertical displacement of the cell. The triaxial cell is centered on a moveable plate, controlled by a motor.

The vertical load was applied to the sample through a 5.08 cm diameter piston that reacted against the frame and the sample top cap as a result of the vertical movement of the cell.

Monitoring Devices

The vertical displacements of the top of the sample, the volume of water that was absorbed by or expelled from the sample, the cell and the back pressures and the vertical load were automatically monitored.

A linear variable displacement transducer (LVDT). (Hewlett Packard - 500 -24 Volts) was attached to the loading piston at the top of the triaxial cell. The LVDT monitored the relative displacement between the loading piston and the top platen of the triaxial cell.

The amount of water that entered or left the oil sand samples during the tests was measured with a volume change monitoring device, SBEL (Structural Behavior Engineering Laboratories Inc.). Figure 4.10 presents a schematic drawing of the volume change device. The volume of water that flows through the device is related to the vertical displacement of the top of the metal bellows, which is monitored by an externally mounted LVDT. The LVDT is calibrated against

volume change inside the metal bellows. Agar, 1984:65, provided detailed information on the volume change device used in this research.

Two pressure transducers, Schaevitz, type P273-0025 were used to monitor the back pressure and the cell pressure. The pore pressure transducer allowed operation in the range of 0-3.5 MPa whereas the cell pressure transducer could operate in the range of 0-7.0 MPa. Both transducers were connected to the bottom plate of the triaxial cell.

The measurement of vertical loads was accomplished through a Durham Instruments load cell, with maximum capacity of 89 KN. It was mounted on the loading frame and provided reaction against the cell piston.

The electronic outputs from the monitoring devices were automatically collected and printed on a Fluke 2240B Datalogger.

The output voltages of the monitoring devices were calibrated and related to physical units such as displacement, volume, pressure and force. The calibrations of the pressure transducers were carried out with a dead weight table hydraulic pressure system. The volume change device LVDT was calibrated against a graduated burette for volume response. The vertical displacement LVDT was calibrated against a micrometer scale.

System Compliance

The values of vertical displacement and the values of the volume of water must be corrected in order to reproduce

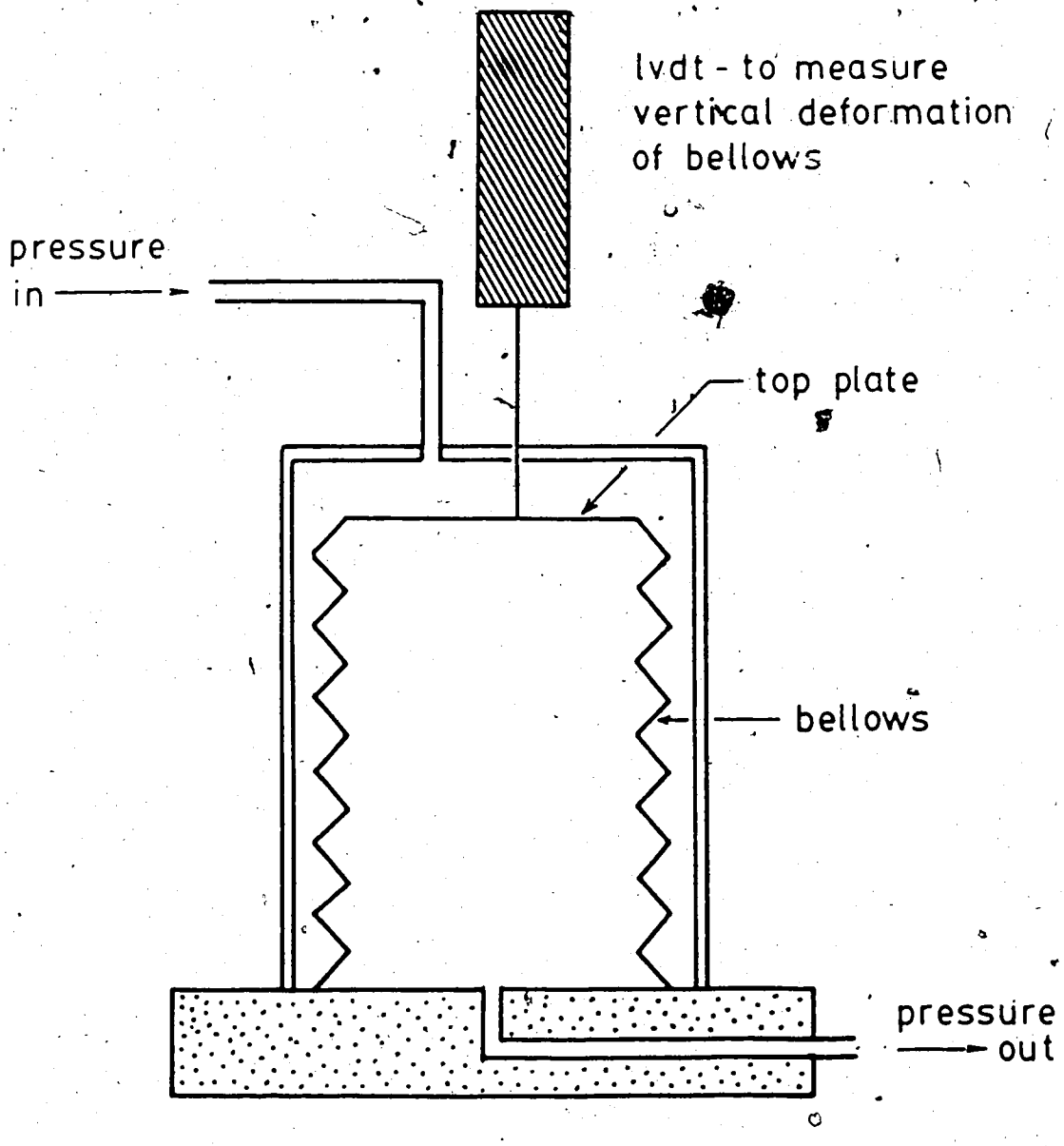

Figure 4.10 Bellows Volume Change

the actual response of the sample being tested.

The vertical displacements, measured by the LVDT that monitored the relative displacement between the loading piston and top platen of the cell, included the vertical compliance of all parts involved in the equilibrium of vertical forces that resulted from the vertical loading of the sample. The filter paper, the top cap, loading piston and bottom platen were responsible for the vertical compliance of the system. An aluminum block was tested and, by comparison of the measured vertical displacements with the theoretical ones, it was possible to quantify the vertical compliance for different vertical loads. Figure E5 depicts the results of the vertical compliance tests.

The volumetric compliance of the back pressure lines was performed by pressurizing the lines up to the pore pressure valve at the bottom plate, which remained closed. The compliance of the lines internal to the bottom platen, the pore pressure transducers and fittings that connected it to the platen was not measured. The volume change measurement with the volume change device, associated with the pressures applied to the back pressure lines is illustrated in Figure E6.

Piston Friction

The piston friction reduces the magnitude of axial load applied to the triaxial sample due to its relative displacement between the loading piston and the "O-ring" seals. If an internal load cell is used, the measured

vertical load is the load acting on the sample and no correction must be made. In this research, however, an external load cell was used and it was therefore necessary to correct the vertical loads for piston friction. The magnitude of piston friction was obtained by applying a constant pressure in the triaxial cell fluid and imposing a downward movement of the loading piston, at a rate similar to the ones at which the triaxial tests were performed. In the absence of the sample and the sample top cap, the vertical load acting on the piston inside the cell was equal to the cell fluid pressure times the cross sectional area of the piston. The value of the friction developed between the "O-ring" seals and the loading piston is the difference between the vertical load acting on the piston inside the cell and the vertical load measured by the external load cell. Figure E7 depicts the friction values obtained for different values of confining pressures. A constant value of 0.25 kN was adopted for the data reduction.

4.3.3.3 Sample Preparation for Testing

The drained triaxial tests took place between 60 and 160 days after sampling. During this period, the samples were kept in the inner core barrel used during sampling, with both ends capped and taped, stored at -20°C in a freezer.

The preparation of a sample for testing started by cutting the sampling tube in 15 cm long sections, after it had been removed from the freezer at -20°C and stored in dry

ice for approximately 24 hours. The 15 cm long tubes were cut on the longitudinal axis, to release the sample from within. Most of the tubes were cut in four sections and numbered sequentially from bottom to top. Each section was double bagged and tagged. The sections not immediately used for testing were placed back into the storage freezer.

The section to be tested was kept in an air tight can in dry ice for an additional 24 hours before trimming started.

The trimming process very closely followed the suggestions proposed by Dusseault et al, 1984 and Agar, 1984:98. After being chilled to approximately -78°C, the 7.3 cm diameter samples had a metal collar placed on one of the ends and were mounted in the chuck of a lathe. A free rotating end cap provided axial pressure along the lathe bed and helped the lathe to retain the sample. A diamond tipped bit was used to trim the samples to the final diameter. In order to minimize disturbance during this process the trimming was performed in 0.250 mm cuts, in its early stages, and in 0.05 to 0.125 mm cuts when finishing the surface. This procedure is illustrated in Plates 4.8 and 4.9.

The samples were then notched using a carbide steel notching bit at a length of approximately 10 cm (except sample 8-2B that was trimmed to a length of 4.5 cm) and then cut with a diamond saw. Samples were finally remounted in the lathe in a thick split ring that had approximately the

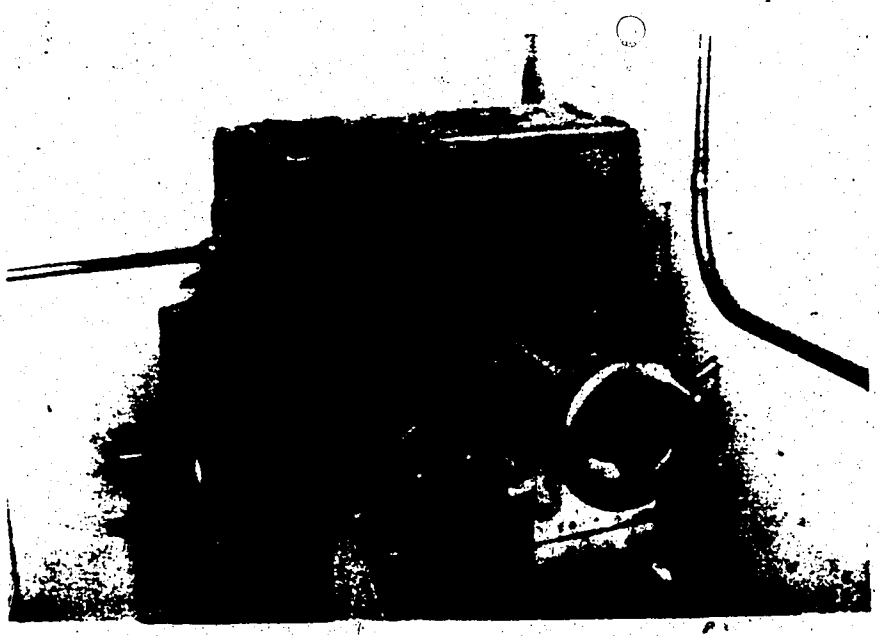

Plate 4.8 Lathe used for Sample Trimming

Plate 4:9 Diamond Bit and Frozen Sample during Trimming

same length as the sample. The ends were trimmed smooth at right angles to the cylindrical axis.

After trimming, the samples were placed back into dry ice, again protected by an air tight can, for a minimum period of 2 hours. After being cooled down to -78°C, the samples were ready to be assembled in the triaxial cell. The bottom platen of the triaxial cell was prechilled in the cold room to -20°C prior to the assembly of samples. All rubber "O-rings" were greased with high vacuum grease prior to the chilling of the platen. The placement of the sample on the triaxial cell pedestal also took place in a cold room, at a temperature of -20°C.

The samples were then removed from the dry ice and had filter paper attached to them at the sides and bottom end as illustrated in Plate 4.10. After being placed on the pedestal, the top cap, two latex membranes (0.4 mm thick each) (Plate 4.11) and two sealing "O-rings" were installed.

The bottom platen, now retaining the sample, was taken out of the cold room to the laboratory where the tests were performed. The bottom platen was positioned in the loading frame, the cell body attached to the bottom platen and immediately filled with water. The monitoring devices were attached to the system. The pressure transducers and pressure lines were deaired and cell pressure and pore pressure were applied to the sample. Thawing and saturation of the samples took place at varying times as described in the following sections.

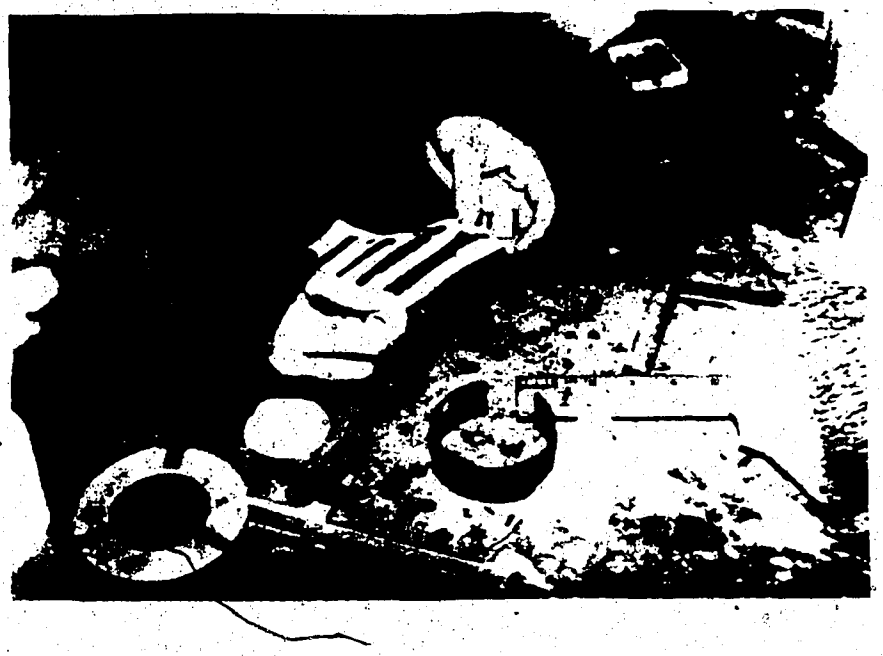

Plate 4.10 Sample Preparation for Testing - Lateral Drains

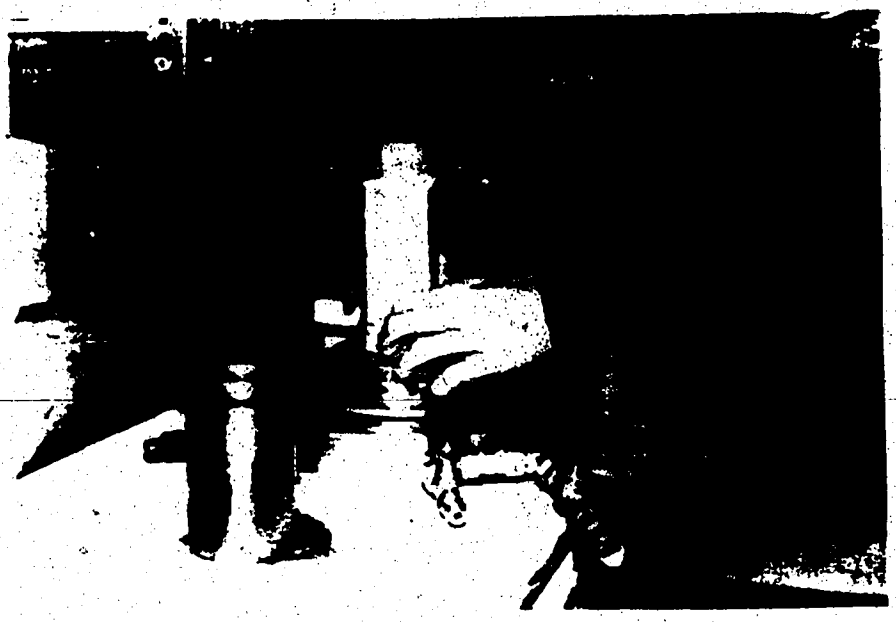

Plate 4.11 Sample Preparation for Testing - Latex Membranes

4.3.3.4 Isotropic Drained Triaxial Tests

Testing Techniques

Table 4.6 summarizes the main characteristics of the isotropic triaxial tests performed. Except for sample 8-28, the samples were trimmed with a height-diameter ratio of approximately 2.

The time and pressures used for thawing and saturation of the samples are also presented in Table 4.6. Immediately after the complete assembly of the triaxial testing system, the samples were subjected to a cell pressure and pore pressure that would allow them to thaw without any further expansion of the skeleton.

Different procedures had been used at the University of Alberta by different researchers in order to saturate the oil sands samples. Dusseault, 1977:138 saturated Athabasca oil sands samples with cell pressures between 300 kPa to 400 kPa and back pressures about 200 to 300 kPa for up to 72 hours. Saturation was assumed to be completed when the pore fluid flow was equilibrated. Sterne, 1981:27 applied a back pressure of 1050 kPa for approximately 1.5 hours and assumed the samples to be saturated when the flow of water into the samples ceased. Agar, 1984:116 saturated oil sand samples at back pressure of at least 2000 kPa for 20 hours.

The saturation of the samples was verified with the comparison of the B values obtained from "B" tests performed with cell pressure increments of 500 to 750 kPa. The constancy of the B value in successive "B" tests would

SAMPLE NO.	DIMENSIONS OF FROZEN SAMPLE			INITIAL EFFECTIVE STRESS	TEST CHARACTERISTICS	THAWING AND SATURATION		
	DIAM. (CM)	HEIGHT (CM)	VOLUME (CC)	SIG' 3 (KPA)		CELL PRESSURE (KPA)	PORE PRESSURE (KPA)	TIME (HOUR)
5-1	5.137	10.755	222.93	520	MONOTONIC UNLOADING	2546 TO 2379	2013 TO 1990	15
7-4	5.401	9.969	228.43	3041	MONOTONIC UNLOADING	3139 TO 4957	2129 TO 1933	18
8-2B	5.110	4.467	91.60	1006	CYCLIC LOADING	172 TO 192 192 TO 1484	86 TO 92 92 TO 1387	19 5
8-3	5.161	10.539	220.50	1032	MONOTONIC UNLOADING	1385 TO 1444 1444 TO 3937	280 TO 486 486 TO 2917	22 2

Table 4.6 Triaxial Drained Isotropic Unloading Tests - Test Characteristics

indicate that the sample is fully saturated. This procedure, originally proposed by Wissa, 1969, is a valuable assessment of the saturation of low compressibility soils. As opposed to most near-surface soils, saturated with water, oil sands can present B values as low as 0.39 (Agar, 1984:115) when fully saturated. The procedure used by Agar was also followed in this research, except that the cell pressure increments were between 80 and 200 kPa during the B tests.

Constant values of B were achieved when samples were nearly fully saturated and ranged between 0.80 and 0.95. The samples were saturated at the testing, effective confining pressures indicated in Table 4.6. Sample 8-2b was subjected to cylic loading whereas the remaining three tests were subjected to monotonic unloading. During the tests, the cell pressures were changed in increments that varied between 50 kPa to 150 kPa and the back pressures were maintained constant. The variation of the cell pressure during the test was defined by the time required for the flow of water into the back pressure line to stabilize. Stabilization was achieved in 20 to 30 minutes after the cell pressure was modified.

Test Results: Presentation and Analysis

The cell pressures, back pressures and pore water volume changes monitored during the tests allowed the association of the volume change of the samples with the effective stresses. No corrections were made for the effect of the membranes on the confining pressure applied to the

sample. The tests, described in Section 4.3.4.3 of this chapter, allowed the evaluation of the pressure acting on the sample and this proved to be approximately 10 kPa higher than the cell pressure applied. This error is considered negligible when compared to the values of cell pressures used during testing.

Figures C.18 to C.21 present the confining effective stress plotted as a function of volumetric strains, with respect to the volume of the samples in the frozen state after trimming.

The data collected from the isotropic drained triaxial tests allowed the evaluation of the elastic bulk modulus, B, which is defined as:

$$B = \frac{d\sigma'_{oct}}{d\epsilon_{vol}} \qquad [4.10]$$

where,

σ'_{oct}= effective octahedral normal stress,

ϵ_{vol}= volumetric strain.

According to Janbu, 1963:22, elastic bulk moduli can be adequately accounted by the formula:

$$M = m\ \sigma_a \left[\frac{\sigma'_v}{\sigma_a}\right]^{1-\alpha} \qquad [4.11]$$

where, according to his notation:

M = constraint modulus = $d\sigma_v/d\epsilon_v$

m = modulus number

σ_a = 1 atmosphere = 101.325 kPa

α = number between 0 and 1

According to the notation used in this thesis, Equation 4.11 is expressed as

$$B = K_b\ P_a\left[\frac{\sigma'_3}{P_a}\right]^m \qquad [4.12]$$

where:

B = bulk modulus

K_B = bulk modulus number

P_a = atmospheric pressure

m = bulk modulus exponent.

Equation 4.11 can be linearized as follows:

$$\log(B/P_a) = \log(K_b) + m\ \log(\sigma'_3/P_a) \qquad [4.13]$$

With the linear regression analysis of the test data, where $\log(\sigma'_3/P_a)$ is treated as the independent variable and $\log(B/P_a)$ is treated as the dependent variable, it is possible to obtain the values of K_B and m for each test, as graphically indicated in Figure 4.11. (Duncan et al., 1980).

Figures C.22 to C.25 present the normalized bulk modulus versus the normalized confining pressure. They

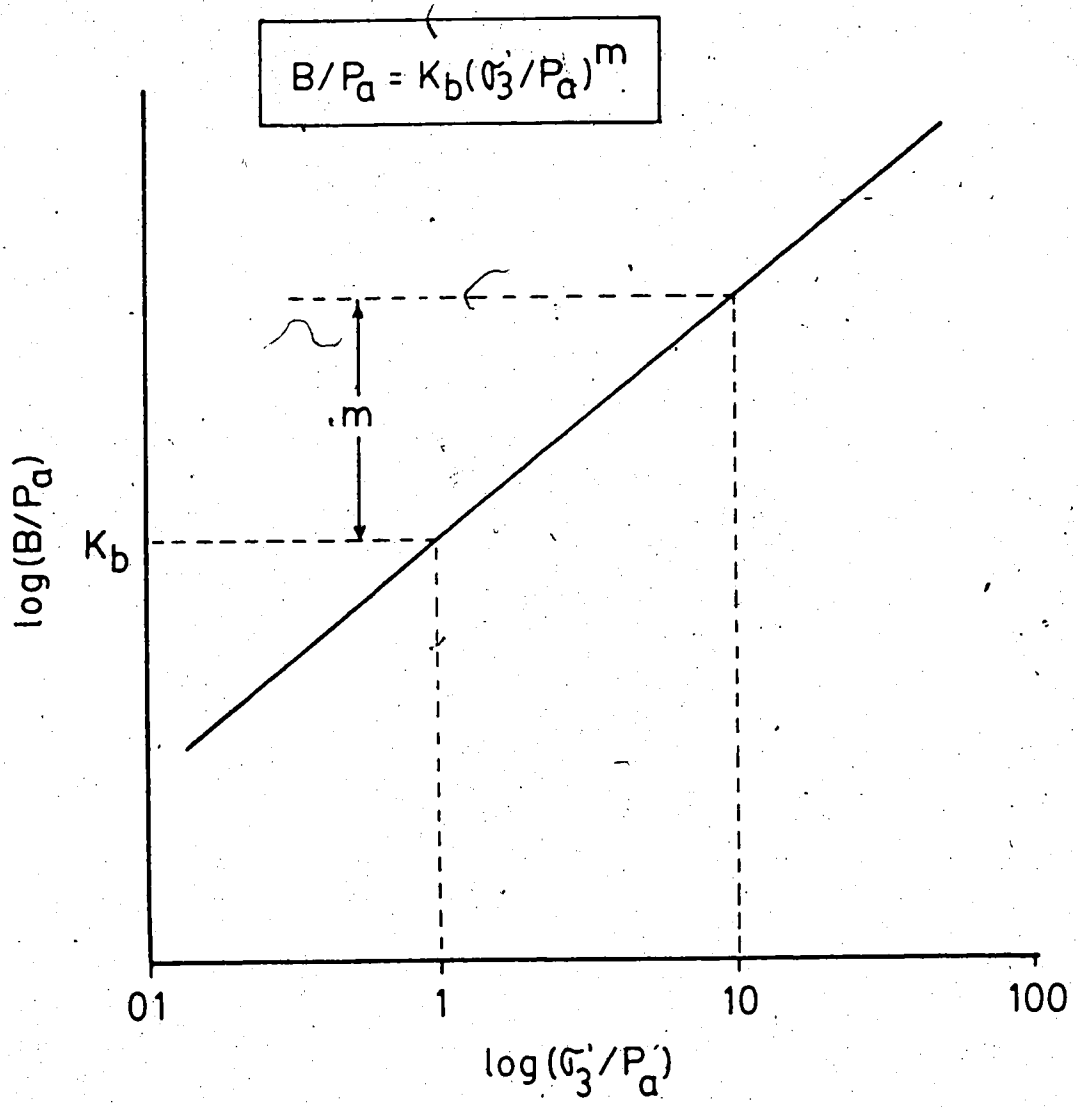

Figure 4.11 Variation of Bulk Modulus with Confining Pressure - Modifified from Duncan, 1980

indicate that the relationship provided by Equation 4.11 can describe well the test results. The curve obtained from the test performed with Sample 8-2b (Figure C.24) represents the last unloading stage, after the sample was subjected to cyclic loading.

Figure 4.12 illustrates and summarizes the statistical analysis of the tests. The consistently higher values of bulk modulus obtained in test 8-2b are a result of the cyclic loading previously mentioned.

Samples 5-1, 8-3 and 7-4 were consolidated at different initial confining stresses, without being subjected to cyclic loading, and presented very similar responses. The average response for these three tests is expressed by the equation:

$$B = 388.4567\ P_a(\sigma'_{oct}/P_a)^{0.9887}$$

as illustrated in Figure 4.12.

For the sake of comparison, the test results obtained by Agar, 1984, in Saline Creek, Athabasca oil sands, and by Domaschuk and Wade, 1969, in dense Chattahoochee Sand (D_R = 90%, e = 0.659), are presented in Figure 4.12.

4.3.3.5 "J1" Drained Triaxial Tests

Testing Techniques

Table 4.7 summarizes the main characteristics of the "J1" tests. It shows that the samples were trimmed with height-diameter ratio of approximately 2 and that the times and pressures used during thawing and saturation of the sample were similar to the ones used with the isotropic

SAMPLE NO.	DIMENSIONS OF FROZEN SAMPLE			MEAN EFFECTIVE STRESS	RATE OF TESTING	THAWING AND SATURATION		
	DIAM. (CM)	HEIGHT (CM)	VOLUME (CC)	SIG' OCT (KPA)	(MM/MIN)	CELL PRESSURE (KPA)	PORE PRESSURE (KPA)	TIME (HOUR)
5-2	5.125	8.125	167.63	2050	0.0087 TO 0.0174	4130 TO 4095	1824 TO 1718	19
5-3	5.110	10.463	214.57	2910	0.0087 TO 0.0174	4987 TO 4767	1987 TO 1954	24
5-4	5.125	10.367	213.86	1820	0.0087 TO 0.0174	3840 TO 3809	2031 TO 2062	18
8-1	5.118	10.411	214.18	2650	0.0087 TO 0.0174	2345 TO 4659	508 TO 2015	44
8-4	5.146	10.616	220.80	2940	0.0087 TO 0.0174	2058 TO 4782	610 TO 1858	26

Table 4.7 Triaxial Drained J1 Tests - Test Characteristics

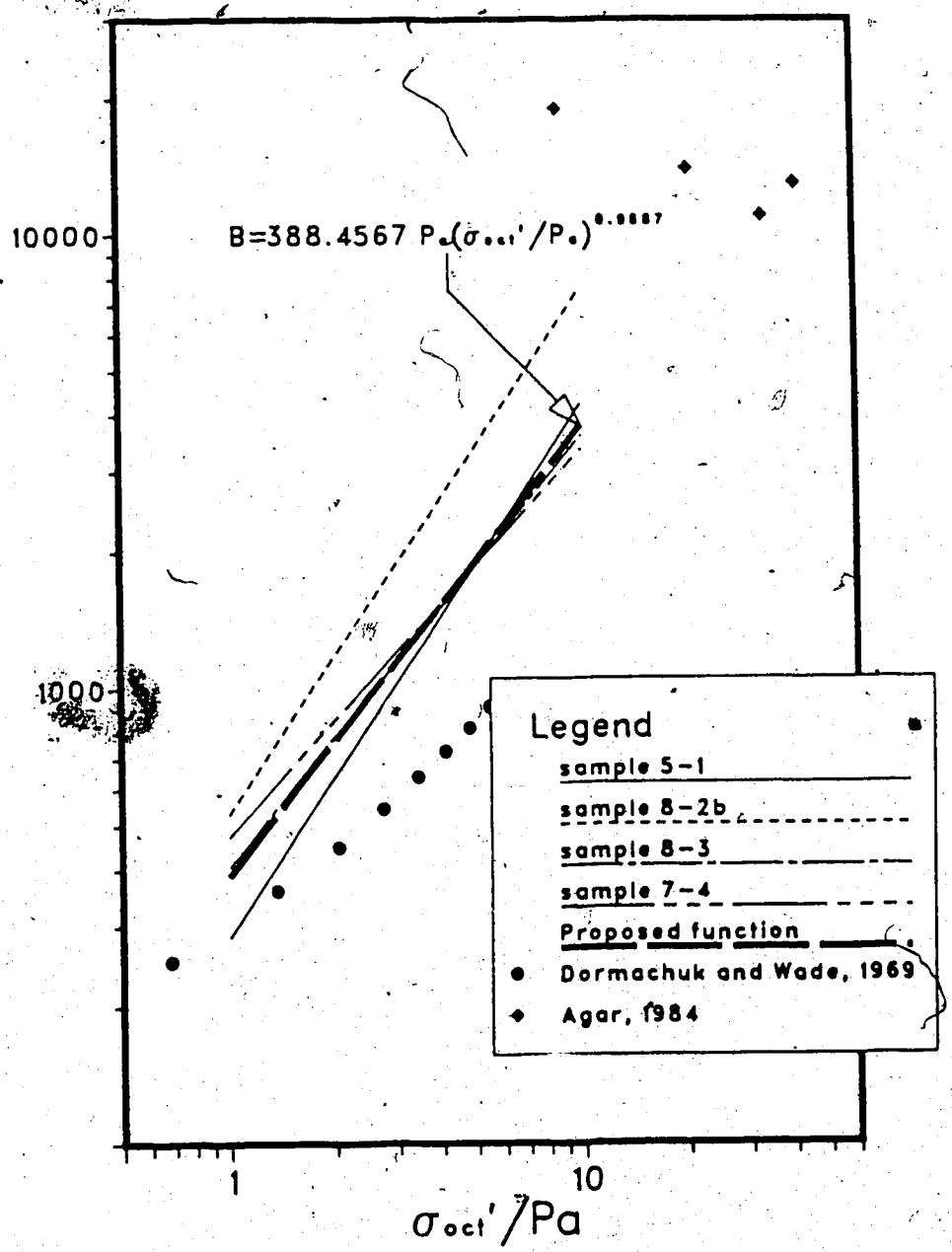

Figure 4.12 Normalized Bulk Modulus versus Normalized Mean Effective stress

triaxial tests. The verification of saturation was also carried out with the performance of successive "B" tests, as described in the preceding section.

The samples were isotropically saturated at the pressures and effective stresses indicated in Table 4.7. The mean effective stresses or octahedral normal stresses depicted in this table were maintained approximately constant throughout the tests.

At the time of performance of the "J1" triaxial tests, a strain controlled Wykeham Farrance stepless compression frame was the only available means of applying axial loads to the samples. This imposed difficulties in performing the "J1" tests, which require the control of stresses, as opposed to strains. The procedure followed to maintain the octahedral mean stress constant during the shearing of samples in the "J1" tests, using a strain controlled axial loading system, is described as follows.

1. With the sample fully saturated and the pore water flow system in equilibrium, a rate of relative vertical displacement between the bottom platen of the triaxial cell and the axial loading system, varying from 0.0087 to 0.0174 mm/min was adjusted in the strain controlled frame machine. These rates of testing were chosen according to suggestions presented by Bishop and Henkel, 1978:125-127. Theoretically, the rate of increase of excess pore pressures during the tests should be compatible with the samples capacity to drain water in

order to dissipate it. The rates of testing were evaluated with conservative values of the coefficient of consolidation (C_v) and with the assumption that sample water drainage took place at one end and radially.

2. The back pressure was maintained constant throughout the test.
3. The cell pressure was maintained constant until the vertical load cell indicated that the load piston made contact with the sample top cap.
4. After the piston contact was made, and the vertical load acting on the sample started to increase, the required value for the cell pressure was calculated as a function of the new vertical stress in order to maintain the initial octahedral normal stress constant.
5. This process of correcting the cell pressure as a function of measured axial stress was carried out throughout the tests, once every minute.

A programmable pocket calculator was used in the evaluation of the required cell pressures. The variation of the cross-sectional area of the sample was taken into account in the evaluation of the average vertical stresses acting on the sample, as suggested by Bishop and Henkel, 1978:29.

The method used to control stresses in a strain controlled apparatus was faulty as far as maintaining the octahedral normal stress constant was concerned. This occurred because corrections of cell pressures were possible

only after the deviation from the desired stress path was detected. Figures C.26 to C.30 present the stress paths that resulted from the performance of the J1 tests. They indicate the octahedral normal stress oscillated about the desired stress.

Test Results: Presentation and Analysis

Figures C.31 to C.35 present the "J1" triaxial test results. They depict the variation of half of the deviatoric shear stress $((\sigma'_1 - \sigma'_3)/2)$, the volumetric strain $(\epsilon_v=\Delta V/V_o)$ and the tangent shear modulus (G_{tan}) as a function of the deviatoric strain $(\epsilon_1-\epsilon_3)$. The effects of the membranes and the lateral paper drains on the stresses actually acting on the sample were neglected. For the sake of comparison, Figure 4.13 graphically summarizes all test results. The values of G_{tan} presented in Figures C.31 to C.35 are the first derivatives of the stress strain curves $[(\sigma'_1-\sigma'_3)/2] \times [\epsilon'_1 - \epsilon'_3]$, which can be described briefly as follows:

$$G = \frac{d\tau_{oct}}{d\gamma_{oct}} \qquad [4.14]$$

where,

$$\tau_{oct} = 1/3\sqrt{(\sigma_1-\sigma_3)^2 + (\sigma_2-\sigma_3)^2 + (\sigma_3-\sigma_1)^2} \qquad [4.15]$$

$$\gamma_{oct} = 2/3\sqrt{(\epsilon_1-\epsilon_3)^2 + (\epsilon_2-\epsilon_3)^2 + (\epsilon_3-\epsilon_1)^2} \qquad [4.16]$$

in the triaxial cell, $\sigma_2=\sigma_3$, hence

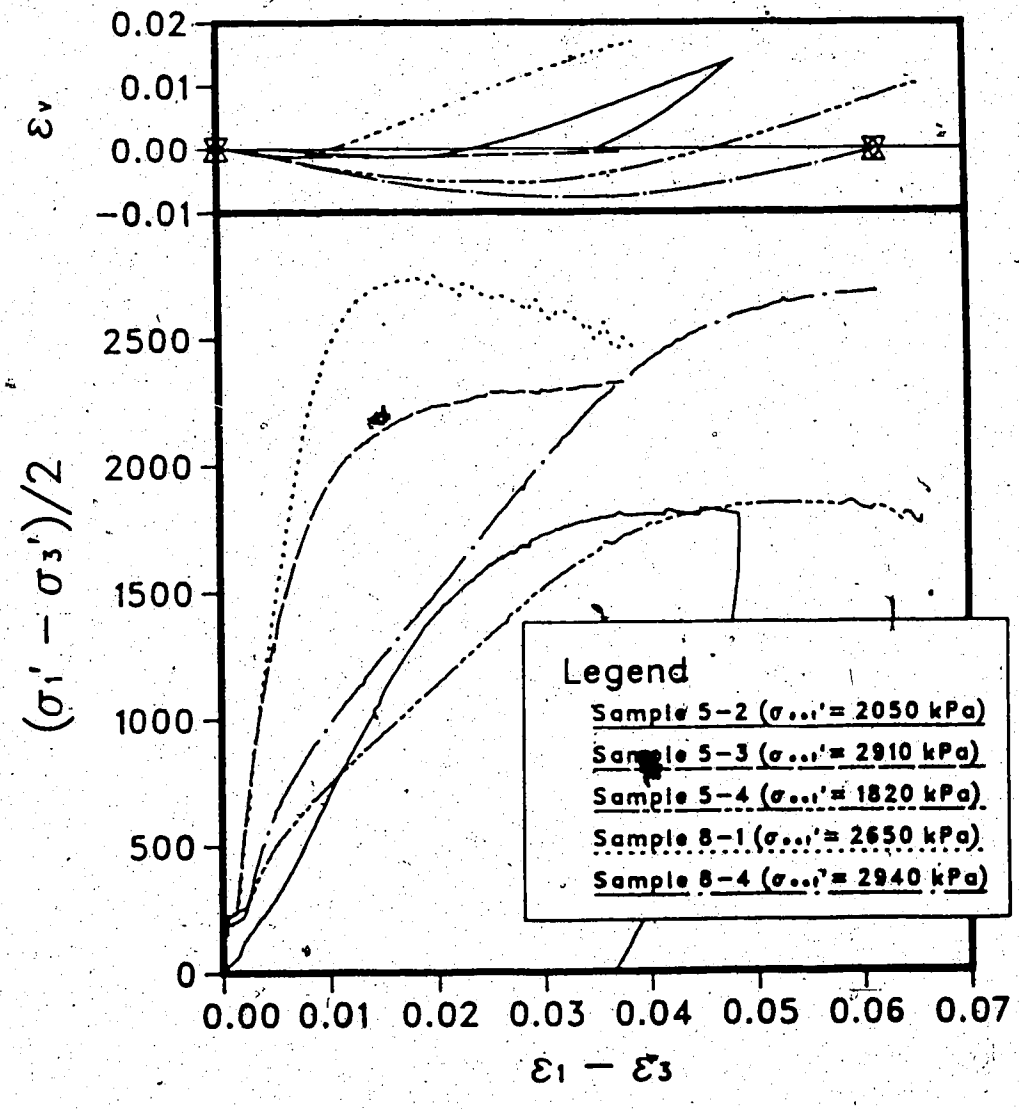

Figure 4.13 J1 Triaxial Tests (Drained) Undisturbed Samples

$$t_{oct} = \sqrt{2}/3 |\sigma_1 - \sigma_3| \qquad [4.17]$$

$$\gamma_{oct} = 2\sqrt{2}/3 \; | \; \epsilon_1 - \epsilon_3 | \; . \qquad [4.18]$$

Therefore, in the triaxial cell,

$$G = \frac{d(\sigma_1 - \sigma_3)}{2d(\epsilon_1 - \epsilon_3)} \qquad [4.19]$$

A non-linear elastic stress strain model was chosen as the constitutive law used to describe the mechanical response of the oil sand skeleton. The numerical simplicity inherent in the use of the elastic models and their wide spread use in the numerical simulation of most different types of geotechnical engineering work were decisive in the choice of these models.

The hyperbolic stress-strain model, originally proposed by Kondner, 1963 and further developed and used by Duncan and Chang, 1970, Kulhawy et al., 1969, Wong and Duncan, 1976, and Duncan et al., 1980, is the most popular non-linear elastic model among geotechnical engineers. The following relationship was proposed for representation of the stress-strain response:

$$(\sigma_1 - \sigma_3) = \frac{\epsilon_1}{(1/E_i + \epsilon_1/(\sigma_1 - \sigma_3)_{ult})} \; . \qquad [4.20]$$

as illustrated in Figure 4.14.

The initial Young's modulus, E_i, was related to σ'_3 according to Janbu, 1963:

$$E_i = K\ P_a\left(\frac{\sigma_3}{P_a}\right)^n \qquad [4.21]$$

where

K = modulus number

n = modulus exponent

and $(\sigma_1 - \sigma_3)_{ult}$ is related to the stress difference at failure as follows,

$$(\sigma_1-\sigma_3)_{ult} = \frac{(\sigma_1-\sigma_3)_{fail}}{R_F} \qquad [4.22]$$

where R_F is the failure ratio and is always less than unity and varies from 0.5 to 0.9 for most soils.

$(\sigma_1-\sigma_3)_F$ can be expressed as a function of σ_3 as follows:

$$(\sigma_1-\sigma_3)_{fail} = \frac{2c\ \cos\phi+2\sigma_3\sin\phi}{1\ -\ \sin\phi} \qquad [4.23]$$

in which c and ϕ are the cohesion intercept and the friction angle respectively, according to the Mohr-Coulomb envelop.

By differentiating Equation 4.20 with respect to ϵ_1 and substituting Equations 4.21, 4.22 and 4.23 into the

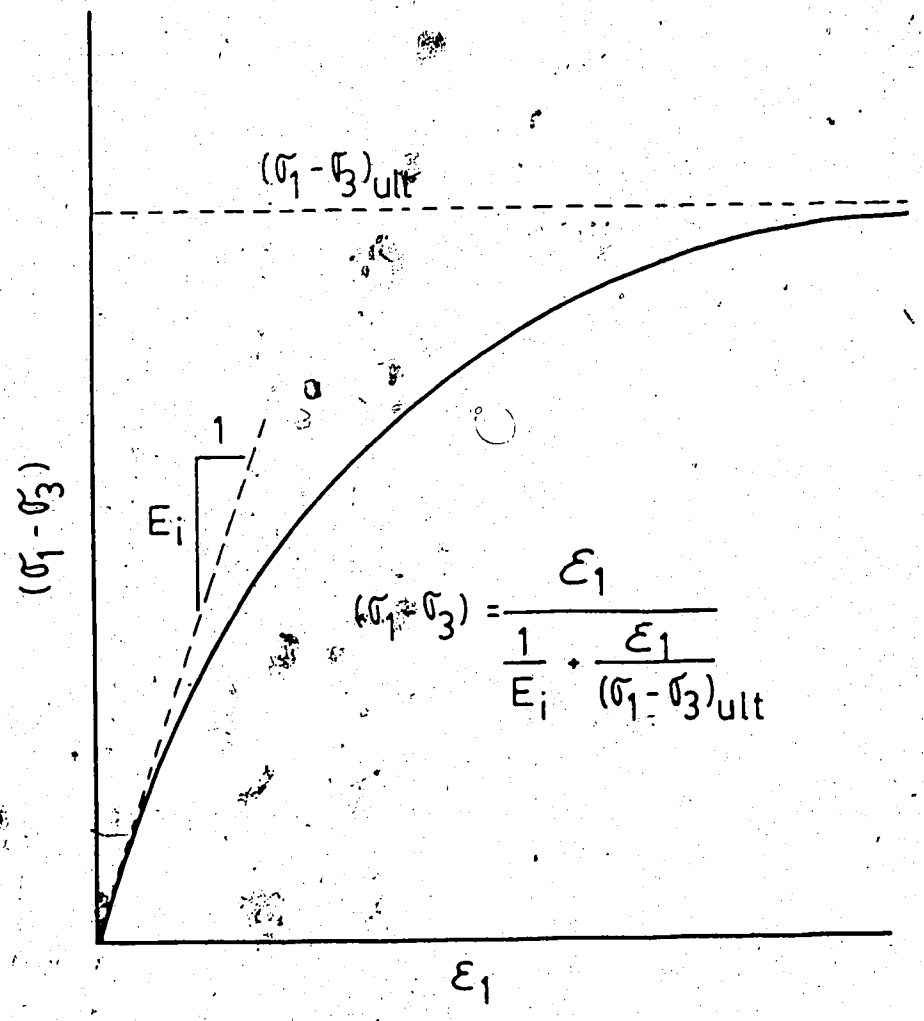

Figure 4.14 Hyperbolic Representation of a Stress-Strain Curve

resulting equation for E_t the following equation can be derived:

$$E_t = [1-\frac{R_f(1-\sin\phi)(\sigma_1-\sigma_3)}{2c\cos\phi + 2\sigma_3\sin\phi}]^2 K.P_a.(\frac{\sigma_3}{P_a})^n \quad [4.24]$$

Therefore, E_t can be derived for values of σ_3 and σ_1, if K, n, c, ϕ and R_F are known. Duncan et al., 1980, presented detailed procedures to obtain the required hyperbolic parameters from standard triaxial tests.

In the present research, however, it was decided to use the bulk modulus, B, and the shear modulus, G, in order to define the constitutive response of the soil, as opposed to the bulk modulus and the Young's modulus, E. The advantage of using B and G, rather than B and E is that the former moduli may be evaluated independently from independent laboratory tests. The evaluation of E from standard triaxial tests is affected by both the hydrostatic and deviatoric stresses, whereas the evaluation of G from the "J1" triaxial tests is not affected by the hydrostatic stresses.

A hyperbolic model expressed in terms of the shear modulus was developed by Domaschuk and Wade, 1969. The proposed expression relates the octahedral shear stress to the octahedral shear strain as follows:

$$\sigma_{oct} = \frac{\gamma_{oct} G_i}{1 + b\gamma_{oct} G_i} \quad [4.25]$$

All variables have been previously presented and are illustrated in Figure 4.15. One can notice that the value of 1/b is equivalent to $(\sigma_1-\sigma_3)_{ult}$ refered to in Figure 4.14. Analogously to Duncan and Chang's derivation, Domaschuck and Wade derived the tangent shear moduli,

$$G=G_i(1 - b\tau_{oct})^2 \qquad [4.26]$$

A series of tests was performed with Chattahoochee River sand at varying relative densities and initial void ratios. The initial shear modulus, G_i, and the stress parameter, "b", were related to the octahedral normal stress through charts. No attempt was made to relate analytically these variables. Christian and Desai, 1977:85, related the tangent shear modulus, G, to σ_3 with an expression almost identical to Equation 4.24.

$$G_t=G_i[1-\frac{R_F(1-\sin\phi)(\sigma_1-\sigma_3)}{2c\cos\phi + 2\sigma_3\sin\phi}]^n \qquad [4.27]$$

It was suggested that the initial tangent shear modulus be obtained according to Hardin and Black, 1968,

$$G_i=1230\ \frac{(2.973 - e)^2}{1 + e}\sigma_{oct}^{1/2} \cdot OCR^k \qquad [4.28]$$

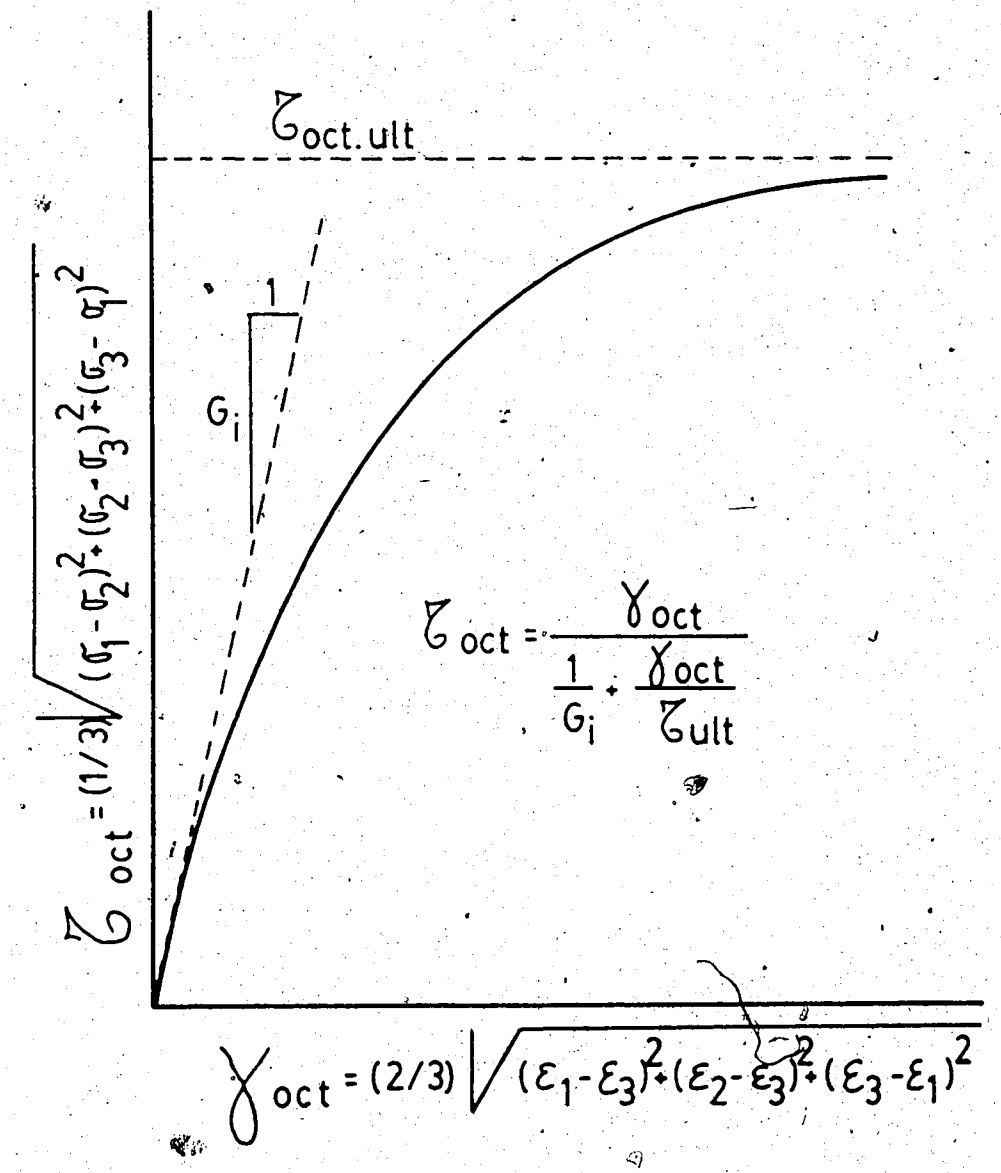

Figure 4.15 Hyperbolic Stress-Strain Curve

where,

e = initial void ratio

σ_{oct} = octahedral normal stress

OCR = overconsolidation ratio

k = number that depends on the plasticity index of the soil. For non-plastic soils k=0

This expression was derived empirically from dynamic vibration tests. Therefore, one might expect that it predicts values higher than the ones obtained from static triaxial tests.

Considering that during the "J1" tests, the octahedral normal stress, σ_{oct}, and not the minimum normal stress, σ_3, is maintained constant, it is desirable to express the tangent shear modulus as a function of σ_{oct}. Thus, the following modifications are proposed in the original derivation by Domaschuk and Wade, 1969.

$$G_t = G_i \left[1 - \frac{\tau_{oct}}{\tau_{oct,ult}}\right]^2 \qquad [4.29]$$

$$\tau_{oct,ult} = R_f \tau_{oct,fail} \qquad [4.30]$$

$\tau_{oct,fail}$ can be obtained with the use of Drucker-Prager yield criterion formulation, as follows:

$$\sqrt{J_2} - aI_1 - K = 0 \qquad [4.31]$$

where,

$$J_2=\tau_{oct}^2 \cdot \frac{3}{2} \qquad [4.32]$$

$$I_1=\sigma_1+\sigma_2+\sigma_3 = 3\sigma_{oct} \qquad [4.33]$$

$$k=0 \text{ for cohesionless soils.} \qquad [4.34]$$

The parameter a can be related to the Mohr-Coulomb's friction angle depending how the Mohr-Coulomb hexagonal surface is approximated by the Drucker-Prager cone. Chen and Saleeb, 1982:485 demonstrate how this approximation should be performed. In this thesis, the two surfaces are made to agree along the compressive meridian (Point A in Figure 4.16) and the following expression results:

$$a=\frac{2 \sin\phi}{\sqrt{3}(3-\sin\phi)} \qquad [4.35]$$

Substituting Equations 4.32 to 4.35 in Equation 4.31 gives:

$$\tau_{oct,fail}=\frac{2\sqrt{2}.\sigma_{oct}\sin\phi}{(3 - \sin\phi)} \qquad [4.36]$$

Substituting 4.30 and 4.36 in 4.29 yields:

$$G_t= G_i\left[1 - \frac{\tau_{oct}R_F(3-\sin\phi)}{2\sqrt{2}\sigma_{oct}\sin\phi}\right]^2 \qquad [4.37]$$

An equation similar to the one used by Duncan and Chang, 1970, is used to relate G_i to the octahedral stress:

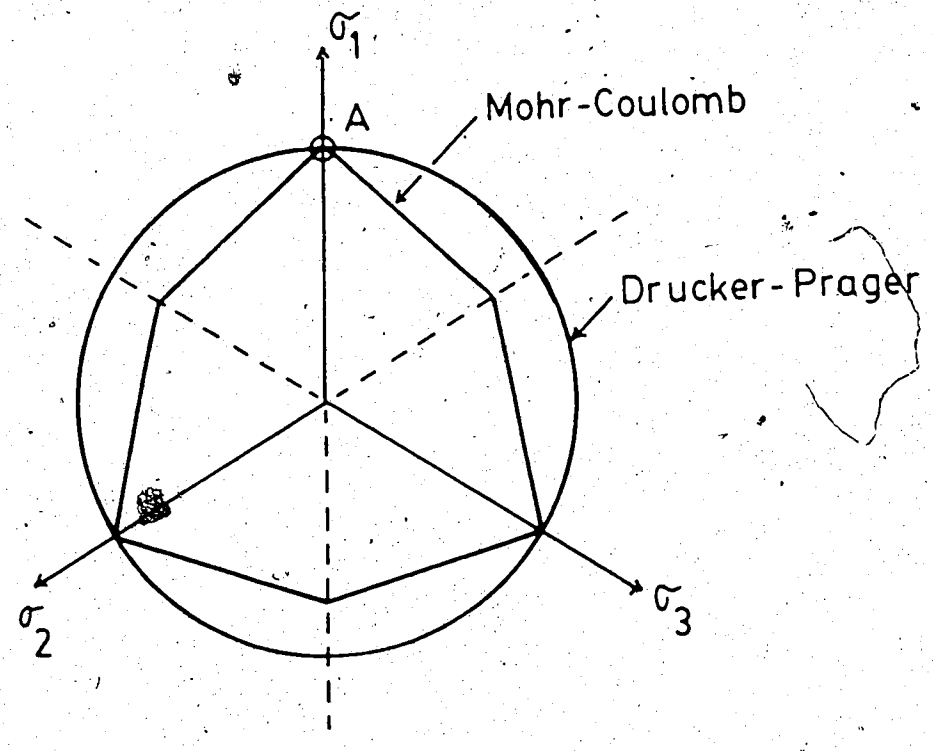

Figure 4.16 Mohr-Coulomb and Drucker-Prager Failure Criteria

$$G_i = K_G P_a \left(\frac{\sigma_{oct}}{P_a}\right)^{n_g} \qquad [4.38]$$

where;

K_G= shear modulus number,

n_G= shear exponent number.

Finally, the tangent shear modulus can be expressed as:

$$G_t = K_G P_a \left(\frac{\sigma_{oct}}{P_a}\right)^{n_g} \left[1 - \frac{\tau_{oct} R_F (3-\sin\phi)}{2\sqrt{2}\sigma_{oct}\sin\phi}\right]^2 \qquad [4.39]$$

This expression indicates that knowledge of K_G, n_G, R_F and ϕ allows the evaluation of G for any stress level defined by σ_{oct} and τ_{oct}. The "J1" triaxial tests performed allowed the evaluation of these parameters, as follows:

Evaluation of ϕ

Several laboratory tests previously performed with Athabasca oil sands indicate that the failure envelope for this material is not represented by a straight line (Dusseault, 1977; Agar, 1984). These experiments show that the friction angle, as illustrated in Figure 4.17, decreases with increases in σ_3 and σ_{oct} at failure. The following relationship has been proposed for the friction angle:

$$\phi = \phi_o - \Delta\phi \log_{10} \frac{\sigma'_3}{P_a} \qquad [4.40]$$

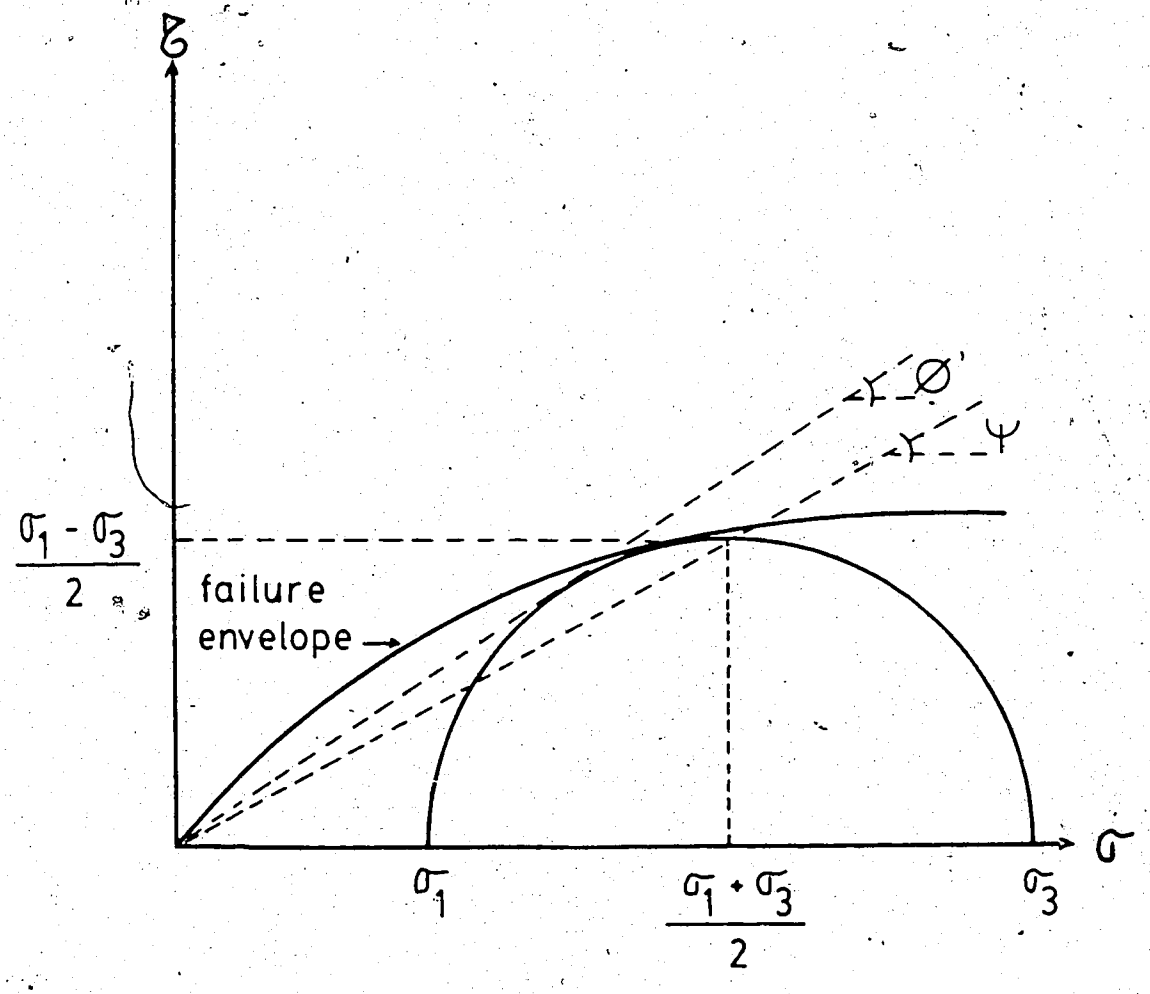

$$\emptyset' = \sin^{-1}(\tan\Psi)$$

Figure 4.17 Curved Failure Envelope

Table 4.8 summarizes the strength parameters obtained from the "J1" and the standard triaxial tests, described in Section 4.3.3.6. The values of the friction angle can be plotted versus the normalized value of the minimum effective stress at failure and the values of ϕ_o and $\Delta\phi$ can be obtained readily by fitting a straight line through the test data, according to Equation 4.40, and according to Figure 4.18. The value of ϕ_o is given by the value of ϕ for $\sigma_3/P_a = 1$ and the value of $\Delta\phi$ is given by the slope of the straight line.

A collection of strength parameters obtained from tests on oil sands is presented in Figure 4.18. It shows the great scatter of friction angles obtained by different authors. The best fit curve for the data obtained in this research is given by the following expression:

$$\phi = 65 - 20\log(\sigma'_3/P_a) \qquad [4.41]$$

The higher friction angles obtained by Agar, 1984, reflected by the Equation presented in Figure 4.16, is a result of the higher quality of the samples obtained from the slopes of Saline Creek.

Table 4.8 also allows one to relate the friction angle with the normalized octahedral stress, as illustrated in Figure 4.19. The following expression follows from this figure:

TEST	SAMPLE	(SIG1'+SIG3')/2	(SIG1-SIG3)/2	SIG-OCT'	SIG-OCT'/PA	SIG3'	SIG3'/PA	FRICTION ANGLE
		AT FAILURE						
J 1	5-2	2646.9	1816.6	2050.0	20.23	830.3	8.19	43.34
	5-3	3731.5	2330.1	2910.0	28.72	1401.3	13.83	38.64
	5-4	2470.0	1850.4	1820.0	17.96	619.6	6.11	48.52
	8-1	3596.3	2749.7	2650.0	26.15	846.6	8.36	49.87
	8-4	3843.9	2686.9	2940.0	29.02	1158.3	11.43	44.35
STANDARD	4-2	1257.0	1119.1	833.9	8.23	137.9	1.36	62.91
	5-1	2555.9	1897.3	1923.5	18.98	658.6	6.50	47.95
	6-2	2199.2	1863.0	1578.2	15.58	336.1	3.32	57.90
	7-4	1784.9	1463.7	1289.4	12.73	298.5	2.95	55.09

Table 4.8 Strength Parameters from Triaxial Tests

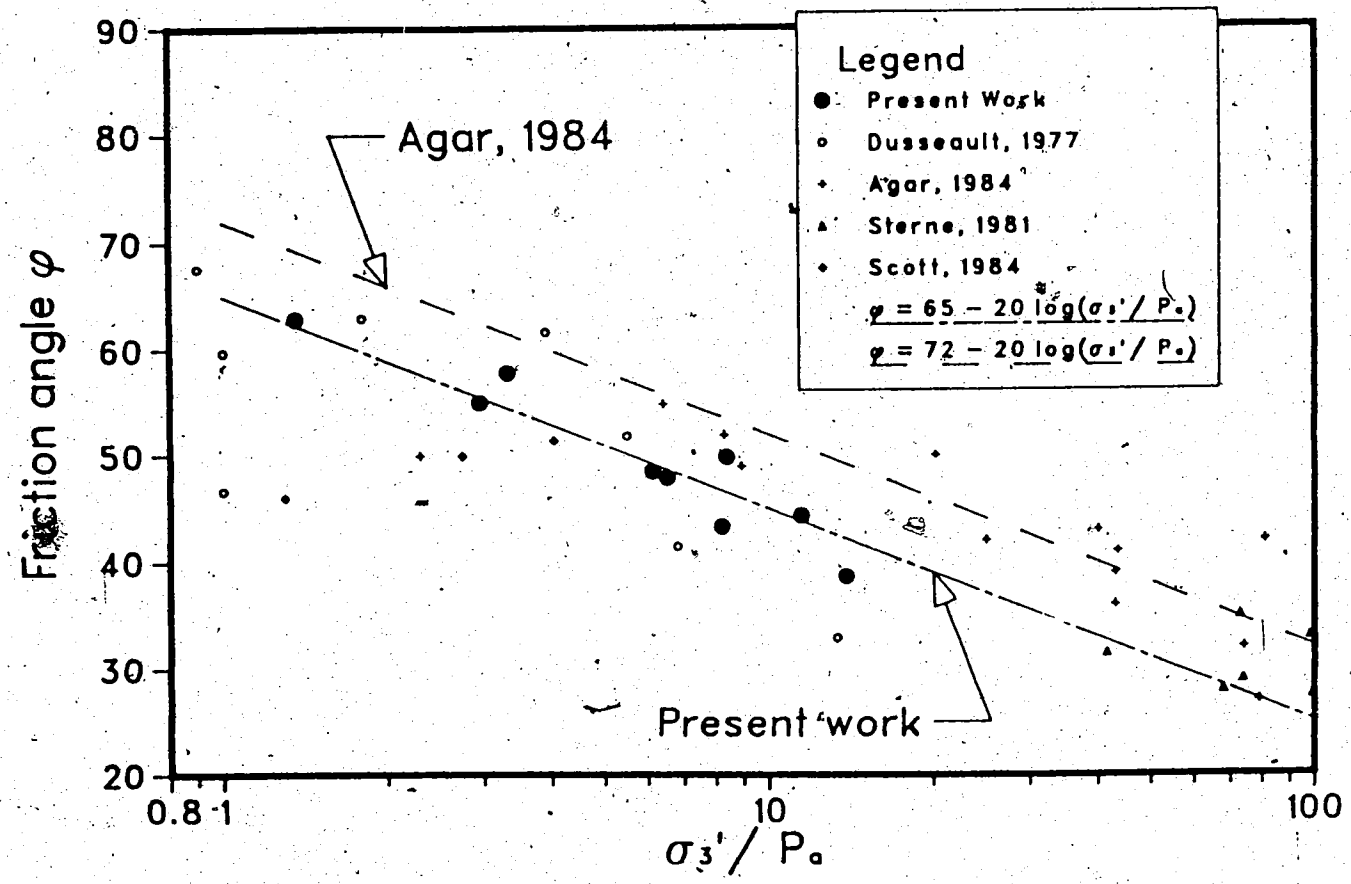

Figure 4.18 Friction Angle versus Normalized Confinement Stress

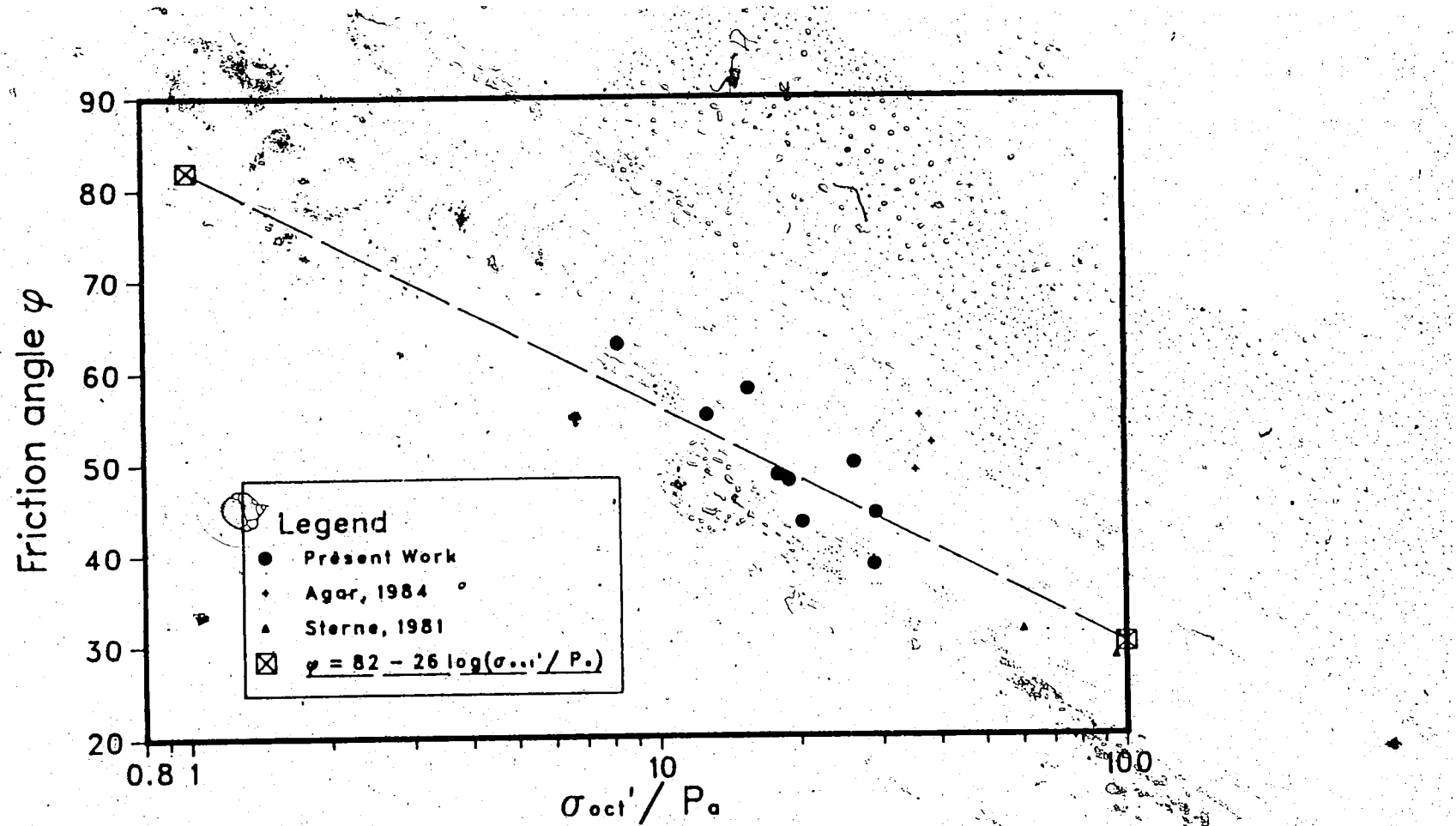

Figure 4.19 Friction Angle versus Normalized Mean Stress

$$\phi = 82 - 26\log(\sigma'_{oct}/P_a) \qquad [4.42]$$

Evaluation of K_G, n_G and R_F

Similar to the procedure presented by Duncan et.al., 1980, two steps are involved in the evaluation of the modulus parameters K_G and n_G. The first is to determine the values of G_i for each test and the second is to plot these values normalized with atmospheric pressure against (σ_{oct}/P_a) on log-log scales to determine the values of K_G and n_G. Theoretically, G_i can be obtained graphically from the linearization of Equation 4.25 as follows:

$$\tau_{oct} = \gamma_{oct} \Big/ \frac{1}{G_i} + \frac{\gamma_{oct}}{\tau_{oct,ult}} \qquad [4.43]$$

$$\frac{1}{G_i} + \frac{\gamma_{oct}}{\tau_{oct,ult}} = \frac{\gamma_{oct}}{\tau_{oct}} \qquad [4.44]$$

By assuming that γ_{oct} is the independent variable and γ_{oct}/τ_{oct} is the dependent variable, Equation 4.44 can be represented graphically as depicted in Figure 4.20. Therefore, it is theoretically possible to obtain the values of G_i and $\tau_{oct,ult}$ directly from the transformed hyperbolic stress-strain plot for each "J1" test. It happens, however, that, on the transformed plot, the test data deviates from the ideal relationship. According to Duncan, 1980:446, tests on dense sands usually plot on a curve which is concave

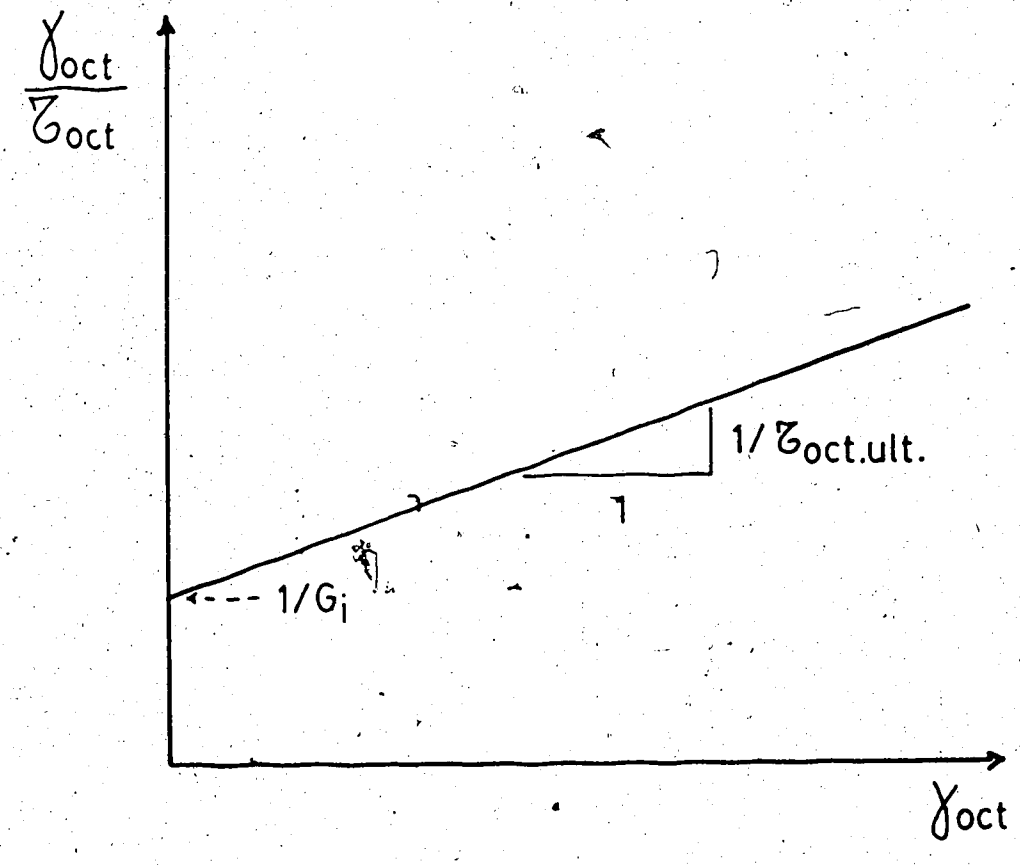

Figure 4.20 Transformed Hyperbolic Stress-Strain Plot

upward, whereas loose sands usually plot on a curve which is concave downward. Duncan reported that past experience with several types of soils indicated that a good match is usually achieved by selecting a straight line that passes through the points where 70% and 95% of the strength are mobilized. Thus, in practice, only two points for each stress-strain curve are required to be plotted on the transformed stress-strain plot.

The data reduction of the "J1" triaxial tests showed that the initial deformations measured at the early stages of the test, not necessarily associated with the deformation of the sample, affected the values of K_G and n_G. The calibration for the vertical compliance of the triaxial cell performed with an aluminum block presented in Figure E5, indicates that the initial strain varies significantly from test to test, despite the fact that all were performed under identical conditions. The random nature of the initial "seating" strains made it difficult to incorporate them in data reduction.

Several authors have recently studied the error involved in the measurement of strains in cylindrical triaxial samples; among them Symes and Burland, 1984; Jardine et.al., 1984; Atkinson and Evans, 1985 and Costa Filho, 1985. These authors identified that there are three sources of movement from which an error in the computed value of sample strain may develop:

1. deflections of the testing apparatus (compliance of the

apparatus: loading piston, load cell, porous stones, filter paper, top cap and other elements included in the measurement of axial displacements).

2. bedding between the end caps and the sample (or contact errors which, according to Costa Filho, 1985:3, may include;
   - non-uniformity of the surface of the specimen ends due to the presence of irregularities.
   - lack of flatness of the specimen ends
   - non-parallelism of the specimen end surfaces
   - lack of squareness of the specimen
   - tilting or misalignment of the top cap).
3. bedding between the porous stone and top cap or pedestal
4. end restraint caused by the restriction of zero lateral movement at the sample ends.

Item 1 can be computed in the data reduction through careful calibration of the apparatus. Item 4 can be avoided with the insertion of sheets of greased rubber at the ends of the sample. However, as reported by Symes and Burland, 1984:49, "benefits of such actions are often outweighted by the associated increase in the bedding errors and creep of the lubricating grease at the interface between the sample and the end platens."

Errors due to items 2 and 3 are unaccountable and cannot be predicted through calibration.

The elimination of these errors at the present moment seems to be possible with the measurement of deformation

directly on the central portion of the triaxial specimens, as opposed to the external measurement of displacements as performed in this thesis. Jardine et.al., 1984 and Costa Filho, 1985, present a summary of the existing techniques to measure strains on cylindrical triaxial specimens.

Triaxial tests performed with the measurement of deformations at the central portion of the samples indicated that the measurement of overall deformations, i.e., between the end platens, leads to an underestimation of the initial modulus.

Jardine et.al., 1984, performed an undrained standard triaxial test on intact low plasticity North Sea clay. The sample was isotropically consolidated to an effective stress of 474 kPa and then undrained shear took place. Overall, or external, and localized axial strains were monitored during the test. The overall strains were corrected for the system compliance, and the corrected strains were compared with the localized strains, as depicted in Figure 4.21. The difference between the two curves is unquestionable and demonstrates that if realistic constitutive parameters are to be obtained, local defofmations on the sample must be measured.

In the present research, however, due to the unavailability of the appropriate devices to monitor locally strains, a simplified approach was adopted in order to minimize the corrected overall strain errors. The initial tangent modulus was assumed to be equal to the modulus

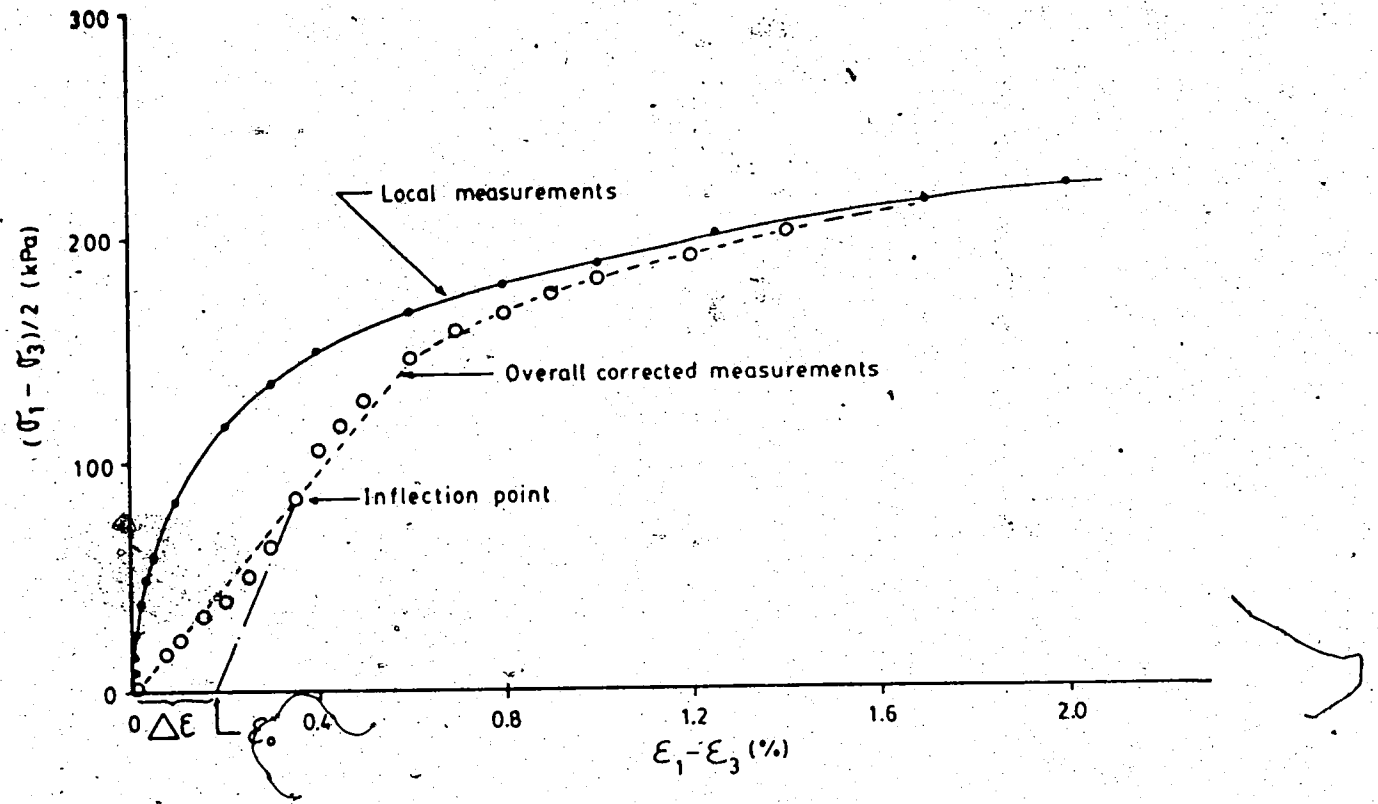

Figure 4.21 Comparison between Overall and Localized Strains (Modified from Jardine et al., 1984)

obtained at the point of inflection, where a change in concavity of the stress-strain curve occurs. The application of this procedure to the test results presented in Figure 4.21 indicates that the inclination of the resultant stress-strain curve still does not resemble the ones obtained by local measurements of strains but, without doubt, represents a significant improvement of the overall corrected stress-strain curve.

With the modified stress strain curves from the J1 triaxial tests it was possible to obtain G_i and $\tau_{oct,ult}$, as explained earlier in this section. For each test, two values of G_i and $\tau_{oct,ult}$ were obtained: one related to the straight line plotted on the transformed hyperbolic stress-strain curve (Figure 4.20), passing through the points where 70% and 95% of the strength is mobilized and the other related to the straight line passing through the points where 40% and 80% of the strength are mobilized. The values of G_i and R_F, obtained from this analysis are summarized in Table 4.9. The purpose of this analysis was to verify if the procedure proposed by Duncan et.al. 1980, (passing through 70% and 95%) was adequate for oil sands. By substituting Equations 4.17 and 4.18 into 4.25 and rearranging 4.25, it is possible to write the hyperbolic expression in terms of G_i and R_F, for the triaxial test, where $\sigma_2=\sigma_3$:

$$\frac{\sigma_1-\sigma_3}{2} = (\epsilon_1-\epsilon_3)/\left[\frac{1}{2G_i}+\frac{(\epsilon_1-\epsilon_3)\ R_F}{(\sigma_1-\sigma_3)_F}\right] \qquad [4.45]$$

By substituting the values of G_i and R_F of Table 4.9 in Equation 4.45, it is possible to express $(\sigma_1-\sigma_3)$ as a function of $(\epsilon_1-\epsilon_3)$ as illustrated in Figures C.36 to C.39. The theoretical hyperbolic curves have been truncated at the shear stress defined by Equation 4.36 for the specific value of σ'_{oct} at which the test was performed. The test results corrected only for the system compliance are presented in these figures and allow one to conclude that, irrespective of the points chosen for the evaluation of G_i and R_F, the hyperbolic curves present a reasonable approximation of the measured curves for shear stresses up to approximately 70% of the theoretical failure shear stresses. Considering this fact, the hyperbolic parameters obtained with Duncan's suggestion (70-95%) were used in the subsequent analyses.

The values of G_i and σ'_{oct}, depicted in Table 4.9 are plotted in Figure 4.22 along with the values obtained from standard triaxial tests, discussed later in this chapter, in order to obtain values for K_G and n_G.

This figure also illustrates the initial moduli measured by other authors. The values of G_i obtained from the J1 triaxial tests varied to an unacceptable extent, as illustrated in Figure 4.22. This variation is probably due to the random cyclic shear to which these samples were submitted during the tests. The data displayed in Table 4.4 indicate that all samples were tested with similar void ratios. This fact excludes the degree of sample disturbance as a reason for such scatter of the initial moduli.

		40% - 80%		70% - 95%	
SAMPLE	σ' oct/Pa	Gi/Pa	Rf	Gi/Pa	Rf
5-3	28.72	4986.48	0.713	6225.12	0.846
8-1	26.15	3879.10	0.337	3941.00	0.358
5-2	20.23	994.68	0.272	1403.87	0.592
5-4	17.96	959.08	0.572	805.29	0.481

Table 4.9 G_i and R_f Obtained from "J1" Triaxial Tests

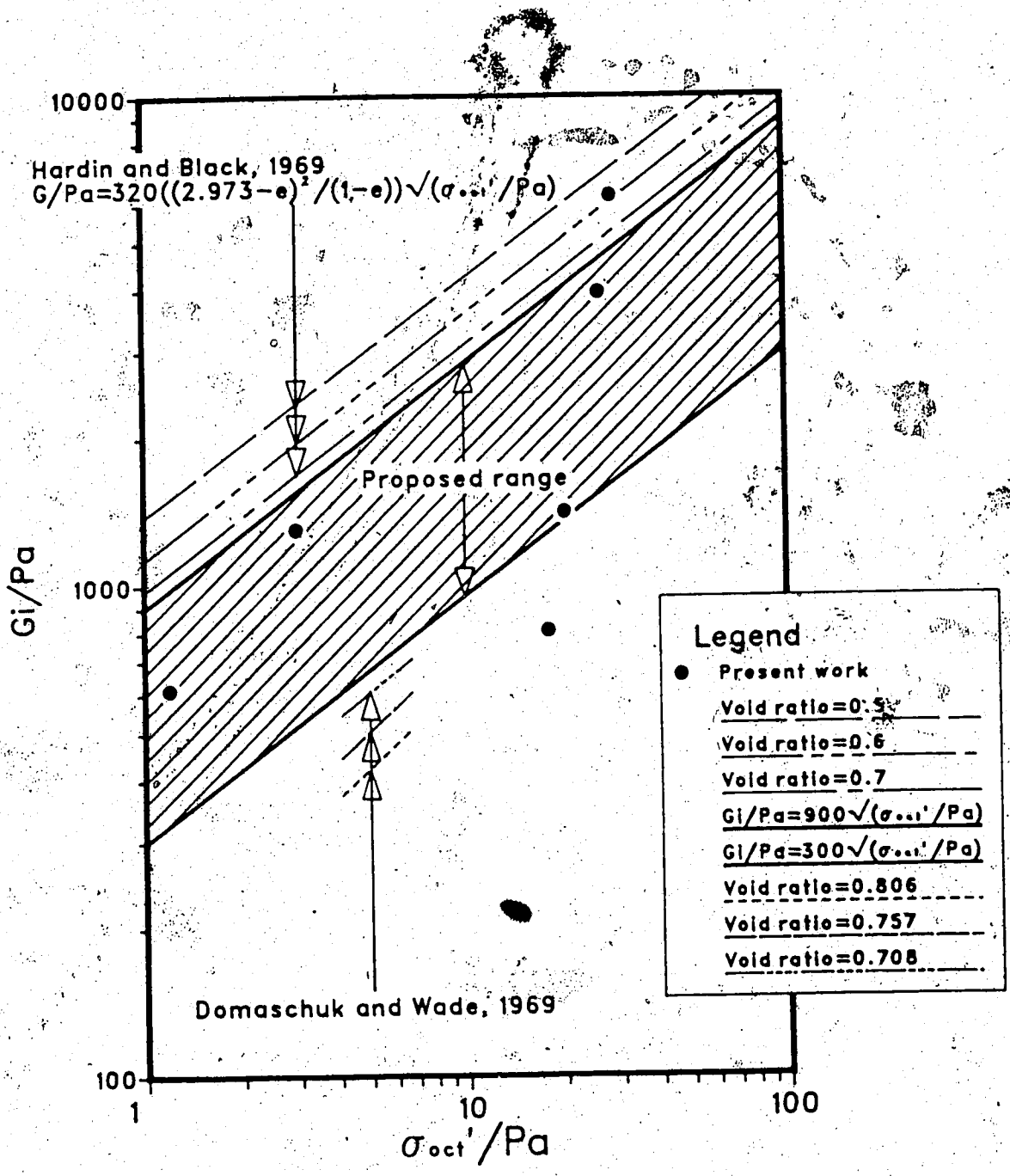

Figure 4.22 Normalized Shear Modulus versus Normalized Mean Effective Stress

The data published by Hardin and Black, 1969, were obtained from dynamic small amplitude vibration tests on crushed Ottawa sands; therefore, they should represent an upper limit to static shear tests. Three theoretical curves, proposed by Hardin and Black, with equivalent void ratios of 0.5, 0.6 and 0.7 are plotted on Figure 4.22.

The moduli obtained by Domaschuk and Wade, 1969, from J1 triaxial tests on Chattahoochee River sand, with characteristics very similar to the oil sands, except a small percentage of mica (<0.5% in weight), are also plotted in Figure 4.22 for three different void ratios, 0.708, 0.757, and 0.806. These should represent a lower limit to the shear moduli of oil sands, due to the fact that the latter does not present any trace of mica and that its locked structure should result in higher moduli.

Based on these considerations, the range of values illustrated in Figure 4.22 is proposed. The upper and lower straight lines are defined by the expression:

$$\log_{10}\frac{G_i}{P_a} = \log_{10}K_G + n_G\log_{10}\left(\frac{\sigma'_{oct}}{P_a}\right) \qquad [4.46]$$

which is, in fact, the transformed version of Equation 4.38. The values of K_G and n_G are 900 and 0.5, respectively, for the upper line, and 300 and 0.5 for the lower line.

4.3.3.6 Standard Drained Triaxial Tests

By definition, standard triaxial tests are tests performed with the confining pressure, i.e. the cell pressure, constant. The reason for the performance of this test was the difficulty encountered in properly controlling the cell pressures during the execution of the J1 tests at lower effective stresses. It was realized that the fluctuation of cell pressures controlled with the Circle-Seal pressure regulators was high when compared to the relatively low octahedral normal stresses at which the tests had to be performed.

In order to obtain stress-strain elastic parameters at lower effective stresses it was decided to perform standard triaxial tests, which are described in the following sections.

Testing Techniques

Table 4.10 summarizes the main characteristics of the standard drained triaxial tests. The procedures followed during thawing and saturation of the samples are identical to the procedures followed during the "J1" triaxial tests described in the preceding section.

Samples 5.1 and 7.4 were subjected to isotropic unloading prior to shear and were not considered in the evaluation of elastic parameters.

Samples 6.1, 7.3 and 7.5 were abandoned due to the excessive tilting observed at the top cap which resulted from localized failure at the top corners of the sample.

SAMPLE NO.	DIMENSIONS OF FROZEN SAMPLE			CONFINING EFFECTIVE STRESS	TEST CHARACTERISTICS	THAWING AND SATURATION		
	DIAM (CM)	HEIGHT (CM)	VOLUME (CC)	SIG' 3 (KPA)		CELL PRESSURE (KPA)	PORE PRESSURE (KPA)	TIME (HOUR)
4-2	5.064	8.940	180.06	120 TO 230		850 TO 920 1900	750 TO 1800	21 2
5-1	5.137	10.755	222.93	650 TO 820	WITH ISOTROPIC UNLOADING	2546 TO 2379	2013 TO 1990	15
6-1	5.087	10.114	205.54	200 TO 260	SAMPLE TILTED TEST ABANDONNED	796 TO 817 2581 TO 2617	586 TO 593 2350 TO 2389	22 3
6-2	5.074	9.755	197.25	310 TO 340		809 TO 862 2729 TO 2844	445 TO 542 2415 TO 2348	18 3
7-3	5.080	9.555	193.66	210 TO 230	SAMPLE TILTED ABANDONNED RESUSTS	795 TO 890 2692 TO 2833	592 TO 617 2464 TO 2599	18 1
7-4	5.401	9.969	228.43	290 TO 300	WITH ISOTROPIC UNLOADING	3139 TO 4957	2129 TO 1933	18
7-5	5.080	8.190	166.00	-----	VALVE LEAKED TEST ABANDONNED	673 TO 698	471 TO 492	19

Table 4.10 Standard Drained Triaxial Tests - Test Characteristics

Test Results: Presentation and Analysis

Figures C.40 to C.44 present the standard triaxial test results. Similar to the "J1" triaxial tests they depict the variation of half of the deviatoric shear stress $(\sigma_1'-\sigma_3')/2$, the volumetric strain ($\epsilon_v=\Delta V/V_o$) and the tangent shear modulus (G_{tan}) as a function of the deviatoric strain. The procedures used to reduce the data from "J1" triaxial tests were used for the standard triaxial tests. Figure C.45 to C.49 illustrate the stress paths that resulted from these tests.

Figure 4.23 graphically summarizes the results from tests that were successfully completed. The test results are in good agreement with those presented by Scott, 1984.

Table 4.11 summarizes the hyperbolic parameters, G_i and R_F, as defined earlier in this chapter, obtained from tests performed with Samples 4.2 and 6.2. The normalized values of G_i are plotted in Figure 4.22 against the normalized values of σ'_3, which in a standard triaxial test is equal to the octahedral normal stress prior to shearing. The scatter of G_i values observed in the J1 tests is also noted in the standard triaxial tests. The data from the two triaxial tests fall within the proposed range of values for K_G and n_G and confirm its validity for the lower ranges of confining stresses.

The volumetric changes observed during these tests indicated that dilation due to shear only occurred at shear stress levels close to failure.

SAMPLE	σ'_3/Pa	G_i/Pa	R_F
4-2	1.184	613.43	0.472
6-2	2.961	1300.67	0.504

σ'_3 = MINIMUM EFFECTIVE CONFINING STRESS
G_i = INITIAL TANGENT SHEAR MODULUS
R_F = FAILURE RATIO
P_a = ATMOSPHERIC PRESSURE

Table 4.11 G_i and R_f Obtained from Standard Triaxial Tests

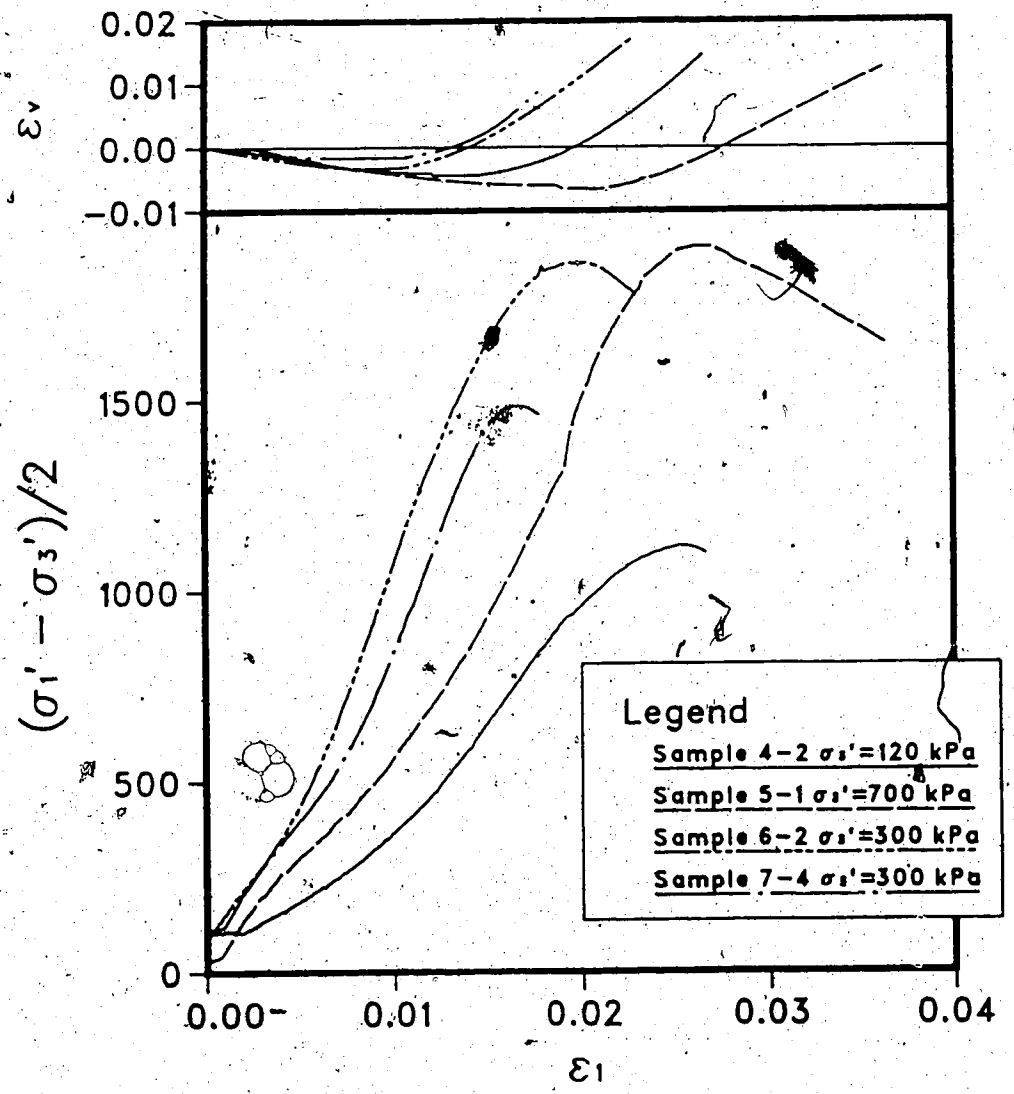

Figure 4.23 Standard Triaxial Tests - Test Results

The angles of friction of the tests are summarized in Table 4.8 and plotted in Figures 4.18 and 4.19.

4.3.3.7 Summary of Stress-Strain Hyperbolic Parameters

The drained triaxial tests described in this section allowed the evaluation of the parameters required for the description of the non-linear elastic parameters B, bulk modulus, and G, shear modulus, as defined by Equations 4.12, 4.39 and 4.40.

The following parameters were obtained:

Bulk Modulus Number, K_b: 388.5

Bulk Modulus Exponent, m: 0.99

Shear Modulus Number, K_G: 300.0 to 900.0

Shear Modulus Exponent, n_G: 0.50

Failure Ratio, R_f: 0.50

Friction Angle at $\sigma'_{oct}=P_{atm}$, ϕ_o: 82°

Friction Angle Increment, $\Delta\phi$: 26°

4.3.4 Gas Evolution Response Tests (Group A)

4.3.4.1 General

The review on the phenomenon of gas evolution (Chapter 2) and on the models available that mathematically describe this model (Chapter 3), reveal that both the time-independent and the time-dependent response characteristics of t[illegible] fluids are required to fully simulate the phenomen[illegible]

The time-independent response of the pore fluids is governed by Boyle's and Henry's law, whereas the time-dependent response is also governed by the fluids viscosity, diffusivity and geometry of pores, among other factors.

It was demonstrated in Chapter 2 that the use of macroscopic model is more appropriate for simulating the transient response of gassy fluids, given the difficulties involved in properly assessing the total number and location of sites where bubbles nucleate and grow.

The mathematical ease of the macroscopic models is counterbalanced by its limitations. The parameters produced from laboratory tests reflect characteristics that are peculiar only to the specific soil sample being tested, saturated with specific fluids, with specific thermodynamic properties. This means that extrapolation of macroscopic time-dependent parameters from one site to another must be made with care.

This section presents the tests performed in order to produce the gas evolution characteristics, both time-independent and time-dependent, of the samples described in Section 4.2. The parameters obtained from these tests, namely the combined solubility coefficient, H_{COMB}, and the time-dependent scaling parameters, E and A', together with the skeleton parameters presented on the previous page are required for the numerical simulation of the model tests described in Section 4.3.5.

To the writer's knowledge, only Sobkowicz, 1982 and Peacock, 1988, have performed tests aimed at the study of gas evolution directly in the pores of the soil samples. Sobkowicz performed undrained triaxial tests in artificially prepared samples of Ottawa sand, saturated with water and CO_2. The main purpose of his test program was to analyse the time-dependent response of gassy soils. The procedure followed by Sobkowicz consisted of saturating the sample with the water/CO_2 fluid and allowing it to consolidate at different stress levels and with pore pressures higher than the bubble point pressure. The samples were consolidated at different stress ratios and subsequently unloaded (decrease in σ'_{oct}) following different stress paths. The tests were performed in a stress controlled manner. After the application of the stress change, the pore pressure and volumetric change of the samples were monitored. A new stress change was applied to the sample only after stabilization of pore pressures and volume changes. During the stages of the test where the value of the confining effective stress was greater than zero and the pore pressures varied with time, it was difficult to separate the time-dependent from the time-independent volume change response of the soil.

Ideally, the pore pressure should be kept constant in order to separate the time-independent volume change of bubbles, governed by Boyle's law, from the time-dependent volume changes. This condition was possible during the last

stages of the isotropic tests, where the confining effective stresses approached zero. At this point, it was possible to control the pore pressure within the sample solely by controlling the cell pressure, since, according to the principle of effective stresses, for $\sigma'=0$, $\Delta u=\Delta\sigma$. Sobkowicz called this stage of the tests pseudo-drained, due to the fact that they were performed with a constant value of pore pressure, as occurs in most drained tests. Five pseudo-drained steps were performed in three different tests. Scaling parameters A' (Section 2.3) varying between 5 and 60 minutes were obtained. Sobkowicz reported inaccuracies in the measurement of the "real" time-dependent response of the fluid mainly due to the loss of gas molecules from the pore fluid through the membrane into the cell fluid. A comprehensive study of the best combination of cell fluid/membrane material led Sobkowicz to use glycerol as the cell fluid and double latex rubber membranes. This combination ameliorated the gas diffusion problem, but did not stop it. The concentration of gas bubbles between the sample and the membrane constituted another difficulty in appropriately measuring the transient growth of the volume of the samples. The growth of large bubbles results in changes in the boundary conditions that govern the gas evolution process to conditions not found in the pores of soils. Therefore, the time-dependent parameters obtained under these conditions do not reflect the transient response that actually takes place in soils.

In order to avoid the diffusion of gas from the sample, Peacock, 1988, performed tests in an oedometer cell. He used Syncrude tailings sands, artificially saturated with water and CO_2, and lean and rich oil sands samples also obtained at the Syncrude mining site. Peacock performed drained and undrained unloading tests in the oil sand samples. The drained tests consisted of maintaining the vertical load on the sample constant and dropping the back pressure instantaneously to atmospheric. The time-dependent volume increase of the sample and the amount of water that left the sample were monitored. The undrained tests consisted of the sequential unloading of the sample with monitoring of back pressures and vertical displacements of the loading piston.

The time-dependent response monitored by Peacock occurred with variations in the pore pressure, making difficult the independent analysis of the transient phenomenon.

This review of the tests performed by Sobkowicz and by Peacock indicates the necessity of appropriately studying the transient gas evolution phenomenon in natural soils. For instance, to date, no time-dependent gas evolution parameters are available for the simulation of transient response of oil sands. Three types of tests were designed in order to measure these parameters:

- oedometer tests
- frictionless oedometer tests
- mercury triaxial tests

Numerous difficulties were encountered in eliminating leaks in the frictionless oedometer cell. Due to time constraints and due to the success of the mercury triaxial tests, the frictionless oedometer cell was abandoned. The following sections present the oedometer and the mercury triaxial tests.

4.3.4.2 Undrained Oedometer Tests

The undrained oedometer tests were performed in a system composed of:

- oedometer cell
- back pressure and axial loading systems
- monitoring devices,

which are described in the following items.

Oedometer Cell

The oedometer cell used in this research was the one used by Peacock, 1988. It is fully machined in stainless steel and consists of a hollow cylinder, pedestal and piston, which confine the sample. Two circular plates hold the cylinder and the pedestal together. The piston travels freely within the cylinder, through the top plate, as indicated in Figures E.8 and E.9.

Ports in the pedestal and piston allow the measurement of pore pressure at the top and bottom of the sample.

More details about the cell can be found in the work by Peacock, 1988.

Back Pressure and Axial Loading Systems

The pressure system schematic for the oedometer tests is presented in Figure 4.24. It depicts that control of the pore pressure is made through the pedestal at the base of the sample. Similar to the triaxial test system, described in Section 4.3.3.2, it was possible to use two different sources of pressure to control the back pressure: the compressed air and the nitrogen sources. The lines, fittings and pressure regulators used in this system are the same as those described in Section 4.3.3.2, and no further reference is made to them here.

The axial loading system consisted of a diaphragm operated air cylinder (Bellofram Products Company, Type S, Sye 24, Series E), connected to a compressed air supply with a capacity of up to 1.0 MPa. Two pressure regulators (Nullmatic Pressure Regulator - More Instruments Co. Ltd.) installed in series controlled the input pressure to the Bellofram. The Bellofram allowed the magnification of the line pressures by a factor which was equal to the ratio of the internal area of the Bellofram (154.838×10^{-4} m^2 and the cross-sectional area of the sample (approximately 42.0×10^{-4} m^2).

Monitoring Devices

The input pressure to the Bellofram, the vertical displacement of the loading piston, the pore pressures at the top and at the base of the sample, the volume of water that was absorbed or expelled from the sample during thawing and saturation and the temperature of the sample were

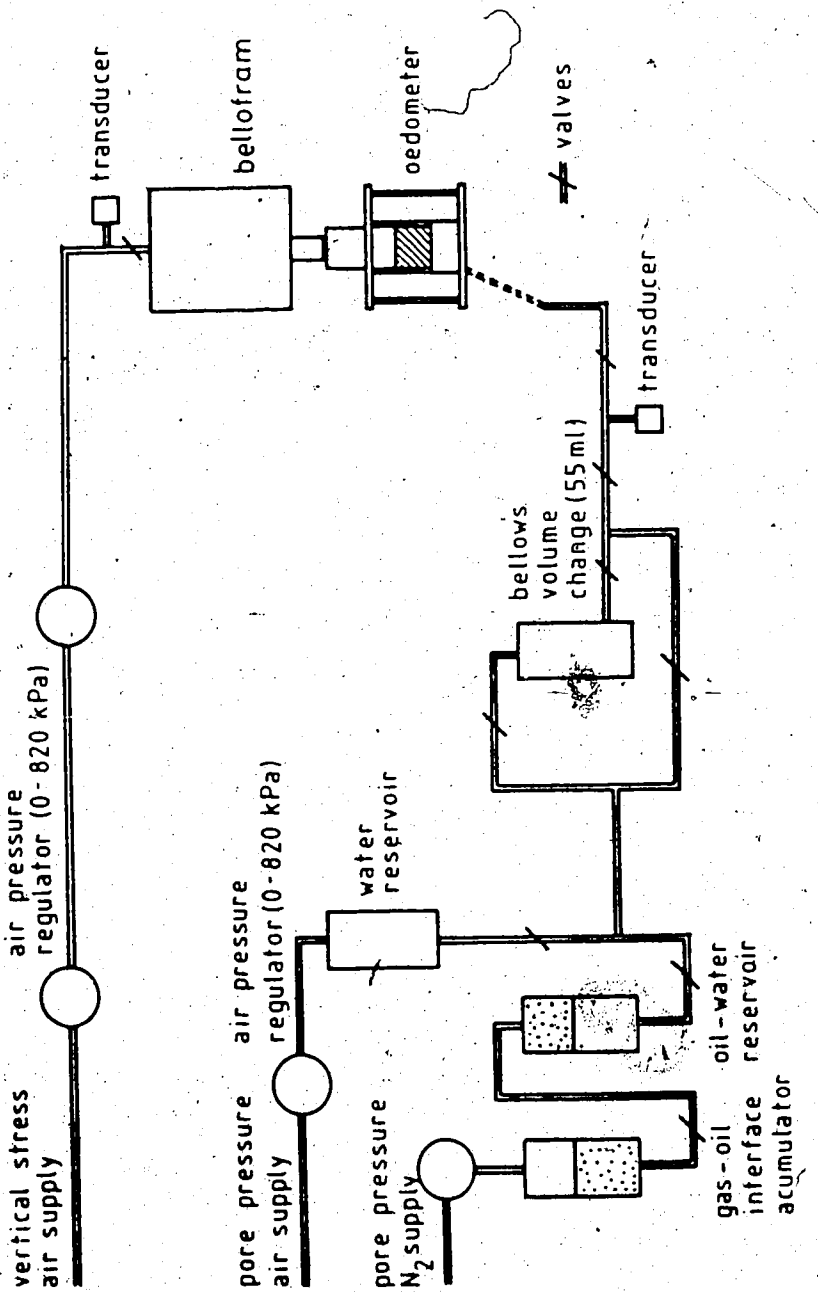

Figure 4.24 Pressure System Schematic for Oedometer Tests

automatically monitored.

A Celesco pressure transducer, type PLC, with a capacity of 1.4 MPa was used to monitor the input pressure in the Bellofram.

A LVDT (Hewlett Packard - 500 - 24 Volts) was attached vertically to the Bellofram piston. It monitored the relative displacement between the loading piston and the top plate of the oedometer cell. The measurement of pore pressures was performed with a Schaevitz, type P273-0025, at the top of the sample, and with a Celesco, type PLC, at the bottom. Both were limited to pressures lower than 2.0 MPa.

The SBEL volume change device used during the drained triaxial tests, described in Section 4.3.3.2, was used to monitor the amount of water that entered or left the oil sand samples during thawing and saturation, prior to the undrained unloading.

Temperature measurements were carried out with a Resistance Temperature Device (RTD) mounted in a stainless steel probe which was inserted in one of the ports of the loading piston, as indicated in Figure E.8.

The electronic output from the monitoring devices was automatically collected and printed by a Fluke 2240B Datalogger.

The calibration of the monitoring devices followed the same procedure described in Section 4.3.3.2.

System Compliance

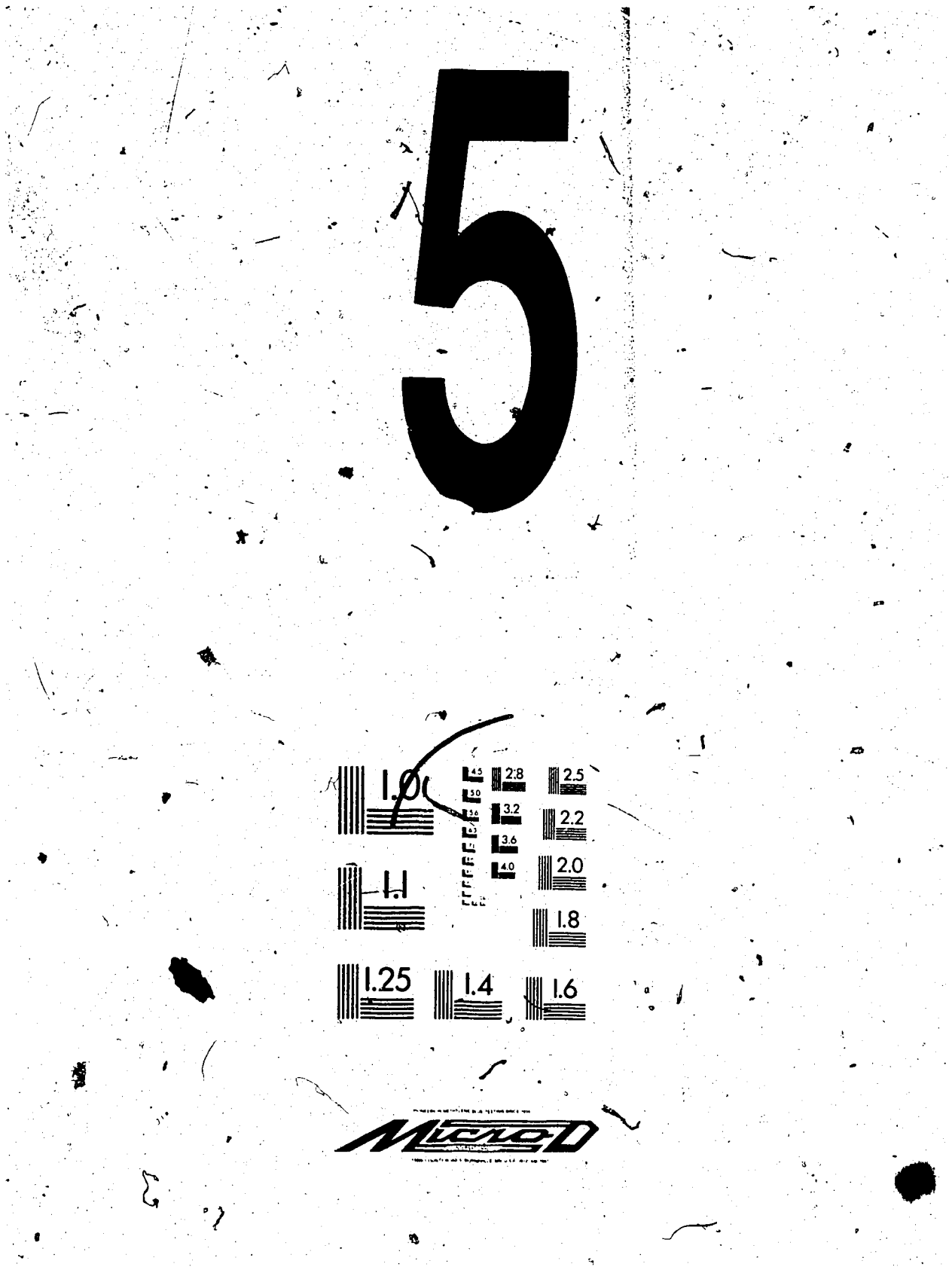
5
1.0
1.1
1.25
1.4
1.6
1.8
2.0
2.2
2.5
2.8
3.2
3.6
4.0
4.5
5.0
5.6
MICROCOPY

Calibration tests were performed in order to relate properly the readings from the monitoring devices with the actual physical quantities that occurred in the sample being tested.

These calibration tests aimed at evaluating the following:

1. Vertical compliance of the cell due to application of vertical loads.
2. Volumetric compliance of the back pressure systems.
3. Temperature effects on the vertical displacements of the piston and on the pore pressure.

The vertical compliance of the system was evaluated through the vertical compression of two materials of well known compressibility properties: aluminum and water. The vertical displacement measured by the LVDT mounted on the Bellofram piston was compared with the theoretical displacement for that specific vertical load. The difference between the two readings gave the vertical compliance of the system.

Non-measureable lateral expansion of the cell took place during the calibration with water and it was assumed that all the water volume change took place in the vertical direction. The assumption proved to be good since the calibrations with water and aluminum, yielded identical vertical compressibility of the system: 0.0002 mm/kPa.

The calibration for the volumetric compliance of the back pressure system was performed with the pressurization of the back pressure lines, maintaining the inlet valve at

the base of the oedometer cell closed, and measuring the associated volume changes. For back pressures higher than 350 kPa, the volumetric compressibility of the system proved to be approximately constant with an average value of 0.0015 cc/kPa.

During the calibration for the system compliance, it was verified that, when the cell was filled with water, the vertical displacements and the back pressure measurements were affected by fluctuations in the temperature of the cell. No direct relationship between temperature and measurement was found; however, it was possible to conclude that for a change in the cell temperature of 1°C, a change of less than 0.005 mm in the vertical displacement and less than 1 kPa in the back pressure, was observed. These corrections were neglected as a result of very small fluctuations of temperatures that were registered during the oedometer tests.

Piston Friction

As illustrated in Figure E8, the loading piston travels inside the oedometer ring, making contact with it through two 'O-ring' seals, installed on the piston. During the unloading steps of the oedometer tests, discussed in the next section, the piston initially moves up, as a result of the expansion of the gas phases, generating downward friction between the 'O-rings' and the walls of the cell.

Towards the end of the unloading steps, as the gas evolution process achieves a point of equilibrium, the

piston gradually stops moving. Bearing this mechanism in mind, it was decided to evaluate the piston friction by filling the cell with water and pressure testing, both loading and unloading it in the undrained mode. The difference between the monitored back pressure and the vertical load was the friction developed. The friction values obtained in the unloading of the piston should be used for the test data reduction. However, due to small fluctuations of the back pressure at stages of calibration where the piston was close to achieving a point of equilibrium, a reversal of the direction of movement of the piston was frequently observed. This fact resulted in the change of the value of the piston friction and, depending on the magnitude of the pressure fluctuation, a reversal of the direction of the resultant of the friction was observed. This fact imposed a major difficulty in assessing the piston friction during the oedometer tests, where similar random pressure fluctuations occurred. Notwithstanding this difficulty, a series of extensive calibration tests were performed, aimed at devising an appropriate procedure to properly assess the piston friction during the tests. Unfortunately, these calibration tests were not conclusive. They indicated, however, that the friction values were always lower than 70 kPa (translated into vertical pressure acting on the sample) for back pressures up to 1.3 MPa and lower than 40 kPa for back pressures up to 0.4 MPa.

Due to the uncertainties associated with evaluating this quantity, the piston friction was not computed in the evaluation of the vertical loads acting on the samples.

Sample Preparation for Testing

The trimming of the samples for the oedometer testing followed exactly the same procedure presented in Section 4.3.3.3 for the preparation of samples for the drained triaxial tests. After being trimmed and prior to assembly in the cell for testing, the samples were cooled to -78°C.

As opposed to the drained triaxial tests, the sample assembly in the cell occurred in the laboratory, at room temperatures. This was possible due to the small amount of time needed for this activity.

Before being positioned into the test cell, a "Rylon" ring was fitted onto the sample, which should provide a low-friction interface between the sides of the sample and the cell walls. The "Rylon" cylinder had a 1.2 mm wall with a height of 35 mm, and outside diameter of 76.2 mm. The samples were trimmed with dimensions that allowed them to fit tightly into the "Rylon" cylinder. The samples were slightly higher than the "Rylon" cylinder in order to avoid contact between the latter and the loading piston.

A #100 wire mesh was placed on the cell pedestal where the samples were placed for testing.

The loading piston was inserted into the oedometer cell until it made contact with the top of the sample. The monitoring devices were mounted in the cell and the two pore

pressure transducers deaired. At this stage, the samples were starting to thaw and ready to be saturated.

Testing Techniques

On three separate occasions, with three different samples, the oedometer cell was prepared for testing. Unfortunately, twice the tests had to be interrupted due to leaking of water between the piston and the cell walls. Therefore, only one test (Sample 11-5) was properly performed. Due to reasons described later in this section, it was decided not to perform any additional tests in the oedometer cell.

As opposed to the procedure described above, Sample 11.5 was installed in the oedometer cell without the "Rylon" cylinder around it. At the time of the sample installation in the cell it was realized tht the "Rylon" cylinder had expanded slightly laterally, and did not fit in the oedometer cell. By comparing the sample diameter, given in Table 4.12, with the cell internal diameter it is possible to evaluate the gap left between the sample and the cell. This gap was prejudicial to the performance of the test. The sample expanded laterally in order to fill this gap and, as a result of vertical compression of the sample during thawing and saturation, it underwent shear strains in the order of 10%; hence, well above the failure shear strains usually observed in oil sands.

Table 4.12 depicts the pressures applied to the sample, and for what extent of time, during its thawing and

SAMPLE NO.	DIMENSIONS OF FROZEN SAMPLE			THAWING AND SATURATION				CHARACTERISTICS BEFORE UNDRAINED UNLOADING			
	DIAM. (CM)	HEIGHT (CM)	VOLUME (CC)	VERTIC. PRESS. (KPA)	PORE PRESS. (KPA)	TIME (HOUR)	WATER INTAKE (CC)	TOTAL VOLUME (CC)	VOID RATIO	FLUID SATURAT.	
										Sbit	Swat
11-5	7.311	4.318	181.26	130	56	19	6.126	160.026	0.679	68.3	31.7
				1400 TO 1700	1200 TO 1400	5					
				1100	900	65					
				1600	1500	24					

Table 4.12 Undrained Oedometer Test - Sample Characteristics

saturation. Careful monitoring of the water that entered the sample and the vertical displacement of the loading piston during thawing and saturation, allowed evaluation of the physical properties and total volume of the sample at the beginning of the undrained stage of the test. These values, shown in Table 4.12, are of extreme importance for the appropriate test data reduction.

The volume of water intake during thawing and saturation was confirmed by the extraction tests performed after testing.

After sample saturation was confirmed by a series of consecutive "B" tests, the back pressure line was closed and the unloading phase of the test started. At this point, the sample had a vertical effective stress of approximately 100 kPa and a pore pressure of approximately 1500 kPa, well above the expected bubble point pressure. The vertical stress was then decreased in steps that varied between 50 and 200 kPa. Full stabilization of pore pressures and vertical displacements of the loading piston was a condition to be observed before modifying the load on the piston for the following unloading step.

Test Results - Presentation and Analysis

The external vertical pressures, the pore pressures and the volume changes that occurred during steps A to F of the test with sample 11-5 are plotted versus time in Figures C.50 to C.55. The lettering of the unloading steps refers to steps that produced a measurable time-dependent volume

increase of the sample.

The volumes of free gas were evaluated from the vertical displacement of the loading piston. These measurements were corrected for the vertical compliance of the apparatus and for the estimated combined compressibility of the bitumen and water phase, which was assumed to be 4.5×10^{-7} kPa^{-1}, based on the compressibility measurements of oil sand pore fluids by Agar, 1984:197. The compressibility of the pore liquids proved to have little effect on the test data corrections. No corrections on the monitored quantities were made due to temperature fluctuations which according to Figures C.50 to C.55 were extremely small.

The initial and final values of external vertical stresses, top pore pressure, gas volume changes and degree of saturation are summarized in Table 4.13. The differences between the values of vertical stresses and pore pressures presented in this table are attributed to the piston friction. At the beginning of Phase A, the effective stress within the sample was probably zero.

Except for Phase B, the external vertical stress during the test was maintained fairly constant, with variations of ± 5 kPa. The variability of the piston friction resulted in a continuous and slow increase in the pore pressure, which, as discussed earlier in this section, makes it impossible to appropriately evaluate the gas evolution transient parameters.

STEP	VERT. STRESS (KPA)		TOP PORE PRESS (KPA)		VOLUME FREE GAS (CC)		DEGREE OF SATURATION	
	INITIAL	FINAL	INITIAL	FINAL	INITIAL	FINAL	INITIAL	FINAL
A	319.59	292.48	420.94	408.50	0.4528	0.5944	0.9929	0.9907
B	292.48	282.85	408.50	399.37	0.5944	0.8545	0.9907	0.9868
C	282.85	245.71	399.37	379.97	0.8545	1.1797	0.9868	0.9819
D	245.71	199.29	379.97	323.84	1.1797	1.8836	0.9819	0.9715
E	199.29	153.30	323.84	282.80	1.8836	2.6073	0.9715	0.9611
F	153.30	54.26	282.80	154.01	2.6073	6.5141	0.9611	0.9084

Table 4.13 Gas Evolution Undrained Oedmeter Test - Sample 11-5

As one can notice from Figures C.50 to C.55, the identification of the actual completion of an unloading step was not an easy task. Except for steps A and B, that produced small quantities of gas, a test step was considered completed when all readings had been stable for approximately 12 hours. The sudden drop in pore pressures observed in Step D, was a result of a sudden drop in the external vertical stress, as a result of a malfunction of the air compressor, which was promptly fixed.

The comparison of the volumes of gas produced immediately after the change of the vertical stress and volume of gas produced with time allowed the preparation of Figure 4.25. It illustrates, for high degrees of saturation, the gas volume changes related to transient processes are responsible for the great majority of the total measured volume changes, as expected. The immediate volume change response refers to the reading taken 2 minutes after the change in vertical load, in order to account for the inertia of the movement of the loading piston.

The equilibrium water pore pressures and volumes of free gas listed in Table 4. [illegible]e plotted in Figure 4.26. This data allows the evalu[illegible] of the combined solubility coefficient of the pore gases into the pore liquids. According to the demonstration in Appendix D, the solubility coefficient is given by:

$$H = \frac{P_{atm}\Delta V_{fg}^{Patm}}{V_i \Delta P} \qquad [D9]$$

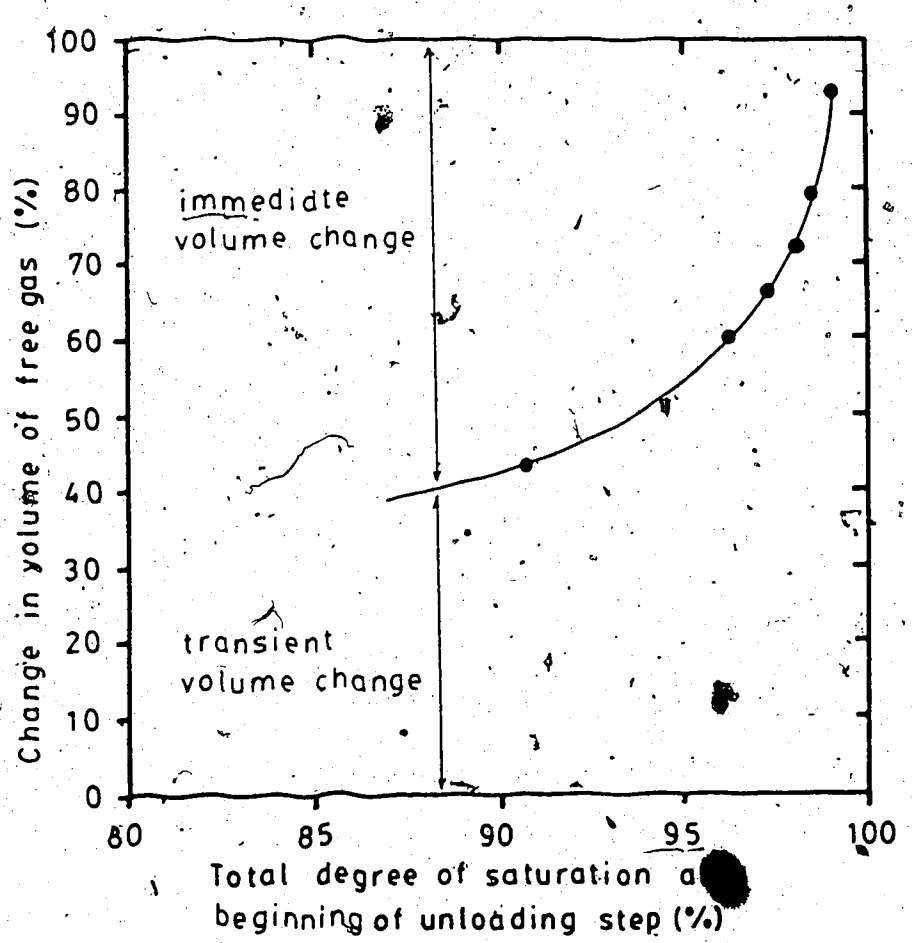

Figure 4.25 Undrained Oedometer Test - Sample 11-5 - Gas Production

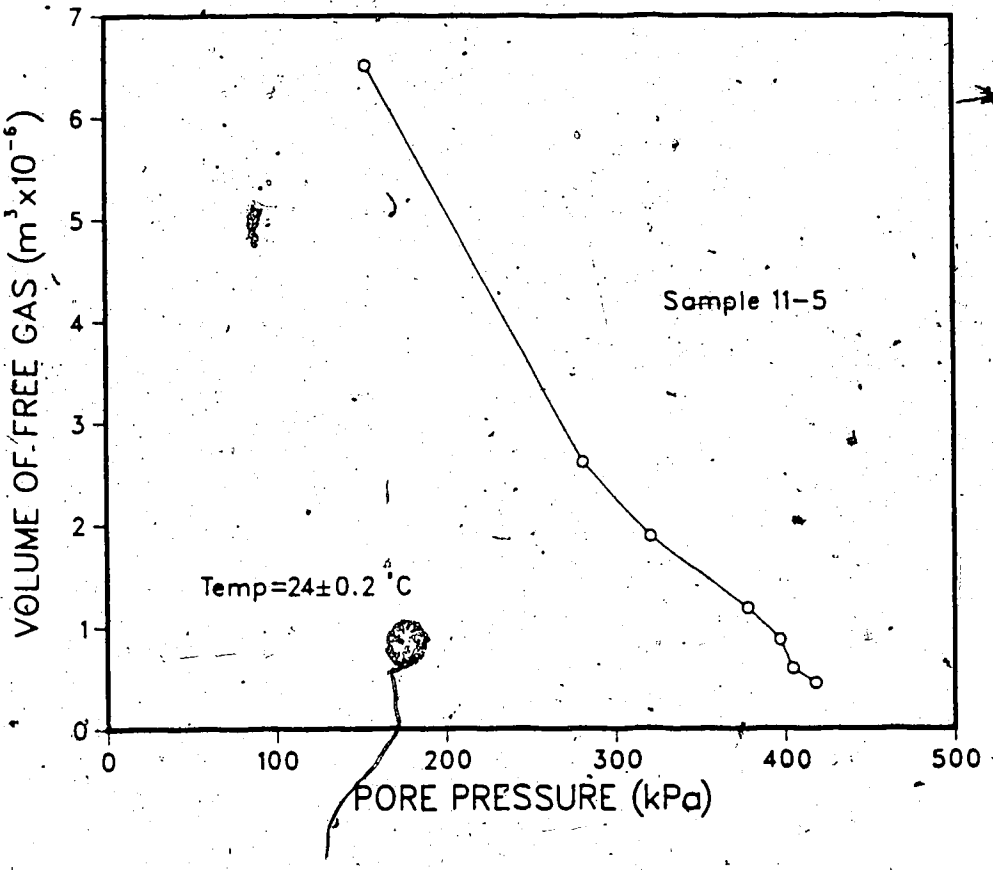

Figure 4.26 Undrained Oedometer Test - Sample 11-5 - Equilibrium Response

where

P_{atm} = atmospheric pressure

ΔV_{fg}^{Patm} = volume change of free gas measured at P_{atm}

P_1, P_2 = equilibrium initial and final absolute pore pressures, respectively

$\Delta P = P_1 - P_2$

V_L = volume of pore liquids

It indicates that the slope of the plot $(\Delta V_{fg}^{Patm}/V_L)$ versus ΔP, times the atmospheric pressure is equal to the solubility coefficient. Figure 4.27 presents this type of plot for sample 11-5, which was prepared with data depicted in Table 4.14. The variability of the solubility coefficients observed in this table are accounted for by the inaccuracies of the measurements of the volume of free gas at the early stages of the test. The uncertainties in the evaluation of the solubility coefficient are increased by the fact that the actual volume of liquids involved in the gas evolution process might be larger than the volume of the pore liquids. The water contained in the cell, the pressure transducers and the pressure lines outside the sample was evaluated to be about 6 cc. If one assumes that bubbles form in these locations, the amount of water should be accounted for in the solubility evaluation. A more comprehensive analysis on the measurement of the solubility coefficient is presented in Section 4.3.4.3.

The impossibility of independently measuring the transient and the time-independent gas volume change was the

GAUGE PORE PRESSURE (KPA) (1)	ABSOLUTE PORE PRESSURE (KPA) (2)	VOLUME OF FREE GAS (CC) (3)	VOLUME OF FREE GAS AT PATM (CC) (4)	(4)/VL (*) (5)	CHANGE IN (5) (6)	CHANGE IN (2) (7)	SOLUBILITY COEFFICIENT (8)
417.94	519.27	0.4528	2.3205	0.0359			
					0.0100	13.57	0.0747
404.37	505.70	0.5944	2.9666	0.0459			
					0.0202	7.46	0.2744
396.91	498.24	0.8696	4.2760	0.0661			
					0.0201	19.14	0.1064
377.77	479.10	1.1799	5.5790	0.0862			
					0.0351	56.97	0.0624
320.80	422.13	1.8836	7.8470	0.1213			
					0.0309	39.40	0.0795
281.40	382.73	2.6073	9.8484	0.1522			
					0.1008	128.06	0.0798
153.35	254.67	6.5154	16.3725	0.2531			

(*)...VL = VOLUME OF PORE LIQUIDS = 64.70 CC

Table 4.14 Undrained Oedometer Test - Sample 11-5 - Calculus of the Solubility Coefficient

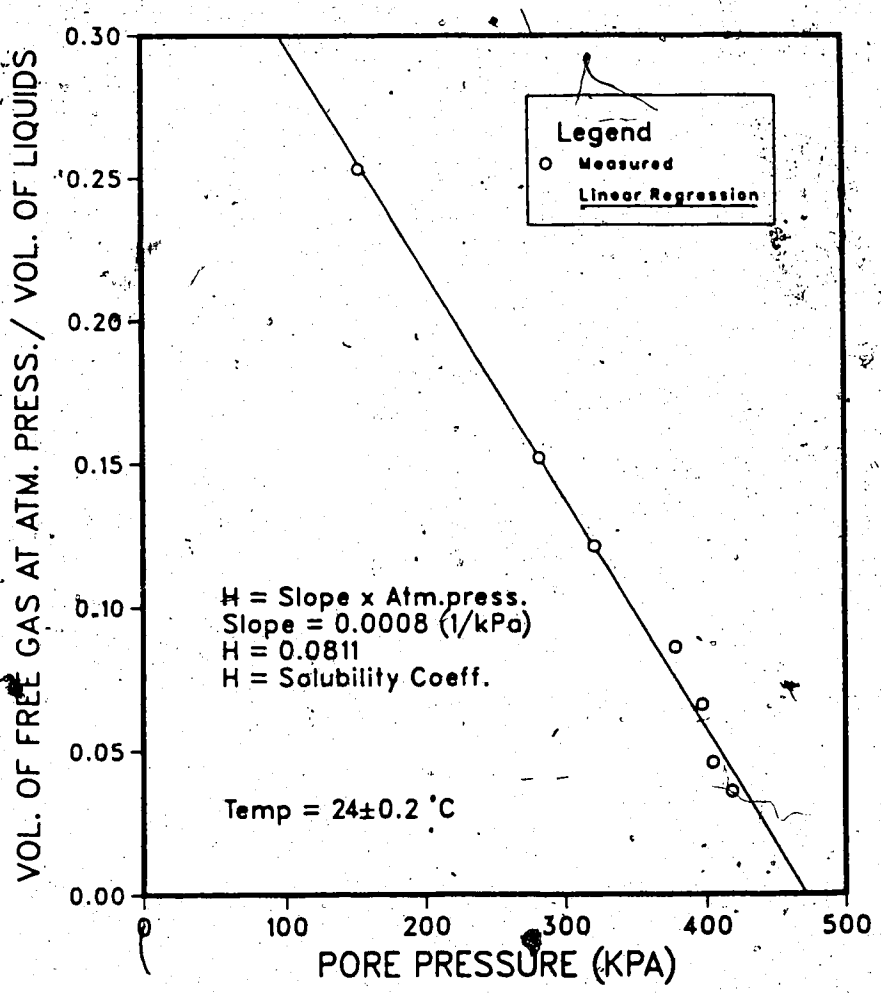

Figure 4.27 Undrained Oedometer Test - Sample 11-5 - Solubility Coefficient

major incentive to look for other means of testing the undrained mechanical response of oil sands. The following section describes the mercury triaxial tests in which the task was successfully performed.

4.3.4.3 Undrained Mercury Triaxial Tests

As it was impossible to maintain the pore pressures constant during the undrained unloading steps performed with the oedometer cell, the appropriate analyses of the time-dependent response of Sample 11-5 was very difficult. The test results indicated that the oedometer cell had the advantage of allowing no losses of gas from the cell, when compared to the triaxial tests performed by Sobkowicz, 1982, but, as opposed to the latter, it did not allow control of the pressure boundary conditions (vertical pressures acting on the sample and pore pressures).

A review of the systems used to perform tests on partly saturated soils indicated that the use of mercury as a cell fluid would efficiently inhibit the gas diffusion from the membrane into the triaxial cell fluid. Sobkowicz discarded the possibility of using mercury due to its electrical conductivity that would damage the electrical transducers used inside the cell for measuring lateral and axial deformations.

The use of a jacket surrounding the sample, with mercury, in triaxial cells, was reported by Bishop and Donald, 1961; Schuurman, 1966; Black and Lee, 1973, Fredlund, 1973 and Bishop and Henkel, 1978. Based on the

success reported by these authors it was decided to implement this approach to the testing of gassy specimens.

Two triaxial testing systems were designed to perform the gas evolution tests. These tests consisted of submitting the samples to isotropic undrained unloading steps, with the samples subjected to "near zero" effective stresses, similar to the procedure followed with the oedometer tests. The following sections present a detailed description of the triaxial cells, pressure systems, monitoring devices, testing techniques and results.

Triaxial Cells

Two Wykeham Farrance, WF40020, triaxial cells were used for the mercury triaxial tests. The cells were capable of withstanding pressures up to 14 MPa. The sample pedestals were specially designed to accommodate the stainless steel jacket, as illustrated in Plates 4.12 and 4.13. Figure E.10 presents further details about the sample pedestal. It was machined in stainless steel in order to avoid corrosion of metals in contact with mercury. Two ports were provided at the base of the sample. One was connected to the back pressure line and the other to the pore pressure transducer line. A #200 wire mesh was installed between the base of the sample and the pedestal in order to minimize the migration of bitumen and grains into the pore pressure lines. Paper filters and porous stones were avoided in this set up in order to minimize the sites outside the sample where bubbles could nucleate.

Plate 4.12 Mercury Triaxial Cell - Stainless Steel Jacket

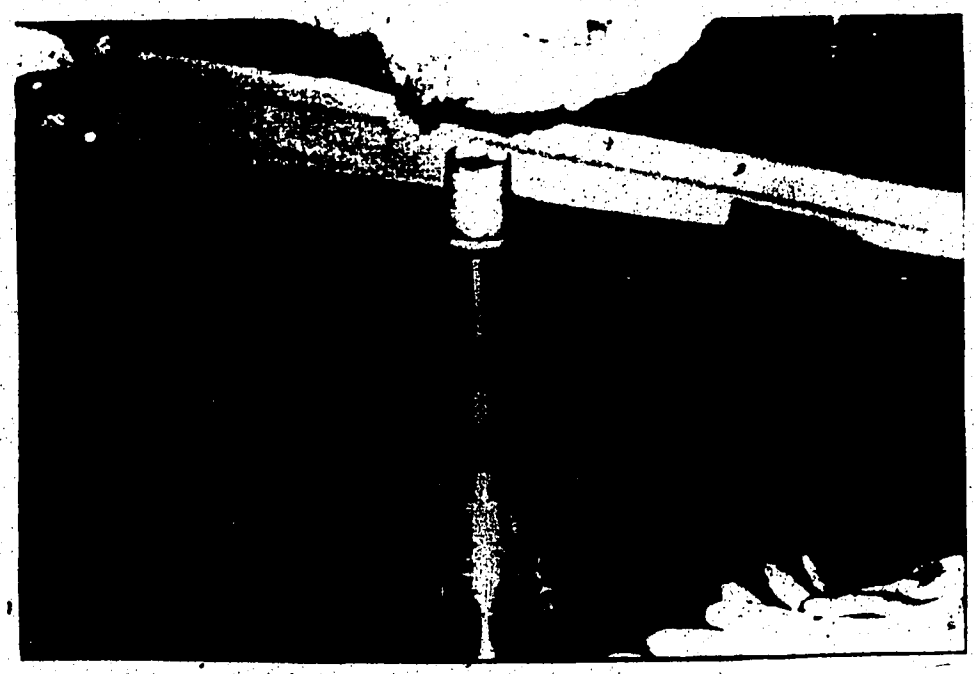

Plate 4.13 Mercury Triaxial Cell - Stainless Steel Jacket and Sample

Pressure Systems

Figure 4.28 presents the schematic of the pressure systems designed to allow the simultaneous performance of two mercury triaxial tests. This figure shows the two triaxial testing cells, three volume change devices, two high pressure (>1 MPa) N_2 independent lines (B and F) and four low pressure (<1 MPa) air independent lines (A, C, D and E).

The two N_2 lines allowed the application of cell pressures and back pressures higher than 1 MPa to either one or the other cell. They were used to saturate the samples.

After the sample saturation was completed and the high pressures were not required any longer, the low pressure air system was activated for that particular cell by setting the appropriate valves. Air regulators, A and D, controlled the cell pressures in cells 1 and 2, respectively, and air regulator C controlled the back pressures in either cell. This set-up, thus, allowed the simultaneous saturation of samples in both cells, one at higher pressures and the other at lower pressures.

Air regulator E was used to pressurize the water refilling reservoir in order to speed up the refilling of the oil-water reservoirs. Each of the N_2 and air pressure systems were assembled with materials and methods identical to those described in Section 4.3.3.2. A general view of the mercury triaxial test system is presented in Plate 4.14.

Monitoring Devices

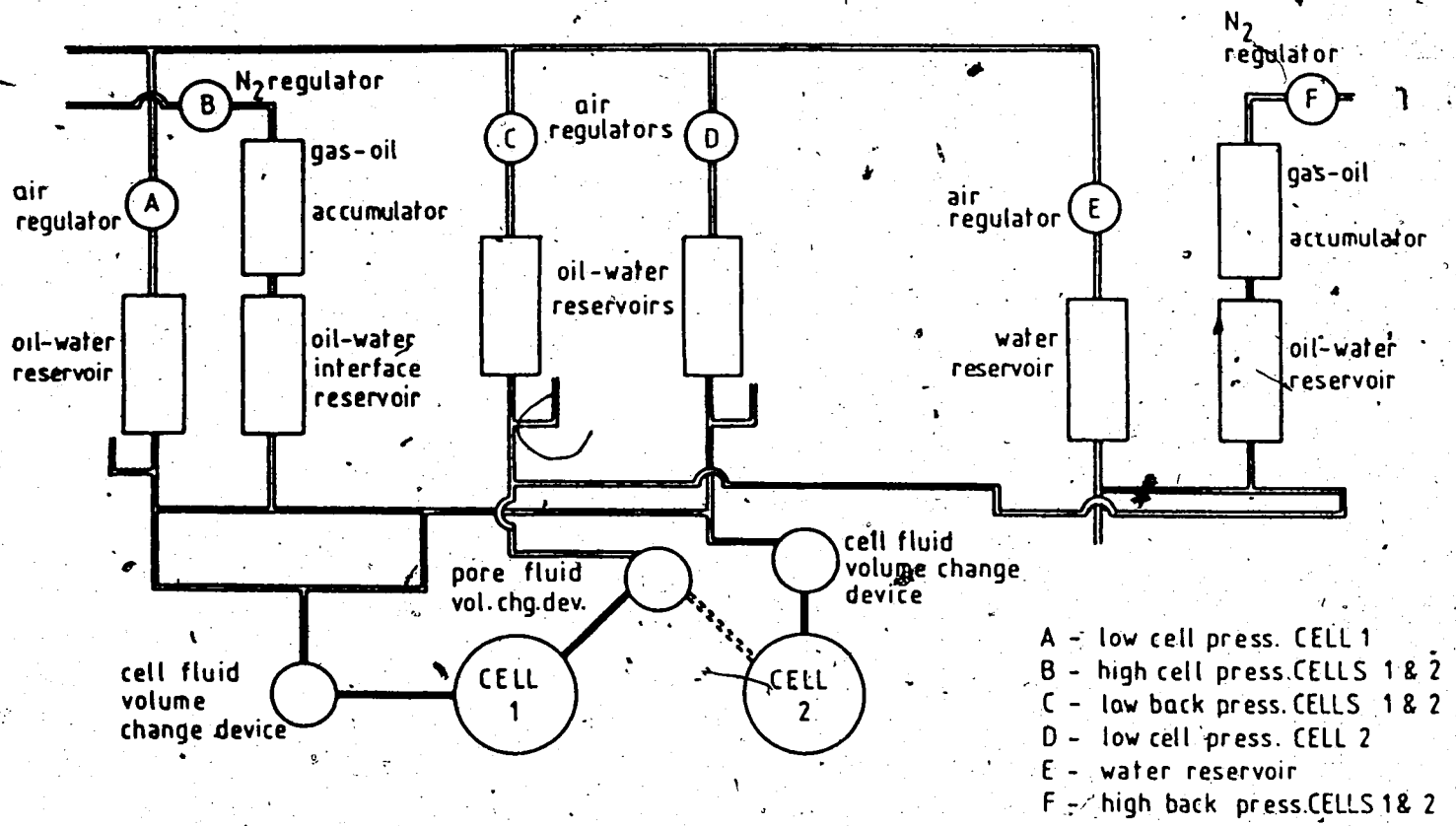

Figure 4.28 Pressure System Schematic for Gas Evolution Tests

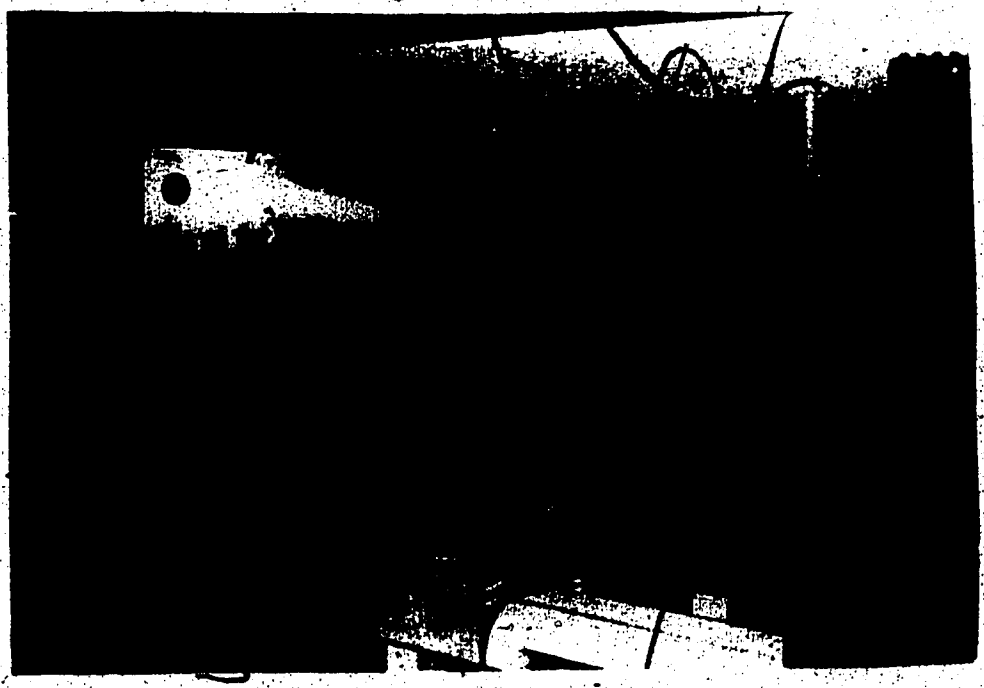

Plate 4.14 Mercury Triaxial Testing System

For each of the triaxial cells, the cell pressures, back pressures, cell water volume change and pore water volume change were automatically monitored.

Pressures in Cell 1 were monitored with Schaevitz pressure transducers, type P273-0025. The pore pressure transducer allowed operation in the range of 0-2.0 MPa whereas the cell pressure transducer had a capacity of 3.5 MPa. Pressures in Cell 2 were monitored with Celesco pressure tranducers, type PLC that allowed the measurement of pressures up to 2.0 MPa and 3.0 MPa, for pore pressures and cell pressures, respectively.

Throughout the undrained phases of the tests, the degree of saturation of samples was higher than 85% assuring the discontinuity of the gas phase. Therefore, the measurement of pore pressures refer to the pore water phase.

During the saturation phases, the water that was absorbed or expelled by the sample was monitored by a volume change device similar to the SBEL volume change device referred to in Sections 4.3.3.2 and 4.3.4.2. Figures E.11 and E.12 present schematics of the volume change device designed and machined at the University of Alberta. It differs from the SBEL in the way it separates the downstream from the upstream lines. Instead of steel bellows it uses a rubber membrane. The cell water volume change was also monitored by this device. It enabled the direct evaluation of the volume change of the sample. During the sample saturation both the pore water volume change of the sample

and the total volume change of the samples allowed the evaluation of the degree of saturation. During the undrained loading phases of the tests, the volume change of the sample was related to the expansion of the gas phase and to the compressibility of the fluid phase as discussed later in this section.

The temperature was monitored with an RTD mounted in a stainless steel probe which was attached to the outside of the wall of Cell 2.

The electronic outputs from the monitoring devices were automatically collected and printed by a Fluke 2240B Datalogger.

The calibration of the volume change devices and pressure transducers followed the same procedure described in Section 4.3.3.2.

System Compliance and Temperature Effects

Calibration tests were performed in order to relate the water volume change measurements at the volume change devices with the actual volume of water that entered or left the sample and with the actual volume change of the sample.

The compliance of the back pressure lines was evaluated by pressurizing the line with the valve that connected it to the closed cell. Figure E.13 presents the average measured volume change versus back pressure observed from these calibration tests. Both loading and unloading curves of the tests presented very similar responses except for a small hysteresis of about 0.04 cc over a pressure range of 900

kPa. For pressures higher than 900 kPa, the system presented negligible compliance.

The compliance of the cell pressure system was evaluated by pressurizing an aluminum block that was mounted on the pedestal with the top cap, membranes and "O-rings" used during a regular test. For each cell pressure increment, the theoretical volume change of the aluminum block was deducted from the measured volume change. The difference between the two volume changes was attributed to the compliance of the system. The average unloading curve obtained from the calibration tests is presented in Figure E.14. The loading curves were similar to the unloading curves except for the first loading portion of the test that, due to the presence of air in the system, resulted in higher measured volume changes. During the first loading portion of the tests, it was verified that for relatively low cell pressures, several hours were required for the bubbles to dissolve into the water. This fact agrees with the observations reported by Lee and Black, 1972.

During some of the calibration tests, the cell pressure system presented significant hysteresis in the volume change versus cell pressure curves. For the full range of pressures used during the cell calibration (0-2.0 MPa), differences of up to 1 cc were observed between successive loading and unloading curves. A detailed analysis of the calibration curves revealed that most of the differences observed in the volume changes occurred at the point where the cell

pressures were reversed, going from loading to unloading or vice versa. At this point, the flow of water in the volume change device was reversed as well. The test data also indicated that the higher hysteresis was observed when this change in direction of flow within the volume change device occurred when the internal piston, to which the LVDT was connected, was located in the middle of the travel range.

When the reversal of flow occurred with the piston positioned near the extremes of the travel range, no hysteresis was observed. An examination of the volume change device revealed that when its internal piston is positioned at the middle of the travel range, the rubber membrane, which separates the internal cell into two separate chambers, folds itself into a loose wrinkled shape. At this stage, if the flow of water is reversed, the membrane can accommodate itself into a different shape and as a result, immeasurable volume changes may occur. If the internal piston is close to either end of the travel range, the internal membrane is stretched and this problem does not occur. Due to this fact, care was taken to have the actual tests performed with the piston positioned away from the middle of the travel range.

The volume change measurements were affected by the thermal expansion of the water inside the cell, pressure lines and downstream chamber of the volume change device. This proved not to be a concern for the tests performed during the winter and early spring, when the laboratory

temperatures were approximately constant. However, late in the spring, temperature fluctuations up to ±2°C were observed in the laboratory. The accurate calibration for the temperature fluctuations was difficult because the temperatures measured by the RTD attached to the outside of the triaxial cell were not necessarily the average temperature of the water in the system. Both temperatures would be approximately equal if the room temperature remained approximately constant long enough to allow the equalization of the system temperature with the room temperature. This situation, however, very seldom occurred. A theoretical temperature correction for the thermal expansion of the system water was evaluated. This was possible with the knowledge of the volume of water in the system (approximately 1200 cc) and the knowledge of the coefficient of thermal expansion of water (0.0002 to 0.0003°C^{-1}) which results in a correction factor of 0.30 cc/°C (1200x0.0025). An insulated cover was placed around the cell in order to minimize the temperature fluctuation.

Sample Preparation for Testing

The techniques used for sample preparation were identical to those described in Section 4.3.3.3, except for the fact that, as opposed to the drained triaxial test samples, the mercury triaxial test samples did not have filter paper installed at the sides and at the bottom. Instead, only a #200 [illegible] mesh was placed between the base of the sample and the pedestal. The dimensions of the frozen

samples are depicted in Table 4.15.

Testing Techniques

After the placement of the samples on the pedestal, the cell base was taken from the cold room to the laboratory. The stainless steel jacket was placed around the sample and filled with mercury. The mercury level was high enough to submerge the upper "O-rings" attached to the top cap. The body of the cell was put into place and the cell filled with water. The pressure transducers were installed on the cell and pore lines and deaired before low cell pressures (≈200 kPa) and pore pressures (≈80 kPa) were applied, to allow the sample to thaw. Both pressures were then increased in 50 kPa increments to the pressures depicted in Table 4.15, with the effective stresses kept approximately constant between 50 and 100 kPa.

The times for saturation, indicated in Table 4.15, were significantly higher than the ones used by other authors, as mentioned earlier in this chapter. This was necessary in order to ensure high degrees of saturation at the beginning of the undrained unloading stages of the test. Throughout the thawing and saturation of samples, care was taken in order to guarantee that water was always flowing into the sample, and not leaving it. This procedure should minimize the loss of gas molecules from the sample to the pressure line system. Saturation was verified with a series of "B tests", as described in Section 4.3.3.4.

SAMPLE NO.	DIMENSIONS OF FROZEN SAMPLE			THAWING AND SATURATION				CHARACTERISTICS BEFORE UNDRAINED UNLOADING			
	DIAM. (CM)	HEIGHT (CM)	VOLUME (CC)	VERTIC. PRESS. (KPA)	PORE PRESS. (KPA)	TIME (HOUR)	WATER INTAKE (CC)	TOTAL VOLUME (CC)	VOID RATIO	FLUID SATURAT.	
										Sbit	Swat
3-1	5.100	5.507	112.507	200 TO 1230	80 TO 1150	74	1.11	80.684	0.485	77.3	19.2
4-1	5.106	5.541	113.470	195 TO 1375	75 TO 1270	21	(*)	(*)	(*)	(*)	(*)
4-3	5.085	5.138	104.35	200 TO 850	50 TO 700	19	(*)	(*)	(*)	(*)	(*)
6-4	5.089	5.376	109.334	-	-	-	(*)	(*)	(*)	(*)	(*)
6-5	5.113	5.199	106.725	270 TO 1300	160 TO 1200	92	-3.350 (**)	101.000 (**)	0.551 (**)	64.0 (**)	35.8 (**)
9-2	5.111	4.978	102.113	180 TO 1370	40 TO 1250	94	-5.069	96.000	0.574	71.4	27.1
11-2	5.079	5.228	105.921	270 TO 1500 1500 TO 850	150 TO 1300 1300 TO 750	24 24	7.239	100.581	0.692	72.8	27.2
11-3	5.055	5.319	106.736	200 TO 930 930 TO 550	65 TO 870 870 TO 500	94 24	3.490	95.630	0.688	68.6	31.2
14-3	5.089	5.300	107.103	470 TO 1300	35 TO 1230	72	7.232	107.227	0.628	69.1	28.6

(*) VALVE FAILURE DUE TO MERCURY CORROSION - TEST NOT COMPLETED

(**)- COULD NOT BE PROPERLY EVALUATED DUE TO LEAK IN CELL AND BACK PRESSURE VALVES DURING SATURATION. VALUES ARE TEMPTATIVES.

Table 4.15 Undrained Mercury Triaxial Tests - Characteristics

The volumes of water absorbed during thawing and saturation are presented in Table 4.15.

After saturation was complete, the cell pressures were decreased to values ranging from 600 to 1300 kPa and the effective stresses were maintained constant. The back pressure valve was closed and the undrained phase of the tests started with decreases in cell pressures of approximately 50 kPa. Another decrement in cell pressure was applied after stabilization of pore pressures and sample volume changes. For pore pressures higher than the bubble point pressure, the decreases in cell pressure resulted in time-independent changes in pore pressure and volume changes. In some tests, however, very small time-dependent volume decreases of the sample and decreases in pore pressures were observed during the first unloading stages. This was attributed to the fact, that, during these unloading stages, the samples might not have been fully saturated and the bubbles were still dissolving with time.

Test Results: Presentation and Analysis

According to Table 4.15, nine samples were prepared for testing. They were all trimmed from very uniform samples and theoretically should produce very similar results, since the test procedures were the same for all tests. On four different occasions, the copper valves used in the cell pressure lines failed during the saturation of samples. It was verified that during the procedure of taking the sample apart, after the completion of the preceding test, some

mercury spilled from the stainless steel jacket into the bottom platen and into the cell pressure line. The mercury that entered the cell pressure line was lodged in the copper valves which resulted in their corrosion and subsequent failure. This accident resulted in the loss of three tests: 4-1, 4-3 and 6-4 and the partial loss of test 6-5. For this latter sample, it was possible to substitute the cell and pore pressure valves without complete relief of the pressures. The volume changes of the sample during saturation, however, could not be properly evaluated due to this fact. This is the most likely reason for the unexpected decrease in the volume of water of the sample during saturation, as depicted in Table 4.15.

The data produced by each of the mercury triaxial tests allow the study of the time-independent and the time-dependent response of the gassy fluids, as discussed below.

Time-Independent Response

Tables C.1, C.4, C.7, C.10, and C.13 present the pressures, volume changes and degrees of saturation at the beginning and end of each unloading stage of the test that produced time-dependent gas volume changes. Tests 4-1, 4-3 and 6-4 were not completed and test 14-3 did not produce gas or a time-dependent response. Therefore, these tests are not presented. The low total degree of saturation of Sample 14-3 in the frozen state indicates that the sample might have lost the pore gases during sampling. The absence of gas in

Sample 14-3 is in agreement with its high sampling quality, as shown in Table 4-3. The equilibrium volumes of free gas and the normalized volumes of free gas are plotted versus the pore pressure for Samples 3-1, 6-5, 9-2, 11-2 and 11-3 in Figures 4.29 to 4.38.

The evaluation of the solubility coefficient from the test data was discussed in the preceding section and presented in Appendix D. The calculation of the combined solubility coefficient for each of the unloading stages of each test is presented in Tables C.2, C.5, C.8, C.11, and C.14. The average combined solubility coefficient of all unloading stages was evaluated from the nearly straight portion of the curves plotted on the normalized volume of free gas versus pore pressure graph (Figures 4.30, 4.32, 4.34, 4.36, 4.38). The extrapolation of these straight lines to the horizontal axis allows the evaluation of the theoretical bubble point pressure for each test. Analysis of the aforementioned figures indicate that the actual pressure at which bubbles started to form was significantly higher than the theoretical bubble point pressure. The reason is not exactly known, but might be attributed to the uneven distribution of the concentration of gas molecules throughout the sample. The procedure of saturating the samples at high back pressures results in the shrinking of bubbles to their eventual complete dissolution in the pore liquids. Immediately after sample saturation is attained, the gas molecule concentration at the sites where the

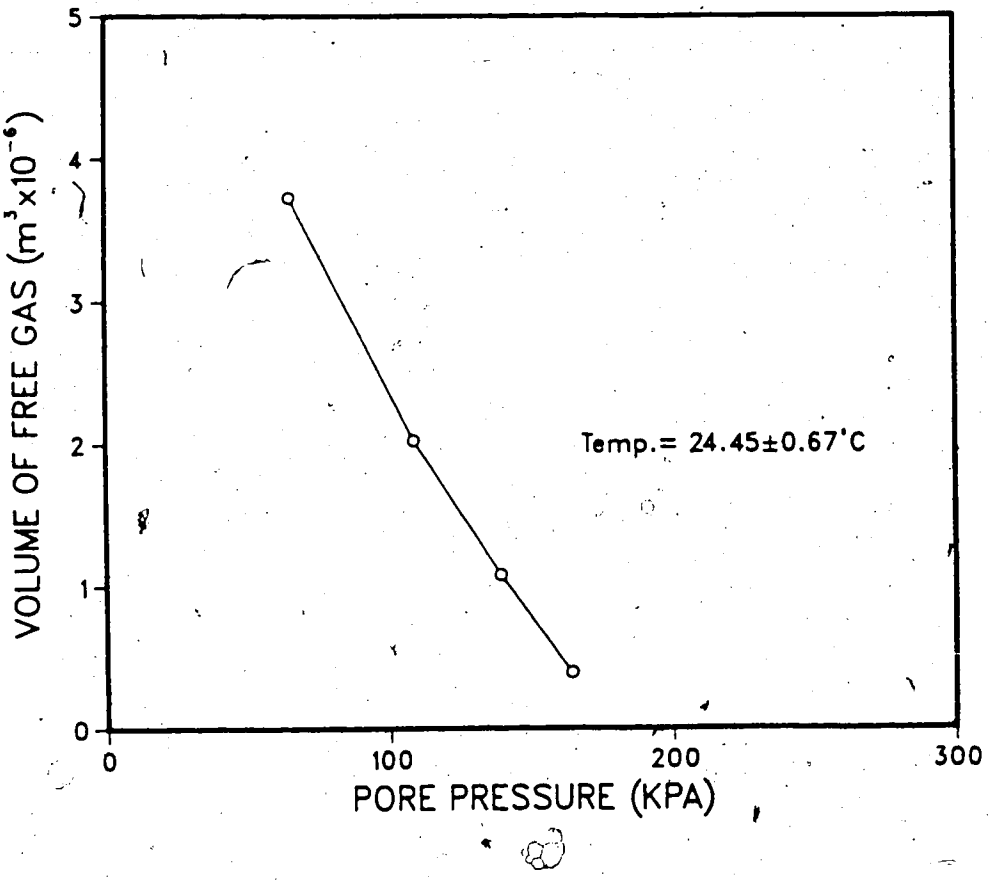

Figure 4.29 Mercury Triaxial Test 3-1 - Equilibrium Response

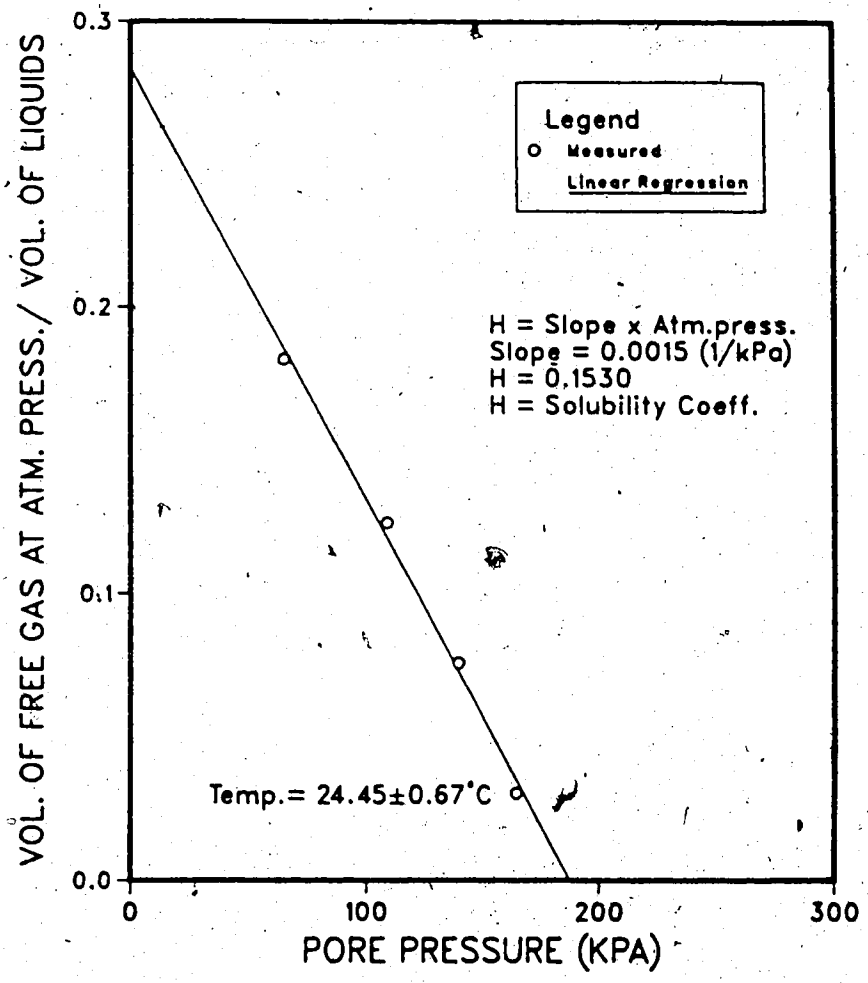

Figure 4.30 Mercury Triaxial Test 3-1 - Solubility Coefficient

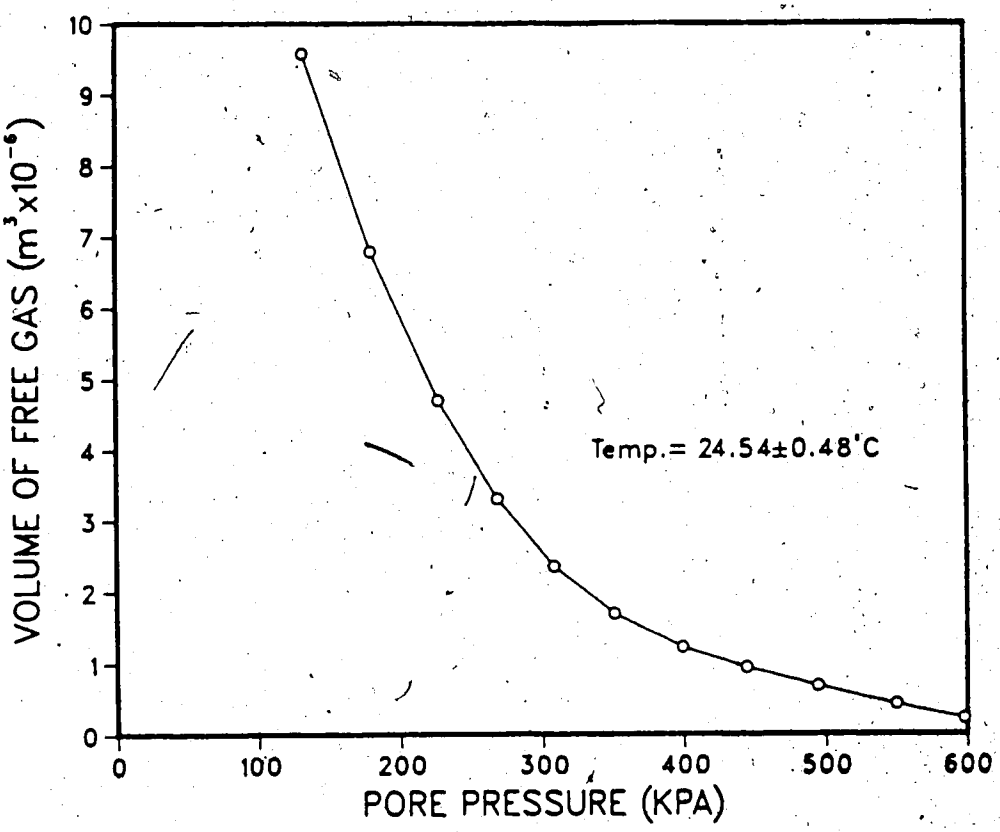

Figure 4.31 Mercury Triaxial Test 6-5 - Equilibrium Response

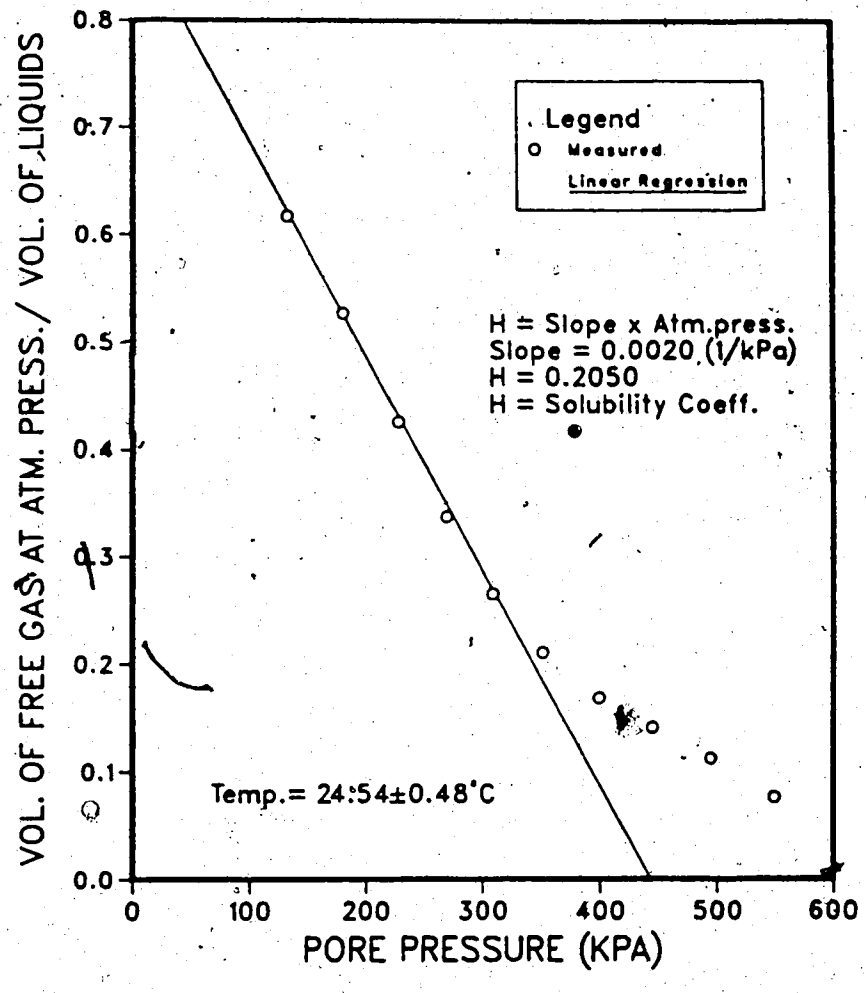

Figure 4.32 Mercury Triaxial Test 6-5 - Solubility Coefficient

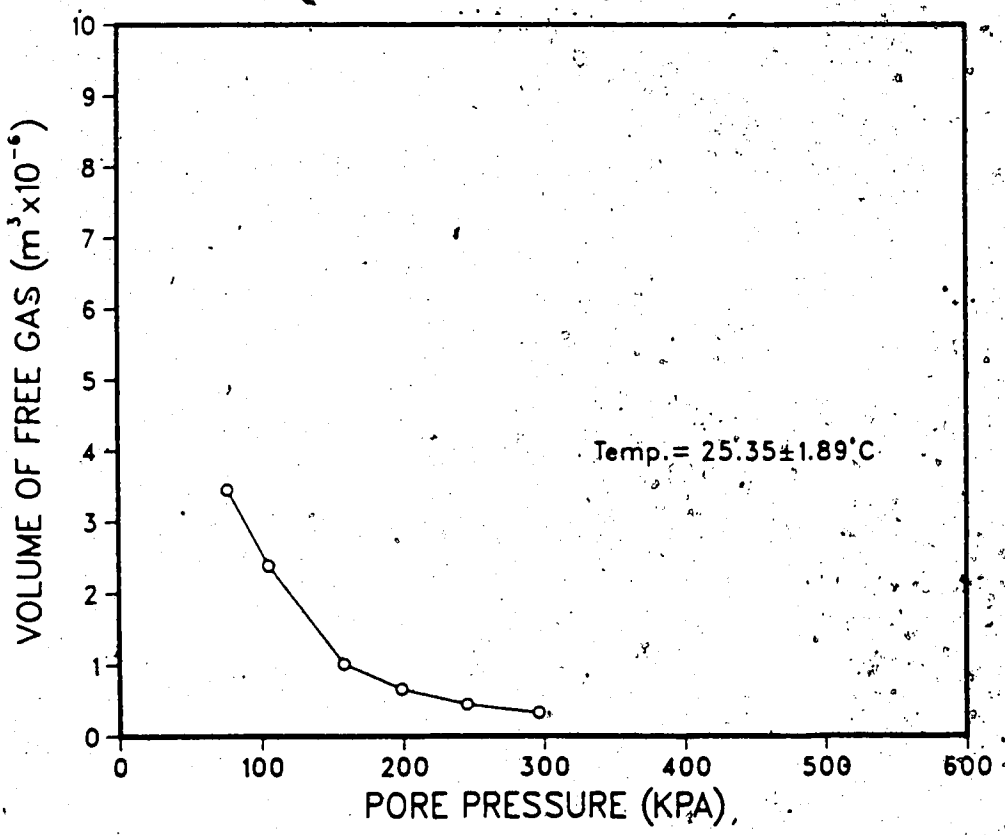

Figure 4.33 Mercury Triaxial Test 9-2 - Equilibrium Response

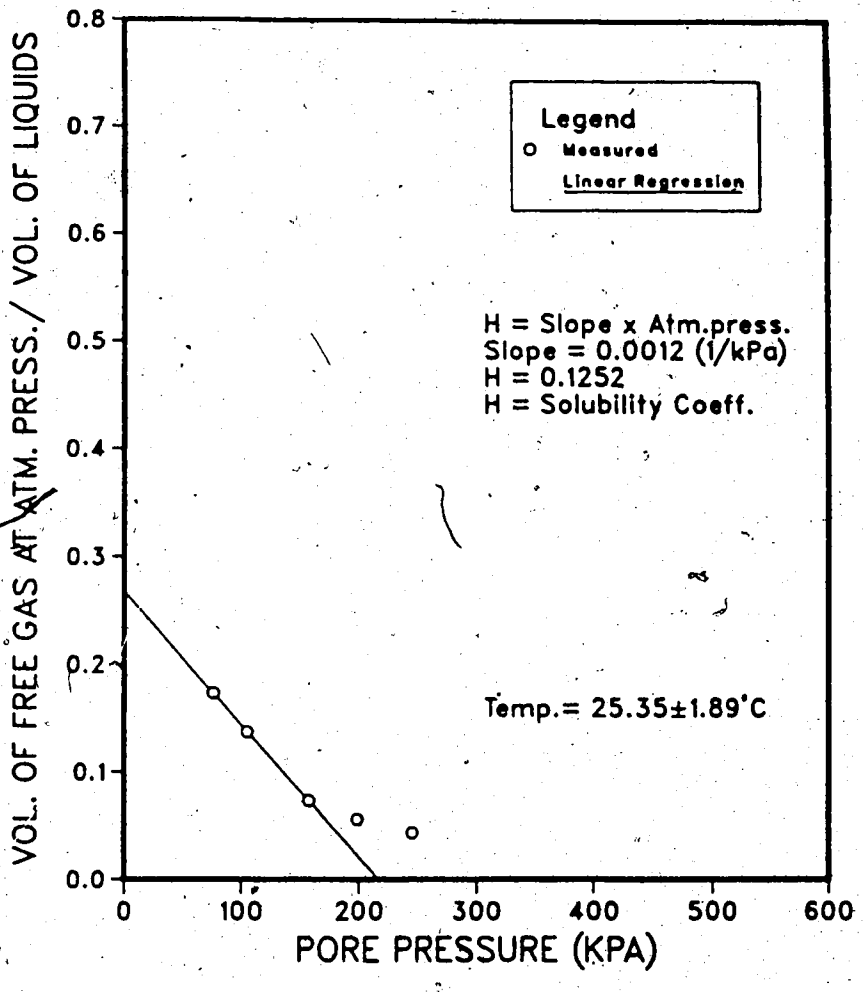

Figure 4.34 Mercury Triaxial Test 9-2 - Solubility Coefficient

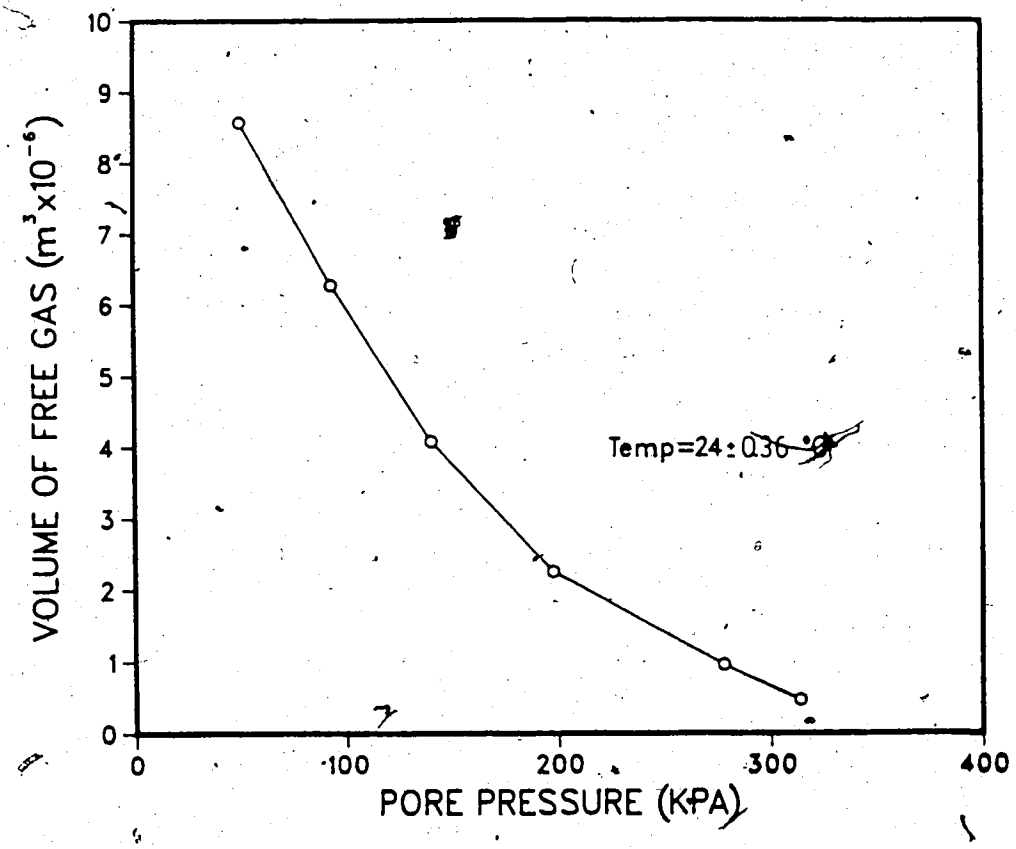

Figure 4.35 Mercury Triaxial Test 11-2 - Equilibrium Response

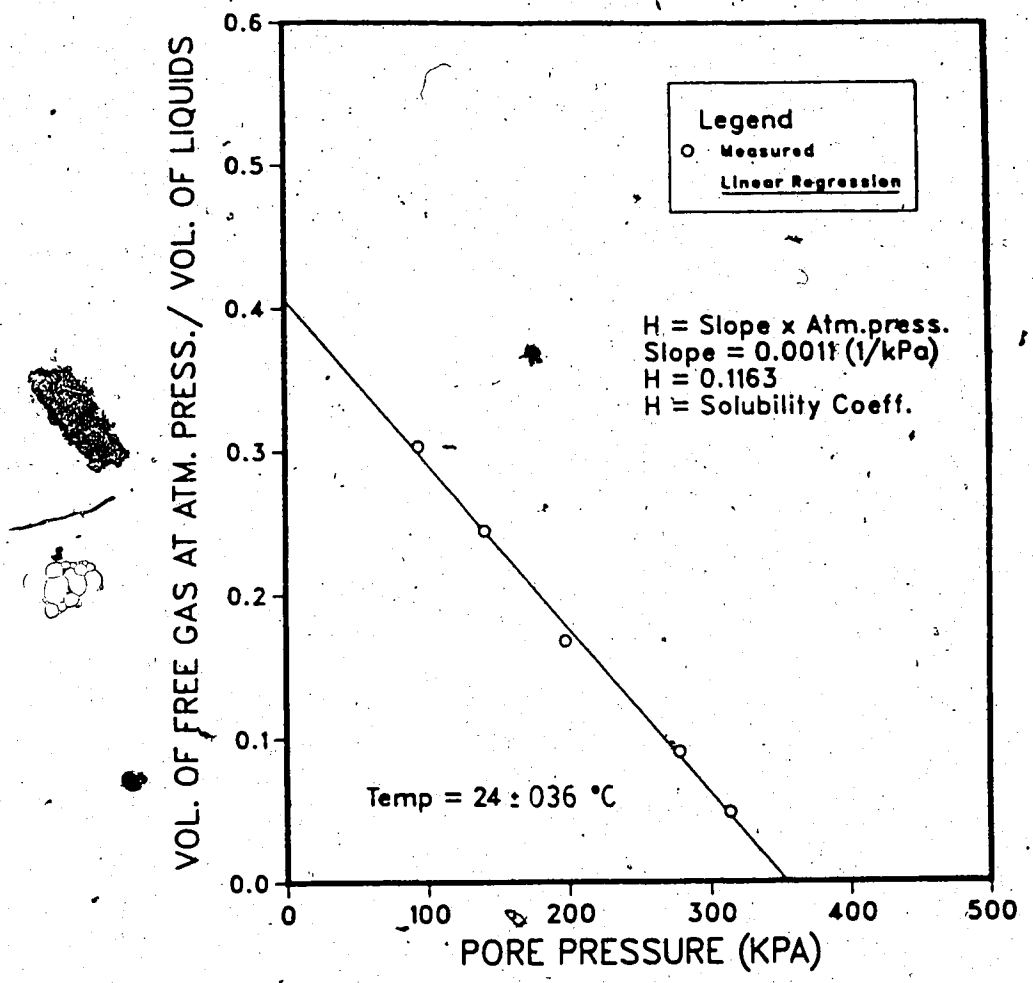

Figure 4.36 Mercury Triaxial Test 11-2 - Solubility Coefficient

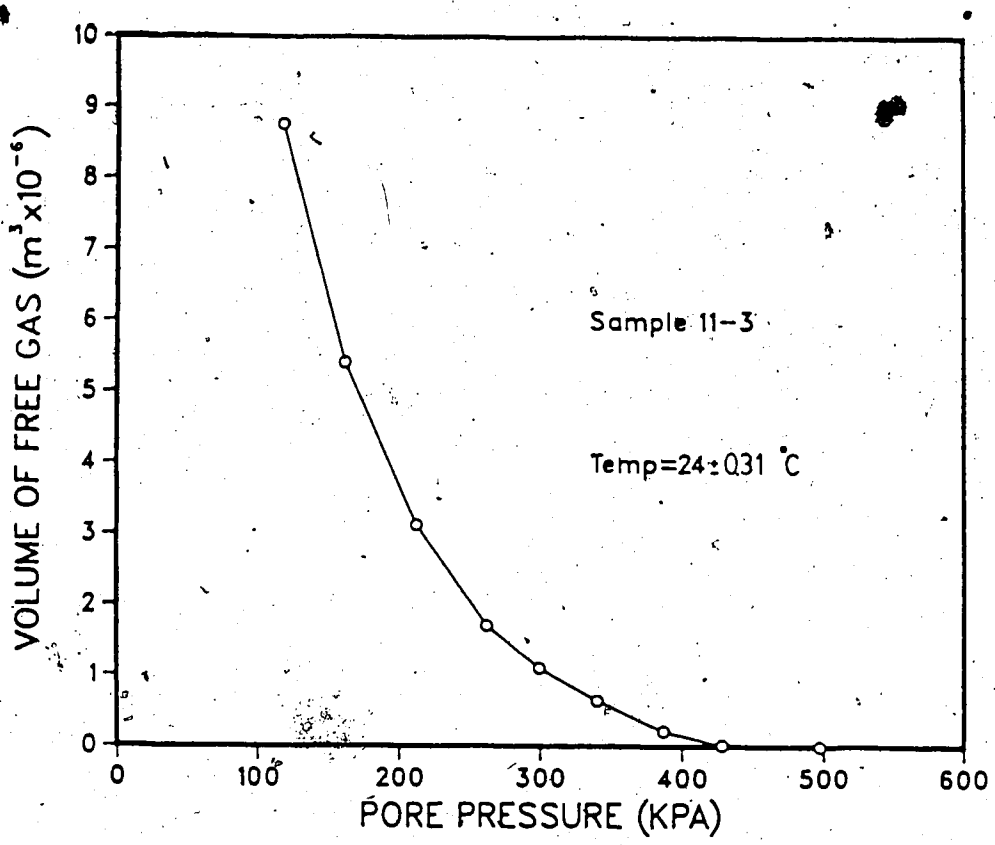

Figure 4.37 Mercury Triaxial Test 11-3 - Equilibrium Response

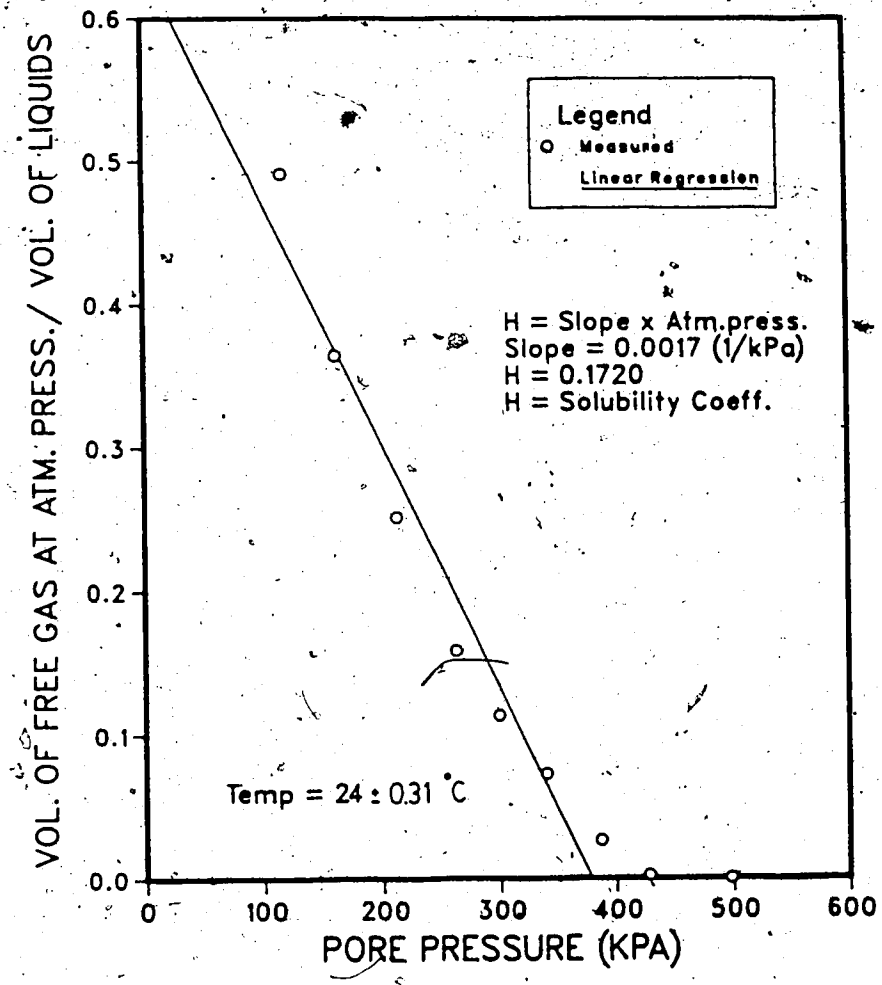

Figure 4.38 Mercury Triaxial Test 11-3 - Solubility Coefficient

bubbles shrunk and disappeared is higher than elsewhere within the pores. Due to the slow diffusivity of gas molecules in bitumen, the diffusion of gas molecules from points of higher to lower concentration is time consuming. Therefore, the time elapsed between the completion of sample saturation and the beginning of the undrained unloading of the samples may not have been sufficient to allow the gas molecules to distribute evenly within the pores. According to Harvey, 1951, as discussed in Section 2.3.1, bubbles can form above the bubble point pressure upon minor fluctuations of the pore pressure, whenever gas molecule concentrations or gas nuclei are present.

If, however, the gas molecules had had enough time to diffuse within the pore liquids and to ensure a uniform gas concentration throughout the sample, the bubble point pressures would probably be very close to the theoretical ones, as discussed earlier. Table 4.16 summarizes the solubility coefficients and theoretical bubble point pressures obtained from both undrained oedometer and mercury triaxial tests. The theoretical bubble point pressures are plotted versus depth in Figure 4.39. Also shown are the hydrostatic pore water pressure from the original ground water level prior to the excavation of the bench and the piezometer readings.

This figure shows that, except for samples 6-5, 9-2 and 14-3, the bubble point pressures obtained are relatively close to the *in situ* original pore pressure, prior to the

SAMPLE	COMBINED SOLUBILITY COEFFICIENT (H)	THEOR. BUBB. POINT PRESSURE (KPa)	TEST
3-1	0.153	187	M.T.T.
6-5	0.205	442	M.T.T.
9-2	0.125	216	M.T.T.
11-2	0.116	353	M.T.T.
11-3	0.172	377	M.T.T.
11-5	0.081	470	O.T.
14-3	(*)	(*)	(*)

M.T.T. - MERCURY TRIAXIAL TEST
O.T. - OEDOMETER TEST
(*) - DEGASSED SAMPLE

Table 4.16 Gas Evolution Tests - Solubility Coefficients and Bubble Point Pressures

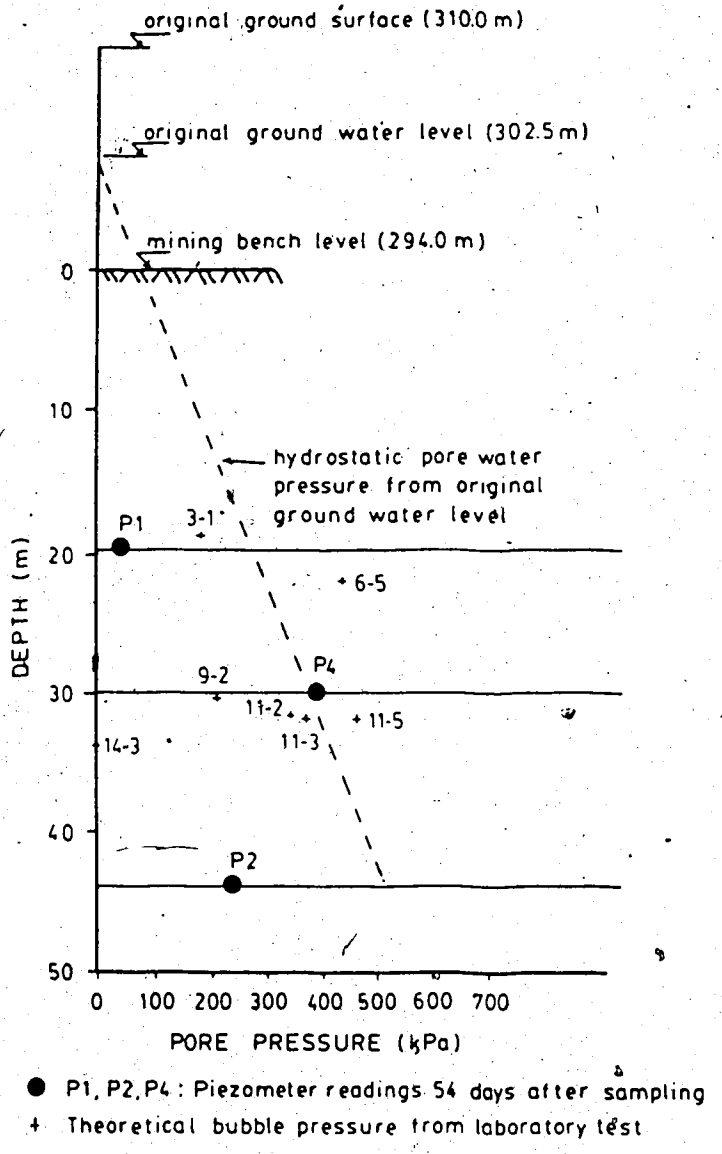

Figure 4.39 Bubble Point Pressures and Measured *in situ* Pore Pressures

bench excavation. This feature was previously observed by Peacock, 1988.

The test on Sample 6-5 experienced leakage during thawing and saturation as described earlier in this section. This accident resulted in difficulties in properly evaluating the volume of water intake, and consequently, the volume of pore liquids required for plotting Figure 4.32. Sample 9-2, on the other hand, was trimmed several weeks prior to testing, and was subjected to losses of gas higher than the other samples that were trimmed not more than 24 hours prior to testing. As discussed earlier in this Chapter Sample 14-3 probably lost the pore gases during sampling.

Excluding these three tests from the bubble point pressure analysis, some scatter in the test results is still noted. The reasons for this scatter are speculative due to the complexity of the phenomenon being observed. Notwithstanding this fact, the following paragraphs describe the errors inherent to the procedures followed.

The observations in the laboratory of bubble point pressures lower than the in situ original pore pressures can be attributed to the fact that during saturation the samples absorb relatively large amounts of water that are air saturated at atmospheric pressure. The extraneous water probably lowered the average gas concentration within the sample which resulted in decreases in the original gas bubble point pressure.

Loss of gas molecules and air contamination during sampling constitute another reason for low bubble point pressures. The degrees of saturation of samples depicted in Table 4.4, after sampling, were about 80% which indicates that the gas bubbles were at least partly connected to the atmospheric gases. Hence, some gas loss and air contamination was inevitable.

Another major source of error in the evaluation of bubble point pressures occurs in the assessment of the volume of liquids used to normalize the volumes of free gas, in the figures discussed above. In these figures, the volume of liquids refers to the volumes of bitumen and water inside the sample pores at the beginning of the undrained unloading stages of the test. Bubble nucleation and growth might, however, take place in the back pressure lines connected to the pore pressure transducer and to the inlet back pressure valve. The volume of water present in these lines was estimated as 3.5 cc. The computation of this extraneous water in the evaluation of the solubility coefficient and bubble point pressure would result in lower parameters than the ones obtained.

Errors in the measurement of sample volume changes due to the formation of air bubbles in the cell fluid was initially considered as a potential source of problems. It was thought that the bubble formation pressures of the cell fluid would change from the initial atmospheric to higher pressures, due to the contamination of air molecules from

the air pressure source. Experiments with the aluminum block and with Sample 14-3, which did not have any gas in solution, showed that the migration of air molecules into the cell pressure system was efficiently prevented by the presence of the silicone oil air-water interface and the rubber membrane of the volume change device.

Errors in the measurement of gas volume changes due to a leak of pore fluids from the sample through the contact between the membranes and top cap and bottom pedestal proved not to be a problem. This assertion is based on a pressure test which showed that the "O-rings" installed outside the membranes, pressing against the top cap and the bottom pedestal, enabled the back pressure to be higher then the cell pressure by 300 kPa, without inducing any leak of water from the sample to the cell.

The solubility coefficients obtained from the mercury triaxial tests, shown in Table 4.16, are also affected by the extraneous water in the back pressure system.

The solubility coefficients varied from 0.08 to 0.21 and are similar to the ones obtained by Meacock, 1988 (0.18 to 0.22), who tested rich Syncrude oil sands at approximately 24°C. The temperatures during the mercury triaxial tests oscillated about 24°C, as indicated in Figures 4.29 to 4.38, with the exception of the tests on samples 9-2 and 14-3, where the temperature oscillated about 25°C.

As discussed in Chapter 2, Section 2.2.1, it is possible to calculate the theoretical combined solubility coefficient if the composition of gases and liquids and the individual solubility constants of each gas component for each liquid are known. The combined solubility coefficient is given by Equation 2.64 which, with the assumption that

$$\frac{n_{dgi/TOT}}{n_{dg/TOT}} = GF_i \qquad [4.47]$$

= volume fraction of gas i.

For the fully saturated liquid (no free gas), GF_i is the ratio between total number of molecules of gas i and the total number of gas molecules that participate in the gas evolution process.

$$\frac{V_{Li}}{V_L} = LF_i \qquad [4.48]$$

= volume fraction of liquid i over the total amount of pore liquids,

can be modified into

$$H_{COMB} = \sum_{i=1}^{N} \left[\frac{GF_i}{H_{i/L1} \cdot LF_1 + H_{i/L2} \cdot LF_2} \right]^{-1} \qquad [4.49]$$

where, N = number of gas components.

The values of the solubility coefficients of each gas component in each liquid component, as given in the literature, are presented in Chapter 2.

As illustrated in Table 4.15, the bitumen and water volume fractions during the tests, after sample saturation, were approximately 70% and 30% respectively, with small variations.

In contrast to the liquid contents, the variability of the gas contents was high, as far as the relative percentages of CH_4 and CO_2 are concerned (Table 4.5). This variability associated with the fact that not all mercury triaxial samples had the gas contents measured, made it difficult to evaluate H_{COMB} for each test.

If, however, one assumes that the gas content of the mercury triaxial samples is given by one of the combinations presented in Table 4.17 and that the individual gas solubility coefficients and the liquid contents are those depicted in Table 4.17, it is possible to evaluate the combined solubility coefficient for each of these gas combinations. The gas content combinations of Table 4.17 were chosen in order to allow a better evaluation of the most probable gas composition of the mercury triaxial samples. By comparing the combined solubility coefficients presented in this table with those obtained from the mercury triaxial tests (Table 4.16) it is possible to conclude that:

- N_2 is not the major gas in solution due to the low H_{COMB} in combination A

COMBINATION	FRACTION OF TOTAL VOLUME OF GAS (%)			COMBINED SOLUBILITY COEFFICIENT (EQUATION 4.49) H_{comb}
	N_2	CH_4	CO_2	
A	90	5	5	0.058
B	0	80	20	0.186
C	0	20	80	0.440
D	10	72	18	0.149

NOTATION: LIQUID 1 (L1) - BITUMEN
LIQUID 2 (L2) - WATER
GAS 1 - N_2
GAS 2 - CH_4
GAS 3 - CO_2
$H_{i/Lj}$ - SOLUBILITY COEFFICIENT OF GAS i IN LIQUID Lj

$H_{1/L1}$	= 0.069	PEACOCK, 1988 (TABLE 5.3)
$H_{1/L2}$	= 0.016	
$H_{2/L1}$	= 0.21	
$H_{2/L2}$	= 0.03	
$H_{3/L1}$	= 0.80	
$H_{3/L2}$	= 0.83	

Table 4.17 Theoretical Combined Solubility Coefficients

- CO_2 is not the major gas in solution due to the high H_{COMB} in combination C
- Variations of combinations B and D, i.e. CH_4 as the major constituent, followed by CO_2 and then by N_2, reflecting the small contamination of air, were most likely present in the samples tested.

These conclusions indicate that the high air content observed at the gas chromotograph tests occurred not due to the presence of air dissolved in the sample pore liquids, but due to actual air contamination that probably took place during the gas sampling.

Time-Dependent Response

The time-dependent change of volume of free gas associated with each of the unloading stages of the mercury triaxial tests are presented in Figures 4.40 to 4.62.

These figures also present the "Quotient+1" and Exponential curves that best fit the test data. These best fit curves were obtained from linear regression analyses, as shown in Section D.2 of Appendix D. Tables C.3, C.6, C.9, C.12 and C.15 present the results of the statistical analyses of the test data. The higher values of the correlation coefficient associated with the "Quotient+1" curves indicate that this form of equation better describes the test data. The same conclusion can be drawn from a visual inspection of Figures 4.40 to 4.62. The laboratory tests performed by Sobkowicz, 1982, described in Section 2.3.2, showed the same trend as the ones presented herein.

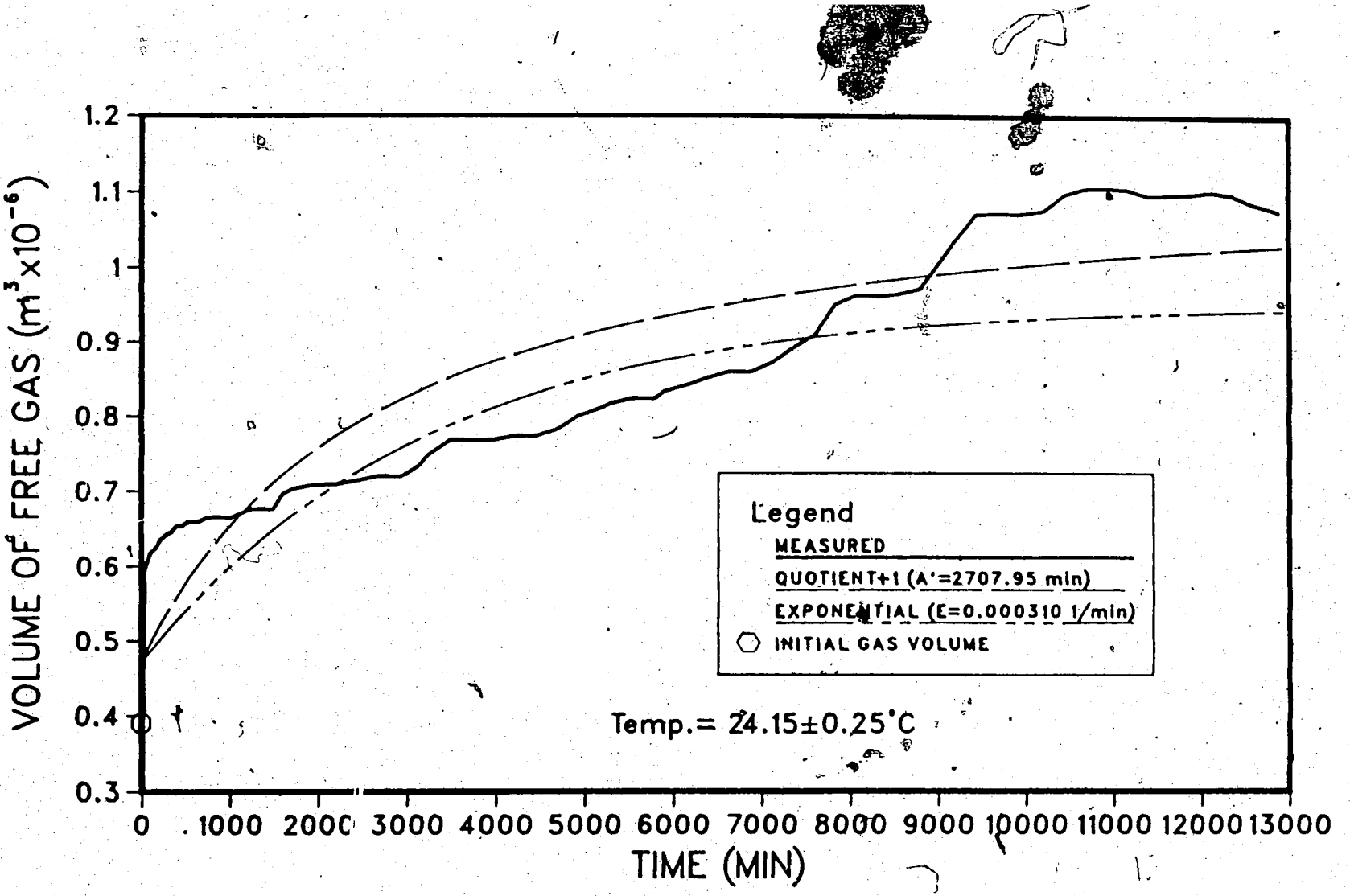

Figure 4.40 Mercury Triaxial Test 3-1 - Step A

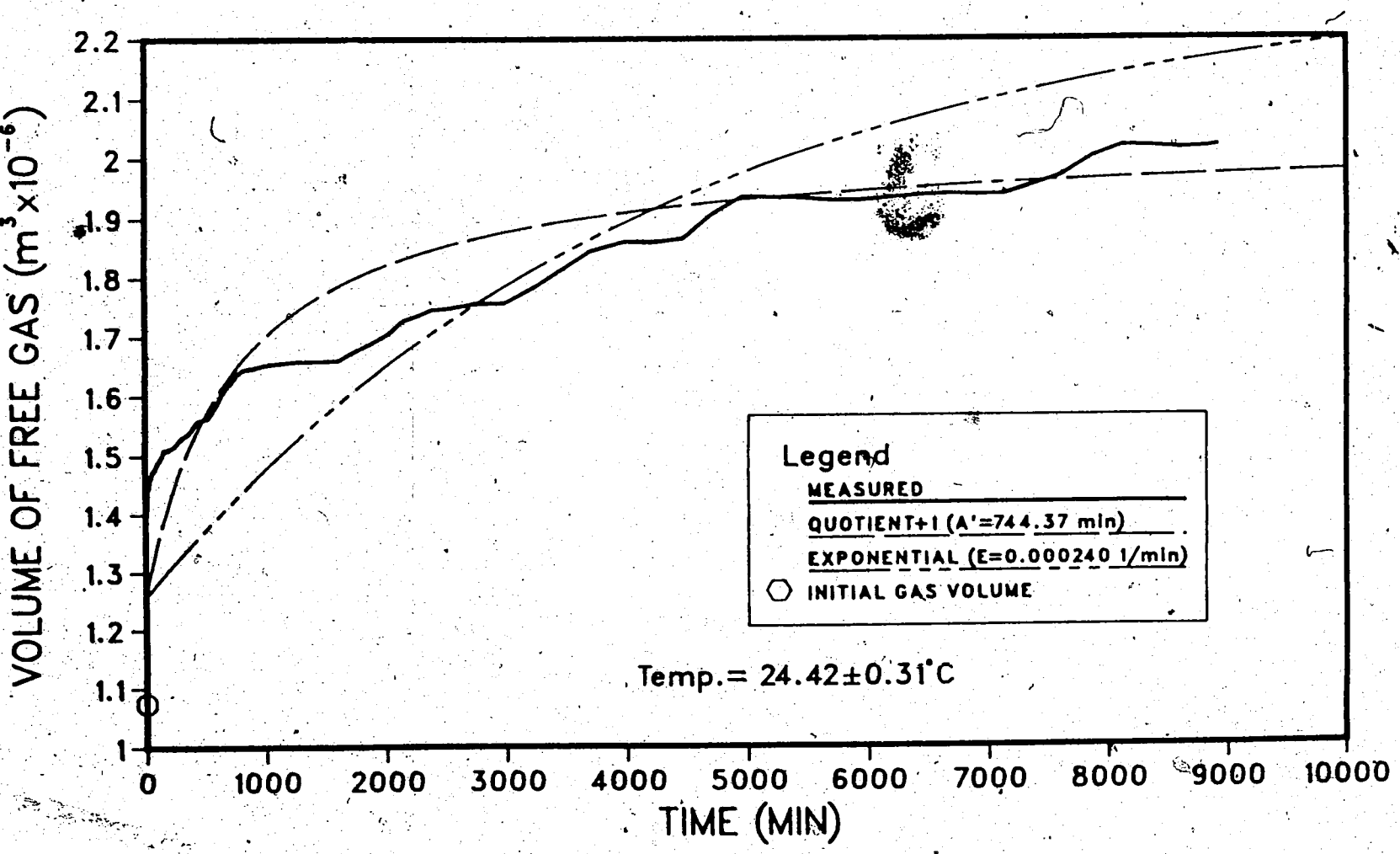

Figure 4.41 Mercury Triaxial Test 3-1 - Step B

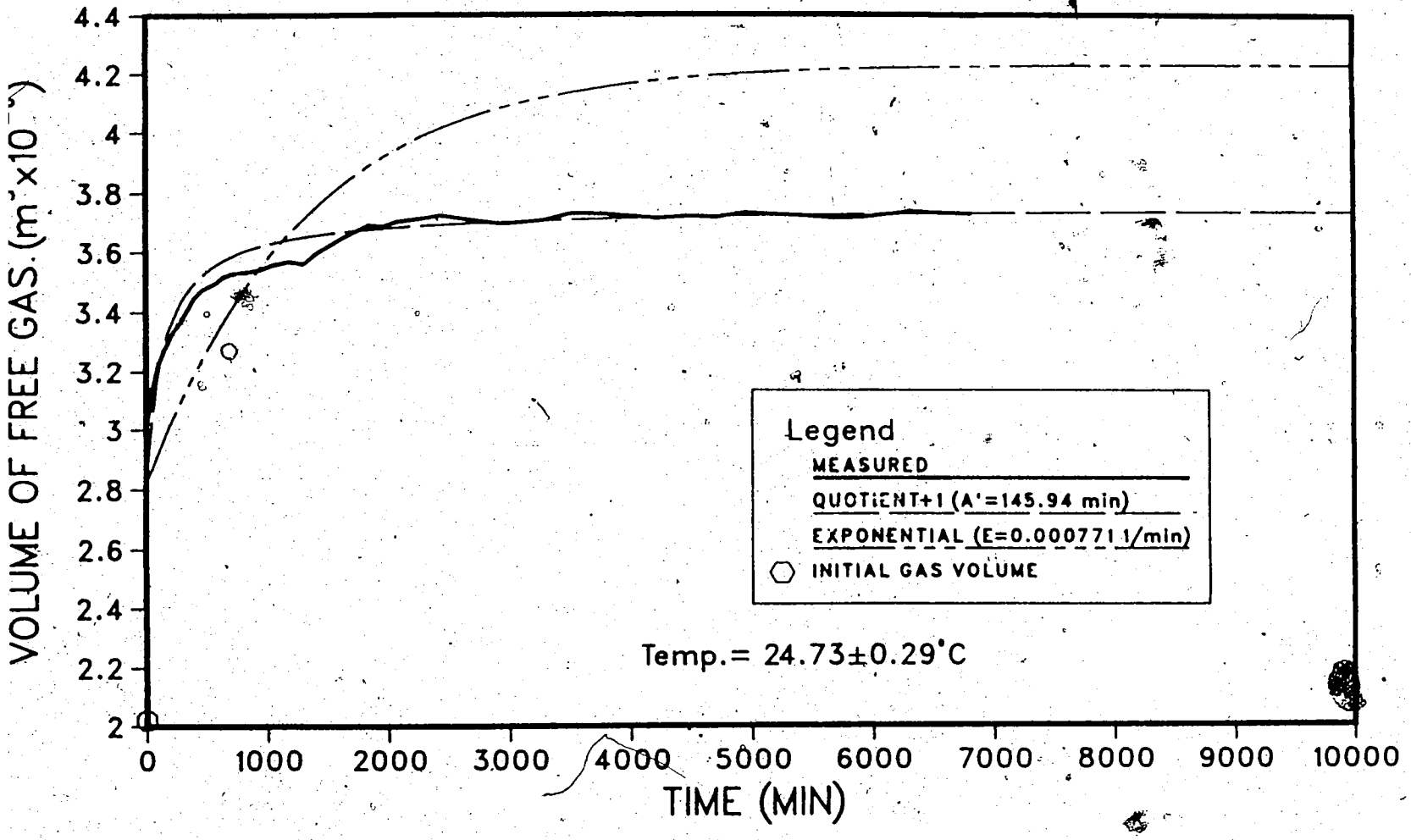

Figure 4.42 Mercury Triaxial Test 3-1 - Step C

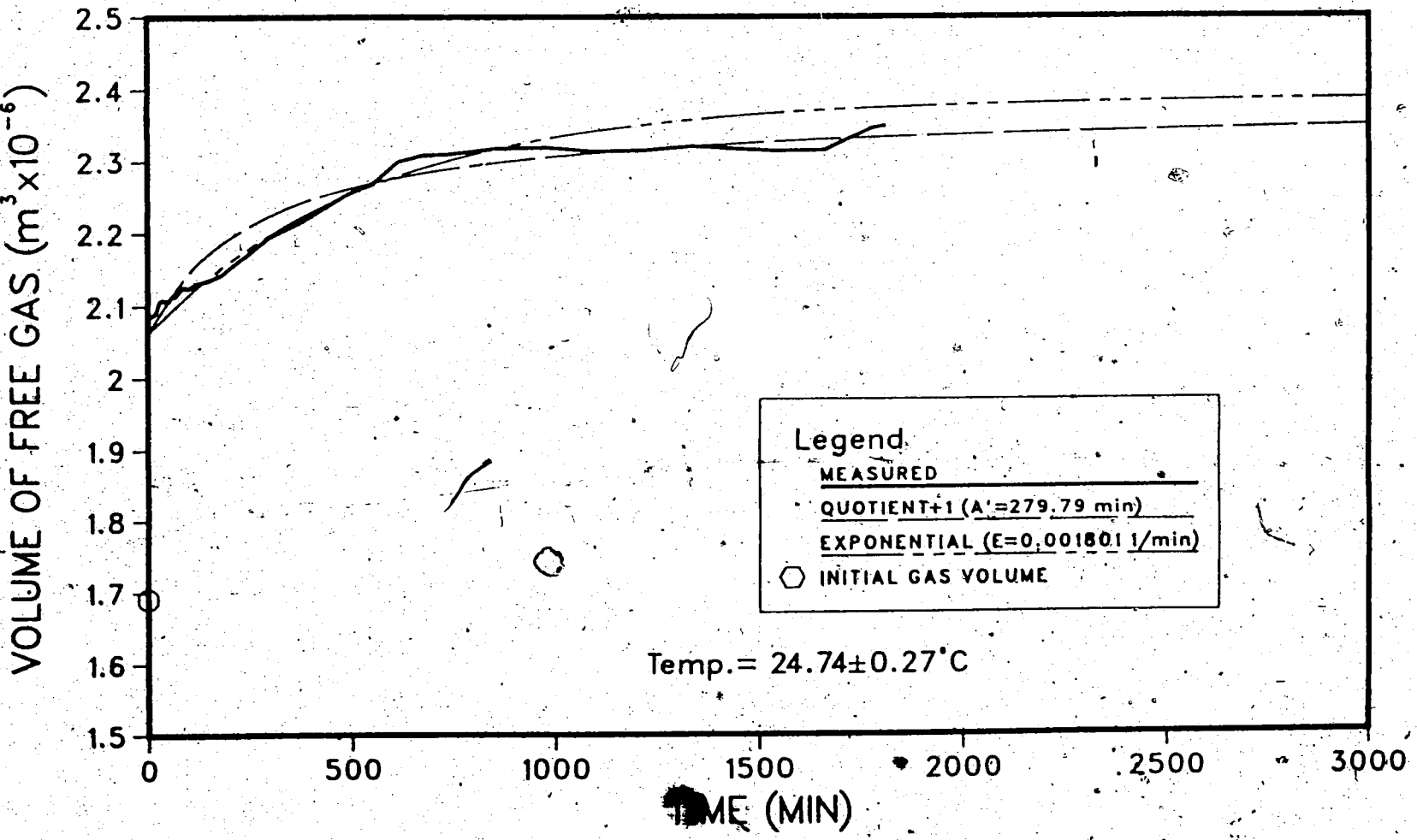

Figure 4.43 Mercury Triaxial Test 6-5 - Step A

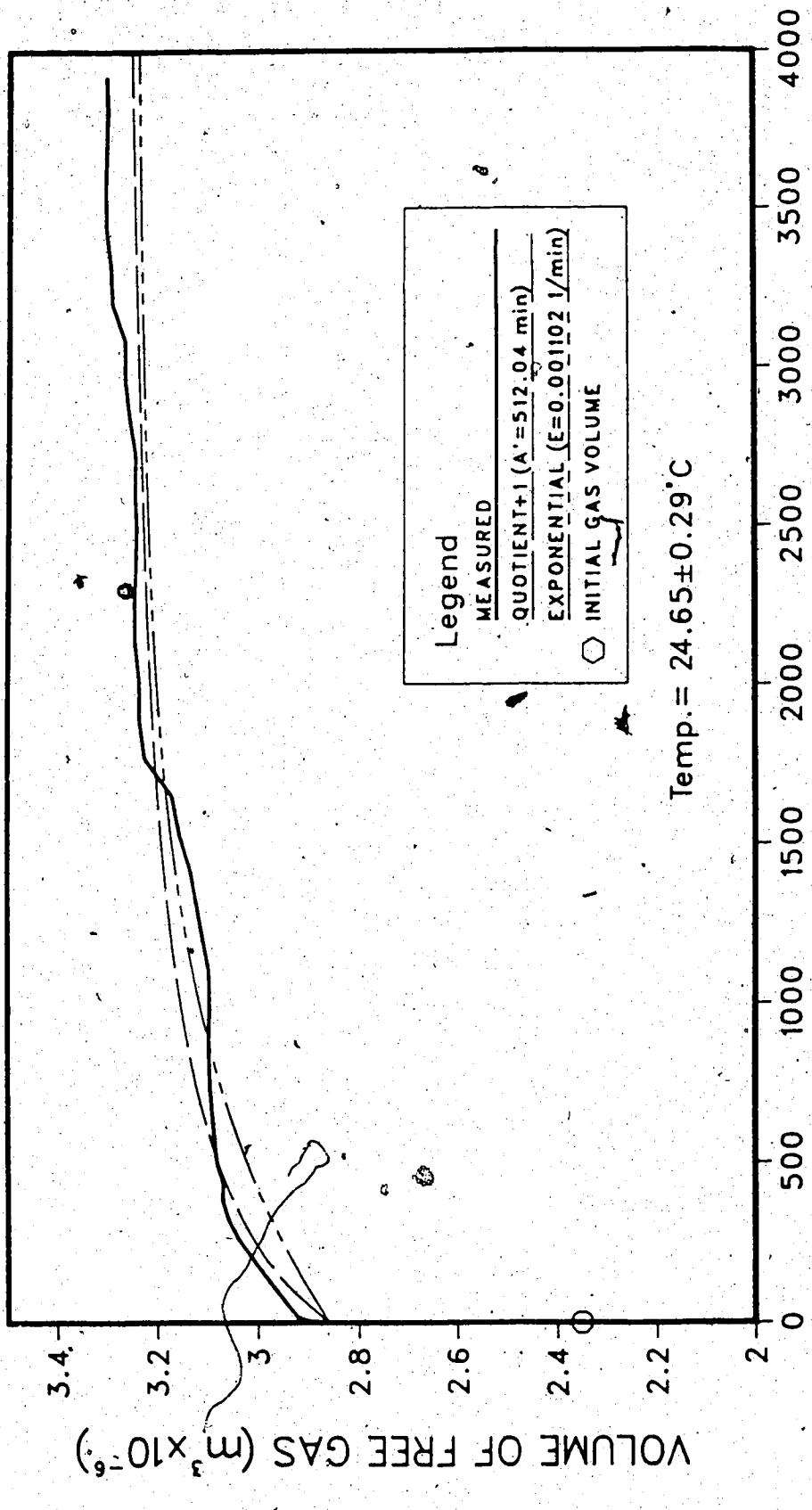

Figure 4.44 Mercury Triaxial Test 6-5 - Step B

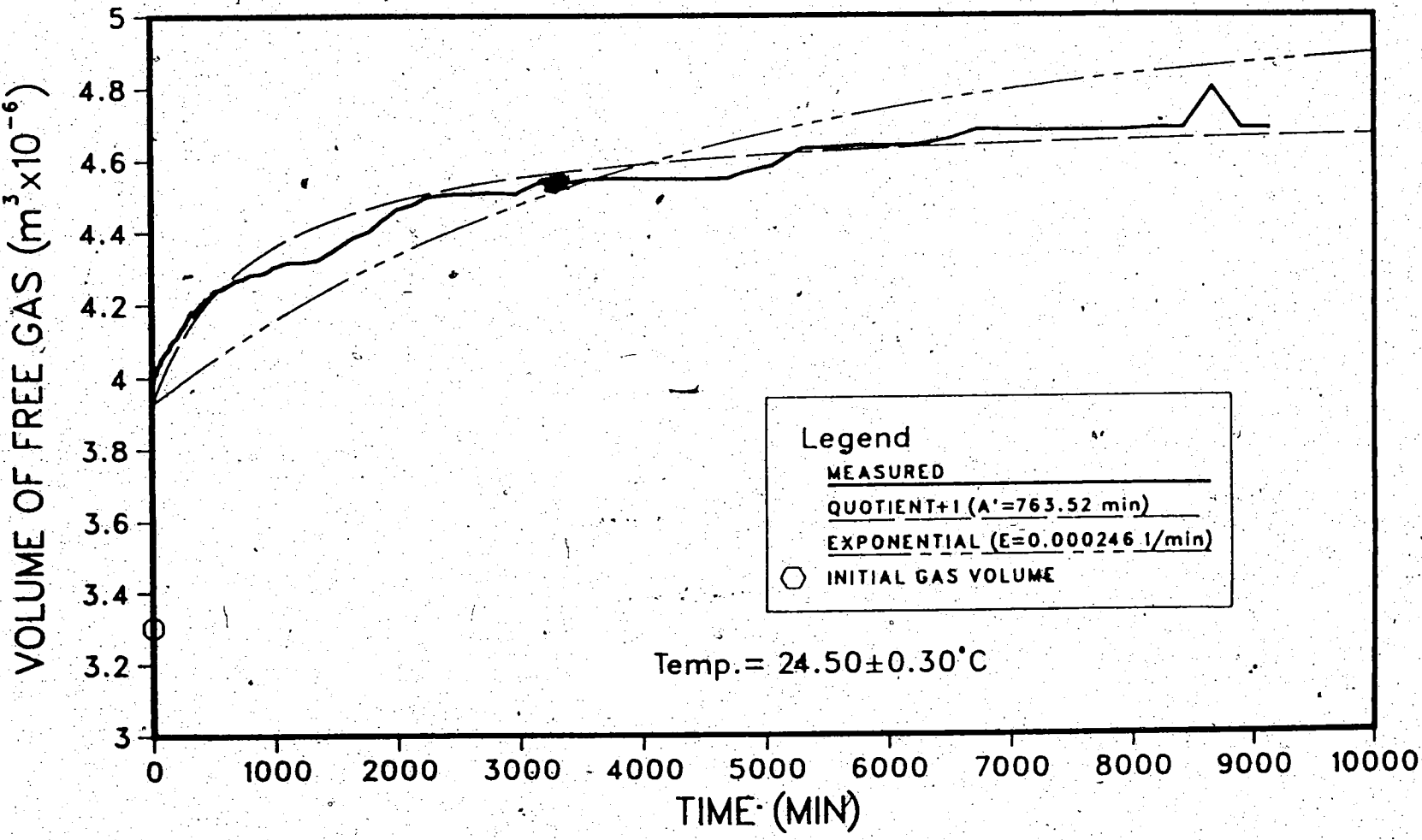

Figure 4.45 Mercury Triaxial Test 6-5 - Step C

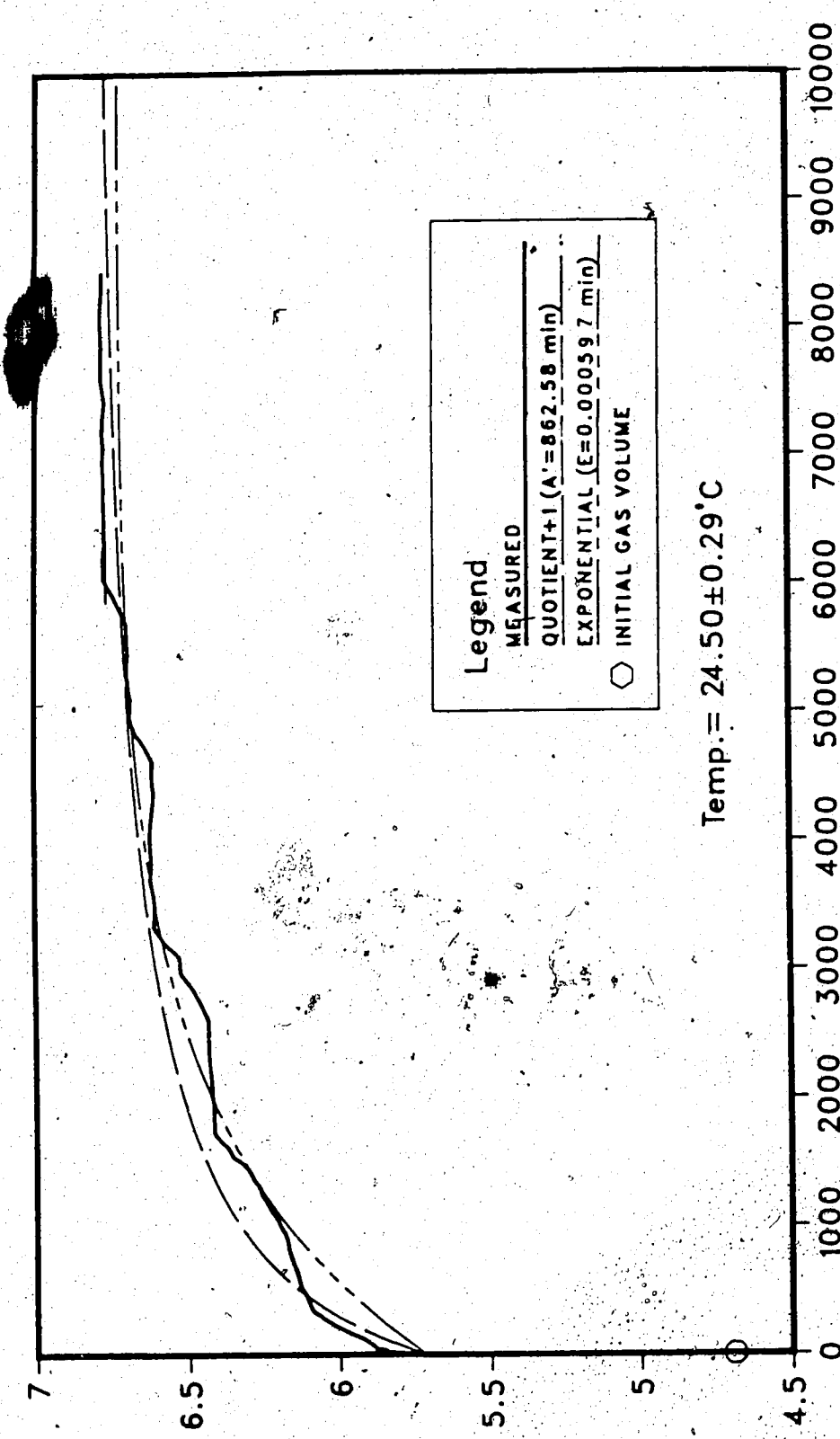

Figure 4.46 Mercury Triaxial Test 6-5 - Step D

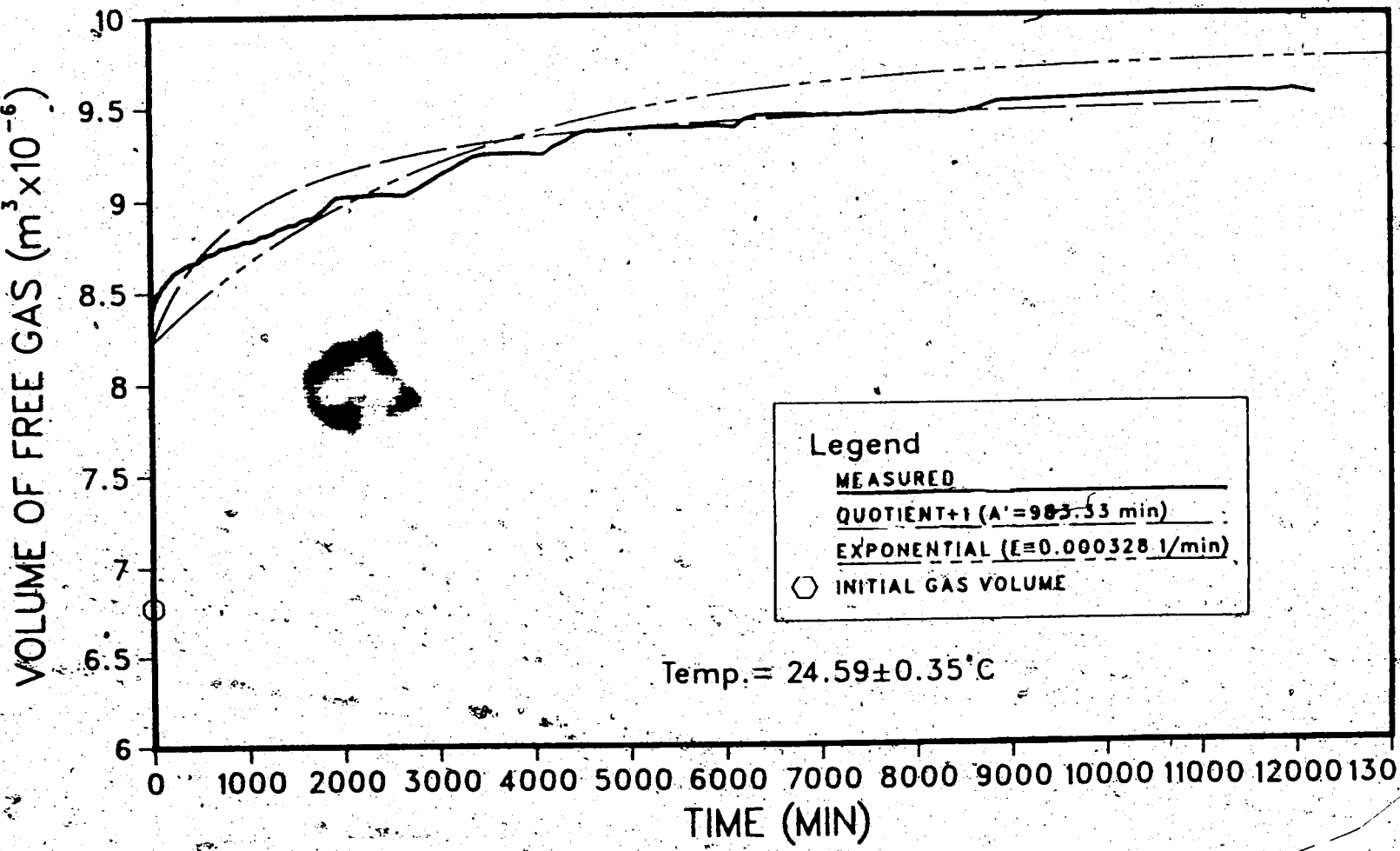

Figure 4.47 Mercury Triaxial Test 6-5 - Step E

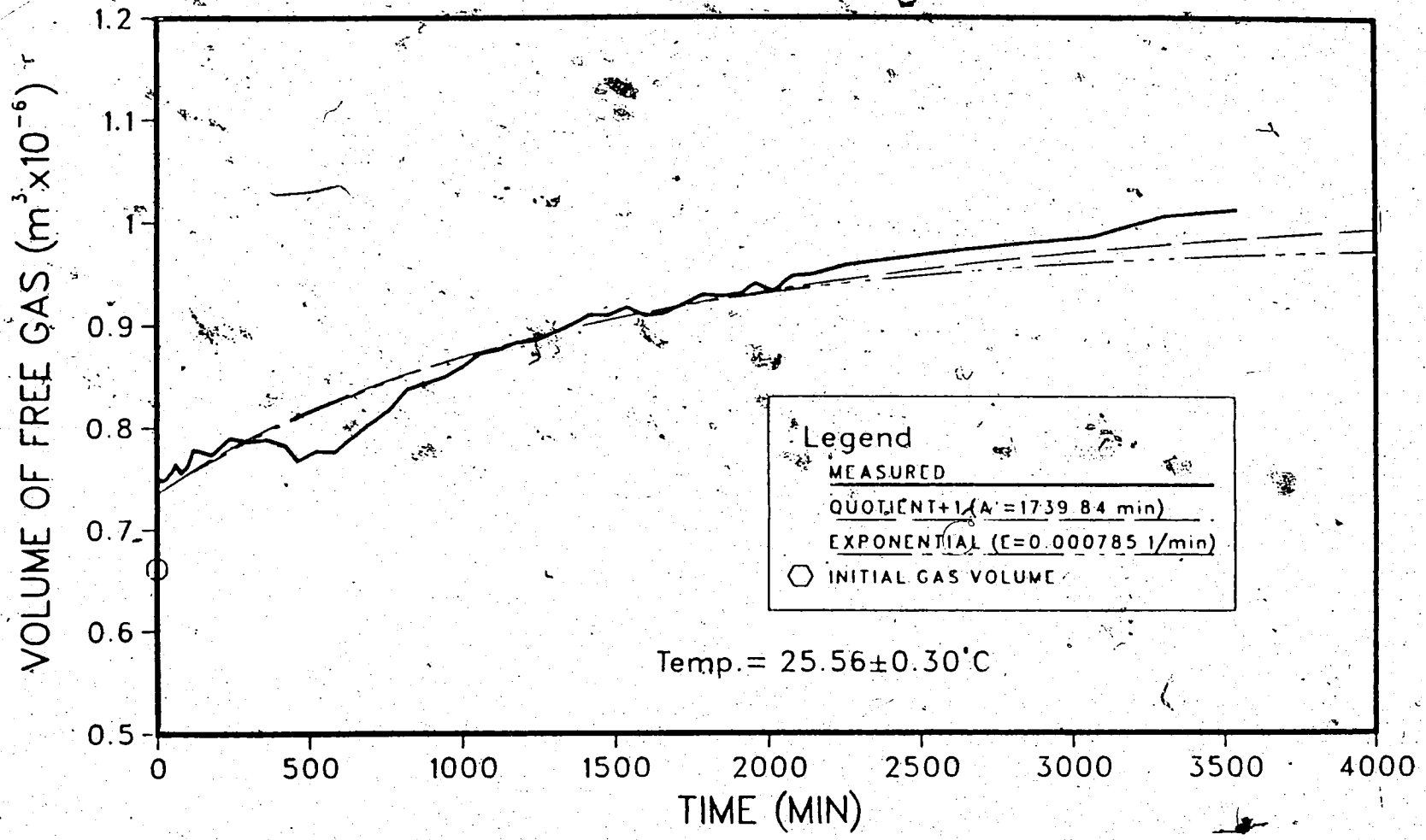

Figure 4.48 Mercury Triaxial Test 9-2 - Step A

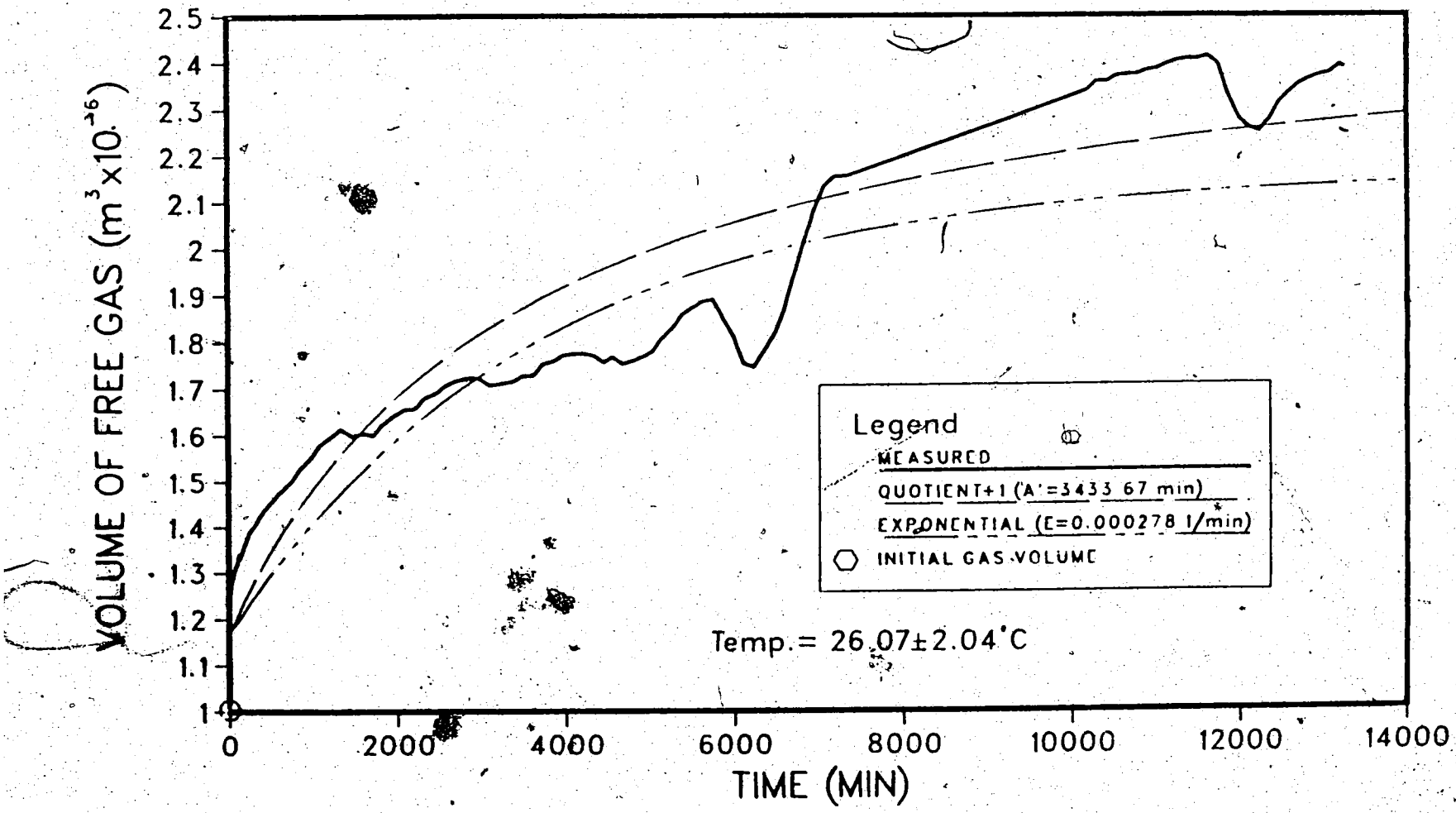

Figure 4.49 Mercury Triaxial Test 9-2 - Step B

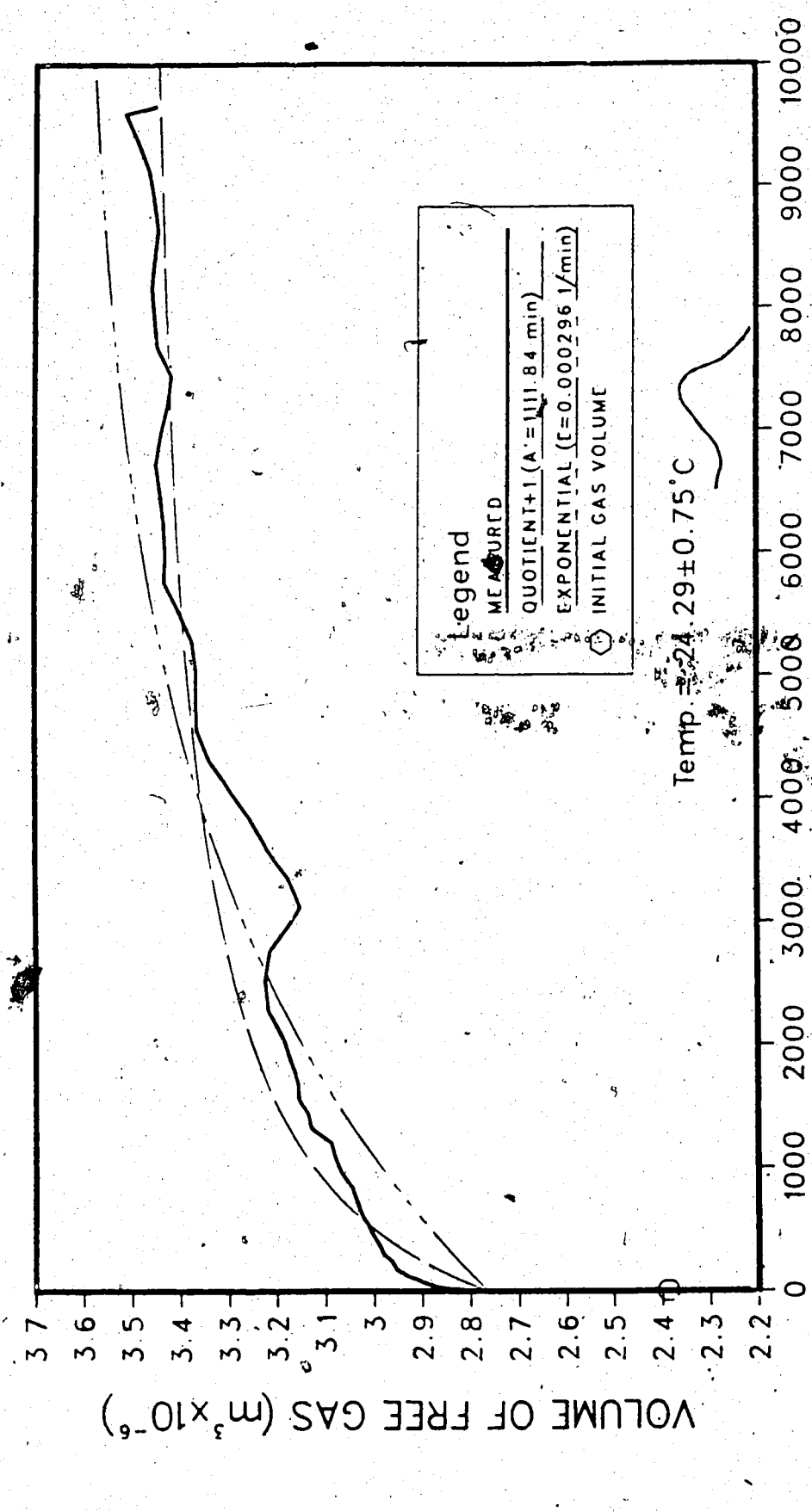

Figure 4.50 Mercury Triaxial Test, Step C

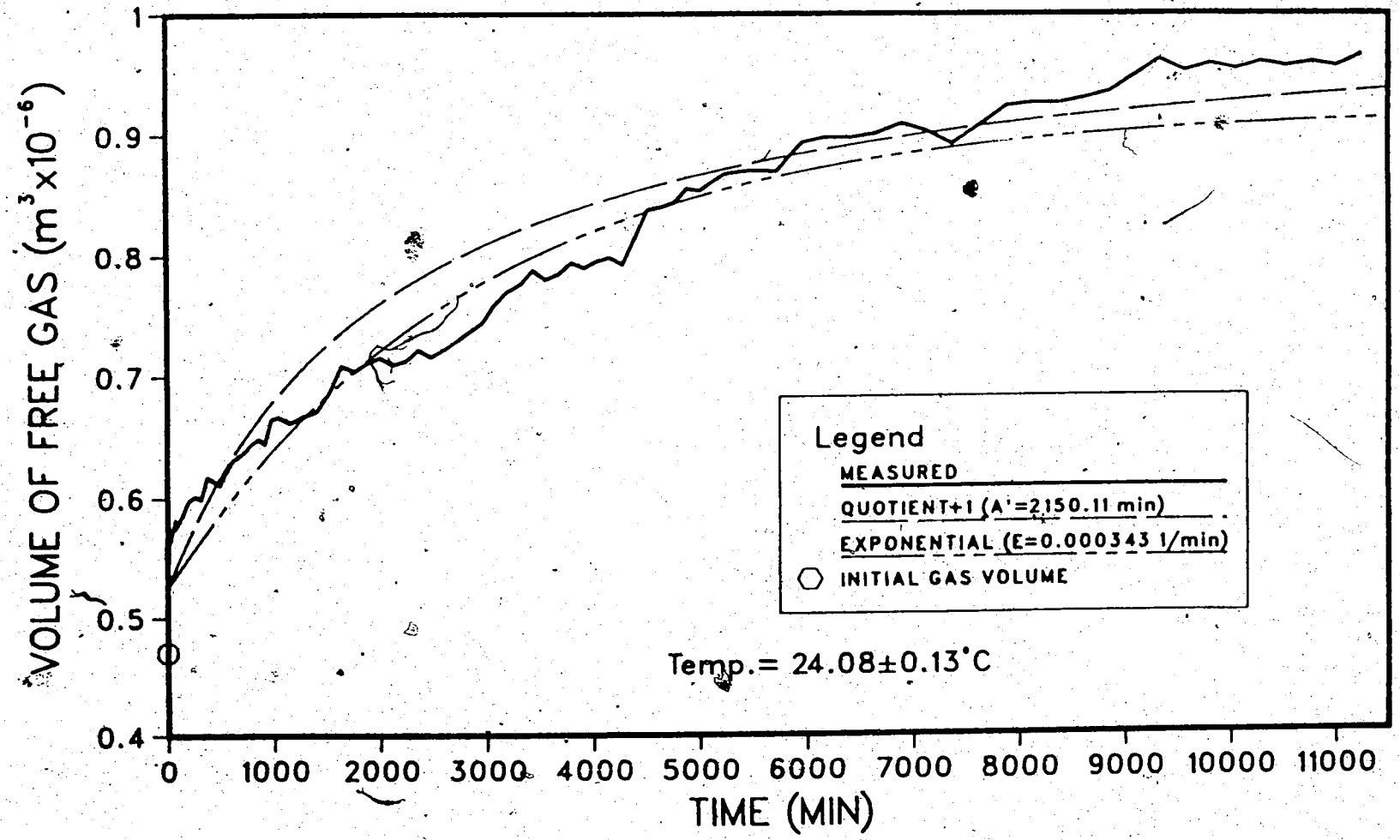

Figure 4.51 Mercury Triaxial Test 11-2 - Step A

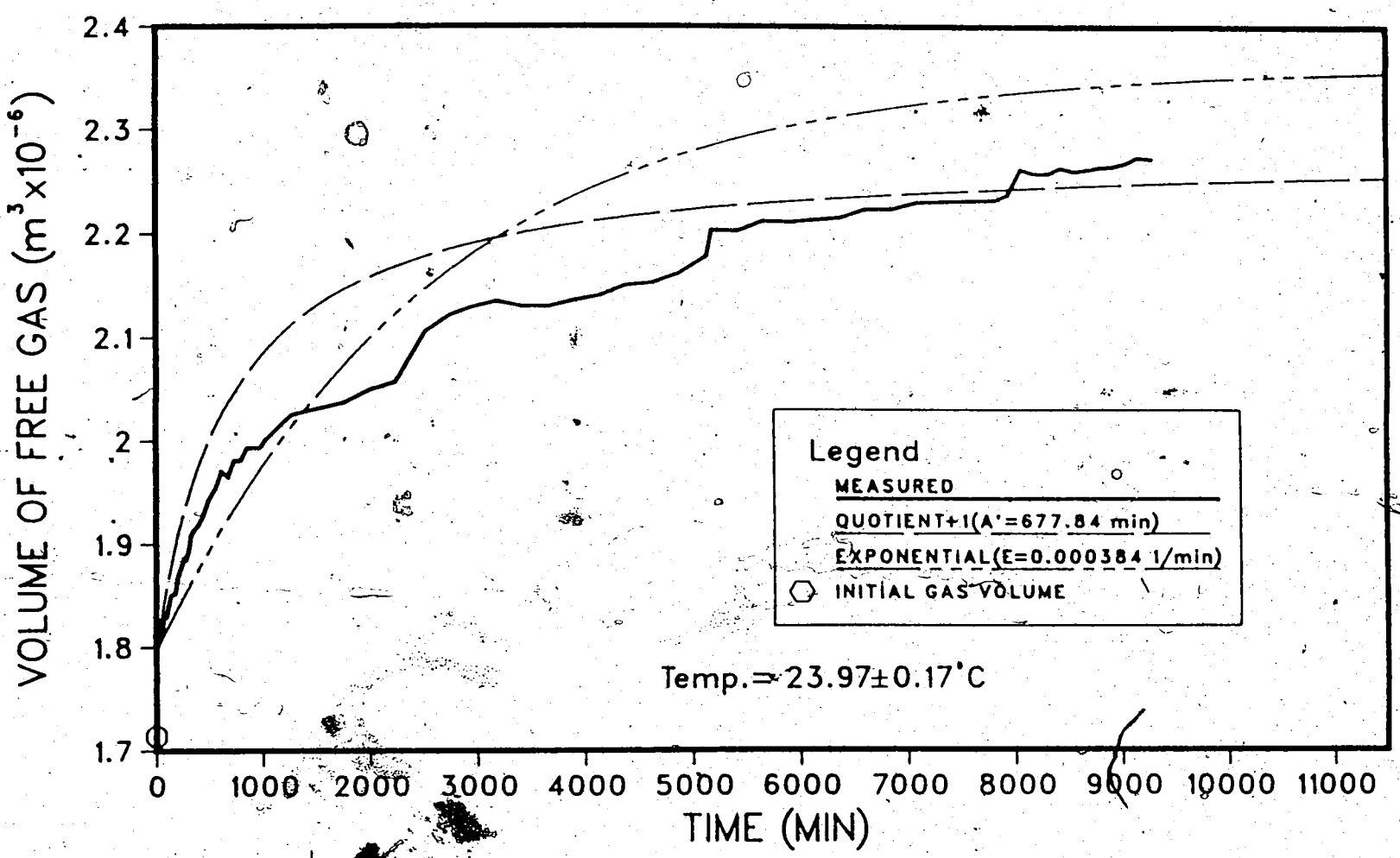

Figure 4.52 Mercury Triaxial Test 11-2 - Step C

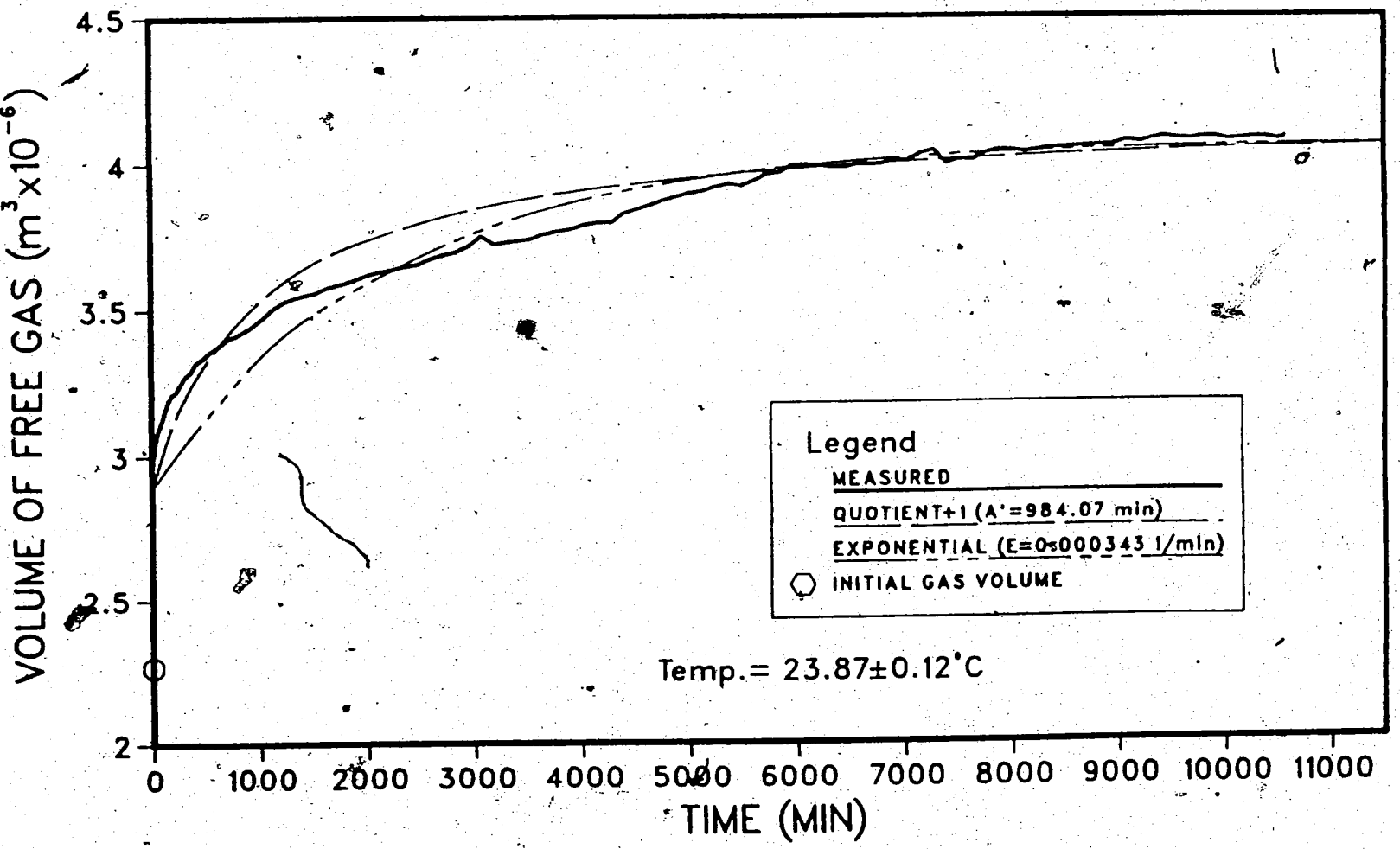

Figure 4.53 Mercury Triaxial Test 11-2 - Step D

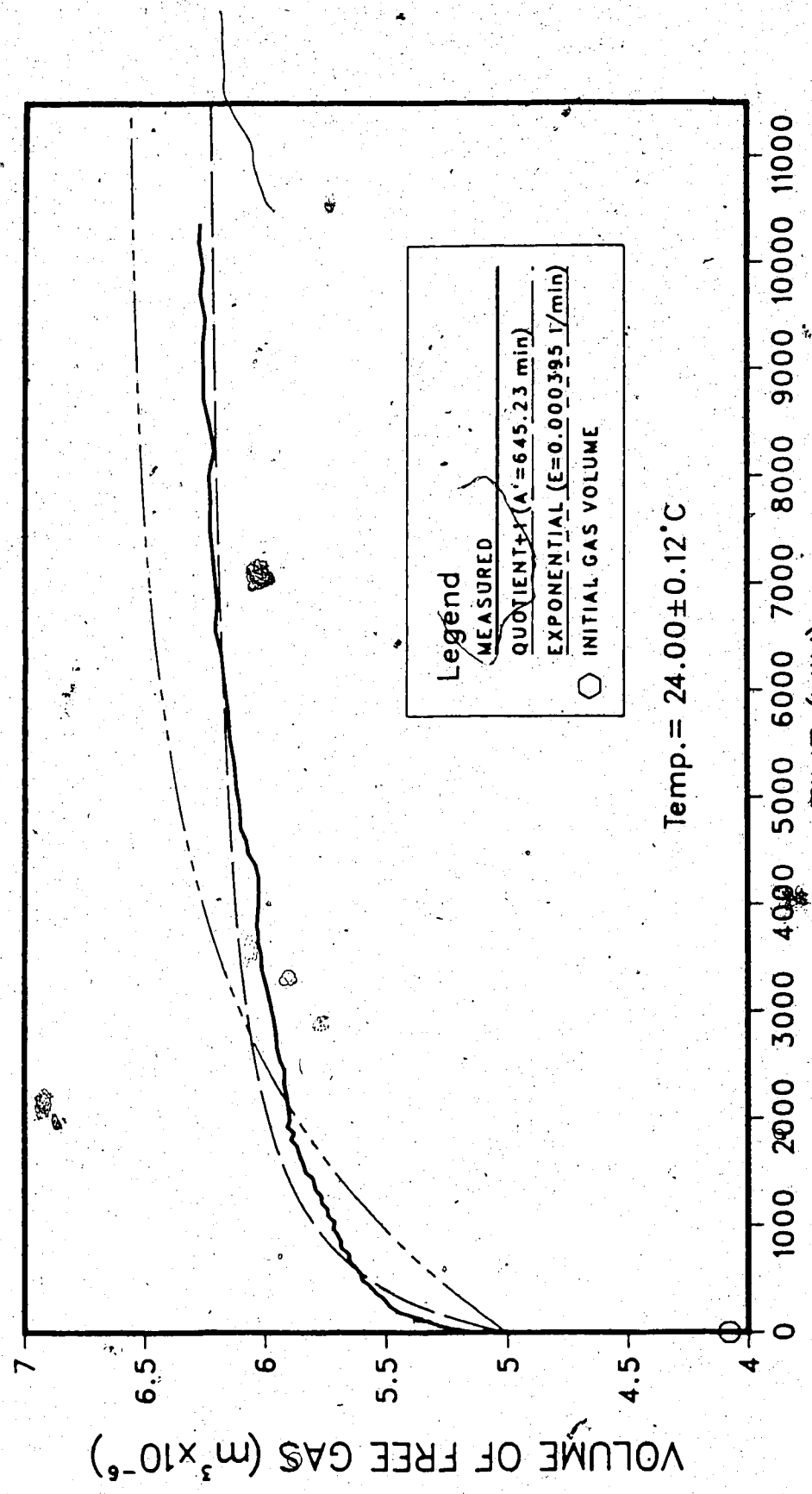

Figure 4.54 Mercury Triaxial Test 11-2 - Step E

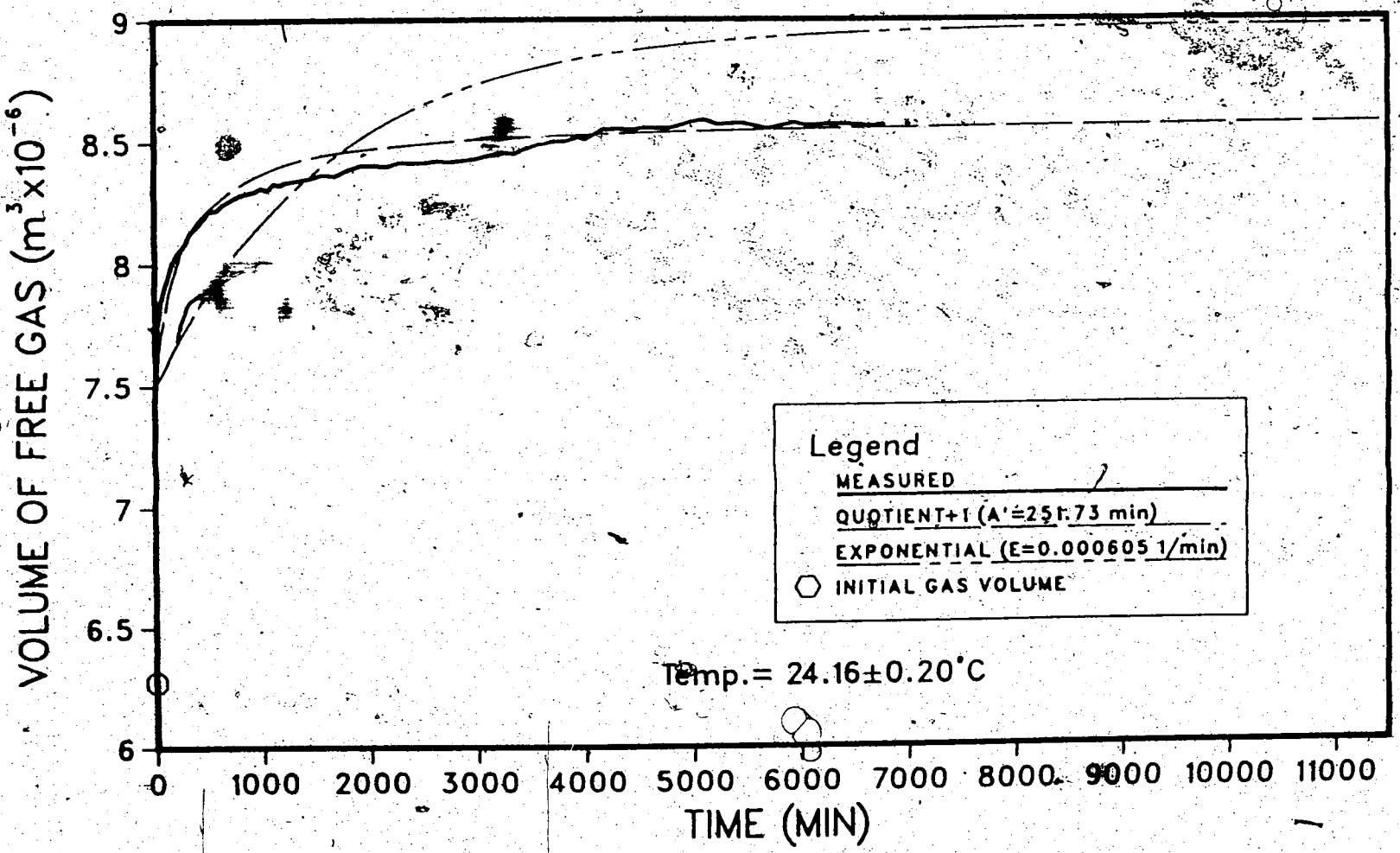

Figure 4.55 Mercury Triaxial Test 11-2 - Step F

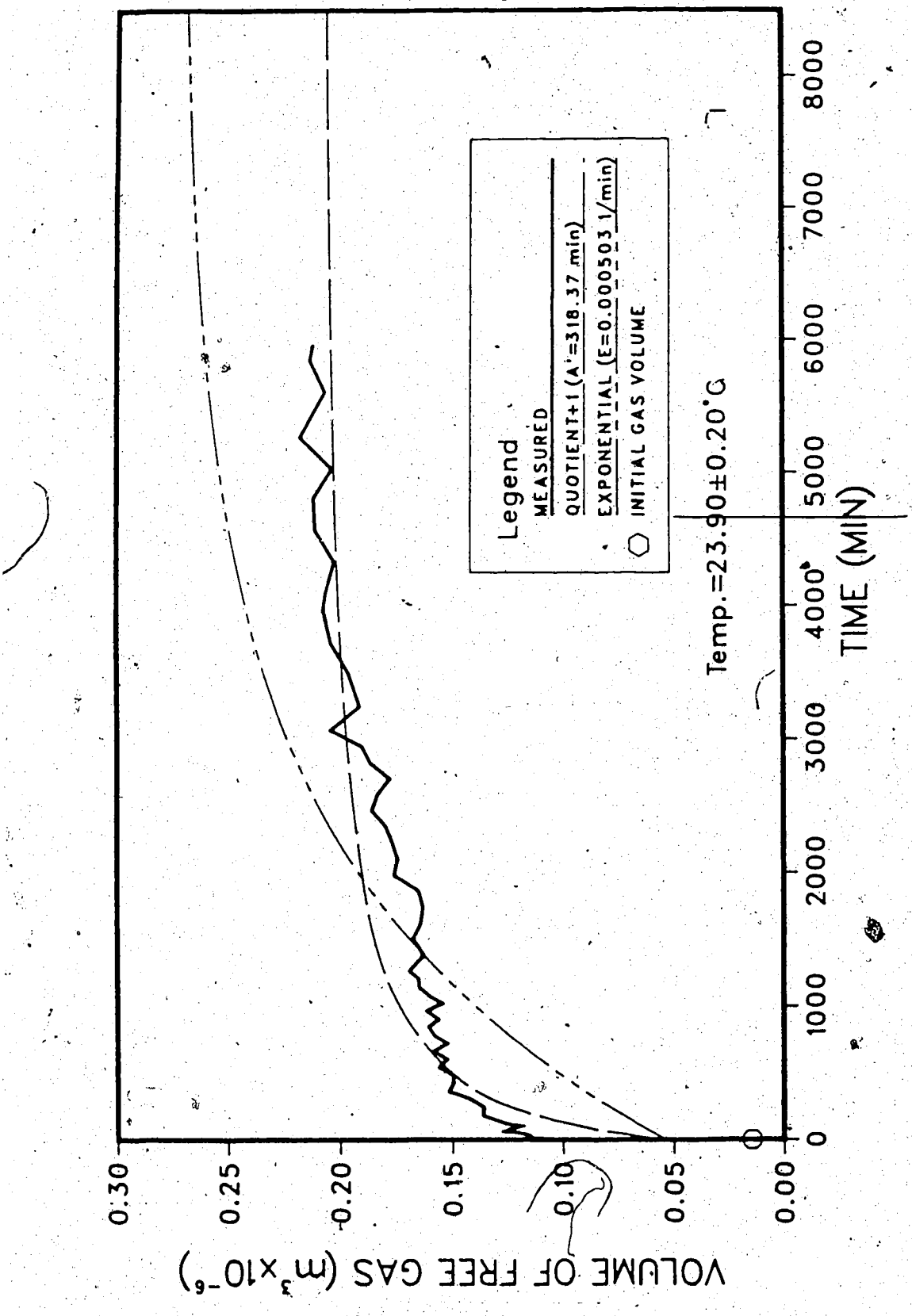

Figure 4.56 Mercury Triaxial Test 11-3 - Step A

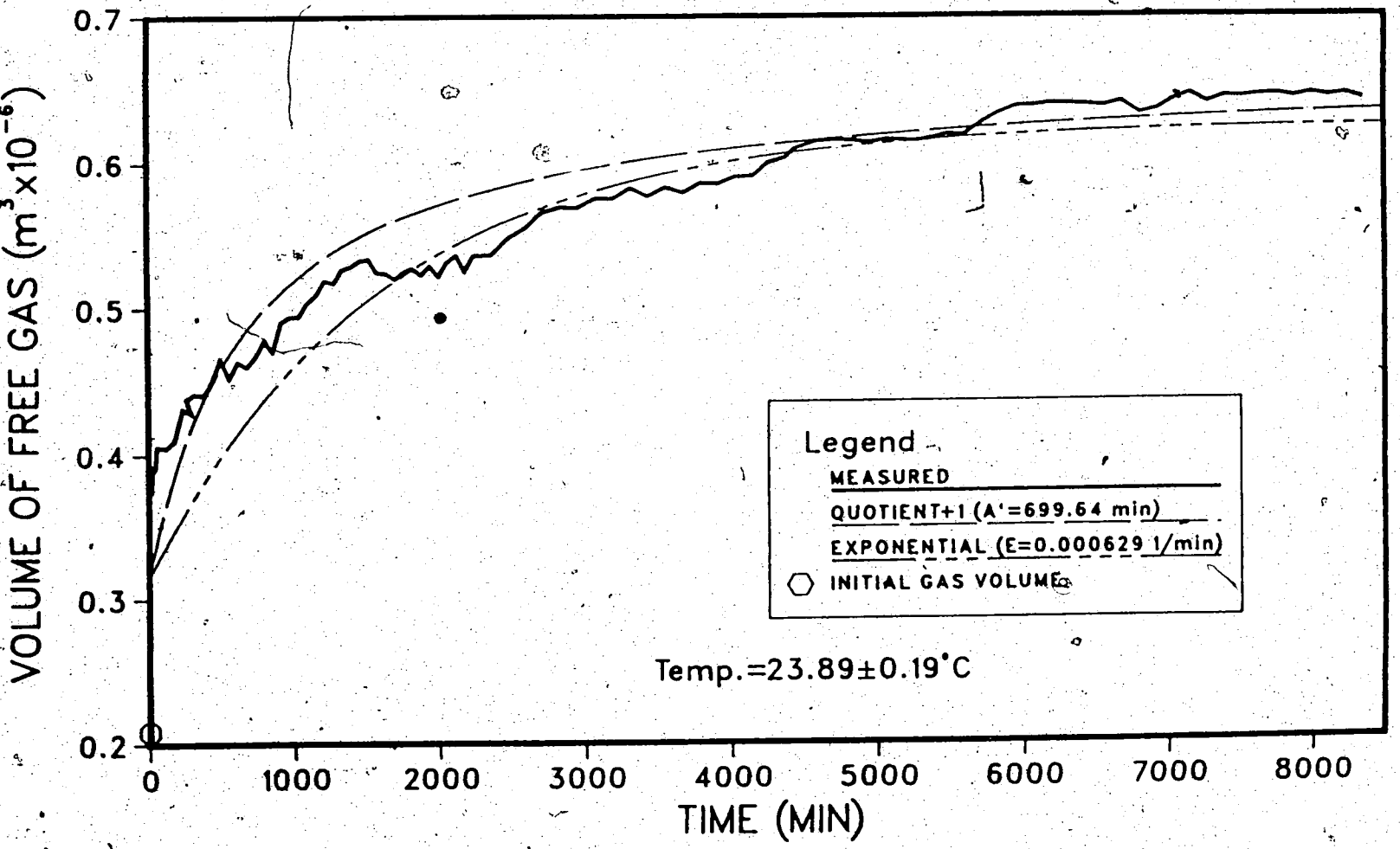

Figure 4.57 Mercury Triaxial Test 11-3 - Step B

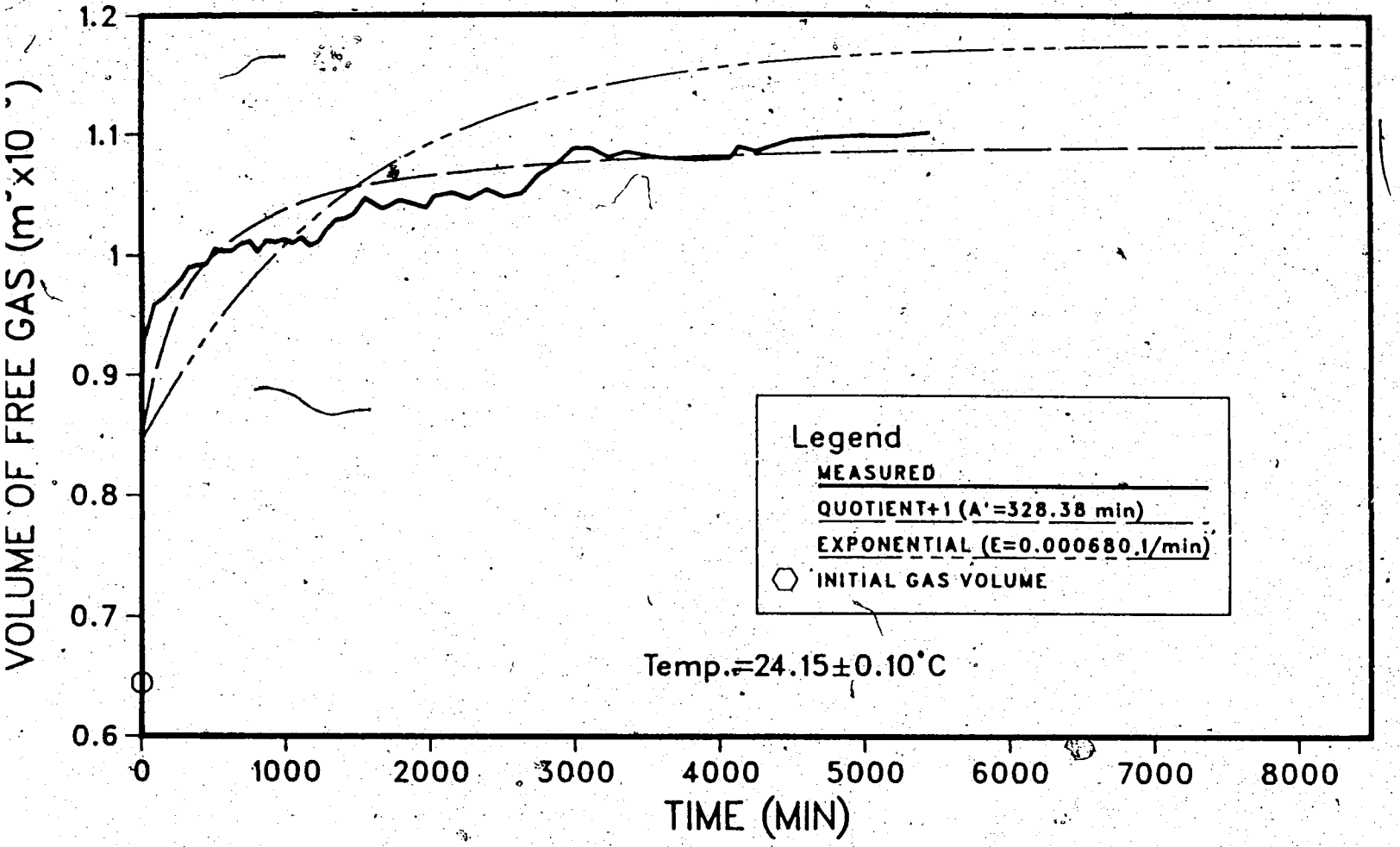

Figure 4.58 Mercury Triaxial Test 11-3 - Step C

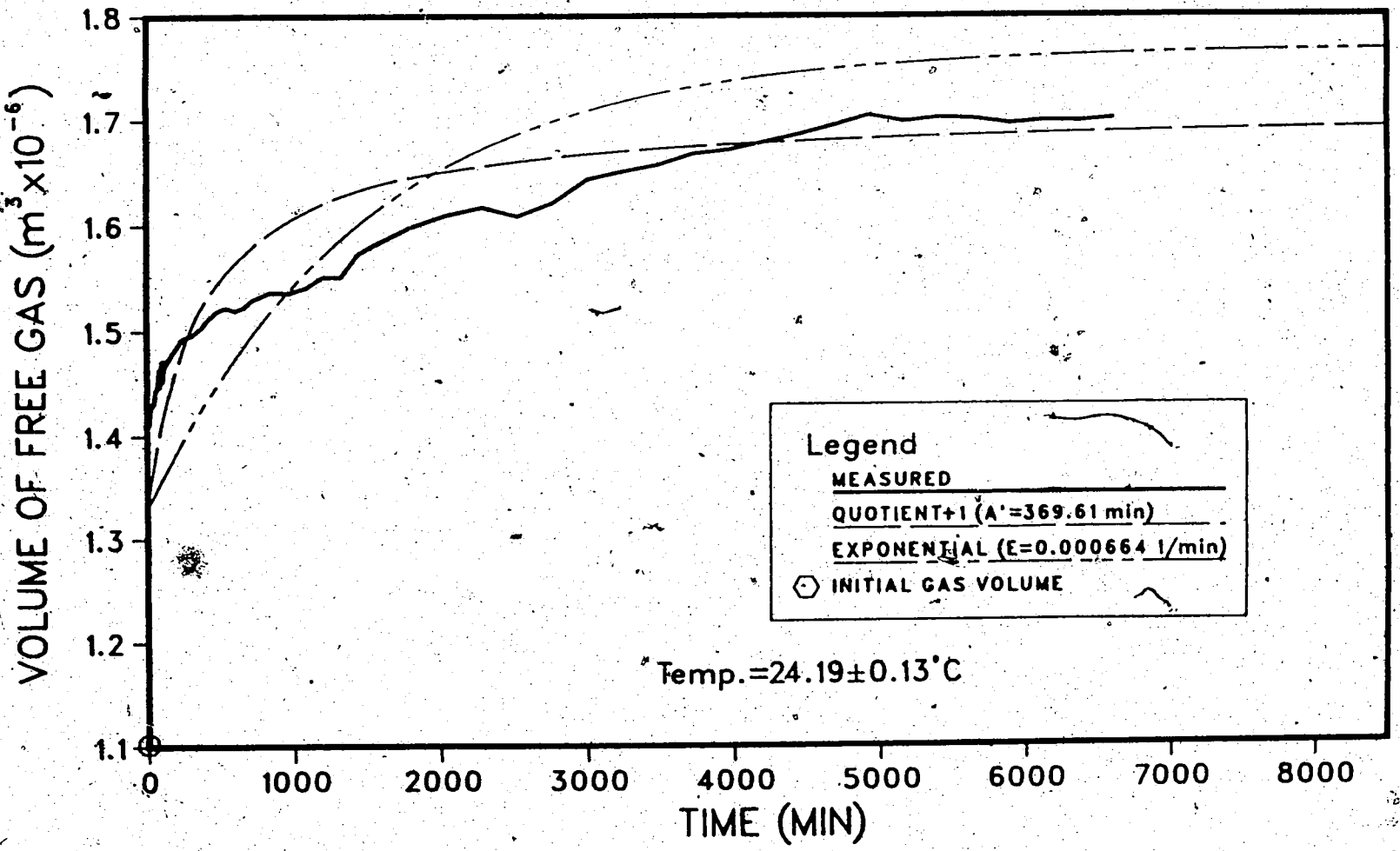

Figure 4.59 Mercury Triaxial Test 1-3 - Step D

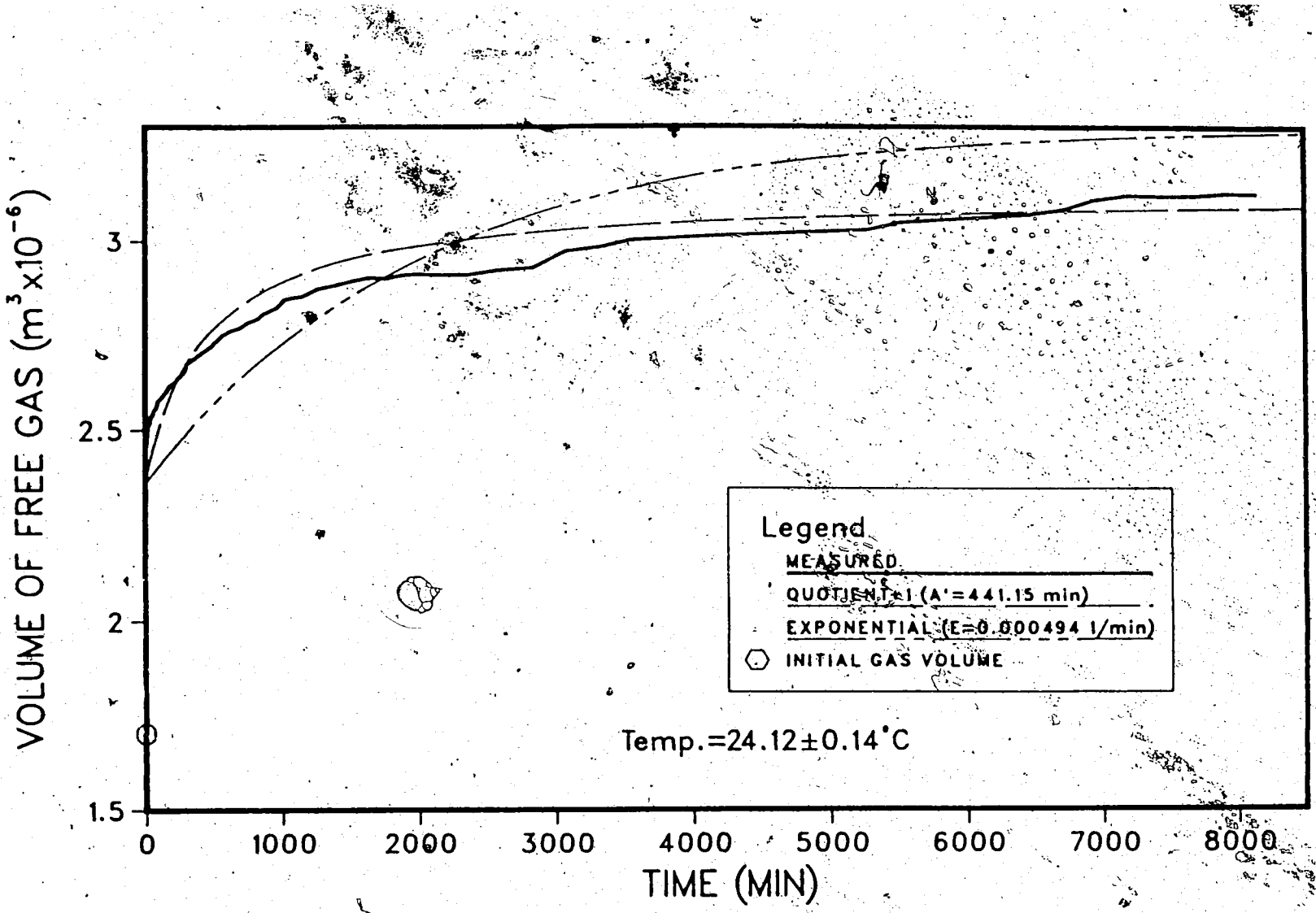

Figure 4.60 Mercury Triaxial Test 11-3 - Step E

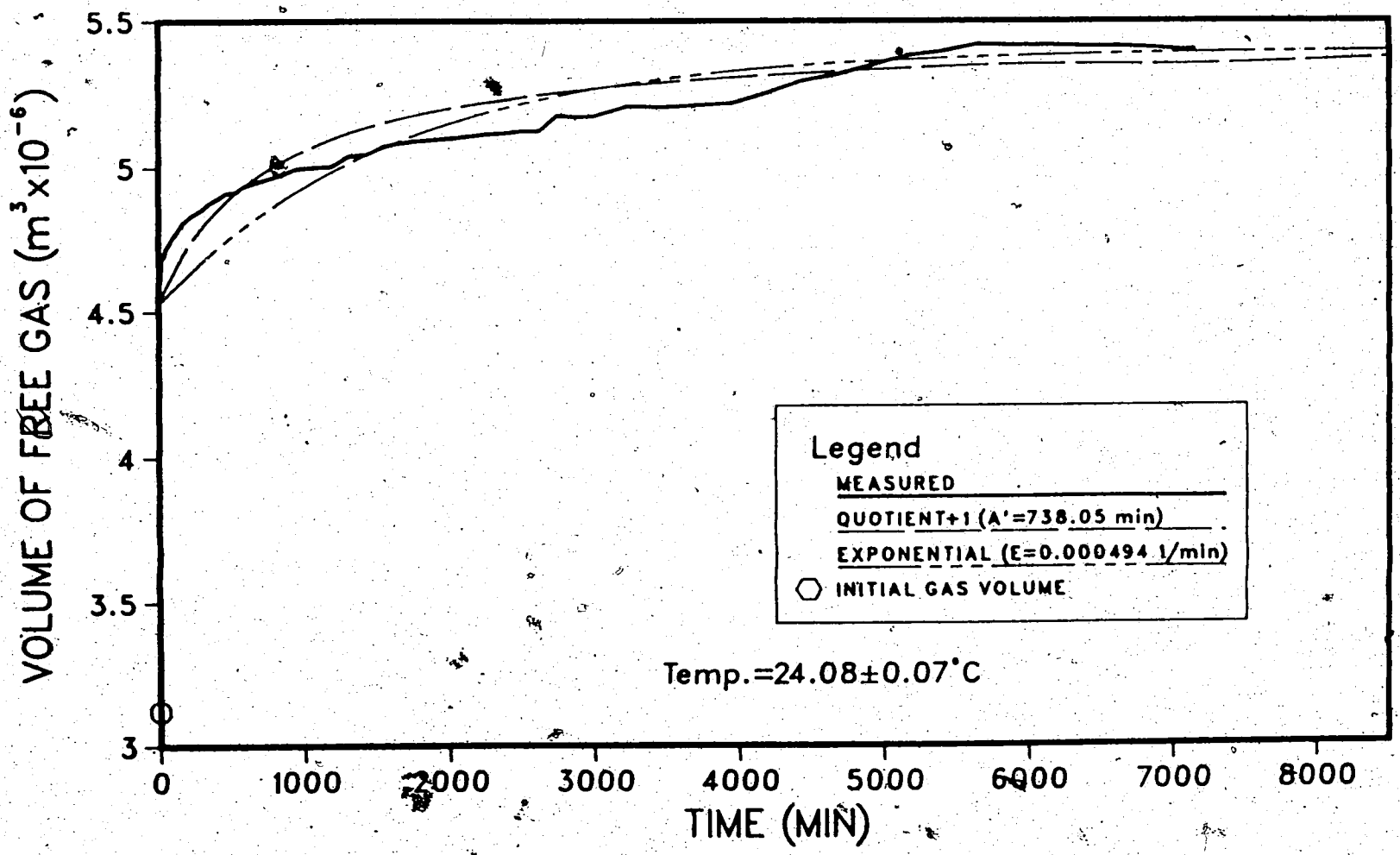

Figure 4.61 Mercury Triaxial Test 11-3 - Step F

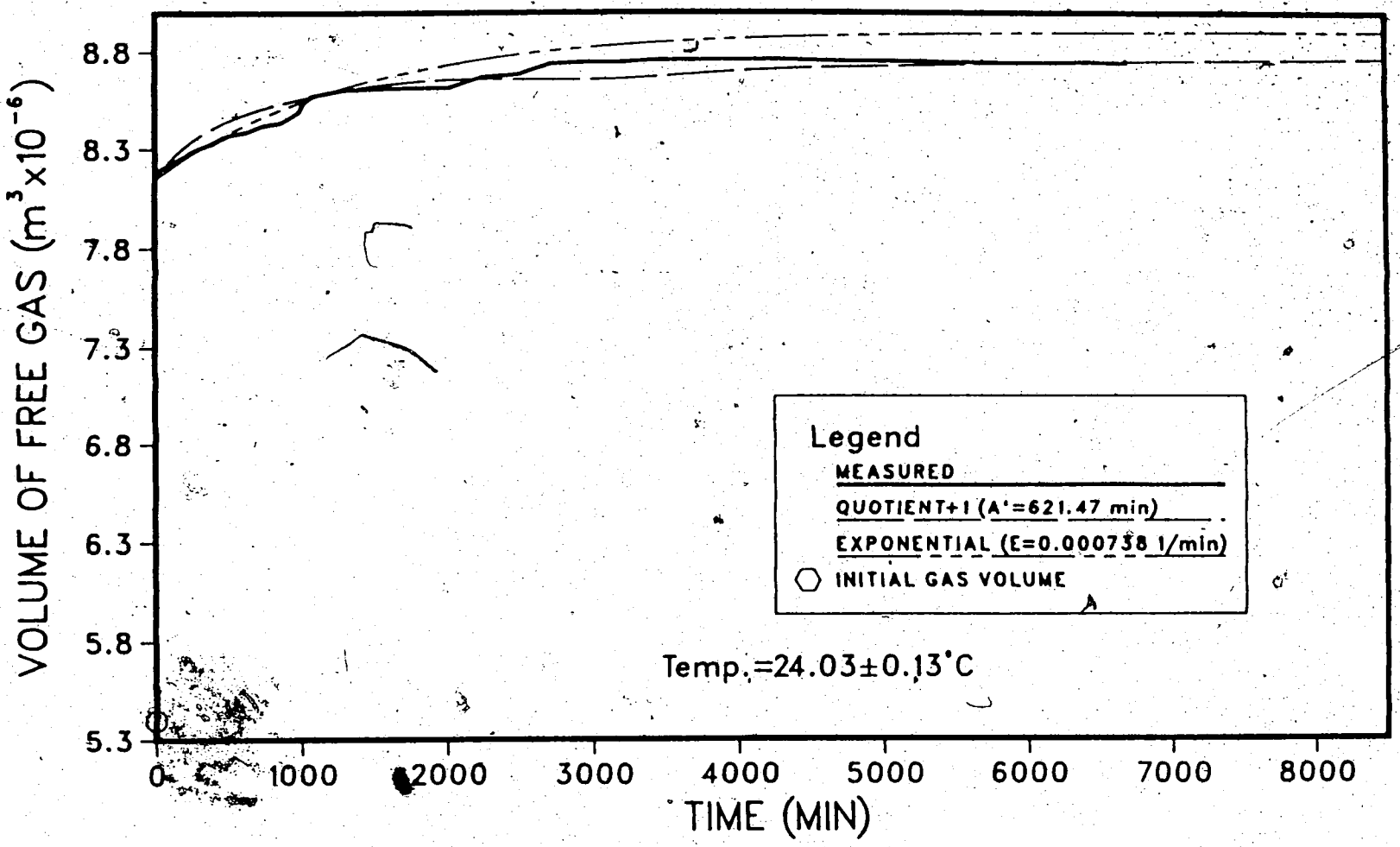

Figure 4.62 Mercury Triaxial Test 11-3 - Step G

For most of the test steps, the volumes of free gas increased faster than the ones predicted by both of the best fit curves during the early stages of the test. This situation reversed with time.

Similar behaviour was observed by Behnke, 1935 and 1951, as discussed in Section 2.3.3. While studying the denitrogenation of human bodies, Behnke concluded that the total elimination of N_2, from a body subjected to decompression, was a result of the N_2 elimination from body fluids and body fats. He noted that the N_2 elimination from body fluids occurred faster than from body fats. This observation induced him to model the total observed behaviour with the sum of the two best fit exponential curves, one obtained from the denitrogenation of body fluids and the other from the denitrogenation of body fats.

Similar to the N_2 elimination in human bodies, the total observed gas evolution in oil sands is a result of the sum of gases that evolve in the water and in the bitumen phases. Assuming that the geometrical boundary conditions are the same for both liquid phases (size and shape of the pores and volume of the bubbles), due to the differences in diffusivity coefficient, the gas evolution process occurs faster in water than in bitumen. Hence, for a constant pore pressure during the growth of the gas phase, as in the case of the mercury triaxial tests, most of the volume change during the early stages of the test is due to the growth of bubbles in the water phase. As time progresses, the bubbles

in the water stop growing and the volume increases are due solely to bubble growth in the bitumen phase. An approach similar to Behnke's could be used herein, i.e., to obtain two best fit curves in order to compose the total volume change response of the gas. However, no data are presently available on the independent study of the time-dependent free gas growth of bitumen-free or lean oil sands. Peacock, 1988, performed some tests with lean oil sands in the oedometer cell described in Section 4.3.4.2. As discussed in that section, the piston friction made it difficult to properly study the time-dependent response of that soil. The tests performed by Sobkowicz would be more helpful in this respect. However, the samples, artificially prepared and saturated with CO_2, might present different behaviour from the lean oil sands.

Due to these reasons, the modelling of the transient gas evolution is performed with a singular exponential or "quotient+1" curve.

The data collected during the tests allowed the construction of Figure 4.63. This figure relates, for all samples tested, the percentage of the total change in the volume of free gas that occurs immediately after the change in the pore pressure and the percentage that occurs with time, with the total degree of saturation at the beginning of the unloading. It illustrates that, for high degrees of saturation, the great majority of the volume changes are transient. As the degree of saturation decreases, the

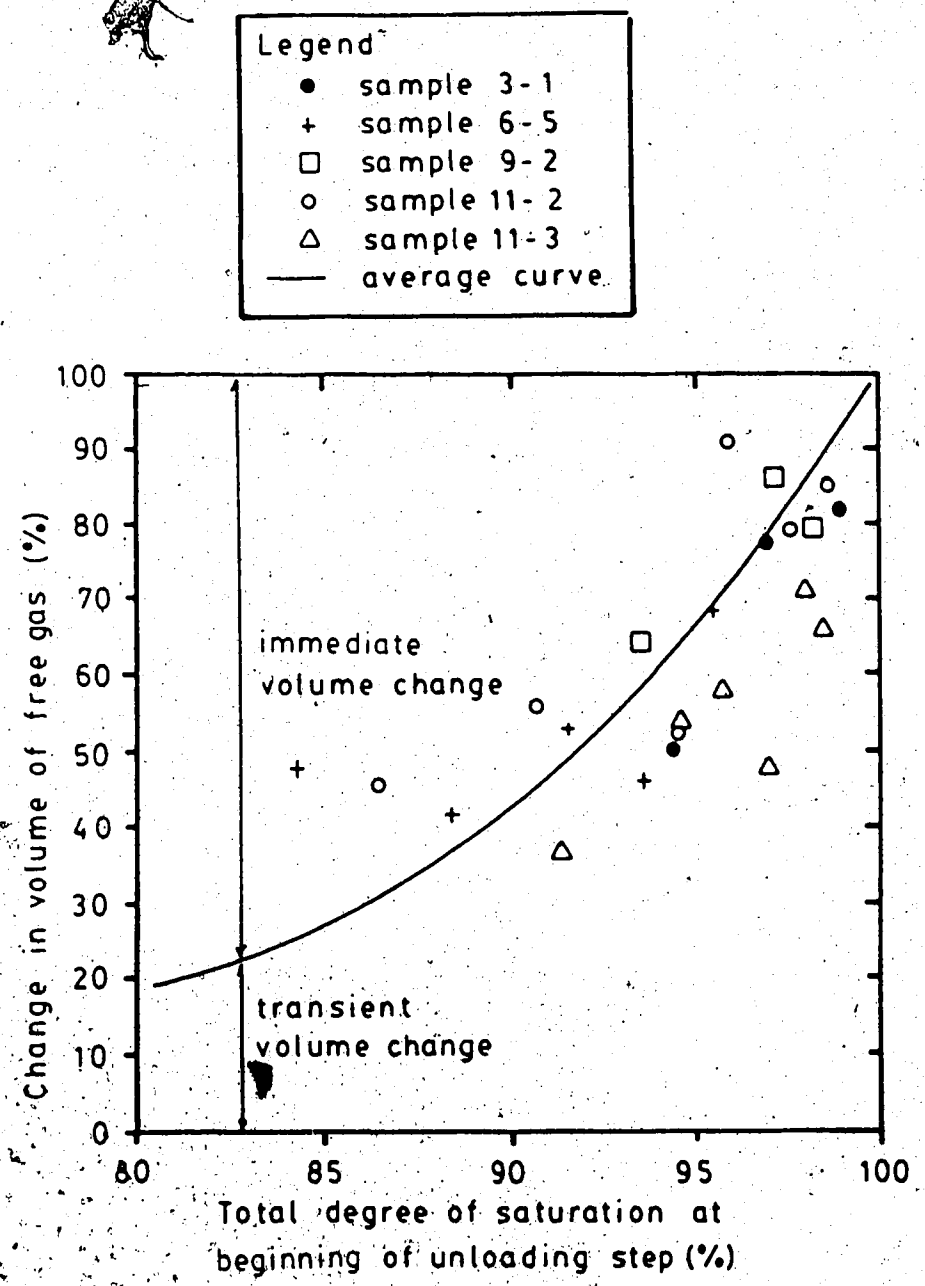

Figure 4.63 Comparison Between Immediate and Time-Dependent

immediate changes in gas volume, due to changes in pore pressure, increase. At a degree of saturation of 85%, the immediate volume change is responsible for approximately 70% of the total volume change. This observation highlights the importance of properly taking into account the time-dependent undrained response of gassy soils, especially at high degrees of saturation.

The variation of the scaling parameter A' with the total degree of saturation at the beginning of the unloading step is illustrated in Figure 4.64. It can be noticed that, for degrees of saturation lower than 95%, the A' values oscillate between 150 and 1100 minutes. For degrees of saturation higher than 95%, the amplitude of oscillation increases significantly from 300 to 3400 minutes. Theoretically, the A' values should be higher for high degrees of saturation, since, for this condition, the radii of bubbles are smaller and the diffusion path for gas molecules to migrate from the liquid phase to the gas bubbles is larger. This might explain the increase in A' values observed at degrees of saturation close to 100%. The laboratory tests performed by Sobkowicz, 1982, indicated the same trend of the test results presented in Figure 4.64.

The time-dependent parameters obtained from the mercury triaxial tests reflect a condition where the soil samples were fully saturated with close to zero effective stresses. In order to achieve this state, the samples expanded and

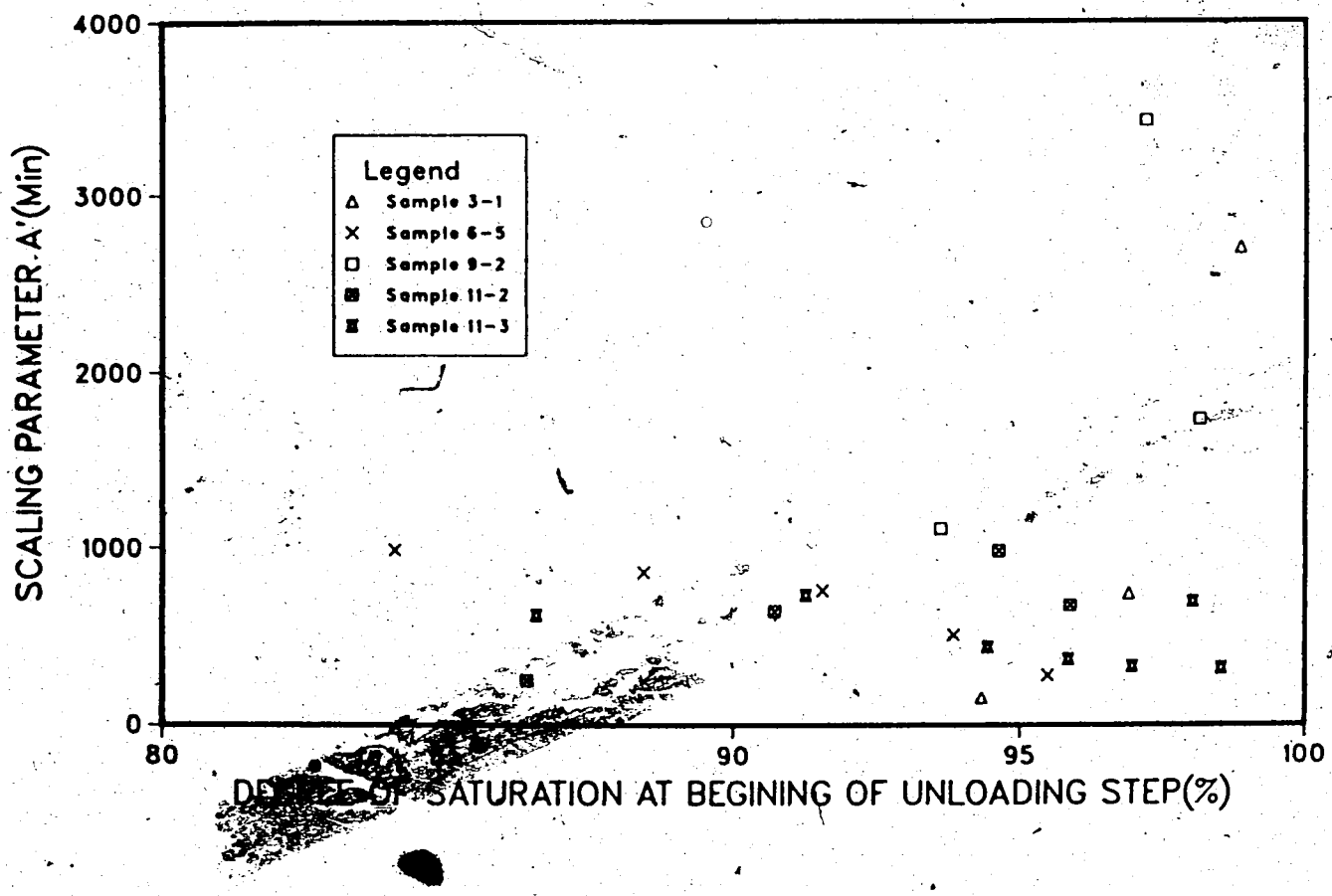

Figure 4.64 Scaling Parameter A' versus Total Degree of Saturation

inspect the changes in behaviour of the time-independent response of the tests, if the samples were saturated at higher effective stresses and consequently have lower water content. This consideration is valuable for the appropriate evaluation of scaling parameters for the hollow cylinder test simulations performed in Chapter 5.

According to the discussion of test results in the preceding paragraphs, the presence of water accelerates the overall observed gas evolution process. Therefore, one might expect that samples saturated at higher effective stresses, thus with lower water content, would present a lower gas evolution rate. On the other hand, the smaller size of pores associated with this condition also affects the transient response of the sample. For the same pore geometry and number of bubbles forming in the pores, the smaller the pore, the faster gas evolution should achieve a condition of equilibrium, due to the shorter path the gas molecules have to travel.

Based on these considerations, one can conclude that the extrapolation of scaling parameters from the conditions in which the tests were performed, to any other hypothetical condition, is difficult. The tests performed herein and the data available in the literature do not allow accurate extrapolations.

4.3.4.4 Summary of the Gas Evolution Test Results

The tests presented in this section allowed the evaluation of the time-independent (equilibrium) and time-dependent (transient) response of Athabasca oil sands samples. The samples were saturated at low effective stresses (approximately zero) and on the average the pores were filled with 30% water and 70% bitumen.

The solubility coefficient varied from 0.08 to 0.21 and with the help of the discussion developed in Section 2.2, indicated that the total amount of gases involved in the gas evolution process is probably composed of large amounts of CH_4 ($\simeq$70%) followed by CO_2 ($\simeq$20%) and small amounts of N_2 and O_2 ($\simeq$10%).

The time-dependent analysis of the tests results indicated that the "quotient+1" equation best describes the observed transient gas volume increase. Scaling factors A', varying from 150 to 1100 minutes were obtained for degrees of saturation lower than 96%, with an average value of 500 minutes. For degrees of saturation higher than 96%, A' values varied from 300 to 3400 minutes.

4.3.5 Model Tests (Group B)

4.3.5.1 General

Hollow cylinder tests were chosen as the model tests in order to allow the evaluation of the simulation capabilities of the numerical model implemented in the computer program,

As already discussed in Section 4.3.1, the choice of this test was based on the possibility to accurately control all boundary conditions involved in the numerical simulation and to simulate situations commonly encountered in underground excavations.

Two types of tests were carried out:

Type I - Consists of the undrained isotropic unloading of the hollow cylinder samples

Type II - Consists of the drained unloading of the internal bore of the hollow cylinder samples.

Type I tests should allow the independent evaluation of the gas evolution model implemented in CONGAS. This is possible because the volume changes of the sample occur mostly due to gas evolution and are not related to the drainage of water, in or out of the sample. The constitutive model chosen to simulate the sand skeleton behaviour should also closely simulate the observed sample behaviour, since shear dilatancy and shear stress reversal, which cannot be simulated by the non-linear elastic model chosen, are not present in this test.

Type II tests, on the other hand, involve the boundary conditions usually encountered in underground excavations in oil sands. Drainage and shear strains within the soil mass are present in this test. The limitations of CONGAS should be stressed when compared with these test results.

The following sections describe the hollow cylinder

4.3.5.2 Hollow Cylinder Testing System

Hollow Cylinder Cell

The cell used for the hollow cylinder tests had previously been designed and machined at the University of Alberta for another research program and later taken to the University of Waterloo. With the development of the research program described herein, the cell was borrowed from Waterloo. To the writer's knowledge, this cell had not been used prior to the testing program described in this Section.

Figures E.15 to E.17 present the drawings and details of this cell.

A load piston, top collar, top cap, top platen, sample pedestal and mercury jacket were specially designed for this research. The drawings and illustrative sketches on the apparatus and assembly sequence are depicted in Figures E.18 to E.23.

This apparatus allows the independent control of pressures in the inner bore (or internal cell), in the external cell and in the load piston. It also allows drainage at the top and bottom platen of the sample, through stainless steel porous stones recessed in the top cap and the bottom pedestal. The following sections describe these pressure systems.

Back Pressure and Confining Pressure Systems

Figures E.20 to E.22 present the details of the top cap and top platen. They were designed to allow the independent

at the top of the sample. Figure E.21 and Plate 4.15 illustrate the top view of the top cap. Four ports are shown in this figure; two are used for the application and measurement of the internal cell pressure and two for the top back pressure.

Two pore pressure ports were also available at the bottom platen. As on the top cap, one port was connected to a pressure transducer and the other to the back pressure system, which in this test program supplied pressures to both the top and bottom of the sample.

A port at the base of the cell was connected to the cell pressure line. The measurement of cell pressure was made with a pressure transducer installed at a port at the top of the cell.

The schematic of the pressure systems used to control the three pressures, i.e., internal, external and back pressures, is presented in Figure 4.65. Each of the pressure systems is similar to the ones used for the execution of drained triaxial tests which were described in Section 4.3.3.2. The only difference between the two systems is that three large water reservoirs were used in the air supply lines. This was because a much larger sample was used in this stage of the testing. These reservoirs had silicone oil at the interface of air/water in order to slow the migration of air molecules to the water in the system.

Axial Loading Systems

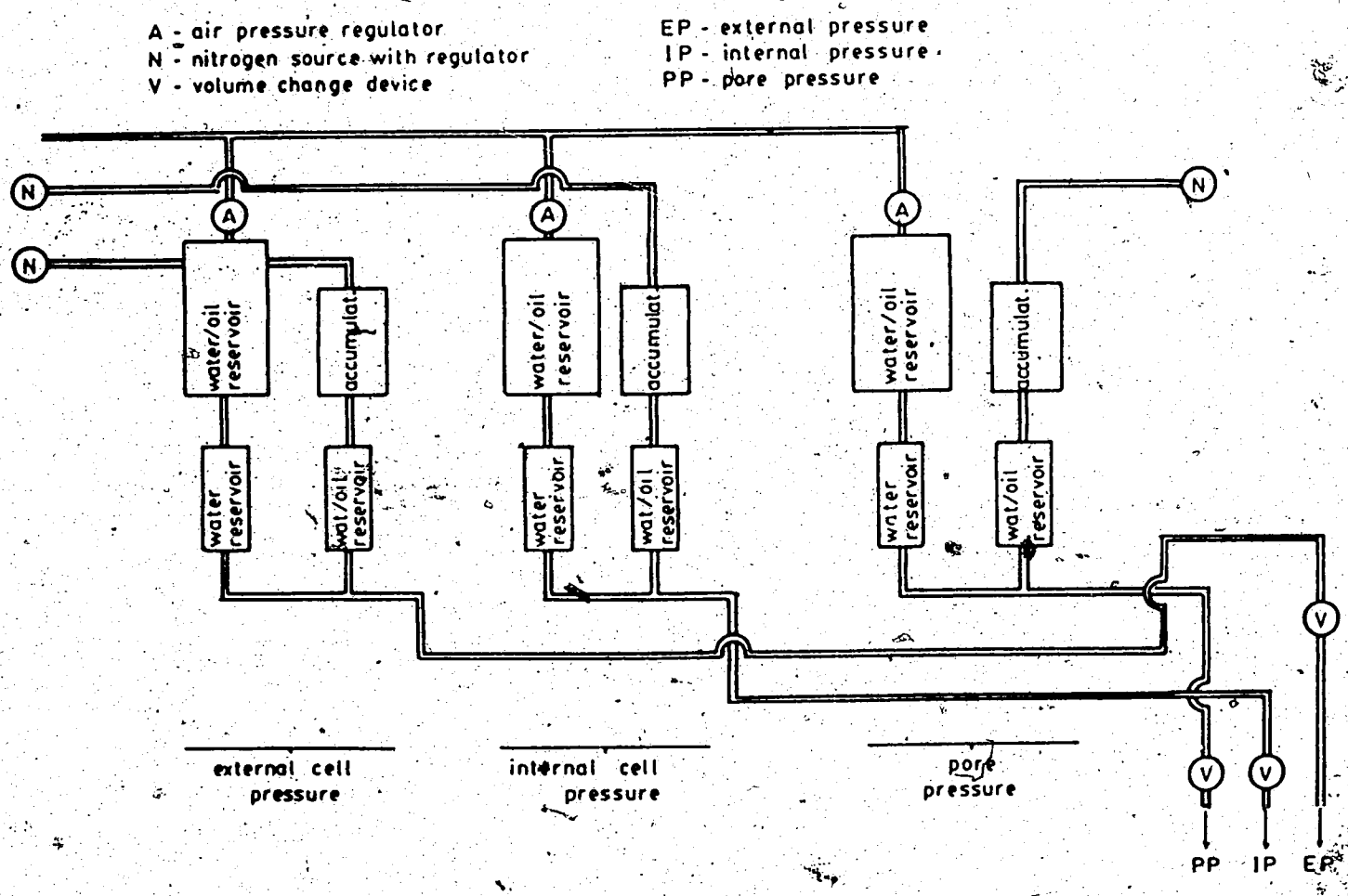

Figure 4.65 Hollow Cylinder Tests - Schematic of Pressure Systems

Axial loading of the samples was provided by a hydraulic pump powered by a Servo-Controlled electric stepping motor which drove a 490 kN capacity hydraulic ram, mounted on a steel frame. The stepping motor was a Mesur-Matic, model 355-760-1600. The hydraulic pump was a Jefri pump, model 1000-1-10-HP, with a pressure capacity of 69 MPa. The hydraulic ram was an O.T.C. model 4144, 2-3/8" stroke.

An electronic servo-control unit used a pressure transducer feedback to control the hydraulic pump pressure rates between preset lower and upper limits.

The electronic servo-control unit could also control the displacement rates of the pump piston.

An aluminum spacer and a load cell, which is described in the following section, were placed between the hydraulic ram and the loading piston. Plate 4.16 presents a view of the hollow cylinder cell and the axial loading system.

Monitoring Devices

During the performance of the tests it was possible to monitor the following quantities:

- vertical displacement of the top of the samples
- average horizontal displacement of the outside wall of the sample
- average horizontal displacement of the inside walls of the centre hole
- pressure applied to the outside wall of the sample
- pressure applied to the inner bore

Plate 4.15 Hollow Cylinder Cell and Top Cap

Plate 4.16 Hollow Cylinder Cell and [illegible]ng System

- vertical load applied to the top of the sample
- pore pressure at the top and bottom of the sample
- temperature outside the cell for Type I tests, and at the base of the cell for Type II tests.

The vertical displacement of the top of the samples was monitored through two LVDTs (Hewlett Packard - 500 - 24 Volts). They were mounted diametrically opposed in a aluminum collar that was attached to the loading piston. The inner bore of the LVDTs rested on the piston guide that was attached to the top of the cell.

The relation between the displacement measured and the actual vertical displacement of the top of the sample is discussed later in this section.

The evaluation of the average horizontal displacement of the outside wall of the samples was accomplished by monitoring the volume of water that entered or left the external cell. This monitoring was performed with a volume change device identical to the one described in Section 4.3.4.3. The horizontal displacement was assumed to be equal to the change in volume of water in the cell divided by the lateral outside area of the sample. The same approach was used to evaluate the horizontal displacement of the walls of the centre hole.

The internal and external cell pressures were monitored by Schaevitz pressure transducers with capacities of 3.5 MPa and 7.0 MPa, respectively.

The top and bottom pore pressures were independently measured by a Celesco and a Viatran pressure transducer, both with capacities of 2.0 MPa.

The vertical load on the load piston, outside of the cell, was monitored with a Durham Instruments load cell, with a maximum capacity of 89 KN. It was mounted on the loading piston and provided reaction against the hydraulic ram.

The Jefri pump pressure and the axial displacement of the pump piston were measured during the test with a 35 MPa capacity Celesco pressure transducer and with a 24V - 2000 Hewlett-Packard LVDT, respectively.

The Jefri pump pressure transducer was calibrated against the piston load cell in order to directly control the axial loads on the piston from the Servo-control unit. Figure E.24 presents the calibration curve.

Temperatures were monitored with a RTD mounted in a stainless steel probe which was initially attached to the outside to the cell and later inserted in a port at the base of the cell.

The calibration of the volume change devices and pressure transducers followed the same procedures described in Section 4.3.3.2.

The electronic outputs from the monitoring devices were automatically collected and printed in a Fluke 2240B Datalogger.

System Compliance and Temperature Effects

A series of calibration tests were performed in order to relate the quantities measured at the monitoring devices with the actual physical quantities at the samples. These tests consisted of evaluation of the:

- vertical compliance of the system in order to relate the vertical LVDT readings with the vertical displacements of the top of the sample;
- volumetric compliance of the external cell, in order to relate the water volume change readings with the horizontal displacements of the outside walls of the sample;
- volumetric compliance of the internal cell, in order to relate the water volume change readings with the horizontal displacements of the inside wall of the centre hole of the sample;
- volumetric compliance of the back pressure system, in order to relate water volume change readings with the actual volumes of water absorbed by the sample.
- effects of the cell temperature fluctuations on the monitored quantities.

All compliance tests were performed with an aluminum block with the same dimensions as the samples. It was assembled in the triaxial cells with the membranes, filter papers and "O-rings" usually used during the regular tests.

Figures E.25 to E.29 present the average system compliance curves for each of the items cited above. These curves were used in the data reduction presented later in

this chapter.

Room temperature fluctuations proved to be a significant source of inaccuracies in the measurement of the volume that flowed into or out of the volume change devices. The hollow cylinder tests were performed late in the spring, when room temperatues varied up to 2°C. With temperature fluctuations, the volume of water in the cell (internal and external) varied as well, independently of the volume changes of the sample. The accurate calibration for the temperature fluctuations was difficult because the temperatures measured by the RTD, installed at the base of the cell, were not necessarily the average temperature of the water in the system. A theoretical temperature correction for the thermal expansion of the three pressure systems was then calculated. This was possible with the evaluation of the volume of water contained in each system and by assuming a coefficient of thermal expansion of water (0.0002 to 0.0003°C^{-1}).

Calculations indicated that the thermal corrections should be approximately:

- back pressure system: 0.018 cc/°C
- internal cell system: 0.059 cc/°C
- external cell system: 3.674 cc/°C

Considering the temperature fluctuations (±2°C), the magnitude of the volume changes observed during the tests (0-40 cc) and the difficulties in properly assessing the average temperatures within the pressure systems, it is

possible to conclude that the errors involved in the measurements of volume changes in the back pressure and internal cell pressure are small, whereas the ones obtained in the external cell pressure system can be unacceptably high.

Piston Friction

The calibration for the friction developed between loading piston and the piston guide aimed at relating the load measured by the load cell, installed outside the cell and the load actually acting on the top of the sample.

The calibration tests for this purpose were performed without any sample or aluminum block inside the cell. This procedure allowed the control of the vertical pressure acting on the piston, which became equal to the cell pressure. The test consisted of applying cell pressures, which were converted to a vertical load acting on the piston by multiplying it by the cross- sectional area of the piston, and comparing it with the load measured by the vertical load cell. The difference between them was attributed to the piston friction.

When the piston travelled upward, the piston friction oscillated between 0.5% and 5% of the load measured by the load cell. However, a change in the direction of piston movement, induced by pressure fluctuations or thermal expansion of the cell water, resulted in the drop of the piston friction to near zero values.

Calibrations were also performed with the piston travelling downward. It indicated that, for this condition, the piston friction was zero.

The low values of piston friction observed resulted in its negligence in the test data reduction.

4.3.5.3 Sample Preparation for Testing

The hollow cylinder tests were performed between 13 and 14 months after the sampling program. During this period, the samples were kept within air-tight PVC tubes inside a freezer at -20°C.

The preparation of a sample typically started three days before testing. Before trimming, the PVC tubes containing the samples were placed in dry ice for approximately 24 hours. After this period, the tubes were removed from the dry ice and, inside a cold room at -20°C, the samples were removed and laid horizontally on a table.

Uniform sections approximately 17 cm long were chosen from the sample and cut with a diamond saw. The unused parts of the sample were used either for classification tests or placed back into the PVC tube for storage.

The 17 cm long sections, with a diameter of approximately 15 cm, were placed in a split-ring mold, attached to the working table of a milling machine. Flat and parallel surfaces, 15.24 cm apart, were milled at both ends of the sample using a carbide bit.

A 3.81 cm external diameter diamond drill core barrel was mounted in the milling machine to drill the central

hole. Its tip was precisely centered with the sample longitudinal axis. The drilling proceeded in advances varying between 0.6 and 1.2 cm, intercalated by the removal of the drill and flushing of the cuttings with compressed air. At this stage, the sample was usually placed back onto dry ice for another 24 hours. The final step consisted of trimming the outside surface of the sample to its final diameter of approximately 14 cm.

An aluminum threaded mandrel was machined especially for this purpose. It was inserted in the central hole of the sample, and fixed tightly with a nut and two washers. This prevented rotation of the sample during the application of tangential forces which occur while trimming. The sample and mandrel assembly was mounted in the chuck of a lathe. A free rotating end pin fit in the free end of the mandrel. It enabled the accurate alignment of the mandrel with the lathe bed and helped the lathe to retain the sample.

A diamond tipped bit was used to trim the samples to the final diameter. The trimming was performed in 0.250 mm cuts in its early stages and in 0.050 to 0.125 mm cuts when finishing the surface.

After trimming, the samples were placed into an air tight can and put into dry ice for approximately 24 hours, before being assembled in the test cell.

The placement of the sample on the hollow cylinder cell pedestal took place in a cold room at -20°C.

The bottom platen of the cell was prechilled, before the assembly of samples, to -20°C. The rubber "O-rings" were greased with high vacuum grease, prior to the chilling of the platen. The top cap and top platen were assembled with the central hole membrane. This was a latex membrane, 0.7 mm thick, moulded in a specially designed mould, illustrated in Figure E.30. The procedure suggested by Vaid and Campanella, 1973, was followed in order to manufacture these membranes.

The external face of the membrane was heavily greased with Dow Corning High Vacuum Grease, a silicone based lubricant, in order to minimize the loss of gases from the samples during testing. Within the cold room, filter paper was placed at the top and bottom ends of the samples, and the top cap/platen/membrane assembly was mounted on the sample as depicted in Plate 4.17. It had been planned originally to place two greased latex discs between each of the sample ends and end platens, in order to guarantee a frictionless boundary condition at these ends. However, during the cell calibration tests, these discs caused difficulties in maintaining the sample and loading piston aligned. It was verified that a small amount of friction was necessary in order to minimize this problem. Hence, a thin film of vacuum grease was applied to the end platens and the latex discs were not used.

With the top cap, platen and internal membrane installed, the sample was placed on the bottom pedestal. An external latex membrane, 0.5 mm thick, was placed around the

sample and kept tight against the top and bottom platens with two "O-rings" installed according to Plate 4.18. The external membrane was heavily greased with vacuum grease in order to minimize the loss of gases from the sample to the external cell during testing (Plate 4.18). Originally, the bottom pedestal had been designed to hold a PVC jacket in which mercury would be placed. The mercury would guarantee efficient containment of the gases within the sample. However, the complete removal of the mercury from the internal membrance and PVC jacket, during the calibration tests, proved to be very difficult. On one occasion, a leak through the internal membrane and the bottom platen resulted in the flow of mercury into the bottom porous stone and back pressure line. The cleaning of the cell was tedious and health hazardous, due to the large amounts of mercury exposed to the atmosphere. For these reasons, it was decided to abandon the use of mercury, and, instead, the membranes were heavily greased with highly viscous vacuum grease. The PVC jacket was still placed around the sample in every test, so that the calibration curves obtained with it could still be used.

After the greasing of the external membrane was completed, the sample assembly was taken out of the cold room to the laboratory where the tests were performed. A vacuum pump was attached to the back pressure port at the base of the cell and vacuum was applied to guarantee good contact between the sample and bottom platen. The base of

Plate 4.17 Hollow Cylinder Test - Sample Preparation for Testing

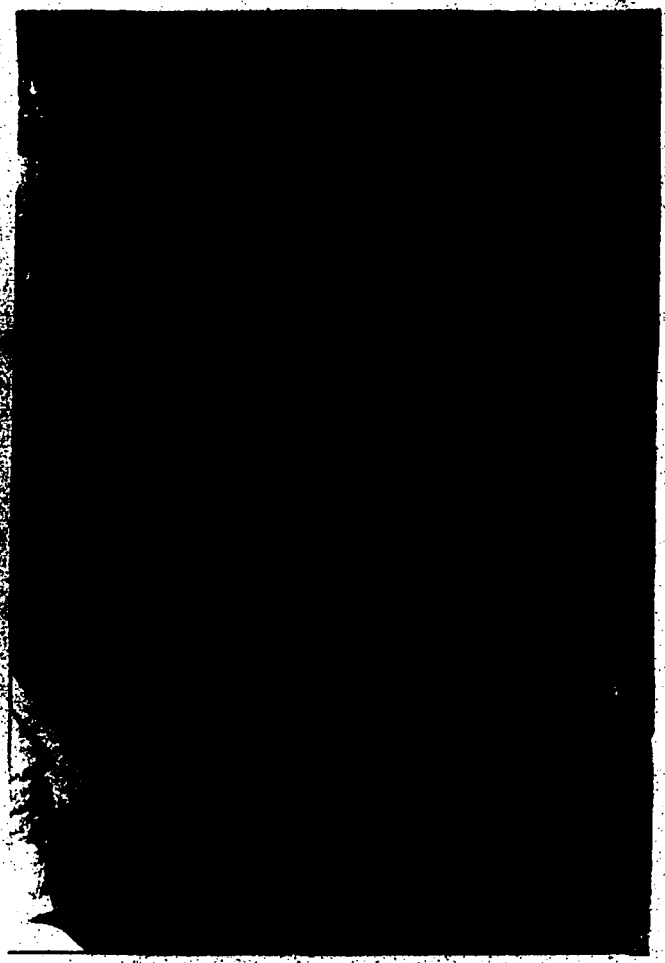

Plate 4.18 Hollow Cylinder Test - Sample Preparation for Testing

the cell was then removed from the cart to the loading frame. The loading piston was lowered in position against the top cap sprayed with silicone oil to guarantee low piston friction during testing.

The external membrane was stretched upward covering the connection between the top cap and loading piston. Another "O-ring" was placed surrounding the membrane against the loading piston. After the PVC jacket was lowered in position, a 25 mm wide and 1 mm thick latex membrane was placed around the connection between the loading piston and top cap. It was held in place by a hose clamp and aimed at avoiding the squeezing of the external membrane against that connection. During the calibration phase, this was a problem that led to the loss of the seal against external cell water flowing into the loading piston central hole.

With the loading piston in place, the body of the cell was lowered onto the bottom plate. The cell was filled by a pump with water and the top plate and collar lowered by crane over the piston as illustrated in Plate 4.19.

Twelve lengths of "all thread" were screwed into the base plate and then nuts were tightened against the top plate (Plate 4.20). Care was taken in order to keep the top plate parallel to the base plate, as any deviation could result in misalignment of the piston and cause eccentric loading. The cell was filled until water flowed through the bleed valve located at the top of the cell. The output voltage of the pressure transducer, attached to the bleed

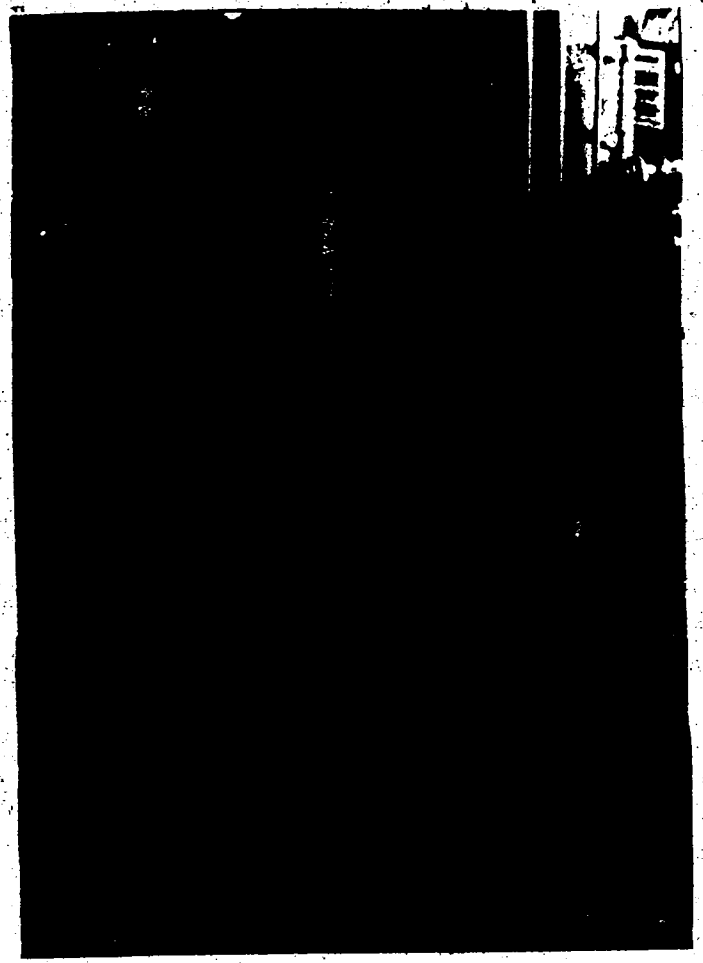

Plate 4.19 Hollow Cylinder Test - Lowering of Top Plate and Collar over the Piston

Plate 4.20 Hollow Cylinder Test - Tightening of the Nuts Against the Collar

valve, was recorded at this point.

To maintain the seal between the piston and the top cap, vertical loads were applied prior to the application of the external cell pressure. When the vertical load (70 kPa) was applied, some vertical compression occurred, which was partially recovered when the external pressure was applied. Both the external and vertical pressures were maintained at 70 kPa until the remainder of the cell preparation was complete. This consisted of filling the inner bore and obtaining the "zero" output voltage. The inner bore was then pressurized to 70 kPa.

The pore pressure lines and transducers were connected to the top cap and bottom platen of the cell, but were not pressurized until time was allowed for the sample to start to thaw (30 minutes). At this point the vertical LVDTs were attached to the load piston and the "zero" output voltages were recorded. It should be noted that the vertical displacement of the sample up to this point was not recorded.

From this point, the procedure for saturation of the samples and the testing techniques were different for each of the two types of tests performed. The following section present details associated with the tests.

4.3.5.4 Test Type I (Undrained Isotropic Unloading)

Test Procedures

Two tests were performed within this group and followed approximately the same procedures, in order to verify

reproducibility of the test results. The original plan was to saturate the samples to an isotropic state of stress with all the boundary pressures equal to 850 kPa and the back pressure equal to 400 kPa.

From this point, the back pressure valves would be closed and the sample submitted to undrained isotropic unloading with boundary pressure decreases of 150 kPa. Tables 4.18 and 4.19 present the pressures and times during which the samples were submitted to these pressures.

The pressures were raised in approximately 35 kPa increments until a pressure of 900 kPa was reached in both the external and internal cells. During loading, the vertical pressure was always increased first; the internal and external pressures were then increased simulaneously. This was accomplished by shutting in the pressures on the downstream side of the volume change devices. The pressures were set on the gauges and the valves then opened. Fine adjustment of the newly applied pressure was done by monitoring the output voltages and carefully adjusting the pressure regulator so that the precalculated voltage was achieved.

There were two reasons for applying the pressures in such small increments:

1. As the vertical pressure had to be applied prior to the application of the external and internal pressures, in order to maintain the seal between the top cap and the piston, a large increment would significantly change the

	VERTICAL PRESSURE (KPA)	EXTERNAL PRESSURE (KPA)	INTERNAL PRESSURE (KPA)	PORE PRESSURE (KPA)	TIME (HOUR)
SATURATION	70	60	60	0	2
	470	[illegible]	450	0	19
	700	650	650	50	1
	715	650	650	200	5
	850	850	850	200	1
	850	850	850	400	46
	1500	1330	1330	920	17
	1715	1630	1630	1200	2
	925	850	850	400	3
TEST	760	620	695	---	46.3
	615	480	555	---	46.4
	465	325	400	---	47.0

Table 4.18 Hollow Cylinder Test - Sample 26-1 - Saturation and Test Characteristics

	VERTICAL PRESSURE (KPA)	EXTERNAL PRESSURE (KPA)	INTERNAL PRESSURE (KPA)	PORE PRESSURE (KPA)	TIME (HOUR)
SATURATION	450	450	450	0	3
	570	515	515	110	21
	770	720	720	300	17
	940	900	900	460	21
	1760	1660	1660	1210	22
	930	840	840	400	28
TEST	770	700	700	---	47.9
	600	545	550	---	46.0
	455	385	395	---	46.3
	320	250	245	---	48.5

Table 4.19 Hollow Cylinder Test - Sample 27-2B - Saturation and Test Characteristics

stress ratio (vertical/horizontal) acting on the sample, as well as eventually subject it to undesirably high shear stresses.

2. At the lower stress ranges, air in the cell and lines was driven into solution resulting in volume changes greater than the one-way capacity of the volume change devices. Small increments were used so that the direction of flow in the volume change device was reversed during a period of stabilization.

When the cell pressure reached 900 kPa, the source was changed from air to N_2. Pressure increments of 70 kPa were then used due to the coarser adjustment capabilities of the N_2 pressure regulator.

The inverse procedure was used for the pressure decreases.

After saturation, as indicated in Table 4.18 and 4.19, the pressures were decreased in greater intervals. The decrease of the cell pressures was done prior to the decrease of the vertical stress in order to guarantee the seal between the piston and top cap. This procedure temporarily induced the development of shear stresses up to 200 kPa within the sample.

The water volume changes at the external cell, internal cell and at the pores of the sample, and the equivalent volume changes measured through the vertical displacement of the top of the sample are presented in Tables 4.20 and 4.21. Unfortunately, a leak detected in the volume change device

VOLUME CHANGES OBSERVED DURING THAWING AND SATURATION

EXTERNAL CELL (CC): - 14.138 (*) (SAMPLE SHRINKING)
INTERNAL CELL (CC): - 4.702 (SAMPLE SHRINKING)
TOP OF SAMPLE (CC): - 2.308 (SAMPLE SHRINKING)
PORE WATER (CC): -65.219 (INTO THE SAMPLE)

(*) APPROXIMATE EVALUATION DUE TO MALFUNCTION OF THE VOLUME CHANGE DEVICE

SAMPLE CHARACTERISTICS

	FROZEN SAMPLE	AFTER THAWING AND SATURATION
OUTSIDE DIAMETER (CM)	13.99	13.97
INSIDE DIAMETER (CM)	8.94	4.00
HEIGHT (CM)	15.15	15.13
TOTAL VOLUME (CC)	2144.02	2122.87
VOLUME OF WATER (CC)	110.48	175.70
VOLUME OF BITUMEN (CC)	556.19	556.19
VOLUME OF GAS (CC)	191.07	104.70
VOLUME OF SAND (CC)	1286.28	1286.28
TOTAL DEG. OF SAT.	0.77	0.88
TOTAL VOID RATIO	0.667	0.650
BITUMEN VOID RATIO	0.432	0.432

Table 4.20 Hollow Cylinder Test - Sample 26-1 - Sample Characteristics

VOLUME CHANGES OBSERVED DURING THAWING AND SATURATION

EXTERNAL CELL (CC):	-34.005	(SAMPLE SHRINKING)
INTERNAL CELL (CC):	+ 2.263	(SAMPLE EXPANDING)
TOP OF SAMPLE (CC):	- 6.469	(SAMPLE SHRINKING)
PORE WATER (CC):	-74.360	(INTO THE SAMPLE)

SAMPLE CHARACTERISTICS

	FROZEN SAMPLE	AFTER THAWING AND SATURATION
OUTSIDE DIAMETER (CM)	14.01	13.96
INSIDE DIAMETER (CM)	3.90	3.71
HEIGHT (CM)	15.30	15.25
TOTAL VOLUME (CC)	2176.49	2138.28
VOLUME OF WATER (CC)	55.50	129.86
VOLUME OF BITUMEN (CC)	646.64	646.64
VOLUME OF GAS (CC)	135.50	22.93
VOLUME OF SAND (CC)	1338.85	1338.85
TOTAL DEG. OF SAT.	0.84	0.97
TOTAL VOID RATIO	0.626	0.597
BITUMEN VOID RATIO	0.483	0.483

Table 4.21 Hollow Cylinder Test - Sample 27-2B - Sample Characteristics

at the external cell pressure line during saturation of Sample 26-1 made it impossible to calculate the volume of the sample after saturation. The values indicated in Table 4.20 were calculated assuming that no volume change occurred after leaking started. The resultant low degree of saturation (0.875), after saturation was thought to be completed; reveals that this assumption was erroneous. Considering the times and pressures used for sample saturation, and the fact that the water had ceased to flow into the sample when the back pressure valves were closed, it is reasonable to assume that the degree of saturation was higher than the one indicated.

The analysis of the first unloading step of the test, presented later in this section, indicates a B value of approximately 0.60, which can be related to a degree of saturation between 0.96 and 0.97, which is the degree of saturation of Sample 27-2B. This is a good indication of the value of the actual degree of saturation of Sample 26-1.

Due to variations of temperature during the saturation of the samples, and the difficulty in relating the temperature measured at the base of the cell with the average temperature of the cell water, the volume changes indicated in Tables 4.20 and 4.21 are subjected to errors of up to 10%. This fact makes the evaluation of the predictive capabilities of CONGAS more difficult, as will be discussed in the following chapter.

Test Results: Presentation and Analysis

The test data collected and reduced according to calibrations discussed in the preceding sections, for Type I tests, are presented in Figures 4.66 to 4.72.

Steps A to C represent the stages of the tests during which the boundary conditions were kept approximately the same for both samples. Therefore, assuming that the two samples have similar geotechnical properties at the beginning of the test, one might expect that, for test stages labelled with the same letter (i.e., A, B or C), the samples should behave similarly. Sample 27-2B was subjected to one additional unloading step, as compared to Sample 26-1.

The analysis of the temperature variations and the volume changes of the water in the external cell, after calibration and thermal corrections were made, indicate that the latter were affected to a significant extent by temperature fluctuations. It is evident that the thermal corrections did not account for all volume change fluctuations observed. According to data published by A.O.S.T.R.A., 1984, for temperature fluctuations of ±2°C about 24°C, the solubility coefficient of the Athabasca oil sands varies less than 5%, and the diffusivity to CO_2 up to 50%. These numbers indicate that temperature fluctuations within these limits should result in negligible fluctuation of the equilibrium volume of free gas but might affect the rate at which this volume is achieved. The data shown in Figures 4.66 and 4.69, however, indicate that the magnitude

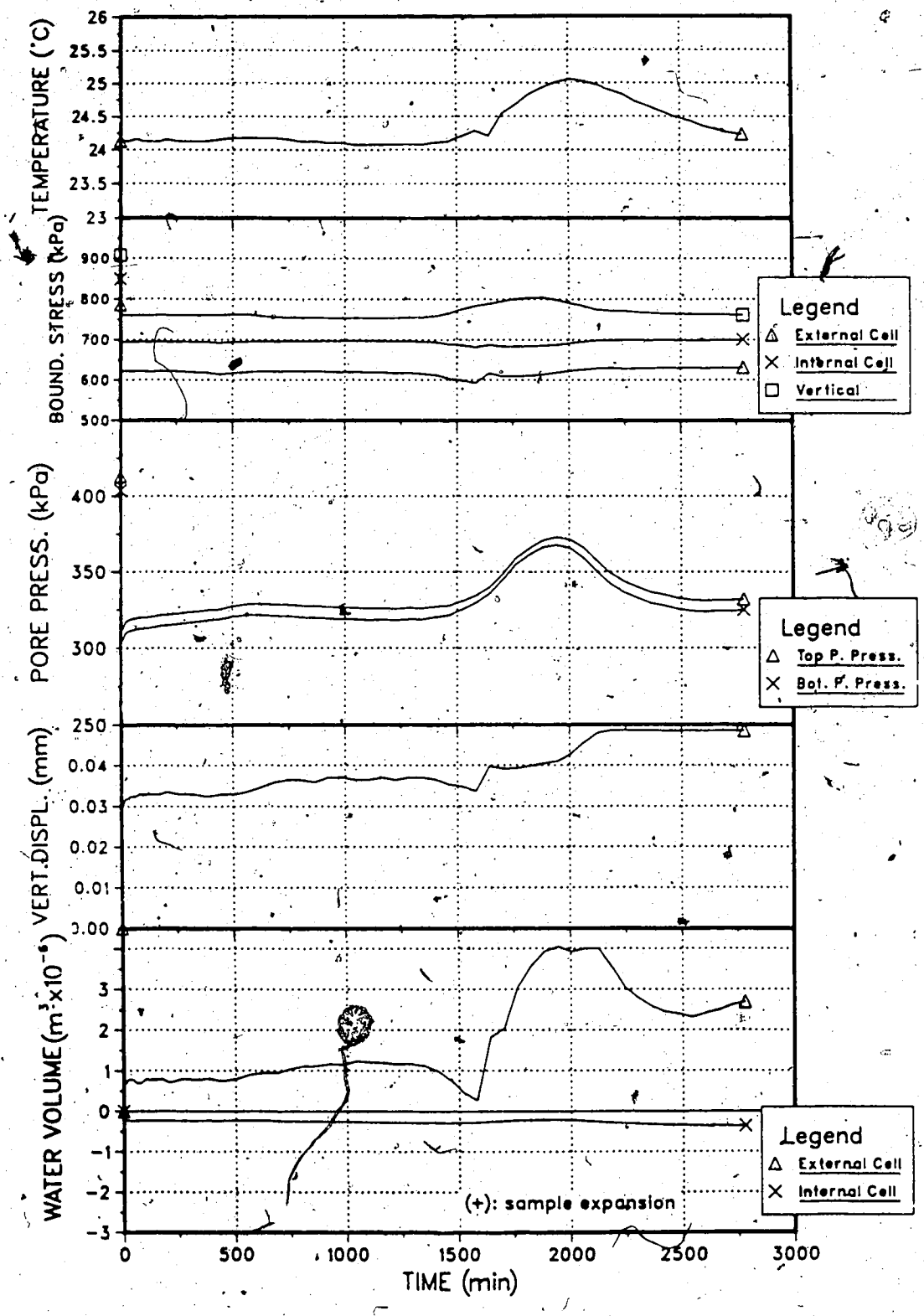

Figure 4.66 Hollow Cylinder Test - Sample 26-1 - Step A

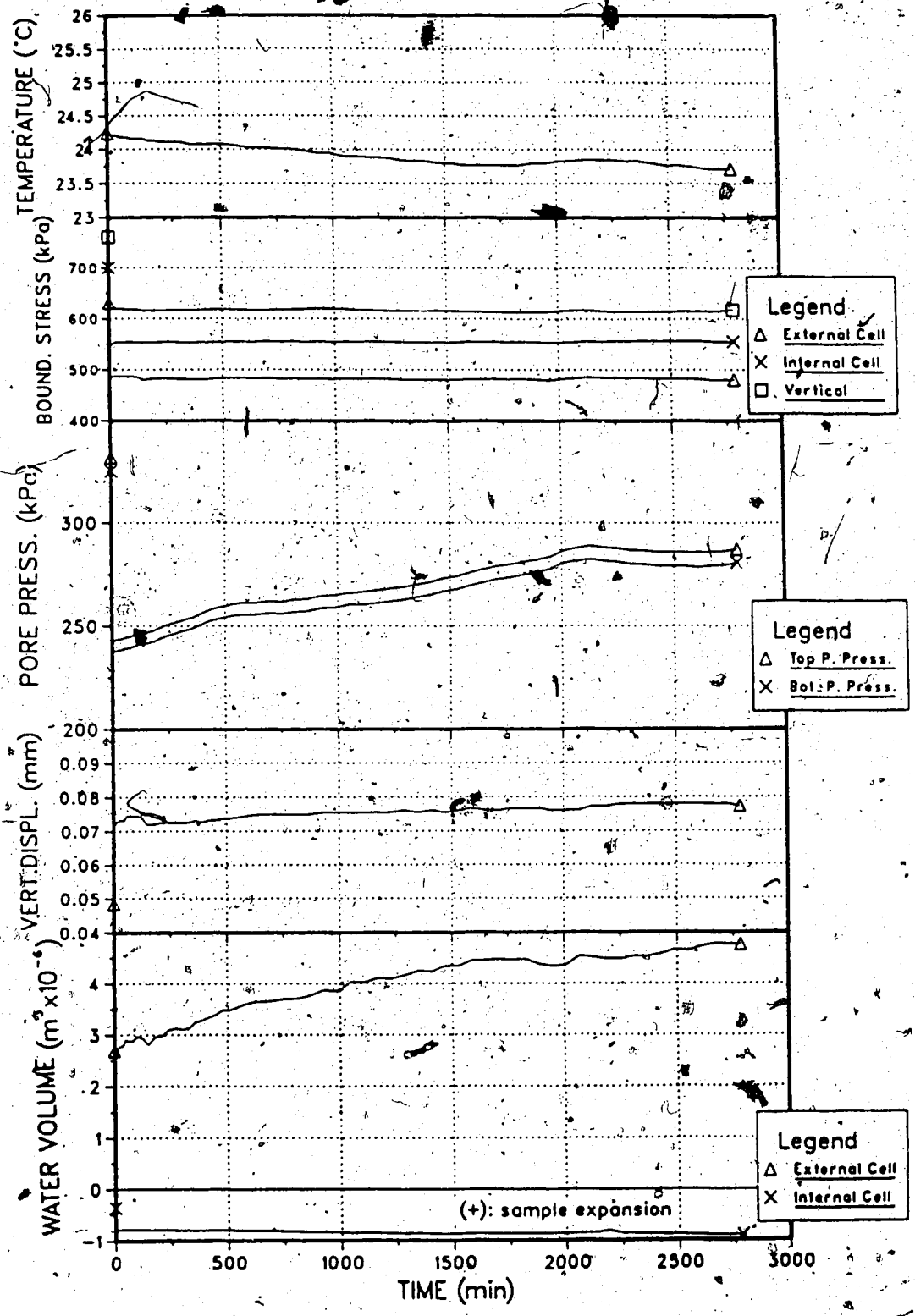

Figure 4.67 Hollow Cylinder Test - Sample 26-1 - Step B

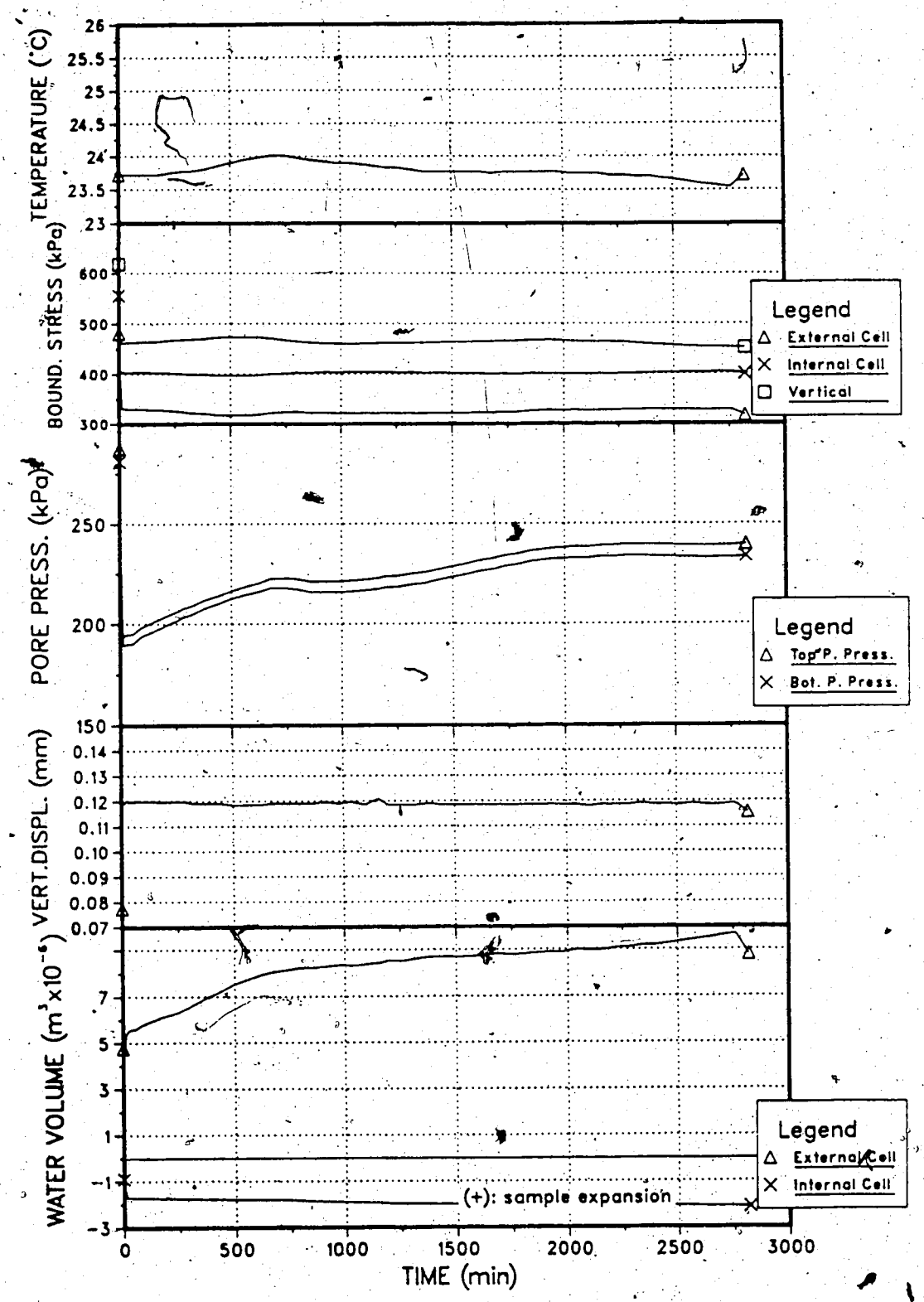

Figure 4.68 Hollow Cylinder Test - Sample 26-1 - Step C

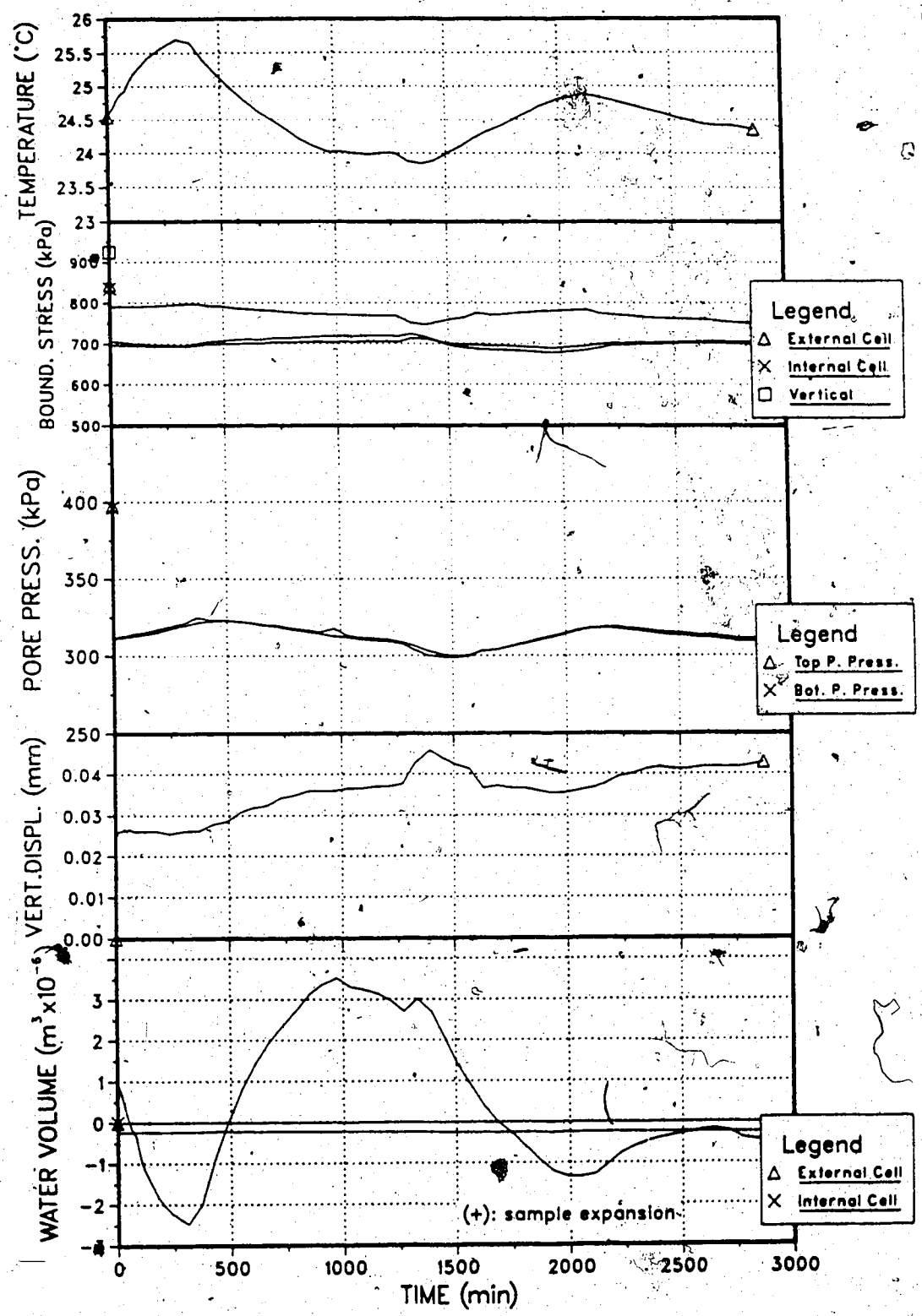

Figure 4.69 Hollow Cylinder Test - Sample 27-2B - Step A

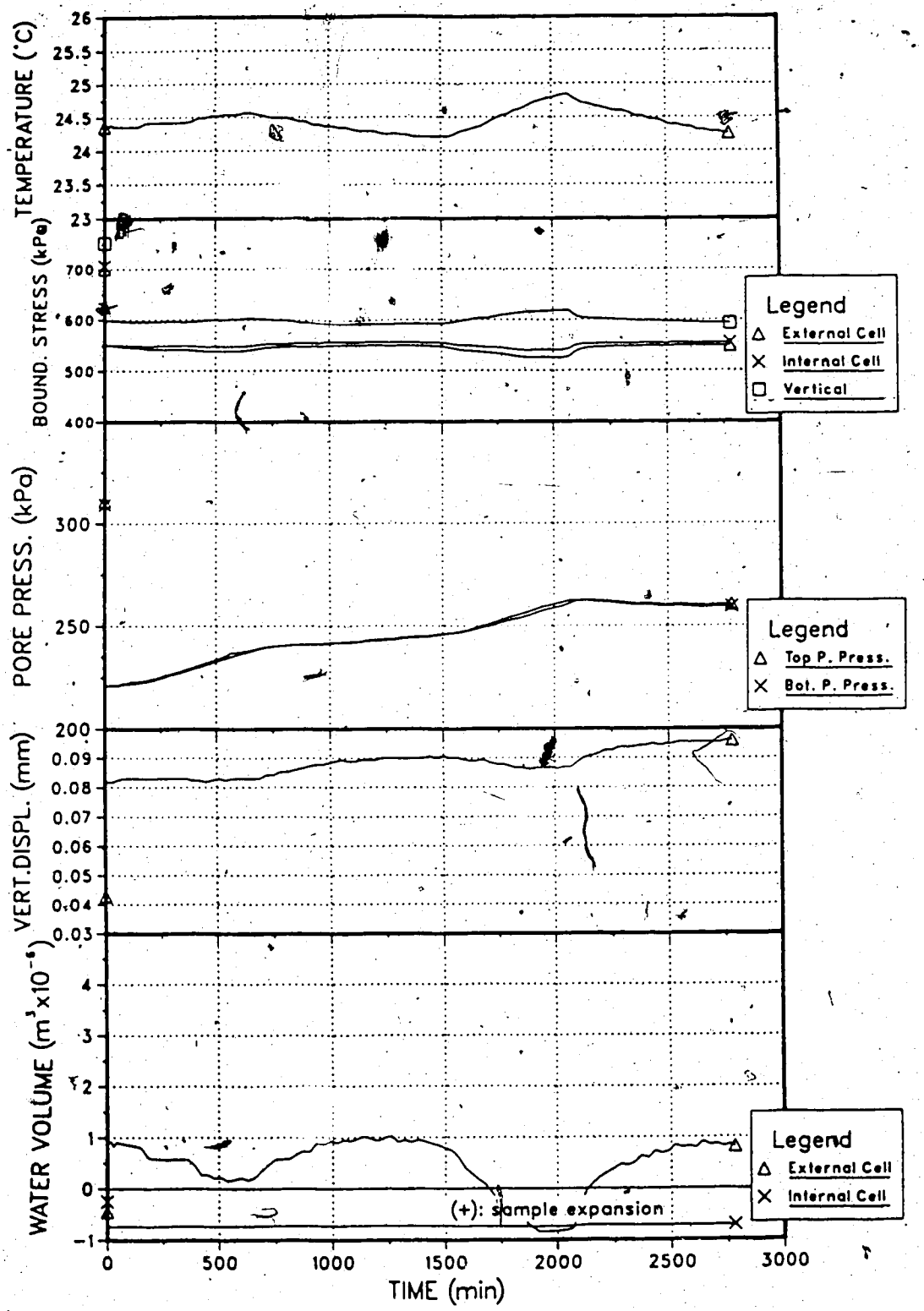

Figure 4.70 Hollow Cylinder Test - Sample 27-2B - Step B

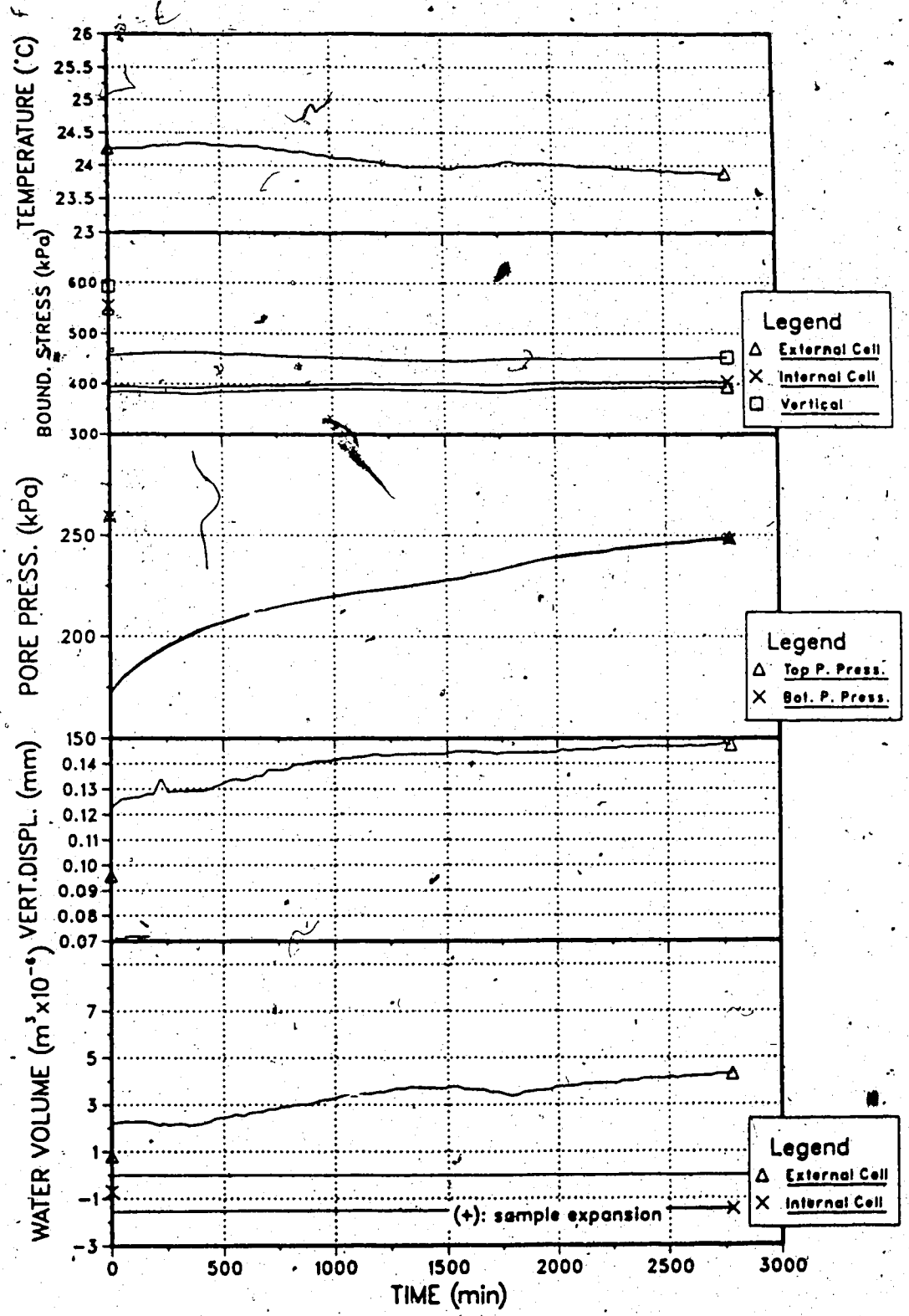

Figure 4.71 Hollow Cylinder Test - Sample 27-2b - Step C

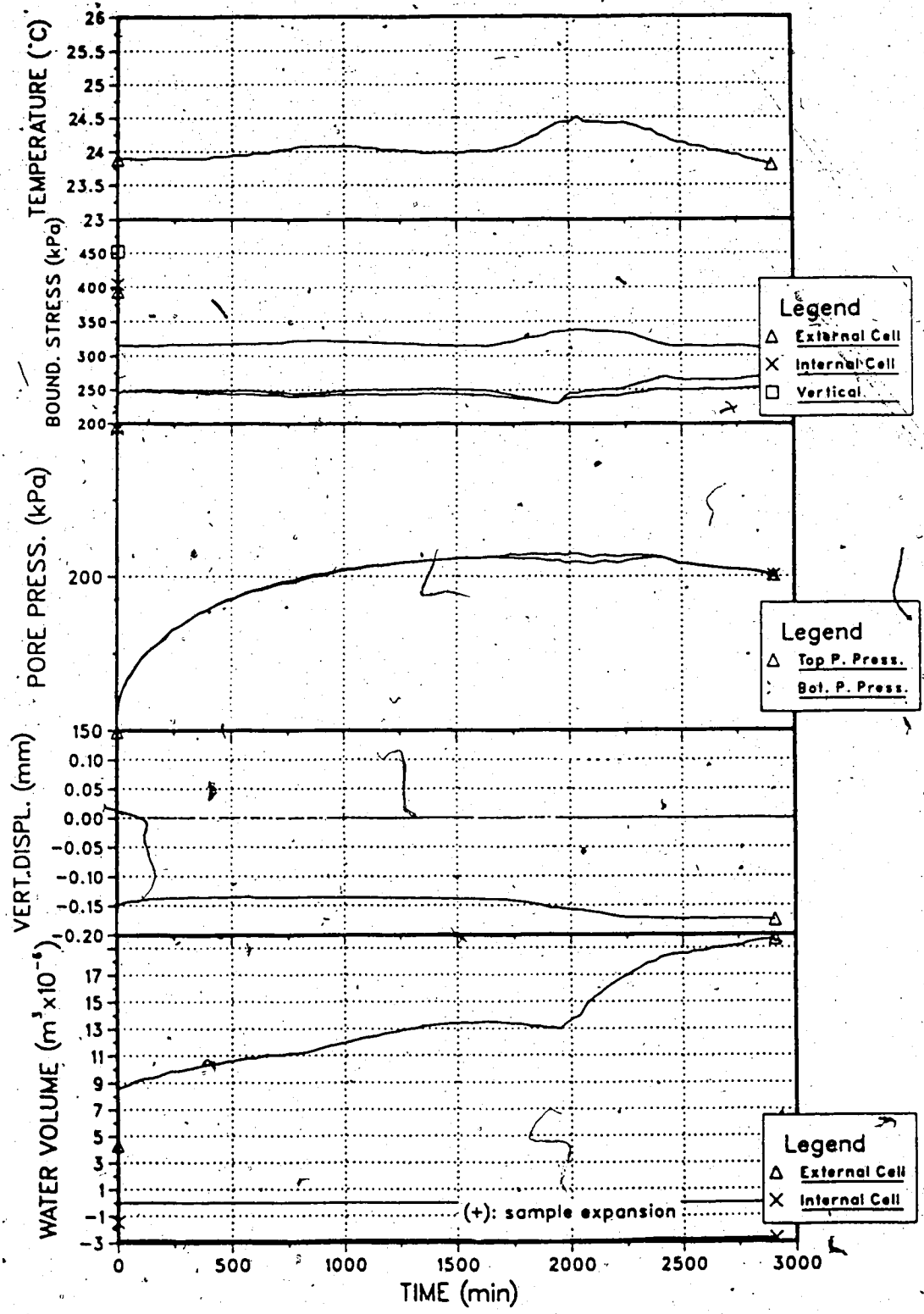

Figure 4.72 Hollow Cylinder Test - Sample 27-2B - Step D

of the changes in the volume of the sample, supposedly primarily related to changes in volume of free gas, were substantially affected by small temperature fluctuations. This leads to the conclusion that the theoretical corrections for water thermal expansion did not correctly reflect the expansions that actually took place during testing.

As previously discussed in this section, the difficulties in assessing the thermal correction to be applied to the volume change readings are partly related to the inability to relate the temperature measured by the RTD, which, for TYPE I tests, was attached to the outside wall of the cell, with the average temperature of the cell water. The rapid change in temperature measured by the RTD during a test was not necessarily associated with the volume increases measured by the volume change device. The data reduction procedure, however, reduced all measured quantities for the current temperatures, forces, and stresses. This procedure seemed to be appropriate for slow increases of temperature (1000 min/1°C), when the average temperature of the cell water could be more representatively measured by the RTD.

Considering the aforementioned facts and the volume changes depicted in Figures 4.66 to 4.72, it is possible to restate the conclusions drawn earlier in this chapter that the inaccuracies of the external cell volume changes were unacceptably high. Therefore, these quantities should not be

referred to for the analysis of the accuracy of prediction of CONGAS.

The other quantities, however, such as pore pressures, vertical displacements of the piston, vertical load and internal cell volume change, were not significantly affected by temperature fluctuations.

Step A of both tests was performed with similar boundary conditions except the external cell pressure for Sample 26-1 that was approximately 100 kPa less than that for Sample 27-2B.

Except for temperature induced fluctuations the pore pressure response in both cases are similar. The small pore pressure increases indicate that during this stage of this test, the pore pressure might be higher than the bubble point pressure. The upward vertical displacements were also similar for both tests and showed a slight increase with time. The internal cell volume change was similar for both tests and did not reflect any time-dependency.

During Step B, the external cell pressure in Test 26-1 was, again, consistently lower than in Test 27-2B, by approximately 60 kPa. The pore pressures responded similarly to the variations in boundary conditions, reflecting some time-dependency. During this stage, the bubble point pressure might have been achieved. Both the vertical displacements and internal volume changes were similar for both tests, reflecting negligible time-dependency.

The observations made for Step B can be extended for Step C, except for the vertical displacement of the piston. As opposed to Sample 27-2B, Sample 26-1 did not present a time-dependent response. Step D was performed only in Sample 27-2B. Here again, no time-dependent vertical displacement of the piston and volume change of the internal cell were noticed, as opposed to the pore pressures.

4.3.5.5 Test Type II (Drained Plane Stress Shearing)

Test Procedures

Similar to TYPE I tests, two TYPE II tests were performed in order to verify the reproducibility of test results. For these tests, the RTD was installed in the base of the cell. It was planned to saturate isotropically the samples with all around pressures of about 2000 kPa and back pressures of 1000 kPa. After saturation, the back pressure would be dropped to 400 kPa and time would be allowed for the pore pressure to equalize within the sample. At this stage, the testing would start with an instantaneous decrease of the internal cell pressures to 1000 kPa, and the back pressures at the top and bottom of the sample to 100 kPa. In the second stage of unloading, the internal pressure would be dropped to 500 kPa. Tables 4.22 and 4.23 depict the boundary conditions imposed on the samples during saturation and testing.

The pressures were modified according to the procedure described in the preceeding section, 4.3.5.4. The water volume changes at the external cell, internal cell, pores of

	VERTICAL PRESSURE (KPA)	EXTERNAL PRESSURE (KPA)	INTERNAL PRESSURE (KPA)	PORE PRESSURE (KPA)	TIME (HOUR)
SATURATION	430	370	370	0	3
	1260	1160	1160	770	67
	2097	1980	1980	1000	23
	2070	2000	2000	400	21
TEST	2070	1930	1000	100	48.0
	2130	1917	500	100	72.0

Table 4.22 Hollow Cylinder Test - Sample 27-2C - Saturation and Testing Characteristics

	VERTICAL PRESSURE (KPA)	EXTERNAL PRESSURE (KPA)	INTERNAL PRESSURE (KPA)	PORE PRESSURE (KPA)	TIME (HOUR)
SATURATION	620	550	550	0	4
	925	820	820	320	17
	2110	1980	1980	1020	5
	2110	1980	1980	410	4
	2110	1980	1980	410	11
TEST	2180	1960	1010	100	48.0
	2160	1950	480	100	48.6

Table 4.23 Hollow Cylinder Test - Sample 28-2C - Saturation and Testing Characteristics

the samples and the equivalent volume change measured through the vertical displacement of the top of the sample are presented in Tables 4.24 and 4.25. A leak was detected in the internal cell system, towards the end of the saturation of Sample 27-2C. Due to this reason, the sample characteristics after saturation, indicated in Table 4.24, are approximate. The relatively low degree of saturation achieved for Sample 27-2C (S=0.94) is probably related to errors in calculation of the total volume of the sample, as a result of the internal cell leak. Considering the similarities between the two samples, and the high degree of saturation obtained in Sample 28-2C, it is reasonable to assume that Sample 27-2C was nearly fully saturated after the saturation phase.

During the saturation phase, the room temperatures fluctuated within ±2°C, which made it difficult to accurately evaluate the changes in volume of water, as discussed in the preceding section. Due to this fact, errors of up to 10% are expected in the volumes indicated in Tables 4.24 and 4.25.

Test Results: Presentation and Analysis

Figures 4.73 to 4.76 present the reduced TYPE II test results. The installation of the RTD in a port at the base of the cell seemed to have significantly improved the thermal correction of the volume change readings of the external cell. This can be concluded by the similarity of these quantities at different tests but at equivalent steps.

VOLUME CHANGES OBSERVED DURING THAWING AND SATURATION

EXTERNAL CELL (CC): -24.098 (SAMPLE SHRINKING)
INTERNAL CELL (CC): - 3.930 (*) (SAMPLE SHRINKING)
TOP OF SAMPLE (CC): - 9.468 (SAMPLE SHRINKING)
PORE WATER (CC): -67.713 (INTO THE SAMPLE)

(*) LEAK WAS DETECTED IN INTERNAL CELL. THE VALUE WAS ESTIMATED

SAMPLE CHARACTERISTICS

	FROZEN SAMPLE	AFTER THAWING AND SATURATION
OUTSIDE DIAMETER (CM)	13.94	[illegible]
INSIDE DIAMETER (CM)	3.98	[illegible]
HEIGHT (CM)	15.25	15.19
TOTAL VOLUME (CC)	2137.70	2100.20
VOLUME OF WATER (CC)	53.98	121.69
VOLUME OF BITUMEN (CC)	628.85	628.85
VOLUME OF GAS (CC)	152.87	47.66
VOLUME OF SAND (CC)	1302.01	1302.01
TOTAL DEG. OF SAT.	0.82	0.94
TOTAL VOID RATIO	0.642	0.613
BITUMEN VOID RATIO	0.483	0.483

Table 4.24 Hollow Cylinder Test - Sample 27-2C - Sample Characteristics

VOLUME CHANGES OBSERVED DURING THAWING AND SATURATION

EXTERNAL CELL (CC):	-75.864	(SAMPLE SHRINKING)
INTERNAL CELL (CC):	+ 1.701	(SAMPLE EXPANDING)
TOP OF SAMPLE (CC):	-10.156	(SAMPLE SHRINKING)
PORE WATER (CC):	-47.501	(INTO THE SAMPLE)

SAMPLE CHARACTERISTICS

	FROZEN SAMPLE	AFTER THAWING AND SATURATION
OUTSIDE DIAMETER (CM)	13.94	13.83
INSIDE DIAMETER (CM)	3.91	3.90
HEIGHT (GM)	15.33	15.21
TOTAL VOLUME (CC)	2156.84	2072.52
VOLUME OF WATER (CC)	87.36	134.86
VOLUME OF BITUMEN (CC)	654.29	654.29
VOLUME OF GAS (CC)	132.65	0.83
VOLUME OF SAND (CC)	1282.54	1282.54
TOTAL DEG. OF SAT.	0.85	1.00
TOTAL VOID RATIO	0.682	0.616
BITUMEN VOID RATIO	0.510	0.510

Table 4.25 Hollow Cylinder Test - Sample 28-2C - Sample Characteristics

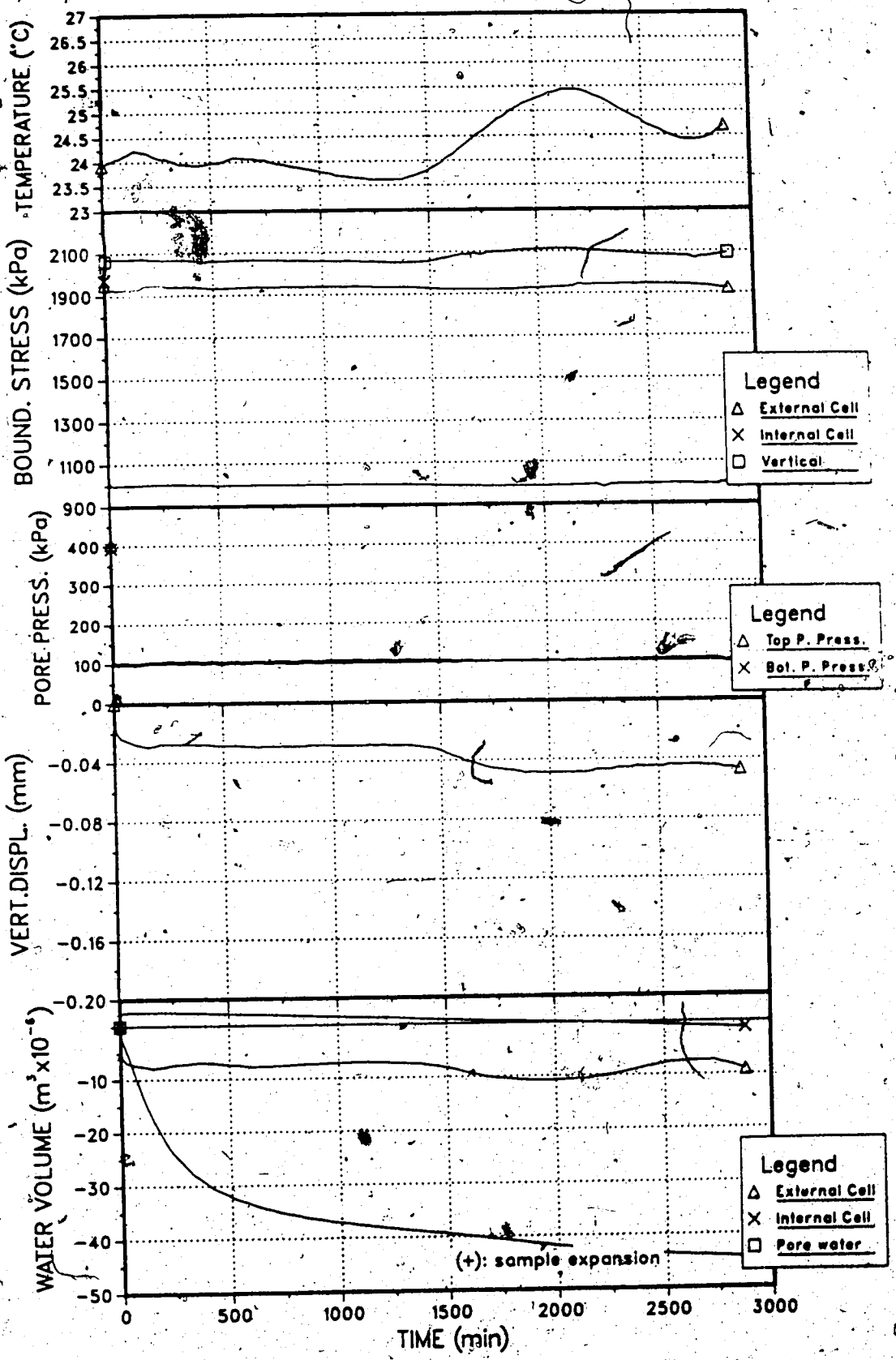

Figure 4.73 Hollow Cylinder Test - Sample 27-2C - Step A

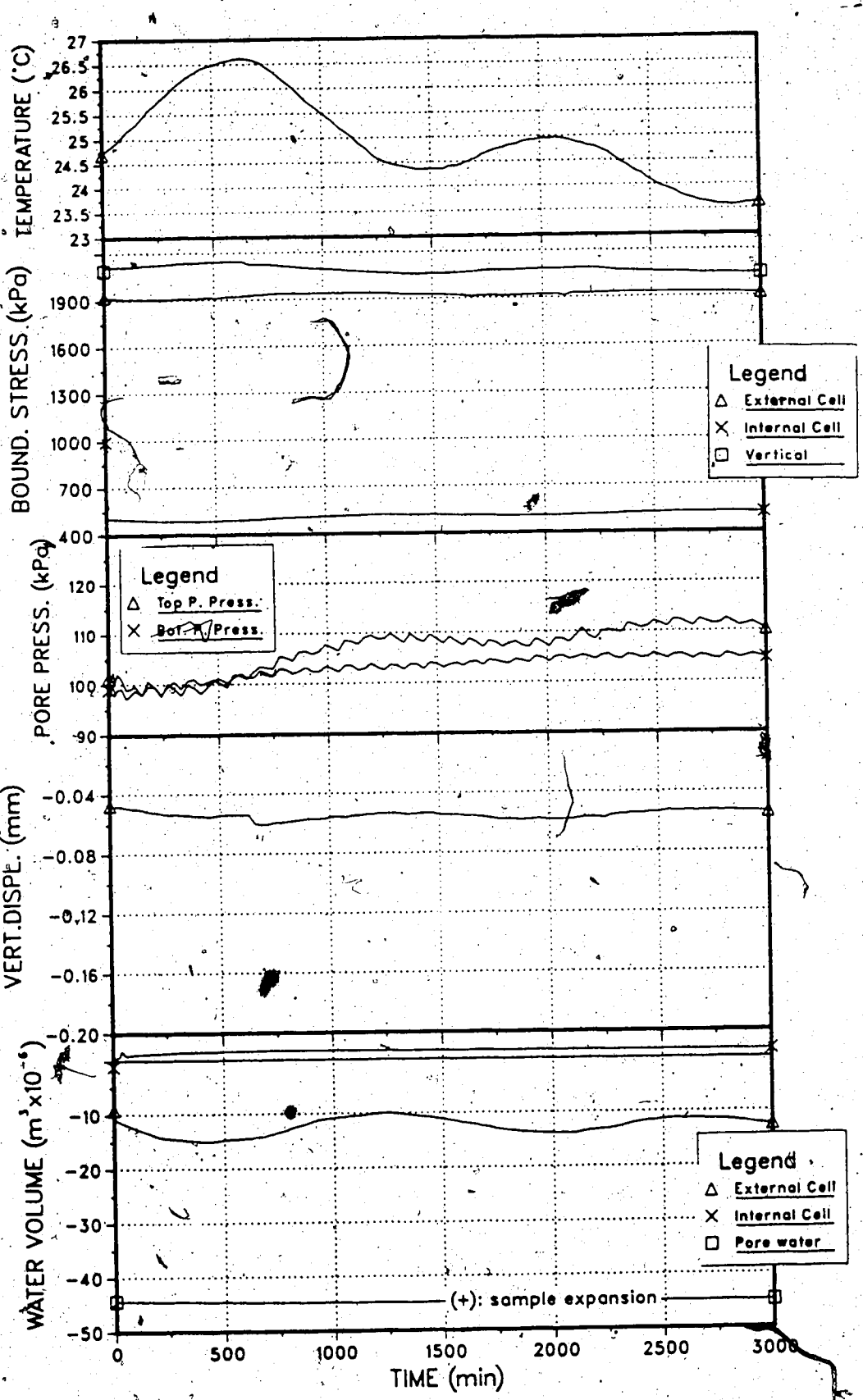

Figure 4.74 Hollow Cylinder Test - Sample 27-2C - Step B

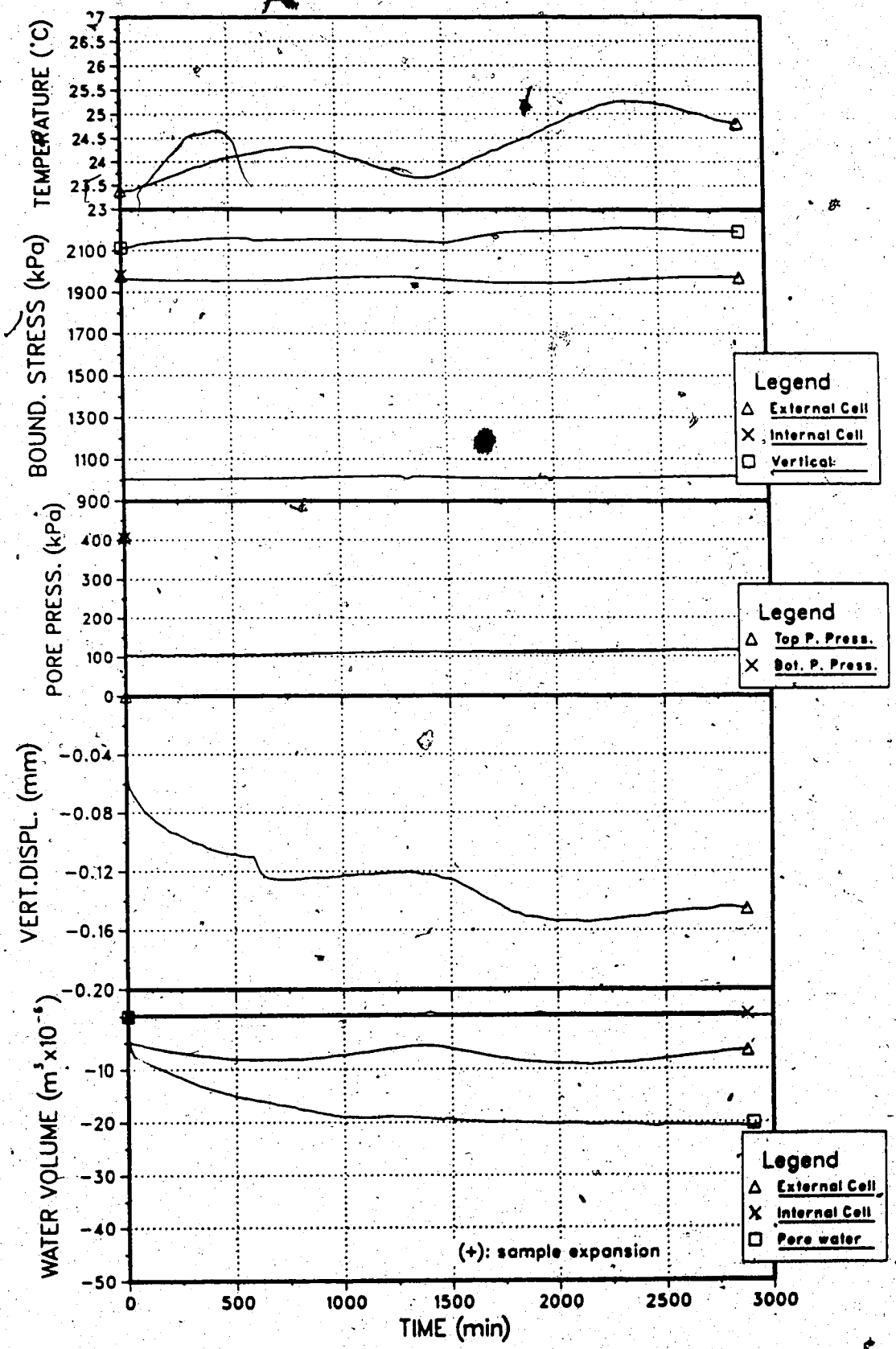

Figure 4.75 Hollow Cylinder Test - Sample 28-2C - Step A

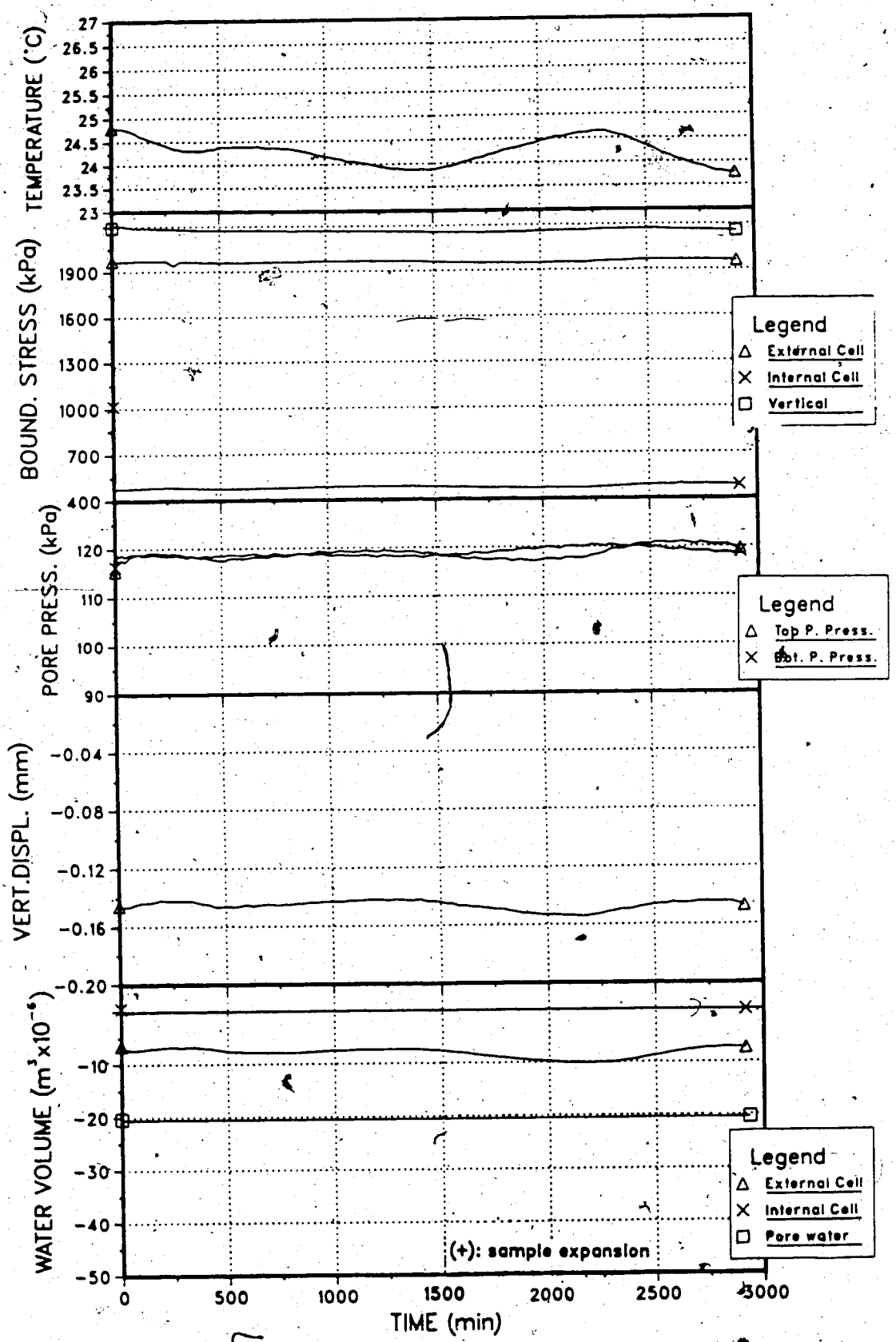

Figure 4.76 Hollow Cylinder Test - Sample 28-2C - Step B

Step A of both tests subjected the samples to low shear stresses, when compared to the failure envelope, and to a significant drop of pore pressure, most likely below the expected bubble point pressure at both extremities. This should result in the combined consolidation and gas evolution in the sample, starting at the extremities and moving inwards with time. The boundary stresses for both tests were almost identical. Sample 27-2C, however, presented downwards vertical displacements lower than the ones observed in Sample 28-2C. On the other hand, the former absorbed twice as much water as the latter. The internal and external volume changes presented very similar responses. Due to leaking in the volume change device on line with the internal bore, results from Sample 27-2C could not be compared with the volume changes of the internal bore of Sample 28-2C.

Step B of this type of test consisted of simply reducing the internal cell pressure to approximately 500 kPa, maintaining the remaining boundary conditions the same. This procedure should induce additional shear straining of the sample near the inner bore, eventually leading to localized yielding. One might expect some additional volumetric straining due to shear in this region.

Figures 4.74 and 4.76 indicate that, for this stage of the test, the boundary conditions are very similar in both tests, except for some fluctutions accompanied by a slow increase of the boundary pore pressures in Sample 27-2C.

These, however, have not affected the test results significantly. The vertical displacements and volume changes of both internal and external cells were stable for both tests, as expected.

4.4 Summary and Conclusions

This chapter presented the sampling and testing programs carried out in order to fulfill two main purposes:

1. to observe the equilibrium and non-equilibrium (transient) mechanical behaviour of a natural gassy sediment, and to verify the applicability of the macroscopic gas evolution model, described in Chapter 2, to simulate the behaviour of gassy sediments.
2. to allow the verification of the predictive capabilities of the numerical model (CONGAS) developed in Chapter 3.

Athabasca oil sands were chosen as the gassy sediment to be tested.

Sample retrieval was carried out at the Syncrude Mining Site, with two types of samplers: a Pitcher and a Christensen barrel. The former retrieved samples with an outside diameter equal to 7.3 cm whereas the latter allowed the sampling of 14.9 cm diameter samples.

The evaluation of the quality of samples according to procedure proposed by Dusseault, 1977, and Dusseault and Domselaar, 1982, indicated most of the samples were of poor quality for geotechnical testing, exhibiting excessive volumetric expansion. The high gas content in the sample

pore fluids was responsible for most of the sample disturbance during sampling.

High gas contents were a desirable characteristic of the samples. The excessive degree of disturbance of samples was not considered a problem to the research program since both the small and the large diameter samples had similar characteristics.

Two groups of laboratory tests were performed:

Group A: tests performed in order to provide basic fundamental geotechnical information about the oil sand samples, such as physical properties, skeleton and pore fluids mechanical response. These properties are required as input for the computer program CONGAS for numerical simulations.

Group B: tests performed in order to produce a case study. In Chapter 5, the results of these tests are compared with the results of similar tests performed numerically with CONGAS.

Group A

The tests performed in order to obtain the physical properties of the oil sand samples indicated that these samples were uniform, as far as bitumen and water content were concerned, exhibiting, in most cases, weight percentages of 14% and 4% respectively, and bitumen and water saturations of 65% and 16% respectively. Void ratios of the frozen trimmed samples varied between 0.57 and 0.89, with 0.65 being the value most often measured. Sieve

analyses showed that samples were uniform, with a uniformity coefficient, CU, varying between 1.4 and 2.5. Gas chromatography tests showed that gas samples were contaminated by large amounts of air. When air components were not considered in the gas tests, CH_4 became the major component followed by CO_2. This fact was confirmed by the mercury triaxial tests which produced combined gas solubilities compatible with high degrees of CH_4 followed by CO_2.

Drained triaxial tests were performed in order to obtain the stress-strain behaviour of the Pitcher samples. Isotropic tests were used to obtain the tangent elastic bulk modulus whereas "J1" and standard tests were used to obtain the tangent elastic shear modulus for the samples. These parameters were obtained based on the assumption that a non-linear elastic constitutive law was suitable to describe the soil response. A hyperbolic stress-strain model based on the tangent bulk and shear moduli was developed. The test results indicated that the bulk moduli were not significantly affected by the varying degree of disturbance of samples. On the other hand, the initial tangent shear moduli varied within a wide range of values. The comparison between the test results and the best fit hyperbolae indicates that the non-linear model chosen was suitable for the sand skeleton modelling. The large volumetric expansions to which the samples were submitted during sampling resulted in the minimization of the sample dilation due to shear.

This could only be observed at shear stresses approaching failure during the "J1" and standard triaxial tests. Before failure, all samples exhibiting contraction when sheared. As discussed in Chapter 5, this fact limits the applicability of the non-linear elastic model to simulate the test model behaviour since these models cannot simulate shear dilation/contraction.

Undrained oedometer and mercury triaxial tests were performed in order to obtain the pore fluids undrained, time-dependent and time-independent responses.

Time-independent combined solubility coefficients were obtained from both types of tests. They varied between 0.08 and 0.21 at room temperature of approximately 24°C. With the theory developed in Chapter 2 for the evaluation of combined solubility coefficients of gas-liquid mixtures, it was possible to conclude that the total amount of gas molecules initially in solution was probably composed of 70 to 80% of CH_4 followed by smaller amounts of CO_2, N_2 and O_2.

The mercury triaxial tests also enabled the theoretical evaluation of the bubble point pressure of the samples. It indicated a considerable variability of the bubble point pressures with depth.

The oedometer cell proved to be unsuitable for the study of the time-dependent phenomenon of gas evolution. This was due to the relatively high friction developed between the loading piston and the surrounding ring. This fact made impossible the accurate control of the pore

pressure within the samples, which were tested at "near-zero" effective stresses.

Undrained triaxial tests, performed with samples surrounded by mercury proved to be suitable for this study. With this apparatus, it was possible to maintain the pore pressures approximately constant within the sample throughout the test stages, and hence, independently study the transient gas volume. The comparison of two "best description curves" previously suggested by Sobkowicz, 1982, indicated that the "Quotient+1" curve better describes the phenomenon. However, the test results indicated that for the early stages of the unloading steps, the gas evolution process was faster than described by the best fit curves. This was attributed to the fact that the gas volume changes measured during the tests were the result of the sum of volume changes that took place in the water and in the bitumen phase. Due to its higher diffusivity coefficient, gas evolution in the water is faster than in the bitumen phase. Therefore, it is believed that the description of the phenomenon by the combination of two "Quotient+1" curves, instead of only one, would be more appropriate. The difficulty involved in separately measuring the time-dependent gas evolution in the water and in the bitumen phases makes this approach impractical.

The mercury triaxial tests also indicated that for degrees of saturation higher than 90%, the transient gas volume changes are responsible for more than 50% of the

total gas volume change. This observation emphasizes the fact that the transient gas evolution process must not be neglected in the modelling of gassy soils, as discussed in Chapter 3.

The scaling parameter A' associated with the "Quotient+1" curve increased with increasing degrees of saturation, confirming the observations previously made by Sobkowicz, 1982. The scatter of results, however, did not allow the definition of a unique relationship between these two parameters.

Group B

Hollow cylinder tests were performed with the Christensen samples, in order to allow evaluation of the simulation capabilities of the numerical model implemented in CONGAS.

Two types of tests were carried out

Type I - Undrained isotropic unloading of hollow cylinder samples;

Type II - Drained unloading of the internal bore of the hollow cylinder samples.

Two tests were performed for each test type, in order to verify test result repeatability.

For type I tests, the inaccuracies in the measurement of the horizontal displacements of the outside wall of the sample were excessively large due to temperature fluctuations. During Type II tests, this problem was ameliorated with the measurement of temperature within the

base of the cell, as opposed to outside the cell ring.

For most test stages, the responses of two samples submitted to similar boundary conditions were alike. Differences in the absolute values of the volume changes and vertical displacement of the top of the sample were observed, as expected. These were attributed to the variability of the geotechnical and thermodynamic properties among samples.

The variability of test results, even for the nearly-ideal conditions found in the laboratory, where almost identical samples were subjected to nearly identical boundary conditions, emphasizes the unavoidable limitations of the predictive capabilities of simulation tools for this kind of problem.

5. NUMERICAL SIMULATION OF MODEL TESTS AND SHAFT SINKING

5.1 General

The finite element program, CONGAS, developed to simulate the transient response of gassy soils due to consolidation and gas evolution, was presented in Chapter 3. It was shown that the computer program is able to simulate ideal situations, where these two processes take place. The verification of CONGAS to simulate real situations where the two transient processes occur, is carried out in this chapter. This verification is possible with the data produced in Chapter 4. Chapter 4 presented results of laboratory tests performed on hollow cylinder samples. These tests are used here as case studies or model tests for the verification of the prediction capabilities of CONGAS. Therefore, in this chapter, the hollow cylinder tests are performed numerically, where the hypothetical samples represented by finite element meshes, with similar geometries and physical properties of the samples tested in the laboratory, are subjected to similar boundary conditions as those imposed during the laboratory tests. The fundamental soil and fluid properties, required for the simulation of the tests, were obtained from tests belonging to Group A, as described in Chapter 4.

The simulation of the hollow cylinder tests, Type I, consisting of the undrained isotropic unloading of the samples, is presented in Section 5.2. Section 5.3 presents

the simulation of the hollow cylinder tests, Type II, which consist of the drained unloading of the internal bore of the hollow cylinder samples. In Section 5.4, the behaviour of oil sands upon stress relief due to shaft sinking is simulated. The numerical results are used to evaluate the efficiency of an alternate shaft sinking construction technique compared to the technique currently used in oil sands.

5.2 Model Test Type I - Isotropic Undrained Unloading

The conditions under which the Type I model tests were performed are described in detail in Section 4.3.5.4. The test procedures were designed in order to ensure that the samples were initially nearly fully saturated, at a back pressure higher than the bubble point pressure. The initial state of equilibrium preceded a series of nearly isotropic unloading steps. This stress path ensured that the soil skeleton was subjected to negligible shear stresses and consequently subjected only to octahedral normal stresses. This procedure eliminated eventual volume changes due to shear that might have occurred during the laboratory test and could not be reproduced by the piecewise linear elastic model used in CONGAS. Consequently Type I tests offered ideal conditions for the calibration of the soil skeleton and gas evolution models of CONGAS.

Two procedures to verify the prediction capabilities of CONGAS were considered herein. The first consists of the

search of the input data, such as soil and fluid parameters, that result in the best match of the response observed in the laboratory. In this case, the analysis of the quality of the simulation is based on the comparison of the final ideal set of input variables with the ones actually obtained from laboratory tests performed to produce these independent variables or parameters (e.g. Group A tests).

In the second procedure, a set of independent input variables, representative of the results obtained from independent laboratory tests, is selected. The resultant predicted response is compared with the one observed in the case study. The former procedure is ideal for situations where the number of input variables is small or in cases where the variability of these variables is small. However, if these conditions are not satisfied, the search for the ideal input parameters can be excessively time consuming. In these cases, the second procedure is preferred.

For the simulation of the model tests, CONGAS requires the following data as input

1. Geometry of the mesh
2. Boundary conditions
   - displacements
   - stresses
   - pore pressures
   - flow
3. Soil and fluid index parameters
   - initial degree of saturation

- total initial void ratios
- bitumen void ratio
- soil unit weight
- water unit weight

4. Initial stresses and pore pressures within the mesh
   - effective stresses in the three directions
   - equilibrium pore pressures at nodal points
5. Soil skeleton stress-strain properties (non-linear)
   7 variables
   (K_G, n, K_F, ϕ_o, $\Delta\phi$, K_B, m)
6. Gas-liquid-skeleton properties
   - bubble point pressure
   - combined solubility
   - time-dependent scaling parameters
   - coefficient of permeability
7. Time discretization

From the items listed above, the initial void ratios, soil skeleton stress-strain and gas-liquid-skeleton properties present high variability. Considering that these three items involve 14 variables, one can conclude that the second procedure of testing the prediction capabilities of CONGAS, discussed above, is more appropriate. Therefore, the numerical simulation of the hollow cylinder tests involved a few computer runs, with input parameters that represented the average of the ones observed in the laboratory. The parameters that more directly affected the results and exhibited large variability had their values varied and

inspected in different numerical tests, as shown later in this section.

Figure 5.1 presents the finite element mesh used for the simulation of both Type I tests. The fact that both samples had dimensions slightly different from the dimensions they had after trimming was neglected. The use of a coarse mesh was possible because in these tests, the samples were not subjected to spatial stress gradients.

The boundary conditions imposed on the mesh were displacement boundary conditions at the bottom of the sample and surface tractions at the remaining surfaces. The nodal points at the lower boundary were restrained from movement in the vertical direction.

The results of both tests, performed with Sample 26-2 and 27-2B, indicated that negligible time-dependent pore pressure and displacements occurred during the first unloading step (i.e. Step A). It was concluded that during this step of the tests, the pore pressures were above the bubble point pressure of the samples. Since CONGAS does not simulate the behaviour of gassy soils at pressures higher than the bubble point pressures, the simulation of the tests began after the conclusion of Step A. The adoption of this simulation procedure was favoured by the fact that the bubble point pressures observed in the laboratory tests (Figure 4.39) are approximately the same as the pore pressures at the end of Step A, for the depth of the samples considered herein.

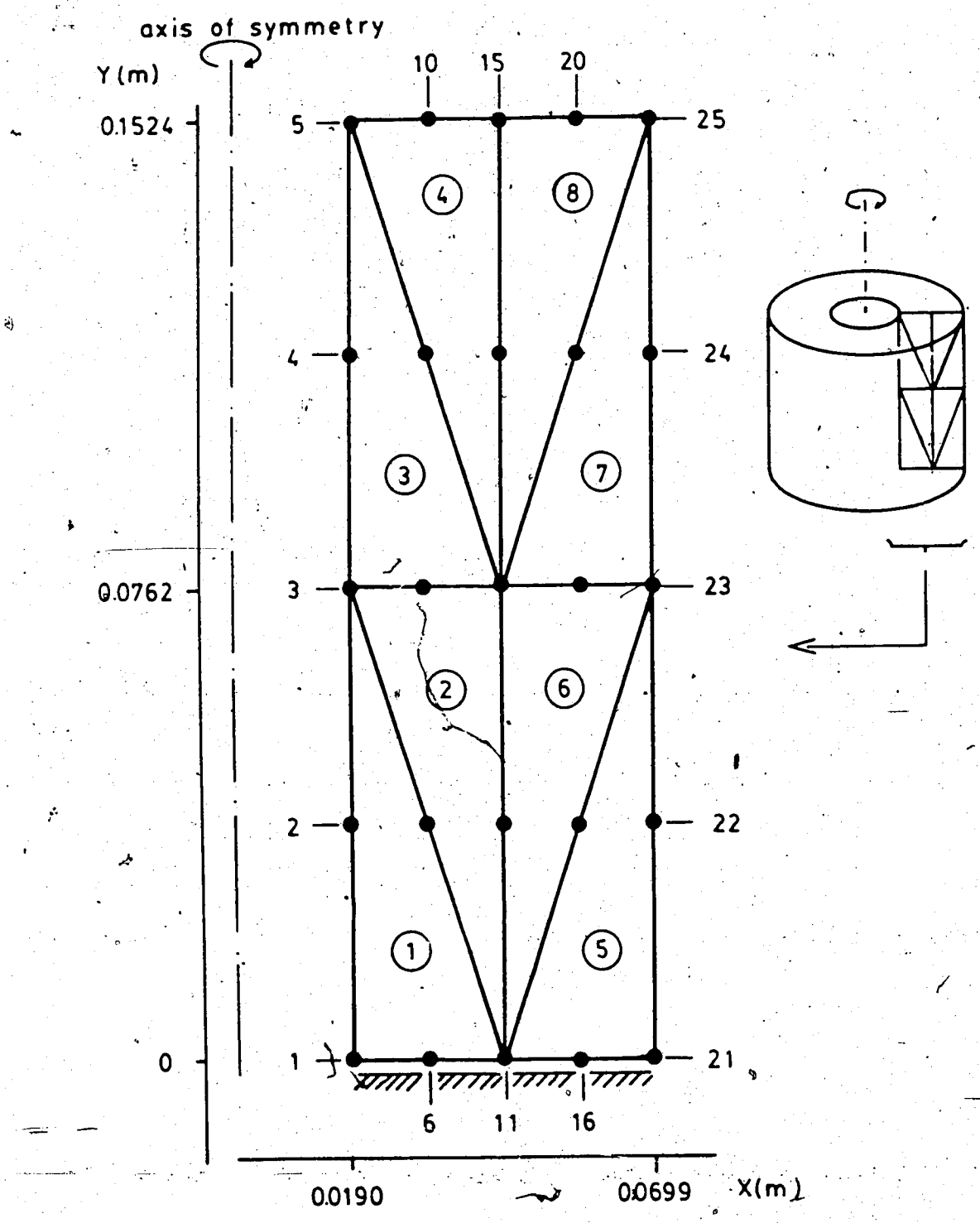

Figure 5.1 Finite Element Mesh - Test-Test16-V16 - Hollow Cylinder Test - Type I

Table 5.1 depicts the boundary stresses, initial pore pressures and void ratios used in the numerical simulation. Except for the boundary stresses at the end of Step A, that were considered equal at both the internal and external walls of the samples, the boundary conditions imposed at the numerical tests were identical to the ones in the laboratory (Tables 4.18, 4.19). The variables used at the end of Step A were assumed to be equilibrium values. Besides the variables indicated in Table 5.1, the initial degree of saturation of the nodes was also necessary as an input parameter. This variable was obtained from parametric analyses as described later in this section.

The simulation proceeded in time increments. The length of the time increments was chosen with the objective of minimizing the errors associated with the incremental elastic simulation, as discussed in Chapter 3, and obtaining stable solutions for the gas volume change iterations. Table 5.2 depicts the time increments that fulfilled these conditions.

The skeleton and liquid-gas-skeleton properties used in the tests are presented in Table 5.3.

Figures 5.2 and 5.3 present the laboratory and numerical simulations of the two unloading stages performed with Sample 26-1. The thicker solid curves represent the laboratory results. The other four curves represent the numerical tests. A parametric analysis indicated that a value of 99.3% for the initial degree of saturation was

		SAMPLE 26-1		SAMPLE 27-2B	
		LAB. TEST	NUM. TEST	LAB. TEST	NUM. TEST
END OF STEP A	Pv	760	760	750	752
	Pe	630	665	700	703
	Pi	700	665	705	703
	u	330	330	310	310
	e_{bit}	0.430	0.430	0.483	0.483
	e_0	0.605	0.605	0.600	0.600
STEP B	Pv	620	620	600	600
	Pe	480	480	545	545
	Pi	555	555	550	550
STEP C	Pv	465	465	455	455
	Pe	325	325	385	385
	Pi	400	400	398	398
STEP D	Pv	-	-	320	320
	Pe	-	-	250	250
	Pi	-	-	245	245

Units : kPa
Pv : Pressure at top of sample
Pe : Pressure at external wall of sample
Pi : Pressure at internal wall of sample
u : Pore pressure
e_{bit}: Void ratio of bitumen
e_0 : Total void ratio

Table 5.1 Boundary Conditions, Initial Void Ratios and Initial Pore Pressures - Hollow Cylinder Tests - Type I

	TIME INTERVAL (MIN)	TIME INCREMENT (MIN)
MODIFICATION OF BOUNDARY STRESSES	0.0 TO 0.1	0.01
BOUNDARY STRESSES MAINTAINED CONSTANT	0.1 TO 180.1 180.1 TO END OF STEP	20.0 100.0

Table 5.2 Temporal Discretization Test Type I

	SAMPLE 26-1	SAMPLE 27-2B
STRESS-STRAIN PARAMETERS	K_G = 300, 600 n = 0.5 R_f = 0.5 $\Delta\Phi$ = 26° Φ_o = 82° K_B = 388 m = 0.99	
GAS-LIQUID PARAMETERS	A^*=10000, 8000 MIN	A^*=10000, 8000, 5000, 3000, 1000 MIN
	H=0.05, 0.10	H=0.02, 0.05, 0.10, 0.15
LIQUIDS COMPRESSIBILITY	Q_{wat} = 4.5 x 10^{-7} 1/kPa Q_{bit} = 20.7 x 10^{-7} 1/kPa	
PHYSICAL PROPERTIES	Sinit=0.997, 0.993 0.992	Sinit=0.995, 0.993
	e_{bit}=0.430 e_o =0.605	e_{bit}=0.483 e_o =0.600

Table 5.3 Hollow CylinderTest Type I - Numerical Simulation - Skeleton - Pore Fluid Properties

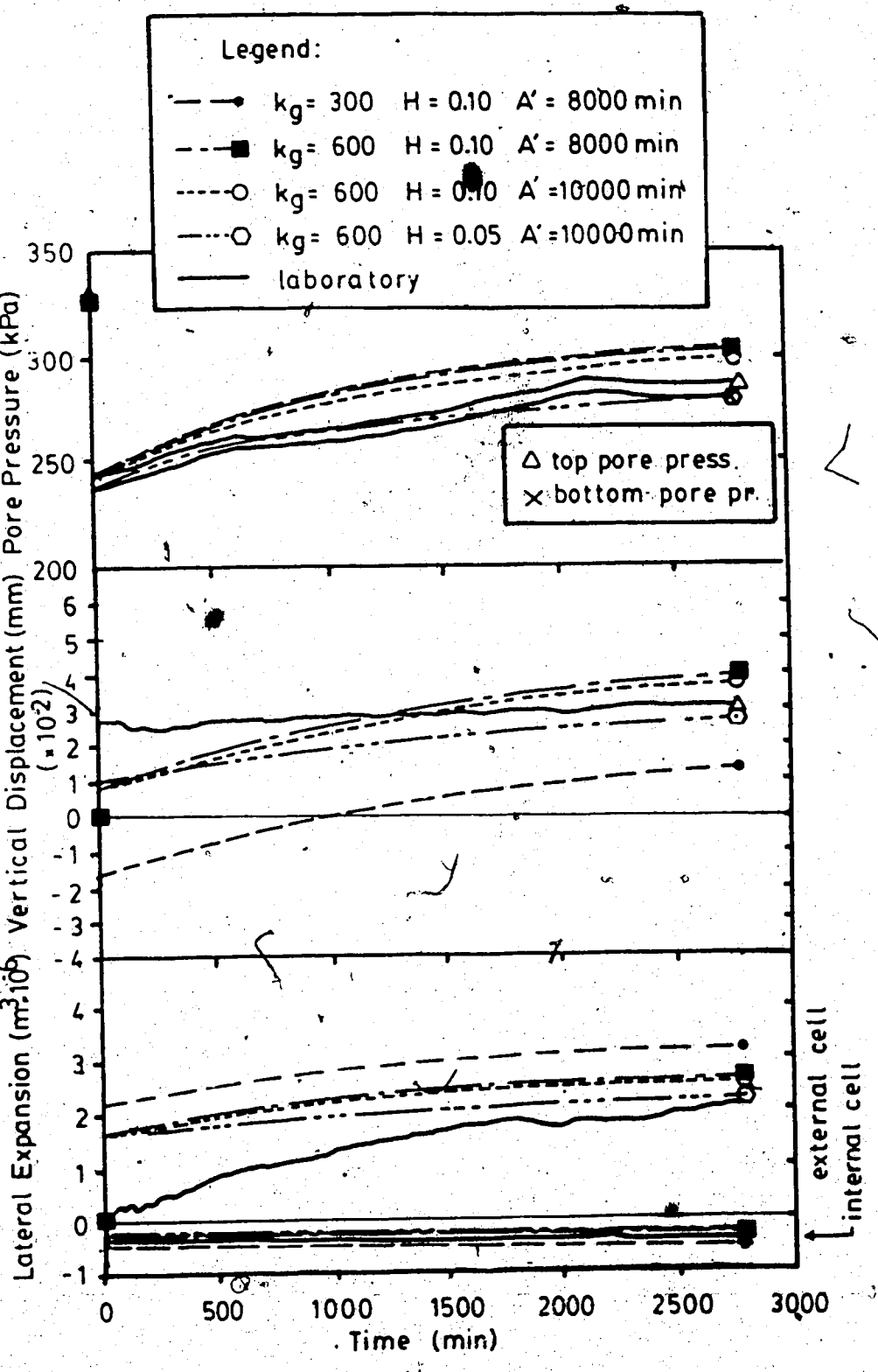

Figure 5.2 Hollow Cylinder Test Type I - Numerical Simulation - Sample 26-1 - Step B

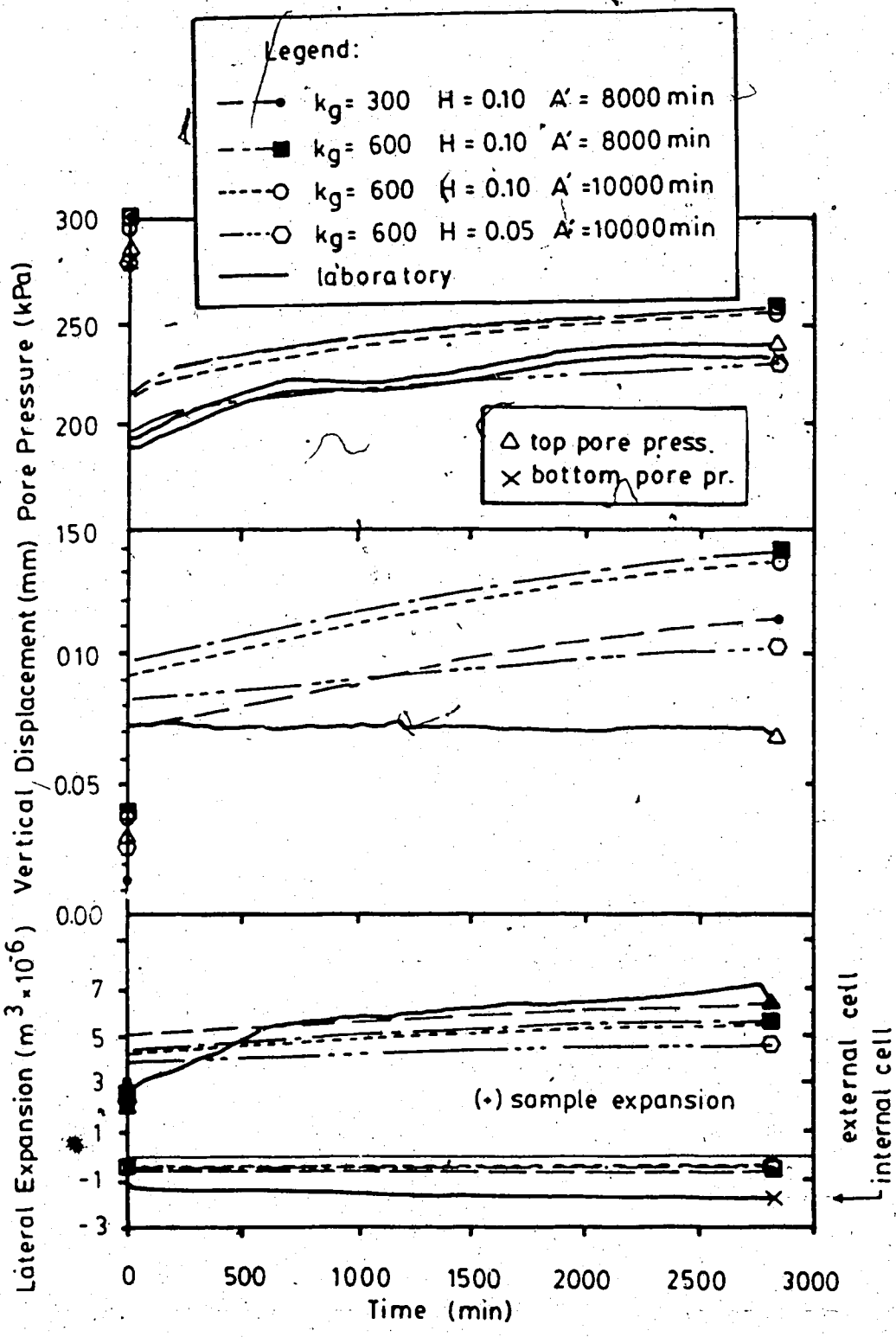

Figure 5.3 Hollow Cylinder Test Type I - Numerical Simulation - Sample 26-1 - Step C

ideal for the match of the immediate pore pressure response observed in the laboratory tests. Pore pressures were used as a basis for comparison for calibrating the initial degree of saturation, due to the high accuracy offered by the pore pressure transducers.

The best overall prediction of results was obtained with the curves represented by the hexagonal symbol, associated with the values:

$K_g = 600$

$H = 0.05$

$A' = 10{,}000$ minutes

The value of K_g is the average shear modulus number obtained from the "J1" drained triaxial tests. The numerical simulation of Step B (Figure 5.2), performed with $K_g = 300$ erroneously predicted that, immediately after the modification of boundary stresses, the piston would move downwards. This was a result of the small shear to which the mesh was subjected to, associated with a low shear modulus.

The comparison of the curves, represented by the solid square and the hollow circle, allows one to conclude that the variation of the scaling parameter, A', between 8000 and 10000 min., did not significantly affect the numerical results. The A' values which resulted in the best prediction of the observed behaviour are higher than the ones obtained in the laboratory tests. However, the measured A' values were associated with degrees of saturation smaller than 99%, as depicted in Figure 4.64. This figure indicates that as

the degree of saturation increased towards unity, the A' value increased significantly. Therefore, the values of A' obtained from the numerical simulation are considered realistic.

A value of 0.10 for the solubility coefficient seemed to be slightly high, as far as the pore pressure prediction was concerned.

The numerical simulation of both unloading steps predicted a gradual upward movement of the piston with time after the immediate response. However, in the laboratory, the piston moved to a position of equilibrium immediately after the change in boundary stresses. The build up of piston friction might be responsible for this behaviour. The calibration of the hollow cylinder cell indicated that when moving upwards, piston friction can be as high as \5% of the external applied load. Considering the vertical loads applied to the samples, listed in Table 5.1, the piston friction during the tests might have been as high as 30 kPa, which is approximately the same magnitude of the decrease in the difference between the external vertical load and internal pore pressure observed during the test. The build up of piston friction might have been enhanced by the long duration of the tests during which the piston did not move. During the calibration of the cell, the friction increased when the piston was kept motionless for an extended period of time.

The prediction of the lateral expansion of the sample was not as accurate as the pore pressure prediction. Considering the temperature fluctuations and the inaccuracies asociated with the volume change measurements, the simulation can be considered good.

All numerical tests predicted a value for the degree of saturation, at the end of Step B, greater than 98%. This value reveals that the gas bubbles within the pores were mostly disconnected, thus validating the hypothesis on which the numerical model was based.

The laboratory and numerical test results of the three unloading steps of Sample 27-2B are presented in Figures 5.4, 5.5 and 5.6. The thicker solid curves represent the laboratory test results. The parametric analysis for the initial degree of saturation revealed that a value of 99.5% resulted in the best match of the immediate pore pressure response.

The best simulation of the pore pressure response during Step B is represented by the curves associated with the hollow circle and the hexagonal symbols. In both cases, the shear modulus number (K_g) is equal to 600 and the scaling parameter is equal to 10,000 min. The solubility coefficients are 0.02 and 0.05, respectively. These values are slightly smaller than expected. A bubble point pressure lower than the initial pore pressure in Step B might result in an apparent smaller solubility coefficient during the laboratory tests. This conclusion is based on the

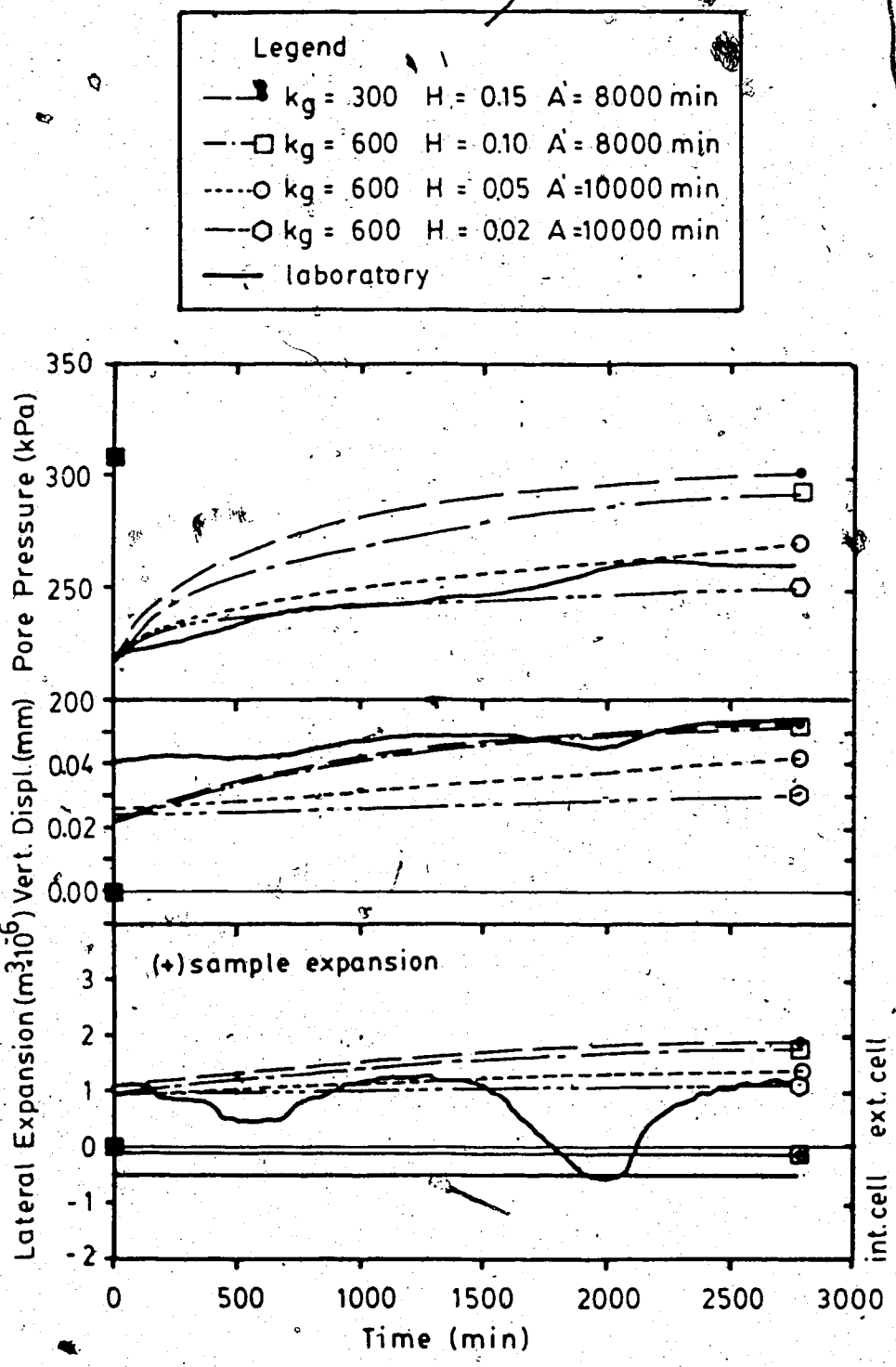

Figure 5.4 Hollow Cylinder Test - Numerical Simulation - Sample 27-2B - Step 8

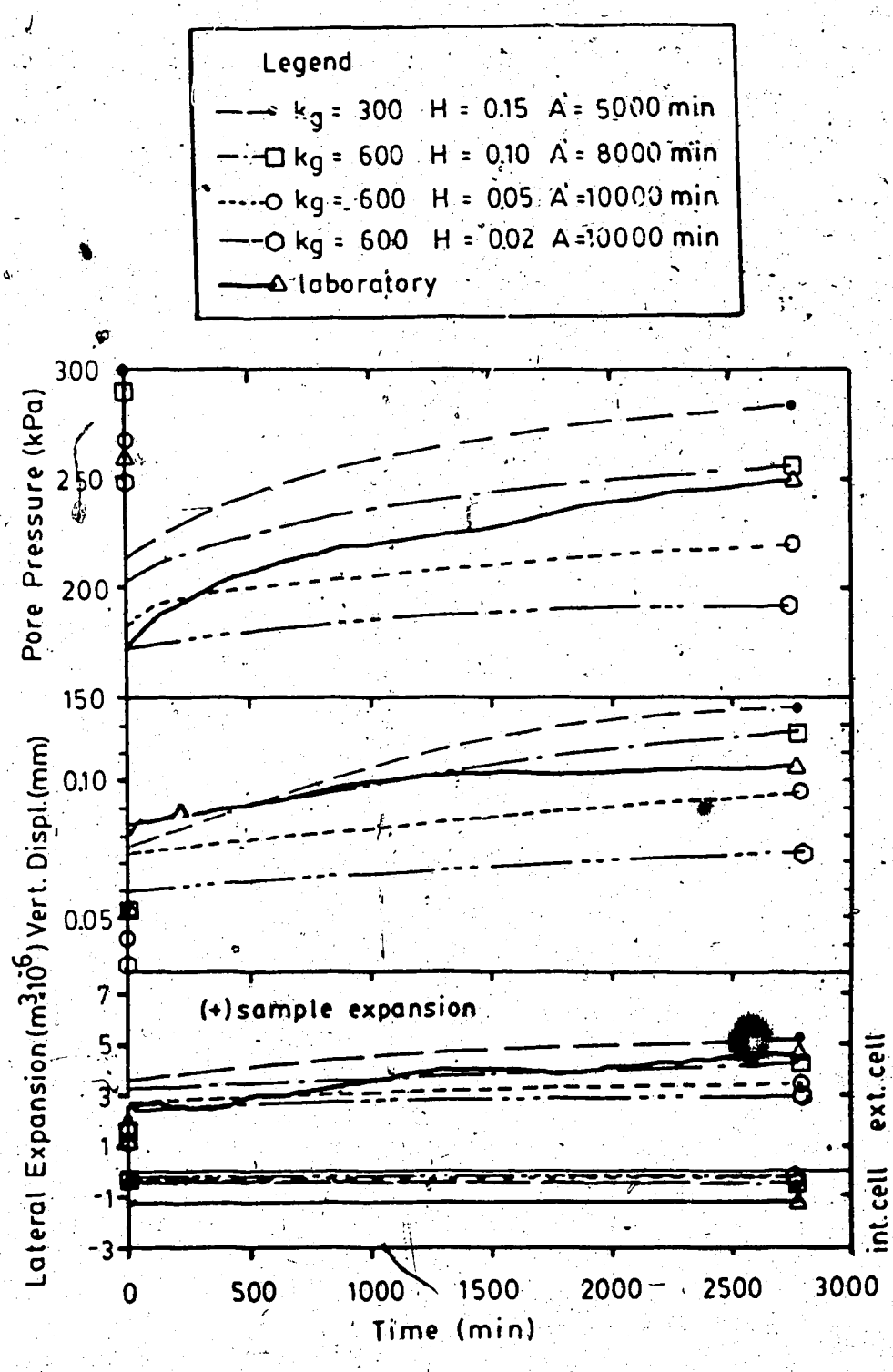

Figure 5.5 Hollow Cylinder Test - Numerical Simulation - Sample 27-2B - Step C

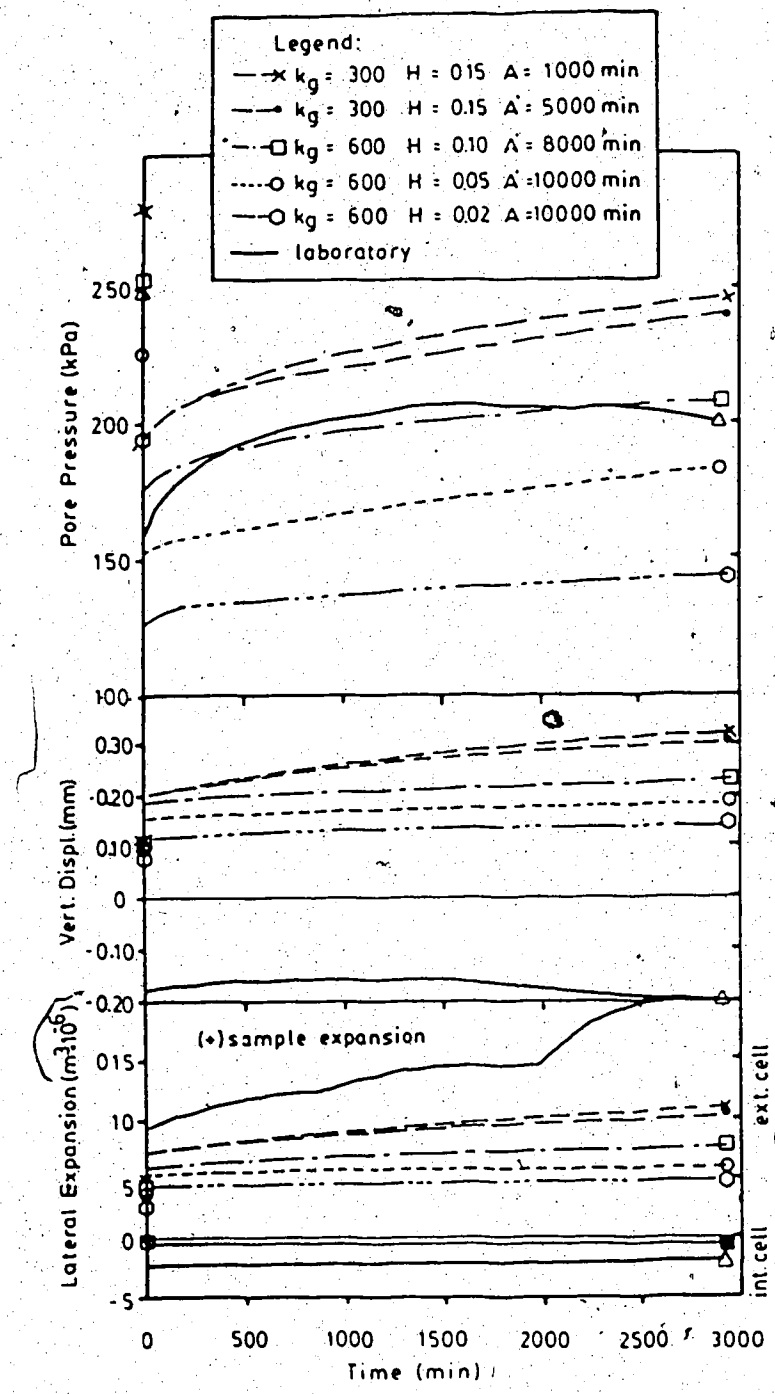

Figure 5.6 Hollow Cylinder Test - Numerical Simulation - Sample 27-2B - Step D

equilibrium solubility coefficient curves presented in Chapter 4. These curves showed that for pore pressures higher than the theoretical bubble point pressures, small amounts of gas formed at pre-existing sites, resulting in small solubility coefficients.

During this step, similar to the test on Sample 26-1, the piston did not exhibit time-dependent response. This observation was once more attributed to piston friction. The large fluctuations in temperature did not allow an accurate measurement of the external lateral extension of the sample. The internal expansion of the bore was underpredicted in all numerical tests. The high degree of disturbance close to the internal wall, due to the procedure used for trimming the internal bore, might have been responsible for the higher observed internal wall movements.

During Step C, (Figure 5.5) the curves associated with the solubility coefficients of 0.02 and 0.05 can no longer reproduce the observed pore pressure response.

Discounting the difference in pore pressures at the beginning of Step C, the curves associated with solubility coefficients (H) 0.10 and 0.15 and scaling parameters (A') 8000 and 10,000 minutes, present the best prediction of the pore pressure response. The increase in the solubility coefficient from Step B to Step C is in agreement with the laboratory tests results presented in Chapter 4, as discussed above.

The vertical movement of the piston showed little time-dependent movement and the final value was reasonably well predicted by CONGAS. A similar conclusion can be extended to the external lateral expansion of the sample. Once again, the expansion of the internal bore was underpredicted by CONGAS.

The overall pore pressure response during Step D, in its early stages, is better predicted by the numerical tests represented by the dashed lines associated with the solid circle and cross symbols. The vertical difference between these curves and the laboratory curve is due to the differences in initial pore pressures associated with each case. As time progressed, after 1500 minutes of testing during Step D, laboratory pore pressures decreased, reflecting a possible leakage of gas molecules from the sample into the cell liquid. Taking this fact into consideration, it seems that values of A' between 1000 and 5000 minutes, and solubility coefficients, H, between 0.10 and 0.15, better reflect the sample behaviour during this last step of the test. All numerical tests predicted degrees of saturation varying between 97.8 and 99.0%, during Step D. According to data presented in Chapter 4 (Figure 4.64) values of A' between 1000 and 5000 minutes, were actually measured from this range of degrees of saturation.

The vertical displacement of the piston observed in the laboratory test, Step D, occurred in the opposite direction of the displacements predicted by the numerical tests. This

apparently odd response was a result of the procedure followed to change the boundary stresses. As explained in Section 4.3.5.4, during changes in the boundary stresses care was taken to maintain the vertical piston pressure higher than the radial pressures, in order to guarantee a good seal between the piston and top cap of the sample. Consequently, during unloading, the vertical pressure was only decreased after both the internal and external cell pressures had been decreased. This resulted in the downward movement of the piston, after the reduction of the radial stresses. As a consequence, the sample was temporarily subjected to additional shear stresses of about 70 kPa.

At the moment, it is not clear why the previous stages of the test did not present the same response. One of the possible reasons, attributed tc this behaviour, is that in the previous test stages, a combination of a higher resistance to shear deformation (higher G values) and piston friction might have counteracted the transient shear stresses.

The oscillation of temperatures, near the end of Step D, introduced excessively large errors in the measurement of the external expansion of the sample. However, prior to this, the numerical t[illegible] simulated the observed results well, provided the d[illegible]nces in the values of lateral extension at the beginning of the step are taken into account.

5.3 Model Test - Type II - Drained Unloading of the Internal Bore

The conditions under which the Type II model tests were performed are described in detail in Section 4.3.5.5. The test procedures were designed to ensure that the samples were initially nearly fully saturated, at a back pressure higher than the bubble point pressure. Under these conditions, both samples tested were, at the beginning of the test, at a state of isotropic effective stress of approximately 1600 kPa and a pore pressure of about 400 kPa.

The first stage of the test consisted of the instantaneous decrease of the internal pressure of the hollow cylinder sample, and a simultaneous decrease in the pore pressures at the top and bottom of the sample. This procedure aimed at subjecting the sample to shear stresses and surface drainage, a condition often present in geotechnical work in gassy soils. The effects of these two features in the prediction capabilities of CONGAS were not verified in the Type I tests. At the end of the first stage of the test (Step A), all boundary conditions were maintained constant except for the internal pressure which was decreased further.

Similar to the simulation procedure used in the preceding section, the simulation of the Type II tests involved a few computer runs, with input parameters that represented the average of the values observed in the laboratory. The parameters which more directly affected the

results and presented large variability had their values varied and inspected. The numerical tests which better described the response of the Type I tests offered a good indication of some of the values of parameters suitable for the simulation of Type II tests. This extrapolation of the experience obtained in Type I tests to Type II tests was possible due to the similarities of the samples.

Figure 5.7 presents the mesh used to simulate the Type II tests. It represents half of the height of a vertical cut through the axis of the sample. The simplification of the design of the mesh was possible due to the axial and half vertical symmetry of the test, with respect to the geometry and boundary conditions. The fact that both samples had slightly different dimensions was neglected, and the same mesh was used to simulate both tests.

The refinement of the mesh considered two aspects:

- stress concentration around the internal cell (horizontal direction)
- pore pressure gradient close to the drainage surface at the top (vertical direction)

The suitability of the mesh refinement in the horizontal direction was verified through the comparison of the time-independent response of the mesh, with elastic stress-strain parameters with the available closed form solutions. The elastic properties in the mesh were set equal to the initial tangent values of the non-linear elastic modulus. The stress and displacement boundary conditions

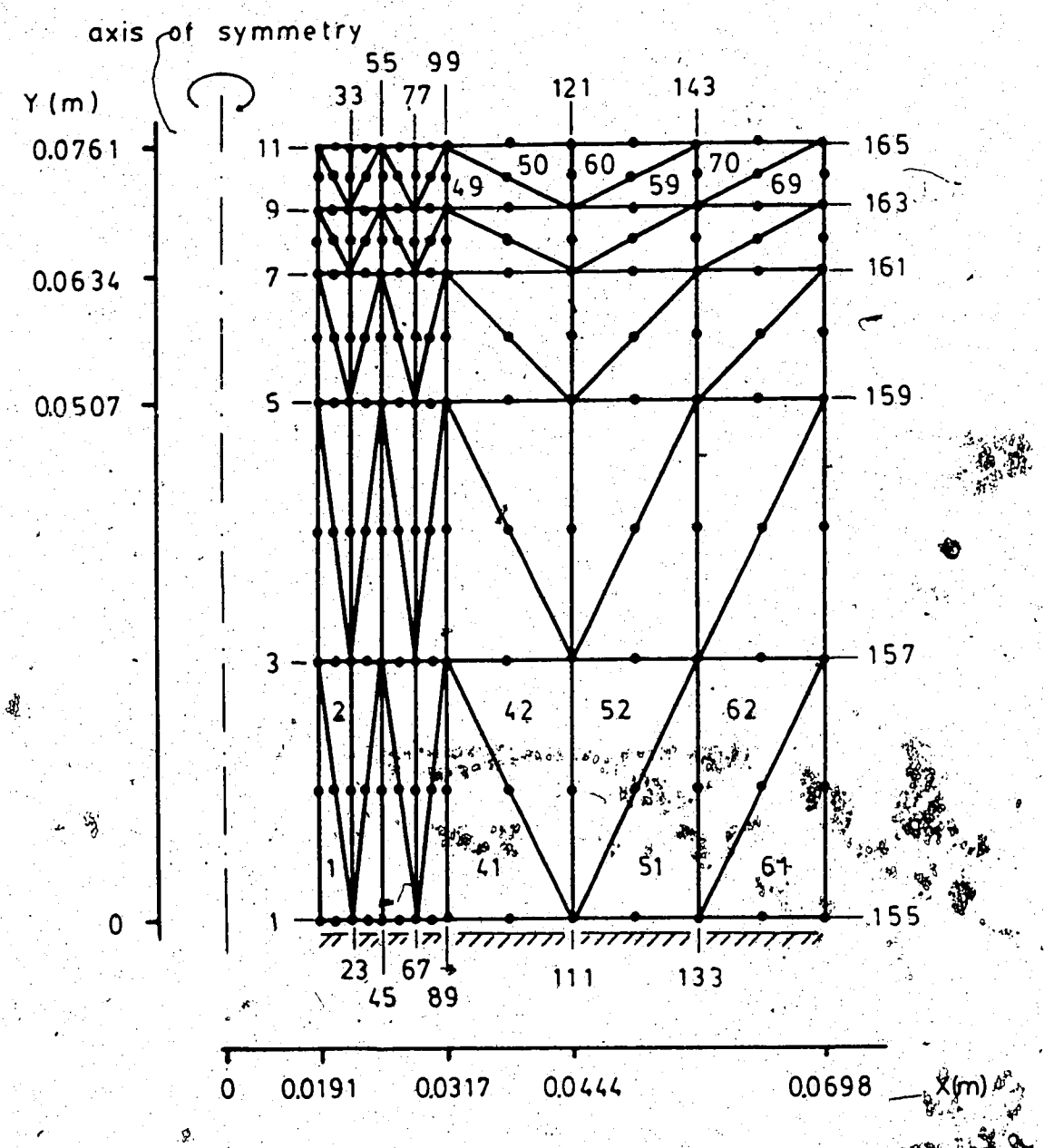

Figure 5.7 Finite Element Mesh - Test 17-V17 - Hollow Cylinder Test - Type II

were identical to the ones used for the simulation of the laboratory tests. This comparison showed that both strains and stresses could be accurately predicted with the horizontal mesh refinement proposed.

The vertical mesh refinement was designed to allow the use of small time increments during the numerical tests. This would allow greater flexibility in the choice of the appropriate time increment and, consequently, ensure accurate and stable solutions.

According to the accuracy condition developed by Vermeer and Verruijt, 1981, as discussed in Section 3.3.4.1, the time increment below which spatial oscillations of pore pressures occur is,

$$\Delta t > \frac{1}{6} \frac{(\Delta h)^2}{a c_v}$$

The meaning of the variables is given in Section 3.3.4.1.

For the mesh of Figure 5.7, the variables have the following values:

$\Delta h = 0.0064$ m

$a = 2/3$

$m_v = 1 \times 10^{-6}$ kPa^{-1}

(calculated for the one-dimensional case based on the tangent moduli G and B, at the beginning of Step A)

$$c_v = \frac{k}{9.8 \times 10^{-6}} \ m^2/s$$

Thus, $\Delta t > \frac{10^{-10}}{k} \ s$

Therefore, for a cofficient of permeability to water varying from 10^{-9} to 10^{-11}, Δt_{crit} varies from 0.1 to 10 seconds.

These values were used as indicators of the minimum time increment since Vermeer and Verruijt's equation was developed for the one-dimensional consolidation case. Moreover, as strains occur in the samples, the tangent elastic moduli vary, thus altering the value of Δt_{crit}.

The boundary conditions imposed on the mesh were zero vertical displacements at the bottom, stresses at the top and lateral walls and pore pressures at the top. Table 5.4 summarizes the boundary conditions, initial void ratios, initial degrees of saturation and initial pore pressures associated with the laboratory and numerical tests.

Due to the similarities of the laboratory tests, it was possible to simulate both of them with only one set of initial values for pore pressures, degree of saturation, void ratios and boundary conditions as depicted in Table 5.4.

Similar to Type I tests, the simulation of Type II tests proceeded in time increments. The length of the time increments was chosen such that the errors associated with the incremental elastic simulation were minimized, as discussed in Chapter 3, and that stable solutions for the

		SAMPLE 27-2C	SAMPLE 28-2C	NUMERICAL TEST
I	Pv	2070	2110	2070
N	Pe	2000	1980	2000
I	Pi	2000	1980	200
T	u	400	410	400
I	ebit	0.483	0.510	0.483
A	eo	0.613	0.616	0.613
L	S	0.940 (*)	0.999	0.995
S T E P A	Pv	2070	2180	2070
	Pe	1930	1960	1924
	Pi	1000	1010	1000
	uB	100	100	100
S T E P B	Pv	2130	2160	2140
	Pe	1917	1950	1917
	Pi	500	480	500
	uB	100	100	100

UNITS: kPa
Pv : PRESSURE AT TOP OF SAMPLE
Pi : PRESSURE AT INTERNAL WALL OF SAMPLE
Pe : PRESSURE AT EXTERNAL WALL OF SAMPLE
u : INTERNAL PORE PRESSURE OF SAMPLE
uB : BOUNDARY PORE PRESSURE AT THE TOP OF SAMPLE
ebit : VOID RATIO OF BITUMEN
eo : TOTAL VOID RATIO
(*) : NOT ACCURATELY EVALUATED DUE TO LEAK IN VOLUME CHANGE CONNECTED TO INTERNAL CELL

Table 5.4 Boundary Conditions, Initial Void Ratios, Initial Degree of Saturation and Initial Pore Pressures - Hollow Cylinder Test - Type II

gas volume change and consolidation iterations were obtained. Table 5.5 depicts the time increments that fulfilled these conditions.

As indicated in this table, the modification of boundary stresses was performed in twenty increments for Step A and ten increments for Step B. This number of increments resulted in errors of up to 7% in the evaluation of octahedral shear stresses according to the error index ERRORG, as defined in Section 3.3.3. Therefore, if iterations had been used to redistribute the unbalanced load vector, (responsible for the aforementioned error), the numerical tests would have predicted slightly larger shear deformations.

The allowable error between successive iterations within each time increment was 0.1%. The DAMP values required for convergence of iterations varied between 0.7 and 0.01.

The skeleton and liquid-gas-skeleton properties used in the analysis are presented in Table 5.6. Given the experience gained through the analysis of the simulation of Type I tests, the scaling parameter, A', and the coefficient of permeability to water, K, were the only parameters varied in the numerical analysis.

The range of values chosen for the scaling factor is in accordance with the discussion of the simulation of the Type I test on Sample 27-2B presented in the preceding section.

		TIME INTERVAL (MIN)	TIME INCREMENT (MIN)
STEP A	MODIFICATION OF BOUNDARY STRESSES	0.0 - 2.0	0.1
	BOUNDARY STRESSES MAINTAINED CONSTANT	2.0 - 2882	10 TO 50
STEP B	MODIFICATION OF BOUNDARY STRESSES	0.0 - 2.0	0.2
	BOUNDARY STRESSES MAINTAINED CONSTANT	2.0 - 200	10 TO 20

Table 5.5 Temporal Discretization - Type II Test

STRESS-STRAIN PARAMETERS	K_G = 600 n = 0.5 R_F = 0.5 $\Delta\Phi$ = 26° Φ_o = 82° K_B = 388 m = 0.99
GAS-LIQUID PARAMETERS	A = 10000, 1000 MIN
	H = 0.15
LIQUIDS COMPRESSIBILITY	β_{wat}= 4.5 x 10^{-7} 1/kPa β_{bit}=20.7 x 10^{-7} 1/kPa
PHYSICAL PROPERTIES	S_{init}=0.995,1000(*)
	e_{bit}=0.483 e_o =0.613
WATER FLOW	k=10^{-9}(**),10^{-10}, 10^{-11} M/S

(*) FOR THE CASE "CONSOLIDATION ONLY"
(**) CONSTANT AND VARIABLE COEFFICIENT OF PERMEABILITY

Table 5.6 Hollow Cylinder Test - Type II - Numerical Simulation - Skeleton-Pore Fluid Properties

The range of values chosen for the coefficient of permeability to water is in accordance with test results published by Dusseault, 1977, 1980, Agar, 1984 and Agar et al., 1988. One might suggest that the values of the coefficient of permeability were slightly low for the degrees of expansion the samples were subjected to during sampling. However, the choice of the range of values above, took into account the fact that the bitumen phase is immobile at 24 °C, that the samples were consolidated to a stress state significantly higher than the original *in situ* ones, that the samples did not have the clay and silt fines removed from the pores, as it occurred in some of the experiments performed by Agar et al., 1988, and that during the test the formation of gas bubbles in the water phase of pores would reduce the permeability to water as well. This latter effect is discussed further in the following paragraphs.

Figure 5.8 presents the progress of the percent consolidation observed in Step A of the laboratory tests on Samples 27-2C and 28-2C, and the ones predicted by five numerical tests. For the laboratory tests, the percent consolidation was evaluated from the amount of water collected from the pores of the samples. The percent consolidation was defined as the volume of water that had left the sample up to a given time, divided by the total volume of water that left the sample when consolidation had ceased. The latter value was assumed to be the water volume

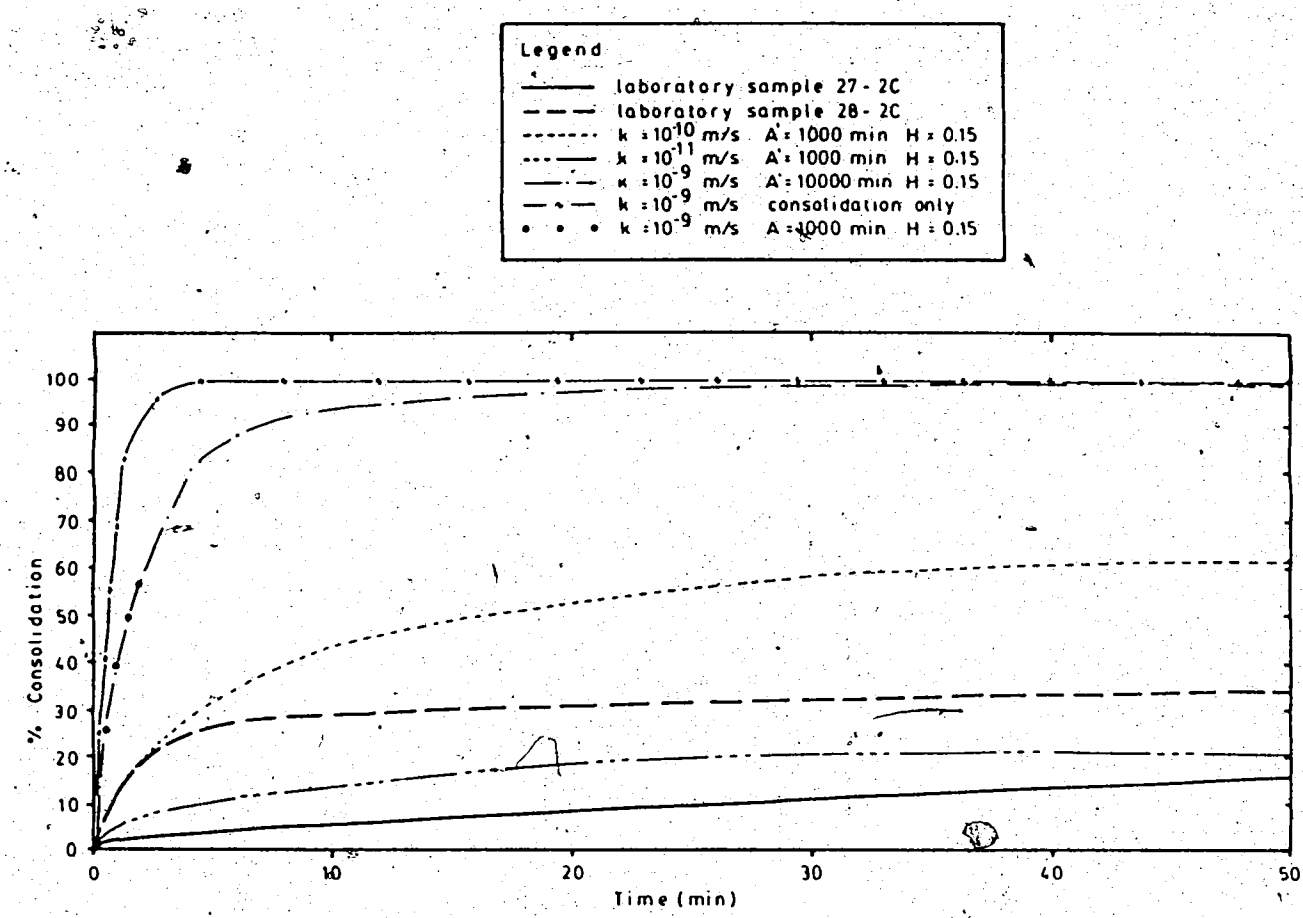

Figure 5.8 Hollow Cylinder Test - Type II - Numerical Simulation - % Consolidation versus Time, 0 to 50 minutes

measured at the end of Step B of the tests.

For the numerical tests, the percent consolidation was calculated based on the pore pressure distribution along a vertical line passing through points 89 to 99, of the finite element mesh of Figure 5.7. Figure 5.9 illustrates how the percent consolidation was evaluated from the numerical test results.

The curves of Figure 5.8 associated with a coefficient of permeability to water equal to 10^{-9} m/s, irrespective of the value of the scaling parameter, A', predicted rates of consolidation significantly faster than the ones observed in the laboratory. The curves with A'=1000 minutes and 10,000 minutes yielded identical results for the first two minutes of the test. After this time, the numerical test with A'=1000 minutes was interrupted.

The improvement of the simulation of the progress of consolidation is most effectively obtained with the variation of the coefficient of permeability to water, the scaling parameter, A', and the bulk modulus. The small variability of the bulk modulus values (Section 4.3.3.4) indicated that the parametric analysis performed with different values of the coefficient of permeability to water would be more realistic. In order to simplify the parametric analysis, the scaling parameter, A', was maintained constant and equal to 1000 minutes. This value was probably lower than the ones that existed during the early stages of the laboratory tests and higher than the ones at the end of Step

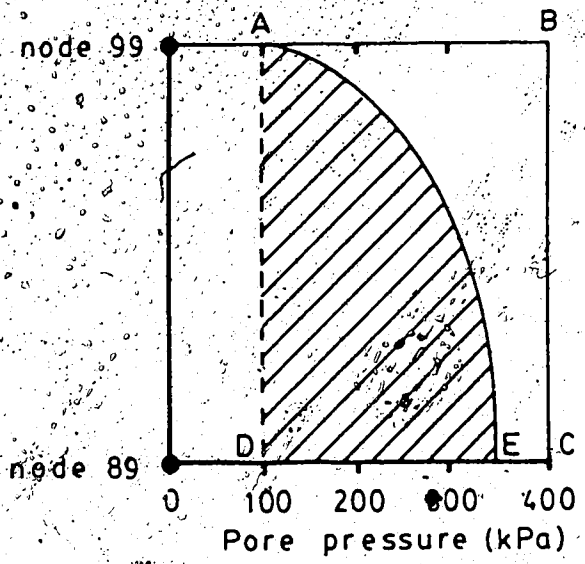

$$U(\%) = 100 \times \frac{\text{Area(ABCD)} - \text{Area(AED)}}{\text{Area(ABCD)}}$$

U(%) = Percentage consolidation

Area(ABCD) = Initial total excess pore pressure

Area(AED) = Excess pore pressure at time t

Figure 5.9 Evaluation of % Consolidation from Numerical Tests

A and throughout Step B, where according to the numerical results, gas evolution took place with degrees of saturation as low as 85% in some regions of the sample.

Two curves, associated with coefficients of permeability to water equal to 10^{-10} m/s and 10^{-11} m/s are shown in Figure 5.8. The comparison of these curves with those observed in the laboratory reveals that the lower values of the coefficient of permeability to water allowed a significantly better simulation of the test.

According to the numerical tests, during the first 50 minutes, the degree of saturation varied from 100 to 98.2%, close to the drainage boundary. Therefore, during this period, the small decrease in the void ratio, due to consolidation occurred simultaneously with the growth of gas bubbles which probably decreased the permeability to water. This might explain why the best numerical simulation was achieved with coefficients of permeability to water usually associated with high quality samples. This is definitely not the case of Samples 27-2C and 28-2C.

The continuation of the curves presented in Figure 5.8, associated with $k=10^{-10}$ m/s and 10^{-11} m/s for longer elapsed times, is presented in Figure 5.10. In this figure, an additional curve was included. It used the same variables for its generation, as the thinner dashed line ($k=10^{-10}$ m/s, $A'=1000$ min) except that the coefficient of permeability to water, K, was allowed to vary according to Equation 3.112 (Section 3.3.3). The comparison between these two curves

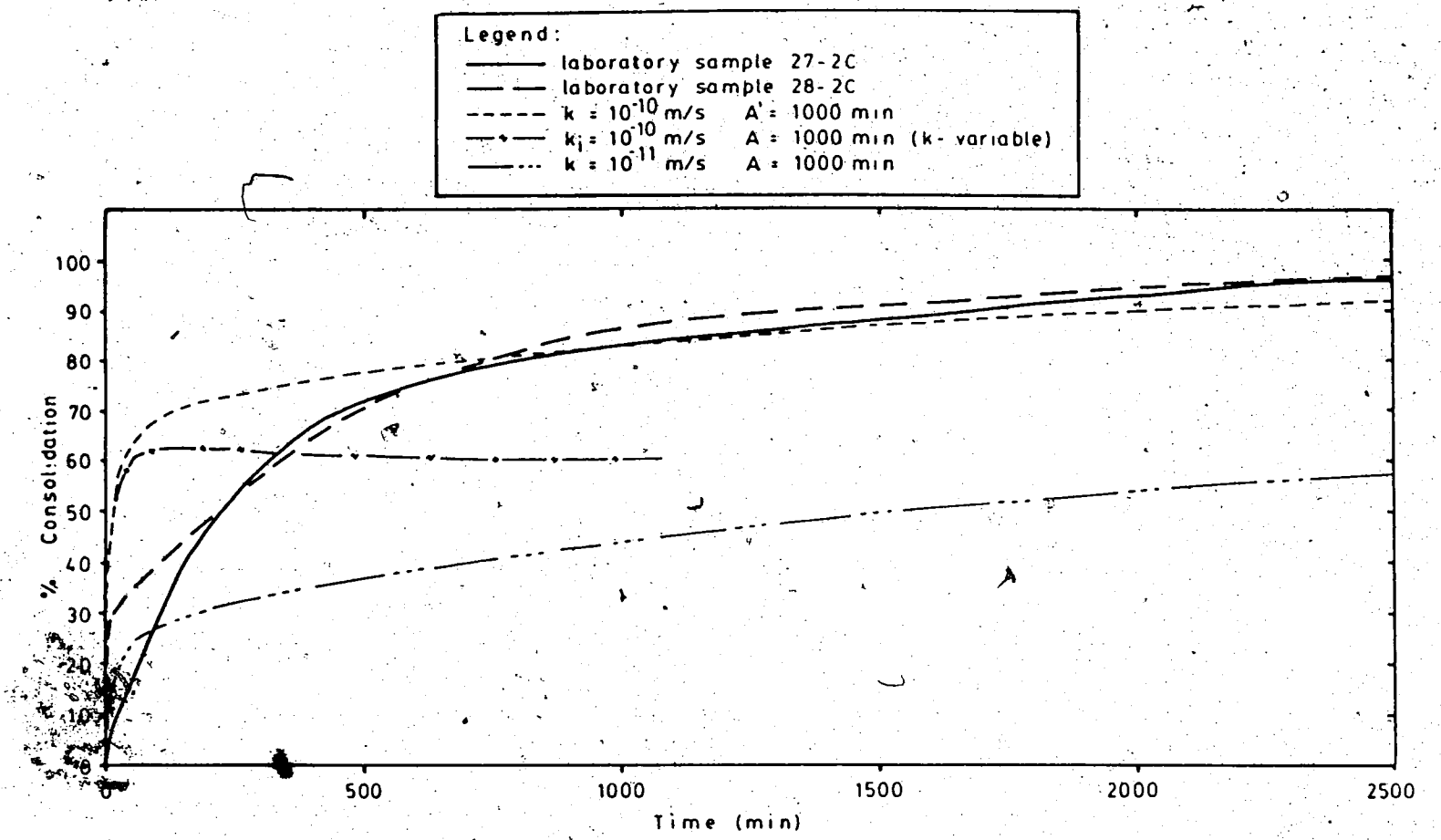

Figure 5.10 Hollow Cylinder Test - Type II - Numerical Simulation - Percent Consolidation versus Time, 0 to 2500 minutes

(constant K and variable K) clearly indicates the effect of the formation of bubbles on the coefficient of permeability to water and consequently, on the dissipation of pore pressures. As discussed earlier in this chapter, as the degree of saturation in the water phase decreases, the coefficient of permeability decreases. With this decrease, the consolidation process occurs at a slower rate, allowing the evolution of gases to take place, which in turn causes an even slower rate of dissipation of excess pore pressures. The numerical test where the coefficient of permeability to water was allowed to vary, indicated that a condition was reached where the degree of consolidation in the early stages of the test was higher than after 1000 minutes of testing. This condition was not observed in the two laboratory samples, indicating that Equation 3.112 most likely does not properly represent the variation of the coefficient of permeability to water with variations of the water void ratios and degree of saturation.

The comparison of the curves from numerical tests where the coefficients of permeability to water were maintained constant, with the two curves from laboratory tests indicate that the former predicted a faster consolidation ratio at the beginning of the test and slower after approximately 100 minutes of elapsed time. Besides the effect of the variability of the coefficient of permeability to water on the consolidation process, the contraction of the pores and the related pore pressure increase associated with shear

strains might have been responsible for the slower rate of consolidation of the laboratory tests. Immediately after the decrease of the internal cell pressure, the samples were subjected to a state of stress similar to the one present in the "J1" tests, (Figure 4.13). In those tests, it was noted when the samples were maintained at constant octahedral normal stress, the application of shear stresses lower than yielding shear stresses resulted in volumetric contraction.

The numerical tests indicated that, after the decrease of the internal cell pressure, the elements close to the internal cell bore were subjected to shear stresses from 6 to 40% of the shear stresses that would induce localized yielding of the soil skeleton (depending on the distance from the drainage boundary). These stresses were associated with maximum deviatoric strains varying from 0.0038 to 0.0044. The data presented in Figure 4.13 indicates that, for these strains and stresses, the soil skeleton exhibits volumetric contraction of 0.001 to 0.002, i.e., 0.1% to 0.2%. In the early stages of the hollow cylinder tests, the shearing of the samples due to the drop of internal stresses took place in a partly undrained mode. Therefore, shearing of the samples most likely resulted in volumetric contraction (since the samples were not fully saturated) and an increase of pore pressures. The increase in pore pressure opposes the consolidation process in which, for the case discussed herein, pore pressure decreases with time. When compared to the numerical test results, with a non-linear

elastic material model and, consequently no volume contraction or dilation due to shear stresses, the pore pressure increase that might have occurred due to shear in the laboratory sample probably resulted in an apparently slower consolidation process. This phenomenon most likely occurred in the early stages of the test, when most of the shear strains and associated volumetric strains took place.

The fact that, in the laboratory samples, the initial pore pressures were higher than the bubble point pressures was also inspected as being a possible reason for the differences between observed and predicted time-dependent response. In the numerical tests, the bubble point pressures were assumed to be higher than the initial pore pressures, since the initial degree of saturation was 99.5% and the sample was at equilibrium. Due to consolidation, as soon as the pore pressure dropped within the finite element mesh, the growth of bubbles took place immediately.

In the laboratory samples, however, the initial state probably was not a state of equilibrium. The samples were most likely undergoing a process of saturation, with pore pressures higher than the bubble point pressures. Therefore, the drop in pore pressure due to consolidation within the sample would not result in the immediate growth of gas bubbles. The growth of bubbles would take place only after the pore pressure dropped below the bubble point pressure. Therefore, one would expect that the laboratory tests would present a faster consolidation rate than the numerical

tests, since in the former the gas evolution responsible for the delay of pore pressure dissipation occurs later than in the numerical tests.

The data presented in Figures 5.8 and 5.9, however, shows the opposite trend for some portions of the tests, indicating that other factors had a greater influence on the overall time-dependent response of the samples.

Figure 5.11 presents the cell volume changes and vertical displacements observed in the laboratory and predicted by numerical simulation. This figure clearly illustrates that the numerical tests consistently underpredicted the lateral and vertical contraction of the samples. Most of the differences between predicted and observed values took place in the early stages of the tests. Thereafter, the behaviour of the numerical tests was very similar to the ones observed in the laboratory.

Table 5.7 depicts the volume changes of the samples observed in the laboratory and predicted by CONGAS. The volume changes indicated in this table were obtained from the lateral and vertical deformation of the samples. The data indicate that shortly after the modification of the internal cell pressure (approximately 10 minutes), the middle point of element 4, of the finite element mesh of Figure 5.7, presented a maximum deviatoric strain of approximately 0.4% and a total sample volumetric strain varying from 0.006% to 0.017%, depending on the coefficient of permeability to water considered.

	LABORATORY				NUMERICAL (*)			
	SAMPLE 27-2C		SAMPLE 28-2C		K=10-10M/S		K=10-11M/S	
	TIME (MIN)		TIME (MIN)		TIME (MIN)		TIME (MIN)	
	10	2880	10	2880	12	2882	12	2882
($\epsilon_1-\epsilon_3$) (%)					0.391	0.389	0.373	0.369
SAMPLE VOLUME CHANGE (CC)	-3.729	-7.153 (***)	-5.334	-8.016	-0.370	-0.755	-0.115	-0.499
SAMPLE VOLUMETRIC STRAIN (%) (**)	-0.178	-0.341	-0.257	-0.387	-0.017	-0.035	-0.006	-0.023

(*) - FROM NUMERICAL SIMULATION - AT CENTRE OF ELEMENT 4 OF FINITE ELEMENT MESH IN FIGURE 5.7

(**) - SAMPLE VOLUMETRIC STRAIN = $\Delta V/Vo$
WHERE : ΔV = SAMPLE VOLUME CHANGE
Vo= INITIAL VOLUME OF SAMPLE
= 2100 CC - SAMPLE 27-2C
= 2073 CC - SAMPLE 28-2C
= 2153 CC - FINITE ELEMENT MESH

(***) - DUE TO LEAK IN THE VOLUME CHANGE DEVICE, CONNECTED TO THE INTERNAL CELL, THE FRACTION OF THE VOLUME CHANGE ASSOCIATED WITH THE INTERNAL CELL WAS EVALUATED AT T=60 MINUTES

Table 5.7 Hollow Cylinder Tests - Type II - Sample Volume Changes, Step A

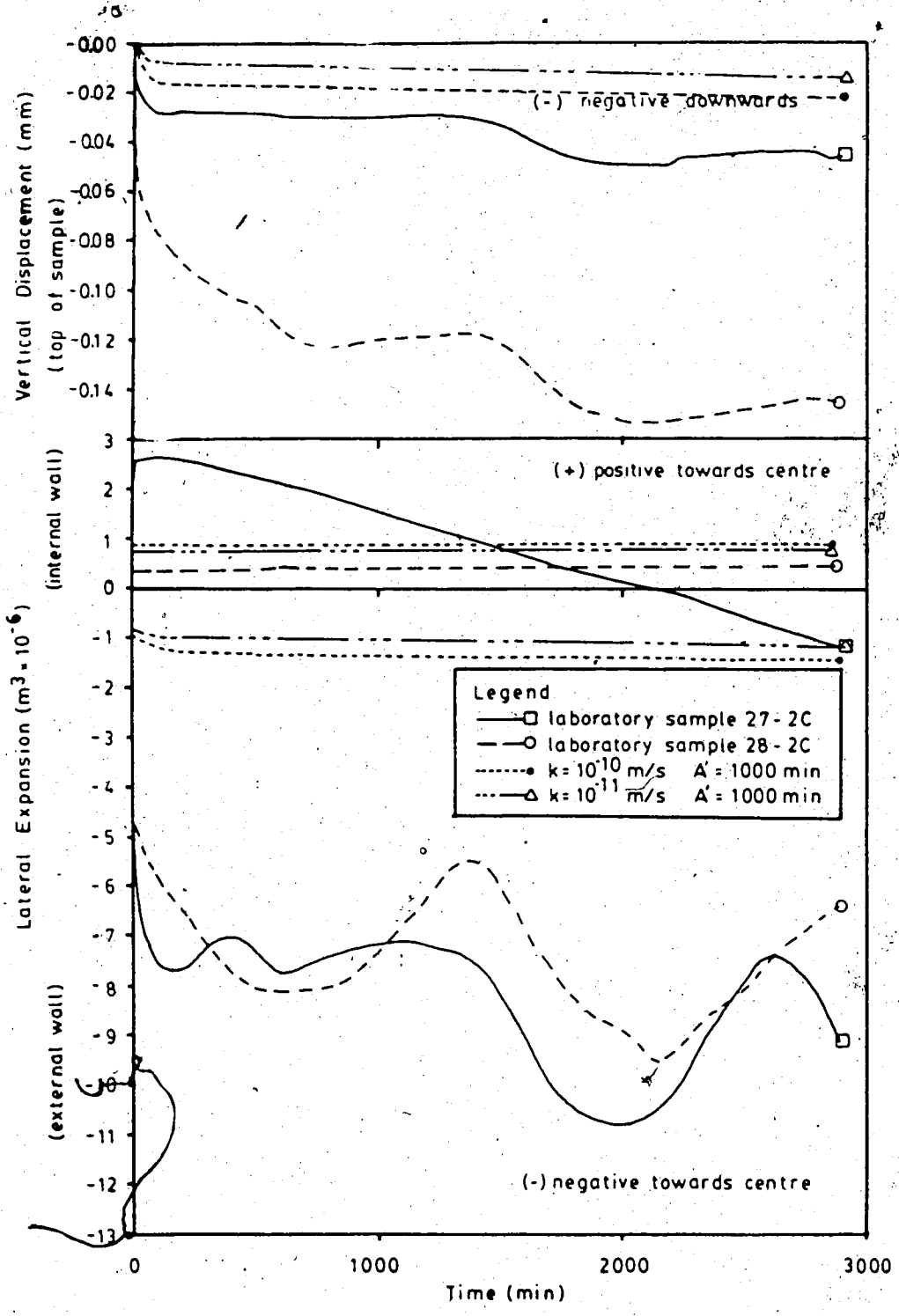

Figure 5.11 Hollow Cylinder Test - Type II - Numerical Simulation, Step A

At an elapsed time of approximately 10 minutes, the laboratory samples exhibited volumetric contraction between 0.1% and 0.25% higher than the numerically predicted ones. If it is assumed that the average shear strain $(\varepsilon_1-\varepsilon_3)$ in the laboratory samples was the same as the ones predicted by CONGAS, i.e., 0.4%, according to the "J1" triaxial tests, the laboratory samples should in fact present volumetric contractions between 0.1 and 0.2% higher than the numerically predicted ones. At the end of Step A, at an elapsed time of 2880 minutes, the difference between predicted and observed volumetric strains increased to 0.3 to 0.4%.

Unfortunately, the data collected during the Type II tests do not allow further analysis of the causes of the differences between measured and predicted values. Localized pore pressures and volumetric strain measurements could probably aid in the analysis of test results.

Finally, Figure 5.12 presents the variation of the degrees of saturation with depth, at the end of Step A, as predicted by the numerical simulations where the coefficient of permeability to water was maintained constant and equal to 10^{-10} m/s and 10^{-11} m/s. The average total degrees of saturation, at the end of Step A, obtained from the laboratory tests results are also shown in this figure. They show that the predicted values associated with the smaller coefficient of permeability to water present an average degree of saturation closer to those observed in the

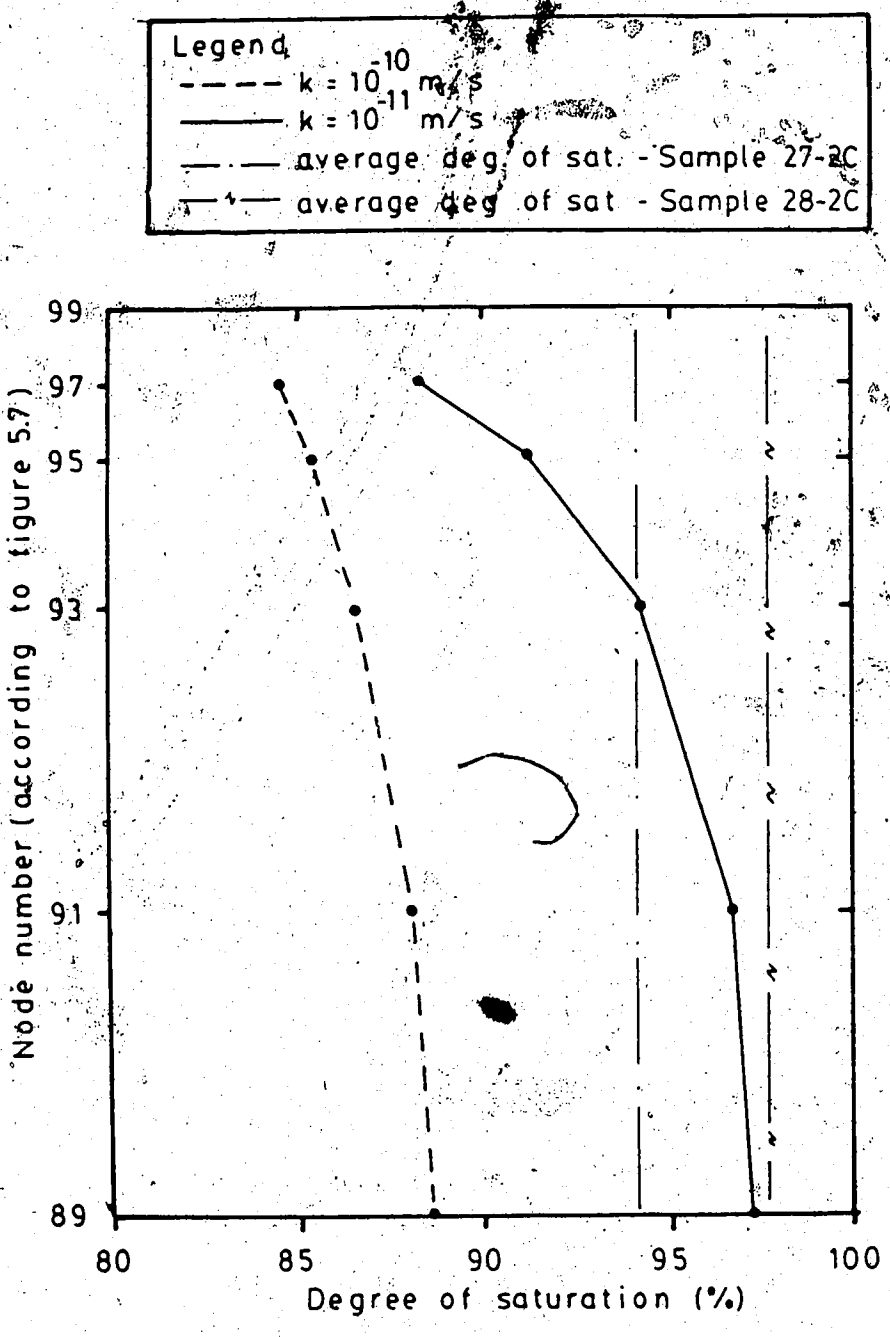

Figure 5.12 Hollow Cylinder Test - Type II - Degree of Saturation versus Depth at the End of Step A - t=2882 minutes

laboratory.

The simulation of Step B, as explained earlier in this section, consisted of the further reduction of the internal cell pressure from 1000 kPa to 500 kPa. All other boundary stresses and pore pressure boundary conditions at the end of Step A were maintained constant.

The temporal discretization depicted in Table 5.5. proved not to be suitable for this step, in the case where the coefficient of permeability to water was equal to 10^{-11} m/s. The use of time increments less than 30 minutes resulted in a general increase in pore pressure within the mesh. This illustrates a limitation of Vermeer and Verruijt's, 1981, equation, when applied to the formulation used in CONGAS. Since in the laboratory, the change in boundary conditions occurred in less than 2 minutes, the exact simulation of the unloading associated with Step B was not possible. Therefore, the numerical test performed with a coefficient of permeability to water equal to 10^{-11} m/s stopped at the end of Step A.

As expected, the numerical test results, performed with a constant coefficient of permeability to water equal to 10^{-10} m/s, indicated that changes in the internal cell pressure induced additional shear stresses in the elements of the finite element mesh. These shear stresses varied from 7% to 65% of the stresses which would induce localized yielding of the soil skeleton. The octahedral shear stresses were associated with maximum deviatoric normal strains of up

to 0.072%.

The modification of the internal boundary stress was performed in ten increments and resulted in an ERRORG index (Section 3.3.3) consistently less than 4.5% for all elements of the mesh.

The sample wall movements as predicted by the numerical test are summarized in Table 5.8. The data indicate that decreases in the internal pressure should result in changes in the water volume in the internal and external cell of approximately 35% and 45%, respectively, provided that no additional shear contraction takes place. However, according to the "J1" triaxial tests discussed earlier in this section, the additional shear strains ($\epsilon_1-\epsilon_3$) (from 0.04% to 0.07%) should induce additional volumetric contraction of the sample. This contraction should be approximately 0.01% or approximately 2 cm^3.

According to the laboratory test data (Section 4.3.5.5), Step B of both Type II tests presented oscillations in the measurements of cell volume water changes of the order of ± 2.5 cm^3. Therefore, the error in the laboratory results probably masked the sample response.

The numerical test predicted an increase of approximately 20% of the downward movement of the piston, after the decrease of the internal pressure. Once again, the accuracy of measurements did not allow the verification of the accuracy of the prediction.

	DISPLACEMENTS (MM x 10^{-2})					
	INTERNAL WALL NODE 4 (*) (**)		EXTERNAL WALL NODE 158 (*) (**)		TOP OF SAMPLE NODE 121 (*) (***)	
	A	B	A	B	A	B
NUMERICAL SIMULATION A'=1000 MIN k=10^{-10}M/S	-4.72	-6.86	-2.17	-2.95	-1.10	-1.35

(*) : REFER TO FIGURE 5.7

(**) : (-) TOWARDS AXIS OF SYMMETRY

(***) : (-) DOWNWARDS

A : BEFORE DECREASE OF INTERNAL PRESSURE (END OF STEP A)

B : AFTER DECREASE OF INTERNAL PRESSURE (BEGINING OF STEP B)

Table 5.8 Hollow Cylinder Test - Type II - Numerical Simulation, Step B

5.4 Simulation of Shaft Sinking in Oil Sands

There are two main objectives in this section:

- To illustrate how CONGAS can be used as an efficient tool to analyse alternative construction techniques for shaft sinking in oil sands.
- To show the importance of proper consideration of the time-dependent evolution of gases in the pores of oil sands, in the simulation of the mechanical response of oil sands.

These objectives are achieved here through the simplified numerical analysis of shaft sinking in oil sands. The simplifications involved in the analysis are discussed in detail in the following sections.

Underground Excavations in the Mining Access Concept

The importance of underground excavations in oil sands has increased with the need of bitumen recovery at depths which are impractical for surface mining. *in situ* recovery processes have been developed to eliminate the need for mining the oil sand deposits for surface treatment. Most of these processes use injection of steam in the formation as a means of decreasing the viscosity of bitumen so it may flow from the sand matrix and be pumped to the surface. Wells for injection of steam and production of bitumen may be drilled from the surface or from a tunnel driven through or underneath the oil sands deposit. The latter technique involves excavation in the oil sands deposit and has been referred to as the Mining Access Concept. Haston, 1985,

presents a brief review of the history of the Mining Access Concept.

In this section, only the shafts used for access and ventilation of the tunnels and underground chambers will be considered.

The implementation of the shafts in the mining access concept involves several activities among which three can be developed in the scope of geotechnical engineering:

- choice of the construction technique;
- assessment of lining loads during construction and during *in situ* production of the bitumen.
- monitoring of the performance of the shaft during construction and during *in situ* production of the bitumen.

Except for the simulation of the behaviour of the lining and surrounding oil sand mass during *in situ* production of the bitumen, which requires the modelling of the process of heat transfer and coupled consolidation, CONGAS can be helpful in the development of these activities. In this section, CONGAS is used to analyse an alternative construction technique for shaft sinking in oil sands. This activity can be classified as part of the first of the three items listed above.

Construction Methods for Shaft Sinking in Oil Sands

The Alberta Oil Sands Technology and Research Authority (AOSTRA) is presently implementing an Underground Test Facility (UTF) located approximately 60 km northwest of the

town of Fort McMurray. The development of this facility aims at generating data on mining access design and providing for field piloting of recovery processes. As part of the project, two shafts with finished diameter slightly over three metres were sunk through the McMurray formation to the underlying Devonian limestone. The local geology has been studied and published by several authors and was summarized by Patterson, 1985. Figure 5.13 summarizes the site geology, *in situ* pore pressures and geotechnical concerns as presented by Patterson, Op.cit. According to the author, the weak properties of the overburden and oil sand deposit demanded a shaft sinking method which would either preconsolidate the mass or provide support during or shortly after excavation. The following methods were considered:

- Conventional excavation (drill and blast) followed closely by ribs and lagging or steel liner plate;
- Preconsolidation grouting;
- Ground freezing;
- Large-diameter drilling with mud for support.

The conventional excavation technique was eliminated due to its time consuming nature and uncertainties concerning the effects of inflow of water and/or fines into the excavation.

The preconsolidation grouting in the local silty and clay materials with low coefficients of permeability to water was considered of questionable efficiency and was also eliminated.

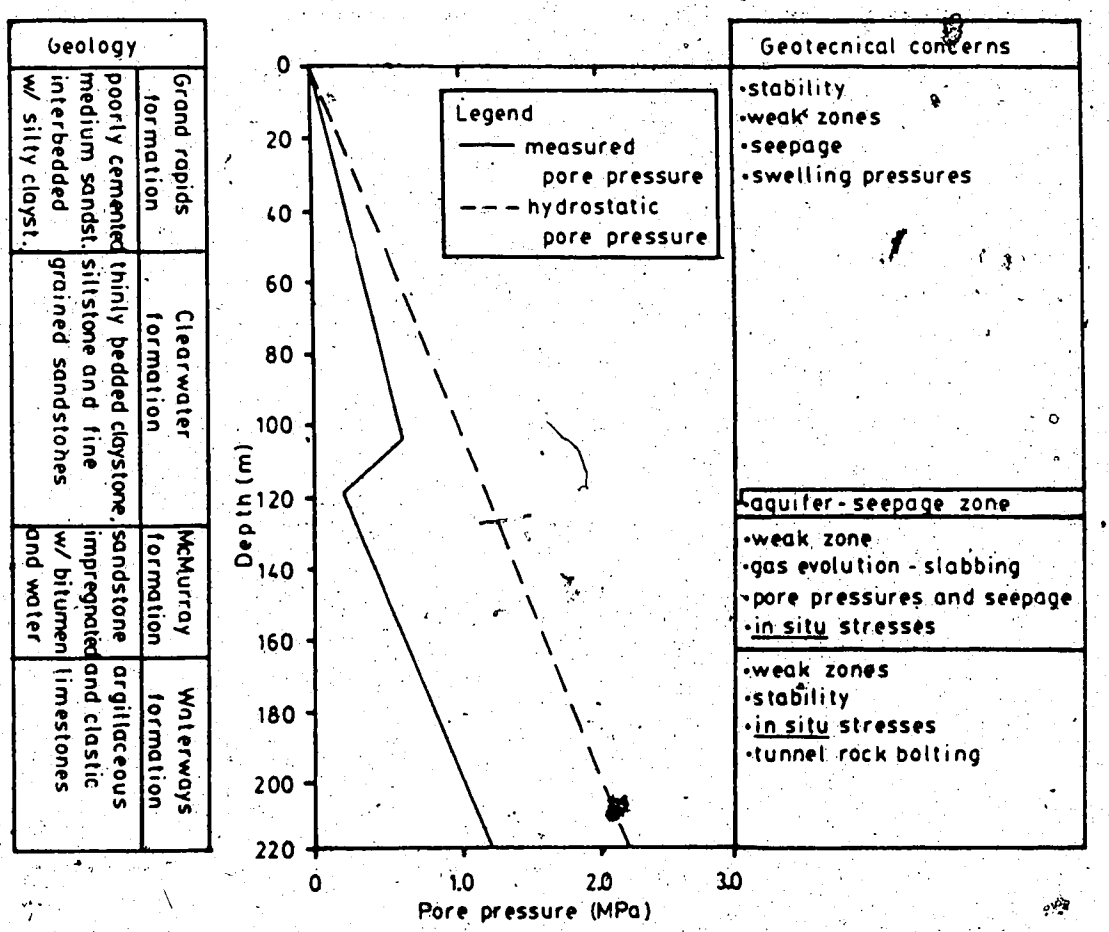

Figure 5.13 UTF Shafts - Geology, Pore Pressures and Geotechnical Concerns

The ground freezing was considered feasible for the overburden materials but of questionable efficiency in the oil sands deposit. Low moisture content, low hydraulic conductivity, inability to control gas evolution and low unconfined strength of frozen disturbed oil sands near the shaft walls were some of the reasons given to eliminate this technique.

Consequently, blind shaft drilling was the construction technique chosen. The ability to control ground water and unstable formations through the appropriate control of the drilling mud, speed of contruction, prevention of gas evolution, preservation of *in situ* strength of oil sands and safety of the workers were cited as important advantages of the chosen method.

Figure 5.14 schematically illustrates the construction stages involved in the blind drilling method.

After the site preparation, the drilling of the UTF shafts was performed with a large diameter (3.96 m) Drilco flat bottomed bit. During drilling, the shafts were maintained flooded with the drilling fluid. Patterson reported average advance rates of 0.2378 m/h in the deposits overlying the oil sands and 0.3122 m/h in the oil sand. After the required depth was reached, the bit was removed and a steel liner was installed. The installation consisted of welding of the liner segments at the surface which were then sunk in the drilling mud by filling the interior with fresh water. After the steel liner reached the bottom of the

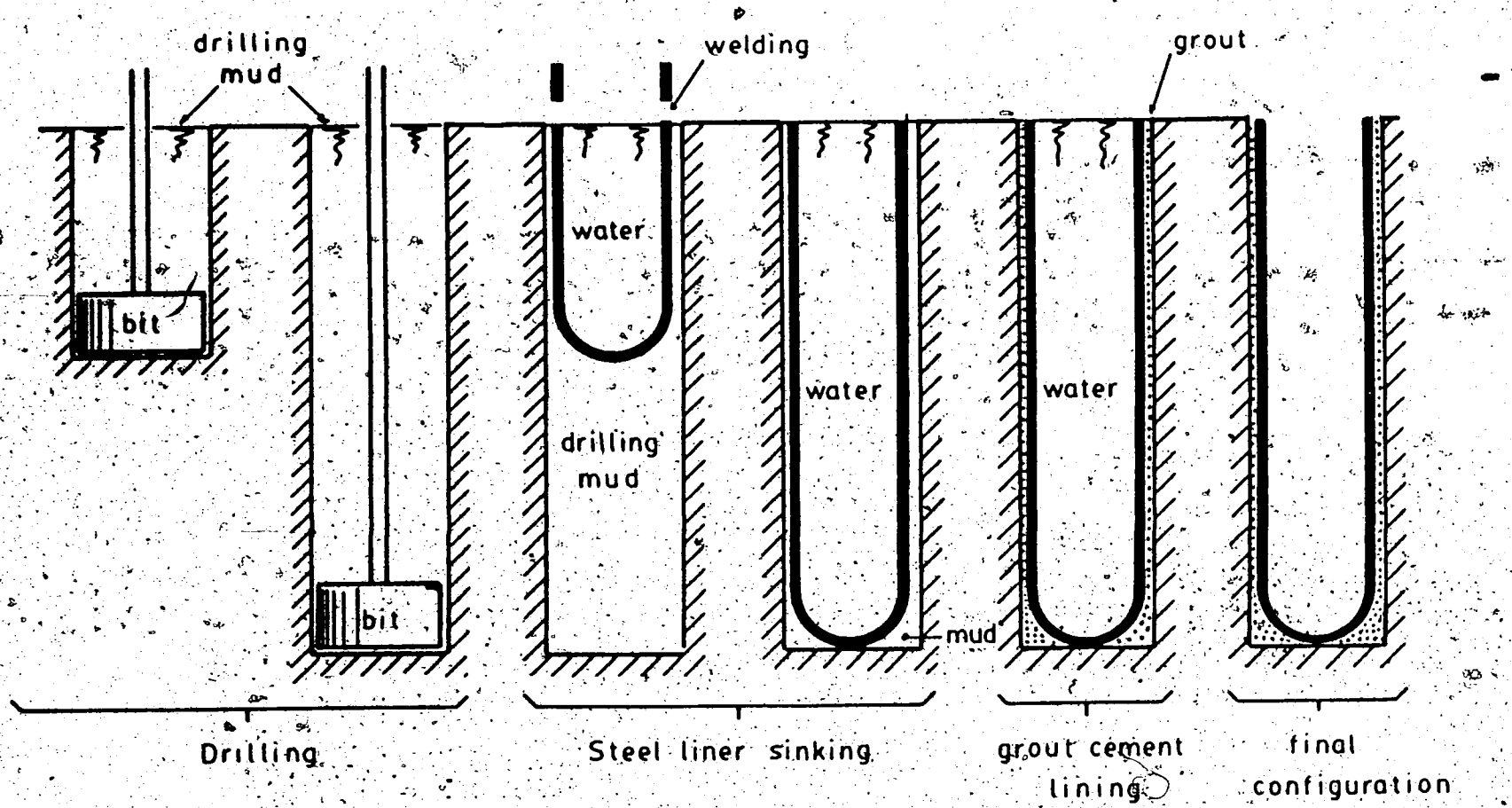

Figure 5.14 Blind Shaft Drilling - Construction Stages

shaft, it was grouted in place. The water inside the steel liner was pumped out and the shaft installation was concluded.

An extensive literature review on shaft sinking and lining installation techniques, published by Branco, 1985, revealed several alternatives to the construction technique used in the UTF. Among them the one that presented greater flexibility of construction and appeared to be suitable for shaft sinking in oil sands, was the one described by Maser, 1981. It was named the Continuous Shaft Lining (CSL) system, developed at Foster-Miller Associates, Massachusetts. The method uses a slipform system that allows the continuous placement of a cast-in-place rapid strength development concrete. The system was developed for three application scenarios:

- lining raised bored shafts
- lining blind drilled shafts after drilling, while the drilling mud is being removed
- lining directly behind a blind shaft boring machine.

Clearly, the latter two cases are applicable to oil sands. In the second scenario, the only variation from the method used at the UTF would be the lining installation. The use of the CSL systems would allow the elimination of the steel liner.

In the third scenario, the circulation of drilling mud and cuttings from the shaft face to the surface must be

carried out consistently with the lining installation procedure. In this latter method, illustrated in Figure 5.15, only the face of the shaft is flooded with mud. The lining placement is continually executed immediately above the fluid mud, at the same advance rate as that of the drilling bit. According to the author, the method allows concreting with large water inflows and allows a wide range of lining thicknesses.

When compared to the method used in the UTF shafts, besides eliminating the need for the steel liner, the CSL allows the minimization of the volumes of drilling fluid required. This might be an important factor during the drilling of deeper and larger shafts. On the other hand, the use of the CSL system results in stress relief of the shaft wall significantly larger than that which occurred at the UTF. Provided that the shaft walls are stable during drilling and lining installation, the stress relief can result in a decrease of lining loads. This conclusion can be drawn from simple ground reaction curves as explained by Scott et al., 1985.

Simulation of Shaft Sinking with the CSL System

The effects of the use of the CSL system for shaft sinking on the mechanical response of oil sands can be studied with CONGAS. This study should aid in the analysis of the efficiency of the construction technique when used in oil sands.

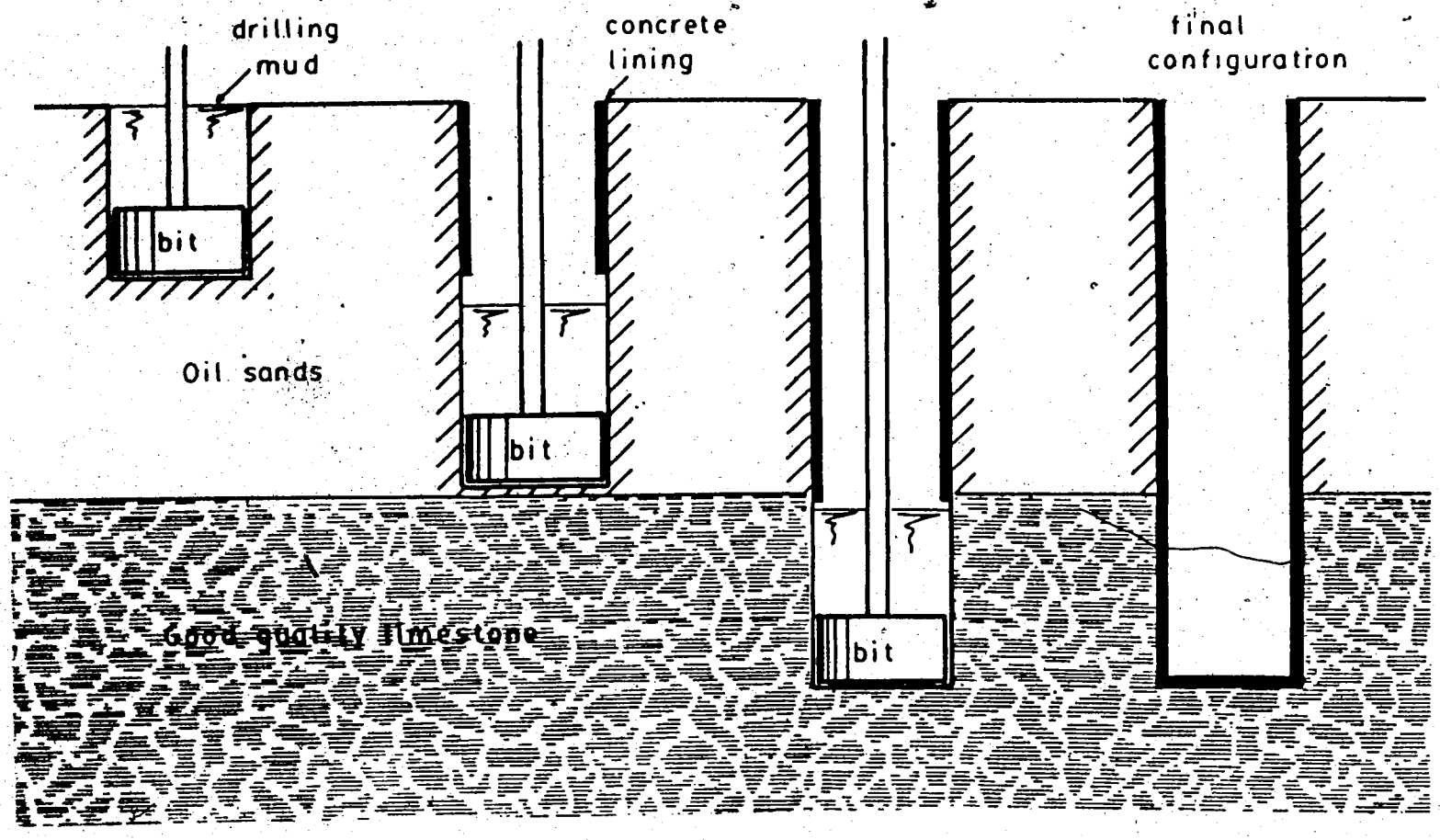

Figure 5.15 Blind Shaft Drilling - Continuous Shaft Lining

The rigorous numerical simulation of shaft sinking, with the CSL system, would require appropriate modelling of the following features:

- Substitution of elements representing the soil excavated by a cavity subjected to boundary pressures applied by the drilling fluid.
- Continuous installation of the concrete lining above the drilling fluid.

In its present state, CONGAS does not allow the exact simulation of these features. Therefore, in order to carry out the numerical simulation in an economic manner, the shaft construction was developed in two independent stages. In the first stage, stage A, a horizontal cross section passing through the shaft axis was studied. In this study, the three dimensional effects of the presence of the advancing face and concrete lining on the behaviour of the oil sands were neglected.

The aim of this stage of the analysis was to study the behaviour of the oil sands located away from the face and lining. Figure 5.16 illustrates the region of the shaft that can be approximately represented by the simulation, stage A.

In the second stage, stage B, the behaviour of the face of the shaft was studied. In order to minimize the horizontal refinement of the mesh and consequently computational time, the side walls of the shaft were restrained from horizontal movement. Therefore, in stage B, only the effect of the decrease in the soil pressures at the

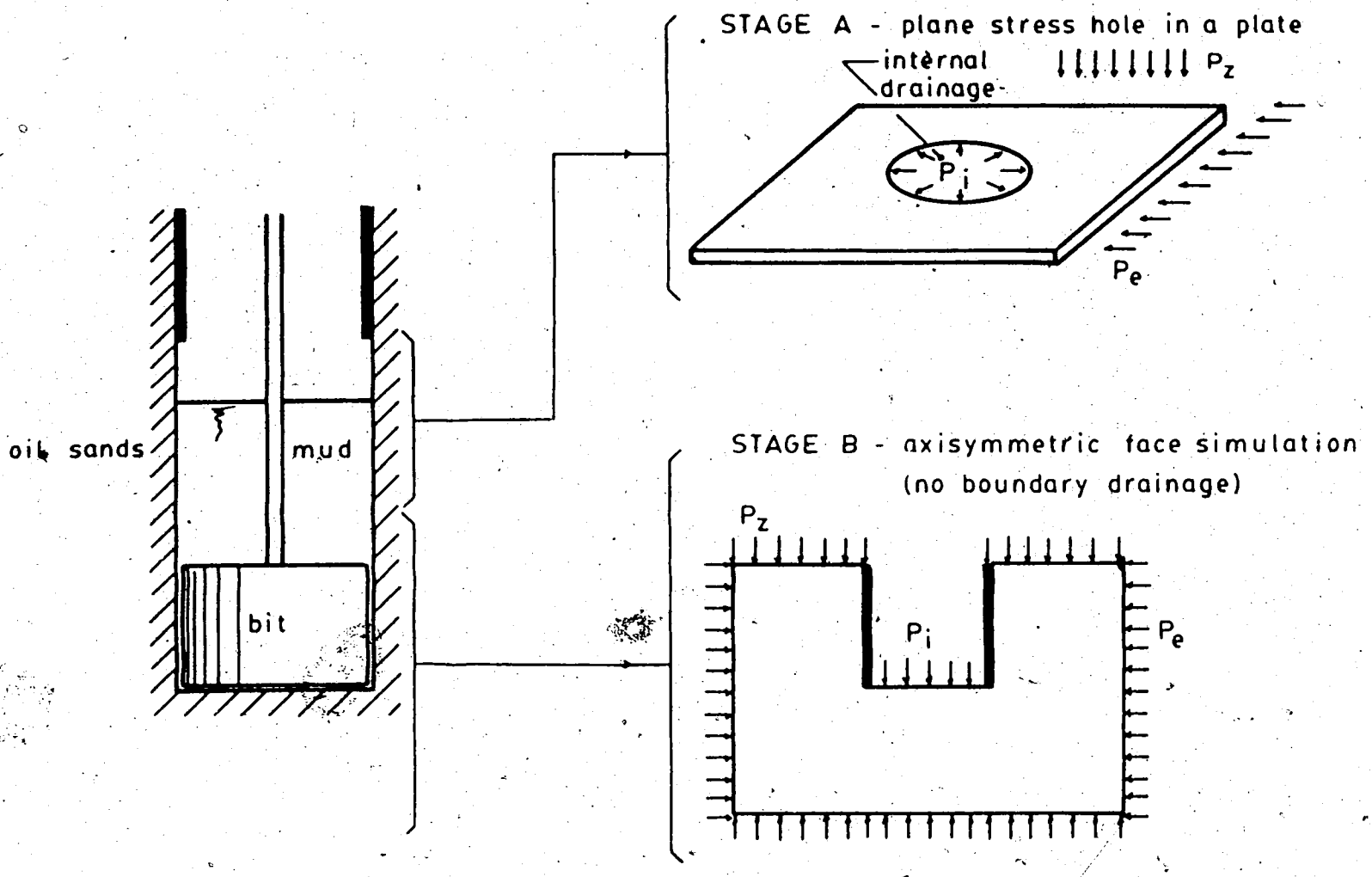

Figure 5.16 Shaft Sinking with the Continuous Shaft Lining System - Numerical Simulation

face of the shaft was analysed. This was thought to be a reasonable simplification to be implemented in stage B, since the behaviour of the side walls of the shaft was studied in stage A of the numerical analysis.

For each of the situations modelled (stages A and B), three time-dependent gas evolution responses were considered:

- No gas evolution takes place (consolidation only);
- Gas evolution takes place at a moderately fast rate (A'=1000 min.);
- Gas evolution takes place at a moderately slow rate (A'= 10,000 min.).

The numerical test with no gas evolution, where consolidation was the only transient process considered, was carried out in order to allow a basis of comparison for the two other situations. The performance of underground openings in which gas evolution does not occur is reasonably well understood. Therefore, this comparison should allow the analysis of the effects of gas evolution on the behaviour of the opening, and consequently the analysis of how the gas evolution process modifies the already existing problems associated with shaft sinking in gas free soils.

Two scaling parameters, A', were selected to study how the rate of gas evolution affects the behaviour of the shaft. The numerical tests that used the lower value of A' simulated the condition where gas evolution occurs at a faster rate. The comparison of these test results, with

tests performed with a higher A' value, should allow the analysis of the importance of the consideration of the transient gas evolution in the simulation of shaft sinking in oil sands. As explained in Chapter 3, most of the techniques available for simulation of the mechanical response of gassy soils assume that the evolution of gases occurs instantaneously. The simulation with a different rate of gas evolution allows the assessment of the limitations of this assumption.

Numerical Tests Stage A

The numerical tests, stage A, were performed with the finite element mesh presented in Figure 5.17. As mentioned earlier in this section, the mesh represents a horizontal plane subjected to a state of plane stress through which the shaft is drilled. The mesh was designed with a ratio of external to internal radius equal to 5, which might be considered small, if after complete modification of the internal boundary stresses, an undisturbed stress field was to be maintained away from the central hole. The choice of this radius ratio was chosen with the consideration that the purpose of this numerical test was to compare results of simulations performed with different parameters and not simulating the actual behaviour of shafts. The minimum time increment, according to Vermeer and Verruijt's, 1981, equation, associated with this mesh, is 85 minutes. Therefore, time increments of 100 minutes were used. The central hole is assumed to exist prior to excavation,

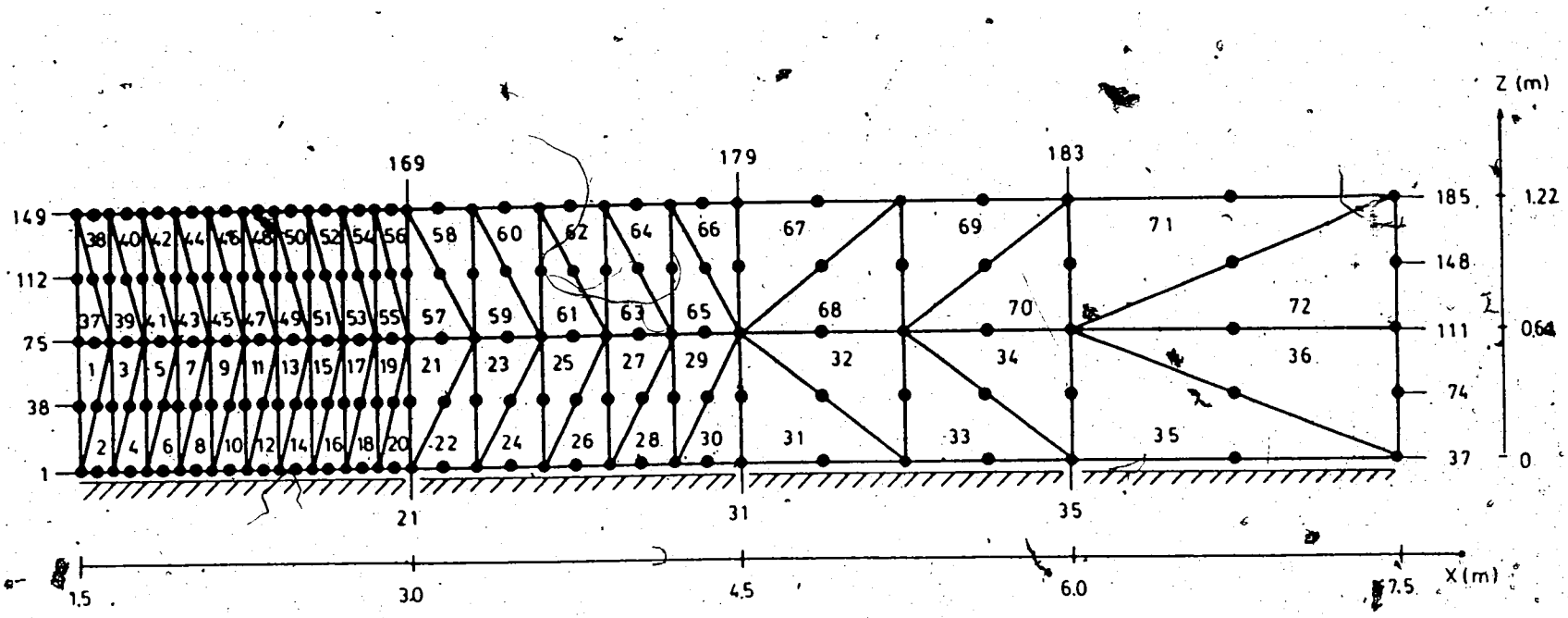

properties: E = 1 GPa
ν = 0.25
k = 10^{10} m/s
e_i = 0.47
S_i = 1.00

boundary condition: Pe = 3 MPa
Pz = 3 MPa
Pi = 3 MPa ⟶ to 0 MPa at t = 0⁺
ui = 1.5 MPa ⟶ to 0 MPa at t = 0⁺

initial internal stresses σ'_x = 1.5 MPa
σ'_y = 1.5 MPa
σ'_z = 1.5 MPa

Figure 5.17 Finite Element Mesh Test 13-V18 - Shaft Simulation - Stage A

subjected to a pressure equal to the *in situ* horizontal stress. Initially, the plate is subjected to an isotropic state of stress equivalent to depths between 140 and 160 metres. In fact, this state of stress is similar to that found in the oil sands deposit at the UTF. At the UTF shafts, the *in situ* pore pressures were lower than hydrostatic, as depicted in Figure 5.13, a fact that was favourable to shaft sinking. Herein, the pore pressures were assumed to be hydrostatic, a condition that might be present during shaft sinking in other regions of the oil sand deposits.

The boundary stresses applied to the finite element mesh are summarized in Table 5.9. Both the internal radial stress and boundary pore pressures were modified to their final values in one single step, i.e., the boundary conditions were assumed to occur instantaneously. This assumption is, in fact, an over-simplification of the actual change of boundary conditions that takes place at the shaft walls when the CSL system is used. However, CONGAS, in its present version, does not allow the modification of pore pressures between successive steps. Therefore, to be consistent with the changes in boundary pore pressures, the boundary stresses were modified in one single step.

The soil skeleton was assumed to behave in a linear elastic manner, with the parameters depicted in Table 5.9. The water flow and physical properties are also shown in this table.

INITIAL STRESSES	σ'	1500 kPa (ISOTROPIC)
	u	1500 kPa
BOUNDARY CONDITION	P_z	3000 kPa
	P_e	3000 kPa
	P_i	3000 kPa TO 0 AT T=0+
	u_i	1500 kPa TO 0 AT T=0+
STRESS-STRAIN PARAMETERS		ν = 0.25 E = 1000 MPa
GAS-LIQUID PARAMETERS		A = 0,1000,10000 MIN H = 0.15
WATER FLOW		$k = 10^{-10}$ M/S
LIQUIDS COMPRESSIBILITY		INCOMPRESSIBLE
PHYSICAL PROPERTIES		S_{init} = 1.00 e_{bit} = 0.33 e_0 = 0.47

σ' = INITIAL EFFECTIVE STRESS
u = INITIAL PORE PRESSURE
P_z = VERTICAL PRESSURE
P_e = EXTERNAL PRESSURE
P_I = INTERNAL PRESSURE
u_i = PORE PRESSURE AT INTERNAL BOUNDARY

Table 5.9 Shaft Simulation - Stage A - Initial Stresses, Boundary Conditions and Parameters

The numerical tests simulated the soil behaviour for a period of 1300 minutes, time during which the soil around the shaft was assumed to undergo stress changes from the virgin *in situ* values to the time the concrete lining is installed. Further details about this assumption are given later in this section. Figures 5.18 and 5.19 and 5.20 present the progress of radial stresses and pore pressure distribution within the soil mass. The difference between the pore pressures within the mesh, immediately after the modification of the boundary stresses (1575 kPa), and the initial pore pressures, are attributed to numerical approximations. Theoretically, both should be equal for the condition where no drainage is allowed at the internal wall, as was the case in the first step of the numerical simulation.

For the tests where gas evolution took place, the degrees of saturation were above 93%.

The data presented in the three figures allow the evaluation of the progress of seepage forces for each case studied. Figure 5.21 depicts the average seepage force between the shaft wall and a point located 0.33 metres from the shaft wall (at sampling point 3 of element 5). Seepage forces within this region act radially, towards the centre of the shaft.

During shaft construction, the seepage forces control the water flow into the shaft, and reduces the factor of safety of the opening. An analysis of Figure 5.21 indicated

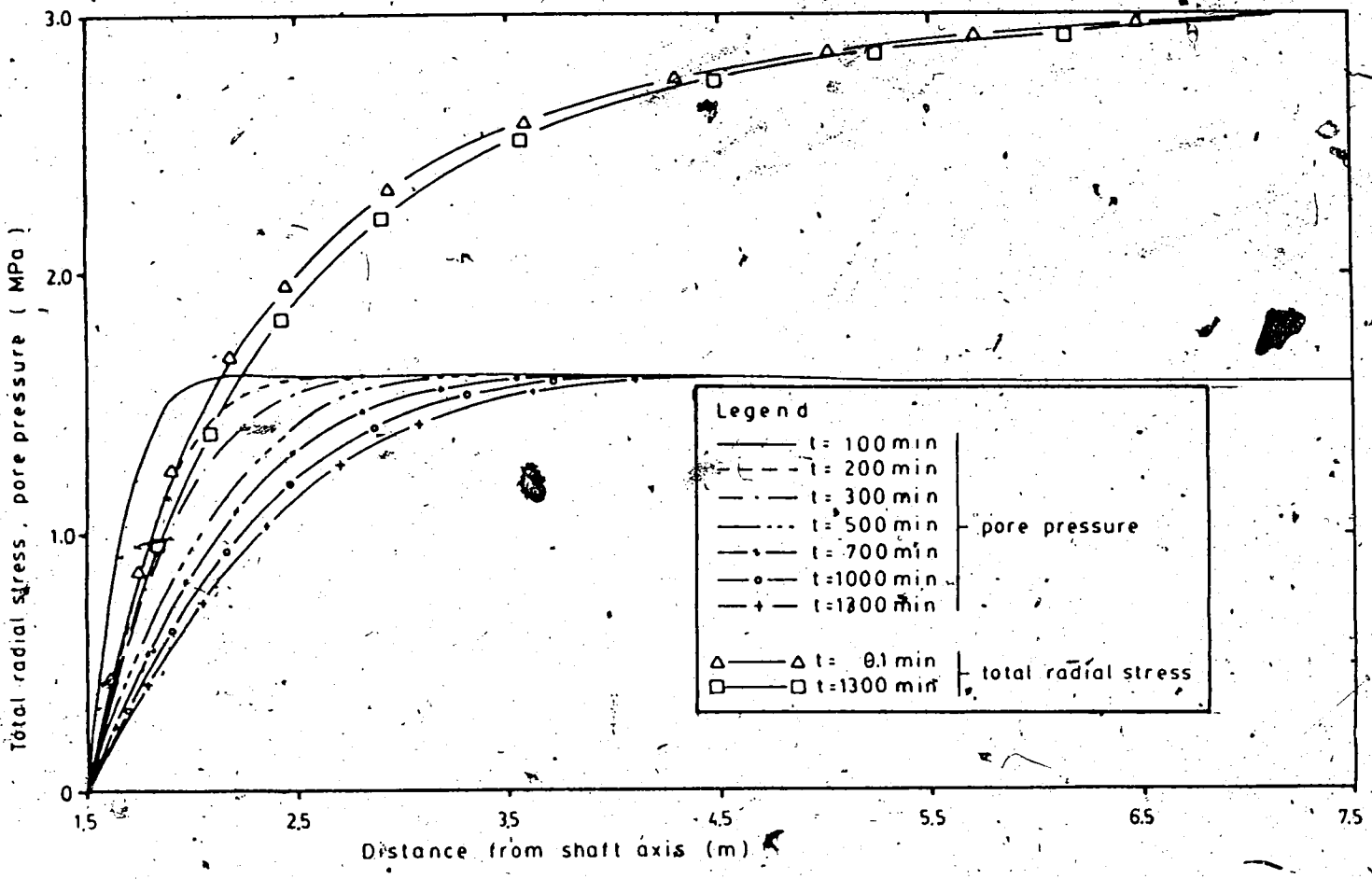

Figure 5.18 Shaft Simulation - Stage A - Radial Stresses and Pore Pressures - Consolidation Only

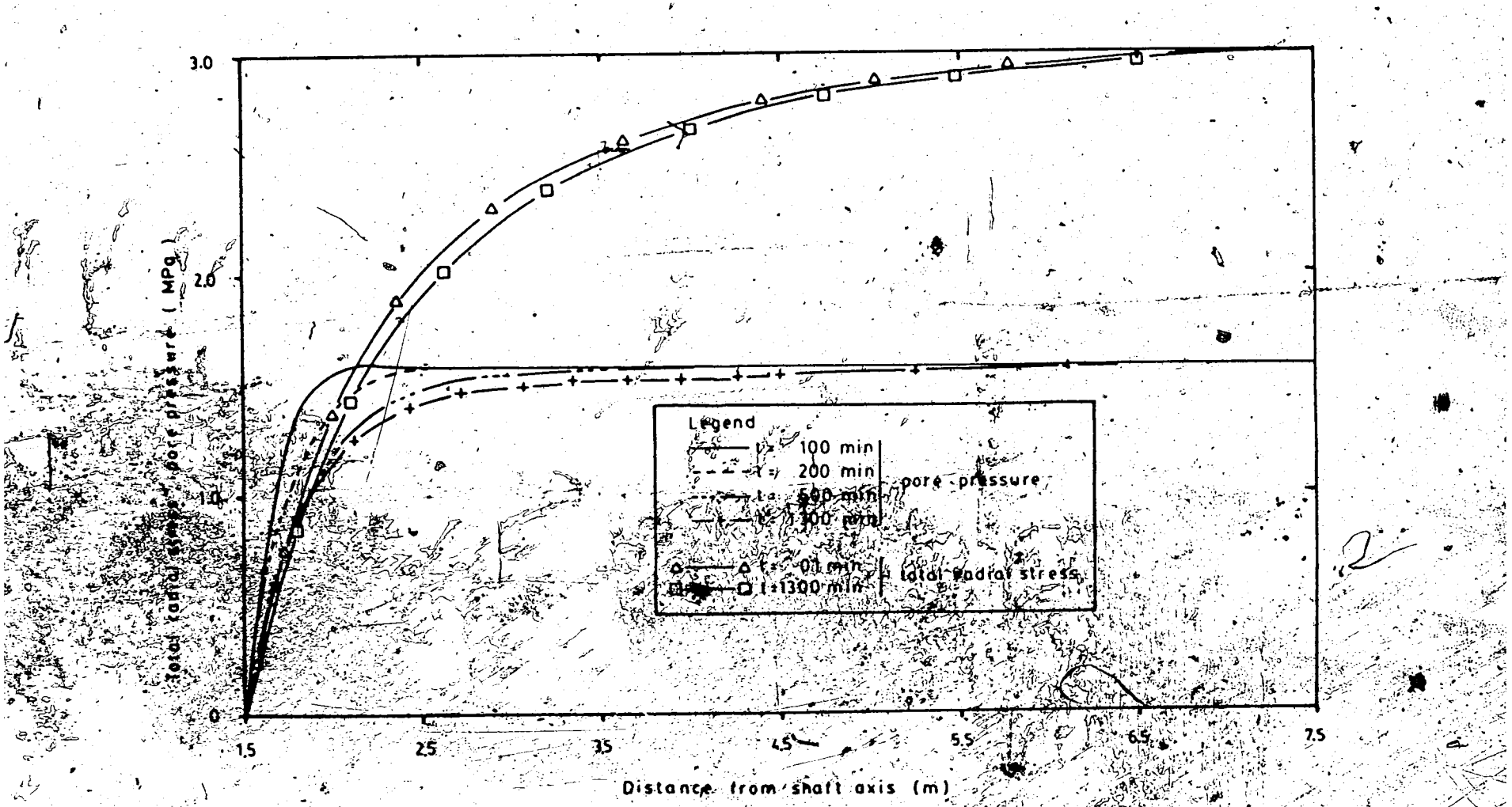

Figure 5.19 Shaft Simulation - Stage A - Radial Stresses and Pore Pressures - A'=10 000 minutes

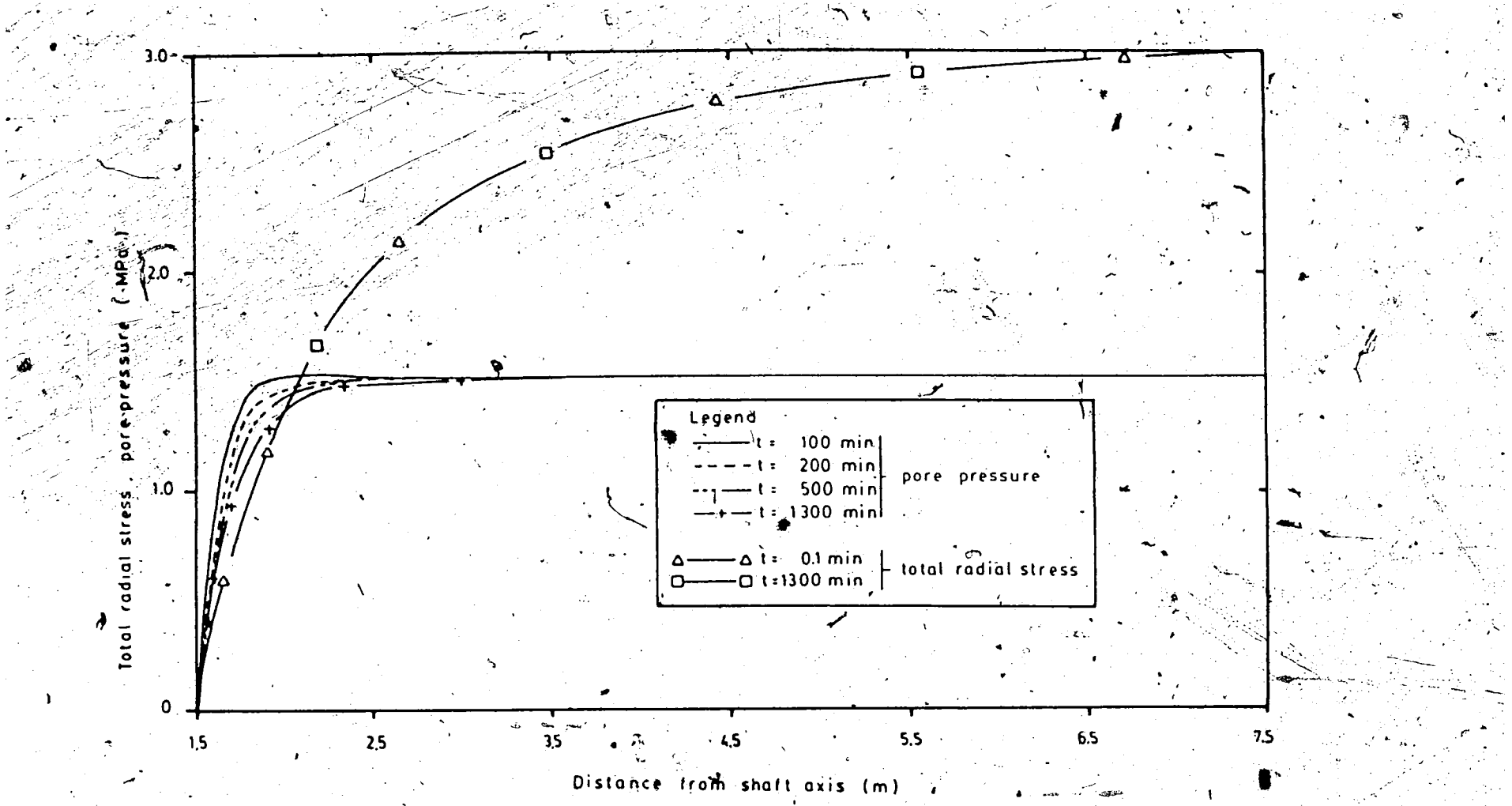

Figure 5.20 Shaft Simulation - Stage A - Radial Stresses and Pore Pressures - A'=1000 minutes

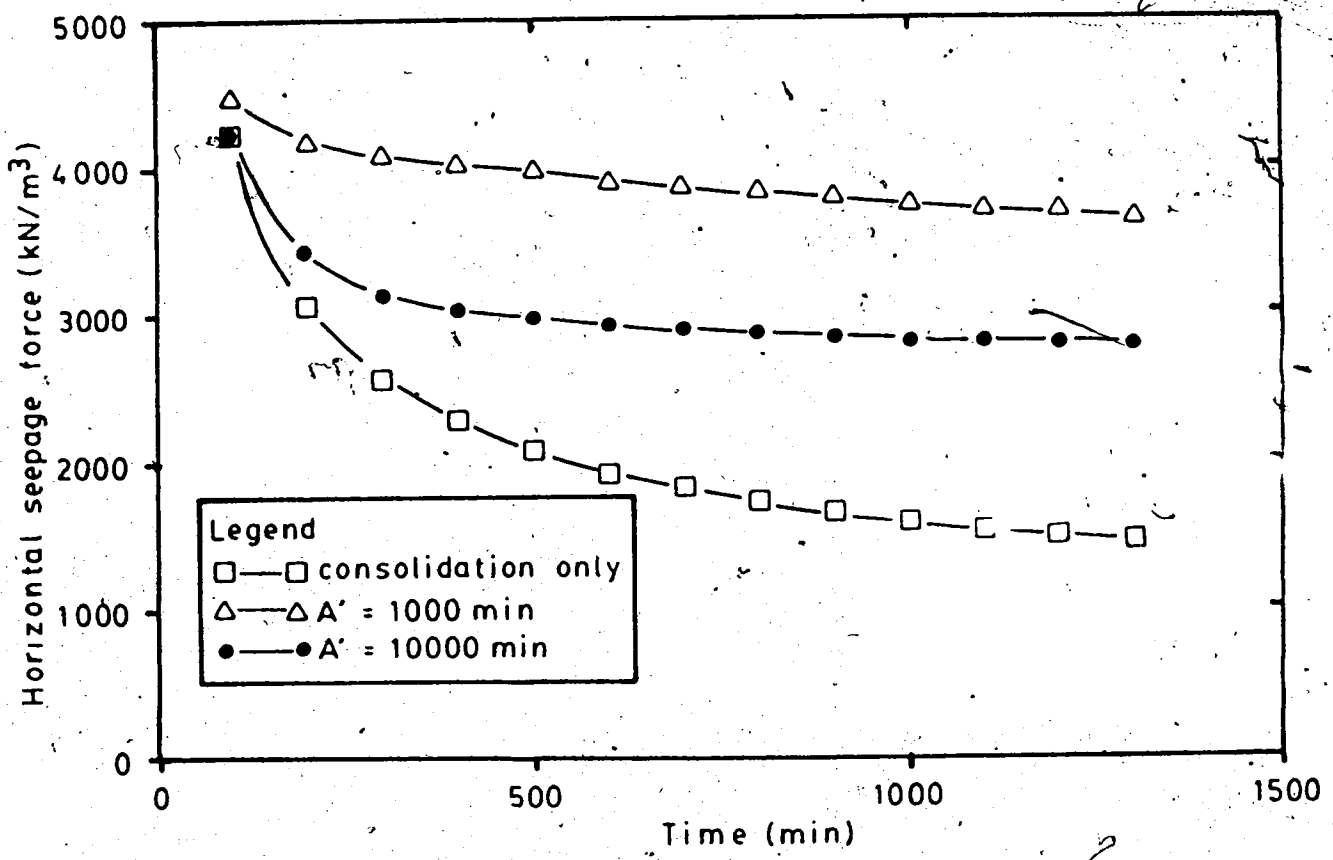

Figure 5.21 Shaft Simulation - Stage A - Average Seepage Forces between the Wall and a Point 0.33 m from the Shaft Wall (Element 5 - Sampling Point 3)

that, immediately after modification of the boundary stresses and pore pressures, the seepage forces were equally high for the three cases analysed. As time progressed, these values decreased. This decrease was faster and more pronounced for the gas free case. The two curves associated with A' values equal to 10,000 and 1000 minutes indicated that, as time progressed, the process of gas evolution resulted in higher seepage forces. Thus, one can conclude that the evolution of gases has a de-stabilizing effect on the shaft walls. The two curves also indicate that the assumption that gas evolution occurs at faster rates (A'=1000 min.) results in higher seepage forces. Therefore, the assumption that gas evolution occurs instantaneously, an assumption present in most of the existing simulation tools available, as discussed in Section 3.2.2, tends to overestimate the de-stabilizing effects of the phenomenon. This might be a reasonable assumption if conservative predictions are to be obtained (i.e., for design purposes). However, if the simulation requires the realistic prediction of the soil mass response, (for example, for the purpose of interpreting field monitoring data), the transient evolution of gases must be considered in the simulation.

Figure 5.22 presents the progress of the region where the total radial stress is lower than the pore pressure. Therefore, in this region, the soil is under traction in the radial direction. Since this condition is not possible in the oil sands mass, in this region cracks develop parallel

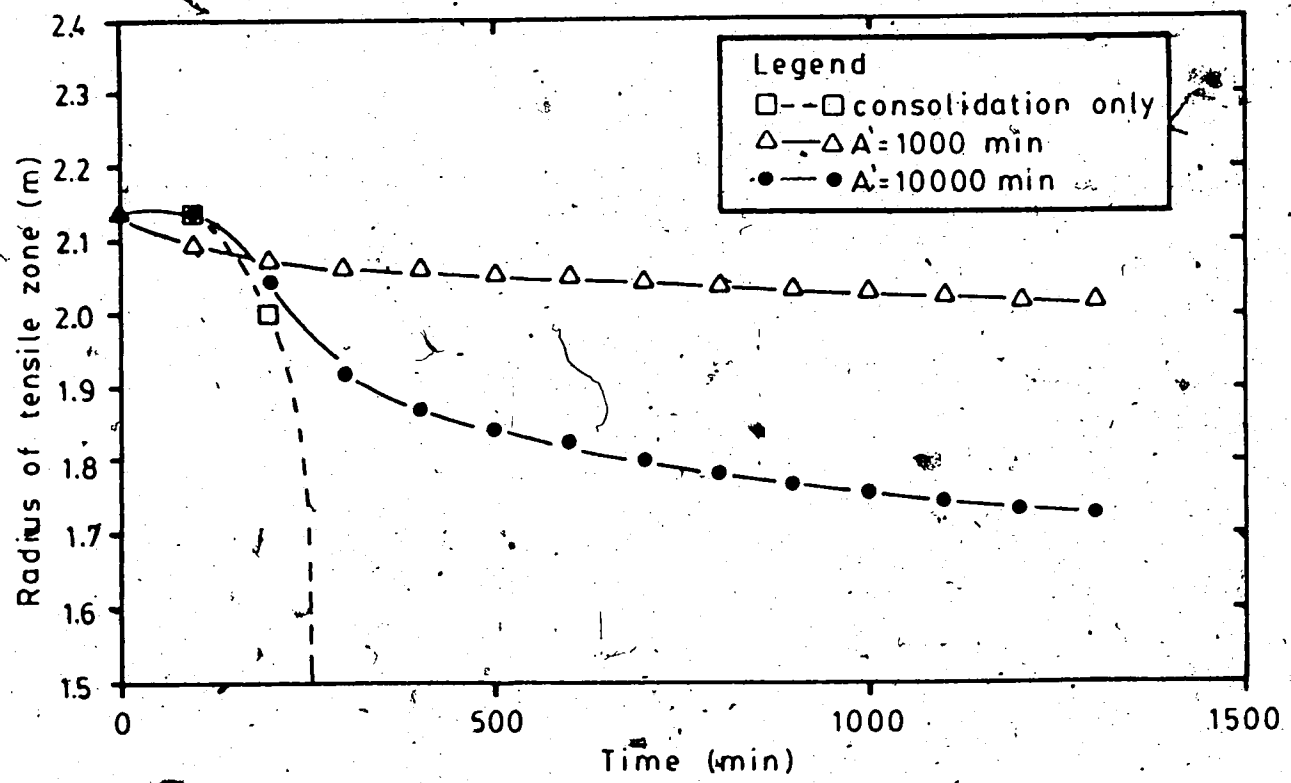

Figure 5.22 Shaft Simulation - Stage A - Progress of Tensile Zone with Time

to the principal stress direction.

The actual size of the zone where this phenomenon takes place cannot be predicted by CONGAS, because the program does not consider the stress redistribution associated with the formation of cracks. Consequently, the size, or the radius of the tensile zone predicted by CONGAS must be interpreted as an index for the potential of the development of crack around the opening. Hoek and Brown, 1980:223, performed a similar analysis in studying the effects of the shape of cavities on the development of zones where the stress state around the opening, obtained from linear elastic analysis, violated the failure criteria. These zones were referred to as zones of potential failure.

Figure 5.22 indicates that the initial radius of the tensile zone is approximately 2.14 metres, i.e., 0.64 metres within the shaft walls. For the gas-free case, this radius rapidly decreases, disappearing 250 minutes after the modification of the boundary stresses. In the case where the evolution of gases occur at a slow rate (A'=10000 min.), the radius decreases at a slower rate but does not disappear. In the case where the evolution of gases occur at a faster rate (A'=1000 min.), the decrease of the radius of the tensile zone is very slow. After 1300 minutes, its value is 2.02 metres, i.e., 0.52 metres within the shaft wall. This value is twice the value obtained after 1300 minutes with A'= 10000 minutes. This fact once again illustrates the de-stabilizing effect of the rate of gas evolution and the

importance of the appropriate consideration of this phenomenon in numerical simulation of oil sands.

Numerical Tests Stage B

The numerical tests, stage B, were performed with the finite element mesh presented in Figure 5.23. The mesh simulates the face of a shaft with walls subjected to no lateral displacement. The bottom and side boundaries of the mesh are located at 3 radii from the face and side walls of the shaft. Ideally, these distances should be larger (more than 10 radii) if a condition of undisturbed stress field is to be maintaind close to the boundaries. However, as already mentioned for stage A, the purpose of the numerical tests presented herein was to compare results of simulations performed with different parameters, and not to simulate the actual behaviour of the soil.

As depicted in Figure 5.23, the mesh was subjected to an isotropic stress state, equivalent to that encountered at the oil sands deposit at the UTF. The nodes at the bottom boundary did not move vertically. The nodes at the walls of the shaft and along the axis of symmetry did not move horizontally. Water flow was not allowed through the boundaries. However, water was allowed to flow within the mesh, whenever hydraulic potential gradients existed.

The initial pore pressures within the mesh were assumed to be hydrostatic, for a depth of approximately 150 metres. This condition is more unfavourable to shaft sinking than the one at UTF, as mentioned earlier in this section.

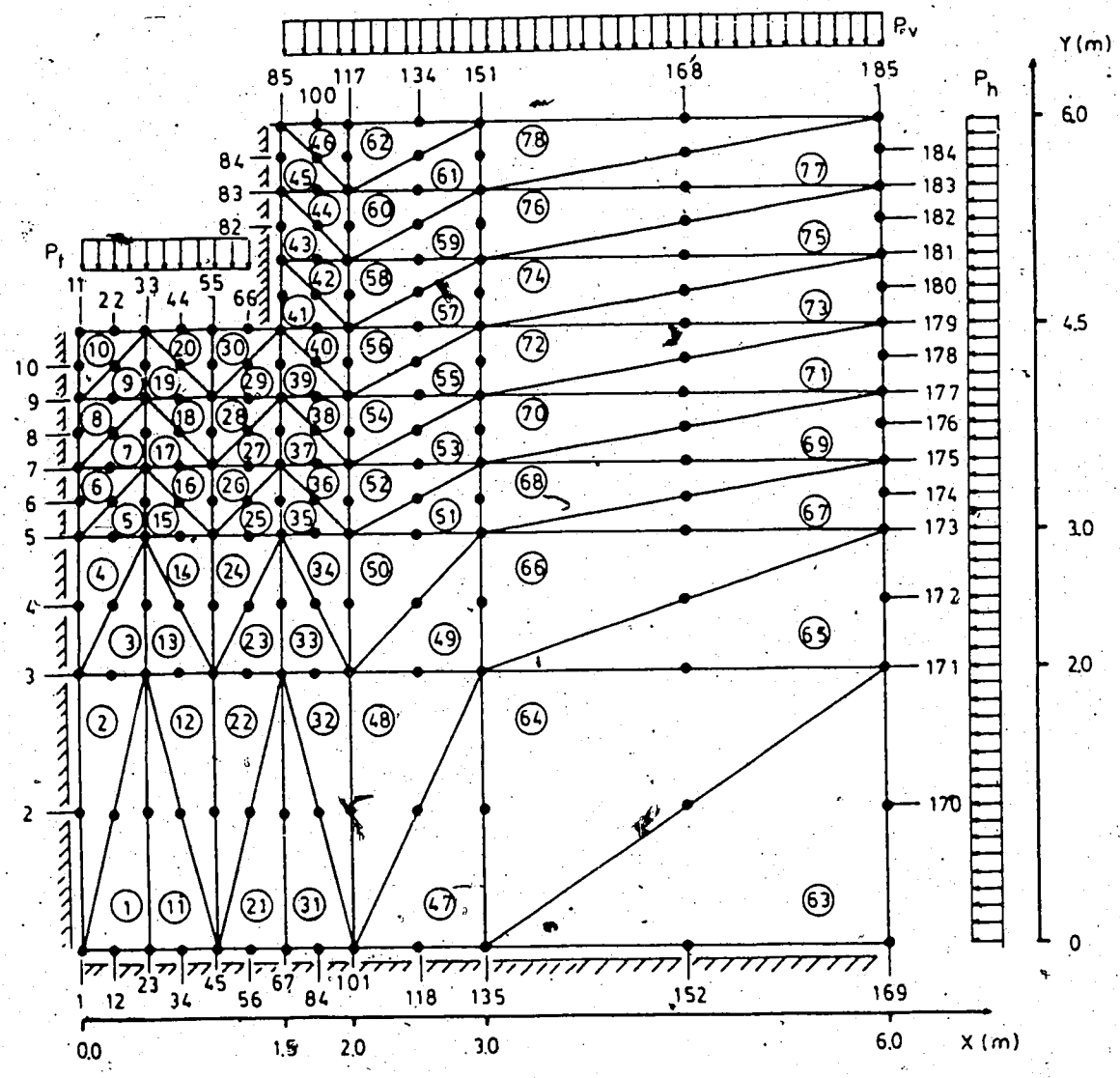

Figure 5.23 Finite Element Mesh - Test18-V18 - Shaft Simulation - Stage B

The simulation of the face advance was performed by imposing a continuous decrease of the boundary stress at the face of the shaft from the initial *in situ* value to 100 kPa. The latter value was equivalent to a height of 7.6 m of drilling fluid assuming it has a unit weight of 13 kN/m³. The decrease of the vertical pressure at the face took place linearly with time over a period of 1400 minutes (approximately 23 hours). This time span was chosen based on the fact that the *in situ* state of stress two diameters (6 metres) ahead of the shaft face was nearly undisturbed, and that the drilling bit advanced at an average of 0.26 m/h, a value similar to that reported by Patterson, at the UTF shafts, as discussed earlier in this section. Time increments between 20 and 100 minutes were used in these analyses. Table 5.10 presents the boundary conditions used for stage B of the numerical tests. All the other variables and parameters used were the same as the ones used for the simulation stage A (Table 5.9). During simulation, the degrees of saturation within the mesh were never below 99%.

The analysis of the test results for stage B was carried out similar to stage A. Herein, the effects of the rate of gas evolution on the behaviour of the shaft construction were studied based on the potential for the formation of cracks in the region below the shaft face. This was done by comparing the values of the total vertical stress with the pore pressures at sampling points located in a vertical line at 10 cm from the shaft axis. Whenever the

INITIAL STRESSES	σ' u	1500 kPA (ISOTROPIC) 1500 kPa
BOUNDARY STRESSES	P_F P_H P_V	3000 TO 100 kPa (LINEAR DECREASE IN 1400 MIN) 3000 kPa 3000 kPa

σ' = EFFECTIVE STRESS
u = INITIAL PORE PRESSURE
P_F = PRESSURE AT SHAFT FACE
P_H = HORIZONTAL BOUNDARY STRESS
P_V = VERTICAL BOUNDARY STRESS

Table 5.10 Shaft Simulation - Stage B - Initial Stresses and Stress Boundary Conditions

vertical effective stress was assumed to be equal to zero, the point under consideration was assumed to belong to the "tensile zone". Figure 5.24 depicts the development of the tensile zone with time and with the decrease of the vertical pressure at the shaft face. From this figure, it is possible to conclude that a minimum pressure of 550 kPa at the shaft face is required for the gas-free case, to ensure that horizontal cracking does not occur below the shaft face. This value increases to 1150 kPa and 1400 kPa, for the cases with A'=10,000 and 1000 minutes, respectively. Therefore, if the development of tensile cracks are to be avoided at the face of the shaft, a minimum height of 42 metres of drilling fluid should be maintained within the shaft ($\gamma_{drilling\ fluid}$ = 13 kN/m^3) for the gas free case, whereas the value increases to 88.5 and 107 metres for A'=10 000 and 1000 respectively.

Figure 5.25 schematically presents the tensile zones at t=1400 minutes, if a height of 7.6 metres of drilling fluid is maintained at the face throughout drilling, for the three different cases studied here. The presence of the tensile zone ahead of the shaft face does not necessarily represent problems for shaft sinking since the region is continously removed during drilling. However, if the lateral walls of the shaft were allowed to move horizontally, the tensile zone would propagate outside the limits of the excavated region and might result in stability problems at the shaft walls before the concrete lining is installed.

Conclusions about Simulation of Shaft Sinking with the CSL

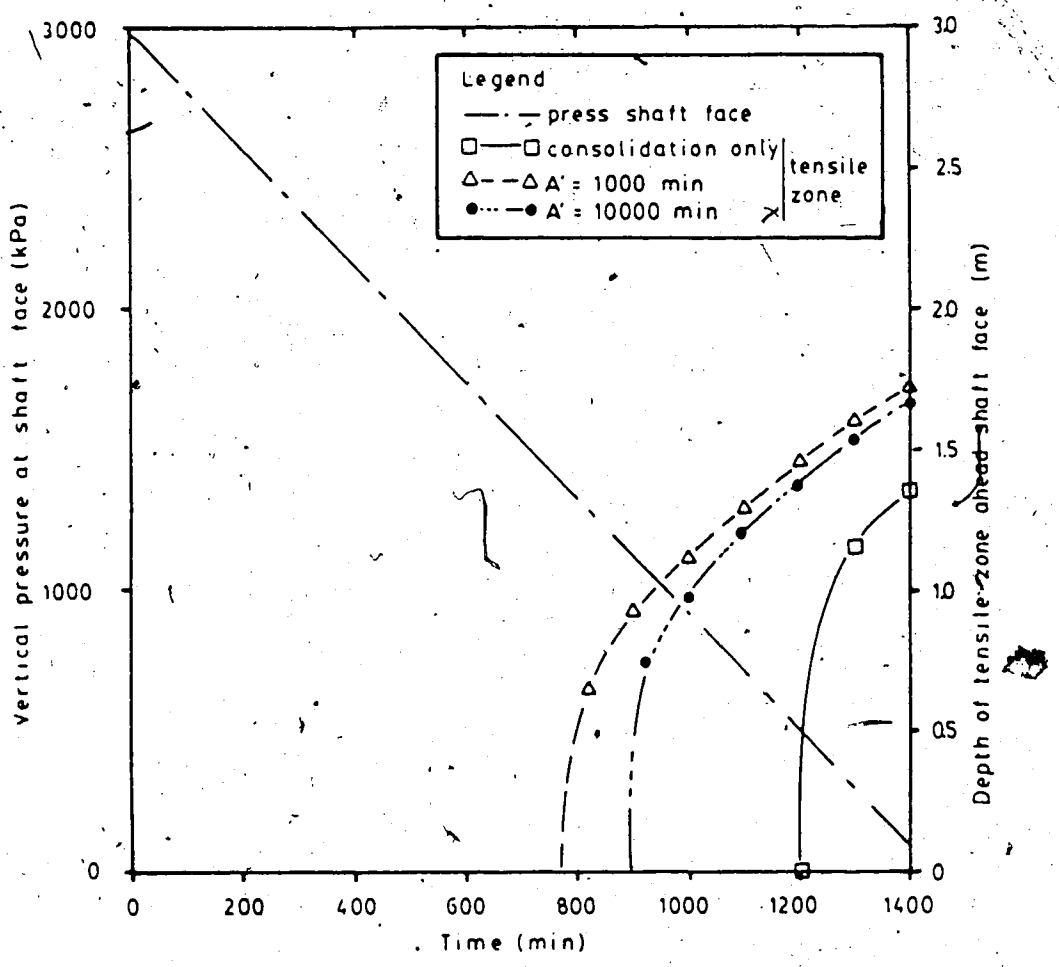

Figure 5.24 Development of Depth of the Tensile Zone along a Vertical Line 10 cm from the Shaft Axis - Stage B

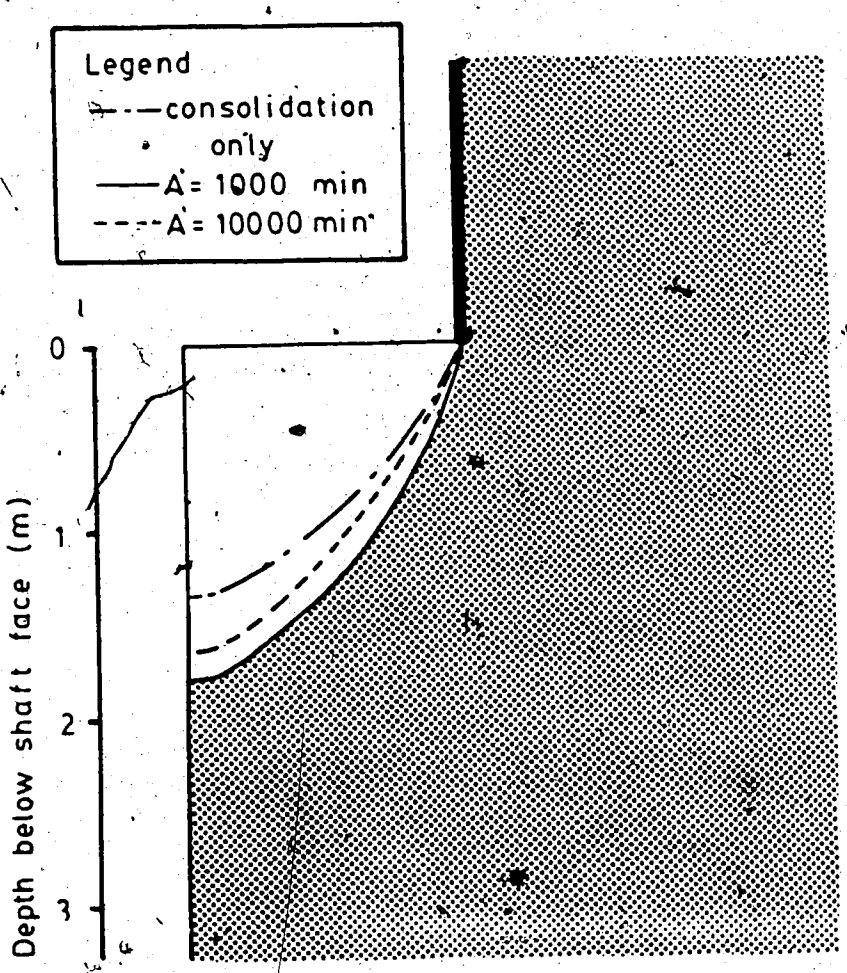

Figure 5.25 Tensile Zone at t=1400 minutes - Stage B

System

The simplified simulation presented above indicated that the use of the CSL system for shaft sinking in oil sands, despite having the advantages discussed earlier in this section, presents the following potential problems:

1. In order to avoid the development of tensile zones ahead of the shaft face, drilling fluid pressures ranging from 550 to 1400 kPa might be necessary. This is equivalent to heights of the drilling fluid from 42 to 107 metres. These heights are excessively high, considering the depth of the shaft considered (≈140 to 160 metres).
2. High seepage forces above the drilling fluid, associated with tensile zones that can advance up to 0.6 metres from the shaft walls, indicate that this region might experience stability problems, before the concrete lining is installed.

Therefore, for the conditions considered here, the use of the CSL system in gas rich oil sands might be of doubtful efficiency. However, this conclusion must not be extrapolated to other situations, which might be favourable for the implementation of this technique.

Similar numerical tests could be performed with other shaft sinking techniques, as presented by Branco, 1985, to search for possible alternatives to the method used for the construction of the UTF shafts. This however, goes beyond the scope of this thesis.

5.5 Summary and Conclusions

In this chapter, the capability of CONGAS to simulate real situations of stress relief problems in oil sands was verified. This was possible with the laboratory data produced in Chapter 4. Chapter 4 presented results of laboratory tests performed on hollow cylinder samples. These tests were used here as case studies, or model tests, to be compared with the hollow cylinder tests performed numerically with CONGAS. The fundamental soil and fluid properties, required for the simulation of the tests, were obtained from tests belonging to group A, presented in Chapter 4.

Hollow cylinder tests - Type I consisted of the undrained unloading of the samples. This stress path favoured the study of the limitation of the gas evolution model used in CONGAS, since the soil skeleton material model, non-linear elastic, should accurately represent the actual observed response of the hollow cylinder samples. This occurred because, during these tests, the samples were subjected to negligible shear stresses, which might induce volume changes due to shear. These volume changes cannot be modelled by elastic formulations.

The numerical analyses indicated that the numerical tests that best reproduced the laboratory data were run with material stress-strain parameters compatible with those obtained from drained triaxial tests. The initial degrees of saturation that best reproduced the initial immediate

response to unloading were 99.3% and 99.5% for Samples 26-1 and 27-2B, respectively.

A value of 0.05 for the solubility coefficient, H, and scaling parameter, A', equal to 10000 minutes resulted in the best reproduction of the laboratory test with Sample 26-1. This solubility coefficient is considered low when compared to those measured in the mercury triaxial tests described in Chapter 4. A high degree of disturbance of the sample and theoretical bubble point pressures lower than the pore pressures within the sample during testing were thought to be responsible for the low solubility coefficients. The high value of the scaling factor, A', was compatible with the high degree of saturation predicted by the numerical test.

Sample 27-2B was subjected to one additional unloading step and, consequently, to lower pore pressures. The numerical tests which best reproduced the laboratory data indicated that during the initial unloading steps, at high degrees of saturation, the solubility coefficient was between 0.02 and 0.05, and the scaling factor, A', equal to 10,000 minutes.

During the last two steps of the test, as the degree of saturation decreased from values higher than 99% to 97.8%, the numerical tests which best reproduced the laboratory data were associated with values of the solubility coefficient between 0.10 and 0.15 and scaling factors, A', that varied from 10,000 minutes, at the beginning of Step C,

to 1000 minutes at the end of Step D. These values were compatible with the values observed in the mercury triaxial tests, Chapter 4.

The numerical tests above indicated that the gas evolution model implemented in CONGAS models accurately the undrained transient response of oil sands.

In hollow cylinder tests - Type II, the samples were submitted to an instantaneous decrease of the top and bottom boundary pore pressures and submitted to shear stresses, induced by the decrease of the internal bore pressure. The numerical results indicated that values of coefficients of permeability to water between 10^{-10} and 10^{-11} m/s resulted in better predictions of the observed laboratory time-dependent response. These values are considered low for the degree of disturbance associated with the samples. The formation of gas bubbles close to the drainage boundary probably decreased the permeability coefficient to water during the laboratory tests.

One numerical test, performed with the assumption that the coefficient of permeability to water varied according to Chang and Duncan's, 1983, equation (Section 3.3.3), indicated that the authors' equation predicted excessive decreases of the coefficient of permeability to water with the formation of bubbles and with the decrease of the void ratios. It was concluded that the proposed equation was not suitable for the simulation developed herein.

The numerical tests consistently underpredicted the volumetric strains observed in the laboratory by values that ranged between 0.1 to 0.4%. The analysis of the results of the "J1" drained triaxial tests indicated that, for the average shear strains encountered within the samples, the samples should indeed present volumetric contraction of approximately 0.2%. Since the non-linear elastic material model does not predict volume changes associated with shear stresses, the difference between measured and predicted values was attributed to the limitations of the material model chosen.

The contraction due to shear stresses was also thought to be responsible for the slightly slower consolidation process observed in the laboratory samples, when compared to the numerical tests. The contraction of pores tends to increase the pore pressures, a behaviour which opposes the consolidation or pore pressure dissipation, in the samples.

Type II tests indicated that more tests are required before the material model used in CONGAS can be used with confidence for simulation purposes. The water flow within the sample and how it is affected by the formation of bubbles is an area that significantly affects the pore pressure dissipation process and requires further research.

In the last part of this chapter, CONGAS was used to simulate the construction of a shaft in oil sands in which the blind drilling technique, associated with the continuous shaft lining system (CSL), was used. The purpose of this

analysis was to illustrate how CONGAS can be used to study alternative construction techniques for shaft sinking and to show the importance of the proper consideration of the time-dependent evolution of gases on the simulation of oil sands.

The response of oil sands to shaft sinking was studied in two separate stages. In the first stage, the stress relief at the walls of the shaft was simulated in a mesh subjected to a state of plane stress. In the second stage, the face of the shaft was studied separately in an axisymmetric mesh. The study was performed assuming that the sections of the shaft under consideration were located at depths between 140 and 160 metres, similar to the depth at which oil sands is encountered in the UTF shaft. As opposed to the UTF shaft, the numerical simulations assumed the pore pressures to be initially hydrostatic, with the water level close to the ground surface. This represented a condition unfavourable to shaft sinking. The numerical results indicated that the region located above the drilling fluid and below the concrete lining, is subjected to seepage forces acting to de-stabilize of the unsupported shaft walls. The value of the seepage forces, for a given elapsed time after the radial stress relief started, was significantly higher for the condition in which the process of gas evolution was assumed to occur at a fast rate ($A'=1000$ minutes). The slower the rate of gas evolution the smaller the seepage forces. These conclusions indicate that

the assumption that gas evolution occurs instantaneously is not reasonable for the prediction discussed herein.

The simulation of the face of the shaft indicated that the vertical stress relief can result in the formation of a tensile zone ahead of the face. The formation of this zone can be inhibited if, at the depth considered, minimum drilling fluid pressures of 1400 kPa and 1150 kPa are maintained at the face, for the cases when gas evolution occurs relatively fast (A'=1000 minutes) and relatively slow (A'=10,000 minutes), respectively. These pressures are equivalent to heights of drilling fluid equal to 107.0 and 88.5 metres which are excessively high, considering the depth of the shaft being considered. Based on the numerical test results, it was finally concluded that, for the conditions considered herein, the use of the CSL system in gas rich oil sands might be of doubtful efficiency.

6. SUMMARY AND CONCLUSIONS

6.1 General

It is the intent of this chapter to summarize the developmen and the major findings of the research herein.

The main purpose of the research was to develop a model that appropriately simulates the transient processes that take place in gassy soils when subjected to isothermal changes in boundary conditions. The need for the development of this model was justified by the increasing number of underground excavations in gassy soils predicted in the near future, associated with the exploration of new hydrocarbon resources, and the lack of models that adequately simulate the transient phenomenon of gas evolution.

This model should aid those engineering projects on gassy soils in many aspects. These include enabling the choice of proper sampling techniques, guiding the design and construction of geotechnical structures, supporting the analyses of field monitoring programs and increasing the understanding of the mechanics of gassy fluids.

The development of the proposed model consisted of the following steps.

1. Identification and study of the processes that control the time-dependent response of gassy soils and development of the governing equations for the problem.
2. Development of a finite element program for the solution of the governing equations, for boundary conditions

usually encountered in gassy soils related works.

3. Verification of the finite element program capability to appropriately simulate the theoretical and the experimental response of oil sands.

These three items constituted the working frame for the research herein and are summarized in the following sections.

6.2 Mechanics of Gassy Fluids

The identification of the processes that govern the transient response of gassy soils consisted of a review of the work previously developed by other researchers. This review indicated that consolidation and the migration of gas molecules between the gas and the liquid phases are the main phenomena involved. The phenomenon of consolidation has been studied by several geotechnical engineers and the associated governing equations are presently well understood. On the other hand, not much attention has been paid to the subject of gas evolution as applied to soil mechanics. This fact resulted in the development of the study on the behaviour of gassy fluids. This study, summarized in Chapter 2, was based on a review of the basic thermodynamic principles that control the behaviour of gassy fluids. The fluid compressibility was used as a comparative basis for the analysis of the validity of simplifying assumptions on the actual response of gassy fluids.

The study revealed that the ideal gas and solution laws are applicable to marine sediments and oil sands, gas saturated with low contents of carbon dioxide, for fluid pressures up to 8 MPa. An exception to this assertion is the evaluation of the combined solubility coefficient (H_{comb}) from individual gas and liquid solubility coefficients. Laboratory experiments have shown that errors of up to 20% can occur in the theoretical evaluation of H_{comb} for methane rich solutions.

The study also revealed that when the surface tensions between the gas and liquid phases are neglected, the errors in the evaluation of the fluid compressibility are small, provided that the carbon dioxide content is small and/or the pore pressures are high. Attention was also paid to the problem of stability of bubbles in the pores of soils. Based on the literature review, it was concluded that extremely small bubbles can exist in a stable condition in the soil pores. This conclusion does not support Fredlund's views, as presented in his thesis in 1973.

The final stage of the study revealed that a proper evaluation of the time-dependent compressibility of gassy fluids in the pores of soils, based on fundamental thermodynamic variables, is a difficult task due to the complexities in assessing the involved boundary conditions. It was shown that more general descriptive, or macroscopic models, are valuable to the solution of the problems dealt with in this thesis, despite their inherent limitations.

The macroscopic model developed by Sobkowicz, 1982, was considered appropriate to simulate the time-dependent gas evolution in soil pores.

The study of the mechanics of gassy fluids allowed a better understanding of the behaviour of gassy soils and, consequently, led to the recognition of the limitations of the assumptions made for the development of the governing equations that describe their behaviour.

6.3 Development of the Finite Element Program CONGAS (CONsolidation and GAS Evolution)

In Chapter 3, a review of analytical and numerical models that aim at simulating the response of gassy soils was presented. This review indicated that all finite element programs that consider the time-dependent response of gassy soils, do not simulate adequately the transient evolution of gases. In these models, the transient pore pressure changes occur solely due to consolidation, whereas the gas evolution is assumed to take place instantaneously, as a function of the pore pressure changes, and not as a function of time.

As a result of this review, a numerical model was developed. The development consisted of the derivation of the governing equations and their solution by the finite element technique. A computer program CONGAS was written. In this program, the mechanical response of the soil skeleton is modelled through a linear elastic or by three different non-linear elastic hyperbolic models. The pore fluid is

assumed to be a two phase system, formed by one liquid and gases. The gases present can be dissolved in the liquid and in the free state. The gas bubbles are assumed to be immobile and the liquid phase is assumed to flow according to Darcy's law. The formulation allows the liquid phase to be considered compressible and the coefficient of permeability to vary as a function of the void ratio and the degree of saturation.

The program is limited to solving cases where the bubbles are not interconnected. Thus, gas venting is not simulated.

6.4 Verification of the Prediction Capabilities of CONGAS

The verification of the prediction capabilities of CONGAS was performed in two phases.

In the first phase, described in Chapter 3, a series of numerical tests was performed, simulating idealized problems. Closed form or approximate solutions, for most of the problems considered, were available in the literature, a fact that made possible the analysis of the performance of CONGAS. The program accurately simulated the idealized conditions.

In the second phase, the capability of CONGAS to simulate the actually observed response of gassy soils was verified. The major difficulty encountered in this phase was the lack of well documented field or laboratory case studies. This fact led to the development of an extensive

sampling and laboratory program. The aim of this program was to generate a model test that would produce results that could be compared with those produced by CONGAS. The laboratory program also included a series of tests that furnished fundamental soil and fluid parameters, required as input data for the numerical simulation of the model tests.

The highlights of the sampling and laboratory programs and of the results of the numerical simulation of the model tests are summarized as follows,

Sampling Program

Athabasca oil sands were chosen as the natural gassy sediment to be tested. Sample retrieval was carried out at the Syncrude mining site with two types of samplers, a Pitcher (I.D.=7.3 cm) and a Christensen (I.D.=14.9 cm) barrel. Most of the samples were of poor quality for stress-strain geotechnical testing, exhibiting excessive volumetric expansion. The high gas content in most samples was responsible, to a large degree, for most of the sample disturbance during sampling and retrieval operations. High gas content was a desirable characteristic of the samples.

The laboratory testing program was designed in such a way that the small diameter samples were used for testing of the fundamental properties and the large diameter samples were used for model testing in the hollow cylinder cell. It was desirable, therefore, that both the large and small samples had similar characteristics, irrespective of their degree of disturbance after sampling. Therefore, the high

degree of disturbance observed was not considered a problem in this research program.

Laboratory Testing Program

A series of tests was performed in order to obtain geotechnical and thermodynamic properties of the oil sands samples. The following types of tests were performed.

- physical properties tests
- skeleton stress-strain properties test
- pore fluid undrained properties test

The physical and skeleton stress-strain properties tests were performed using standard equipment and following standard procedures. The pore fluid undrained properties test, however, required the development of new equipment and testing procedures. The test results, generated by the latter type of tests, allowed the detailed analysis of the time-independent and time-dependent response of the oil sands pore fluid. The test data revealed the large variability of the bubble point pressures with depth. Most of the tests, however, yielded bubble point pressures approximately equal to the original hydrostatic pressures before excavations at the sampling site started. A considerable scatter of the solubility coefficients was also observed.

The time-dependent response of the gas evolution process was found to be reasonably well described by the macroscopic model suggested by Sobkowicz, 1982.

Hollow cylinder tests were used as model tests. Two types of tests were performed.

- Test Type I - Undrained Isotropic Unloading
- Test Type II - Drained unloading of the internal bore.

These tests enabled the limitations of the numerical simulation of CONGAS to be identified.

Numerical Simulation of the Hollow Cylinder Tests

The isotropic stress path imposed on type I tests, allowed a separate assessment of the capacity of the gas evolution model to predict the time-dependent response of the hollow cylinder samples. It was concluded that CONGAS very closely reproduced the observed sample response to modifications in the stress boundary conditions.

The simulation of type II tests revealed that volumetric contractions due to shear might have played an important role in the displacements and pore pressure generation and dissipation observed in the hollow cylinder samples. The non-linear elastic material models, implemented in CONGAS, do not simulate volume changes induced by shear stress changes. This limited the prediction capabilities to cases where volume changes due to shear do not play a major role in the overall behaviour of the soil mass.

The structure of CONGAS facilitates the future implementation of material models that take into account the plastic and dilation/contraction strains observed in oil sands. The simulation of type II tests also revealed that the growth of bubbles in the pore fluids was most likely

responsible for the decrease in the water permeability, which might have played a major role in the time-dependent response of the hollow cylinder samples.

6.5 Simulation of Shaft Sinking in Oil Sands

A simulation of the construction of a shaft in oil sands, in which a novel technique of concrete lining placement is used, was carried out. The simulation was useful in illustrating how CONGAS can be used effectively to study alternative construction techniques for shaft sinking. Through the shaft simulation, it was shown that the assumption adopted by all the currently available finite element programs for simulation of gassy soils, namely that gas evolution occurs instantaneously, is not reasonable for the study of underground excavations. The rate of gas evolution proved to have a significant impact on the behaviour of the shaft excavation. Faster rates of gas evolution resulted in higher de-stabilizing seepage forces at the shaft walls and larger zones subjected to tensile stresses around the shaft.

6.6 Suggestions for Future Research

With regard to laboratory testing, the following topics should be investigated in order to allow further understanding of the time-dependent response of oil sands:

1. The time-dependent gas evolution process should be independently measured in the bitumen and in the

water phase. This procedure would enable the extrapolation of results from one site, with specific gas/bitumen/water contents to sites with different physical properties.

2. A method of collecting gas samples from the oil sands samples that minimizes the air contamination of the sample should be designed.
3. Permeability tests should be performed on good quality samples, at different degrees of saturation. Apparently, the formation of bubbles has a major effect on the coefficient of permeability and consequently on the pore pressure dissipation process in gassy oils.
4. The measurement of the time-dependent gas evolution at lower temperatures might generate valuable information for the future simulation of colder zones of the oil sands deposits.
5. The measurement of the lateral displacement of the external walls of the hollow cylinder tests through the measurement of the variation of the volume of cell fluid was sensitive to temperature fluctuations. Excessively high errors were associated with this technique. For future tests, it would be preferable to use other techniques for measurements of the lateral displacement of the sample.

With regard to the finite element program CONGAS, the following items should be implemented in order to improve its performance and prediction capabilities.

1. The choice of the DAMP constant should be adjusted automatically within the program, in order to avoid the divergence of solutions.
2. Create an option for bubble point pressures lower than the initial *in situ* pore pressures.
3. Implementation of a material model that simulates plastic strains and volumetric strains due to shear.
4. Implementation of a more efficient solution technique for the finite element equations.

REFERENCES

Agar, J.G., 1984. Geotechnical behaviour of oil sands at elevated temperatures and pressures. PhD thesis, Department of Civil Engineering, The University of Alberta, 906 pp.

Agar, J.G., Morgenstern, N.R. and Scott, J.D., 1988. Fluid transport properties of Athabasca oil sand at elevated temperatures and confining stresses. Unpublished.

Amix, J.W.; Bass, D.M. and Whiting, R.L., 1960. Petroleum reservoir engineering - Physical properties. McGraw-Hill Book Company, 610 pp.

Atkinson, J.H. and Evans, J.S., 1985. The measurement of soil stiffness in the triaxial apparatus: Discussion. Geotechnique, September 1985, Vol. 35, No.3, pp 378-382.

Baguelin, F.; Jezequel, J.F. and Shields, D.H., 1978. The pressuremeter and foundation engineering. Series on Rock and Soil Mechanics, Vol. 2, No. 4, Trans Tech Publications.

Barron, R.A., 1948. Consolidation of fine-grained soils by drain wells. ASCE, Transactions, 1948, Paper 2346, pp. 718-754.

Bathe, K.J., 1982. Finite element procedures in engineering analysis. Prentice-Hall, 735 pp.

Behnke, A.R., Thomson, R.M. and Shaw, L.A., 1935. The rate of elimination of dissolved nitrogen in man in relation to the fat and water contents of the body. American Journal of Physiology, No. 114, pp. 137-146.

Behnke, A.R., 1951. Decompression sickness following exposure to high pressures. Decompression Sickness-Caisson Sickness, Diver's and Flier's Bends and Related Syndromes. W.B. Sounders Company. pp. 53-89.

Biot, M.A., 1941. General theory of three dimensional consolidation. Journal of Applied Physics, Volume 12, No. 2.

Biot, M.A., 1955. Theory of elasticity and consolidation for a porous anisotropic solid. Journal of Applied Physics, Volume 26, No. 2.

Bishop, A.W. 1957. Some factors controlling the pore pressures set up during the construction of earth pressure dams. Proceedings of the Fourth International Conference on Soil Mechanics and Foundation Engineering,

London, Vol.II, pp. 294-300.

Bishop, A.W. and Donald, I.B., 1961. The experimental study of partly saturated soils in the triaxial apparatus. Proceedings of the Fifth International Conference on Soil Mechanics and Foundation Engineering, Paris, Vol.I, 1961, pp. 13-22.

Bishop, A.W. and Henkel, D.J., 1978. The measurement of soil properties in the triaxial test. Edward Arnold Lts, Second edition, 1978.

Black, D.K. and Lee, K.L., 1973. Saturating laboratory samples by back pressure. Journal of the Soil Mechanics and Foundation Division, ASCE, Vol. 99, No. SM1, pp. 75-93.

Bolton, M.D., 1986. The strength and dilatancy of sands. Geotechnique 36, No. 1, pp. 65-78.

Booker, J.R. and Small, J.C., 1975. An investigation of the stability of numerical solutions of Biot's equation of consolidation. International Journal for Solids and Structures. Vol. 11, pp. 907-917.

Branco, P., 1985. Construction methods for shaft sinking in rock masses (in portuguese). Revista de Engenharia FAAP, Agosto 1985, Ano III, No. 7.

Br[illegible]o, P., 1988. CONGAS - A finite element program for simulation of coupled consolidation and gas evolution. Department of Civil Engineering, The University of Alberta, Internal Report.

Brescia, F., Arents, J., Meislich, H. and Turk, A., 1970. Fundamentals of chemisty - A modern Introduction. Academic Press, 796 pages.

Byrne, P.M. and Eldridge, T.L., 1982. A three parameter dilatant-elastic stress-strain model for sand. International Symposium on Numerical Models in Geomechanics, Zurich, 1982.

Byrne, P.M. and Grigg, R., 1980. OILSTRESS - A computer program for analysis of stresses and deformations in oil sands. Soil Mechanics Series, University of British Columbia, Vancouver, B.C.

Byrne, P.M. and Janzen, W.F., 1984. INCOIL - A computer program for nonlinear analysis of stresses and deformations in oil sand masses. A Report Submitted to the Oil Sands Technology and Research Authority, Department of Civil Engineering, University of British Columbia, Vancouver, 104 pp.

Byrne, P.M., Janzen, W.F. and Mittal, H.K., 1982. Finite element analysis of excavation in oil sands. 33rd Annual Technical Meeting, Canadian Institute of Mining and Metallurgy. Calgary, pp. 93-98.

Byrne, P.M., Smith, B.L., Grigg, R.F. and Stewart, W.P., 1980. A computer model for stress-strain and deformation analysis of oilsands. Proceedings of Applied Oilsands Geoscience Conference, University of Alberta, Edmonton, 38 pages.

Byrne, P.M. and Vaziri, H., 1985. Stress, deformation and flow analysis in oil sand masses. Soil Mechanics, Series No. 88. Department of Civil Engineering, University of British Columbia, Vancouver, Canada.

Carrigy, M.A. and Kramers, J.W., 1974. Geology of the Alberta oil sands. Athabasca Oil Sands Conference Proceedings, Engineering Institute of Canada, Western Region, pp. 13-24.

Chaney, R.C., Kenneth, R.D. and Fang, F.Y., 1985. Toward a unified approach to soil property characterization: in situ versus laboratory. Strength Testing of Marine Sediments: Laboratory and In Situ Measurements, ASTM, STP 883, pp. 425-439.

Chang, C.S. and Duncan, J.M., 1983. Consolidation analysis for partly saturated clay by using an elastic-plastic effective stress-strain model. International Journal for Numerical And Analytical Methods in Geomechanics, Vol. 7, pp. 35-55.

Chen, W. and Saleeb, A.F., 1982. Constitutive equations for engineering materials, Vol.I, Elasticity and Modeling. John Wiley and Sons, 1982.

Christian, J.T. and Boehmer, J.W., 1970. Plane strain consolidation by finite elements. ASCE - Journal of the Soil Mechanics and Foundation Division, SM4, pp. 1435-1457.

Christian, J.T. and Desai, C.S., 1977. Constitutive laws for geologic media. Numerical Methods in Geotechnical Egineering. Editors: Desai, C.S. and Christian, J.T., Chapter 2, pp. 65-115.

Cividini, A., 1981. An alternative finite element approach for soil consolidation. Numerical Methods for Coupled Problems - Proceedings of the International Conference, University College, Swansea, pp. 688-698.

Costa Filho, L.M., 1985. Measurement of axial strains in triaxial test on London clay. Geotechnical Testing

Jounal, GTJODJ, Vol. 8, No. 1, March 1985, pp. 3-13.

Cowper, G.R., 1973. Gaussian quadrature formulas for triangles. International Journal for Numerical Methods in Engineering, Vol. 7, pp. 405-408.

Davies, R. (Editor), 1964. Cavitation in Real Liquids. Proceedings of the Symposium on Cavitation in Real Liquids, General Motors Research Laboratories, Warren, Michigan, 1962, 189 pp.

Davies, J.T. and Rideal, E.K., 1961. Interfacial phenomena. Academic Press.

Denness, B. (Editor), 1983. Seabed Mechanics. Proceedings of Symposium, University of Newcastle upon Tyne, 281 pp.

Desai, C.S. and Johnson, L.D., 1973. Evaluation of some numerical schemes for consolidation. International Journal for Numerical Methods in Engineering, Vol. 7, pp. 243-254.

Dickin, E.A. and King, G.J.W., 1982. The behavior of hyperbolic stress-strain models in triaxial and plane strain compression. International Symposium on Numerical Models in Goemechanics, Zurich.

Dodson, C.R. and Standing, M.B., 1944. Pressure-volume-temperature and solubility relations for natural gas-water mixtures. Drilling and production practice, American Petroleum Institute.

Domaschuk, L. and Valliappan, P., 1975, Nonlinear settlement analysis by finite element. ASCE Journal of the Geotechnical Division, GT7, pp. 601-614.

Domaschuk, L. and Wade, N.H., 1969. A study of bulk modulus and shear moduli of a sand. Journal of the Soil Mechanics and Foundation Division, ASCE, Vol. 95, No. SM2, Proceedings Paper 6461, pp. 561-581.

Dorsey, N.E., 1940. Properties of ordinary water-substance. American Chemical Society Series, Reinhold Publishing Corporation.

Duncan, J.M., 1980. Hyperbolic stress-strain relationships. Limit equilibrium, plasticity and generalized stress-strain in geotechnical engineering. McGill University, May 28-30, 1980, pp. 245-253 and 443-460.

Duncan, J.M., Byrne, P., Wong, K.S. and Mabry, P., 1980. Strength, stress-strain and bulk modulus parameters for finite element analyses of stresses and movements in soil masses. Report No. UCB/GT/80-01.

Duncan, J.M. and Chang, Y.Y., 1970. Nonlinear analysis if stress and strain in soils. Journal of the Soil Mechanics and Foundation Division, ASCE, Vol. 96, No. SM5, September 1970.

Duncan, J.M., D'Orazio, T.B., Chang, C.S., Wong, K.S. and Namig, L.I., 1981. CON2D: A finite element computer program for analysis of consolidation. Dept.of Civil Engineering, Univerity of California, Berkeley, Report No. UCB/GT/81-01 to U.S. Army Engineers Waterways Experiment Station, Vicksberg, Mississippi, and Nikken-Sekkei, Japan.

Dusseault, M.B., 1977. The geotechnical characteristics of the Athabasca Oil Sands. Ph.D. Thesis, Department of Civil Engineering, University of Alberta, 472 pp.

Dusseault, M.B., 1979. Undrained volume and stress change behaviour of unsaturated very dense sands. Canadian Geotechnical Journal, Vol. 16, No. 4, Nov. 1979, pp. 627-640.

Dusseault, M.B., 1980. Sample disturbance in Athabasca oil sand. Journal of Canadian Petroleum Technology, Vol. 19, No. 2, pp. 85-92.

Dusseault, M.B., 1988. Personal communication.

Dusseault, M.B. and Domselaar, H.R.V., 1982. Unconsolidated sand sampling in Canadian and Venezuelan oil sands. Second International Conference: The Future of Heavy Crude and Tar Sands. Caracas, Venezuela, Chapter 39, pp. 336-348.

Dusseault, M.B. and Morgenstern, N.R., 1978. Shear strength of Athabasca oil sands. Canadian Geotechnical Journal, Vol. 15, pp. 216-238.

Dusseault, M.B., Soderberg, H. and Sterne, K., 1984. Preparation techniques for oil-sand testing. Geotechnical Testing Journal, GTJODJ, Vol. 7, No. 1, pp. 3-9.

Epstein, P.S. and Plesset, M.S., 1950. On the stability of gas bubbles in liquid gas solutions. Journal of Chemical Physics, Vol. 18, No. 11, pp. 1505-1509.

Eisenberg, D. and Kauzmann, W., 1969. The structure and properties of water. Oxford University Press, Ely House, London, W1.

Esrig, M.I. and Kirby, R.C., 1977. Implications of gas content for predicting the stability of submarine slopes. Marine Geotechnology: An International Journal

of Seafloor Science and Engineering, Vol. 2, 1977, pp. 81-100.

Fredlund, D.G., 1973. Volume change behaviour of unsaturated soils. PhD thesis, Department of Civil Engineering, University of Aberta.

Fredlund, D.G., 1976. Density and compressibility characteristics of air-water mixtures. Canadian Geotechnical Journal, Vol. 13, pp. 386-396.

Ferris, E.B., Engel, G.L. and Romand, J., 1951. The clinical nature of high altitude decompression sickness. Decompression Sickness - Caisson Sickness, Diver's and Flier's Bends and Related Syndromes. W.B. Saunders Company, pp. 4-52.

Gerrard, W., 1976. Solubility of gases and liquids; A. graphic approach - data - causes - prediction. Plenum Press, 275 pp.

Gerrard, W., 1980. Gas solubilities, widespread applications. Pergamon Press, 497 pp.

Ghaboussi, J. and Kim, K.J., 1982. Analysis of saturated and partially saturated soils. International Symposium on Numerical Models in Geomechanics, Zurich, Switzerland, pp. 377-390.

Ghaboussi, J. and Wilson, E.L., 1972. Variational formulation of dynamics of fluid-saturated porous elastic solids. Journal of the Engineering Mechanics Division - Proceedings of the ASCE. 98-EM4.

Ghaboussi, J. and Wilson, E.L., 1973. Flow of compressible fluid in porous elastic media. International Journal for Numerical Methods in Engineering. Vol. 5, pp. 419-442.

Griffin, G.D., 1986. The heave and settlement of foundations on oil sands: three case histories. Master of Engineering Report. Department of Civil Engineering, University of Alberta, Edmonton, Canada. 121 pp.

Hardin, B.O. and Black, W.L., 1968. Vibration modulus of normally consolidated clay. Journal of the Soil Mechanics and Foundation Division, ASCE, SM2, pp. 353-369.

Hardy, R.M. and Hemstock, R.A., 1963. Shearing strength characteristics of Athabasca oil sands. Karl A. Clark Volume, Edited by M.A. Carrigy, Information Series No. 45. Research Council of Alberta, Edmonton, pp. 109-122.

Harris, M.C. and Smith, L.B., 1979. Computer model for

stress-strain analysis of oilsand - (the N.E.A.T. program). Submitted to Canada Department of Energy, Mines and Resources.

Harris, M.C. and Sobkowicz, J.C., 1977. Engineering behavior of oil sand. The Oil Sands of Canada - Venezuela - 1977, The Canadian Institute of Mining and Mettalurgy. pp. 271-283.

Harvey, E.N., 1951. Physical factors in bubble formation. Decompression Sickness - Caisson Sickness, Diver's and Flier's Bends and Related Syndromes, W.B. Saunders Company, pp. 90-114.

Haston, J.A., 1985. Advances in petroleum recovery and upgrading technology, A.O.S.T.R.A., June 6-7, 1985, Session 1.

Hilf, J.W., 1948. Estimating construction pore pressures in rolled earth dams. Proceedings of the Second International Conference on Soil Mechanics and Foundation Engineering, Rotterdam, Vol. 3, pp. 234-240.

Hiroyasu, O. and Kamemura, K., 1985. An application of coupled stress flow analysis to the field problem. Proceedings of the Fifth International Conference on Numerical Methods in Geomechanics, Nagoya, pp. 597-604.

Hoek, E. and Brown, E.T., 1980. Undergroun excavations in rock. The Institution of Mining and Metallurgy, London.

Hughes, J.M.O.; Wroth, C.P. and Windle, D., 1977. Pressuremeter tests in sand. Geotechnique, Vol. 27, No. 4, Dec. 1977, pp. 455-477.

Hulbert, M.H. and Bennett, R.H., 1982. Anomalous pore pressures in Mississippi delta sediments: gas and electrochemical effects. Marine Geotechnology - An International Journal of SeaFloor Science and Engineering, Vol. 5, No. 1, pp. 51-62.

Hunt, R.E., 1984. Geotechnical Engineering Investigation Manual. McGraw-Hill Book Company, 983 pp.

Hwang, C.T., 1970. Plane strain consolidation program by finite element method. Department of Civil Engineering, University of Alberta, Internal Report, Sept. 1970.

Hwang, C.T., Morgenstern, N.R. and Murray, D.W., 1971. On solution of plane strain consolidation problems by finite element methods. Canadian Geotechnical Journal, No. 8, PP. 109-118.

Hwang, C.T., Morgenstern, N.R. and Murray, D.W., 1972.

Application of the finite element method to consolidation problems. Proceedings of the Symposium on the Applications of Finite Element Methods in Geomechanical Engineering, Vickburg, USA, pp. 739-765.

Janbu, N., 1963. Soil compressibility as determined by oedometer and triaxial tests. European Conference on Soil Mechanics and Foundation Engineering, Vol. 1, pp. 19-25.

Jardine, D., 1974. Cretaceous oil sands of Wertern Canada. Oil Sands, Fuel of the Future - Canadian Society of Petroleum Geologists, Memoir 3, pp. 50-67.

Jardine, R.J., Symes, M.J. and Burland, J.B., 1984. The measurement of soil stiffness in the triaxial apparatus. Geotechnique 34, No. 3, pp.323-340.

Jessberger, H.L., 1979. Shaft sinking in oil sand formation. Design Parameters in Geotechnical Engineering, British Geotechnical Society, London, Vol. 1, pp.189-194.

Kaplan, I.R. (Editor), 1974. Natural Gases in Marine Sediments. Plenum Press. 324 pages.

Keller, J.B., 1964. Growth and Decay of Bubbles. Proceedings of the Symposium on Cavitation in Real Liquids, General Motors Research Laboratories, Warren, Michigan, 1962, pp.19-29.

Khaled, M.Y., Beskosi, D.E. and Aifantis, E.C., 1984. On the theory of consolidation with double porosity - III A finite element formulation. International Journal for Numerical and Analytical Methods in Geomechanics, Vol. 8, pp. 101-123.

Kondner, R.L., 1963. Hyperbolic stress-strain response: cohesive soils. Journal of the Soil Mechanics and Foundation Division, ASCE, Vol. 89, No.SM1, Feb. 1963.

Kujawski, J. and Desai, C.S., 1985. A quasi-explicit modification of the two time level family of schemes for non-linear transient analysis. International Journal for Numerical and Analytical Methods in Geomechanics, Vol. 9, pp. 437-451.

Kulhawy, F.H.; Duncan, J.M. and Seed, H.B., 1969. Finite Element Analysis of stresses and movements in embankments during construction. Report No. TE69-4, Office of Research Services, University of California, Berkeley.

Kunar, R.R. and Minowa, N., 1981. A comparison between finite element and finite difference explicit

formulations for triangular and quadrilateral plane-strain elements. International Journal for Numerical and Analytical Methods in Geomechanics, Vol. 5, pp. 217-224.

Lalonde, G., 1983. The installation and performance of some deep piezometers. M.Eng Report, Department of Civil Engineering, University of Alberta, April 1983, 62 pp.

Lambe, T.W., 1967. The stress path method. Journal of the Soil Mechanics and Foundation Division, ASCE, Vol. 93, SM6, Nov. 1967, pp. 309-331.

Lambe, T.W. and Marr, W.A., 1979. Stress path method: Second edition. ASCE Journal of the Geotechnical Division, June 1979, GT6, pp. 727-738.

Lee, K.L. and Black, D.K., 1972. Time to dissolve air bubble in drain line. Journal of the Soil Mechanics and Foundation Division, ASCE. Vol. 98, No. SM2, pp. 181-194.

McArdle, W.D., Katch, F.I. and Katch, V.L., 1981. Exercise physiology: energy, nutrition and human performance. Lea & Febiger, Philidelphia.

Martschuk, J., Chan, W.K. and Slawinski, A., 1985. Basal aquifer dewatering at the Suncor oil sands mine. Heavy Oil and Oil Sands Technical Symposium. Challenges and Innovations 1985. Paper No. 3, University of Calgary, Calgary, Alberta.

Maser, K.R. 1981. Advanced techniques for rapidly placing concrete linings in tunnels and shafts. Rapid Escavation and Tunneling Conference, San Francisco, California, May 3-7, pp.449-467.

Mehrotra, A.K. and Svrcek, W.Y., 1982. Correlation for properties of bitumen saturated with CO_2,CH_4 and N_2 and experiments with combustion gas mixtures. Journal of Canadian Petroleum Technology, Vol. 21, pp. 95-104.

Meijer, K.L., 1984. Comparison of finite and infinitesimal strain consolidation by numerical experiments. Internaltional Journal for Numerical and Analytical Methods in Geomechanics, Vol. 8, pp. 531-548.

Morgenstern, N.R., 1981. Twenty first rankine lecture: Geotechnical engineering and frontier resource development.Geotechnique, Vol.31, No.3, pp. 305-365.

Mori, Y., Hijikata, K. and Nagatani, T., 1977. Fundamental study of bubble dissolution in liquid. International Journal of Heat and Mass Transfer. Vol. 20, pp. 41-50.

Mossop, G.D.; Kramers, J.W.; Flash, P.D. and Rottenfusser, B.A., 1979. Geology of Alberta's oil sand and heavy oil deposits. Proceedings of the First International Conference on the Future of Heavy Crude and Tar Sands, June 4-12, 1979, pp. 197-207.

Okumura, T., 1977. Stress change in soil sample taken from sea floor. Ninth International Conference of Soil Mechanics and Foundation Engineering, Specialty Session 2, Soil Sampling, Tokyo, pp. 141-145.

Osaimi, A.E. and Clough, G.W., 1979. Pore-pressure dissipation during excavation. ASCE Journal of Geotechnical Division, No. GT4, pp. 481-498.

Owen, D.R.J. and Damjanic, F., 1981. The stability of numerical time integration techniques for transient thermal problems with special references to reduced integration effects. Numerical Methods in Thermal Problems - Proceedings of the Second International Conference, Venice, Italy. pp. 487-505.

Patterson, M.A., 1985. Blind boring through oil sands. Advances in Petroleum Recovery and Upgrading Technology, Edmonton, June 6-7, 1985, Session 1, Paper 6, 38 pp.

Peacock, D., 1988. Gas evolution in the Athabasca oil sands. MSc thesis, Department of Civil Engineering, University of Alberta.

Piche, R., 1980. Testing of the NEAT program. Report MRP/MRL 80-66 (TR).

Plesset, M.S., 1964. Bubble dynamics. Proceedings of the Symposium on Cavitation in Real Liquids, General Motors Research Laboratories, Warren, Michigan, 1962, pp. 1-18.

Prigogine, I., 1964. Molecular theory of surface tension. Proceedings of the Symposium on Cavitation in Real Liquids, General Motors Research Laboratories, Warren, Michigan, 1962, pp. 147-163.

Prior, D.B. and Coleman, J.M., 1978. Disintegrating retrogressive landslides on very low-angle subaqueous slopes, Mississippi Delta. Marine Geotechnology, Vol. 3, No. 1, pp. 37-60.

Reed, M.B., 1982. Techniques for the analysis of seepage in porous elastic media using parabolic isoparametric elements. Proceedings of the International Conference on Finite Element Methods. Shangai, China. pp. 534-539.

Reed, M.B., 1984. An investigation of numerical errors in the analysis of consolidation by finite elements.

International Journal for Numerical and Analytical Methods in Geomechanics. Vol. 8, pp. 243-257.

Richards, A.F., (Editor), 1967. Marine Geotechnique. University of Illinois Press. 327 pages.

Robinson, D.B., Kalra, H. and Sim, S.K., 1980. Behaviour of bitumen-water-gas systems. Final report on A.O.S.T.R.A. research agreement 43, September 1980.

Rowe, P.W., 1971. Theoretical meaning and observed values of deformation parameters for soil, stress-strain behaviour of soils. Proceedings Roscoe Memorial Symposium, Cambridge University, 1971, pp. 143-194.

Rowe, R.K.; Lo, K.Y. and Than, L.G., 1982. The analysis of tunnels and shafts in dense (oil) sand. Proceedings of the Fourth International Conference on Numerical Methods in Geomechanics, Edmonton, Alberta, Canada, Vol. 2, pp. 587-596.

Sandhu, R.S., 1968. Flow in saturated soil. PhD thesis, Department of Civil Engineering, University of California Berkeley.

Sandhu, R.S., Liu, H. and Singh, K.J., 1977.Numerical performance of some finite element schemes for analysis of seepage in porous elastic media. International Journal for Numerical and Analytical Methods in Geomechanics, Vol. 1, pp. 177-194.

Sandhu, R.S., Lee, S.C. and The, H., 1985. Special finite elements for analysis of soil consolidation. International Journal for Numerical and Analytical Methods in Geomechanics. Vol. 9, pp. 125-147.

Sandhu, R.S. and Pister, K.S., 1970. A variational principle for linear coupled field problems in continuum mechanics. International Journal of Engineering Science, Vol. 8, pp. 989-999.

Sandhu, R.S. and Wilson, E.L., 1969. Finite element analysis of seepage in elastic media. Journal of the Engineering Mechanics Division, ASCE, Vol. 95, June 1969, pp. 641-652.

Sangrey, D.A., 1977. Marine geotechnology: state of the art. Marine Geotechnology: An International Journal of Seafloor Science and Engineering, Vol. 2, pp. 45-80.

Schuurman, I.E., 1966. The compressibility of an air/water mixture and a theoretical relation between the air and water pressures. Geotechnique. Vol. 16, No. 4, pp. 269-281.

Scott, J.D., 1984. Oil sand tests for Syncrude foundation design. Letter to Syncrude, Sept. 40.

Scott, J.D., Eisenstein, Z., Branco, P. and Peacock, D., 1985. Heave in foundation excavations in oil sands. 38 Canadian Geotechnical Conference. Theory and Practice in Foundation Engineering. Session 4, pp. 123-133.

Shchupakov, N.N., 1967. Prevention and treatment of caisson disease. English translation of Russian Language Book: Profilaktika i Lecheniye Kessonnoy Bolezni, Byschupakov, Moscow, 187 pages.

Shineda, K., 1978. Principles of solution and solubility. Editor: Marcel Dekker Inc.

Silver, H.F. and Nydahl, J.E., 1976. Introduction to engineering thermodynamics. West Publishing Company, 557 pp.

Siriwardane, H.J. and Desai, C.S., 1981. Two numerical schemes for nonlinear consolidation. International Journal for Numerical Methods in Engineering, Vol. 17, pp. 405-426.

Skempton, A.W., 1954. The pore pressure coefficients A and B. Geotechnique Vol. 4, pp. 143-147.

Smith, L.B. and Byrne, P.M., 1980. Convergence-confinement method of design for shafts and tunnels in oilsands. Applied Oilsands Geoscience, June, 1980. Edmonton, Alberta.

Smith, L.B., Chatterji, P.K., Insley, A.E. and Sharma, L., 1978. Construction of saline creek tunnel in Athabasca oil sand. AOSTRA Seminar on Underground Excavation in Oil Sand, University of Alberta, Edmonton, Alberta, Paper No. 7, 58 pages.

Smith, R.E. and Morales, M.F., 1944. On the theory of blood-tissue exhanges. Bulletin of Mathematics and Biophysics. No. 6, pp. 125-152.

Sobkowicz, J.C., 1982. The mechanics of gassy sediments. Ph.D. Thesis, Department of Civil Engineering, University of Alberta. 531 pp..

Sobkowicz, J.C. and Morgenstern, N.R., 1984. The undrained equibrium behavior of gassy sediments. Canadian Geotechnical Journal, Vol. 21, pp. 439-438.

Sobkowicz, J.C. and Morgenstern, N.R., 1987. An experimental investigation of transient pore pressure behaviour in soils due to gas exsolution. Prediction and Performance

in Geotechnical Engineering. Calgary, June 17-19, pp. 267-275.

Sparks, A.D.W., 1963. Various aspects of moisture. Third Regional Conference for Africa on Soil Mechanics and Foundation Engineering. Vol. 1, pp. 210-214.

Sparks, A.D.W., 1963. Theoretical considerations of stress equations for partly saturated soils. Third Regional Conference for Africa on Soil Mechanics and Foundation Engineering. Vol. 1, pp. 215-218.

Specht, H., 1958. Physiological effects of abnormal atmospheric pressure. Industrial Hygiene and Toxicology. Vol. 1, Editor: Patty, F.A., Interscience Publishers Inc. N.Y.

Sterne, K., 1981. Stress-deformation behaviour of oil sands. MSc thesis, Department of Civil Engineering, University of Alberta.

Stewart, G.A. and MacCallum, G.T., 1978. Athabasca oil sands guide book, Canadian Society of Petroleum Geologists, International Conference, Facts and Principles of World Oil Occurrence, 33 pp.

Strausz, O.P., Jha, K.N. and Montgomery, D.S., 1977. Chemical composition of gases in Athabasca bitumen and in low-temperature thermolysis of oil sand, asphaltene and maltene. Fuel, Vol. 56, pp. 114-122.

Svrcek, W.Y. and Mehrotra, A.K., 1982. Gas solubility, viscosity and density measurements for Athabasca bitumen. Journal of Canadian Petroleum Technology. Vol. 21, pp. 31-38.

Symes, M.J. and Burland, J.B., 1984. Determination of local displacements on soil samples. Geotechnical Testing Journal, Vol. 7, No. 2, June 1984, pp. 49-59.

Taylor, D.W., 1948. Fundamental of soil mechanics, John Wiley and Sons, N.Y., 700 pp.

Teunissen, J.A.M., 1982. Mechanics of a fluid-gas mixture in a porous medium. Mechanics of Materials 1, pp. 229-237. North-Holland Publishing Co.

Tikuisis, P., Ward, C.A. and Venter, R.D., 1983. Bubble evolution in a stirred volume of liquid closed to mass transport. Journal of Applied Physics, Vol. 54, No. 1, pp. 1-9.

Tobias, C.A., 1951. Decompression sickness in actual flights. Decompression Sickness - Caisson Sickness,

Diver's and Flier's Bends and Related Syndromes. W.B. Saunders Company. pp. 360-377.

Tucker, A.S. and Ward, C.A., 1975. Critical state of bubbles in liquid-gas solutions. Journal of Applied Physics, Vol. 46, No. 11, pp. 4801-4808.

Vaid, Y.P. and Campanella, R.G., 1973. Making rubber membranes. Canadian Geotechnical Journal, Vol. 10, pp. 643,644.

Vaziri, H., 1986. Mechanics of fluid and sand production from oil sand reservoirs. Paper submitted for publication to the Petroleum Society of the C.I.M.

Vermeer, P.A., Verruijt, A., 1981. An accuracy condition for consolidation by finite elements. International Journal for Numerical and Analytical Methods in Geomechanics, Vol. 5, pp. 1-14.

Vigras, L.W., 1968. Geology of Canadian heavy oil sands. The American Association of Petroleum Geologists Bulletin, Vol. 52, No. 2, October 1968, pp. 1984-1999.

Walder, D.N. and McCallum, R.I., 1975. Medical hazards of tunneling. Hazards in Tunnelling and on Fa[illegible] Work. Proceedings of the Third International Safet[illegible]e held at the Institution of Civil Engineers, L[illegible] 67-73.

Wan, R., 1985. Finite element implementation of some conventional geotechnical problems. MSc thesis, Department of Civil Engineering, Faculty of Science and Engineering, University of Ottawa, July 1985.

Ward, C.A., Balakrishnan, A. and Hooper, F.C., 1970. On the thermodynamics of nucleation in weak gas-liquid solutions. Transactions of the A.S.M.E. - Journal of Basic Engineering. Series B, pp. 695-704.

Ward, C.A., Johnson, W.R., Venter, R.D., Ho, S., Forest, T.W. and Fraser, W.D., 1983. Heterogeneous bubble nucleation and conditions for growth in a liquid-gas system of constant mass and volume. Journal of Applied Physics, Vol. 54, pp. 1833,1843

Ward, C.A. and Levart, E., 1984. Conditions for stability of bubble nuclei in solid surfaces contacting a liquid-gas solution. Journal of Applied Physics, Vol. 56, No. 2, pp. 491-500.

Ward, C.A. and Tikuisis, P. and Venter, P.D., 1982. Stability of bubbles in a closed volume of liquid-gas solution. Journal of Applied Physis, Vol. 53, No. 9, pp.

6076-6084.

Ward, C.A., Yee, D. and Tikuisis, P., 1985. Maximum stress produced by bubble growth in a condensed phase. Journal of Applied Physics. Vol. 58, No. 1, pp. 273-279.

Westwater, J.W., 1964. Measurements of bubble growth during mass transfer. Proceedings of the Symposium on Cavitation in Real Liquids, General Motors Research Laboratories, Warren, Michigan, 1962, pp. 34-54.

Whelan, T. III, Coleman, J.M., Suhayda, J.N. and Roberts, H.H., 1977. Accoustical penetration and shear strength in gas-charged sediment. Marine Geotechnology, Vol. 2. Marine Slope Stability, pp. 147-159.

Wissa, A.E.Z, 1969. Pore pressure measurement in saturated stiff soil. ASCE Journal of Soil Mechanics and Foundation Engineering, SM4, July 1969, pp. 1063-1073.

Wong, K.S. and Duncan, J.M., 1974. Hyperbolic stress-strain parameters for nonlinear finite element analyses of stresses and movements in soil masses. Report No. TE74-3, University of California, Berkeley.

Yamagami, T., Veta, Y. and Harumoto, S., 1986. Elasto-plastic uncoupled procedure for consolidation analysis and its comparison with coupled procedures. Fifth International Conference on Numerical Methods in Geomechanics, Nagoya. pp. 605-612.

Yen, B.C. and Allen, R.L, 1977. Spreading of submarine slopes caused by trenching. Marine Geotechnology, Vol. 2, Marine Slope Stability, pp. 101-116.

Yokoo, Y., Yamagata, K. and Nagaoka, H., 1971-a. Finite element method applied to Biot's consolidation theory. Soils and Foundations, Japanese Society of Soil Mechanics and Foundation Engineering. Vol. II, No. 1.

Yokoo, Y., Yamagata, K, and Nagaoka, H., 1971-b. Variational principles for consolidation. Soils and Foundations - Japanese Society of Soil Mechanics and Foundation Engineering. Vol. II, No. 4.

Yokoo, Y., Yamagata, K, and Nagaoka, H., 1971-c. Finite element analysis of consolidation following undrained deformation. Soils and Foundations - Japanese Society of Soil Mechanics and Foundation Engineering. Vol. II, No. 4.

Zienkiewicz, O.C., 1982. Finite element methods for coupled problems in engineering. Numerical Methods for Coupled Problems in Engineering - Proceedings of the

International Conference, University College, Swansea. pp. 1-15.

Zienkiewicz, O.C., 1983. The Finite Flement Method - Third Editon. McGraw-Hill Book Company, pp. 787.

Zienkiewicz, O.C. and Cormeau, I.C., 1974. Visco-plasticity - plasticity and creep in elastic solids - a unified numerical solution approach. International Journal for Numerical Methods in Engineering. Vol. 8, pp. 821-845.

Zienkiewicz, O.C. and Shiomi, T., 1984. Dynamic behavior of saturated porous media; the generalized Biot formulation and its numerical solution. International Journal for Numerical and Analytical Methods in Geomechanics. Vol. 8, pp. 71-96.

Zienkiewicz, O.C., Watson, M. and King, I.P., 1968. A numerical method of visco-elastic stress analysis. International Journal of Mechanical Sciences, Vol. 10, pp. 807-827.

APPENDIX A - COMPRESSIBILITY OF GASSY FLUIDS

In this appendix, the compressibility of gassy fluids is evaluated for some hypothetical cases with Equation 2.69, by Schuurman, 1966, presented in Chapter 2.

The following fluids are considered:

a) liquid : water
   gas : CO_2

b) liquid : bitumen
   gas : CH_4

In both cases, it is assumed that there is no flow of mass through the element of fluid being considered (i.e. undrained condition).

This element of fluid has the size of a typical void encountered in a hypothetical sand matrix. The volume of this void is assumed to be equal to D_{10} of the sand, which in our case is assumed to be equal to 0.1 mm (according to grain size distribution of samples collected).

It is also assumed that only one bubble grows per void. This assumption is partly supported by the coalescence principle (Schuurman, 1966:272) and by experiments performed by the Soviet astronaut Colonel Nikolayev (Keller, 1964:20) in the absence of gravitational forces.

It is assumed that the bubble pressure is the *in situ* pore pressure which, according to Schuurman, 1966, is also the maximum allowable gas pressure (u_{max}).

The values calculated according to Equation 2.69 and presented in Tables A.1 to A.4 refer to conditions of

equilibrium.

The use of the equation presented in this Appendix is restricted to the cases where the bubbles are occluded and spherical. If the bubbles are not occluded the surface tension cannot be directly related to the average radius of the bubble.

Controlling equations:

1)Static equilibrium of a bubble

$$P_{fg}-P_L = \frac{2q}{r_B}$$

2)Boyle's law

$$P_i V_{Tgi} = P_{fg}(V_{dg}+V_{fg})$$

3)Henry's law

$$V_{dg} = HV_L$$

4) Volume of a bubble (1 bubble per void)

$$V_{fg} = \frac{4}{3}\pi r_o^3$$

5) Degree of saturation

$$S = \frac{V_L}{V_L+V_{fg}}$$

6) Compressibility of the fluid

$$\beta_T = \frac{1}{V_{fg} + V_L}\left[\frac{P_{fg}}{(V_{fg} + V_{dg})} - \frac{2q}{3r_o V_{fg}}\left[\frac{V_{fgo}}{V_{fg}}\right]^{1/3}\right]^{-1}$$

where,

P_{fg}= absolute pressure in the bubble

P_L= absolute pressure in the liquid

q = surface tension (assumed to be constant)

r_o= radius of the bubble

P_i= bubble pressure and initial liquid pressure for S = 1.0

V_{Tgi}= total volume of free gas

V_{dg}= volume of dissolved gas

V_{fg}= volume of free gas

H= coefficient of solubility

β_F= coefficient of compressibility of fluid assuming the liquid incompressibility

a) liquid - water

gas - carbon dioxide

(Tables A.1 and A.2)

H = 0.86

q = 70 dynes/cm = 7.000111 x 10^{-5} kN/m (Sobkowicz, 1982)

P_{atm} = 101.325 kPa

b) liquid : Athabasca bitumen

gas : CH_4

(Tables A.3 and A.4)

H=0.22 (Svrcek and Mehrotra, 1982:35, Run 8)

q = 40 dynes/cm = 4.000634 x 10^{-5} KN/m (Bowman, 1967).

Table A.1 Fluid Compressibility P_i = (300 + 101.325) kPa

u_L	P_L	u_{fg}	P_{fg}	ro	S	β_{fnt}	β_{fte}
kPa				m*10-5		kPa*10-3	
280.00	381.33	290.00	391.33	1.4005	0.979	2.2054	-3.3047
279.32	380.65	289.00	390.33	1.4470	0.976	2.118	-5.2353
278.60	379.93	288.00	389.33	1.4908	0.974	2.2182	-9.5819
277.86	379.19	287.00	388.33	1.5324	0.972	2.2247	-2.8295
277.09	378.42	286.00	387.33	1.5721	0.970	2.2313	48.632
276.30	377.63	285.00	386.33	1.6101	0.968	2.2378	15.040
275.49	376.82	284.00	385.33	1.6465	0.966	2.2444	9.5534
274.67	376.00	283.00	384.33	1.6814	0.963	2.2510	7.3198
273.84	375.16	282.00	383.33	1.7154	0.961	2.2577	6.0985
273.00	374.32	281.00	382.33	1.7481	0.959	2.2644	5.3409
272.13	373.46	280.00	381.33	1.7798	0.957	2.2711	4.8249
263.17	364.51	270.00	371.33	2.0555	0.935	2.3405	3.2136
253.87	355.19	260.00	361.33	2.2831	0.913	2.4138	2.9073
244.36	344.69	250.00	351.33	2.4825	0.891	2.4913	2.8250
234.75	336.07	240.00	341.33	2.6636	0.869	2.5735	2.8218
225.05	326.38	230.00	331.33	2.8319	0.842	2.6606	2.8570

β_{fte}: fluid compressibility with interfacial tensions
β_{fnt}: fluid compressibility with no interfacial tensions
u : gauge pressure
P : absolute pressure
S : degree of saturation
ro : bubble radius

Table A.2 Fluid Compressibility - P_i = (3000 + 101.325) kPa

u_L	P_L	u_{fg}	P_{fg}	ro	S	β_{fnt}	β_{fte}
kPa				m*10-5		kPa*10-3	
2983.50	3064.80	2979.00	3080.33	0.9015	0.994	0.2795	-0.9161
2946.60	3047.90	2959.00	3060.33	1.1293	0.989	0.2815	-0.8520
2928.20	3029.50	2939.00	3034.33	1.2920	0.983	0.2837	0.9081
2909.20	3010.50	2919.00	3020.33	1.4232	0.977	0.2858	0.5102
2889.90	2991.20	2899.00	3000.33	1.5353	0.972	0.2880	0.4102
2840.80	2942.10	2848.70	2950.00	1.7670	0.958	0.2935	0.3465
2791.50	2892.80	2798.70	2900.00	1.9540	0.944	0.2993	0.3309
2692.50	2793.80	2698.70	2800.00	2.2617	0.915	0.3114	0.3215
2642.90	2744.20	2648.70	2750.00	2.3948	0.901	0.3178	0.3305
2593.10	2694.40	2598.70	2700.00	2.5187	0.887	0.3244	0.3348
2543.40	2644.70	2548.50	2650.00	2.6360	0.872	0.3313	0.3400
2493.60	2594.90	2498.70	2600.00	2.7470	0.858	0.3384	0.3459
2443.80	2545.10	2448.70	2550.00	2.8540	0.843	0.3459	0.3524

β_{fte}: fluid compressibility with interfacial tensions
β_{fnt}: fluid compressibility with no interfacial tensions
u : gauge pressure
P : absolute pressure
S : degree of saturation
ro : bubble radius

Table A.3 Fluid Compressibility - P_i = (300 + 101.325) kPa

u_L	P_L	u_{fg}	P_{fg}	r_0	S	β_{rnt}	β_{rte}
kPa				m*10-5		kPa*10-3	
281.00	382.33	290.00	391.33	0.8891	0.994	0.5733	-1.1470
280.32	381.60	289.00	390.33	0.9185	0.994	0.5780	-2.0520
279.60	380.90	288.00	389.33	0.9460	0.993	0.5786	-5.3222
278.80	380.10	287.00	388.33	0.9730	0.993	0.5812	20.0950
278.00	379.30	286.00	387.33	0.9980	0.992	0.5839	4.1406
277.20	378.50	285.00	386.33	1.0221	0.992	0.5866	2.5103
276.40	377.70	284.00	385.33	1.0450	0.991	0.5893	1.8934
275.50	376.80	283.00	384.33	1.0680	0.990	0.5920	1.5708
274.70	376.00	282.00	383.33	1.0890	0.990	0.5947	1.3735
273.80	375.10	281.00	382.33	1.1100	0.989	0.5975	1.2411
272.90	374.20	280.00	381.33	1.1200	0.989	0.6003	1.1467
263.90	365.20	270.00	371.33	1.3050	0.983	0.6292	0.8329
254.50	355.80	260.00	361.33	1.4490	0.976	0.6602	0.7793
245.00	346.30	250.00	351.33	1.5760	0.970	0.6936	0.7761
235.30	336.60	240.00	341.33	1.6916	0.963	0.7296	0.7924
225.60	326.90	230.00	331.33	1.7977	0.956	0.7686	0.8193
215.80	317.10	220.00	321.33	1.8989	0.948	0.8107	0.8534
206.00	307.30	210.00	311.33	1.9958	0.940	0.8565	0.8936
196.20	297.50	200.00	301.33	2.0898	0.932	0.9062	0.9394
186.40	287.70	190.00	291.33	2.1816	0.923	0.9605	0.9907
176.50	277.80	180.00	281.33	2.2721	0.914	1.0199	0.0478
166.60	267.90	170.00	271.33	2.3619	0.905	1.0850	1.1112
156.80	258.10	160.00	261.33	2.4515	0.895	1.1566	1.1815
146.90	248.20	150.00	251.33	2.5413	0.884	1.2356	1.2596
137.00	238.30	140.00	141.33	2.6320	0.873	1.3231	1.3464
127.00	228.40	130.00	131.33	2.7239	0.861	1.4203	1.4433
117.20	218.50	120.00	121.33	2.8175	0.842	1.5289	1.5516

β_{rte}: fluid compressibility with interfacial tensions
β_{rnt}: fluid compressibility with no interfacial tensions
u : gauge pressure
P : absolute pressure
S : degree of saturation
r_0 : bubble radius

Table A.4 Fluid Compressibility - P_i = (300 + 101.325) kPa

u_L	P_L	u_{fg}	P_{fg}	ro	S	β_{rnt}	β_{rte}
kPa				m*10-5		kPa*10-5	
2965.80	3067.80	2980.00	3081.33	0.5630	0.999	7.1759	-2.4296
2948.80	3050.10	2960.00	3061.33	0.7109	0.997	7.2595	-2.9275
2930.20	3031.50	2940.00	3041.33	0.8156	0.996	7.3445	2.0194
2911.10	3012.40	2920.00	3021.33	0.8990	0.994	7.4303	12.3070
2891.80	2993.10	2900.00	3001.33	0.9713	0.993	7.5192	10.3400
2872.30	2973.60	2880.00	2981.33	1.0344	0.991	7.6089	9.5321
2852.70	2954.00	2860.00	2961.33	1.0914	0.990	7.7002	9.1278
2833.00	2934.30	2840.00	2941.33	1.1437	0.988	7.7932	8.9114
2813.30	2914.60	2820.00	2921.33	1.1922	0.987	7.8879	8.7971
2793.60	2894.90	2800.00	2901.33	1.2376	0.985	7.9844	8.7443
2744.10	2845.40	2750.00	2851.33	1.3409	0.981	8.2334	8.7614
2694.40	2795.70	2700.00	2801.33	1.4334	0.977	8.4943	8.8921
2644.80	2746.10	2650.00	2751.33	1.5181	0.973	8.7680	9.0840
2595.00	2696.30	2600.00	2701.33	1.5969	0.965	9.0551	9.3163
2545.20	2646.50	2550.00	2651.33	1.6712	0.964	9.3567	9.5787
2495.40	2596.70	2500.00	2601.33	1.7420	0.959	9.6737	9.8668
2445.60	2546.90	2450.00	2551.33	1.8099	0.955	10.0073	10.1780
1345.90	2447.20	2350.00	2451.33	1.9390	0.945	10.7286	10.8687
2296.00	2397.30	2300.00	2401.33	2.0010	0.940	11.1192	11.2482
2246.20	2347.50	2250.00	2351.33	2.0623	0.934	11.5316	11.6516
2196.30	2297.60	2200.00	2301.33	2.1220	0.924	11.9677	12.0802
2096.50	2197.80	2100.00	2201.33	2.2403	0.918	12.9180	13.0192
1996.60	2097.90	2000.00	2101.33	2.3566	0.905	13.9875	14.0807
1896.80	1998.10	1900.00	2001.33	2.4725	0.892	15.1971	15.2848
1796.90	1898.20	1800.00	1901.33	2.5890	0.878	16.5726	16.6567
1697.10	1798.40	1700.00	1801.33	2.7070	0.863	18.1463	18.2228
1597.20	1698.50	1600.00	1701.33	2.8290	0.847	19.9587	20.0399

β_{rte}: fluid compressibility with interfacial tensions
β_{rnt}: fluid compressibility with no interfacial tensions
u : gauge pressure
P : absolute pressure
S : degree of saturation
ro : bubble radius

APPENDIX B - DETAILS OF CONGAS

B.1 Introduction

This appendix presents the procedures followed for the evaluation of the element matrices in CONGAS and the procedure used to impose displacement and pore pressure boundary conditions.

B.2 Development of the Element Matrices in CONGAS

The development of the element matrices $[K_1]$, $[K_2]$, $[C]$, $\{M_1\}$, $\{M_2\}$, $\{M_3\}$, $\{T\}$, $\{Q\}$, $\{\epsilon_v^{fg}\}_{tN-1}^{tN}$ and $[E]$ (Chapter 3), require the integration of functions over the volume of the element as shown in Equations 3.70 to 3.79. The type of functions to be integrated vary with the type of formulation (plane strain or axisymmetric), the material model (linear or non-linear), and the permeability model (constant or variable). The choice of the procedure, for the integration of the referred functions, requires the development of the basic element matrices as follows:

Figure B1 displays the triangular element 6-3 and the area coordinates used in the present derivation. Based on this figure, the element displacement shape functions can be expressed as follows:

$$W_x = \langle \phi_w \rangle_{1x6} \begin{Bmatrix} Wx_1 \\ \vdots \\ W_{x6} \end{Bmatrix}_{6x1}$$

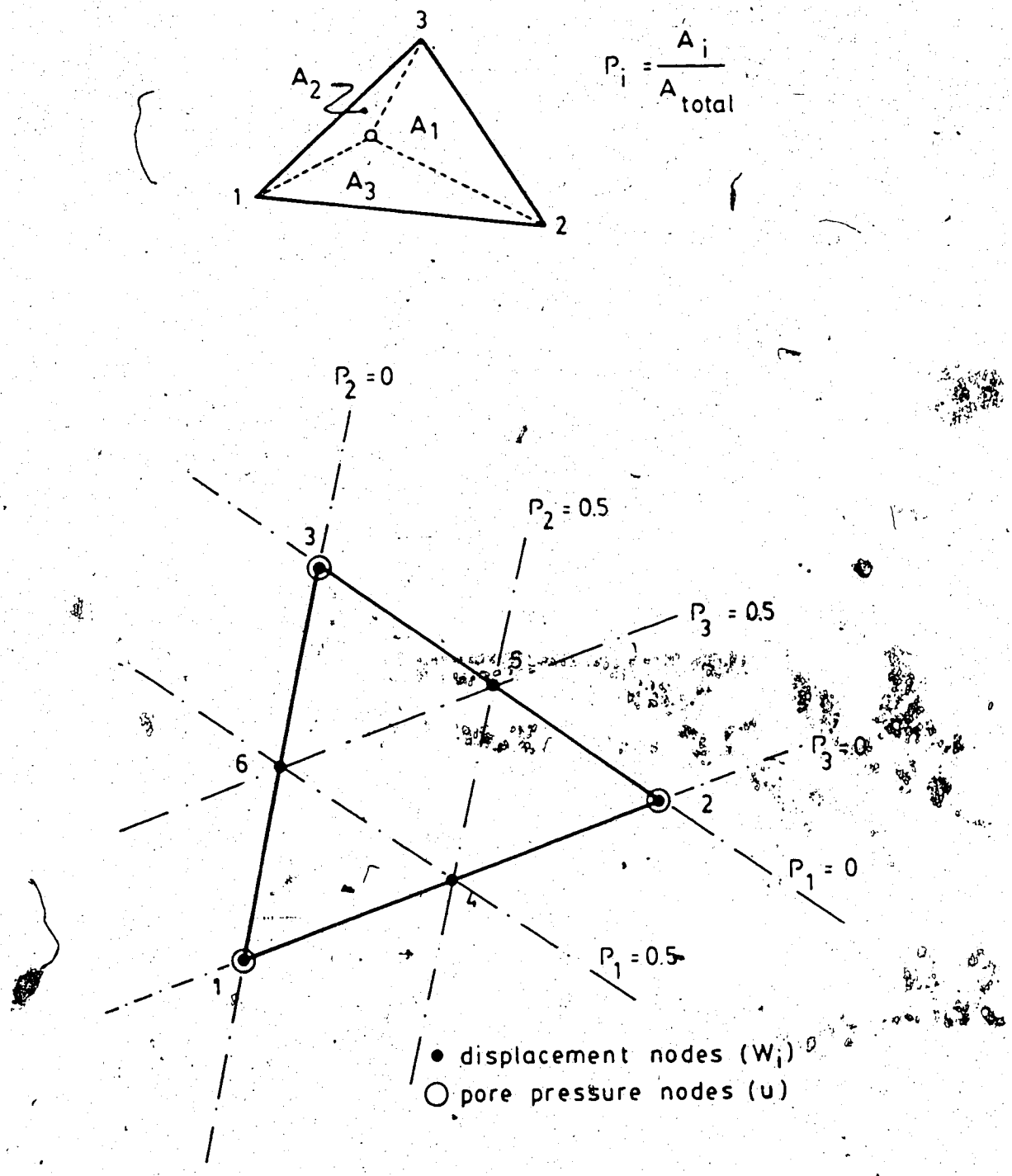

Figure B.1 Triangular Element - 6-3 - Area Coordinates

$$w_y = \langle \phi_w \rangle_{1x6} \begin{Bmatrix} w_{y1} \\ \vdots \\ w_{y6} \end{Bmatrix}_{6x1}$$

where,

$\langle \phi_w \rangle_{1x6} = \langle \rho_1(2\rho_1-1),\ \rho_2(2\rho_2-1),\ \rho_3(2\rho_3-1),\ 4\rho_1\rho_3,\ 4\rho_2\rho_3,\ 4\rho_3\rho_1 \rangle$

and,

w_x and w_y = horizontal and vertical displacements within the element

w_{xi}, w_{yi} = horizontal and vertical displacements at node i.

In a more general form,

$$\begin{Bmatrix} w_x \\ w_y \end{Bmatrix} = \begin{bmatrix} \langle \phi_w \rangle_{1x6} & \langle 0 \rangle_{1x6} \\ \langle 0 \rangle_{1x6} & \langle \phi_w \rangle_{1x6} \end{bmatrix} \begin{Bmatrix} w_{xi} \\ w_{yi} \end{Bmatrix}$$

or,

$$\begin{Bmatrix} w_x \\ w_y \end{Bmatrix} = [N] \begin{Bmatrix} w_{xi} \\ \vdots \\ w_{yi} \end{Bmatrix}$$

In the present formulation, the axisymmetric strain tensor is defined as,

$$\langle \epsilon \rangle_{1x4} = \langle \epsilon_x,\ \epsilon_y,\ \epsilon_{xy},\ \epsilon_z \rangle$$

where,

$$\epsilon_x = \frac{\partial w_x}{\partial x}$$

$$\epsilon_y = \frac{\partial w_y}{\partial y}$$

$$\epsilon_{xy} = \frac{\partial w_x}{\partial y} + \frac{\partial w_y}{\partial x}$$

$$\epsilon_z = \frac{w_x}{x}$$

It is then possible to write the following relationships:

$$\{\epsilon\}_{1x4} = \begin{bmatrix} \delta\langle\phi\rangle/\delta x & \langle 0\rangle_{1x6} \\ \langle 0\rangle_{1x6} & \delta\langle\phi\rangle/\delta y \\ \delta\langle\phi\rangle/\delta y & \delta\langle\phi\rangle/\delta x \\ \langle\phi\rangle/x & \langle 0\rangle_{1x6} \end{bmatrix} \begin{Bmatrix} W_{xi} \\ W_{yi} \end{Bmatrix}_{12x1}$$

or simply,

$$\{\epsilon\}_{4x1} = [B_e]_{4x12} \begin{Bmatrix} W_{xi} \\ W_{yi} \end{Bmatrix}_{12x1}$$

where $[B_e]$ is the strain-displacement matrix, which is fully developed in Figure B.2.

In the plane strain formulation, since $\epsilon_z=0$, the strain tensor and the strain-displacement matrix are reduced to a 3x1 and 3x12 matrices, respectively.

The volumetric strain within the element can also be expressed in terms of the nodal displacements as follows:

$$\epsilon_v = \epsilon_x + \epsilon_y + \epsilon_z$$

$$= \frac{\partial w_x}{\partial x} + \frac{\partial w_y}{\partial y} + \frac{w_x}{x}$$

$$= \langle (\frac{\partial\langle\phi\rangle}{\partial x} + \frac{\langle\phi\rangle}{x}), \frac{\partial\langle\phi\rangle}{\partial y} \rangle_{1x12} \cdot \begin{bmatrix} W_{xi} \\ W_{yi} \end{bmatrix}_{12x1}$$

or,

$$\epsilon_v = \langle B_v \rangle_{12x1} \begin{bmatrix} W_{xi} \\ W_{yi} \end{bmatrix}_{1x12}$$

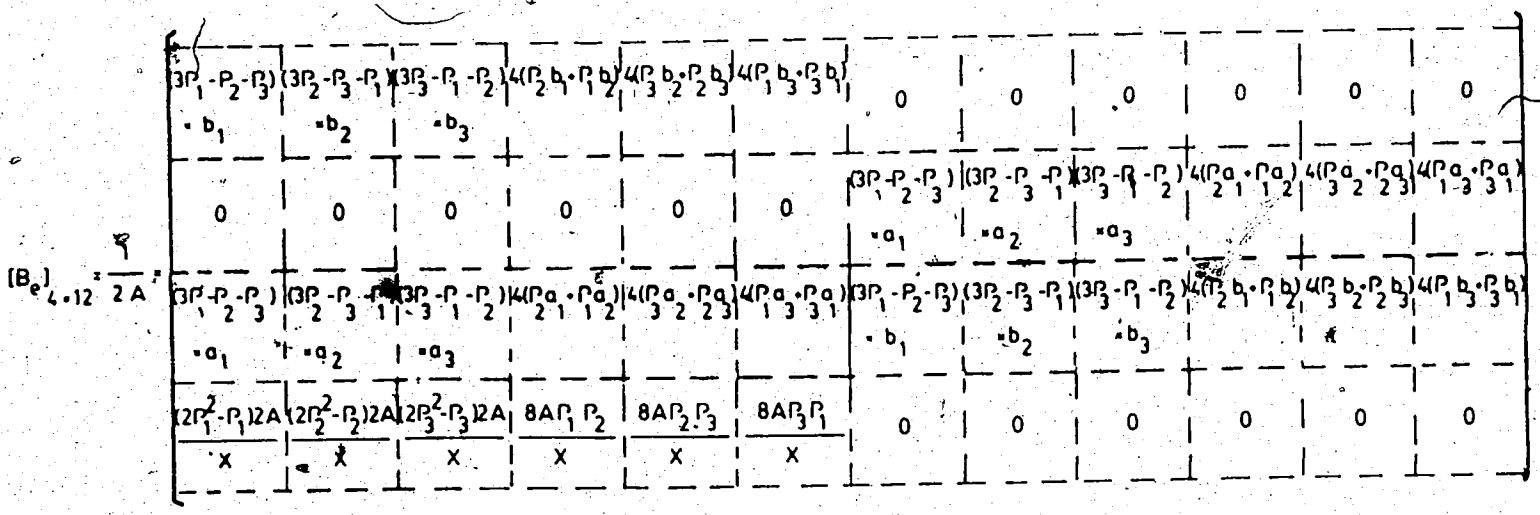

where, $b_i = y_j - y_k$
$a_i = x_k - x_j$
$x = P_1x_1 + P_2x_2 + P_3x_3$

i, j, k are even permutations of 1, 2, 3, the external nodes

Figure B.2 Strain - Displacement Matrix - Triangular Element

6-3 - Axisymmetric Formulation

The elements of $\langle B_v \rangle$ are displayed in Figure B3. In the plane strain formulation $\epsilon_z=0$ and the term $\langle \phi \rangle / x$ disappears from the volumetric strain-displacement matrix.

The pore pressures are assumed to vary linearly within the element, according to the following equation:

$$u = \langle \phi_u \rangle_{1x3} \begin{Bmatrix} u_1 \\ u_2 \\ u_3 \end{Bmatrix}_{3x1}$$

where $\langle \phi_u \rangle$ is the shape function for pore pressures.

$$\langle \phi_u \rangle_{1x3} = \langle \rho_1, \rho_2, \rho_3 \rangle$$

and u_i are the pore pressures at the three external loads.

Another basic matrix required for the current analyses is the matrix that relates the first derivative of the pore pressures with the pore pressures at the nodes:

$$\begin{Bmatrix} \frac{\partial u}{\partial x} \\ \\ \frac{\partial u}{\partial y} \end{Bmatrix} = 1/2A \begin{bmatrix} b_1 & b_2 & b_3 \\ \\ a_1 & a_2 & a_3 \end{bmatrix} \begin{Bmatrix} u_1 \\ \\ u_2 \\ \\ u_3 \end{Bmatrix}$$

where a_i, b_i are defined in Figure B2

or,

$$\begin{Bmatrix} \frac{\partial u}{\partial x} \\ \\ \frac{\partial u}{\partial y} \end{Bmatrix} = [\phi_q]_{2x3} \{u_i\}_{3x1}$$

$$[B_v]^T_{12\times 1} = \begin{bmatrix} (1/2A)(3P_1 - P_2 - P_3)b_1 + (2P_1^2 - P_1)/x \\ (1/2A)(3P_2 - P_3 - P_1)b_2 + (2P_2^2 - P_2)/x \\ (1/2A)(3P_3 - P_1 - P_2)b_3 + (2P_3^2 - P_3)/x \\ (2/A)(P_2 b_1 + P_1 b_2) + 4P_1P_2/x \\ (2/A)(P_3 b_2 + P_2 b_3) + 4P_2P_3/x \\ (2/A)(P_1 b_3 + P_3 b_1) + 4P_1P_3/x \\ (3P_1 - P_2 - P_3)a_1/2A \\ (3P_2 - P_3 - P_1)a_2/2A \\ (3P_3 - P_1 - P_2)a_3/2A \\ 2(P_2 a_1 + P_1 a_2)/A \\ 2(P_3 a_2 + P_2 a_3)/A \\ 2(P_1 a_3 + P_3 a_1)/A \end{bmatrix}$$

a_i, b_i, x are defined in figure B.2

Figure B.3 Volumetric Strain - Displacement Matrix - Triangular Element 6-3 - Axisymmetric Formulation

Matrices $\langle\phi_v\rangle$, $[N]$, $[B_e]$, $\langle B_v\rangle$, $\langle\phi_u\rangle$ and $[B_g]$ allow the integration of the element matrices as follows:

$[K_1]$ (material element stiffness matrix)

According to Equation 3.70:

$$[K1]= \int_v [B_e]^T[H]\,[B_e]dV$$

There are four cases to be considered for the evaluation of [K1]:

1st Case - Axisymmetric-Linear Material Model

In this case, the equation above reduces to

$$[K_1]= \int_A [B_e]^T_{12x4}\,[H]_{4x4}\,[B_e]_{4x12}\,2\pi x\,dA$$

where, $x = (\rho_1 x_1 + \rho_2 x_2 + \rho_3 x_3)$

and, $dA= 2A\,d\rho_1 d\rho_2$

The analysis of the terms of the matrix $[B_e]$ indicates that the function to be integrated above, is composed of polynomials of up to the 4th degree and complete polynomials of up to the 3rd degree.

According to Cowper, 1973, the numerical integration of a function "f" over a triangle of area A can be performed according to the following equation:

$$\int\int f dA= A \sum_{i=1}^{N} W_i\, f(\rho_{1i},\ \rho_{2i},\ \rho_{3i})$$

where W_i is the weight associated with the i-th sampling point and ρ_{1i}, ρ_{2i} and ρ_{3i} are the area coordinates associated with that point.

According to Cowper, a 3rd degree complete polynomium can be numerically integrated exactly over a triangle, with four sampling points, with the location and weights indicated in Figure B4.

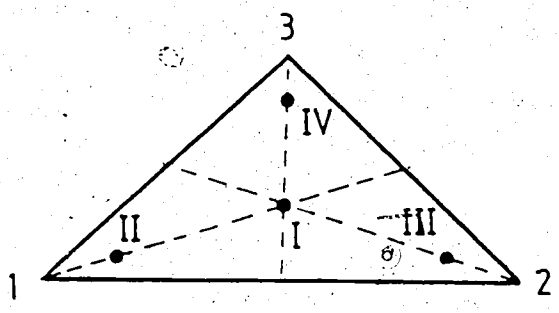

SAMPLING POINT	AREA COORDINATE			WEIGHT
	p_1	p_2	p_3	W_i
I	1/3	1/3	1/3	-27/48
II	0.6	0.2	0.2	+25/48
III	0.2	0.6	0.2	+25/48
IV	0.2	0.2	0.6	+25/48

Figure B.4 Numerical Integration of a Complete 3rd Degree Polynomial over a Triangle

Therefore, in CONGAS, in the axisymmetric formulation, [K1] is obtained as follows:

$$[K_1] = 2\pi A \sum_{1}^{4} W_i [B_e]_i [H] [B_e]^t_i \; x_i$$

where $[B_e]_i$ is the strain-displacement matrix evaluated at the sampling point i, with abssiss x_i, and the area coordinates and W_i given by Figure B4.

2nd Case - Axisymmetric Non-Linear Material Model

According to Bathe, 1982:401, the introduction of non-linearity in an analysis (geometric or material non-linearity), might require an increase in the order of integration in order to increase the accuracty of the solution. A review of the literature, however, indicates that in most finite element programs, the order of integration is maintained the same, for linear and non-linear material models. This is probably due to the fact that the gain in accuracy associated with the higher order integration is not significant and represents an increase in the computational costs.

In CONGAS, the same four-point formula, presented in the preceding sub-section is used for the axisymmetric non-linear material model case.

3rd Case - 2D Linear Material Model

$$[K_1] = \text{width} \int [B_e]^T_{12x3} [H]_{3x3} [B_e]_{3x12} \, dA$$

As discussed earlier in this appendix, the two dimensional formulation is in fact a simplification of the axisymmetric formulation. The elimination of the terms $<\phi>/x$ of the strain-displacement matrix and, the fact that the

constitutive matrix [H] is constant within the element, allows the direct integration of the terms of $[K_1]$.

4th Case - 2D Non-Linear Material Model

The fact that [H] varies within the element, eliminates the possibility of integrating the components of $[K_1]$ directly. In this case, the integrants of $[K_1]$ are complete polynomials of the 2nd degree, which according to Cowper, 1973, can be integrated exactly with a three-point formula.

However, for the sake of consistency within the computer program, the four-point formula used in the first case (Axisymmetric - Non-Linear Material Model), is used in the 2D case as well.

$[K_2]$ (permeability matrix)

According to Equation 3.71

$$[K_2] = \int_V [B_q][R][B_q]^T dV$$

There are two cases to be considered in this situation:

1st Case - Constant Coefficient of Permeability

In this case, irrespective of the type of formulation being considered (axisymmetric or 2D), the integrants of $[K_2]$ are simple polynomials which can be integrated by direct means. This procedure was therefore used in CONGAS.

2nd Case - Variable Coefficient of Permeability

The fact that the coefficient of permeability varies within the element, as a function of the void ratios and degrees of saturation, as expressed in Equation 3.114, eliminates the possibility of using direct integration of the components of $[K_2]$. The analysis of Equation 3.71 and

the matrix $[B_q]$ indicates that the highest complete polynomial is of first degree. For the sake of consistency with the remainder of the computer program, the same four-point formula described earlier was used to evaluate the integrants of $[K_2]$:

$$2D \Rightarrow [K_2] = A*Width \sum_1^4 [B_q]_i[R]_i[B_q]_i^T W_i$$

$$Axisymmetric \Rightarrow [K_2] = 2\pi A \sum_1^4 [B_q]_i[R_i][B_q]_i^T x_i W_i$$

where $[B_q]_i$ is the matrix that relates the first derivative of the pore pressures with the pore pressures at the nodes, evaluated at the sampling points, $[R_i]$ is the permeability coefficient evaluated at the sampling points and x_i is the x coordinate of the sampling point being considered.

[C] (Coupling Matrix)

$$[C] = \int_V [B_v]\langle\phi_u\rangle dV$$

There are two case to considered for the evaluation of [C]

1st Case - Axisymmetric Formulation

$$[C] = 2\pi \int_A \phi [B_v]_{12x1}\langle\phi_u\rangle_{1x3}\, xdA$$

In this case, the integrants of [C] are polynomials of up to the 3rd degree (complete). Therefore, the four-point formula can be used again for its exact integration:

$$[C] = 2\pi A \sum_1^4 [B_v]_i\langle\phi_u\rangle_i x_i W_i$$

where $[B_v]_i$ is the volumetric strain-displacement matrix, $\langle\phi_u\rangle_i$ is the shape function and x_i is the x coordinate, all three evaluated at the sampling point under consideration.

2nd Case - Plane Strain Formulation

$[C] = \text{width} \int_A [B_v]^T \langle \phi_u \rangle dA$

In this case, the integrands of [C] are simple 2nd degree polynomials that in CONGAS, were integrated exactly.

{M₁} (initial effective stresses matrix)

$\{M_1\} = \int_V [B_e]^T \{\sigma_o\} dV$

Two cases are to be considered:

1st Case - Axisymmetric Formulation

$\{M_1\}_{12x1} = 2\pi \int_A [B_e]^T_{12x4} \cdot \{\sigma_o\}_{4x1} \, x dA$

where

$$\{\sigma_o\} = \begin{Bmatrix} \sigma_{xo} \\ \sigma_{yo} \\ \sigma_{xyo} \\ \sigma_{zo} \end{Bmatrix} = \text{initial effective stresses}$$

The initial effective stresses are extrapolated from the external nodes, which are input of the program. Therefore:

$$\{\sigma_o\} = \begin{bmatrix} \sigma_{x1} & \sigma_{x2} & \sigma_{x3} \\ \sigma_{y1} & \sigma_{y2} & \sigma_{y3} \\ \sigma_{xy1} & \sigma_{xy2} & \sigma_{xy3} \\ \sigma_{z1} & \sigma_{z2} & \sigma_{z3} \end{bmatrix} \begin{Bmatrix} \rho_1 \\ \rho_2 \\ \rho_3 \end{Bmatrix}$$

σ_{xi}, σ_{yi}, σ_{xyi} and σ_{zi} are the nodal values of the initial effective stresses.

Similarly to the numerical integrations previously executed herein, the integrants of $\{M_1\}$ are obtained with the four-point formula:

$$\{M_1\} = 2\pi A \sum_1^4 [B_e]^T_i \{\sigma_o\} x_i W_i$$

where, similarly to previous derivations, the subscript i,

of the matrices, indicates the value of that matrix evaluated at the sampling point.

2nd Case - Plane Strain Formulation

$\{M_1\}_{12x1} = \text{width} \int_A [B_e]_{12x3}\{\sigma_o\}_{3x1} dA$

where,

$$\{\sigma_o\} = \begin{Bmatrix} \sigma_{xo} \\ \sigma_{yo} \\ \sigma_{xyo} \end{Bmatrix} = \text{initial effective stresses}$$

Similarly to the axisymmetric case, the effective stresses are assumed to vary linearly within the element:

$$\{\sigma_o\} = \begin{Bmatrix} \sigma_{xo} \\ \sigma_{yo} \\ \sigma_{xyo} \end{Bmatrix} = \begin{bmatrix} \sigma_{x1} & \sigma_{x2} & \sigma_{x3} \\ \sigma_{y1} & \sigma_{y2} & \sigma_{y3} \\ \sigma_{xy1} & \sigma_{xy2} & \sigma_{xy3} \end{bmatrix} \begin{Bmatrix} \rho_1 \\ \rho_2 \\ \rho_3 \end{Bmatrix}$$

σ_{xi}, σ_{yi} and σ_{xyi} are the nodal values of the initial effective stresses.

The simplicity of the polynomials that compose $\{M_1\}$, for the 2D case, made possible the use of direct integration.

$\{M_2\}$ (soil total unit weight matrix)

$\{M_2\} = \int_V [N]^T \{\rho_s F_i\} dV$

Two cases are to be considered:

1st Case: Axisymmetric Formulation

$\{M_2\} = 2\pi \int_A [N]^T_{12x2} \{\rho_s F_i\}_{2x1} x dA$

where,

$$\{\rho_s F_i\} = \int \begin{bmatrix} F_x \\ F_y \end{bmatrix}$$

F_x, F_y = total unit weight in the x and y directions.

In the present derivation, the unit weight is assumed to vary quadratically within the element. Therefore,

$$\begin{bmatrix} F_x \\ F_y \end{bmatrix}_{2x1} = [N]_{2x12} \cdot \begin{Bmatrix} \gamma_1 G_x \\ \gamma_2 G_x \\ \gamma_3 G_x \\ \gamma_4 G_x \\ \gamma_5 G_x \\ \gamma_6 G_x \\ \gamma_1 G_y \\ \gamma_2 G_y \\ \gamma_3 G_y \\ \gamma_4 G_y \\ \gamma_5 G_y \\ \gamma_6 G_y \end{Bmatrix}_{12x1}$$

where, γ_i = values of unit weight at the nodal points i, which are part of the program input.

G_x = cosine of the angle between direction of gravity and the x-axis.

G_y = sine of the angle between the direction of gravity and the x-axis.

The components of $\{M_2\}$ are polynomials of up to the 3rd degree (complete) which can also be integrated with the four-point formula:

$$\{M_2\} = 2\pi A \cdot \left[\sum_{1}^{4} [N]^T_{12x2} \cdot [N]_{i\ 12x12}\ W_i x_i\right]_{12x2} \begin{Bmatrix} \gamma_i G_x \\ \gamma_i G_y \end{Bmatrix}_{12x1}$$

The subscript, i, in the 12x12 matrix indicates the value of that matrix evaluated at the sampling point.

2nd Case - Plane Strain Formulation

$\{M_2\} = \text{width} \int_A [N]^T \{\rho_s F_i\} dA$

In this case, the simplicity of the polynomials of $\{M_2\}$ allowed the use of direct integration for the evaluation of its components:

$$\{M_2\} = \text{width} \left[\int [N]^T [N]\ dA\right] \begin{Bmatrix} \gamma_i G_x \\ \gamma_i G_y \end{Bmatrix}$$

$\{M_3\}$ (water unit weight matrix)

$\{M_3\} = \int_V [B_q]^T [R] \{\rho_w F_i\}\ dV$

where $\{\rho_w F_i\} = \begin{Bmatrix} \gamma_w G_x \\ \gamma_w G_y \end{Bmatrix}$

Here, similarly to the procedure followed for the evaluation of $[K_2]$, two cases are to be considered:

1st Case - Constant Coefficient of Permeability

For both formulations, i.e. axisymmetric and plane strain, it was possible to obtain the components of $\{M_3\}$ through direct integration:

Axisymmetric:

$$\{M_3\}_{3x1} = 2\pi\gamma_w [B_q]^T [R]\ (\int_A x dA) \cdot \begin{bmatrix} G_x \\ G_y \end{bmatrix}_{2x1}$$

Plane Strain:

$$\{M_3\}_{3x1} = \text{width}\ \gamma_w\ [B_q]^T[R](\int_A dA).\begin{bmatrix}G_x\\G_y\end{bmatrix}_{2x1}$$

2nd Case - Variable Coefficient of Permeability

In this case, since the matrix [R] is not constant within the element, the integration of the components of $\{M_3\}$ has to be performed numerically. For the sake of consistency with the previous numerical integrations performed in CONGAS, the four-point formula is used again:

Axisymmetric:

$$\{M_3\} = 2\pi\gamma_w A\left[\sum_1^4 W_i[B_q]_i[R]_i\ x_i\right]\begin{Bmatrix}G_x\\G_y\end{Bmatrix}$$

Plane Strain:

$$\{M_3\} = \text{width}\ \gamma_w A\left[\sum_1^4 W_i[B_q]_i[R]_i\ \right]\begin{Bmatrix}G_x\\G_y\end{Bmatrix}$$

{T} (surface traction matrix)

$$\{T\}_{12x1} = \int_{St}[N]^T_{12x2}\{\bar{T}_i\}_{2x1}\ dS$$

where,

$$\{\bar{T}_i\} = \begin{bmatrix}\bar{T}_x\\\bar{T}_y\end{bmatrix} = [N]_{2x12}\ .\ \{SIG_i\}_{12x1}$$

SIG_i are the surface stresses at the element nodal points. However, in order to simplify the procedure of data input in CONGAS, surface tractions are applied only to the side to the element composed on nodes 2-5-3.

Figure B5 illustrates the surface traction matrix {T}. Since only the side 2-5--3 of the element is submitted to tractions, according to Figure B5 it follows:

$$T_1, T_4, T_6, T_7, T_{10}, T_{11} = 0$$

Two cases are to be considered for the solution of integration of the non-zero terms of {T}:

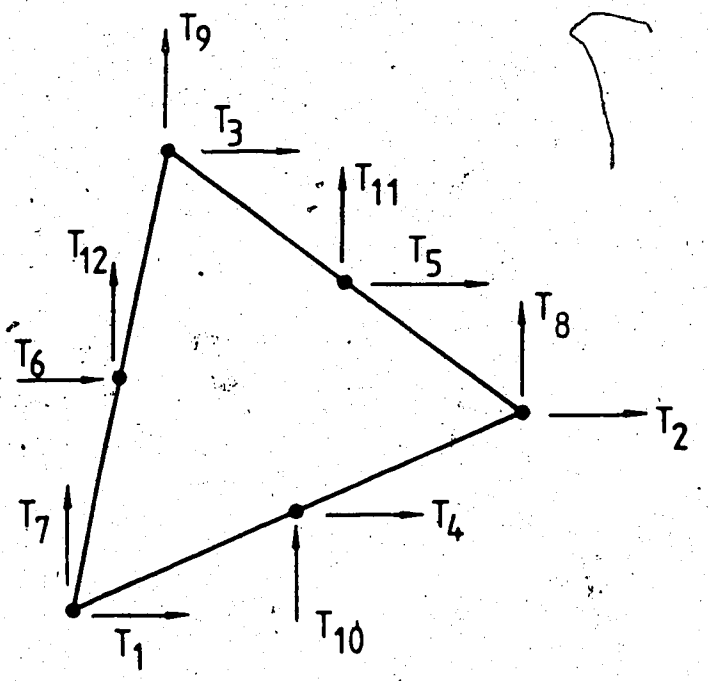

surface tractions = $\{T\}_{12\times 1}$

Figure B.5 Surface Tractions

1st Case: Axisymmetric Formulation

$$\{T\}_{12x1} = 2\pi \int_{1t} [N]^T_{12x2} [N]_{2x12} \{SIG_i\}_{12x1} \times dl$$

Since along side 2-5-3 $\rho_1=0$ and $\rho_2=1-\rho_3$, it is possible to express all the elements of the equation above in terms of ρ_3. The highest polynomial found after the multiplication of the terms of the equation above is of order 5. According to Bathe, 1983:273, a polynomial of 5th degree can be integrated exactly with 5 sampling points, equally spaced along side 2-5-3, according to the Newton-Cotes method. Figure B6 illustrates this integration procedure. Therefore, the following equation can be obtained.

$$\{T\}_{12x1} = 2\pi l_{2-3} \left[\sum_{i=1}^{5} [N]^T_i [N]_i x_i W_i \right]_{12x12} \{SIG_i\}_{12x1}$$

where l_{2-3} is the length of side 2-5-3.

2nd Case: Plane Strain Formulation

$$\{T\}_{12x1} = \text{width} \left[\int_{1t} [N]^T_{12x2} [N]_{2x12} \, dl \right] \{SIG_i\}_{12x1}$$

In this case, the integration of the non-zero terms of {T} were performed with direct integration.

{Q} (boundary flow matrix)

$$\{Q\} = \int_{sb} \{\phi_u\} \bar{q} \, dS$$

where $\bar{q}$ is assumed to vary linearly along the sides of the element. Thus:

$$\bar{q} = \langle \phi_u \rangle \begin{bmatrix} q_1 \\ q_2 \\ q_3 \end{bmatrix}$$

and the boundary flow matrix can be rewritten:

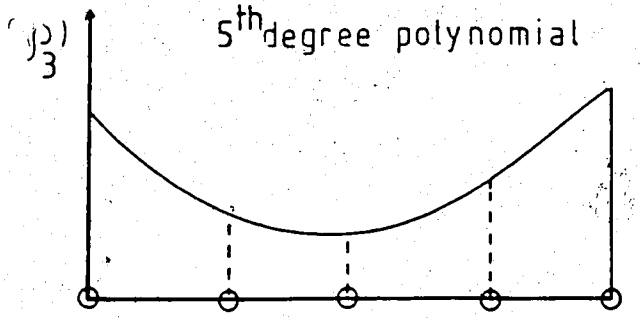

NODAL POINT	2		5		3
SAMPLING POINT	I	II	III	IV	V
p_3	1	0.75	0.5	0.25	0
WI	7/90	32/90	12/90	32/90	7/90

$$\int f(p_3)\, dp_3 = L_{2\text{-}5\text{-}3} \sum_{i=1}^{5} (W_i\ f(p_3)_i)$$

Figure B.6 Numerical Integration along Side 2-5-3 - Newton-Cotes

$$\{Q\}_{3x1} = \left[\int_{sq}\{\phi_u\}_{3x1}\langle\phi_u\rangle_{1x3}dS\right]_{3x3}\{q_i\}_{3x1}$$

There are two cases to be considered herein:

1st Case - Axisymmetric Formulation

$$\{Q\}_{3x1} = 2\pi\left[\int_{lq}\{\phi_u\}_{3x1}\langle\phi_u\rangle_{1x3} \times dl\right]\{q_i\}_{3x1}$$

In CONGAS, the evaluation of the boundary flow matrix is performed separately for each side of the triangle. By following this procedure, one of the terms of $\{q_i\}$ and one of the area coordinates becomes zero, along the side of the element being considered. It is, therefore, possible to express the terms of the $\{Q\}$ matrix as a function of only one area coordinate. The resulting polynomials, components of $\{Q\}$ were directly integrated in CONGAS.

2nd Case: Plane Strain Formulation

$$\{Q\}_{3x1} = \text{width}\left[\int_{lq}\{\phi_u\}_{3x1}\langle\phi_u\rangle_{1x3}\,dl\right]\{q_i\}_{3x1}$$

Similarly to the axisymmetric case, the integration of the integrants of $\{Q\}$ were obtained through direct integration.

$\{\epsilon_v^{fg}\}_{t_{N-1}}^{t_N}$ (gas volumetric strain matrix)

$$\{\epsilon_v^{fg}\}_{t_{N-1}}^{t_N} = \int_V \{\phi_u\}_{3x1}\epsilon_v^{fg}\Big|_{tN-1}^{tN} dV$$

$\epsilon_v^{fg}\Big|_{tN-1}^{tN}$ is assumed to vary linearly within the element, therefore it can be expressed in terms of the external node values $\{\bar{\epsilon}_{vi}^{fg}\}_{tN-1}^{tN}$:

$$\epsilon_v^{fg}\Big|_{tN-1}^{tN} = \langle\phi_u\rangle_{1x3}\{\bar{\epsilon}_{vi}^{fg}\}_{tN-1\ 3x1}^{tN}$$

and the gas volumetric strain matrix can be expressed as:

$$\{\epsilon_v^{fg}\}_{t_{N-1}}^{t_N} = \left(\int_{lq}\{\phi_u\}_{3x1}<\phi_u>_{1x3}\, dV\right) \cdot \{\bar{\epsilon}_{vi}^{fg}\}_{tN-1}^{tN}$$

Two cases are to be considered:

1st Case: Axisymmetric Formulation

$$\{\epsilon_v^{fg}\}_{t_{N-1}}^{t_N} = 2\pi\left(\int_A \{\phi_u\}_{3x1}<\phi_u>_{1x3} \times dA\right) \cdot \{\bar{\epsilon}_{vi}^{fg}\}_{tN-1}^{tN}$$

Due to its simple form, the polynomials of the matrix above were integrated exactly.

2nd Case: Plane Strain Formulation

$$\{\epsilon_v^{fg}\}_{t_{N-1}}^{t_N} = \text{Width}\left(\int_A \{\phi_u\}_{3x1}<\phi_u>_{1x3}\, dA\right) \cdot \{\bar{\epsilon}_{vi}^{fg}\}_{tN-1}^{tN}$$

Similarly to the axisymmetric case, the equation above was developed by direct integration.

[E] (Liquid Compressibility Matrix)

$$[E] = \int 1/Q\, \{\phi_u\}_{3x1}<\phi_u>_{1x3} dV$$

According to the derivation presented in Section 3.3.3, the combined liquid compressibility is evaluated as a function of the individual compressibility of the liquids, the initial void ratios and the initial degree of saturation. Since the initial values of void ratios and degrees of saturation vary within the element, for the sake of simplicity it was assumed that the combined liquid compressibility within the element can be evaluated from the

combined liquid compressibilities evaluated at the three external nodes of the element:

$$\frac{1}{Q} = \langle \phi_u \rangle \{1/\bar{Q}_i\}$$

There are two cases to be considered:

1st Case: Axisymmetric Formulation

$$[E] = 2\pi \int_A 1/Q \{\phi_u\} \langle \phi_u \rangle \, x \, dA$$

The four-point formula is used here once more to integrate the components of [E]:

$$[E] = 2\pi A . \sum_1^4 (1/Q)_i \{\phi_u\}_i \langle \phi_u \rangle_i x_i W_i$$

Plane Strain Formulation

$$[E] = \text{width} \int_A (1/Q) \{\phi_u\} \langle \phi_u \rangle dA$$

For the sake of consistency, the same four-point formula is used again:

$$[E] = \text{Width} . A . \sum_{i=1}^4 (1/Q)_i \{\phi_u\}_i \langle \phi_u \rangle_i W_i$$

B.3 Specification of Boundary Conditions in CONGAS

Two types of boundary conditions can be specified in CONGAS:

- boundary displacements
- boundary pore pressures

The procedures followed to numerically impose these boundaries are described in the following sections:

SPECIFIED DISPLACEMENTS

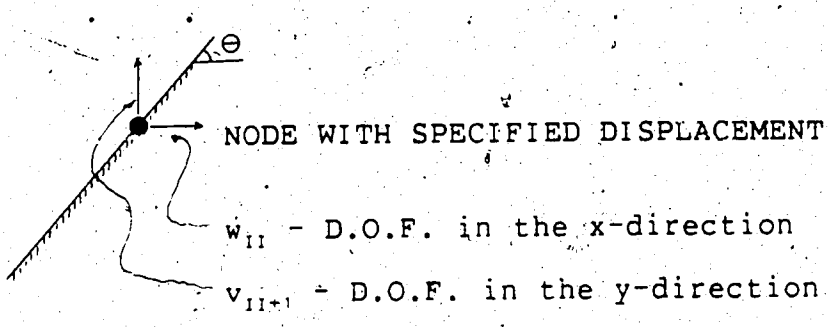

For $0<\theta<90$ (inclined boundary)

$$\begin{bmatrix} \ddots & & \\ & A(LL1)\ A(LL2) & \\ & & A(LL2+1) \\ & & \ddots \end{bmatrix} \begin{Bmatrix} \\ W_{II} \\ V_{II+1} \\ \\ \end{Bmatrix} = \begin{Bmatrix} \\ F_{II} \\ F_{II+1} \\ \\ \end{Bmatrix} \begin{matrix} \\ \leftarrow \text{Equation II} \\ \leftarrow \text{Equation II+1} \\ \\ \end{matrix}$$

stiffness matrix × displacement vector

Assuming tht $v_{II+1} = W_{II} \tan\theta$, the stiffness matrix can be rearranged as follows:

Equation II:

$$..... + A(LL1) \cdot W_{II} + A(LL2).V_{II+1} + ... = F_{II}$$

and

$$..... + (A(LL1) + A(LL2)\tan\theta).W_{II} + 0.V_{II+1} + ... = F_{II}$$

Equation II+1:

$$..... + A(LL2) \cdot W_{II} + A(LL2+1).V_{II+1} + ... = F_{II+1}$$

which can be modified into

$$..... + A(LL2).V_{II+1}/\tan\theta) + A(LL2+1).V_{II+1} + ... = F_{II+1}$$

and finally,

$$..... + 0.W_{II} + \left[A(LL2)/\tan\theta + A(112+1)\right].V_{II+1} + ... = F_{II+1}$$

Therefore the new modified components of the stiffness matrix are:

$$A(LL1) = A(LL1) + A(LL2).\tan\theta$$

$$A(LL2) = 0$$

$$A(LL2+1) = A(LL2)/\tan\theta + A(LL2+1)$$

For $\theta = 0$ or $90°$, the components of the finite element equation are modified as follows

$$\begin{bmatrix} \ddots & & \\ & 0 & \\ & 0 & \\ & 1\,0\,0\,0 & \end{bmatrix} \times \begin{bmatrix} \\ W \\ \\ \end{bmatrix} = \begin{bmatrix} \\ 0 \\ \\ \end{bmatrix} \longleftarrow \text{D.O.F. with displac. = 0}$$

SPECIFIED PORE PRESSURES

For the inclusion of known pore pressures, the finite element equations are modified as follows:

$$\begin{bmatrix} \ddots & & \\ & 0 & \\ & 0 & \\ & 1000 & \end{bmatrix} \times \begin{bmatrix} \\ r(II) \\ \\ \end{bmatrix} = \begin{bmatrix} \\ AUP(II) \\ \\ \end{bmatrix} \quad * = AUP(LJ) = AUP(LJ) - r(II).K(II,J)$$

column II

where,

AUP(II) = known pore pressure

K(II,LJ) = components of the stiffness matrix, as indicated

r(II) = pore pressure d.o.f. with known pore pressure

APPENDIX C - LABORATORY TEST DATA

STEP	CELL PRESSURE (KPA)		PORE PRESSURE (KPA)		VOLUME FREE GAS (CC)		DEGREE OF SATURATION		SCALLING PARAMETER	
	INITIAL	FINAL	INITIAL	FINAL	INITIAL	FINAL	INITIAL	FINAL	A' (MIN)	E (1/MIN)
A	188.65	138.80	164.43	139.42	0.390326	1.074101	0.9885	0.9691	2707.95	0.000310
B	138.80	109.19	139.42	108.72	1.074101	2.020687	0.9691	0.9433	744.37	0.000240
C	109.19	65.71	108.72	64.92	2.020687	3.721877	0.9433	0.9004	154.93	0.000771

Table C.1 Mercury Triaxial Test - Sample 3-1

GAUGE PORE PRESSURE (KPA) (1)	ABSOLUTE PORE PRESSURE (KPA) (2)	VOLUME OF FREE GAS (CC) (3)	VOLUME OF FREE GAS AT PATM (CC) (4)	(4)/VL (*) (5)	CHANGE IN (5) (6)	CHANGE IN (2) (7)	SOLUBILITY COEFFICIENT (8)
164.43	265.76	0.390326	1.0237	0.0304			
					0.0454	25.01	0.1839
139.42	240.75	1.074101	2.5520	0.0759			
					0.0487	30.70	0.1606
108.72	210.05	2.020687	4.1888	0.1245			
					0.0570	43.80	0.1318
64.92	166.25	3.721877	6.1065	0.1816			

(*)...VL = VOLUME OF PORE LIQUIDS = 33.63 CC

Table C.2 Mercury Triaxial Test - Sample 3-1 - Calculus of Solubility Coefficient

		QUOTIENT+1 FIT			EXPONENTIAL FIT		
STEP	V2 MEASURED (CC)	A' (MIN)	V2 PROJECTED (CC)	CORRELATION COEFFICIENT	E (1/MIN)	V2 PROJECTED (CC)	CORRELATION COEFFICIENT
A	1.0741	2707.9480	1.1450	0.8318	0.000310	0.9506	0.7207
B	2.0207	744.3733	2.0316	0.9684	0.000240	2.2923	0.9676
C	7.7219	145.9439	3.7436	0.9999	0.000771	4.2295	0.8119

Table C.3 Mercury Triaxial Test - Sample 3-1 - Test Data Regression

STEP	CELL PRESSURE (KPA)		PORE PRESSURE (KPA)		VOLUME FREE GAS (CC)		DEGREE OF SATURATION		SCALING PARAMETER	
	INITIAL	FINAL	INITIAL	FINAL	INITIAL	FINAL	INITIAL	FINAL	A' (MIN)	E (1/MIN)
-	597.49	549.28	587.36	540.66	0.226633	0.425299	0.9937	0.9883	*	*
-	549.28	494.45	540.66	487.49	0.425299	0.684260	0.9883	0.9812	*	*
-	494.45	444.27	487.49	440.54	0.684260	0.940075	0.9812	0.9744	*	*
-	444.27	399.17	440.54	398.45	0.940075	1.223545	0.9744	0.9676	*	*
-	399.17	351.11	398.45	352.08	1.223545	1.691005	0.9676	0.9549	*	*
A	351.11	308.54	352.08	313.15	1.691005	2.349831	0.9549	0.9384	279.79	0.001801
B	308.54	268.93	313.15	174.38	2.349831	3.302765	0.9384	0.9155	512.04	0.001101
C	268.93	227.92	274.38	232.86	3.302765	4.684359	0.9155	0.8843	763.51	0.000246
D	227.92	180.42	232.86	186.64	4.684359	6.778456	0.8843	0.8408	862.58	0.000597
E	180.42	132.35	186.64	139.78	6.778456	9.575361	0.8408	0.7890	983.33	0.000328

* - SCALING PARAMETERS COULD NOT BE APPROPRIATELY EVALUATED AT THESE STEPS

Table C.4 Mercury Triaxial Test - Sample 6-5

Table C.5 Mercury Triaxial Test - Sample 6-5 - Evaluation of Solubility Coefficient

GAUGE PORE PRESSURE (KPA) (1)	ABSOLUTE PORE PRESSURE (KPA) (2)	VOLUME OF FREE GAS (CC) (3)	VOLUME OF FREE GAS AT PATM (CC) (4)	(4)/VL (*) (5)	CHANGE IN (5) (6)	CHANGE IN (2) (7)	SOLUBILITY COEFFICIENT (8)
549.28	650.61	0.425299	2.7302	0.0763			
					0.0361	54.83	0.0667
494.45	595.78	0.684260	4.0233	0.1124			
					0.0290	50.18	0.0586
444.27	545.60	0.940075	5.0619	0.1414			
					0.0274	45.10	0.0616
399.17	500.50	1.223545	6.0437	0.1688			
					0.0421	48.06	0.0888
351.11	452.44	1.691005	7.5507	0.2109			
					0.0546	42.57	0.1300
308.54	409.86	2.349831	9.5052	0.2655			
					0.0716	39.61	0.1832
268.93	370.26	3.302765	12.0687	0.3371			
					0.0881	41.01	0.02177
227.92	329.25	4.684359	15.2213	0.4252			
					0.1013	47.50	0.2161
180.42	281.75	6.778456	18.8482	0.5265			
					0.0903	48.07	0.1903
132.35	233.68	9.575361	22.0826	0.6168			

(*)...VL = VOLUME OF PORE LIQUIDS = 35.80 CC

Table C.6 Mercury Triaxial Test - Sample 6-5 - Test Data Regression

		QUOTIENT+1 FIT			EXPONENTIAL FIT		
STEP	V2 MEASURED (CC)	A' (MIN)	V2 PROJECTED (CC)	CORRELATION COEFFICIENT	E (1/MIN)	V2 PROJECTED (CC)	CORRELATION COEFFICIENT
A	2.3498	279.7879	2.3760	0.9567	0.001801	2.3857	0.8706
B	3.3027	512.0430	3.3355	0.9542	0.001101	3.2422	0.8188
C	4.6844	763.5109	4.7326	0.9807	0.000246	4.9836	0.9516
D	6.7785	862.5757	6.8632	0.9755	0.000597	6.7329	0.9357
E	9.5754	983.3282	9.6140	0.9769	0.000328	9.7879	0.9617

STEP	CELL PRESSURE (KPA)		PORE PRESSURE (KPA)		VOLUME FREE GAS (CC)		DEGREE OF SATURATION		SCALLING PARAMETER	
	INITIAL	FINAL	INITIAL	FINAL	INITIAL	FINAL	INITIAL	FINAL	A' (MIN)	E (1/MIN)
-	310.79	253.63	296.33	245.06	0.326460	0.444657	0.9908	0.9875	*	*
-	253.63	203.93	245.06	198.62	0.444657	0.661334	0.9875	0.9815	*	*
A	203.93	162.29	198.62	157.75	0.661334	1.011034	0.9815	0.9719	1739.84	0.000785
B	162.29	113.70	157.75	105.24	1.011034	2.387884	0.9719	0.9361	3433.66	0.000278
C	113.70	82.85	105.24	76.73	2.387884	3.448895	0.9361	0.9102	1111.84	0.000296

Table C.7 Mercury Triaxial Test - Sample 9-2

Table C.8 Mercury Triaxial Test - Sample 9-2 - Evaluation of Solubility Coefficient

GAUGE PORE PRESSURE (KPA) (1)	ABSOLUTE PORE PRESSURE (KPA) (2)	VOLUME OF FREE GAS (CC) (3)	VOLUME OF FREE GAS AT PATM (CC) (4)	(4)/VL (*) (5)	CHANGE IN (5) (6)	CHANGE IN (2) (7)	SOLUBILITY COEFFICIENT (8)
245.06	346.39	0.444657	1.5201	0.0434			
					0.0125	46.44	0.0273
198.62	299.95	0.661334	1.9577	0.0559			
					0.0174	41.11	0.0429
157.51	258.84	1.004198	2.5652	0.0733			
					0.0640	52.27	0.1241
105.24	206.57	2.387884	4.8069	0.1373			
					0.0359	28.51	0.1276
76.73	178.06	3.448895	6.0606	0.1732			

(*)...VL = VOLUME OF PORE LIQUIDS = 35.00 CC

Table C.9 Mercury Triaxial Test - Sample 9-2 - Test Data

Regression

		QUOTIENT+1 FIT			EXPONENTIAL FIT		
STEP	V2 MEASURED (CC)	A' (MIN)	V2 PROJECTED (CC)	CORRELATION COEFFICIENT	E (1/MIN)	V2 PROJECTED (CC)	CORRELATION COEFFICIENT
A	1.0110	1739.840	1.1038	0.5021	0.000785	0.9812	0.9170
B	2.3879	3433.665	2.5667	0.8154	0.000278	2.1608	0.7828
C	3.4489	1111.837	3.5208	0.9555	0.000296	3.6212	0.9629

STEP	CELL PRESSURE (KPA)		PORE PRESSURE (KPA)		VOLUME FREE GAS (CC)		DEGREE OF SATURATION		SCALLING PARAMETER	
	INITIAL	FINAL	INITIAL	FINAL	INITIAL	FINAL	INITIAL	FINAL	A' (MIN)	E (1/MIN)
A	329.26	290.08	313.79	277.78	0.470602	0.965054	0.9883	0.9764	2150.11	0.000343
B	290.08	231.44	277.78	220.23	0.965054	1.713995	0.9764	0.9588	•	•
C	231.44	206.07	220.23	197.81	1.713995	2.267099	0.9588	0.9462	677.84	0.000384
D	206.07	146.87	197.81	140.99	2.267099	4.078717	0.9462	0.9072	984.07	0.000452
E	146.87	97.96	140.99	93.89	4.078717	6.274645	0.9072	0.8640	645.23	0.000395
F	97.96	52.43	93.89	50.42	6.274645	8.568137	0.8640	0.8231	251.73	0.000605

• - THIS STEP WAS ACCIDENTLY INTERRUPTED. DISREGARD DATA.

Table C.10 Mercury Triaxial Test - Sample 11-2

Table C.11 Mercury Triaxial Test - Sample 11-2 - Evaluation Solubility Coefficient

GAUGE PORE PRESSURE (KPA) (1)	ABSOLUTE PORE PRESSURE (KPA) (2)	VOLUME OF FREE GAS (CC) (3)	VOLUME OF FREE GAS AT PATM (CC) (4)	(4)/VL (*) (5)	CHANGE IN (5) (6)	CHANGE IN (2) (7)	SOLUBILITY COEFFICIENT (8)
313.79	415.12	0.470602	1.9280	0.0484			
277.78	379.11	0.965054	3.6108	0.0906	0.0422	36.01	0.1187
220.23	321.56	1.713995	**	**	**	**	**
197.81	299.14	2.267099	6.6930	0.1679	**	**	**
140.99	242.32	4.078717	9.7543	0.2447	0.0768	56.58	0.1375
93.89	195.22	6.274645	12.0892	0.3033	0.0586	47.10	0.1261
50.42	151.75	8.568137	12.8321	0.3219	0.0186	43.47	0.0434

(*)...VL = VOLUME OF PORE LIQUIDS = 39.86 CC
(**)..STEP B WAS ACCIDENTLY INTERRUPTED. DISREGARD DATA.

Table C.12 Mercury Triaxial Test - Sample 11-2 - Test Data Regression

		QUOTIENT+1 FIT			EXPONENTIAL FIT		
STEP	V2 MEASURED (CC)	A' (MIN)	V2 PROJECTED (CC)	CORRELATION COEFFICIENT	E (1/MIN)	V2 PROJECTED (CC)	CORRELATION COEFFICIENT
A	0.9651	2150.1100	1.0138	0.9121	0.000343	0.9205	0.9220
B	1.7952	•	•	•	•	•	•
C	2.27134	677.8477	2.2805	0.9854	0.000384	2.3621	0.9479
D	4.0787	984.0706	4.1561	0.9841	0.000452	4.0639	0.9151
E	6.2746	645.2276	6.3012	0.9870	0.000395	6.5828	0.9620
F	8.5681	251.7325	8.5921	0.9954	0.000605	8.9737	0.9352

STEP	CELL PRESSURE (KPA)		PORE PRESSURE (KPA)		VOLUME FREE GAS (CC)		DEGREE OF SATURATION		SCALLING PARAMETER	
	INITIAL	FINAL	INITIAL	FINAL	INITIAL	FINAL	INITIAL	FINAL	A' (MIN)	E (1/MIN)
A	446.95	400.72	428.00	386.88	0.014522	0.211546	0.9853	0.9803	318.37	0.000503
B	400.72	350.40	386.88	340.26	0.211516	0.641586	0.9803	0.9697	699.65	0.000629
C	350.40	294.44	340.26	299.39	0.641586	1.101669	0.9697	0.9585	328.38	0.000680
D	294.44	252.02	299.39	262.32	1.101669	1.701777	0.9585	0.9444	369.61	0.000664
E	252.02	201.70	262.32	212.22	1.701777	3.123286	0.9444	0.9126	441.15	0.000494
F	201.70	146.31	212.22	161.15	3.123286	5.401005	0.9126	0.8657	738.05	0.000627
G	146.31	100.36	161.15	117.28	5.401005	8.750028	0.8657	0.8050	621.48	0.000738

Table C.13 Mercury Triaxial Test - Sample 11-3

Table C.14 Mercury Triaxial Test - Sample 11-3 - Calculus of Solubility Coefficient

GAUGE PORE PRESSURE (KPA) (1)	ABSOLUTE PORE PRESSURE (KPA) (2)	VOLUME OF FREE GAS (CC) (3)	VOLUME OF FREE GAS AT PATM (CC) (4)	(4)/VL (*) (5)	CHANGE IN (5) (6)	CHANGE IN (2) (7)	SOLUBILITY COEFFICIENT (8)
497.36	598.69	0	0	0			
					0.0020	69.36	0.0029
428.00	529.33	0.014522	0.0759	0.0020			
					0.0245	41.12	0.0604
386.88	488.21	0.211516	1.0191	0.0265			
					0.0463	46.62	0.1006
340.26	441.59	0.641589	2.7961	0.0728			
					0.0406	40.87	0.1007
299.39	400.72	1.101669	4.3569	0.1134			
					0.0451	37.07	0.1233
262.32	336.65	1.701777	6.0908	0.1585			
					0.0930	50.10	0.1881
212.22	313.55	3.123286	9.6650	0.2515			
					0.1126	51.07	0.2234
161.15	262.48	5.402131	13.9941	0.3641			
					0.1271	43.87	0.2936
117.28	218.61	8.750028	18.8783	0.4912			

(*) VL = VOLUME OF PORE LIQUIDS = 38.43 CC

Table C.15 Mercury Triaxial Test - Sample 11-3 - Test Data Regression

		QUOTIENT+1 FIT			EXPONENTIAL FIT		
STEP	V2 MEASURED (CC)	A (MIN)	V2 PROJECTED (CC)	CORRELATION COEFFICIENT	E (1/MIN)	V2 PROJECTED (CC)	CORRELATION COEFFICIENT
A	0.2174	318.3749	0.2117	0.9797	0.000503	0.2711	0.8278
B	0.6454	699.6471	0.6611	0.9791	0.000626	0.6258	0.8331
C	1.1017	328.3836	1.1014	0.9814	0.000680	1.1776	0.9275
D	1.7048	369.6120	1.7092	0.9811	0.000664	1.7690	0.9372
E	3.1248	441.1506	3.1249	0.9869	0.000494	3.2999	0.9225
F	5.4191	738.0508	5.4530	0.9639	0.000627	5.4017	0.8473
G	8.7577	621.4760	8.8139	0.9874	0.000738	8.9051	0.7800

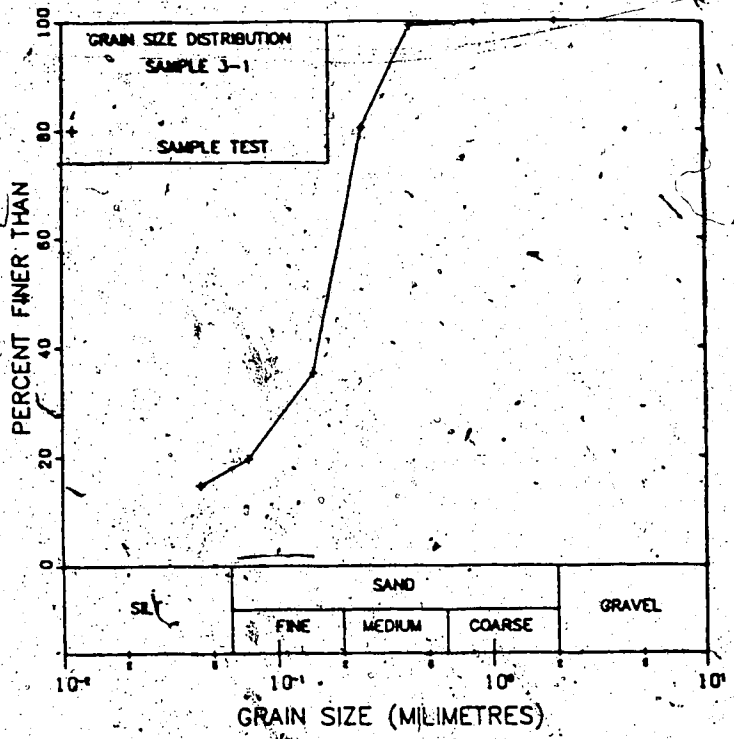

Figure C.1 Grain Size Distribution - Sample 3-1

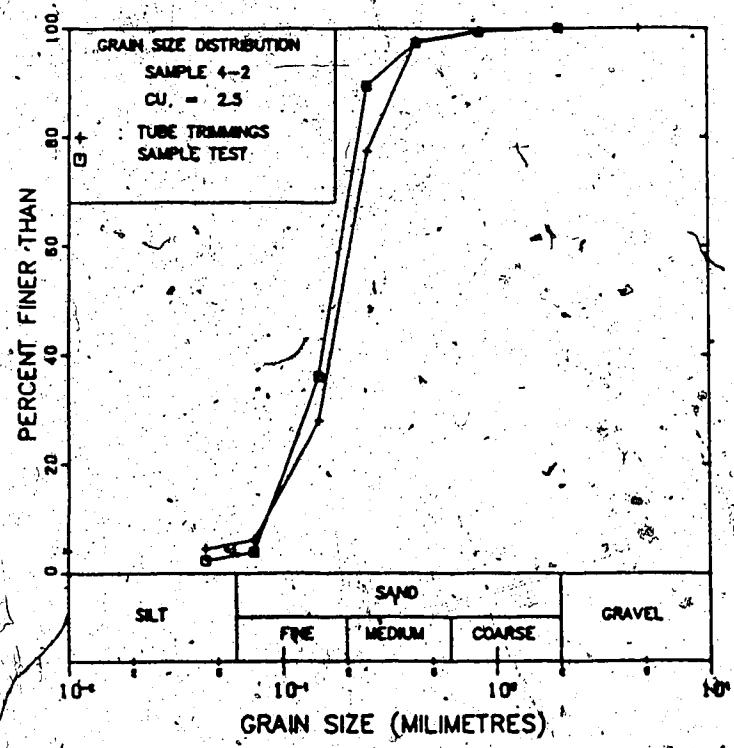

Figure C.2 Grain Size Distribution - Sample 4-2

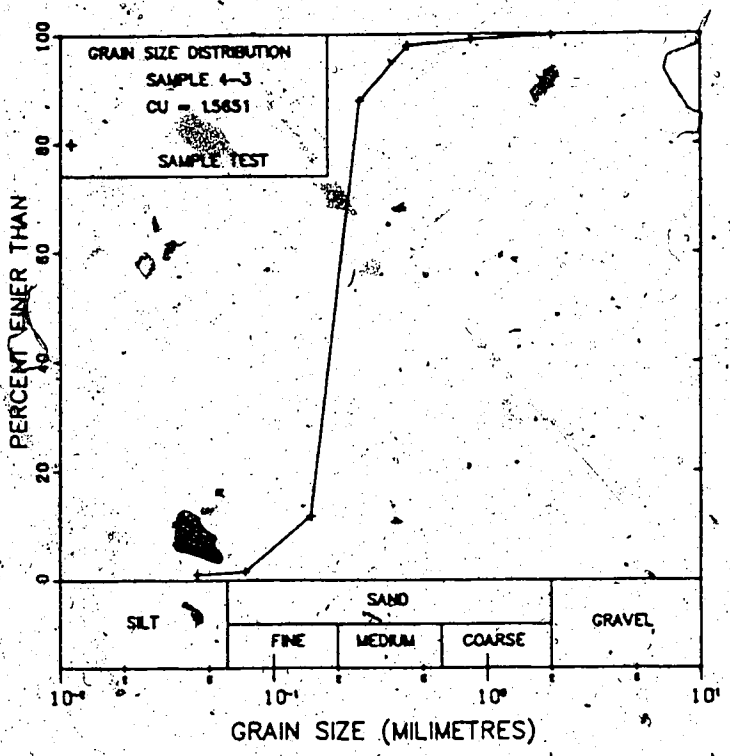

Figure C.3 Grain Size Distribution - Sample 4-3

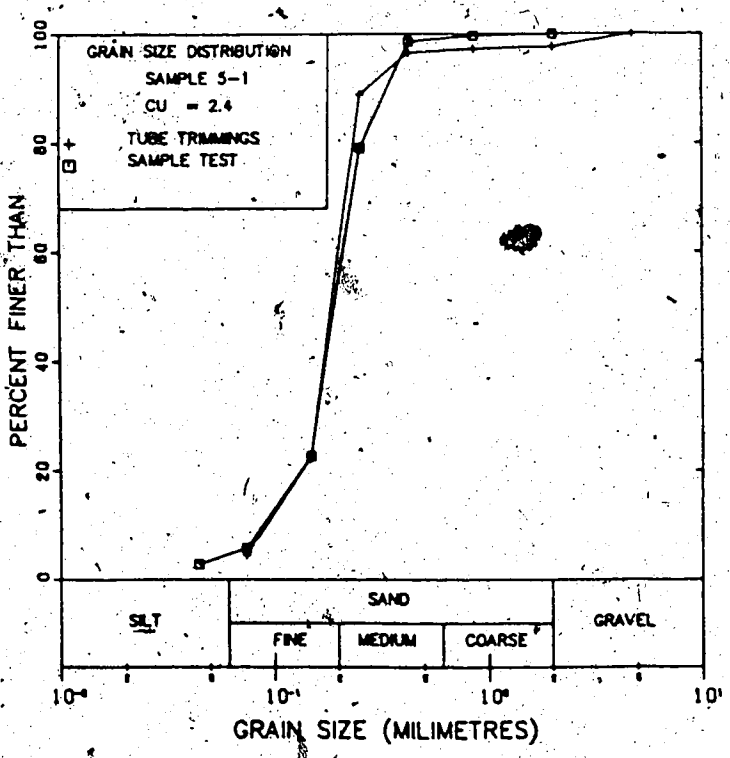

Figure C.4 Grain Size Distribution - Sample 5-1

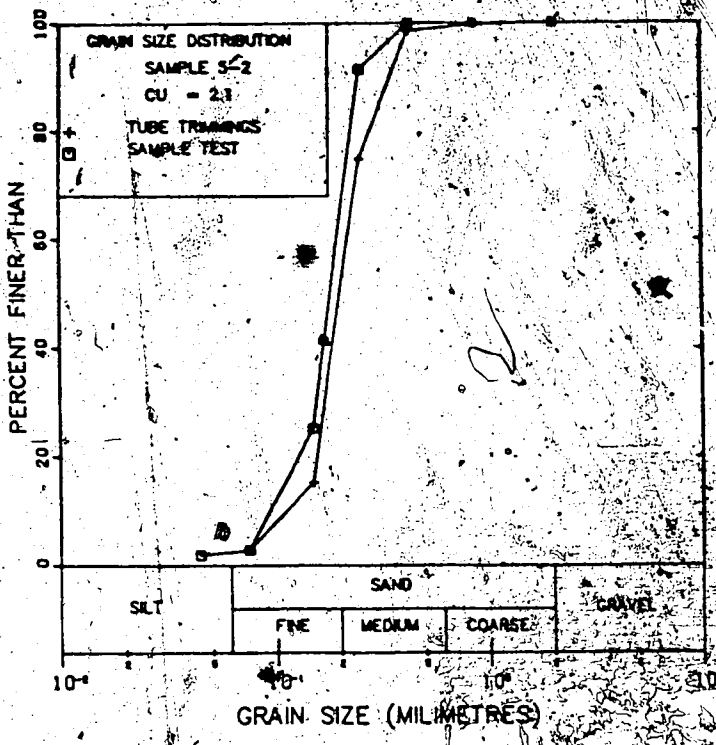

Figure C.5 Grain Size Distribution - Sample 5-2

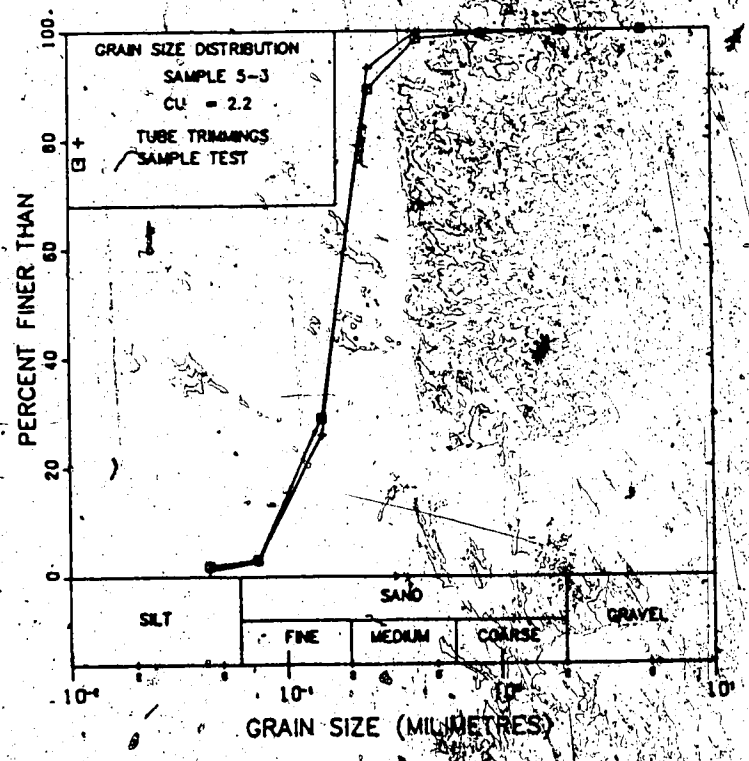

Figure C.6 Grain Size Distribution - Sample 5-3

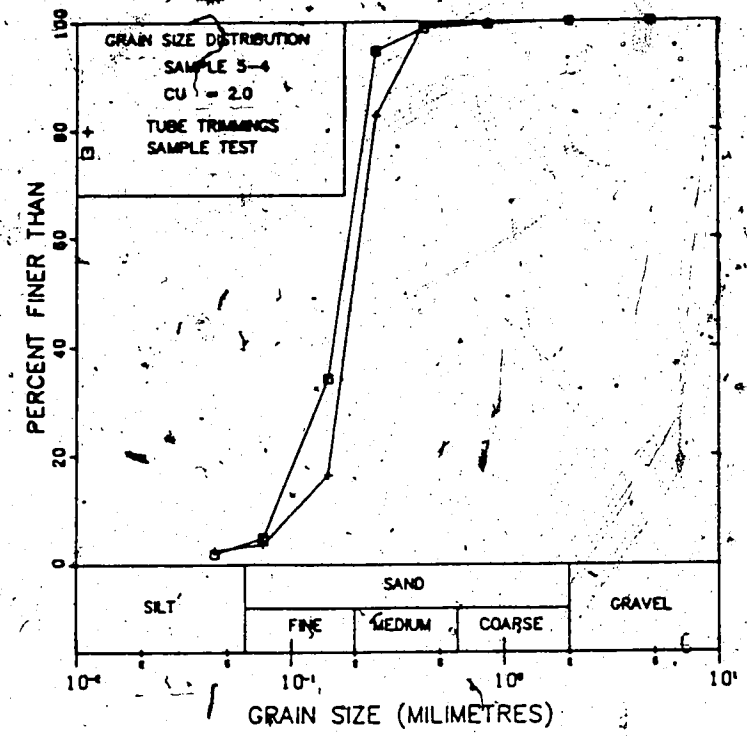

Figure C.7 Grain Size Distribution - Sample 5-4

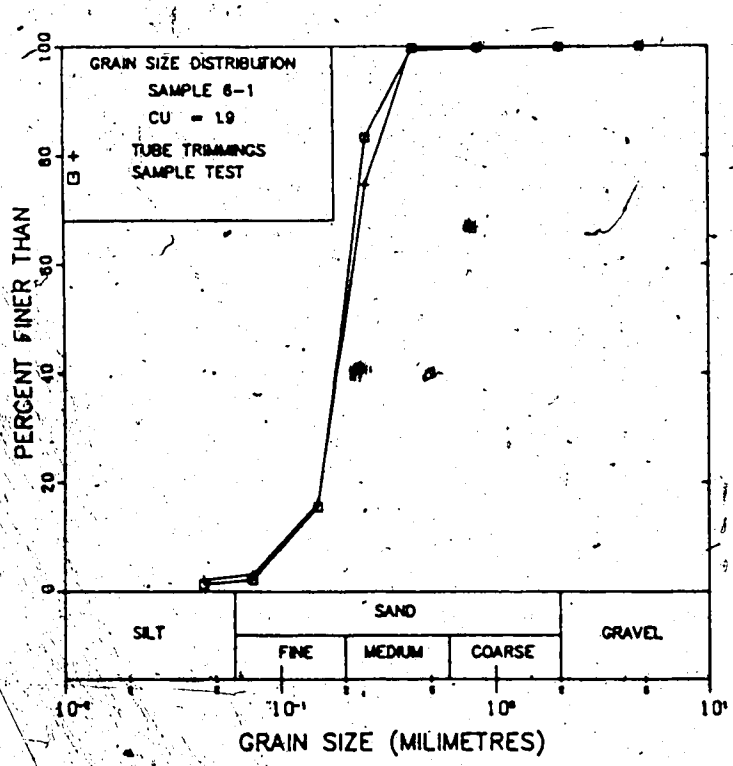

Figure C.8 Grain Size Distribution - Sample 6-1

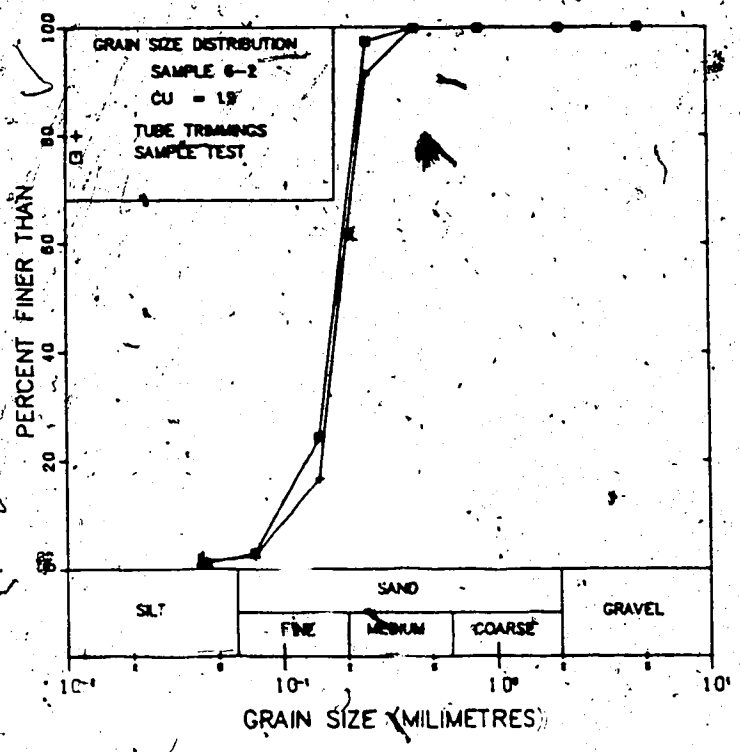

Figure C.9 Grain Size Distribution - Sample 6-2

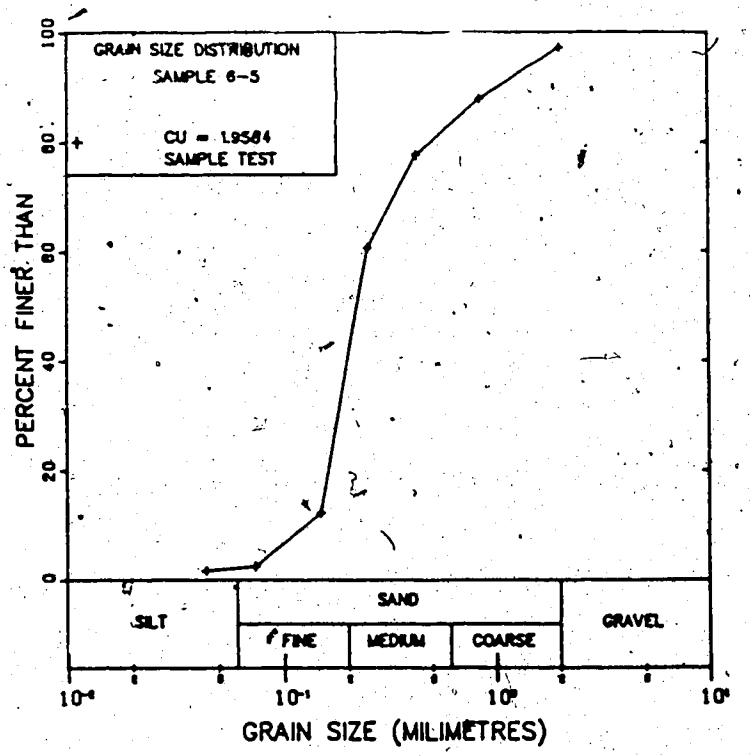

Figure C.10 Grain Size Distribution - Sample 6-5A

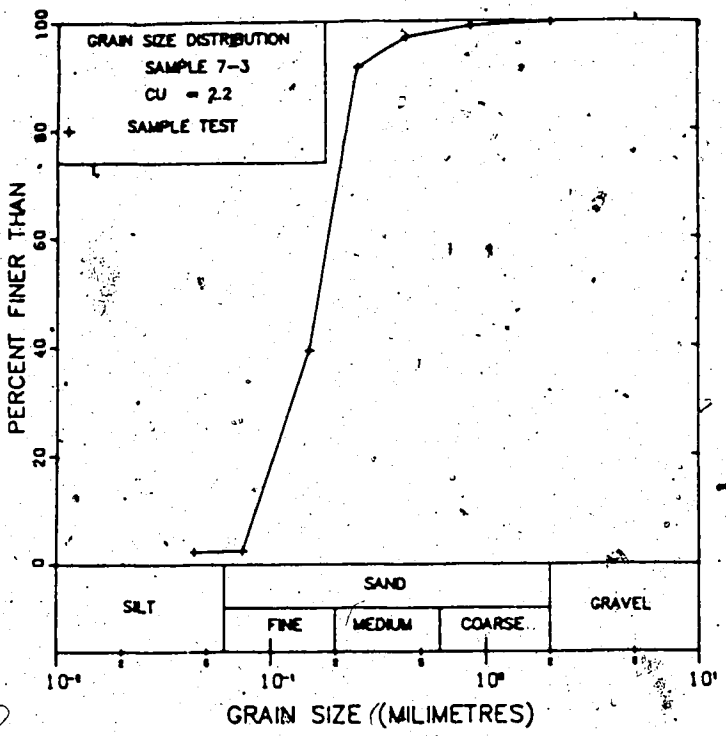

Figure C.11 Grain Size Distribution - Sample 7-3

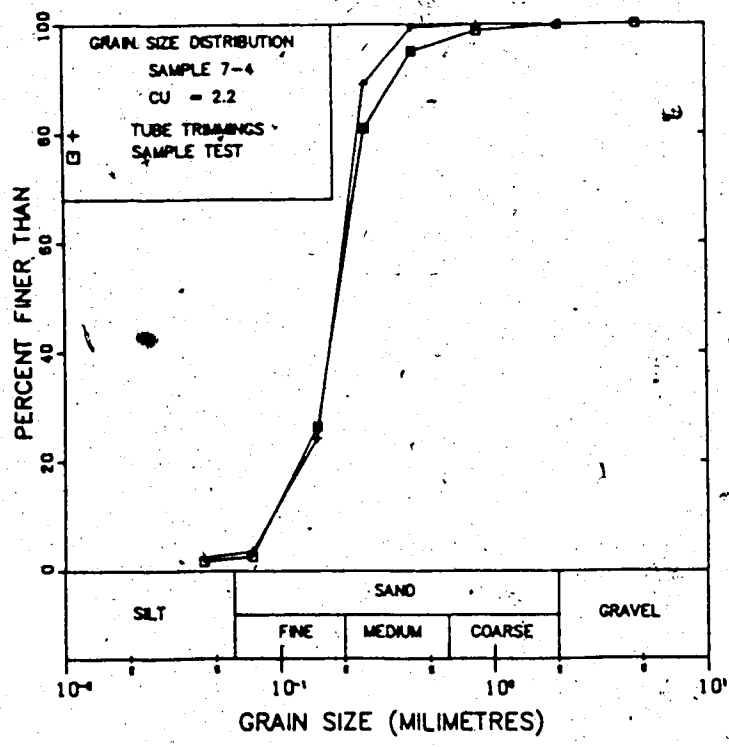

Figure C.12 Grain Size Distribution - Sample 7-4

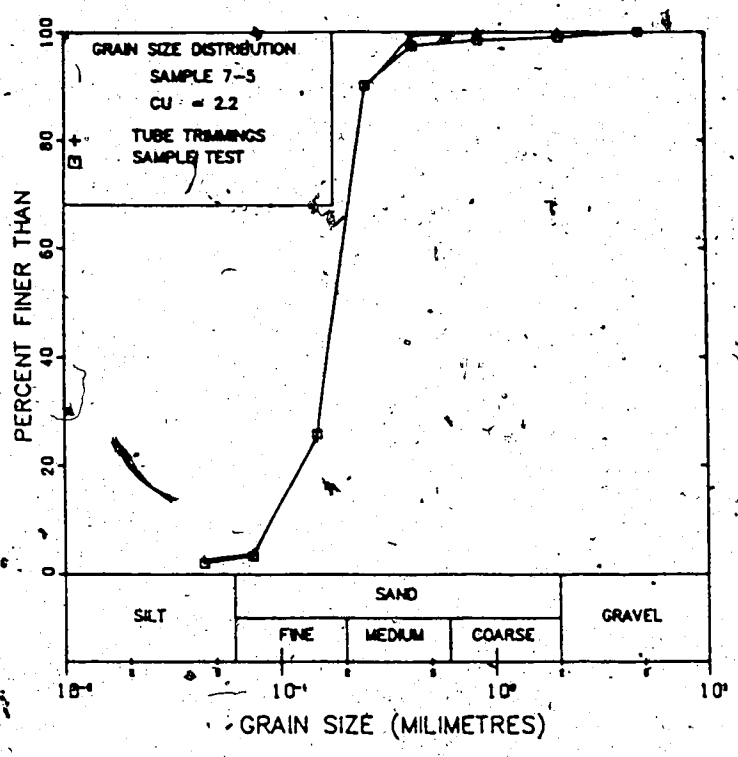

Figure C.13 Grain Size Distribution - Sample 7-5.

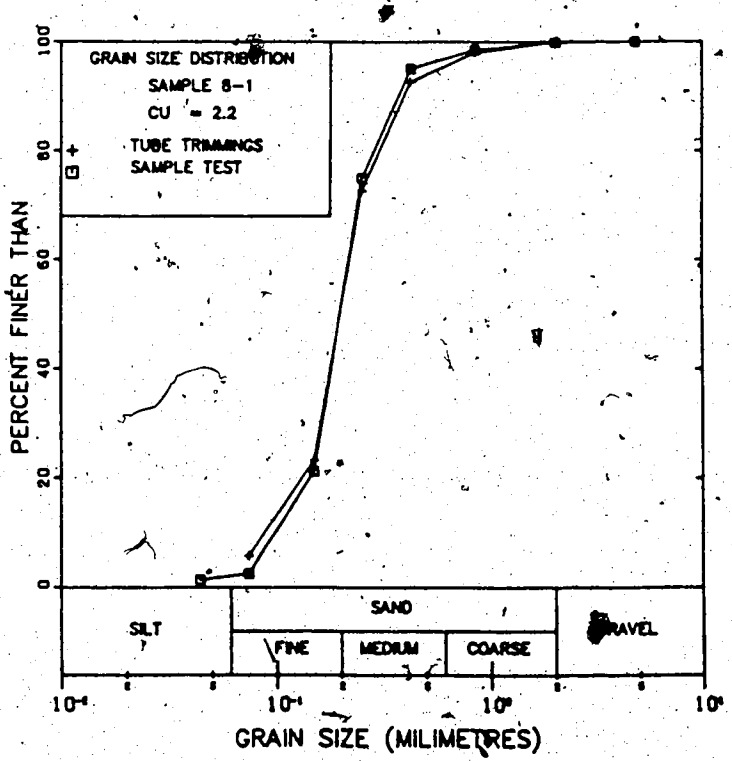

Figure C.14 Grain Size Distribution - Sample 8-1

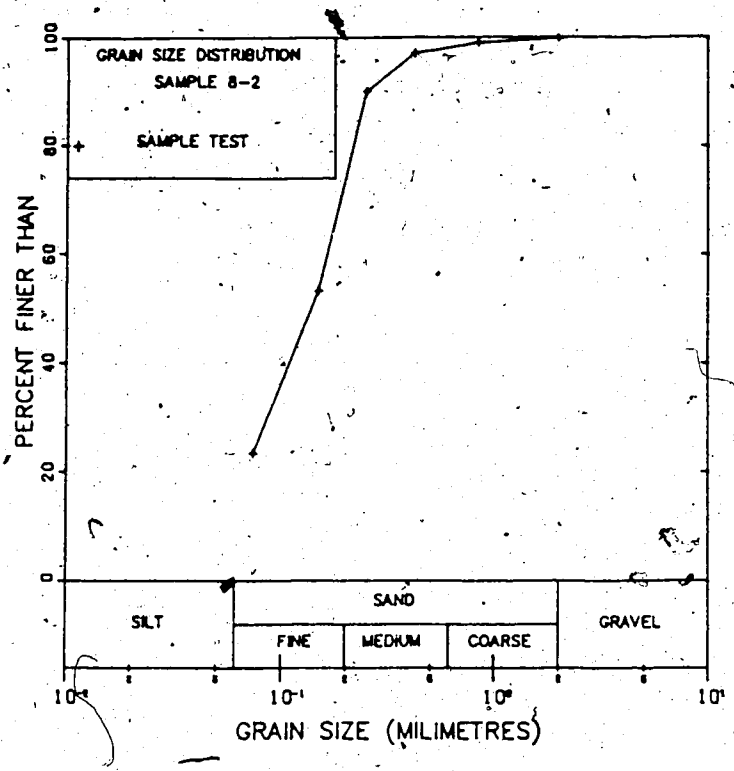

Figure C.15 Grain Size Distribution - Sample 8-2

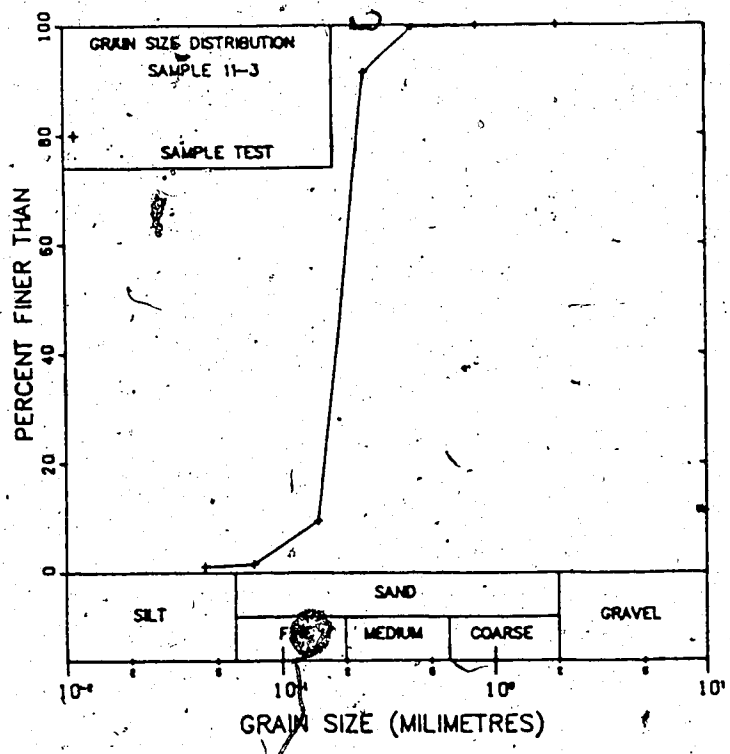

Figure C.16 Grain Size Distribution - Sample 11-3

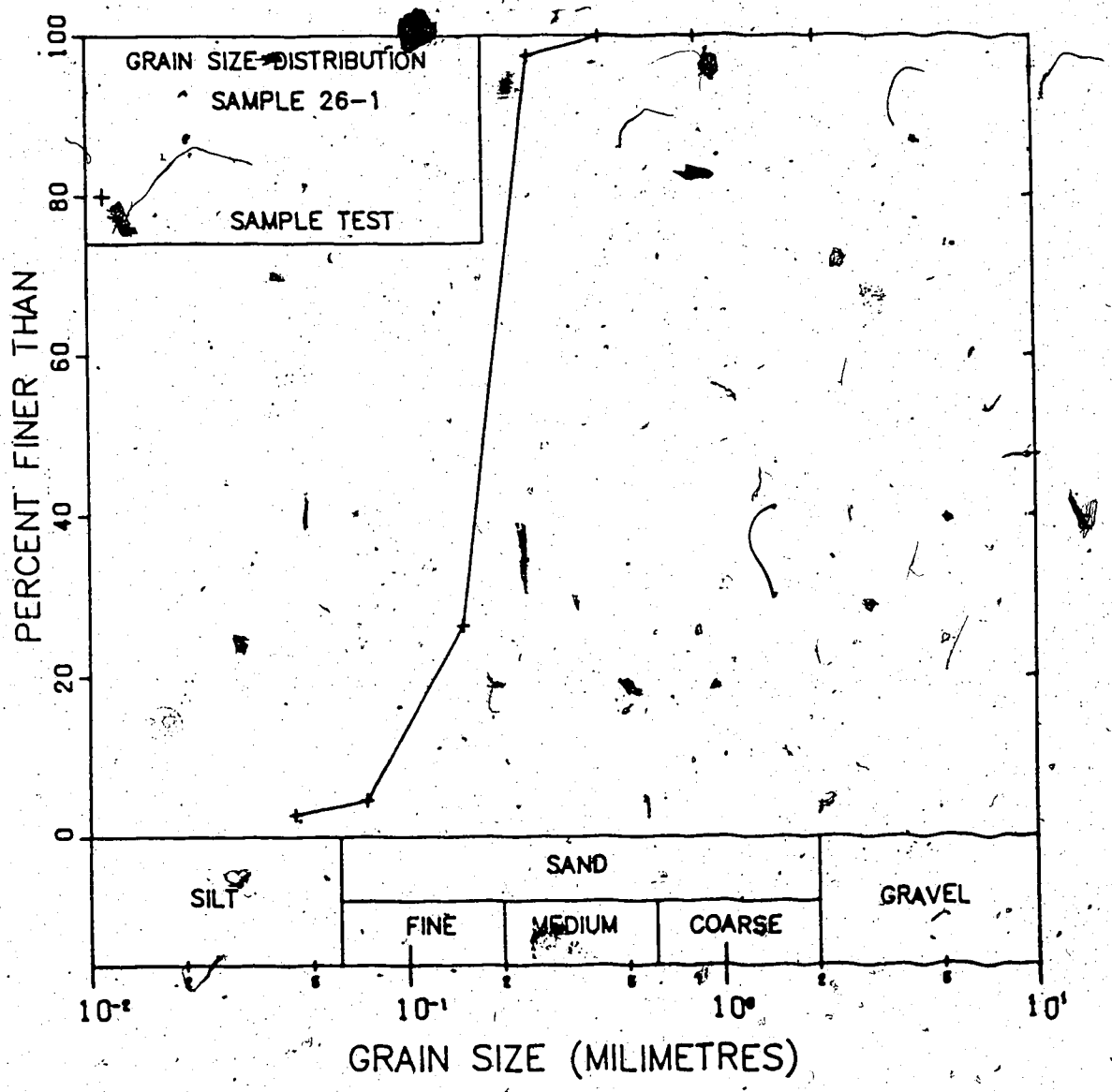

Figure C.17 Grain Size Distribution - Sample 26-1

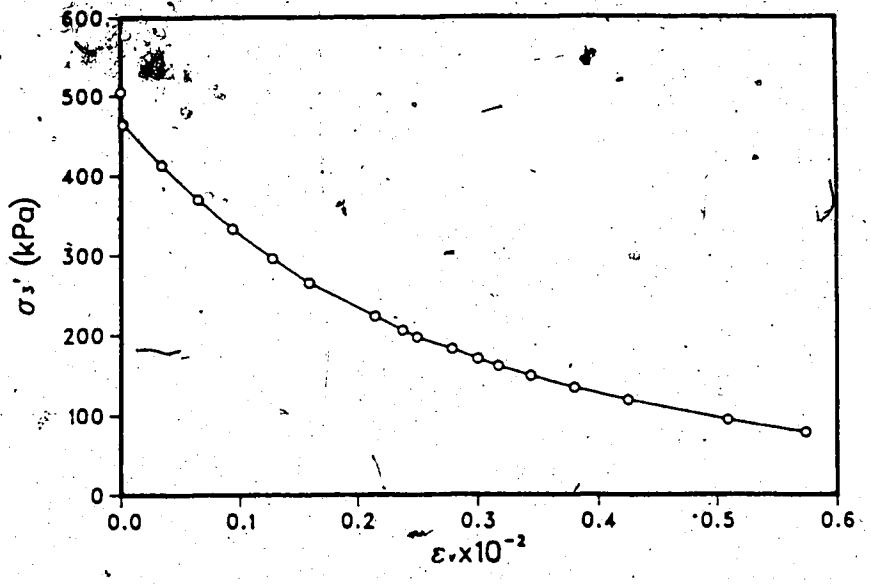

Figure C.18 Triaxial Drained Isotropic Unloading Test - Sample 5-1

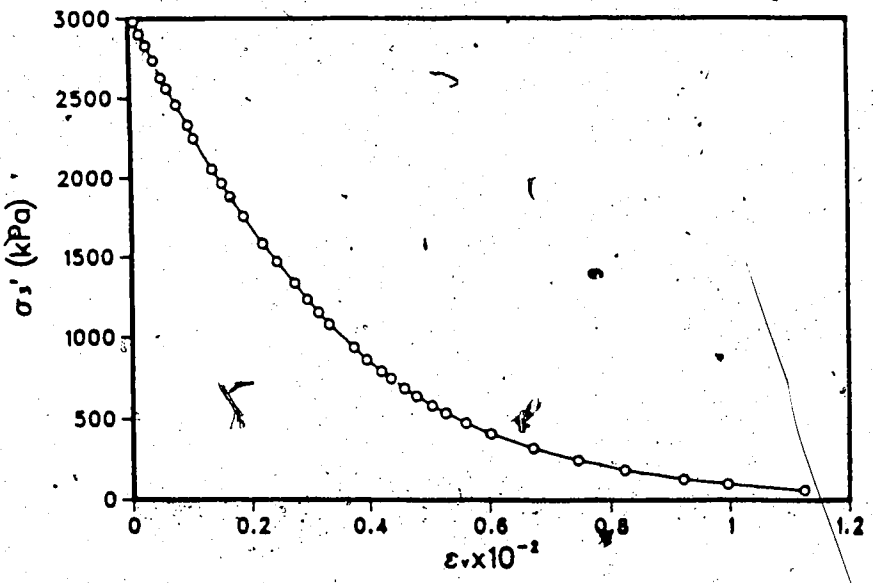

Figure C.19 Triaxial Drained Isotropic Unloading Test - Sample 7-4

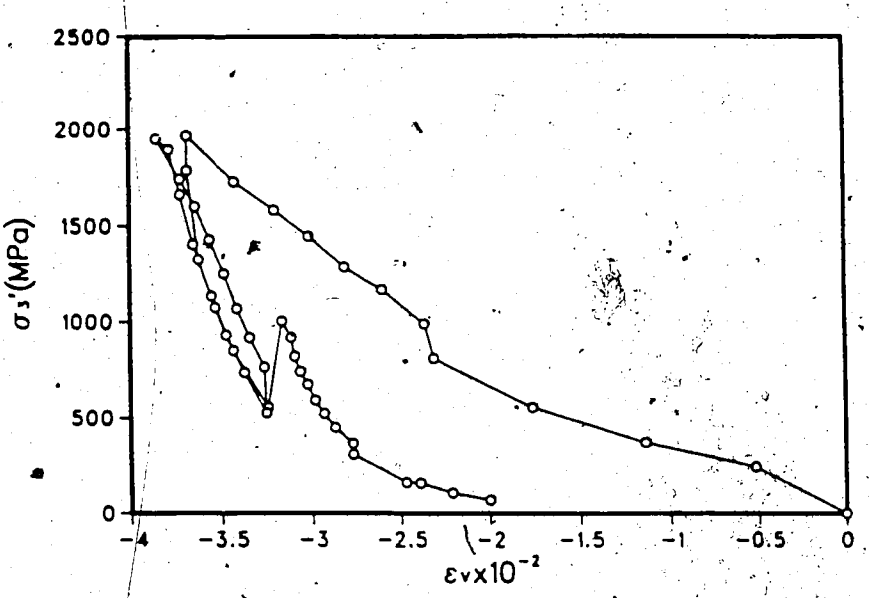

Figure C.20 Triaxial Drained Isotropic Unloading Test - Sample 8-2B

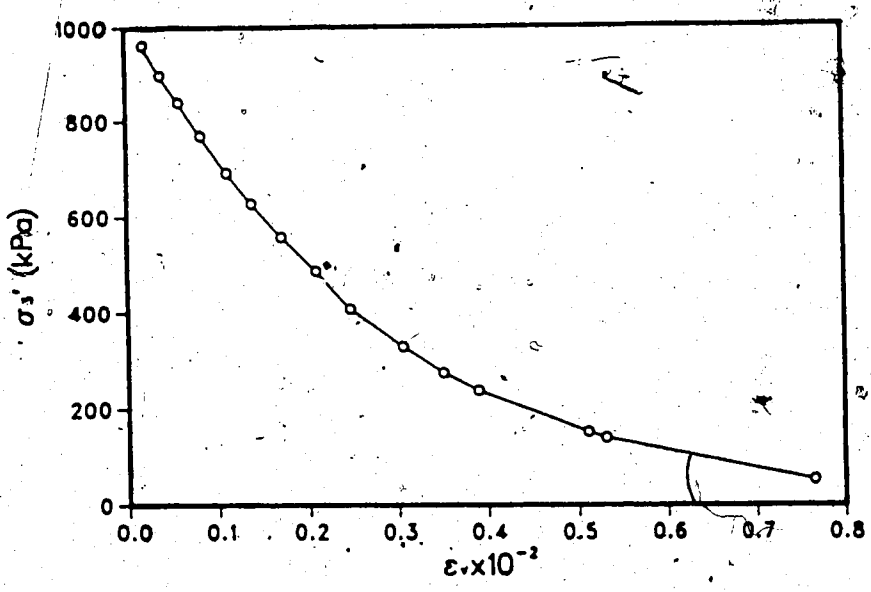

Figure C.21 Triaxial Drained Isotropic Unloading Test - Sample 8-3

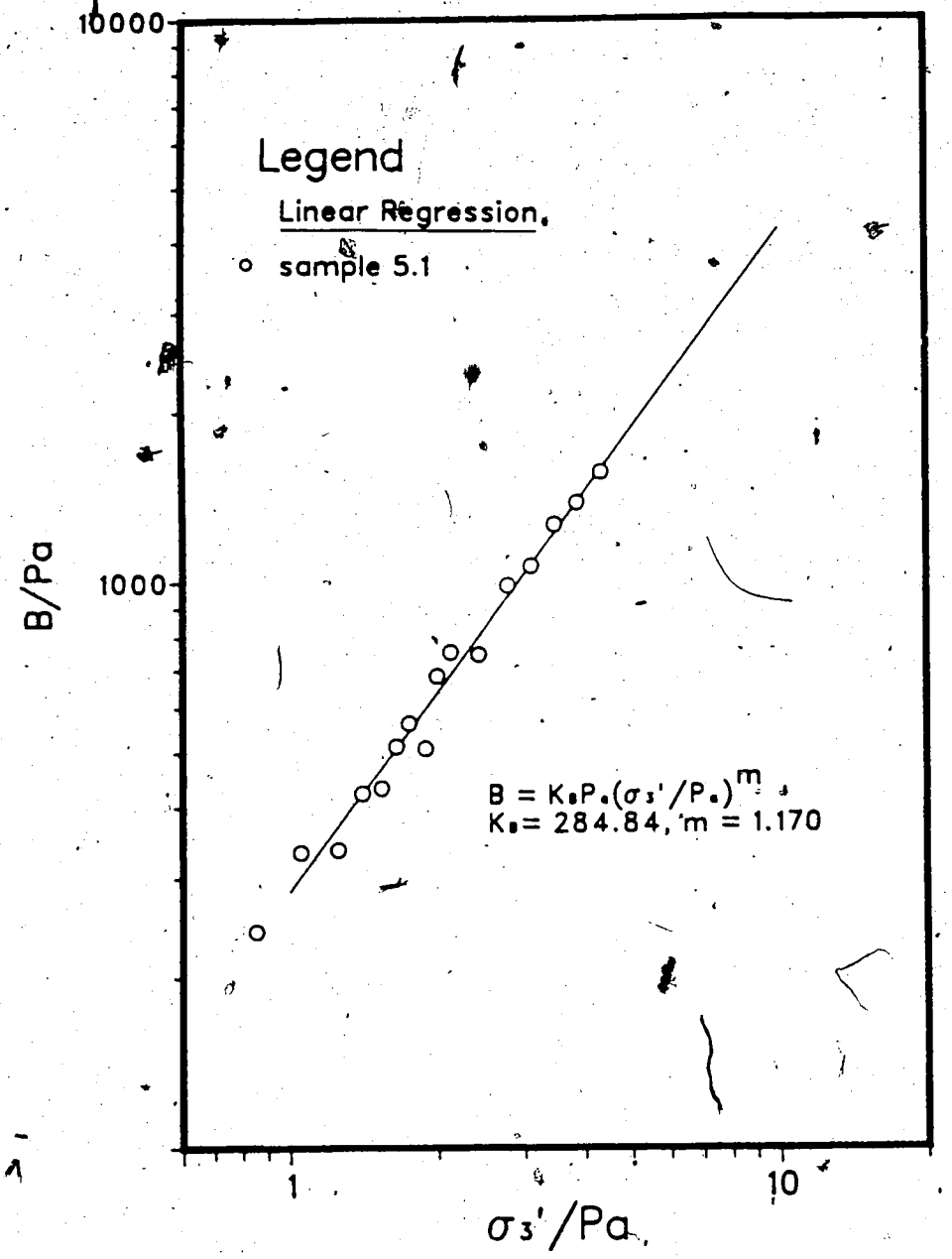

Figure C.22 Normalized Bulk Modulus versus Normalized Mean Effective Stress - Sample 5-1

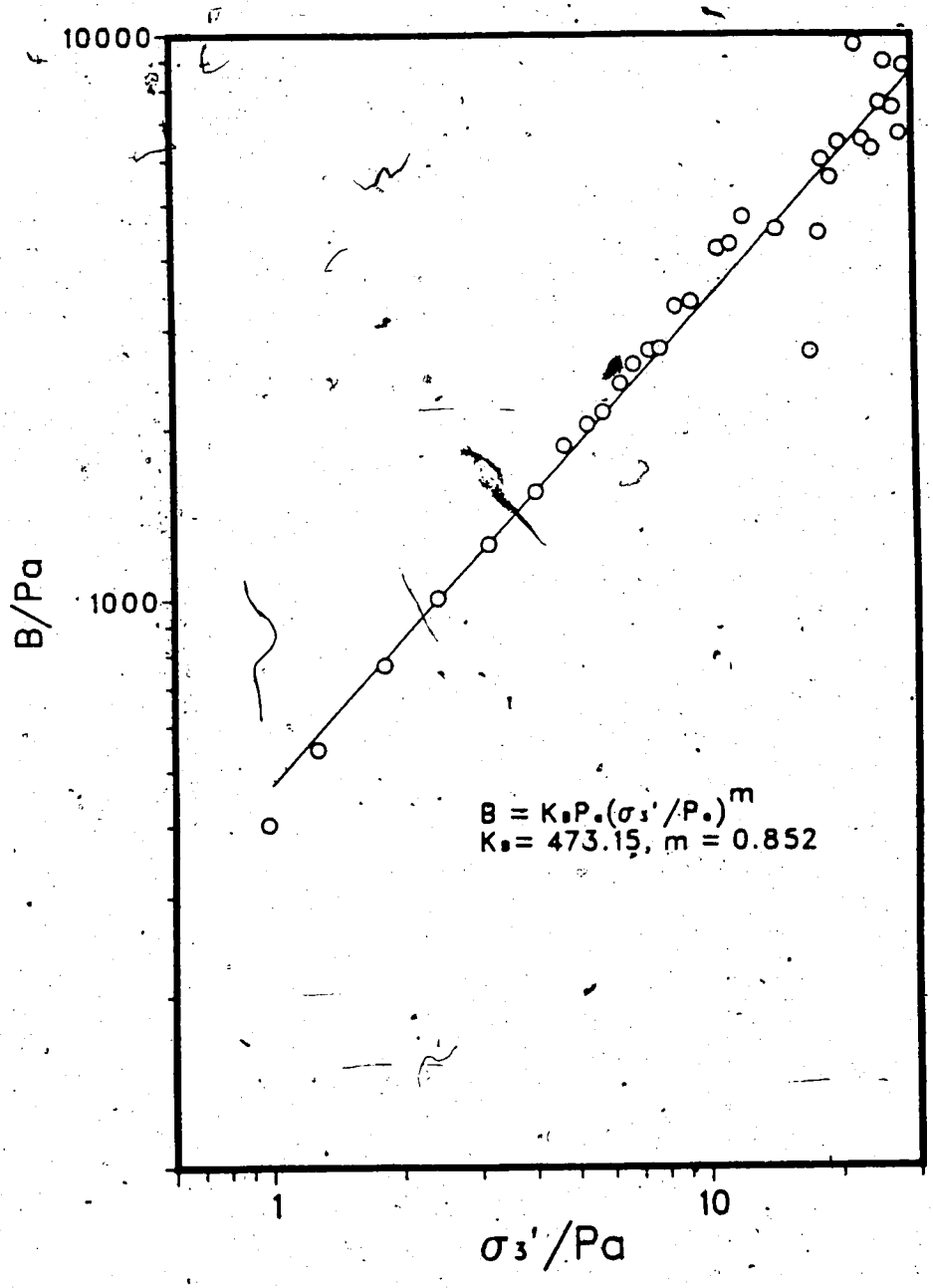

Figure C.23 Normalized Bulk Modulus versus Normalized Mean Effective Stress - Sample 7-4

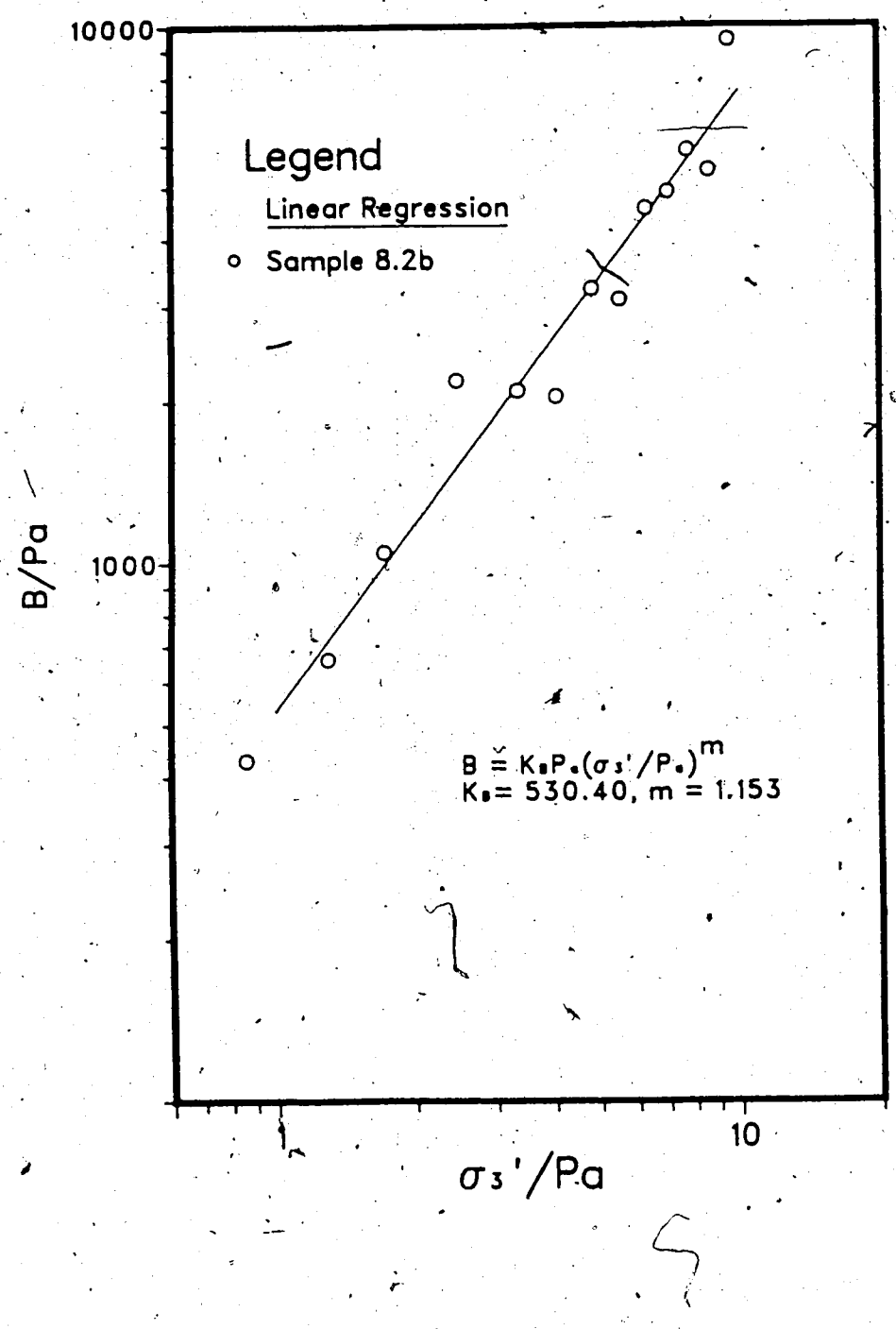

Figure C.24 Normalized Bulk Modulus versus Normalized Mean Effective Stress - Sample 8-2B

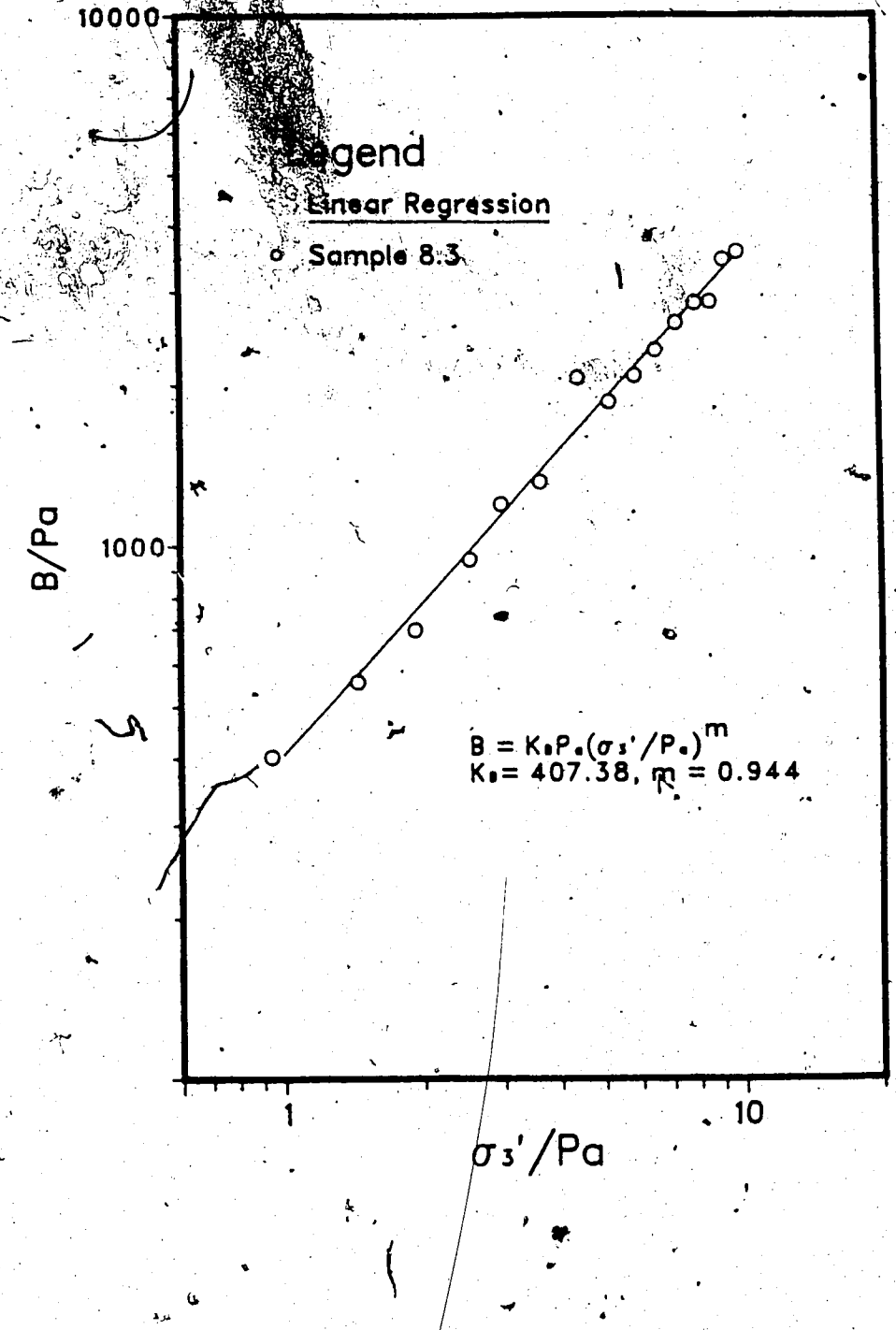

Figure C.25 Normalized Bulk Modulus versus Normalized Mean Effective Stress - Sample 8-3

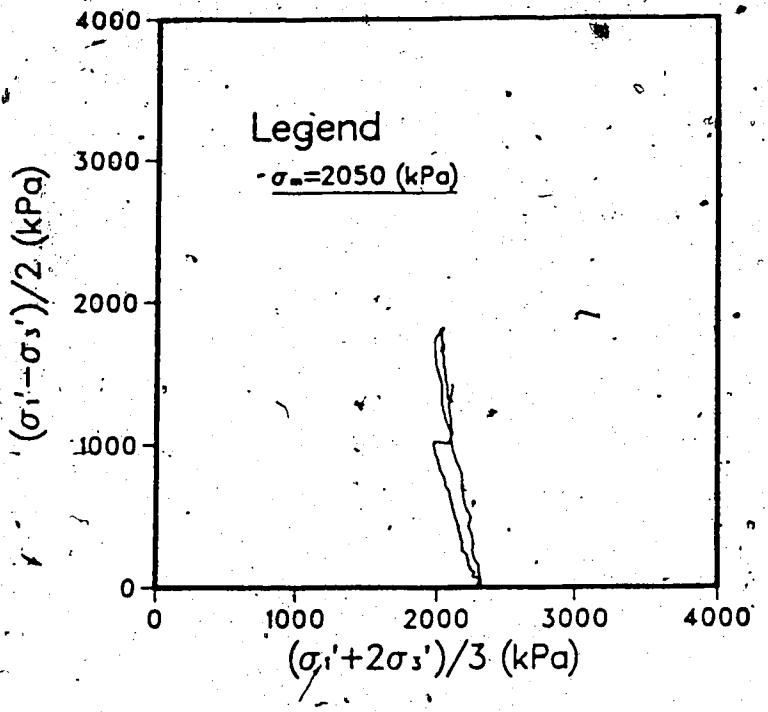

Figure C.26 Triaxial J1 Test - Stress Path - Sample 5-2

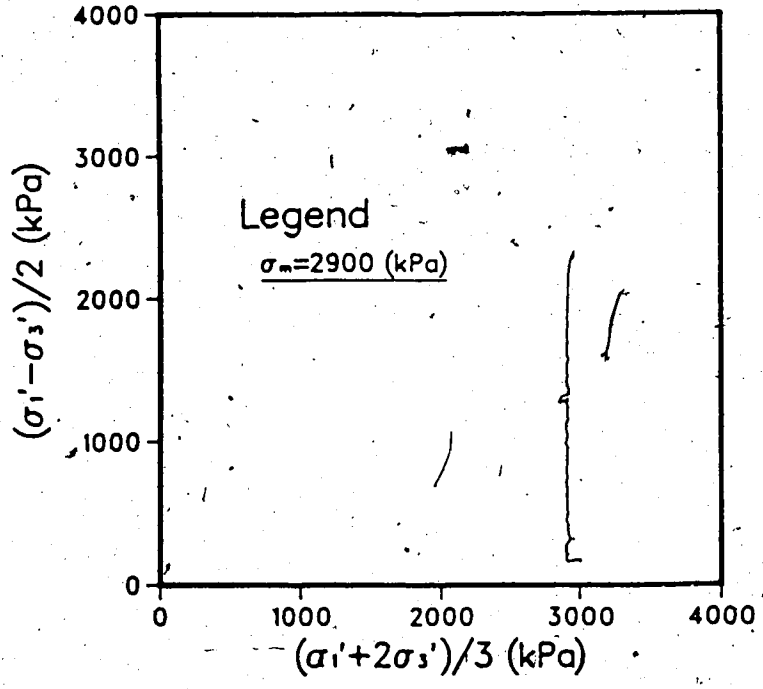

Figure C.27 Triaxial J1 Test - Stress Path - Sample 5-3

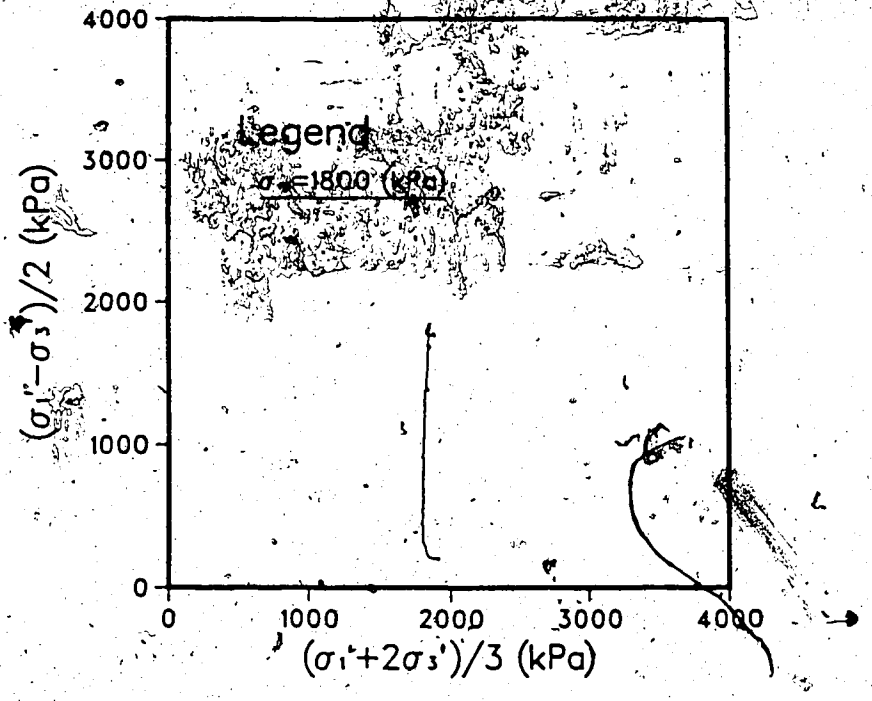

Figure C.28 Triaxial J1 Test - Stress Path - Sample 5-4

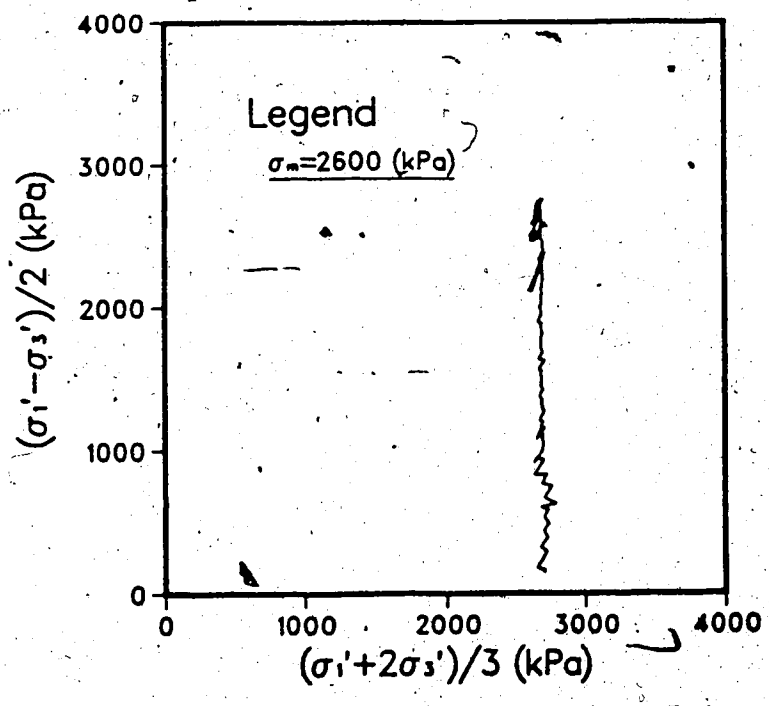

Figure C.29 Triaxial J1 Test - Stress Path - Sample 8-1

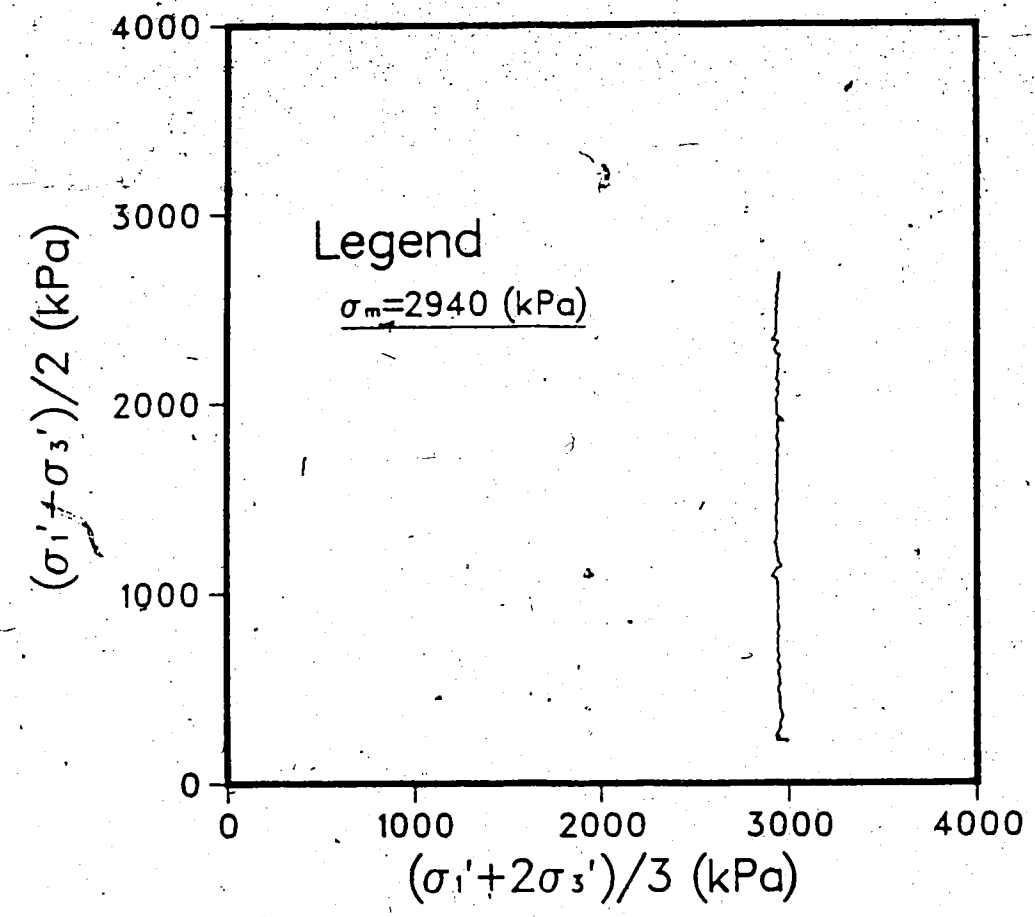

Figure C.30 Triaxial J1 Test - Stress Path - Sample 8-4

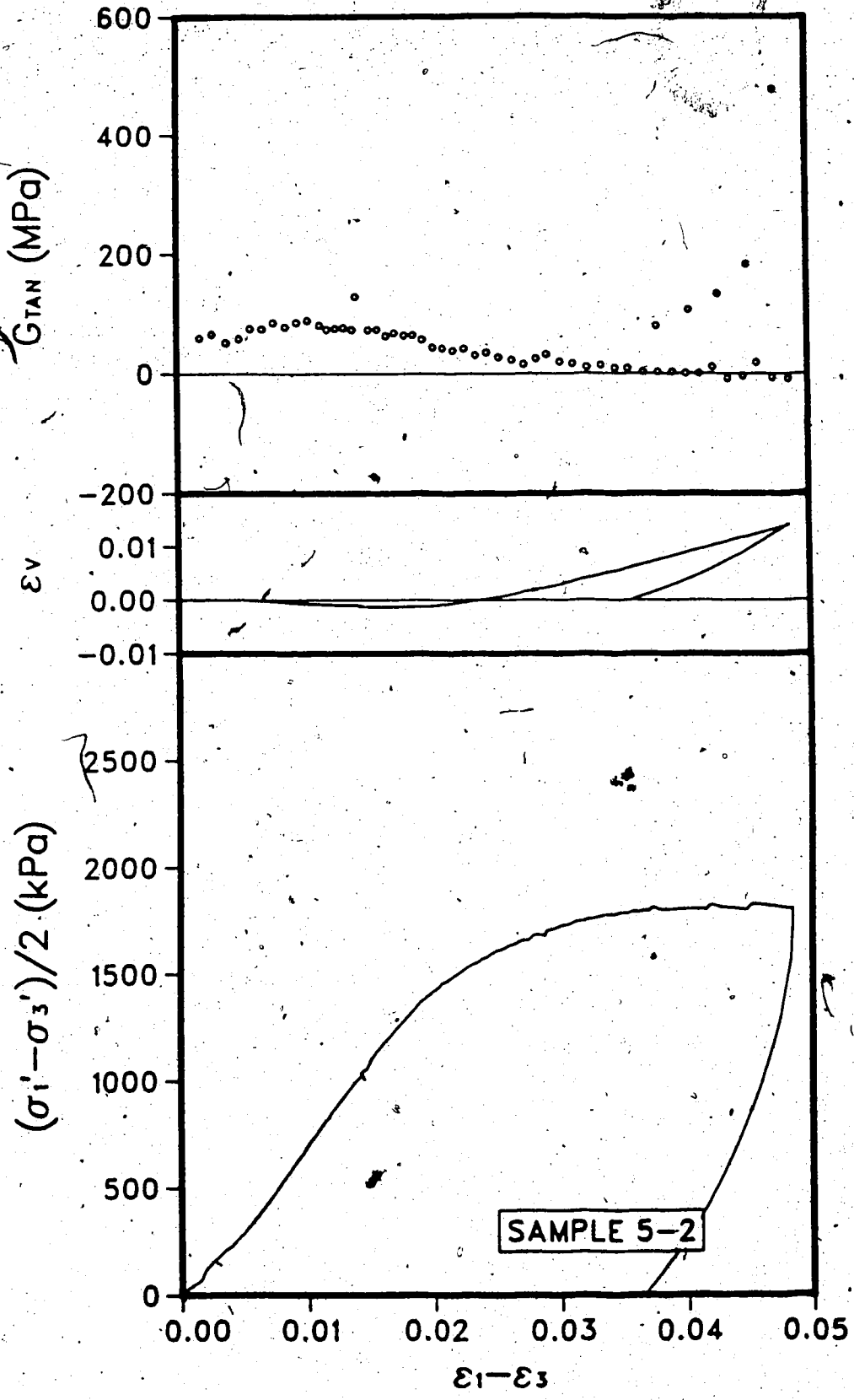

Figure C.31 Triaxial J1 - Sample 5-2

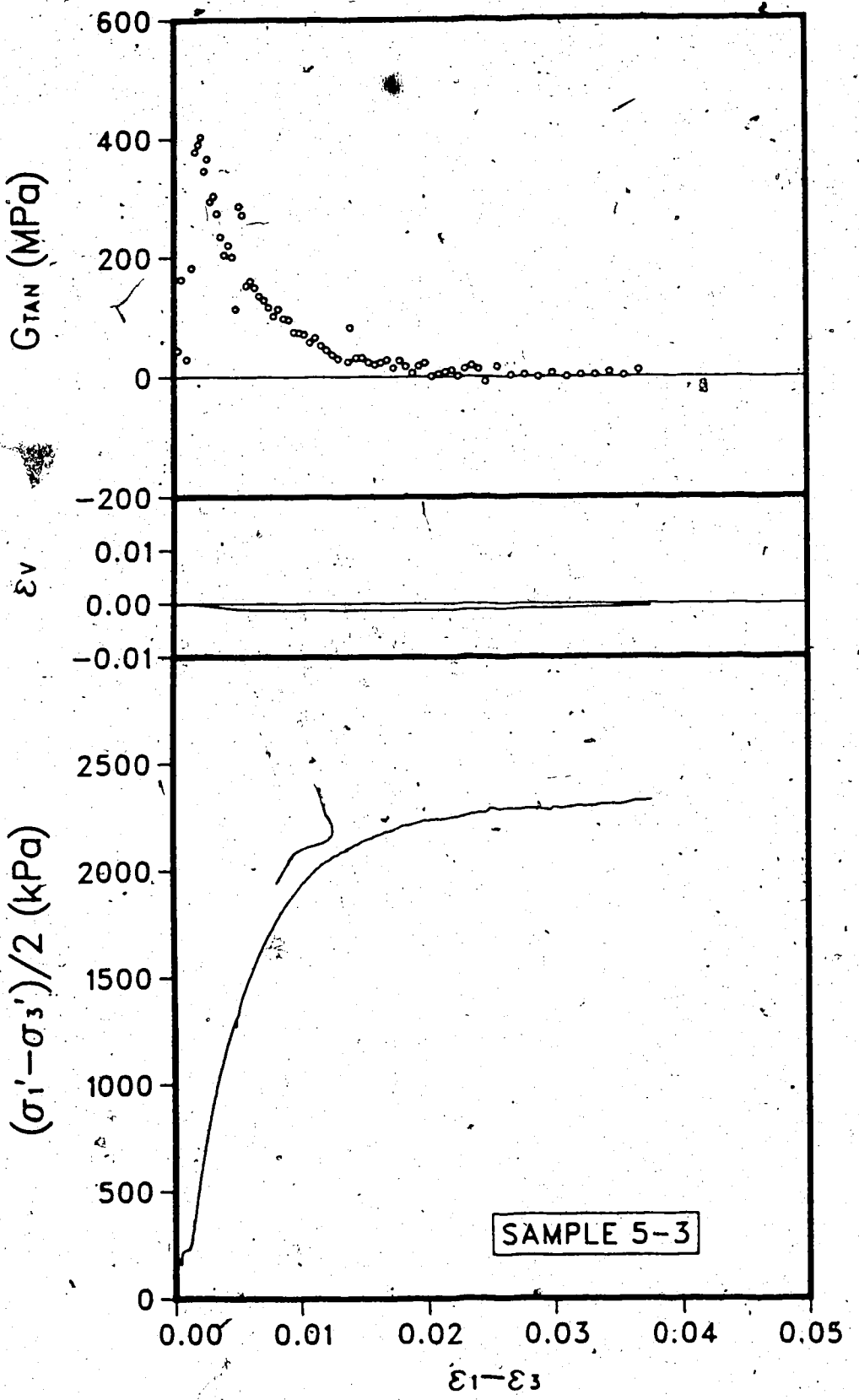

Figure C.32 Triaxial J1 - Sample 5-3

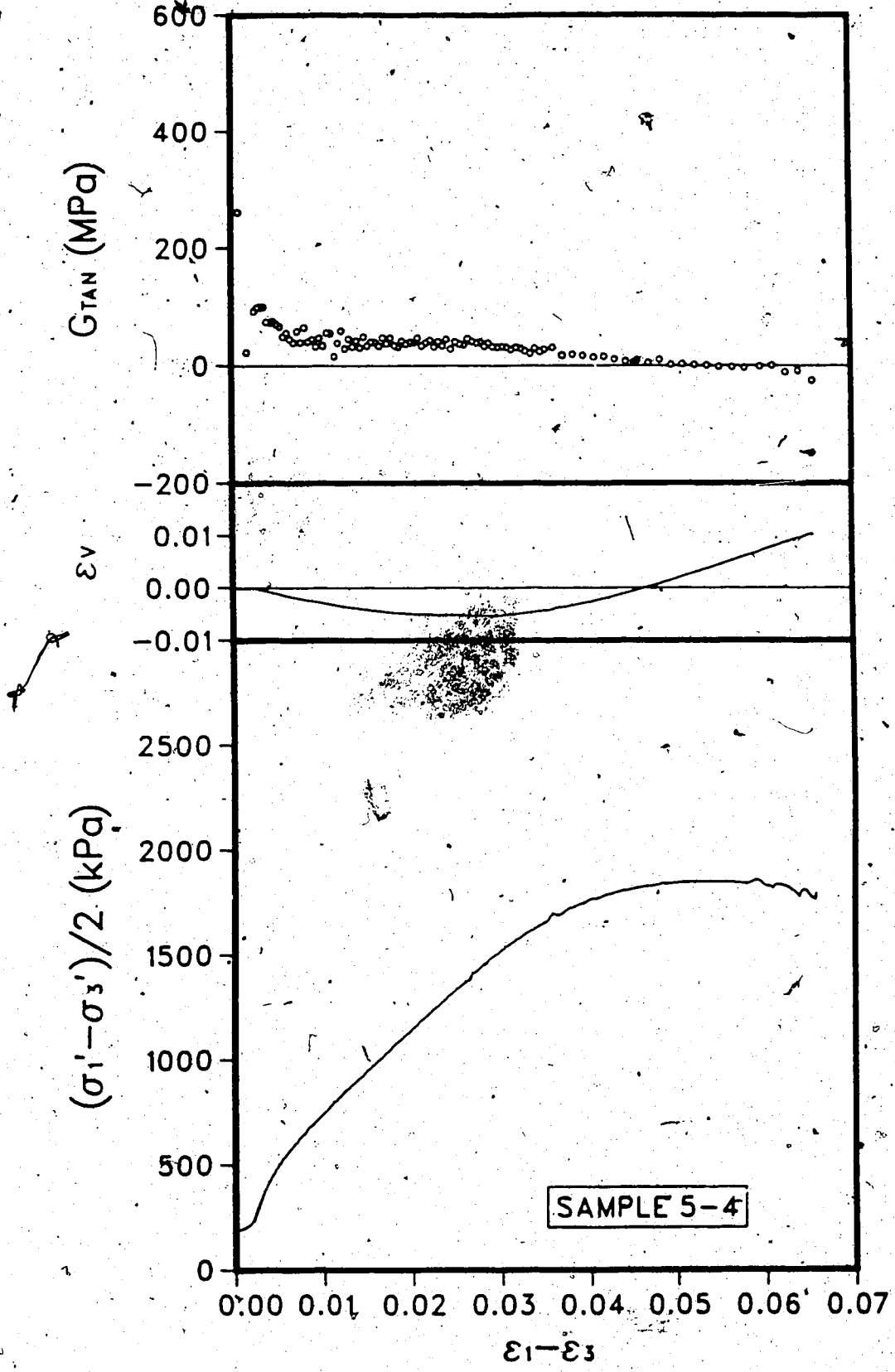

Figure C.33 Triaxial J1 - Sample 5-4

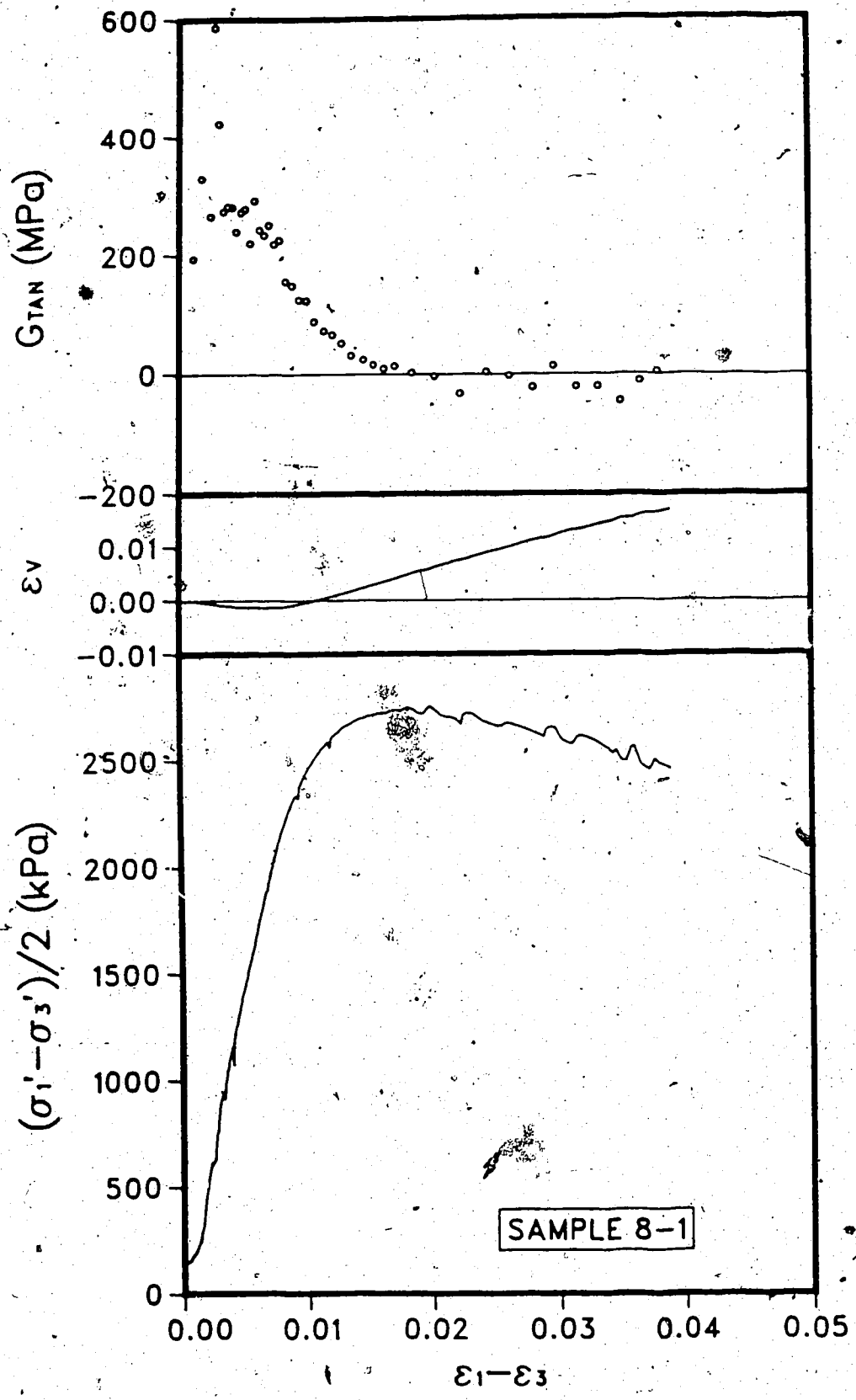

Figure C.34 Triaxial J1 - Sample 8-1

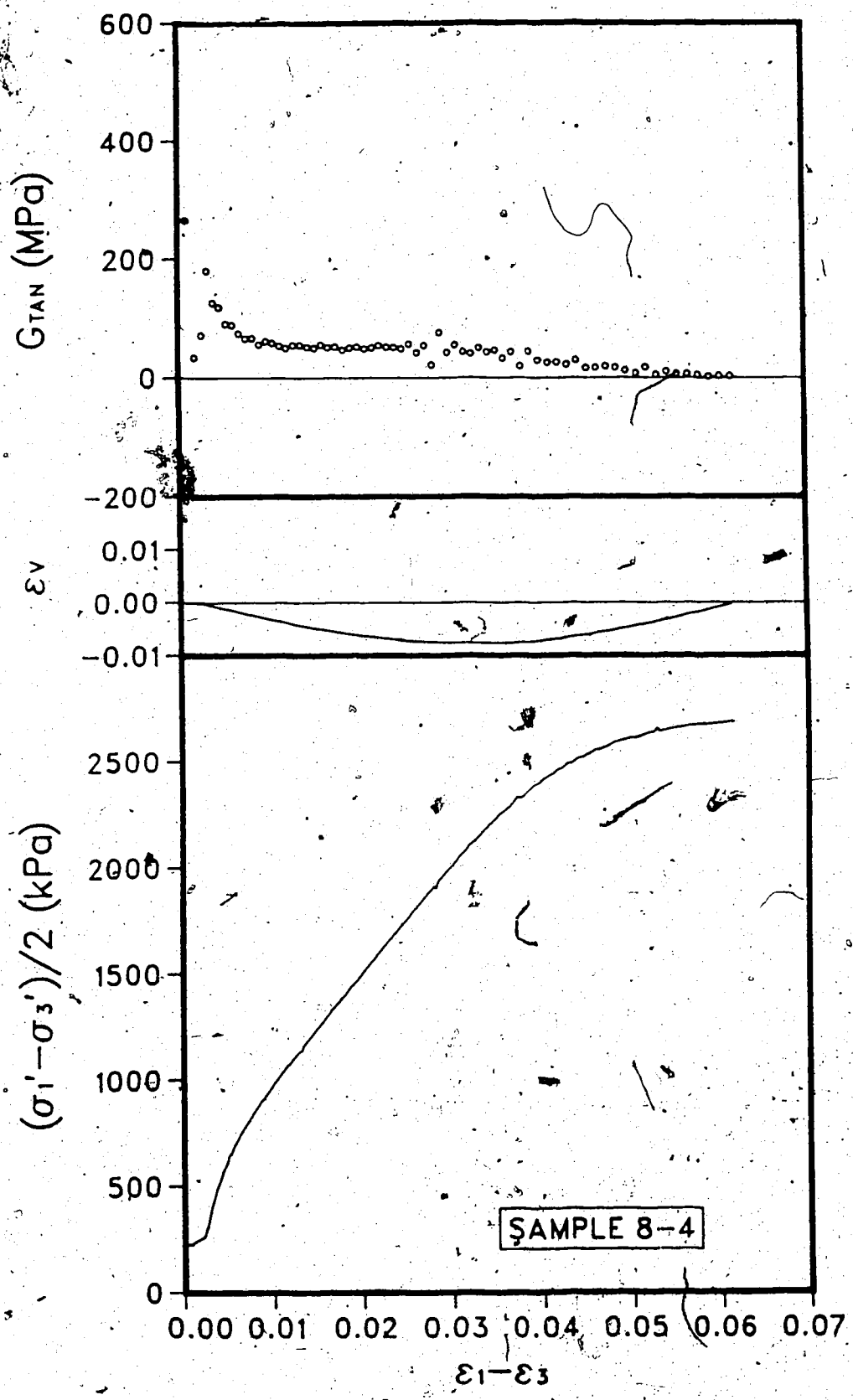

Figure C.35 Triaxial J1 - Sample 8-4

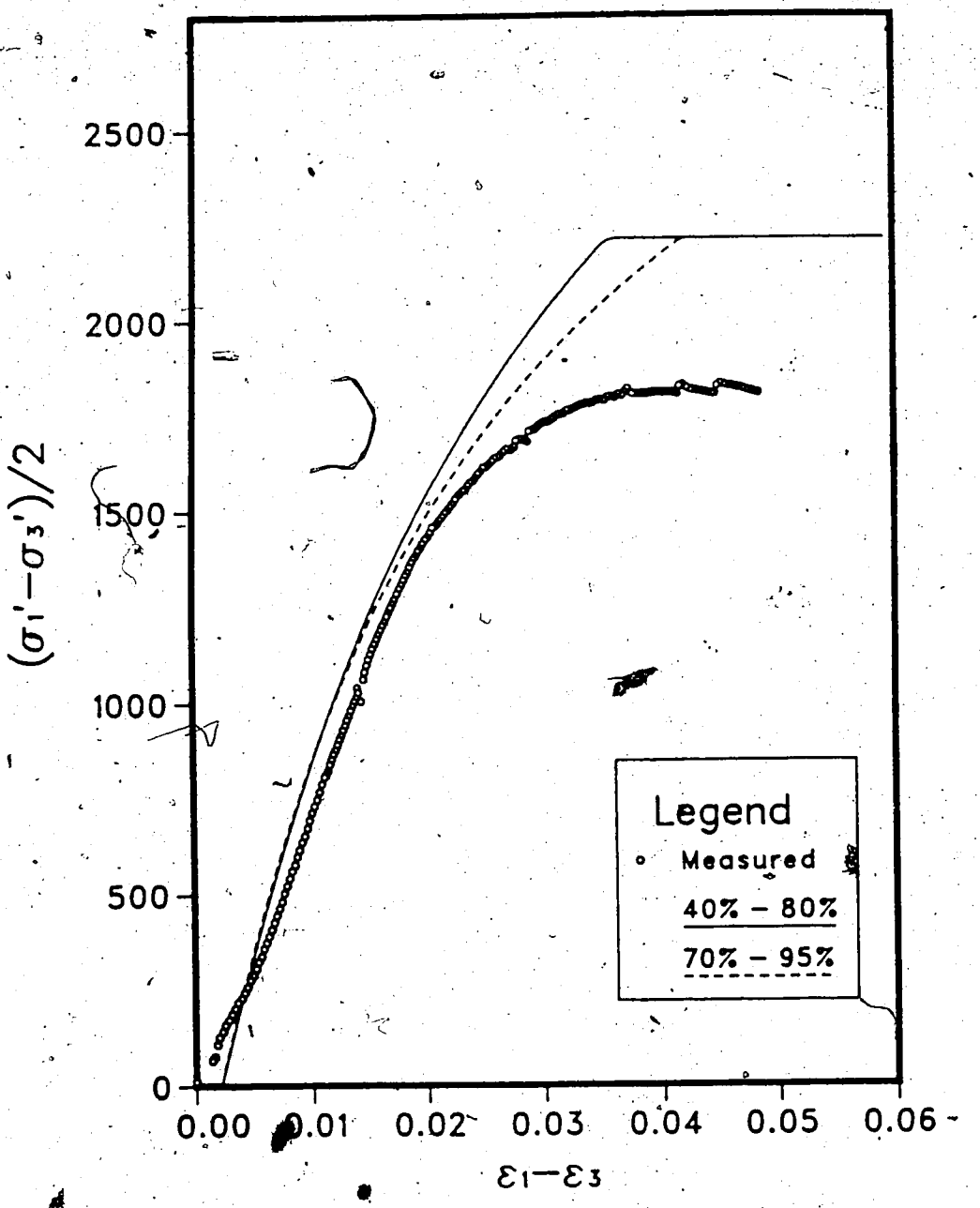

Figure C.36 Hyperbolic Fit - Sample 5-2

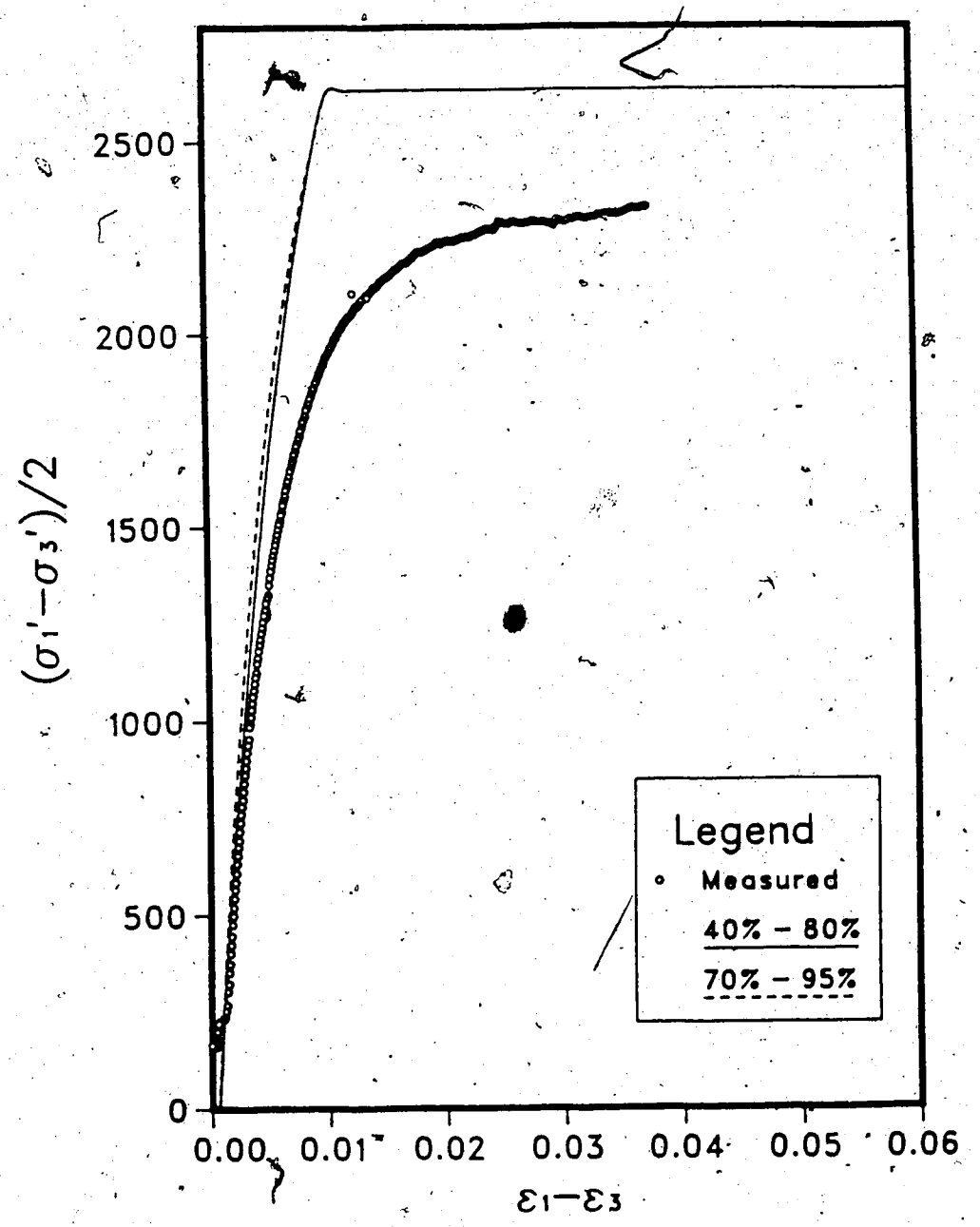

Figure C.37 Hyperbolic Fit - Sample 5-3

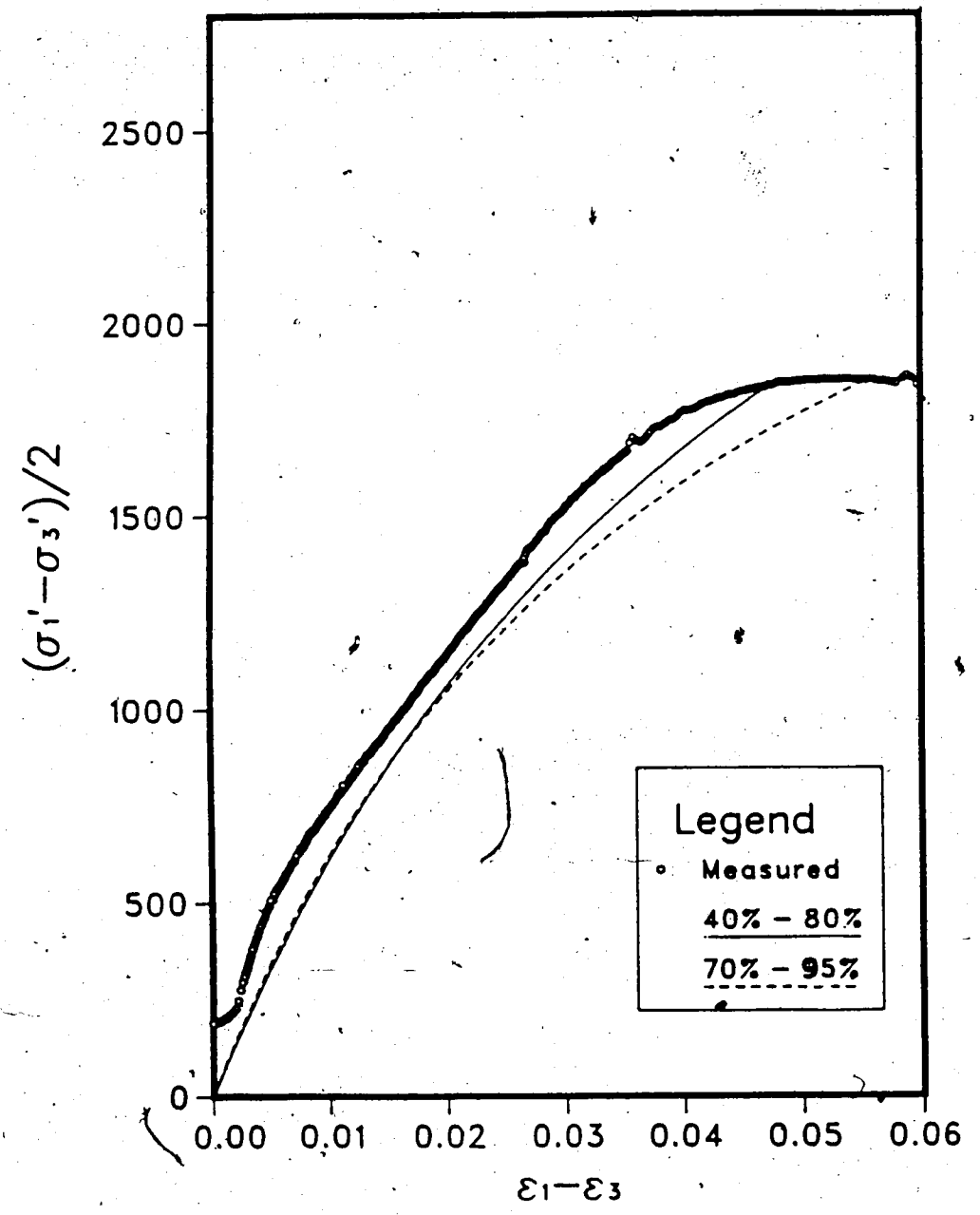

Figure C.38 Hyperbolic Fit - Sample 5-4

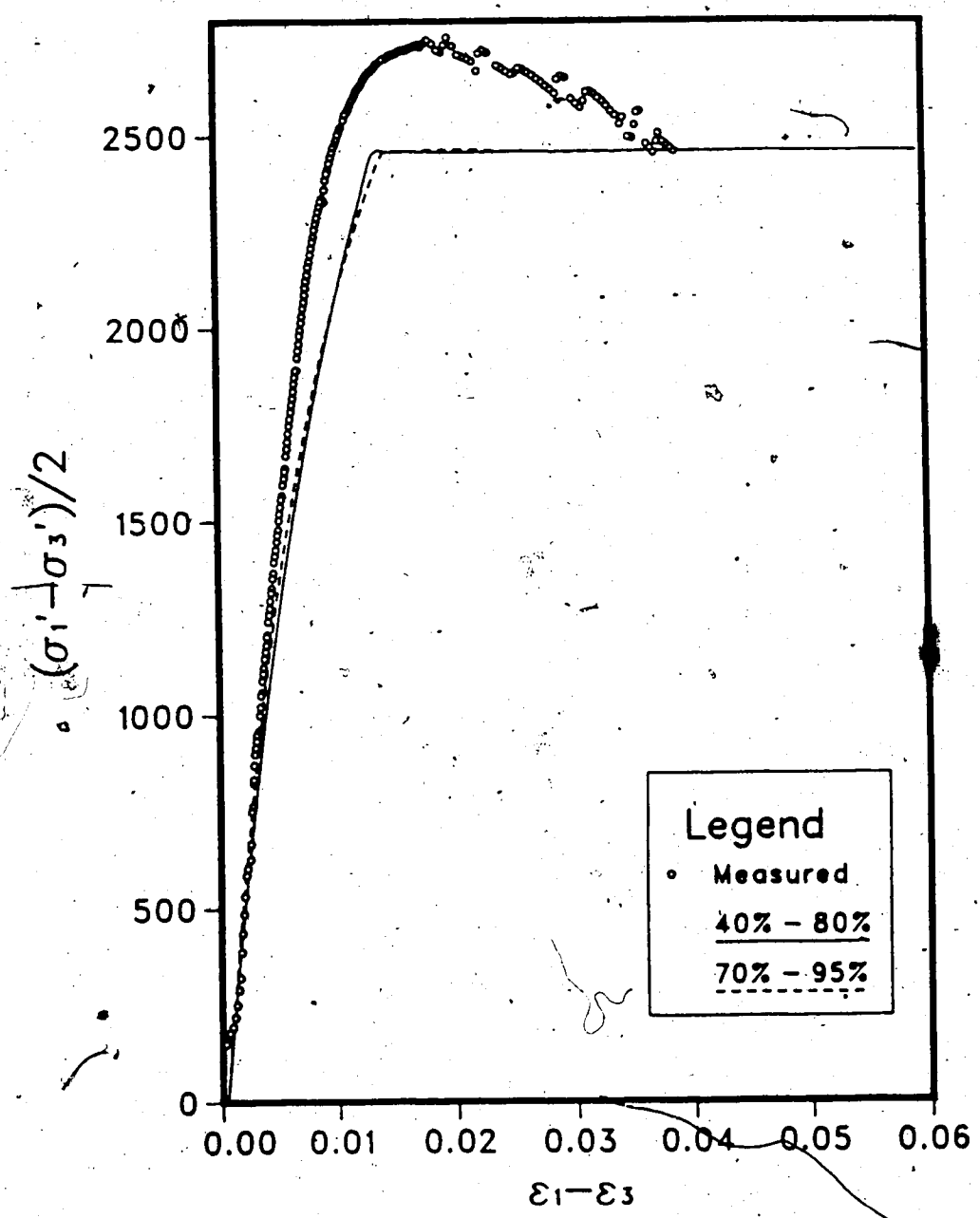

Figure C.39 Hyperbolic Fit - Sample 8-1

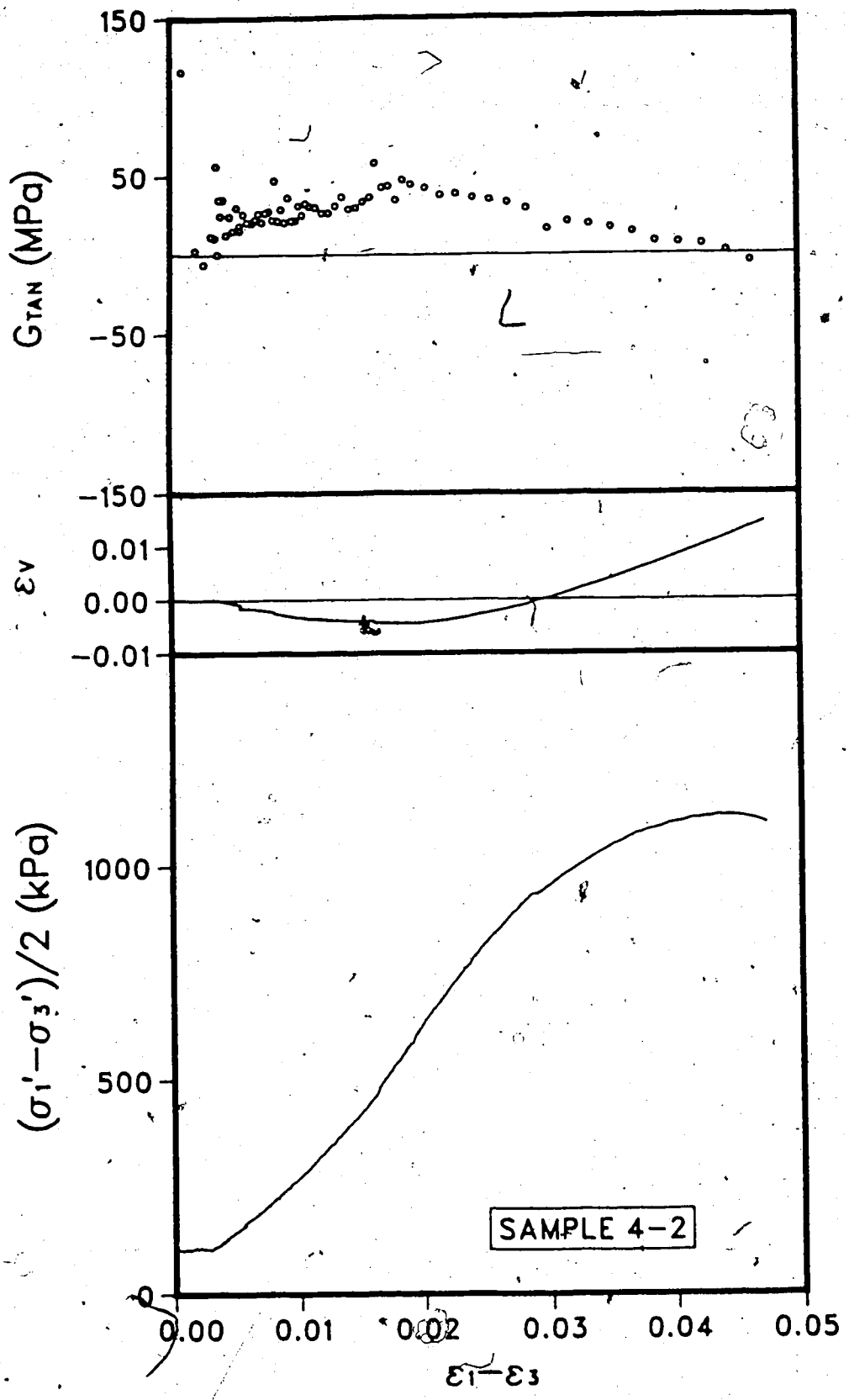

Figure C.40 Standard Triaxial Test - Sample 4-2

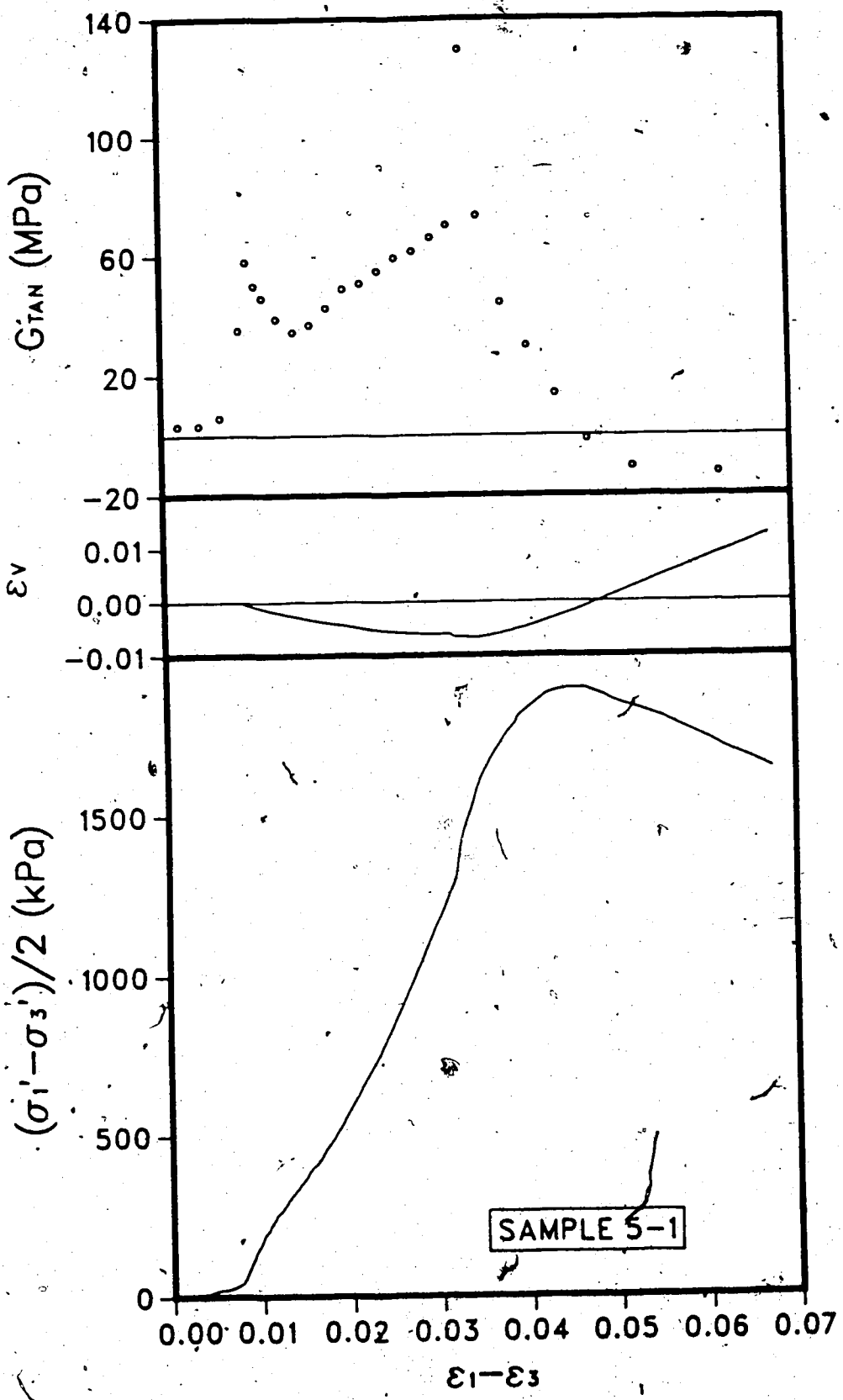

Figure C.41 Standard Triaxial Test - Sample 5-1

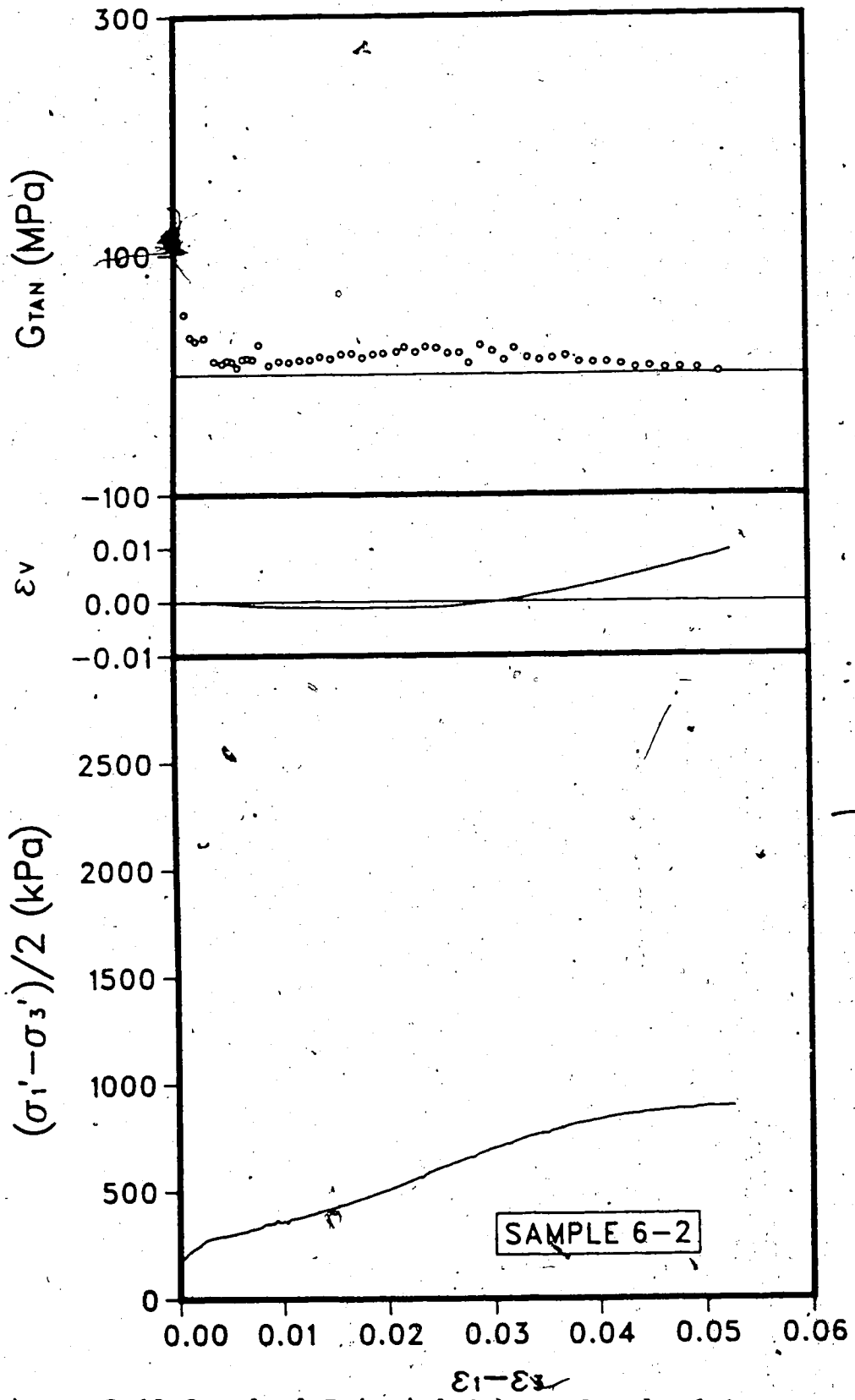

Figure C.42 Standard Triaxial Test - Sample 6-1

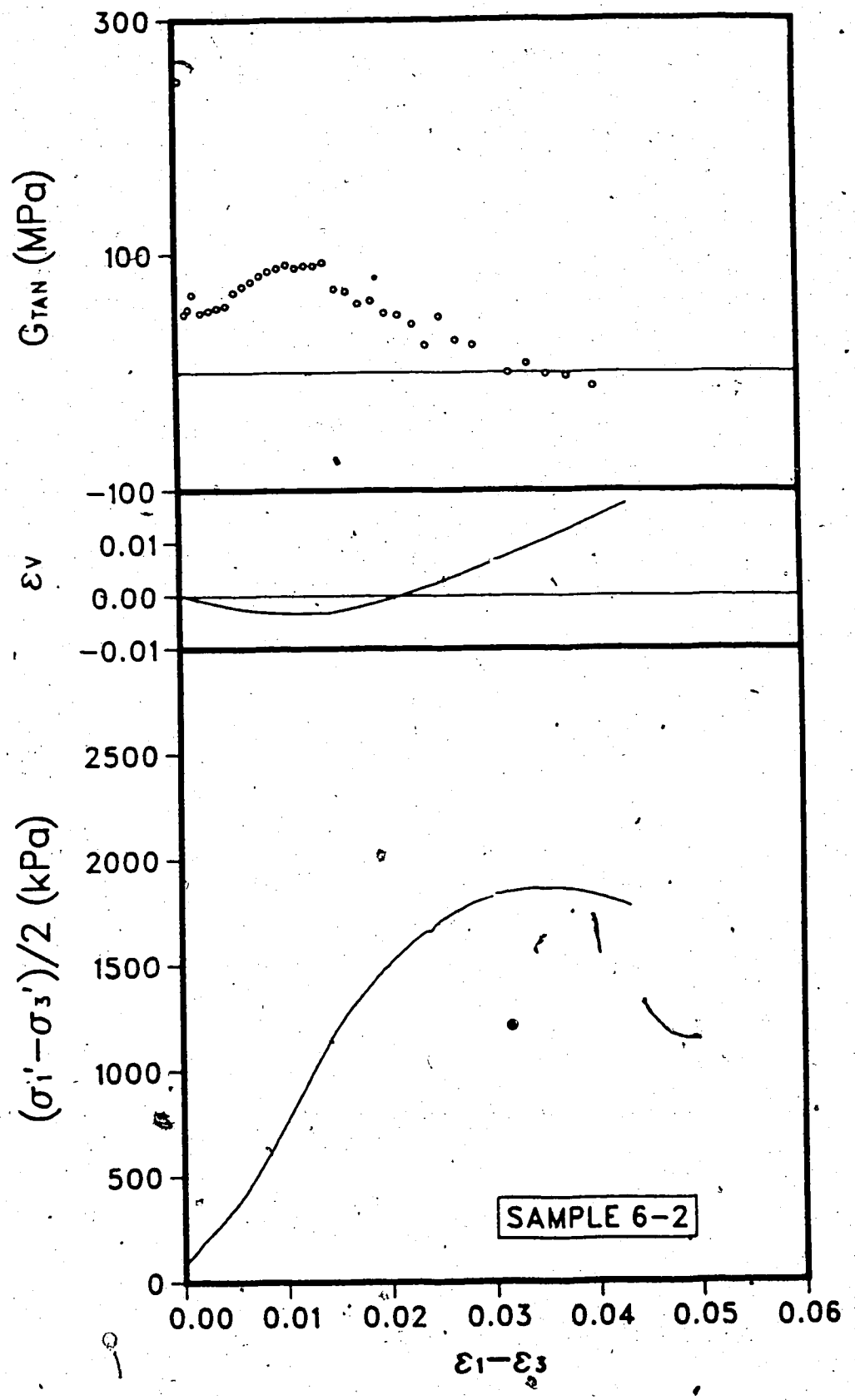

Figure C.43 Standard Triaxial Test - Sample 6-2

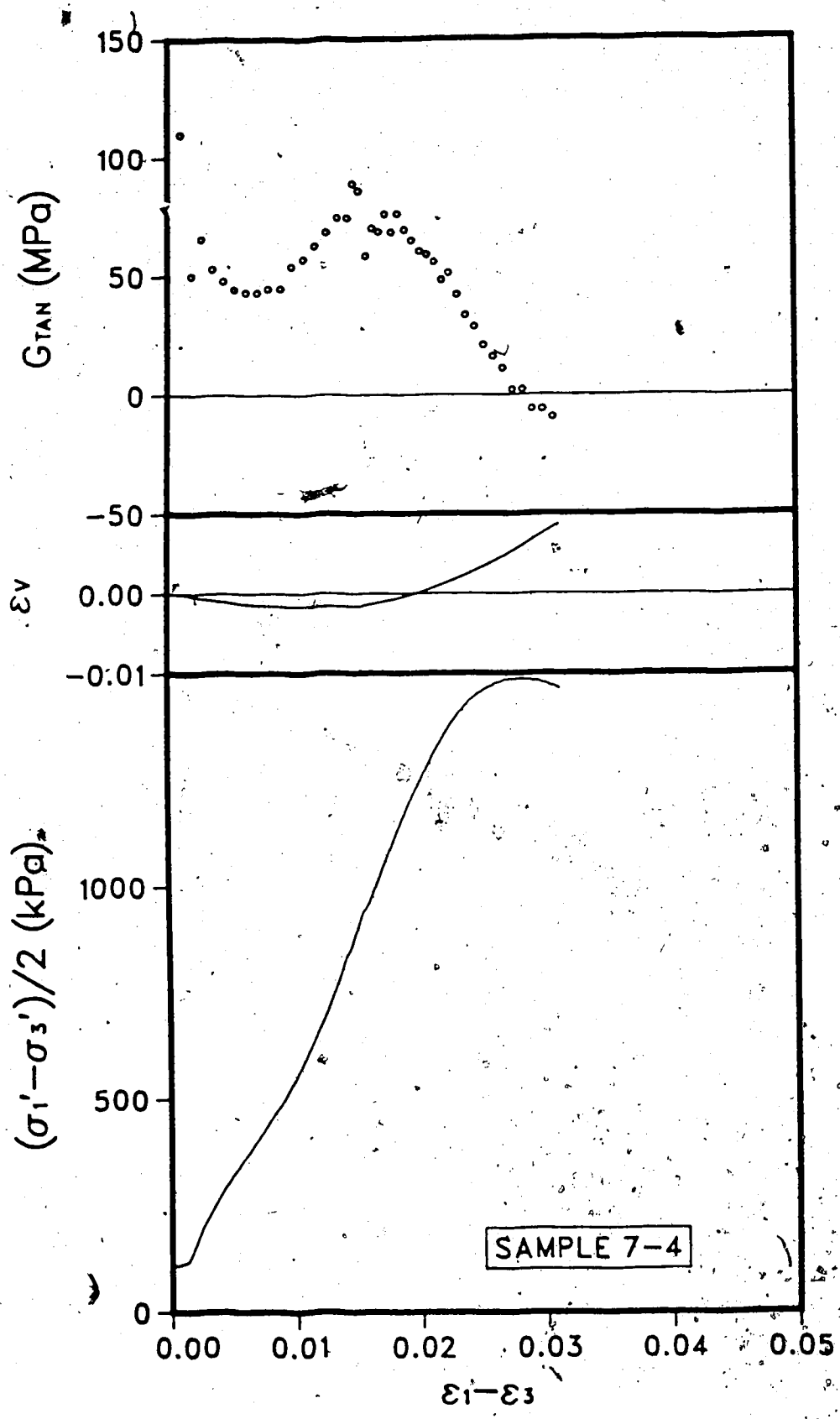

Figure C.44 Standard Triaxial Test - Sample 7-4

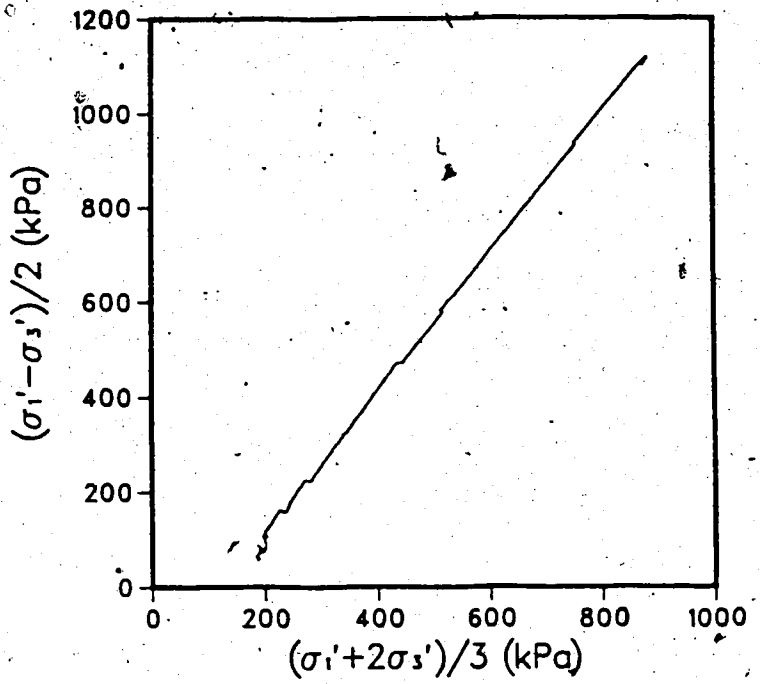

Figure C.45 Standard Triaxial Test - Stress Path - Sample 4-2

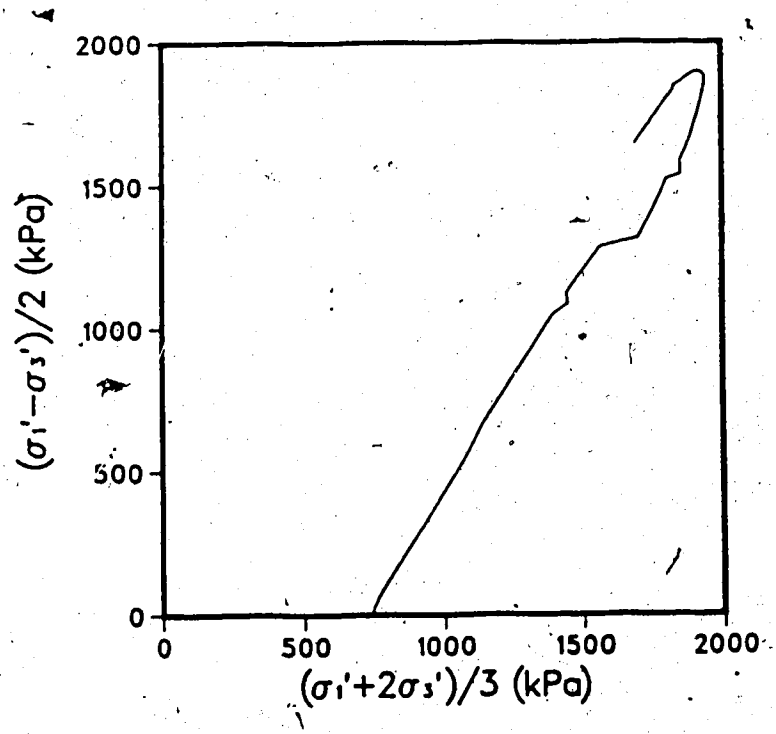

Figure C.46 Standard Triaxial Test - Stress Path - Sample 5-1

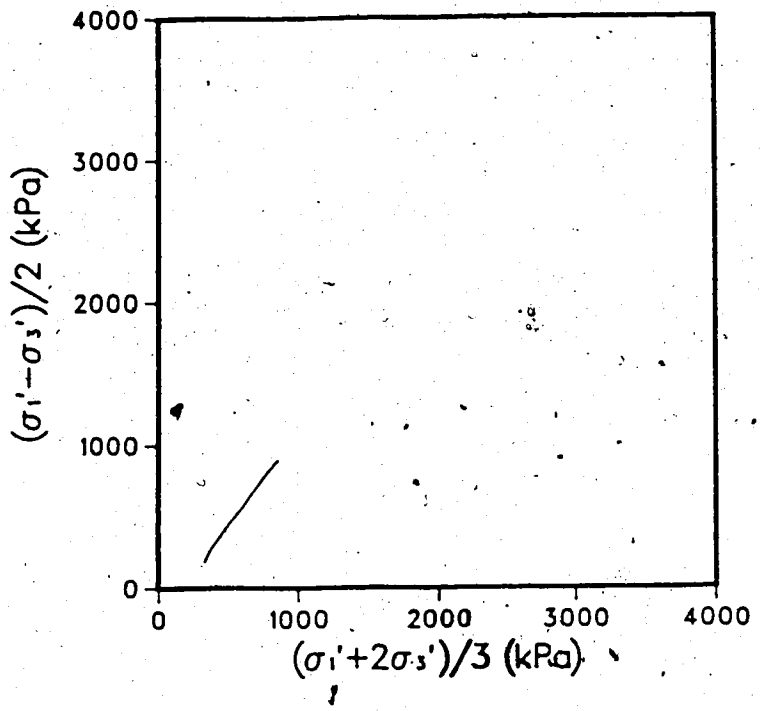

Figure C.47 Standard Triaxial Test - Stress Path - Sample 6-1

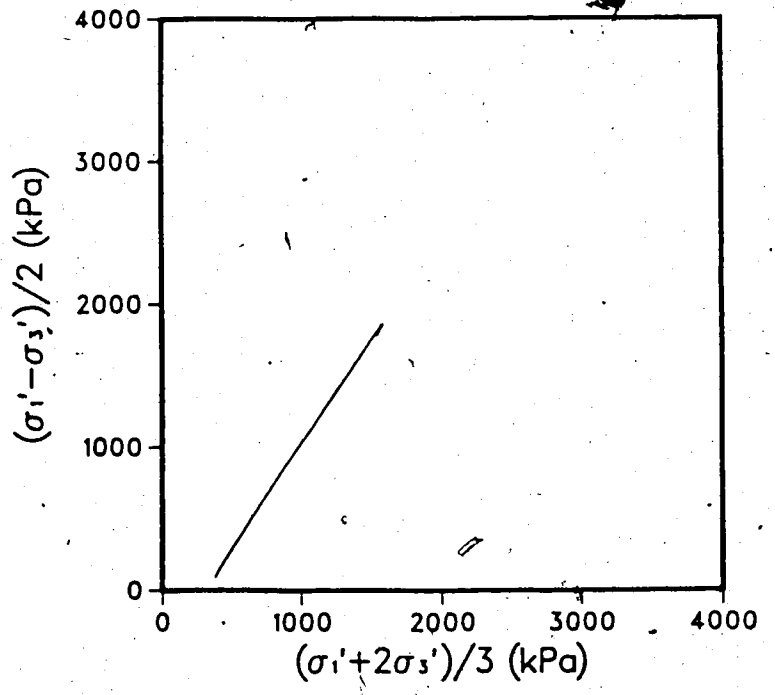

Figure C.48 Standard Triaxial Test - Stress Path - Sample 6-2

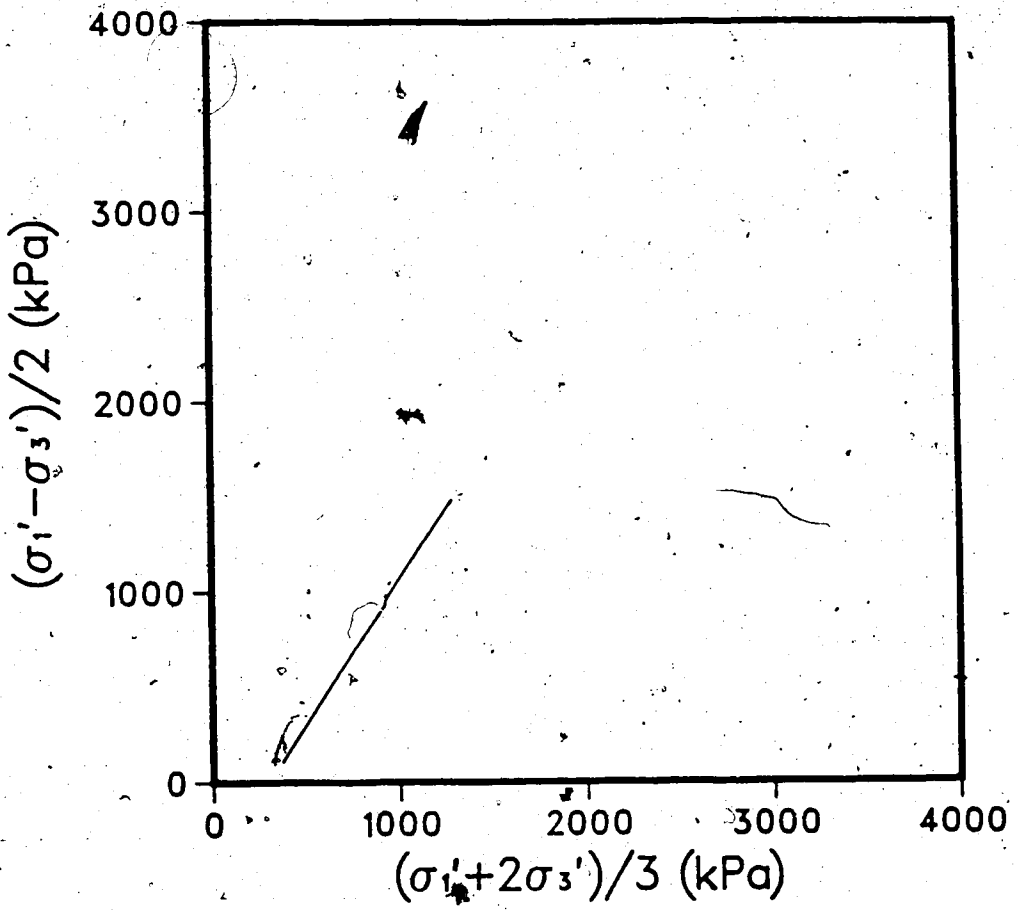

Figure C.49 Standard Triaxial Test - Stress Path - Sample 7-4

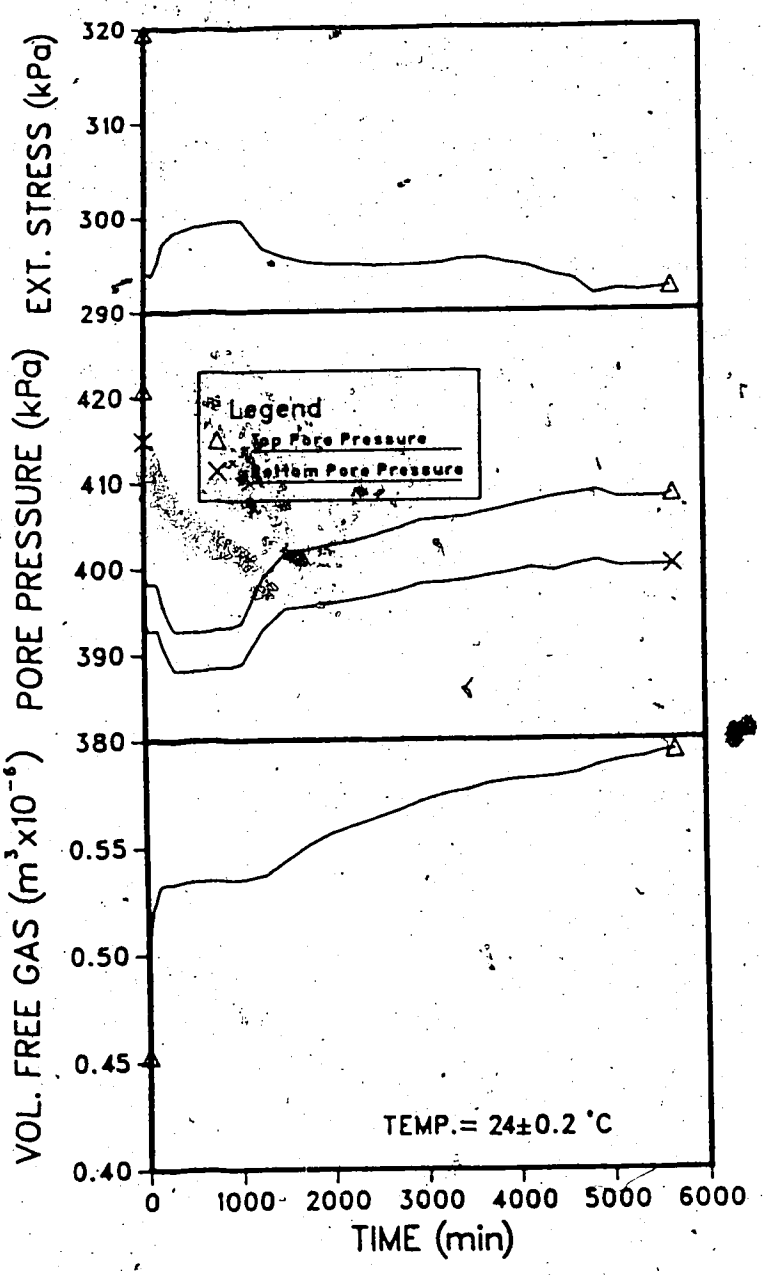

Figure C.50 Undrained Oedometer Test - Sample 11-5 - Step A

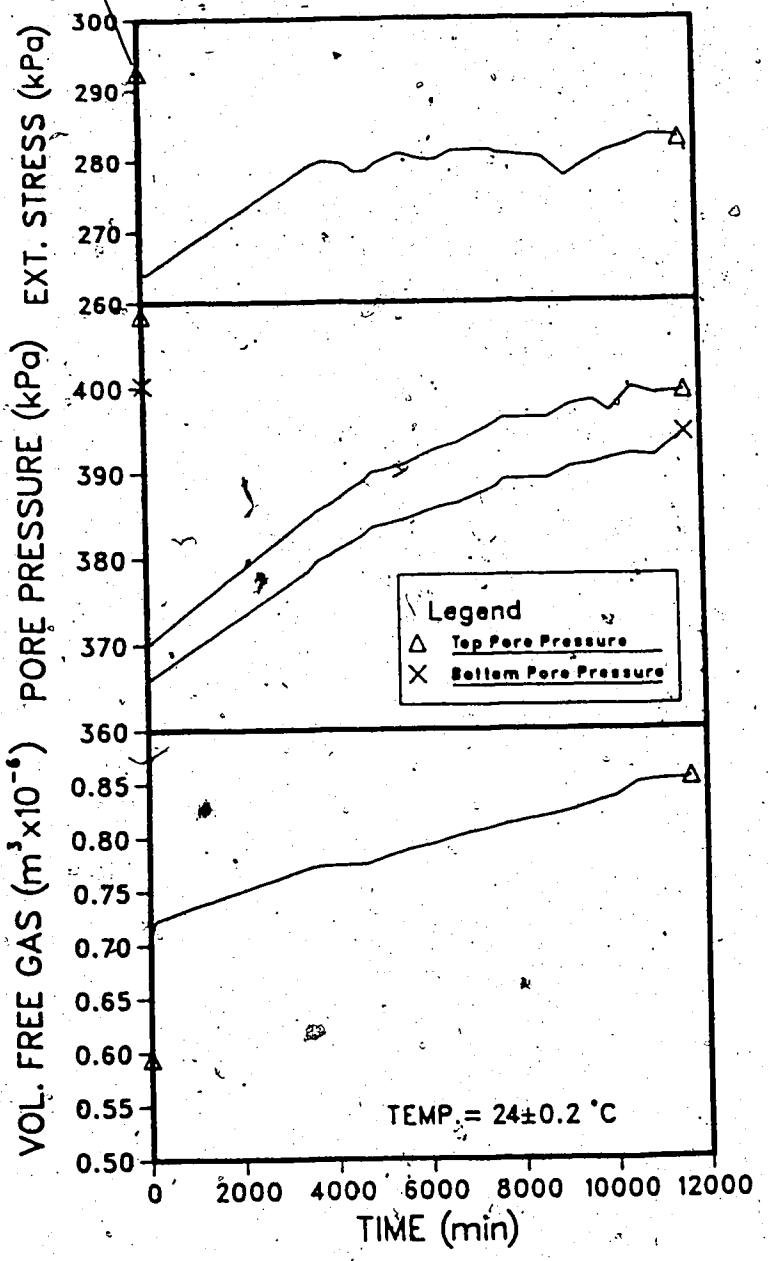

Figure C.51 Undrained Oedometer Test - Sample 11-5 - Step B

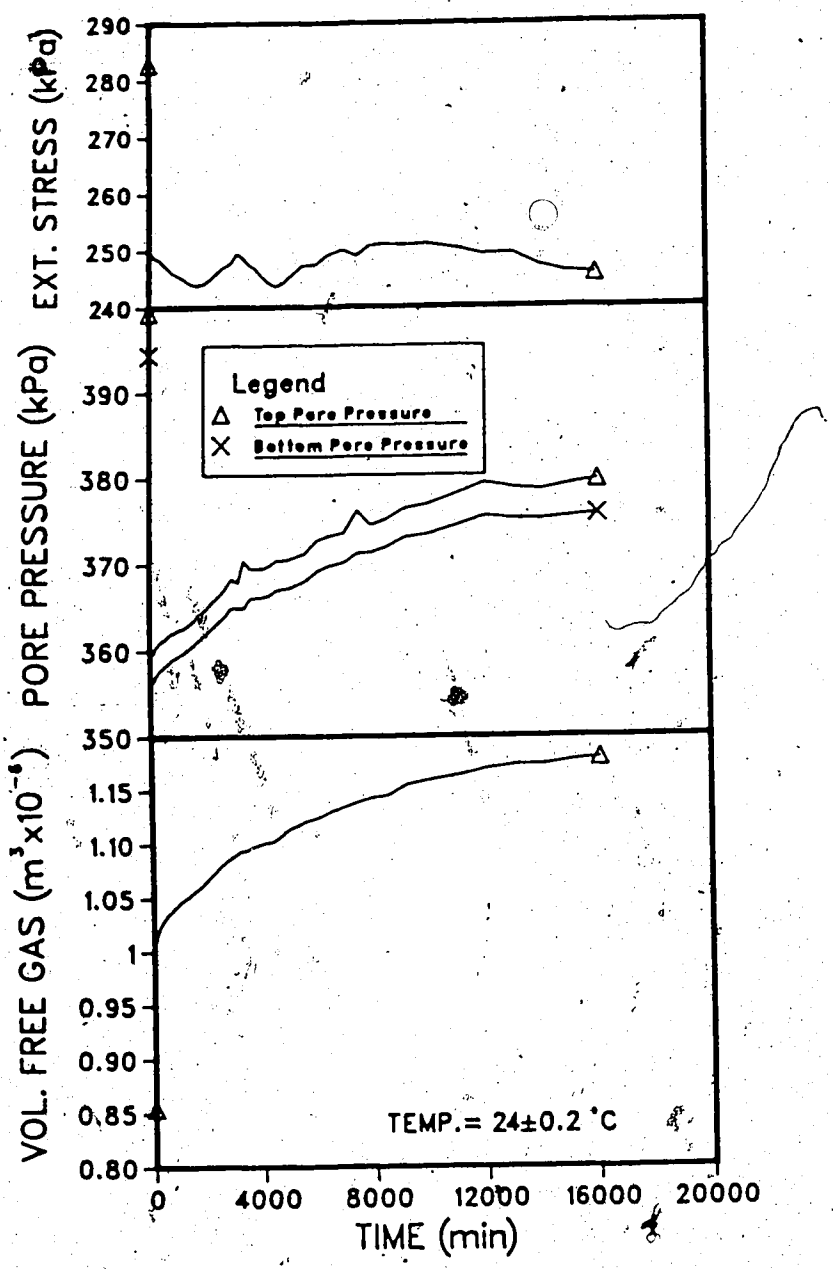

Figure C.52 Undrained Oedometer Test - Sample 11-5 - Step C

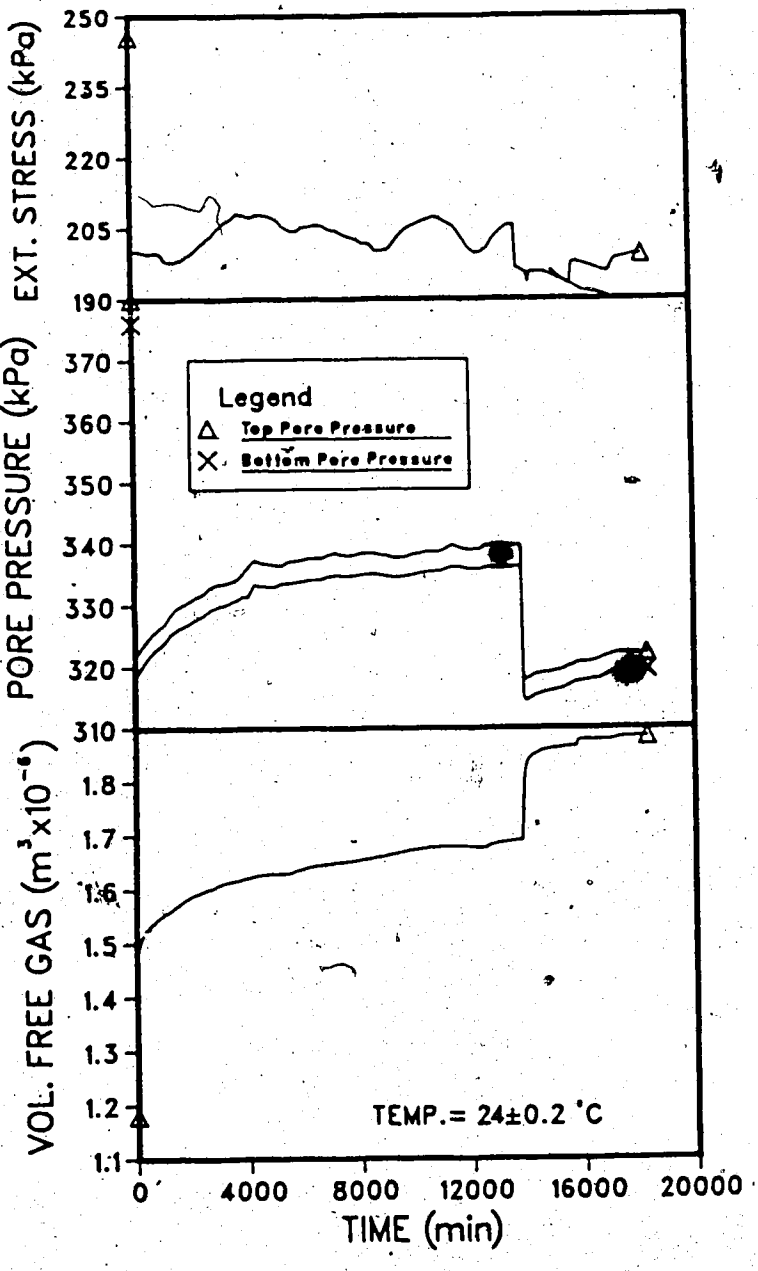

Figure C.53 Undrained Oedometer Test - Sample 11-5 - Step D

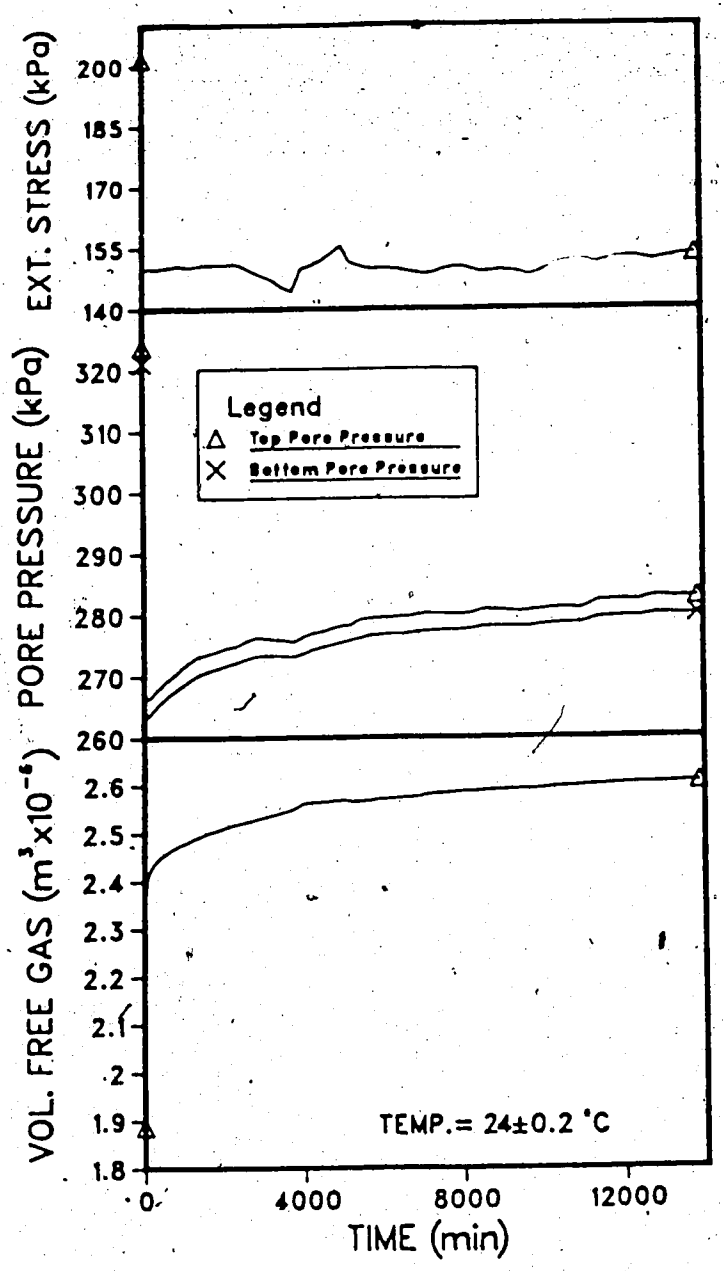

Figure C.54 Undrained Oedometer Test - Sample 11-5 - Step E

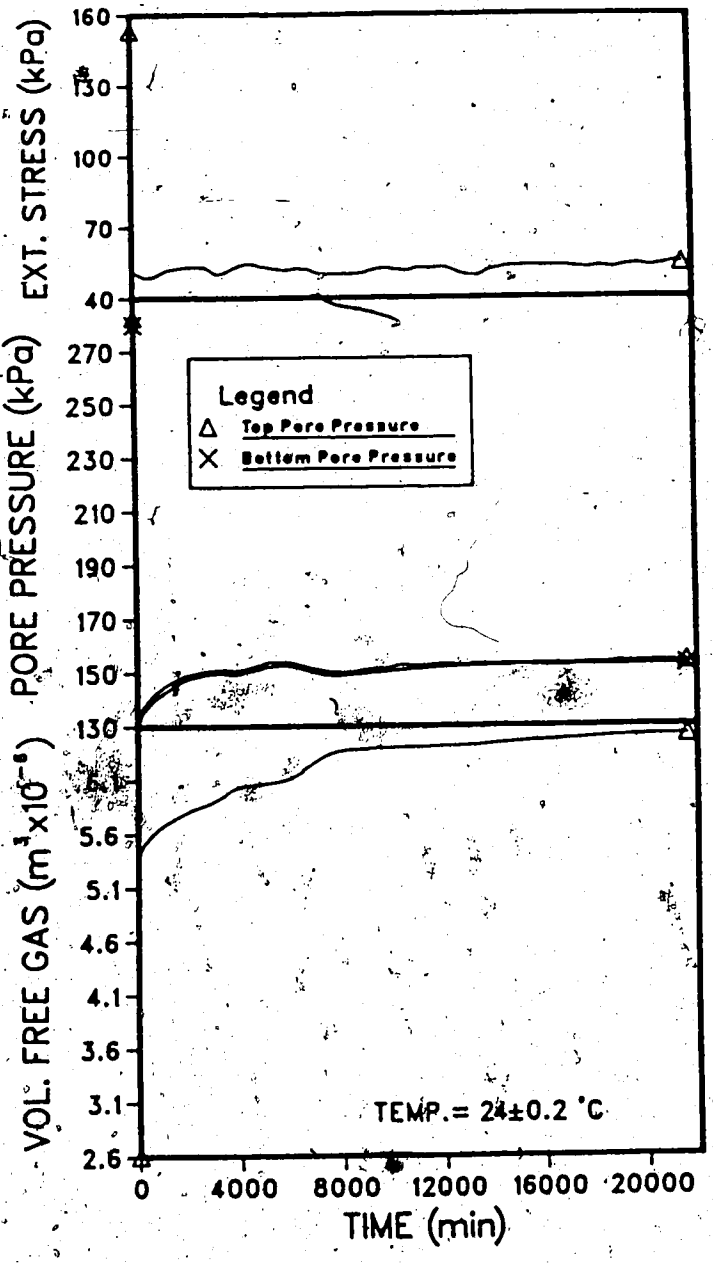

Figure C.55 Undrained Oedometer Test - Sample 11-5 - Step F

APPENDIX D - ANALYSIS OF GAS EVOLUTION TEST DATA

D.1 Evaluation of Combined Solubility Coefficient from Laboratory Tests

According to derivations presented in Chapter 2, Section 2.2.1.

$$V_{Tg} = V_{fg} + HV_L \qquad [2.33]$$

All variables are defined in Chapter 2.

Let us imagine a laboratory test with a gassy soil subjected to undrained isotropic unloading steps in which the absolute pore pressure (assumed equal in all fluid phases) is decreased from P_1 to P_2. The following equations can then be written.

$$\text{at } P_1 \ldots V^1_{Tg} = V^1_{fg} + HV_L \qquad [D.1]$$

$$\text{at } P_2 \ldots V^2_{Tg} = V^2_{fg} + HV_L \qquad [D.2]$$

According to Equation 2.35, Boyle's law can be applied to the total volume of gas V_{Tg}, hence,

$$V^2_{Tg} = \frac{V^1_{Tg} \cdot P_1}{P_2} \qquad [D.3]$$

Substituting D.1 and D.2 in D.3:

$$(V^1_{fg} + HV_L)\frac{P_1}{P_2} = V^2_{fg} + HV_L \qquad [D.4]$$

$$V^1_{fg}\frac{P_1}{P_2} + HV_L\frac{P_1}{P_2} = V^2_{fg} + HV_L \qquad [D.5]$$

The solubility coefficient can now be obtained.

$$H = \frac{V^1_{fg}(P_1/P_2) - V^2_{fg}}{V_L(1-(P_1/P_2))} \qquad [D.6]$$

The numerator of Equation D.6 is in fact the volume of gas that comes out of solution, or the change in volume of free gas measured at P_2,

$$H = \frac{\Delta V^{P2}_{fg}}{V_L(\Delta P/P_2)}$$

$$= \frac{P_2\ \Delta V^{P2}_{fg}}{V_L \Delta P} \qquad [D.7]$$

but,

$$P_2 \Delta V^{P2}_{fg} = P_{atm}\ \Delta V^{Patm}_{fg} \qquad [D.8]$$

Substituting D.8 in D.7:

$$H = \frac{P_{atm}\ \Delta V^{Patm}_{fg}}{V_L \Delta P} \qquad [D.9]$$

Equation D.9 demonstrates that the slope of the curve $(\Delta V^{Patm}_{EVOL}/V_L)$ x ΔP, multiplied by P_{atm} is the solubility coefficient.

D.2 Regression Analysis of Gas Evolution Test Data

This section presents the procedure used for the statistical analysis of gas exsolution test data.

According to Sobkowicz's macroscopic gas evolution model, the time-dependent volume change of free gas under constant pressure can described by the following equations:

1) "Quotient + 1" function:

$$V_{fg}(t) = V_1 + (V_2 - V_1)\frac{t}{t + A'}$$ (Sobkowicz, 1982:233)

where,

t = elapsed time after immediate response,

$V_{fg}(t)$ = volume of free gas at time t

V_1 = initial volume of free gas after immediate response

V_2 = final volume of free gas after transient process ceases (unknown)

A' = scaling parameter (unknown)

2) Exponential function

$V_{fg}(t) = V_2 - (V_2 - V_1)e^{-Econst.t}$ (Sobkowicz 1982:239).

E_{const} = gas evolution parameter

All other variables have been previously defined. The following two items describe the approach followed for the statistics analysis using these two functions.

"Quotient + 1" function

This function has the same form as the hyperbolic function, often used in nonlinear elastic constitutive models for soils. It can be transformed to a linear function with the following modifications (similarly to procedure by Duncan et al., 1980).

$$V_{fg}(t) = V_1 + (V_2 - V_1)\frac{t}{t + A}$$

$$V_{fg}(t) - V_1 = \frac{(V_2 - V_1)}{t + A} \cdot t$$

$$\frac{t + A}{V_2 - V_1} = \frac{t}{V_{fg}(t) - V_1}$$

$$\frac{t}{V_{fg}(t) - V_1} = \frac{A}{V_2 - V_1} + \frac{t}{V_2 - V_1}$$

This equation has the form of a linear function with the form:

$$y = a + bx$$

where:

$$y = \frac{t}{V_{fg}(t) - V_1}$$

$$a = \frac{A}{V_2 - V_1}$$

$$b = \frac{1}{V_2 - V_1}$$

$$x = t$$

Figure D1 illustrates the linearized "Quotient + 1" function. The "$V_{fg}(t)$ x t" data produced by the tests can now be analyzed by linear regression, where:

$$x \Rightarrow t$$

$$y \Rightarrow \frac{t}{V_{fg}(t) - V_1}$$

Once the best fit linear function is obtained from linear regression from laboratory data, the scaling factor 'A' and the projected final volume of free gas are evaluated as follows.

$$V_2 = V_1 + \frac{1}{b}$$

and

$$A' = \frac{a}{b}$$

Exponential Function

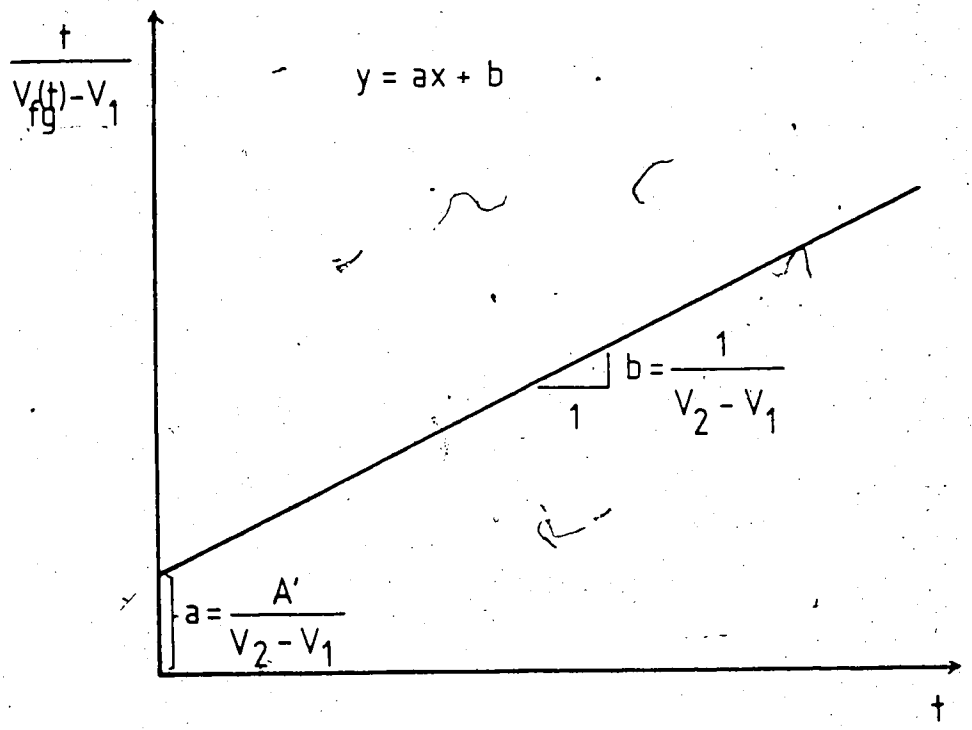

Figure D.1 Linearized "Quotient + 1" Function

The exponential function also can be linearized as follows:

$$V_{fg}(t) = V_2 - (V_2 - V_1)e$$

$$V_2 - V_{fg}(t) = (V_2 - V_1)e^{-Econst.t}$$

$$\ln(V_2 - V_{fg}(t)) = \ln(V_2 - V_1) - E_{const} \cdot t$$

This equation has the form of a linear function with the form:

$$y = a + bx$$

where,

$$y = \ln(V_2 - V_{fg}(t))$$

$$a = \ln(V_2/V_1)$$

$$b = -E_{const}$$

$$x = t$$

Figure D.2 illustrates the linearlized Exponential function. The "V_{fg} x t" data produced by the tests can now be analysed by linear regression where,

$x \rightarrow t$

$y \rightarrow \ln(V_2 - V_{fg}(t))$

According to this procedure, the value of V_2, the final volume of free gas, is a known value, when in fact, it should be obtained from the statistical analysis. In order to eliminate this inconvenience, the following procedure is used.

Assume V_2 is the highest volume of free gas measured during

the test.

With linear regression analysis obtain E_{const} and V_1 as follows:

$E = -b$

$V_1 = V_2 - e^a$

Compare the value of V_1 obtained from this linear regression (V_{1LR}) with the real value of V_1 ($V_{1,REAL}$ at the beginning of that specific stage of the test.

Obtain $\Delta V_1 = V_{1REAL} - V_{1LR}$

Correct V_2

$V_{2\ PROJECTED} = V_{2\ MAX.MEASURED} + \Delta V_1$

Finally, the projected volume of free gas, V_2, and the gas evolution parameter, E_{const}, can be obtained.

$E_{const} = -b$

$V_2 = V_{2\ MAX.MEASURED} + V_{1REAL} - (V_{2\ MAX.MEAURED} - e^a)$

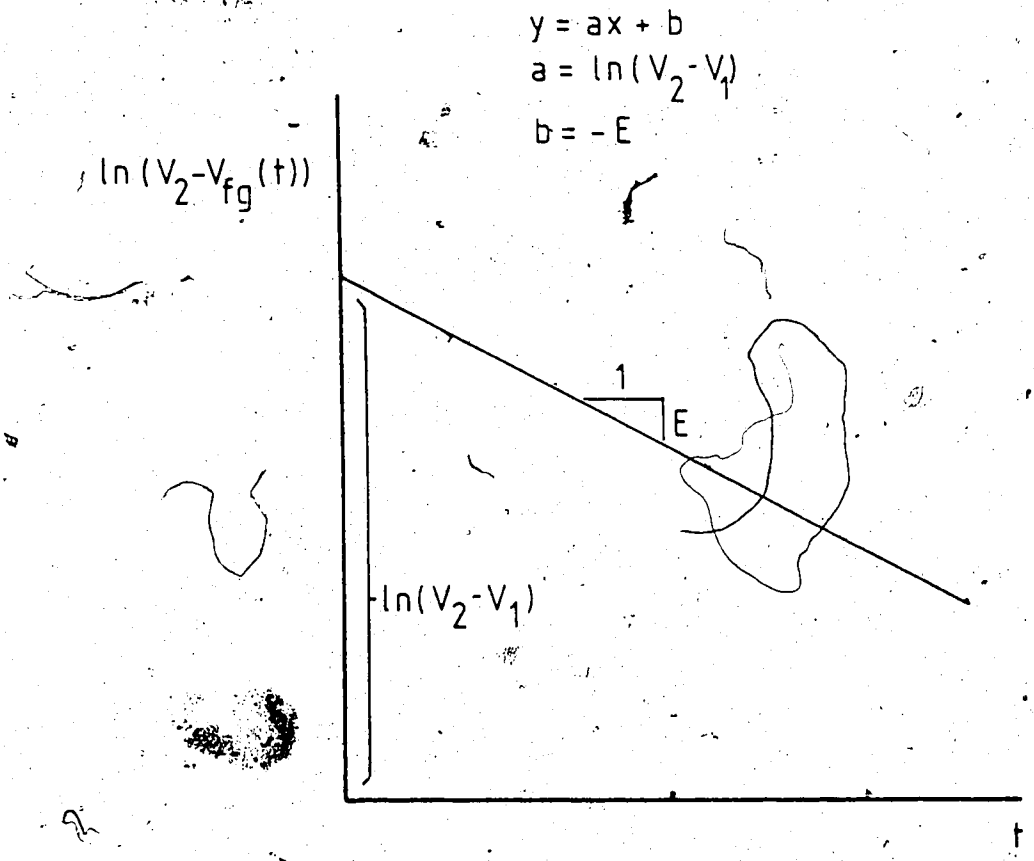

Figure D.2 Linearized Exponential Function

APPENDIX E - LABORATORY EQUIPMENT DATA

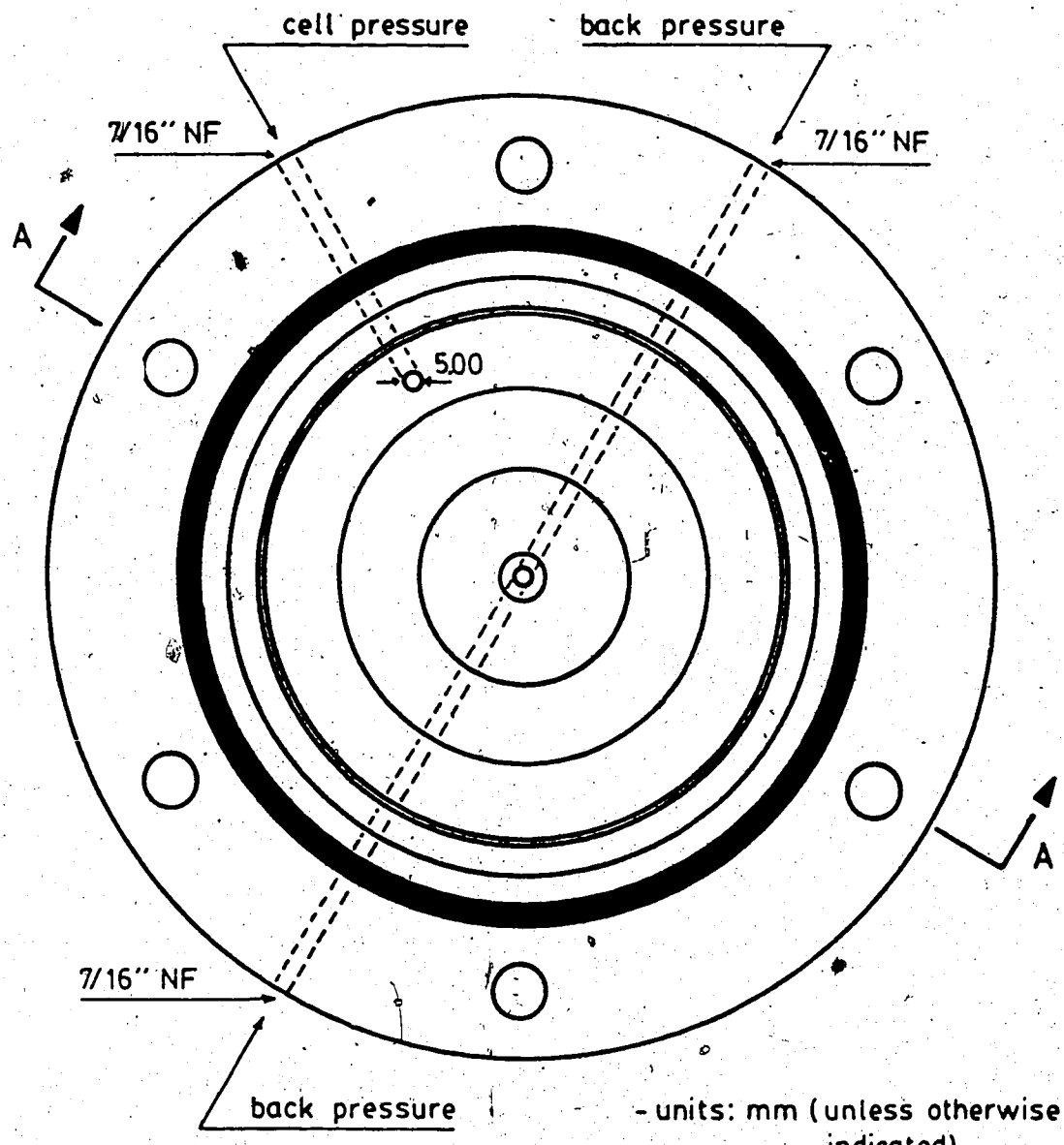

Figure E.1 Triaxial Cell - Base Platen and Pedestal - Top View

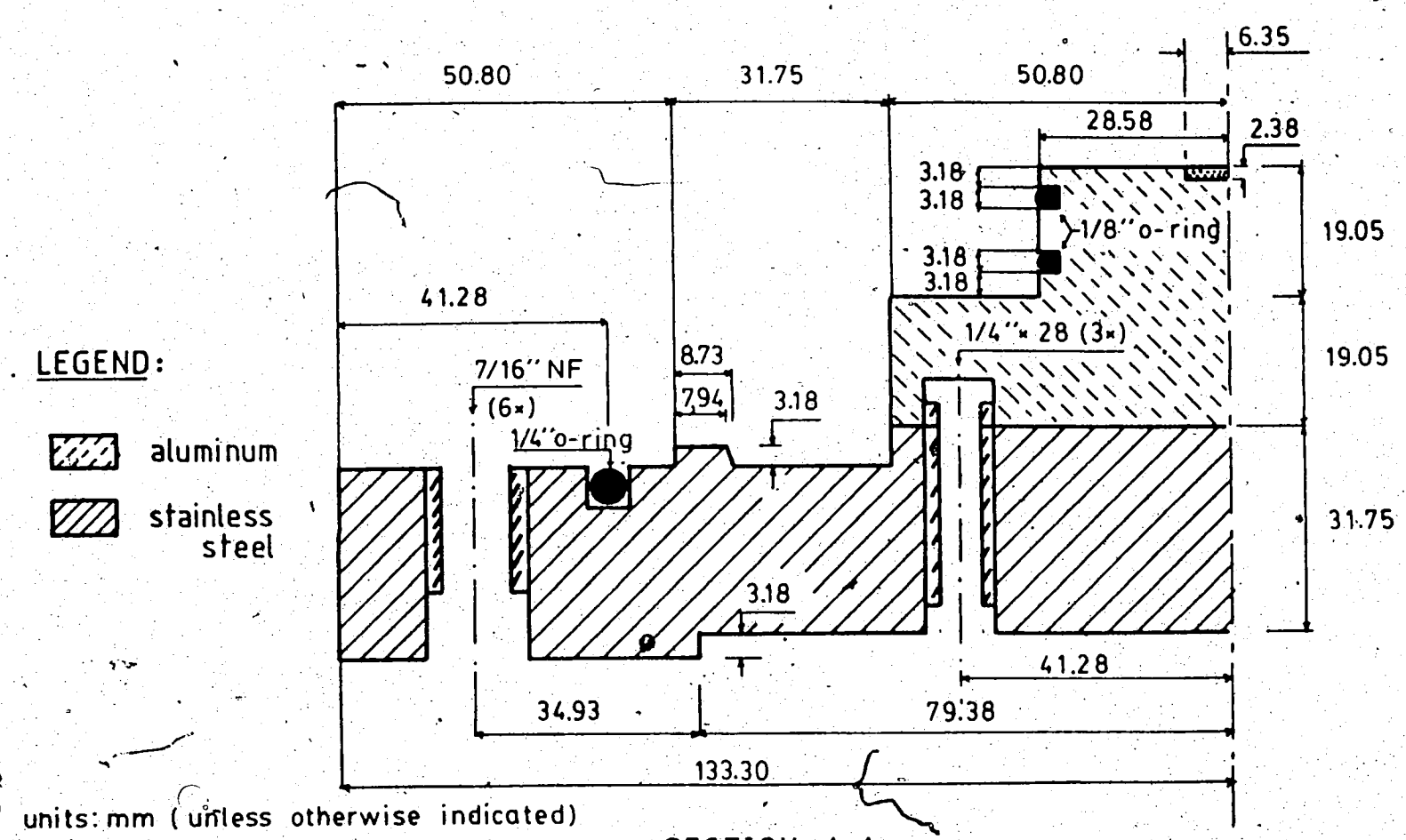

Figure E.2 Triaxial Cell - Base Plate and Pedestal

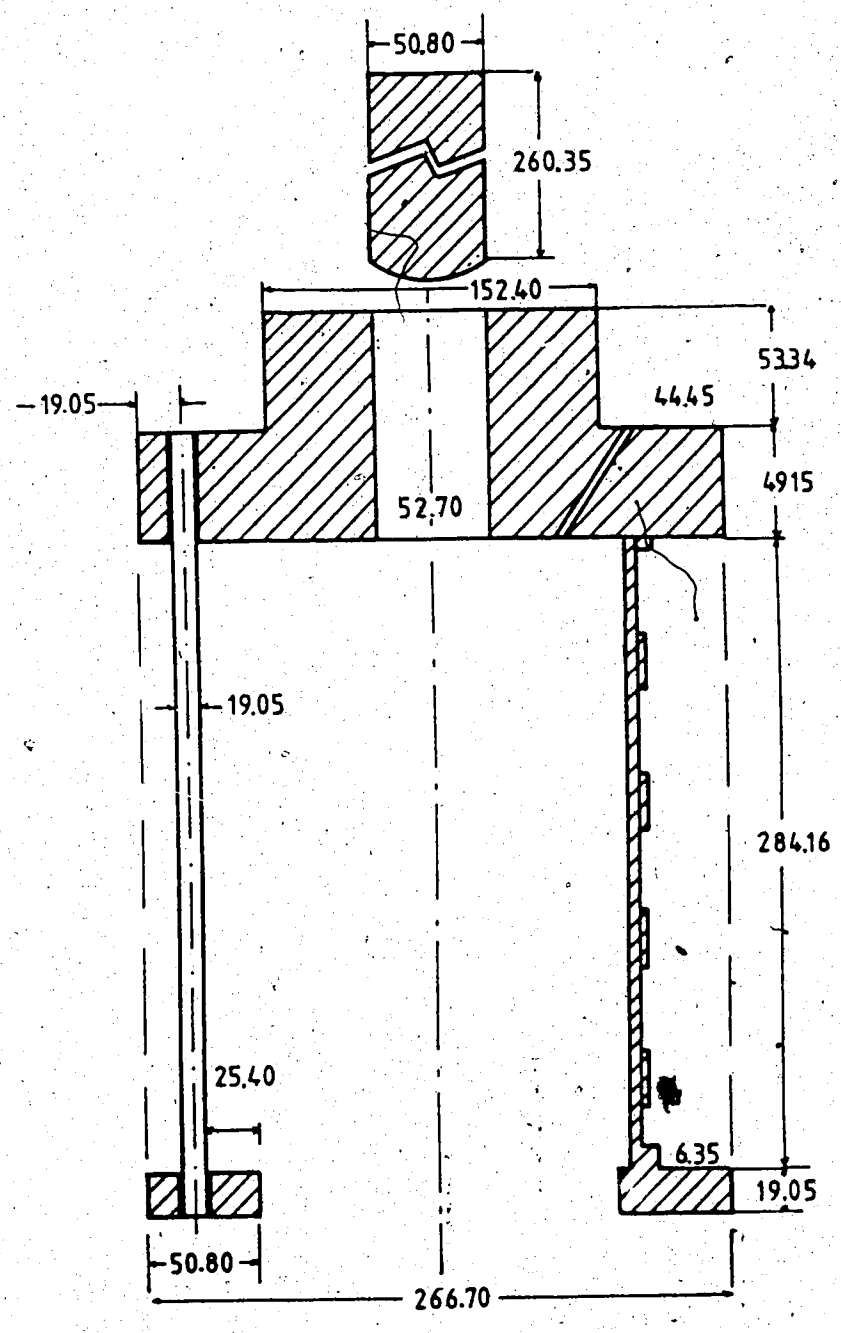

SECTION B-B

Figure E.3 Triaxial Cell - Section B-B

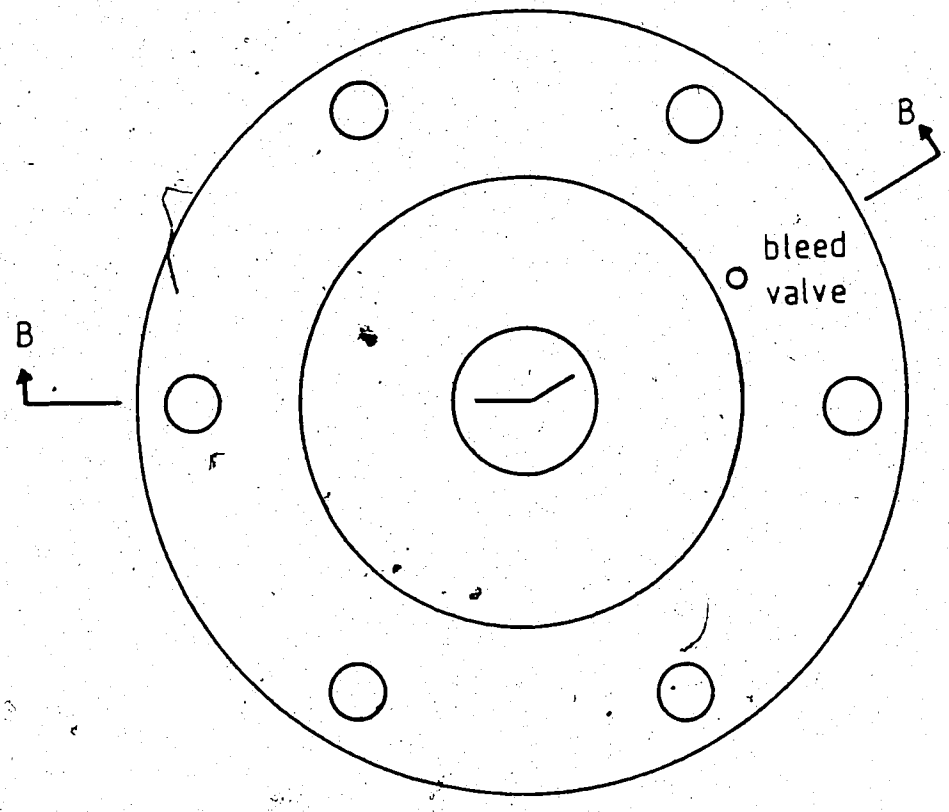

details in figure E3

Figure E.4 Triaxial Cell - Top Platen

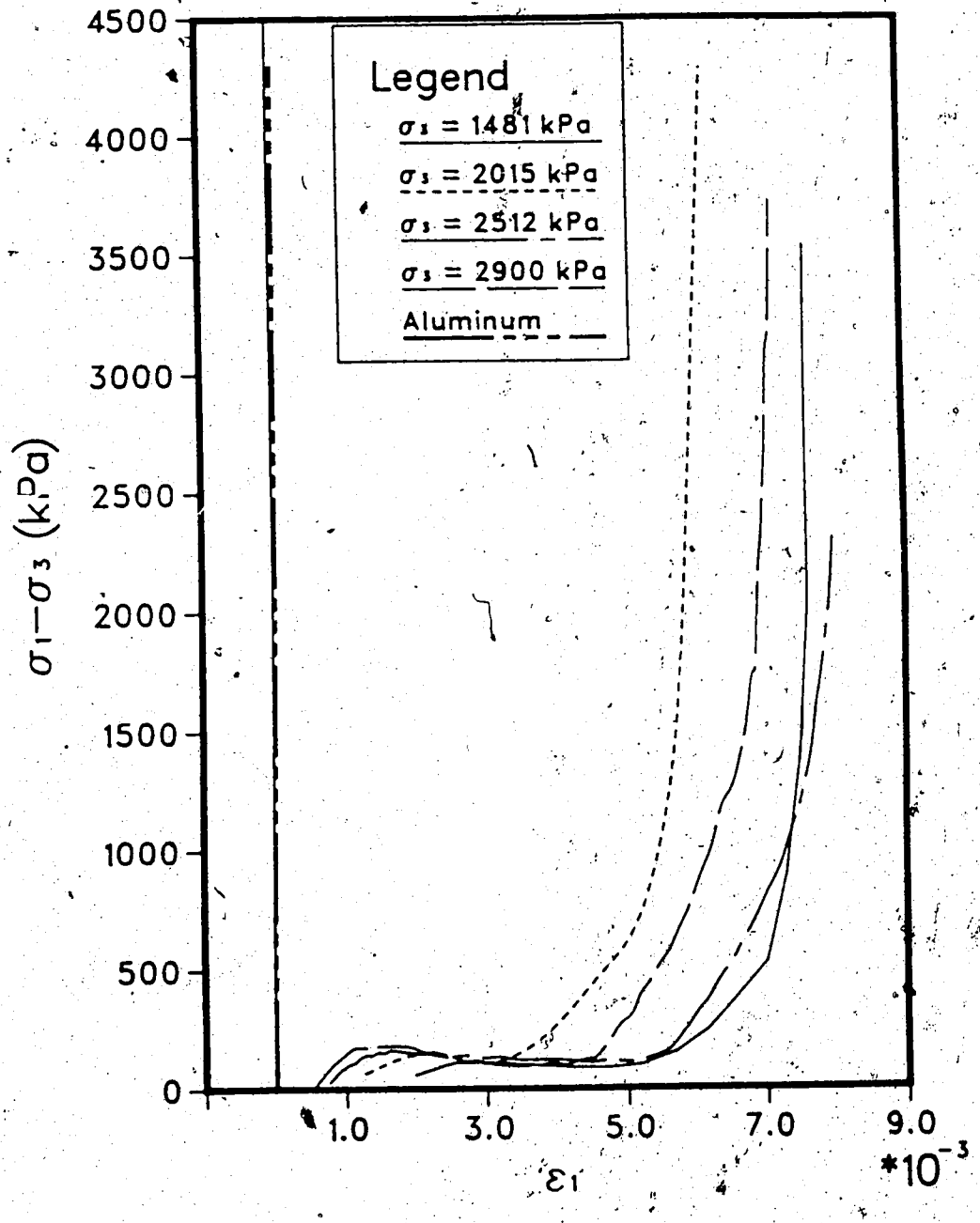

Figure E.5 Vertical [illegible]iance of the Triaxial Apparatus

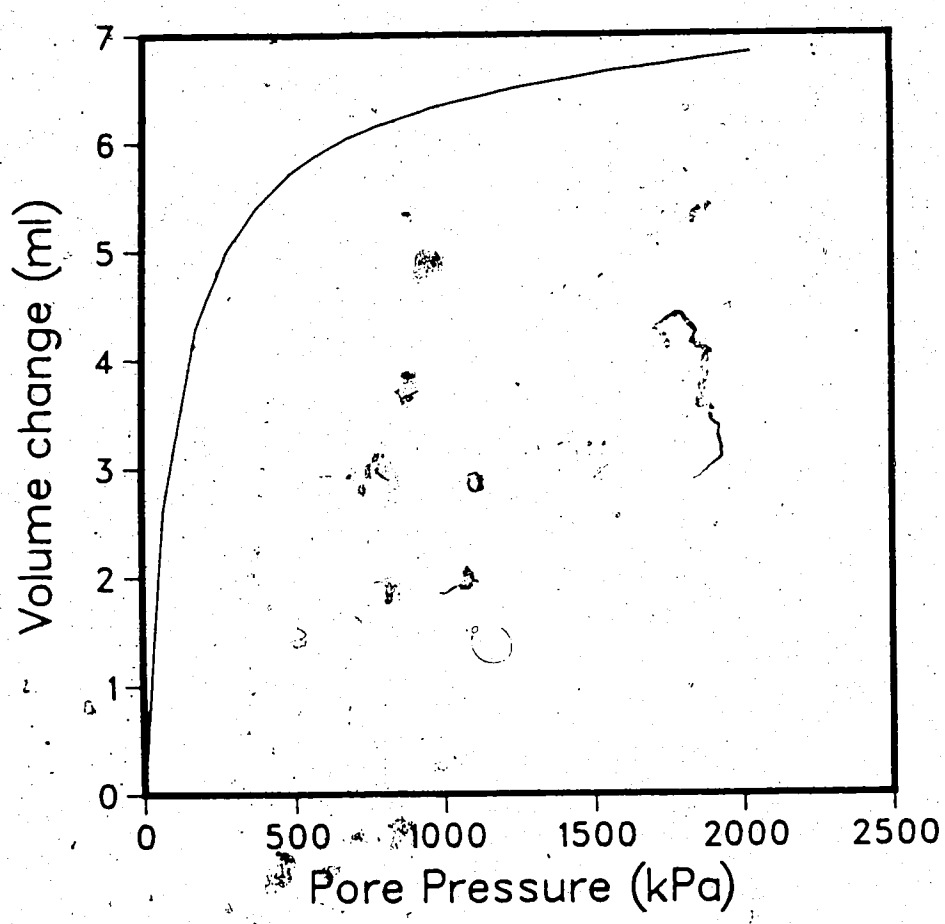

Figure E.6 Volumetric Compliance of the Back Pressure Lines

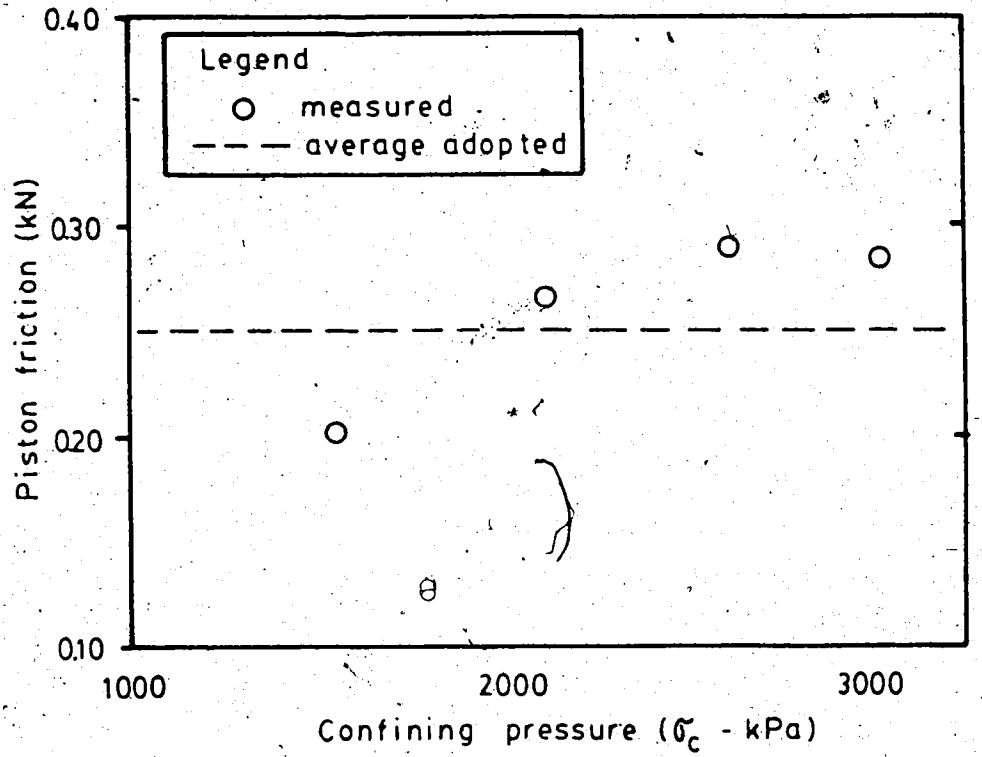

Figure E.7 Axial Load Correction for Piston Friction - Triaxial Apparatus

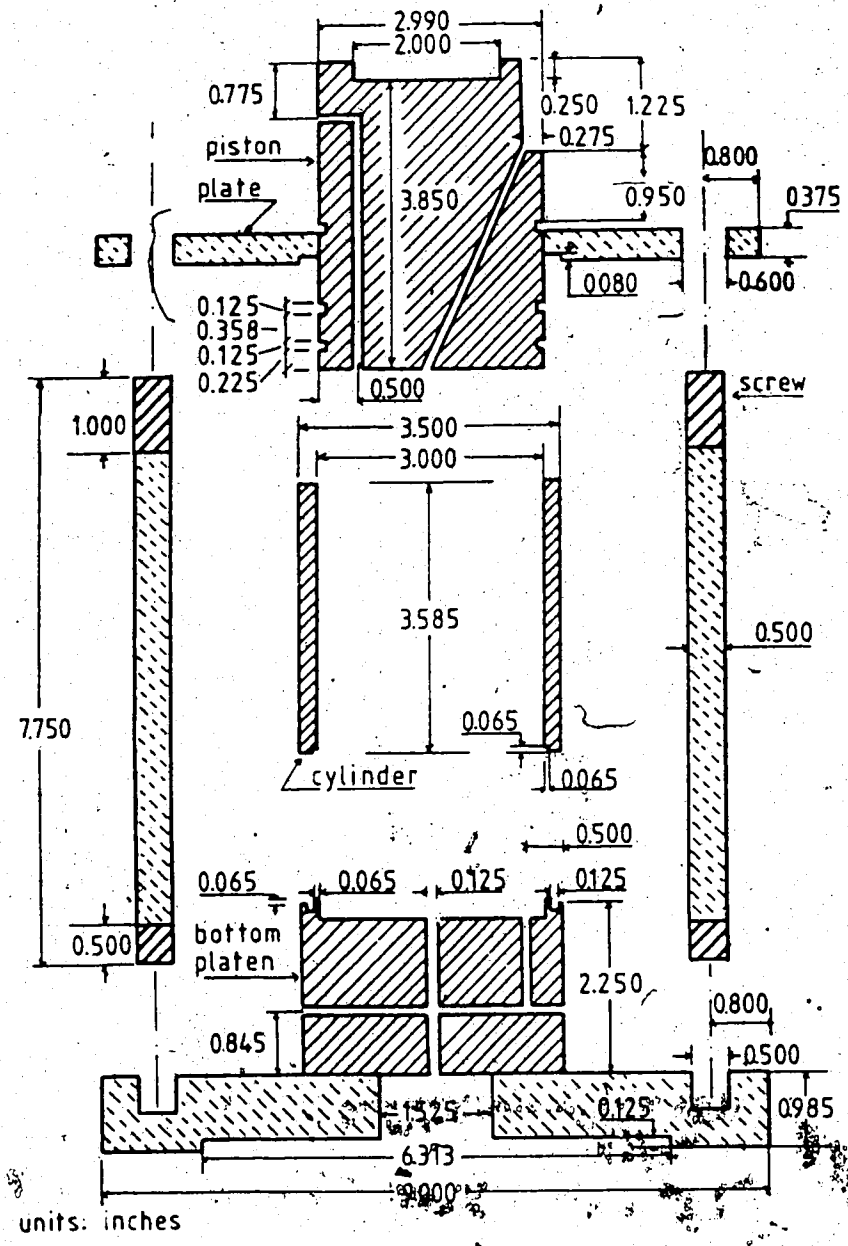

Figure E.8 Oedometer - Expanded Cross Section

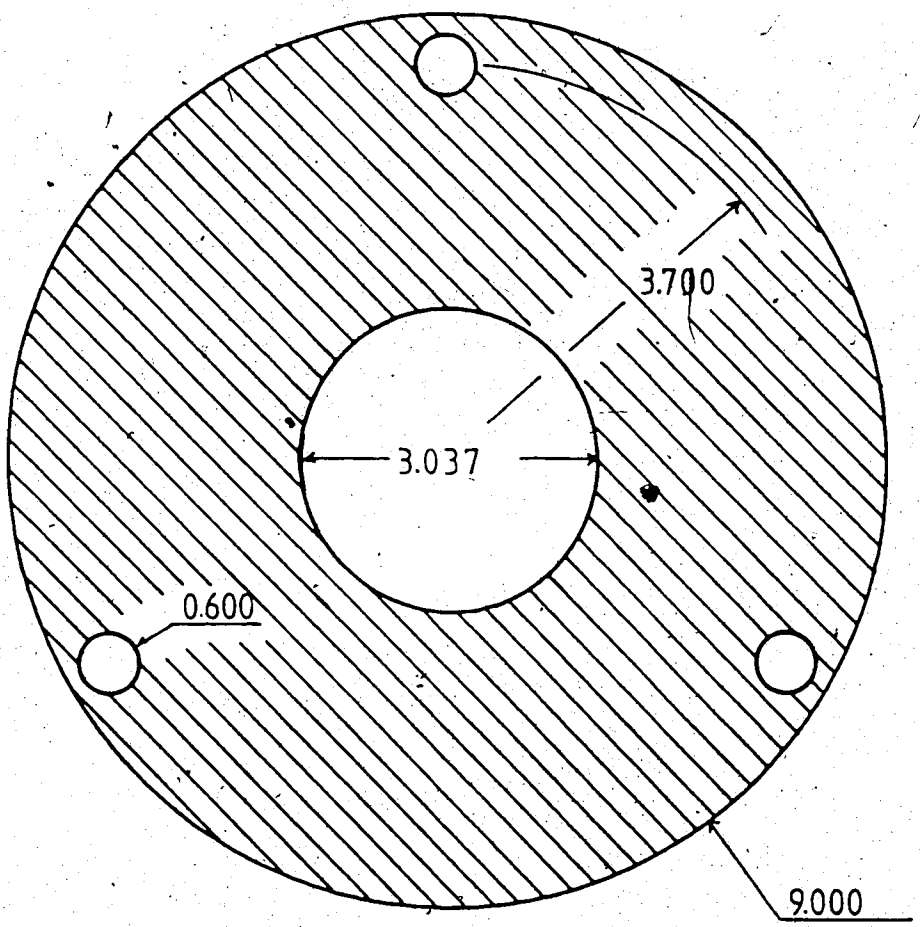

units: inches

Figure E.9 Oedometer - Top Plate

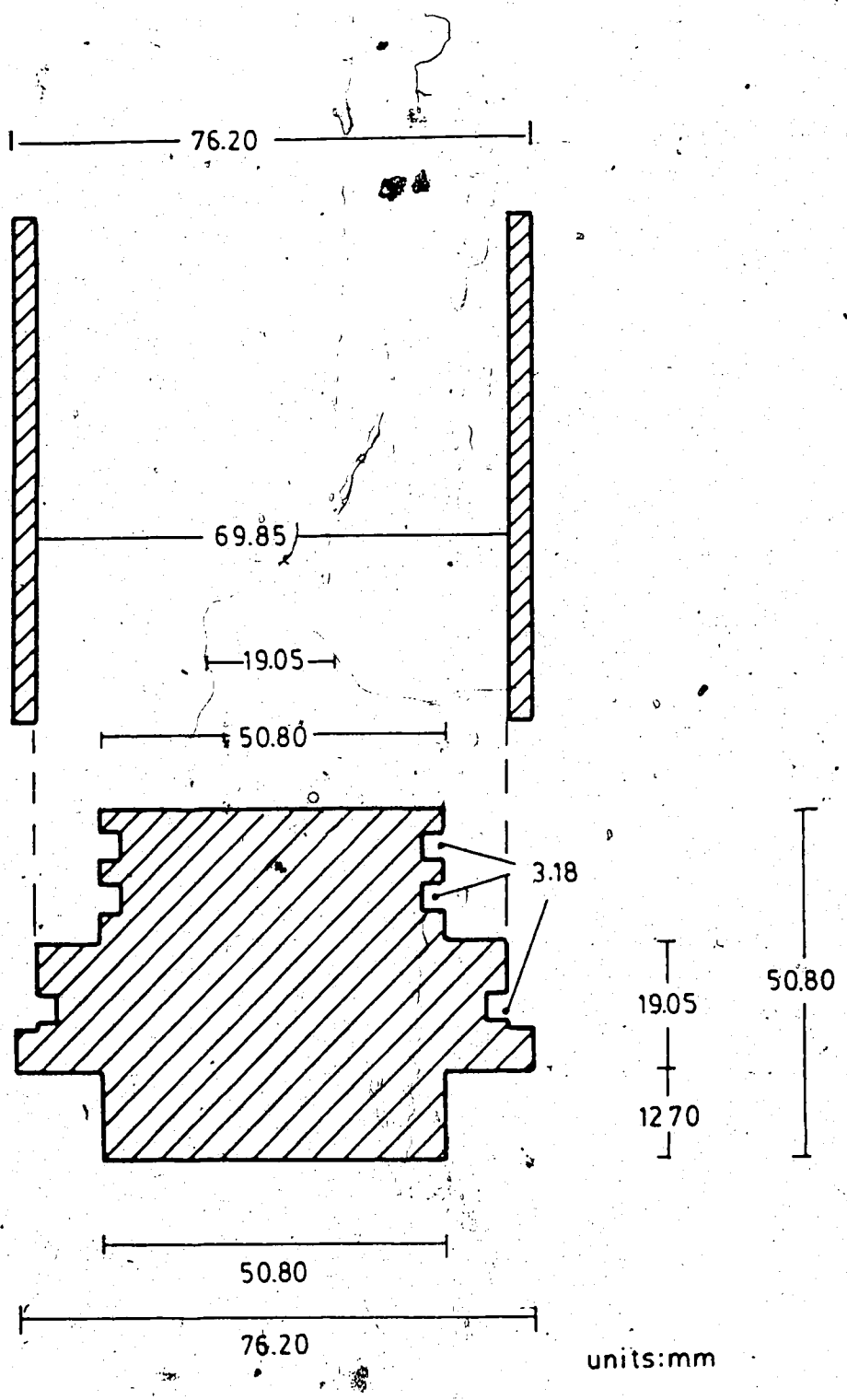

Figure E.10 Mercury Triaxial - Sample Pedestal

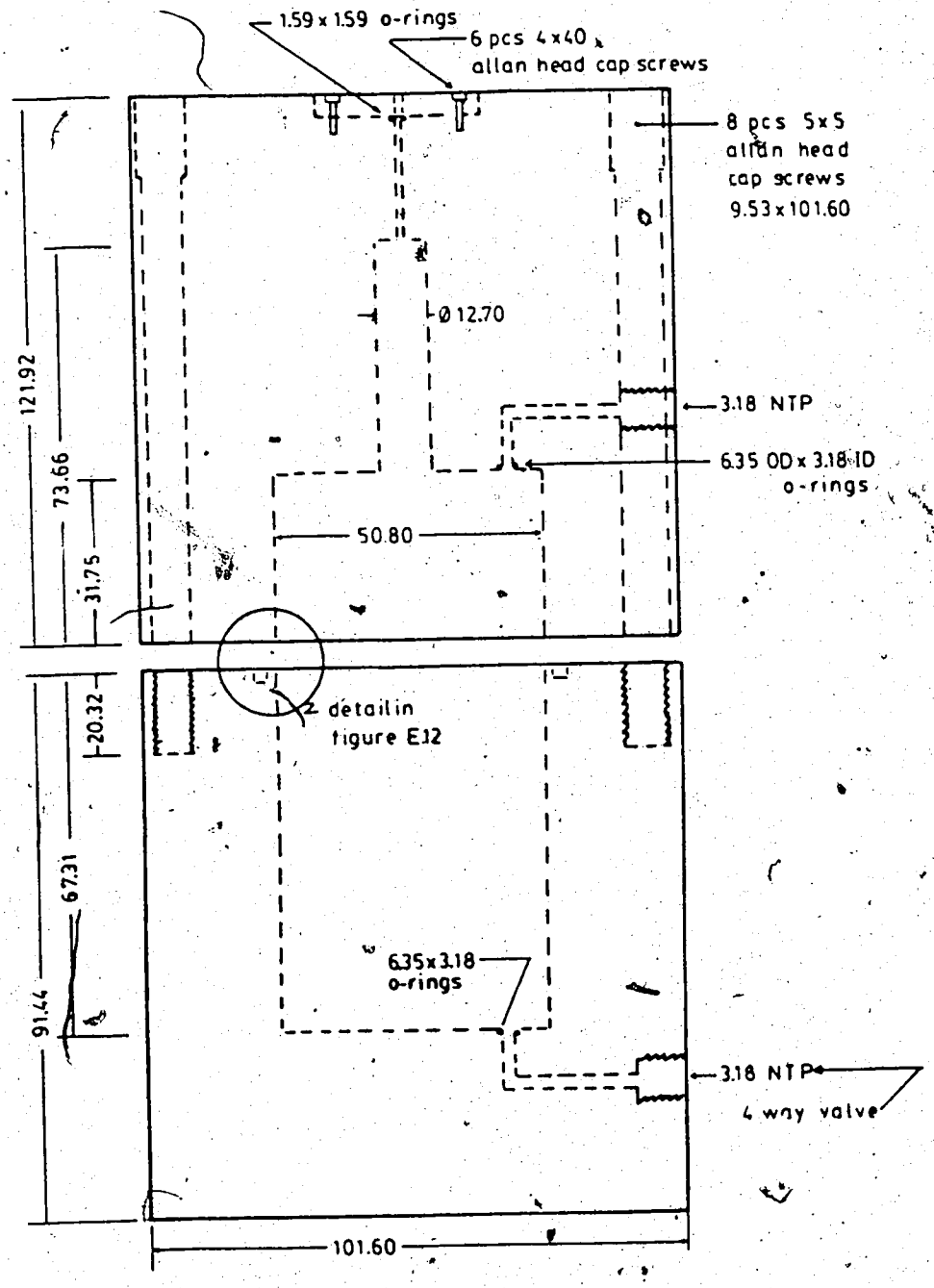

Figure E.11 U. of A. Volume Change Device

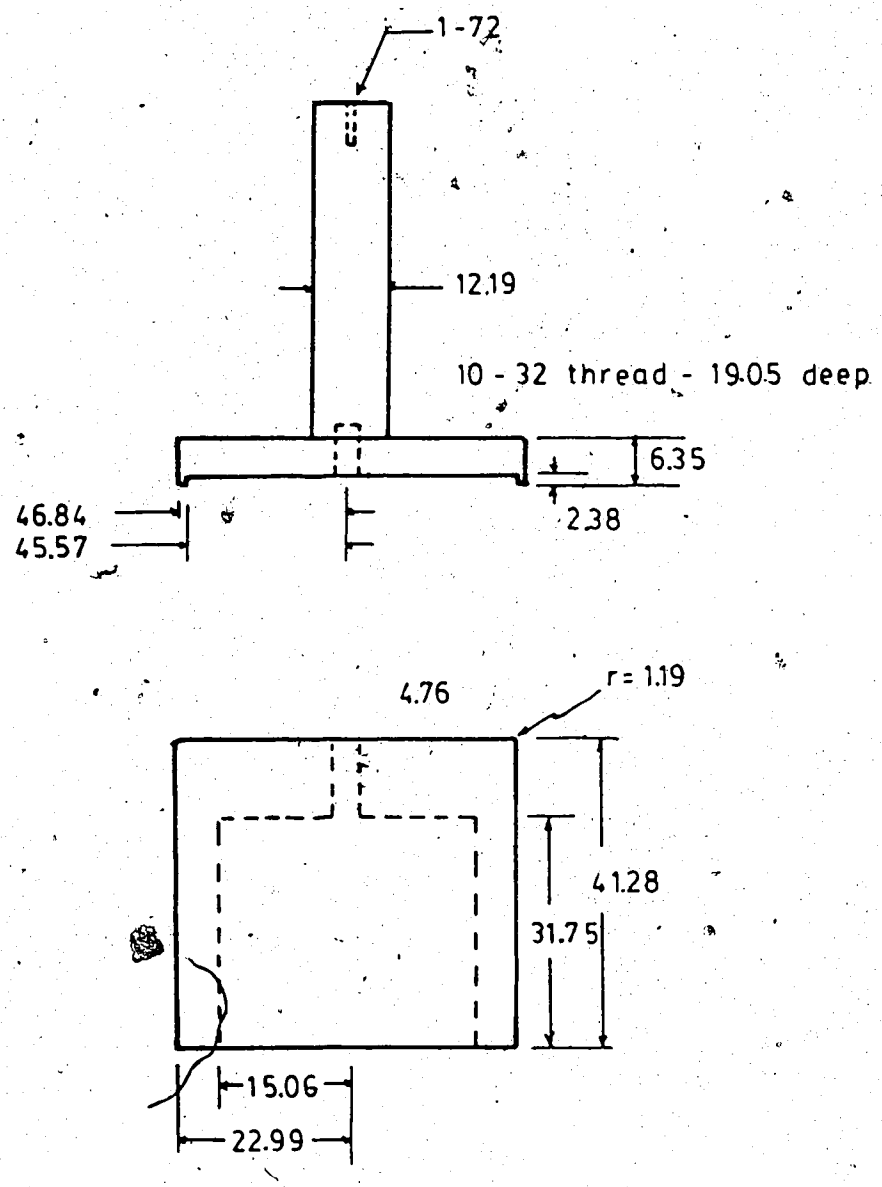

Figure E.12 U. of A. Volume Change Device - Piston

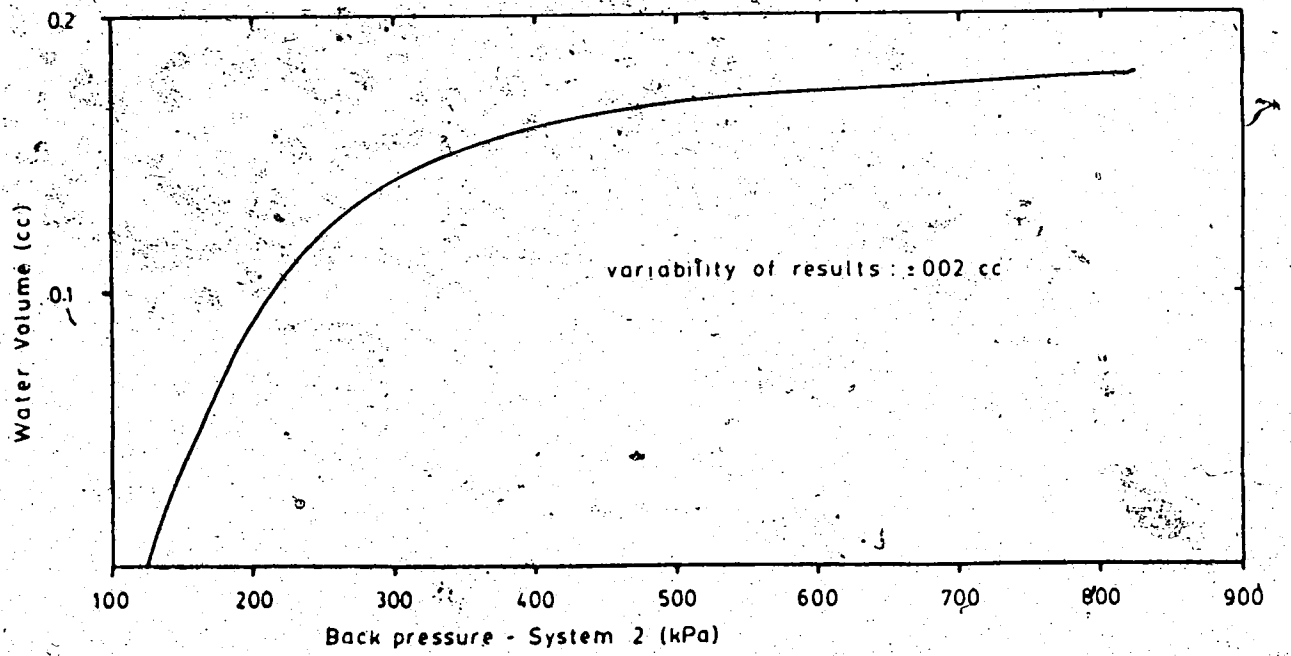

Figure E.13 Volumetric Compliance - Back Pressure System No. 2

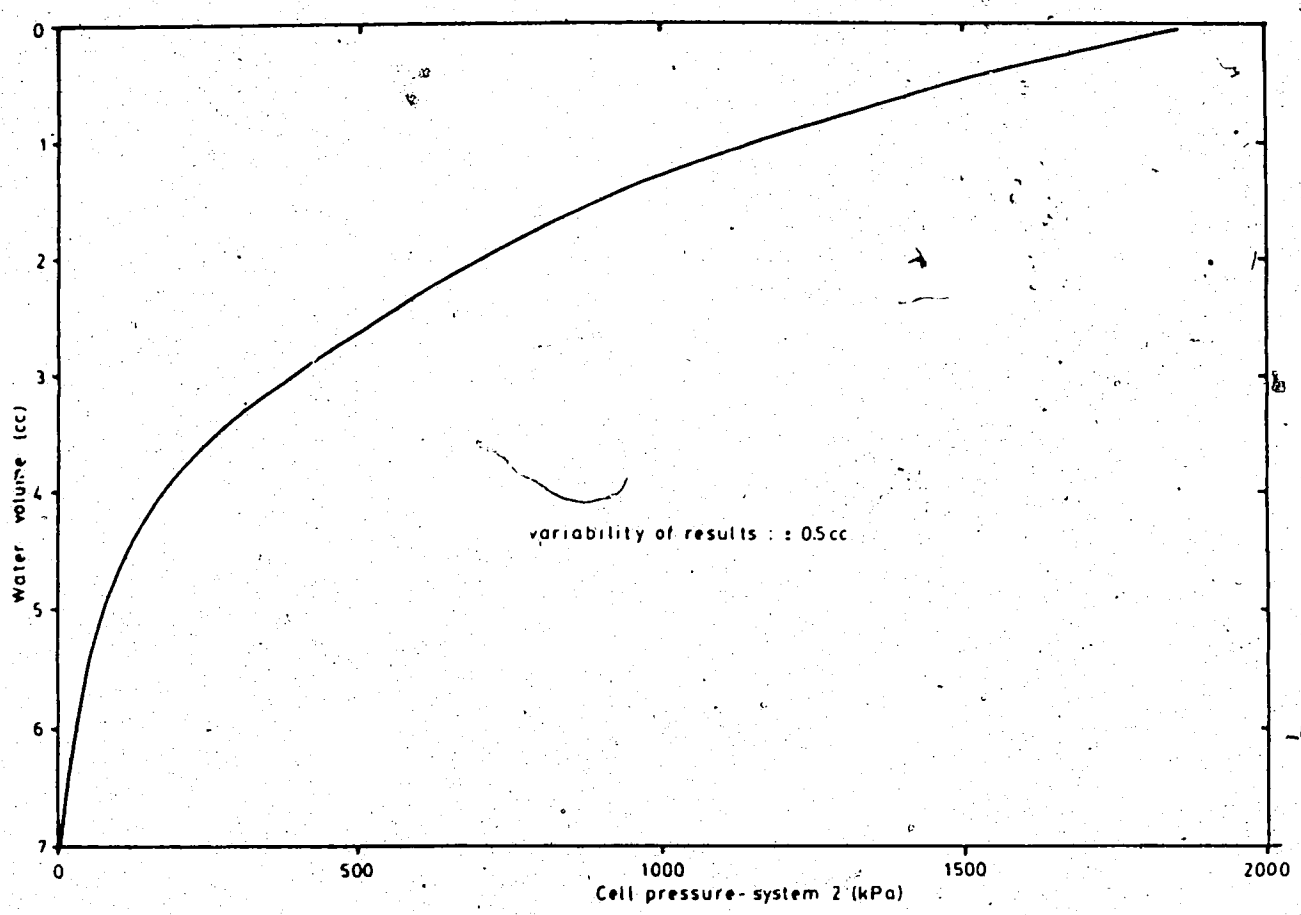

Figure E.14 Volumetric Compliance - Cell Pressure System No. 2

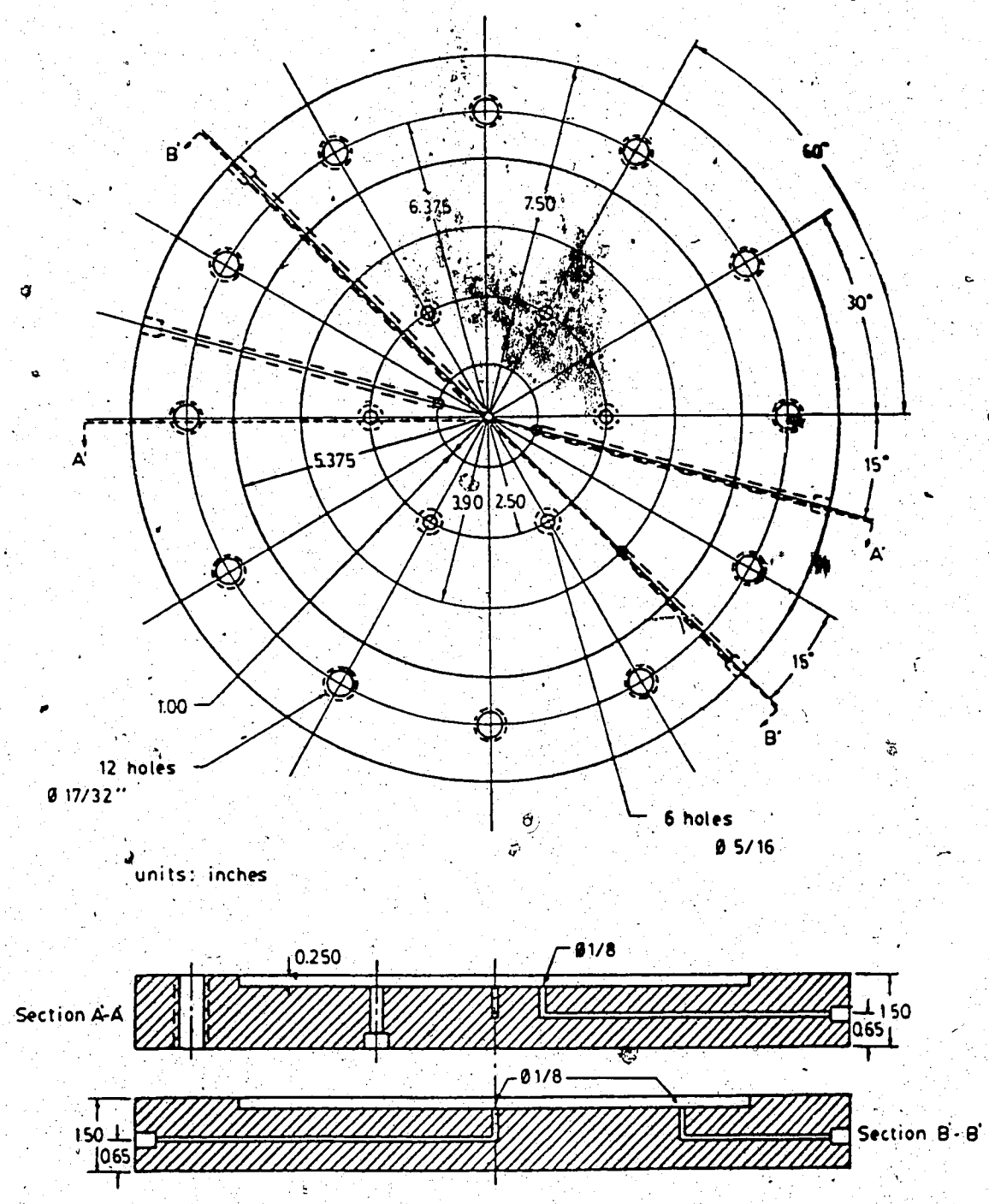

Figure E.15 Hollow Cylinder Cell - Bottom Platen

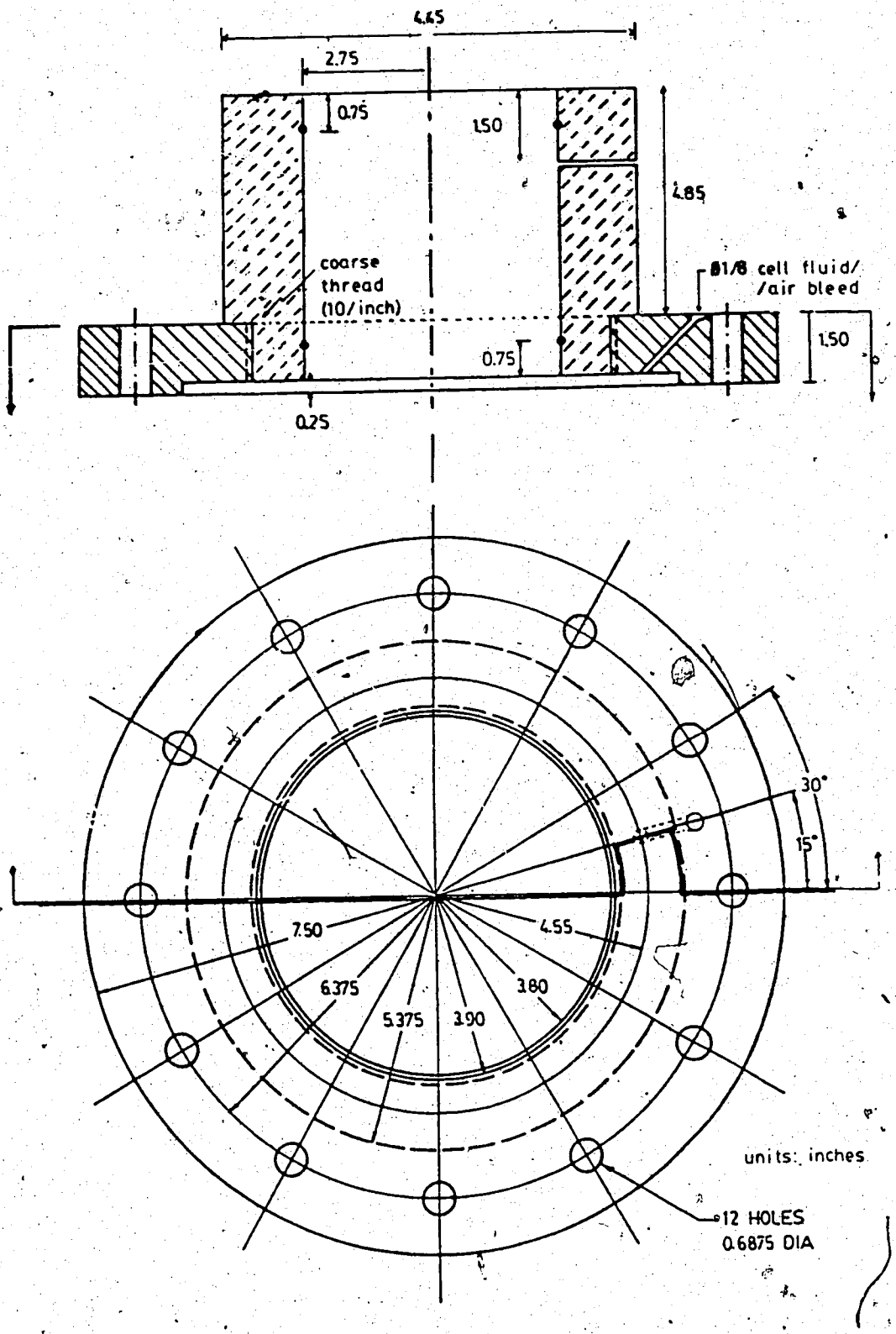

Figure E.16 Hollow Cylinder Cell - Top Platen

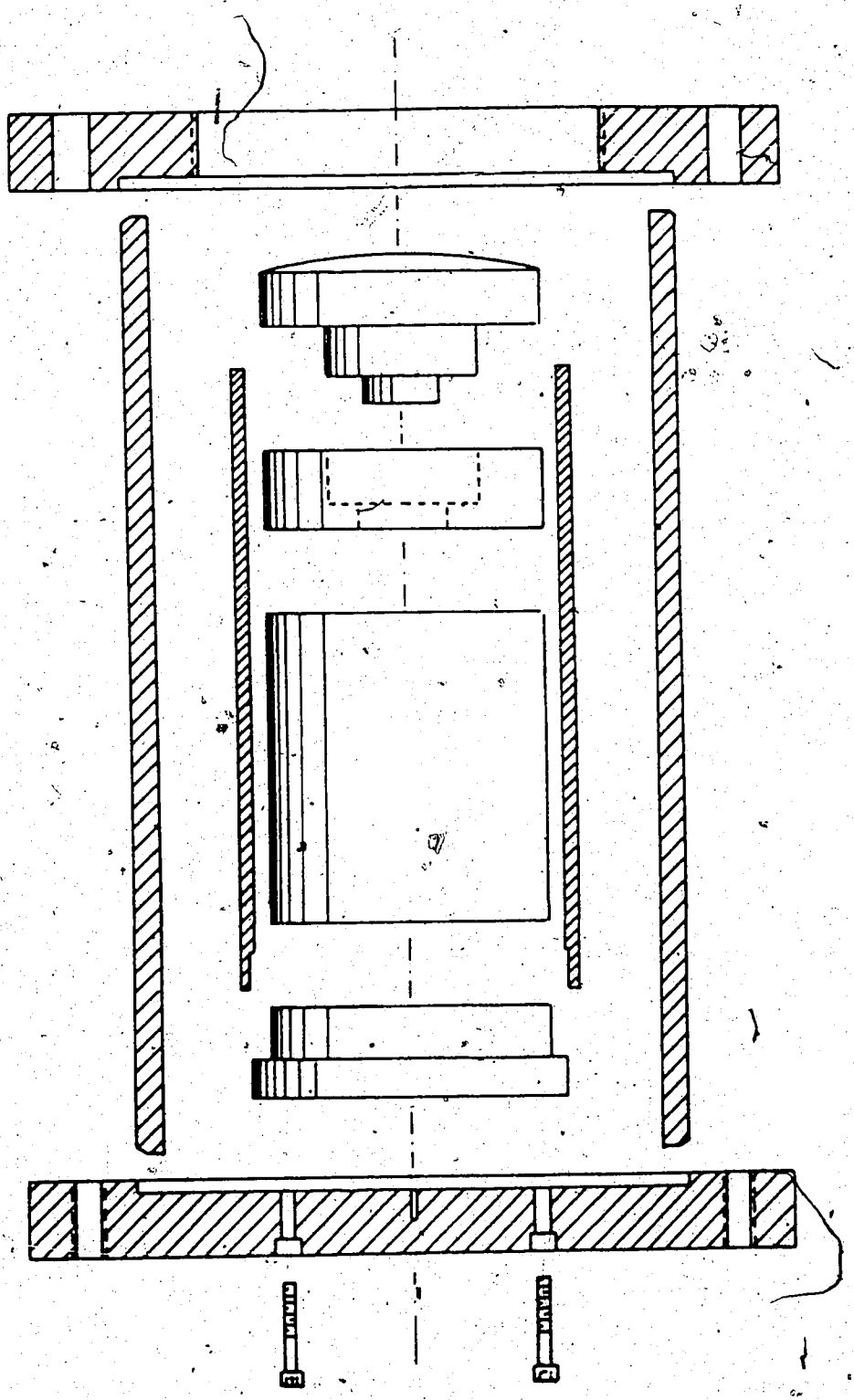

Figure E.17 Hollow Cylinder Cell - Sketch Cross Section

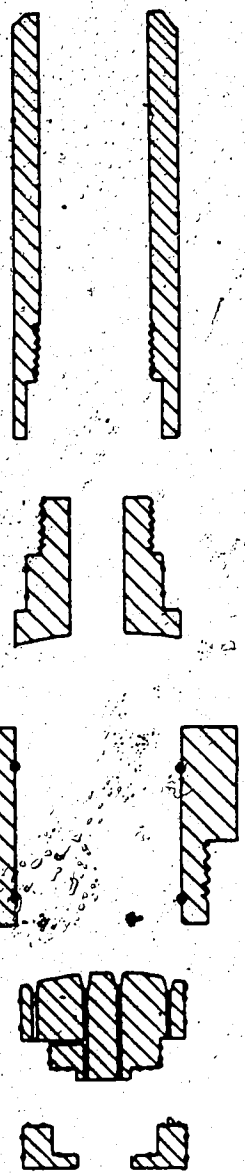

Figure E.18 Hollow Cylinder Cell - Sketch of Piston, Sample and Cap Assembly

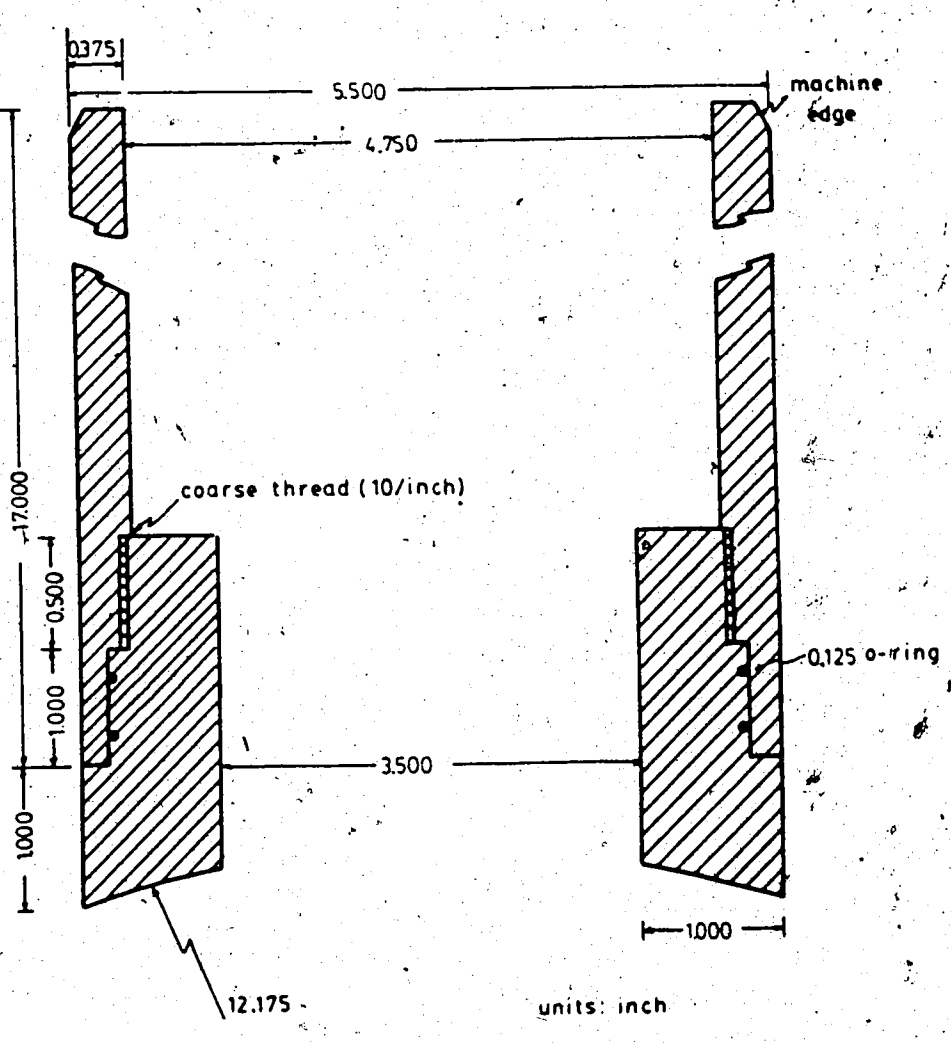

Figure E.19 Hollow Cylinder Cell - Piston

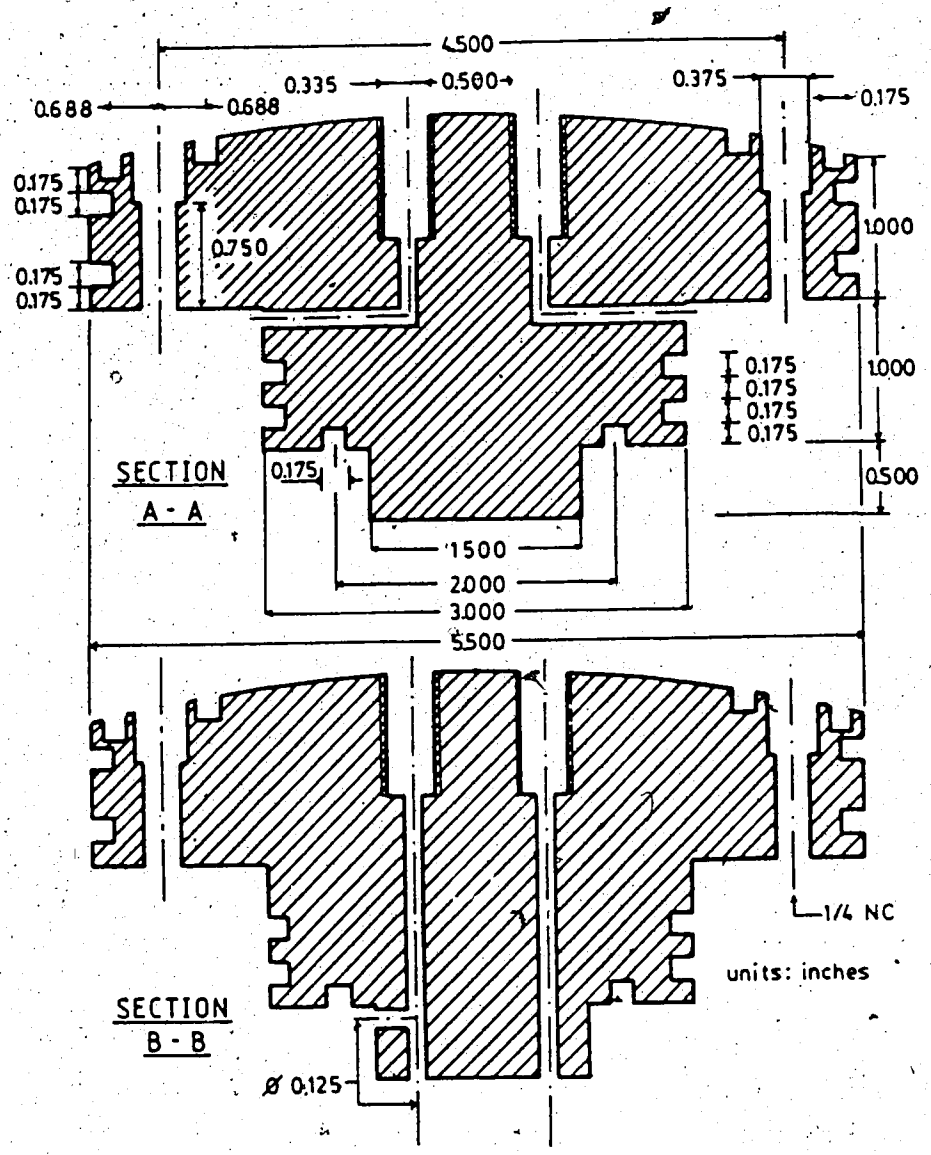

Figure E.20 Hollow Cylinder Cell - Top Cap - Cross Sections A-A and B-B

Note: refer to sections A-A and B-B for dimentions

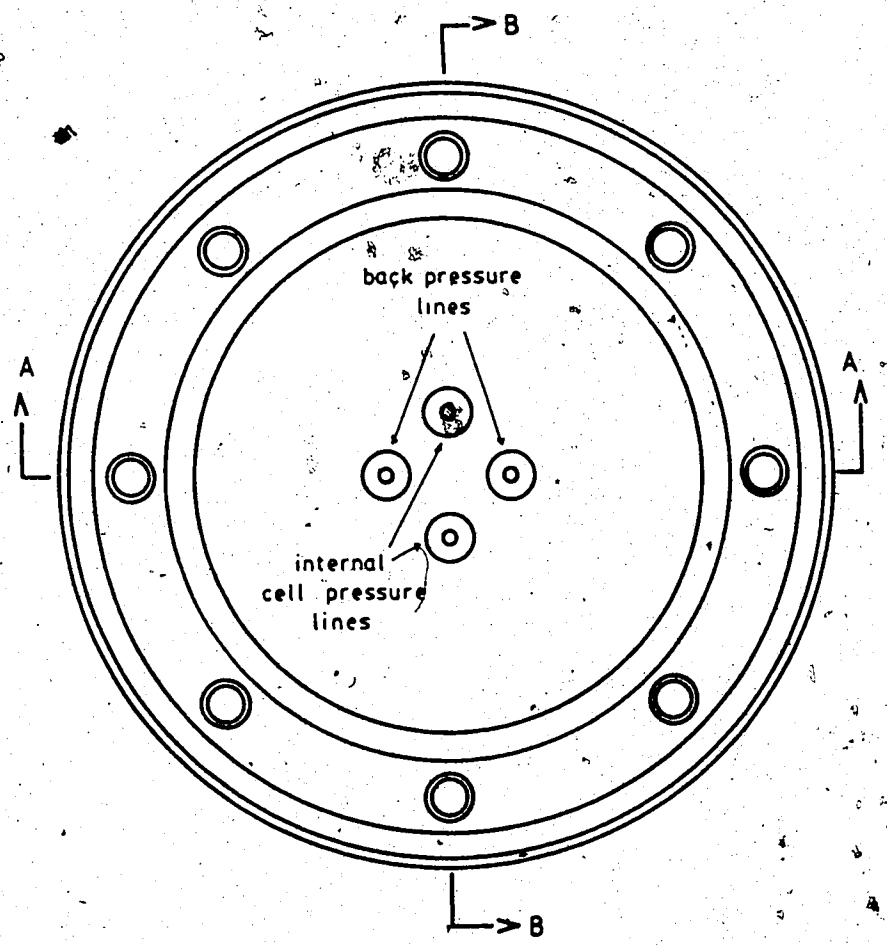

Figure E.21 Hollow Cylinder Cell - Top Cap - Top View

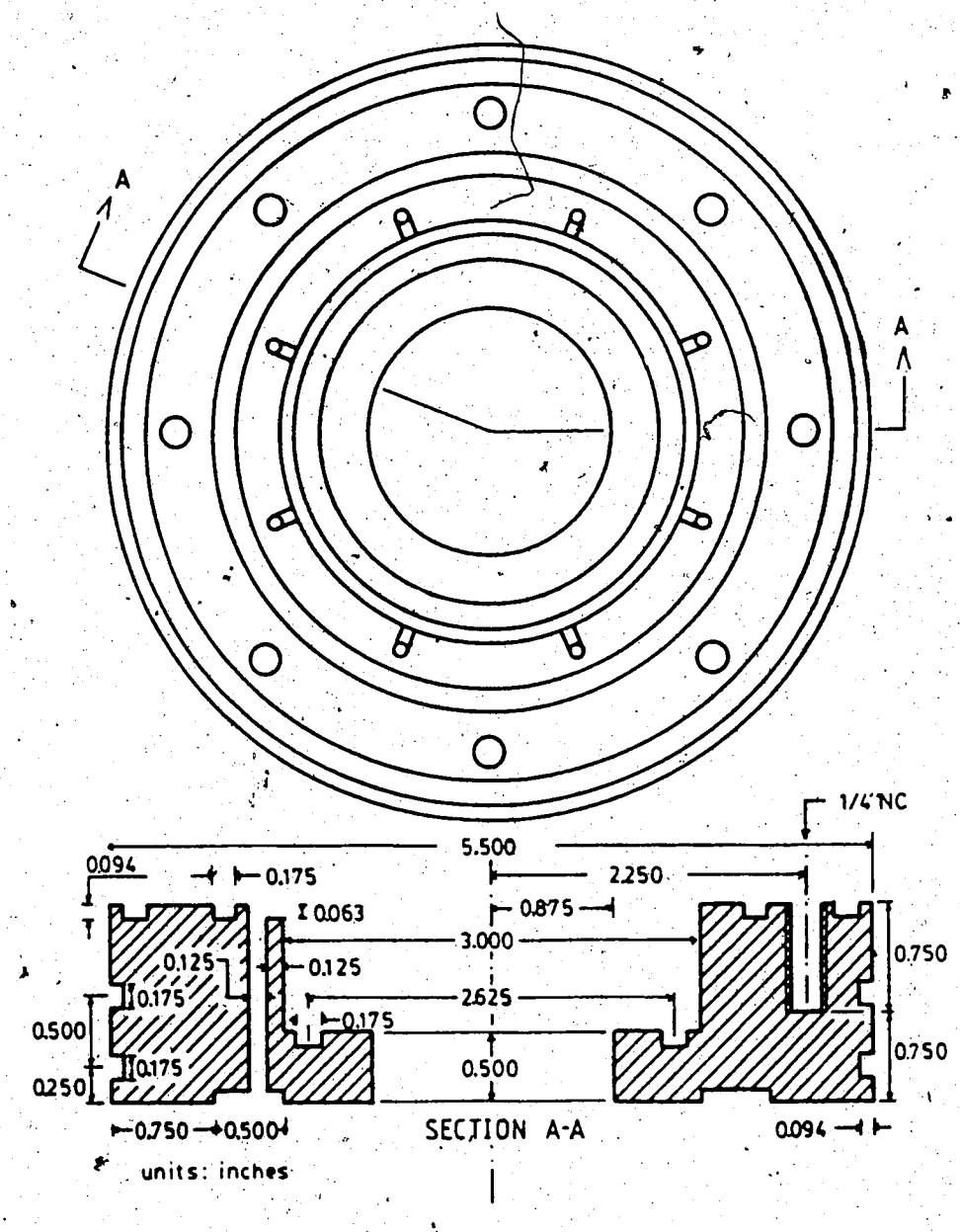

Figure E.22 Hollow Cylinder Cell - Sample Top Platen

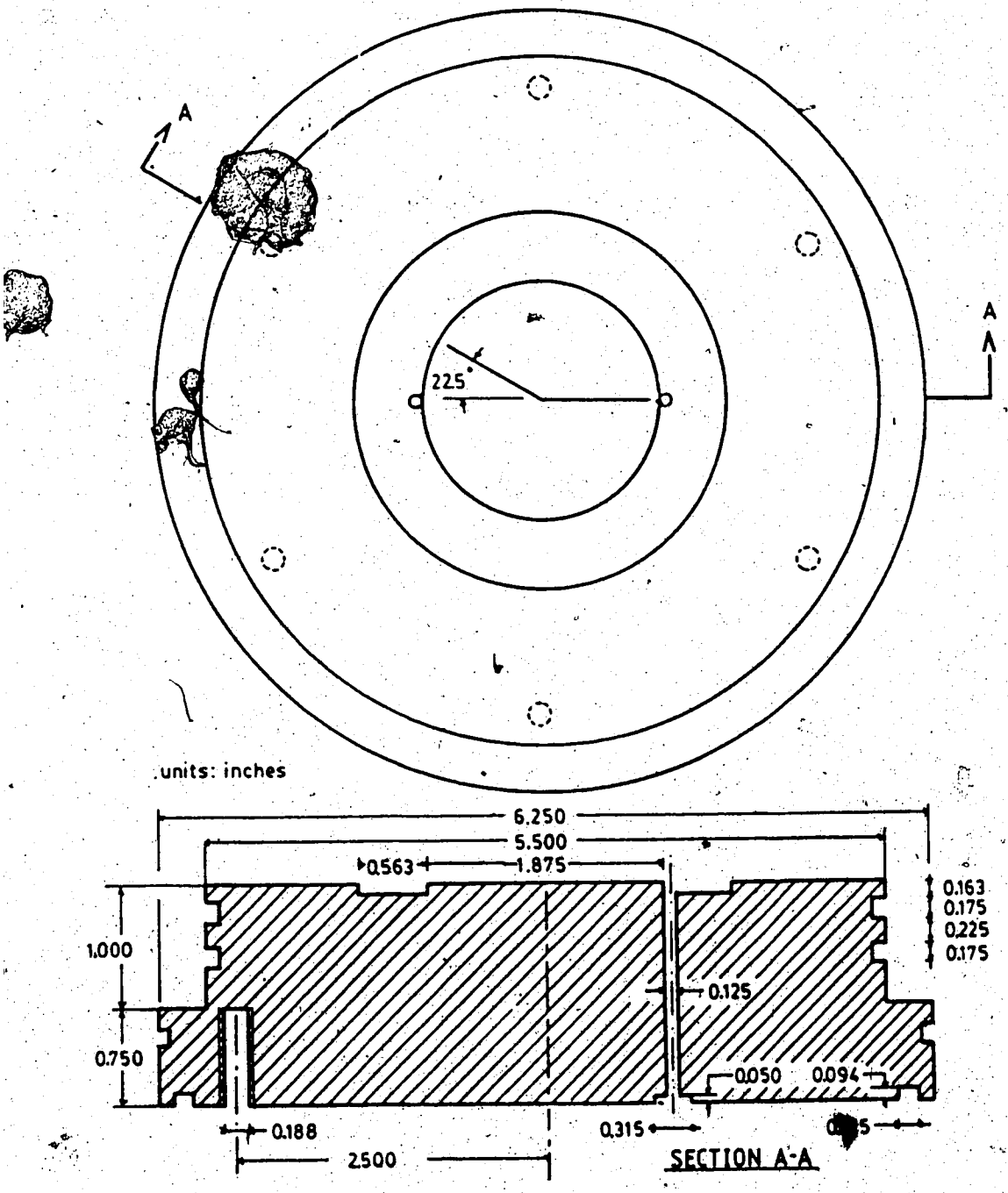

Figure E.23 Hollow Cylinder Cell - Sample Bottom Platen

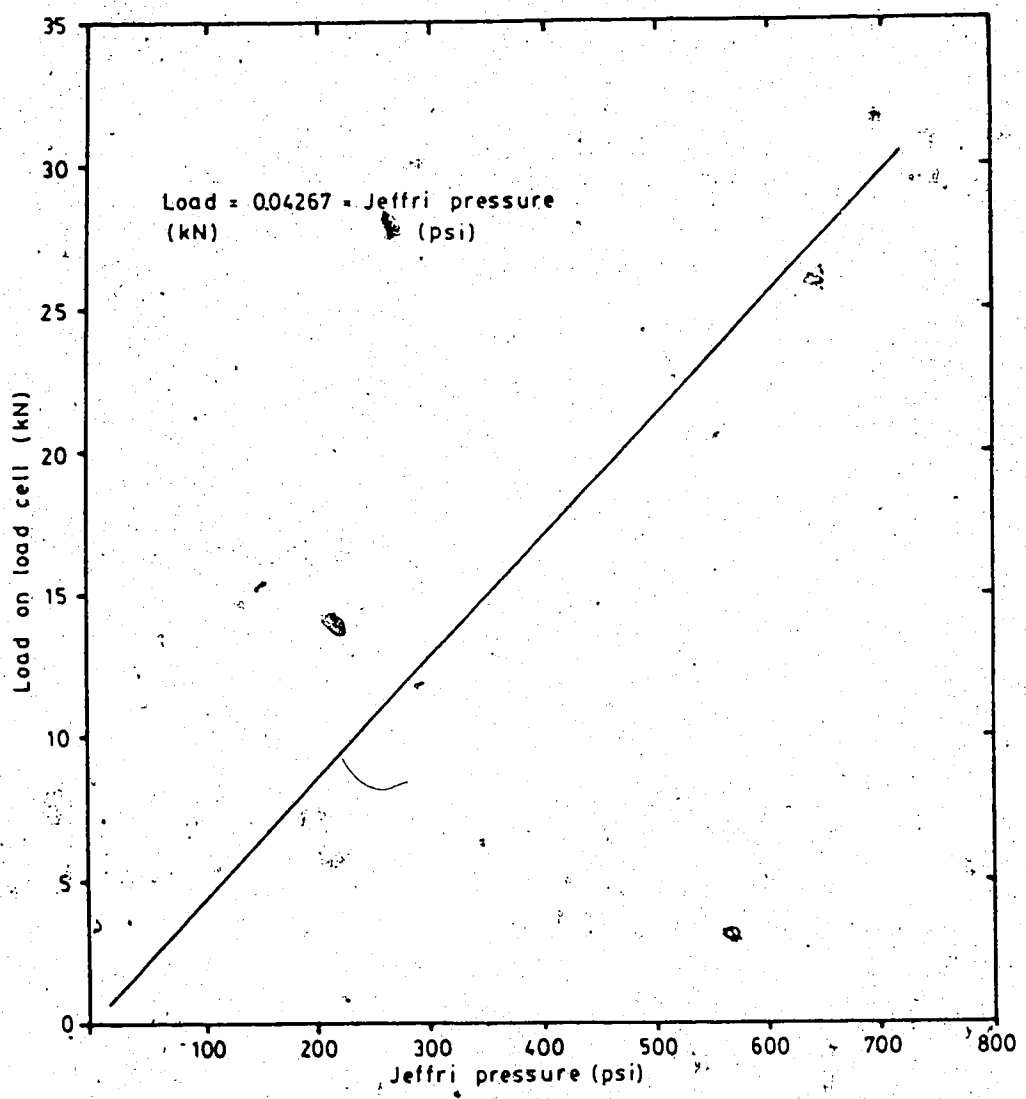

Figure E.24 Load Cell Reading versus Jefri Pump Pressure

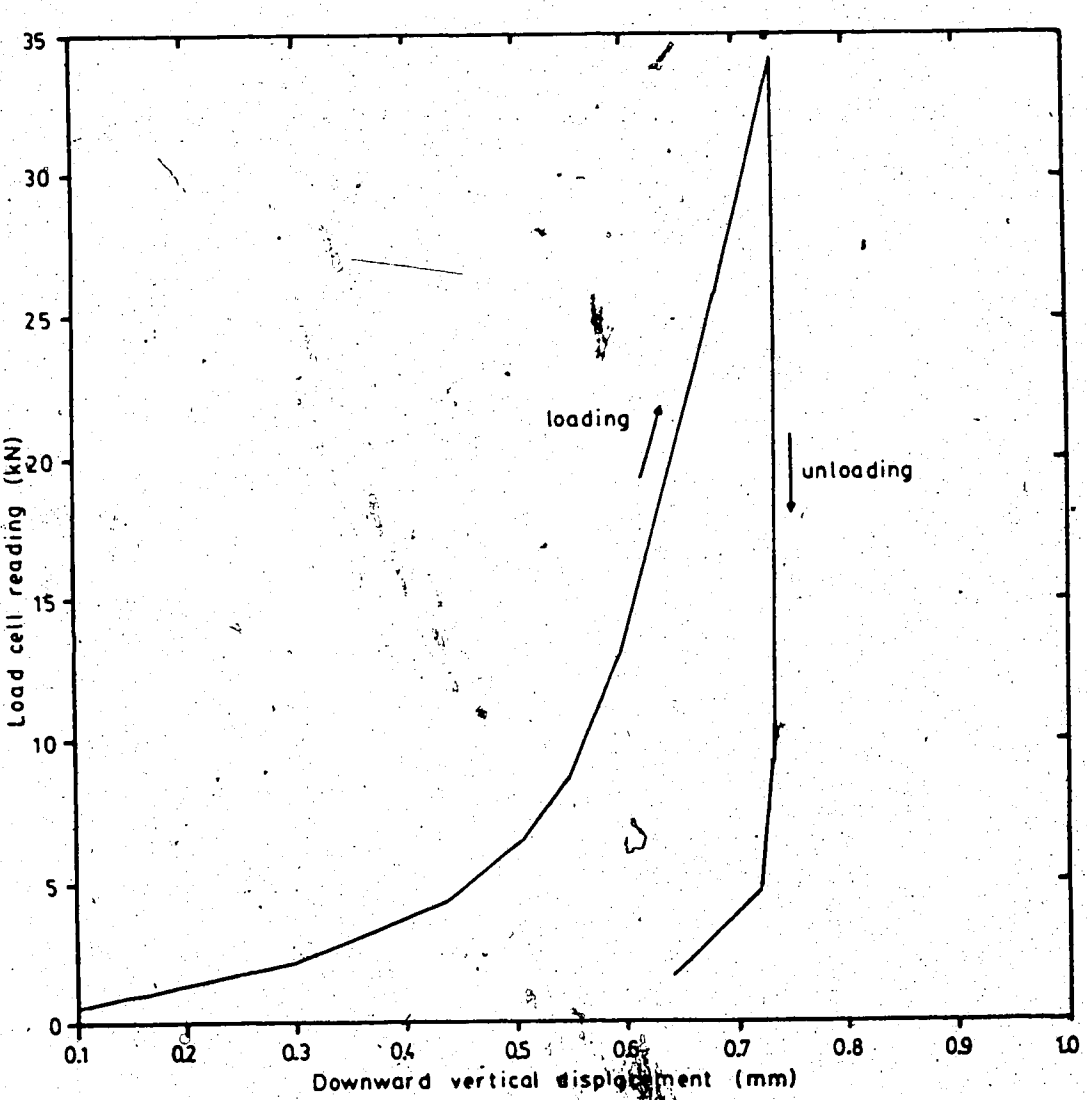

Figure E.25 Hollow Cylinder Cell - Vertical System Compliance

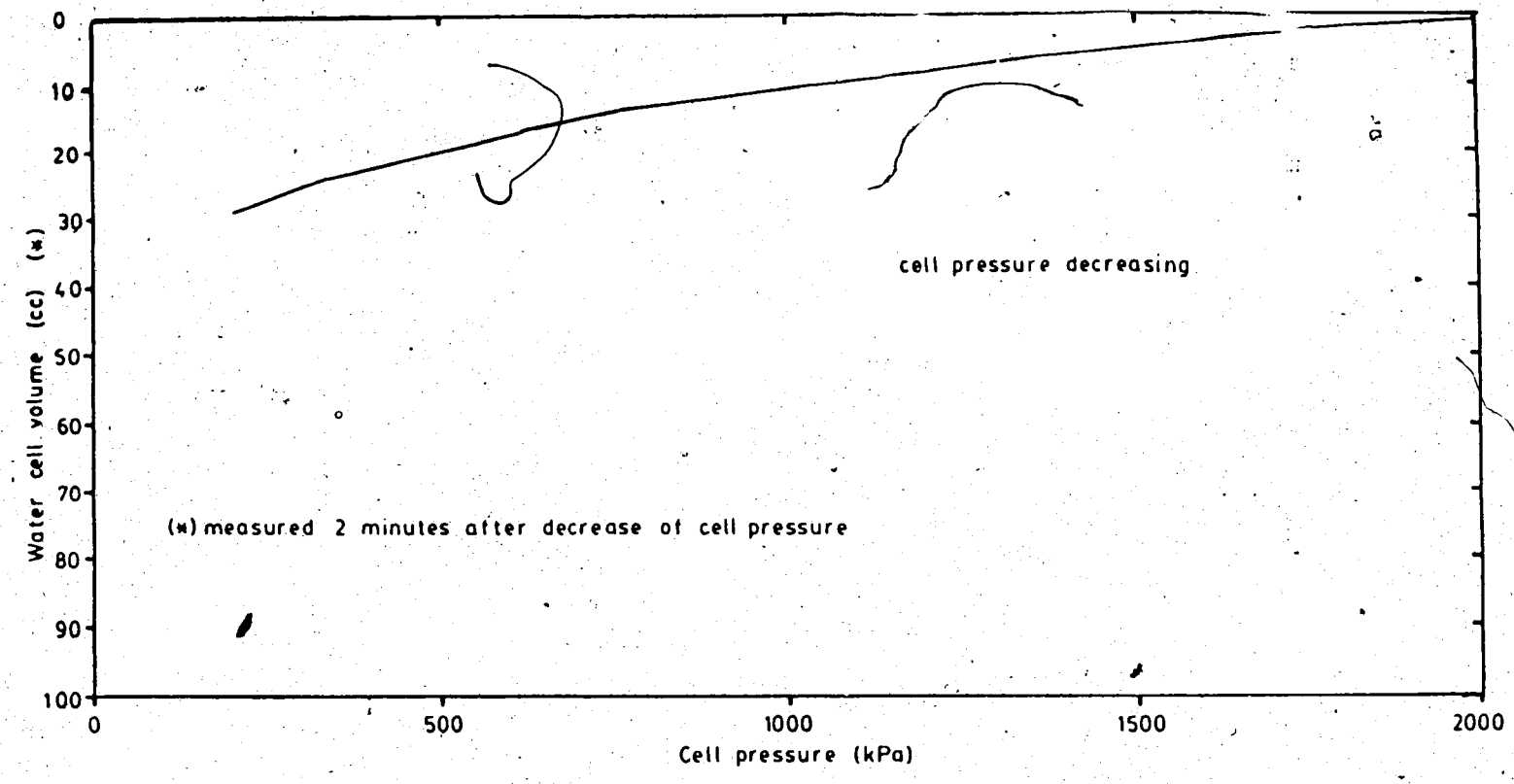

Figure E.26 Hollow Cylinder Cell - Volumetric Compliance of External Cell Cell System

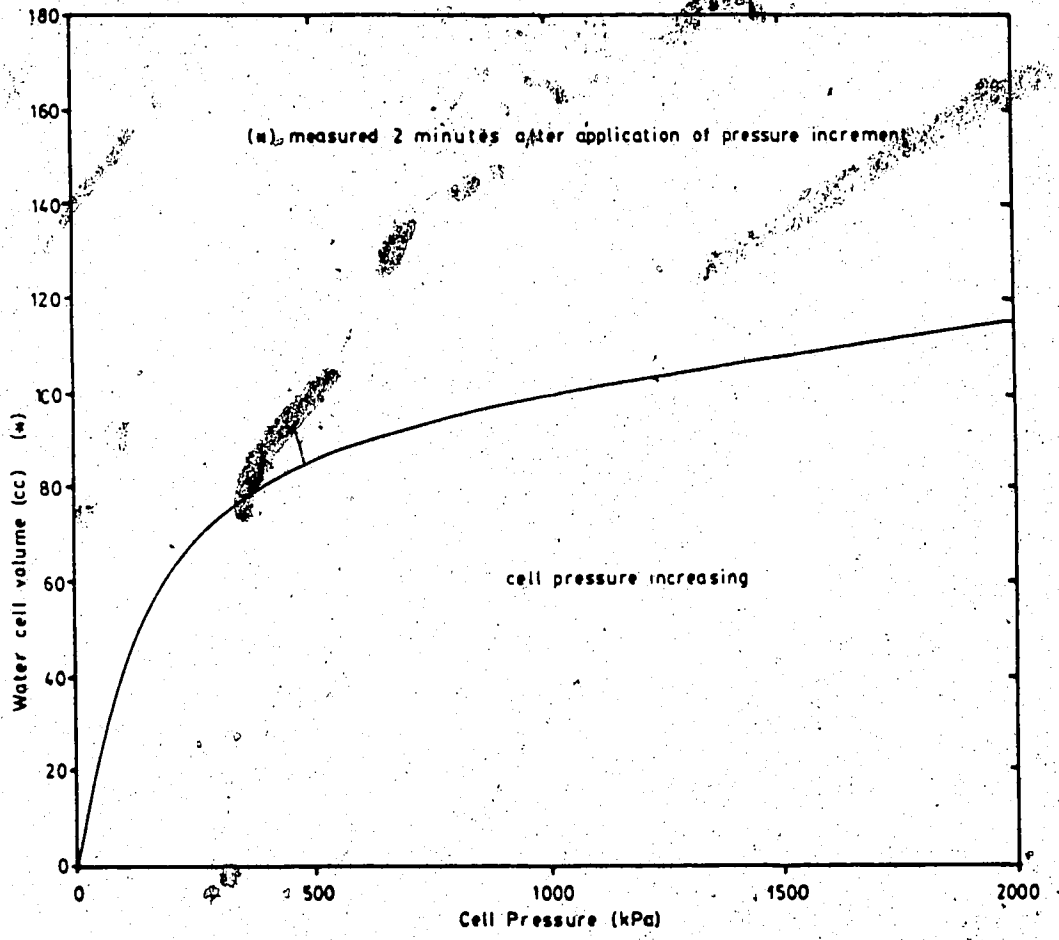

Figure E.27 Hollow Cylinder Cell - Volumetric Compliance of External Cell Cell System

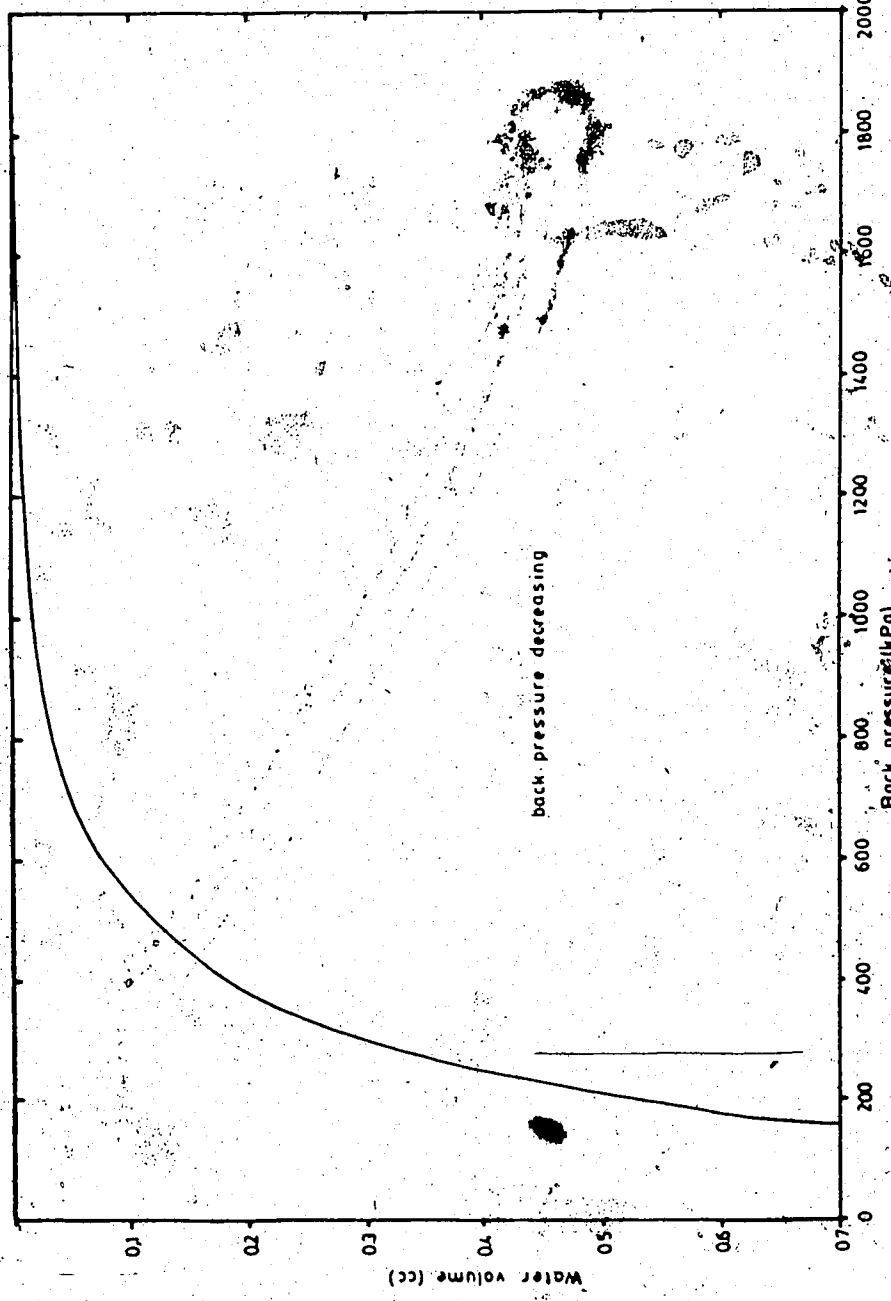

Figure E.28 Hollow Cylinder Cell - Volumetric Compliance of Back Pressure System

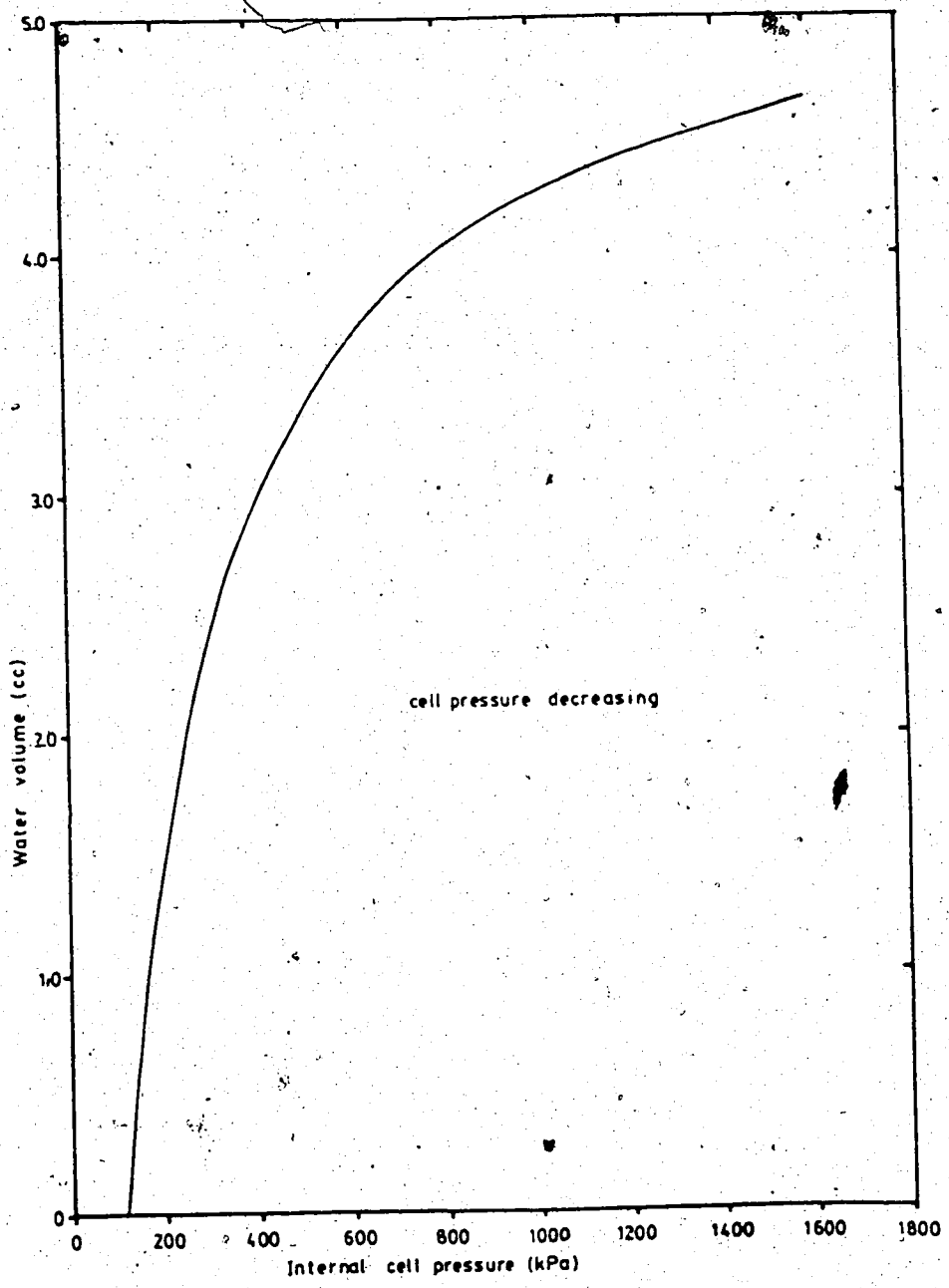

Figure E.29 Hollow Cylinder Cell - Volumetric Compliance of Internal Cell System

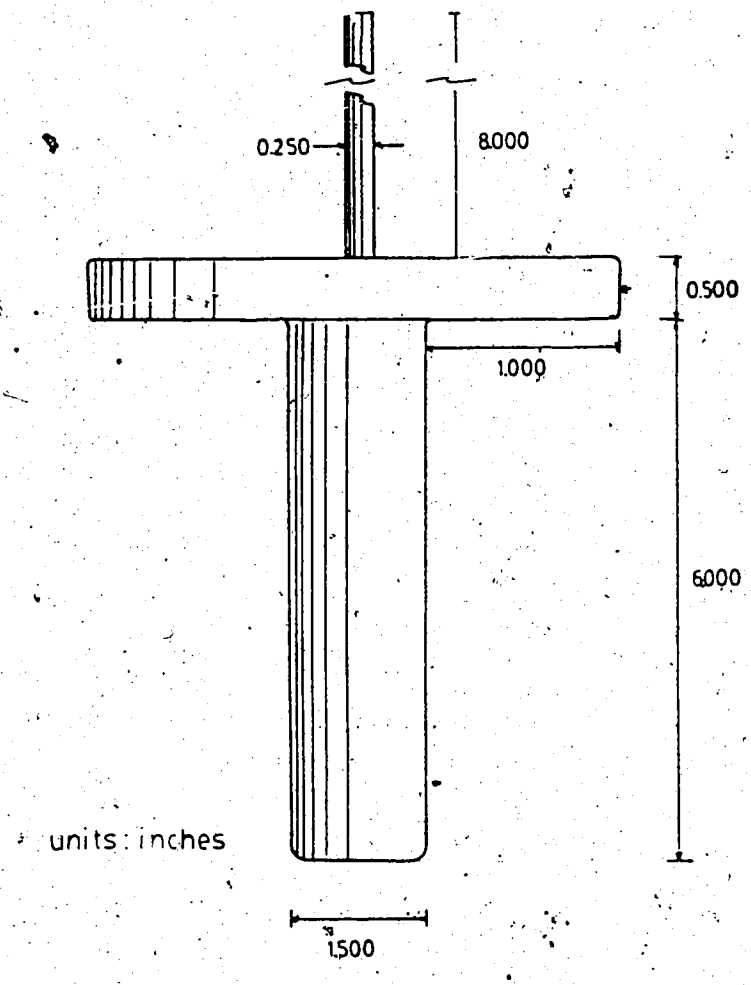

Figure E.30 Hollow Cylinder Cell - Internal Cell Latex Membrane Mold